frontiers | Research Topics

Innovative approaches in precision radiation oncology

Edited by
Abdul K. Parchur and Poonam Yadav

Published in
Frontiers in Oncology
Frontiers in Medicine

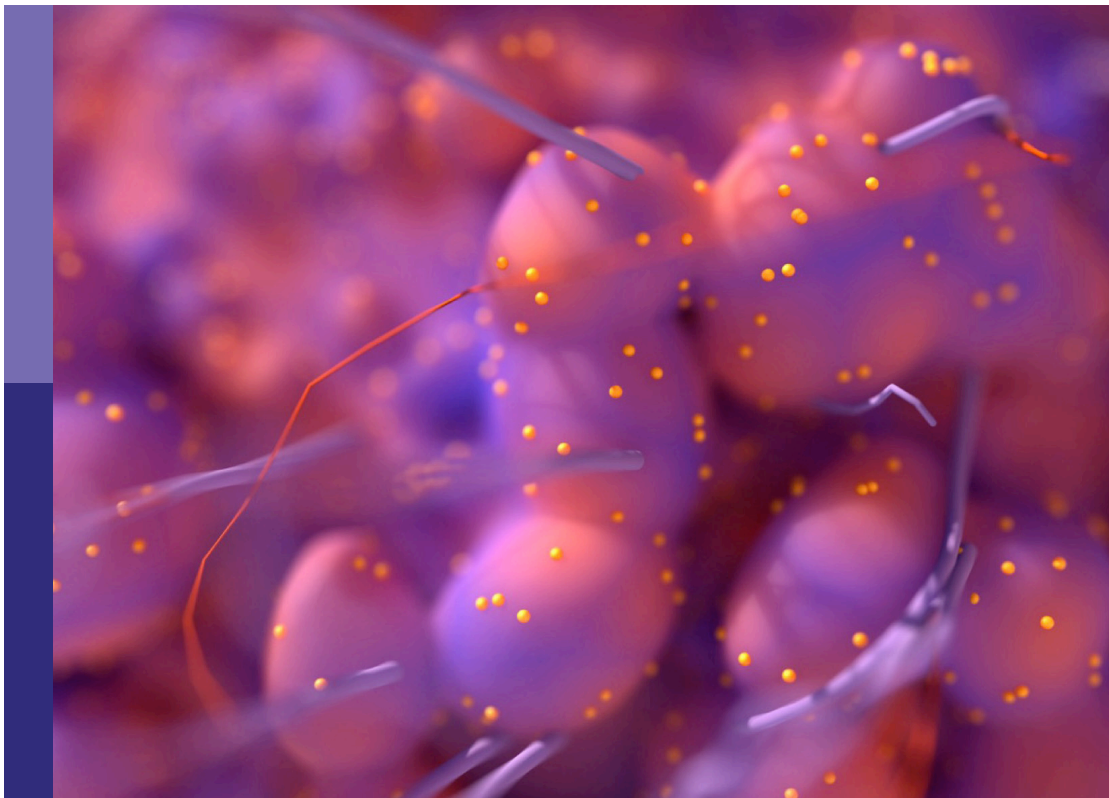

FRONTIERS EBOOK COPYRIGHT STATEMENT

The copyright in the text of individual articles in this ebook is the property of their respective authors or their respective institutions or funders. The copyright in graphics and images within each article may be subject to copyright of other parties. In both cases this is subject to a license granted to Frontiers.

The compilation of articles constituting this ebook is the property of Frontiers.

Each article within this ebook, and the ebook itself, are published under the most recent version of the Creative Commons CC-BY licence. The version current at the date of publication of this ebook is CC-BY 4.0. If the CC-BY licence is updated, the licence granted by Frontiers is automatically updated to the new version.

When exercising any right under the CC-BY licence, Frontiers must be attributed as the original publisher of the article or ebook, as applicable.

Authors have the responsibility of ensuring that any graphics or other materials which are the property of others may be included in the CC-BY licence, but this should be checked before relying on the CC-BY licence to reproduce those materials. Any copyright notices relating to those materials must be complied with.

Copyright and source acknowledgement notices may not be removed and must be displayed in any copy, derivative work or partial copy which includes the elements in question.

All copyright, and all rights therein, are protected by national and international copyright laws. The above represents a summary only. For further information please read Frontiers' Conditions for Website Use and Copyright Statement, and the applicable CC-BY licence.

ISSN 1664-8714
ISBN 978-2-8325-7471-3
DOI 10.3389/978-2-8325-7471-3

Generative AI statement
Any alternative text (Alt text) provided alongside figures in the articles in this ebook has been generated by Frontiers with the support of artificial intelligence and reasonable efforts have been made to ensure accuracy, including review by the authors wherever possible. If you identify any issues, please contact us.

About Frontiers

Frontiers is more than just an open access publisher of scholarly articles: it is a pioneering approach to the world of academia, radically improving the way scholarly research is managed. The grand vision of Frontiers is a world where all people have an equal opportunity to seek, share and generate knowledge. Frontiers provides immediate and permanent online open access to all its publications, but this alone is not enough to realize our grand goals.

Frontiers journal series

The Frontiers journal series is a multi-tier and interdisciplinary set of open-access, online journals, promising a paradigm shift from the current review, selection and dissemination processes in academic publishing. All Frontiers journals are driven by researchers for researchers; therefore, they constitute a service to the scholarly community. At the same time, the *Frontiers journal series* operates on a revolutionary invention, the tiered publishing system, initially addressing specific communities of scholars, and gradually climbing up to broader public understanding, thus serving the interests of the lay society, too.

Dedication to quality

Each Frontiers article is a landmark of the highest quality, thanks to genuinely collaborative interactions between authors and review editors, who include some of the world's best academicians. Research must be certified by peers before entering a stream of knowledge that may eventually reach the public - and shape society; therefore, Frontiers only applies the most rigorous and unbiased reviews. Frontiers revolutionizes research publishing by freely delivering the most outstanding research, evaluated with no bias from both the academic and social point of view. By applying the most advanced information technologies, Frontiers is catapulting scholarly publishing into a new generation.

What are Frontiers Research Topics?

Frontiers Research Topics are very popular trademarks of the *Frontiers journals series*: they are collections of at least ten articles, all centered on a particular subject. With their unique mix of varied contributions from Original Research to Review Articles, Frontiers Research Topics unify the most influential researchers, the latest key findings and historical advances in a hot research area.

Find out more on how to host your own Frontiers Research Topic or contribute to one as an author by contacting the Frontiers editorial office: frontiersin.org/about/contact

Innovative approaches in precision radiation oncology

Topic editors

Abdul K. Parchur — University of Maryland Medical Center, United States

Poonam Yadav — Northwestern University, United States

Citation

Parchur, A. K., Yadav, P., eds. (2026). *Innovative approaches in precision radiation oncology*. Lausanne: Frontiers Media SA. doi: 10.3389/978-2-8325-7471-3

Table of contents

06 Editorial: Innovative approaches in precision radiation oncology
Abdul K. Parchur and Poonam Yadav

10 Baseline cross-sectional imaging of locally advanced high-risk breast cancer facilitates highly customized radiation therapy in surgically inaccessible anatomical areas
Tomasz Borowiec, Rafał Matkowski, Bożena Cybulska-Stopa, Tomasz Kuniej, Andrzej Kołodziejczyk, Dorota Dupla and Adam Maciejczyk

20 Study of predictive factors for response to ^{177}LU-PSMA in patients with metastatic castration-resistant prostate cancer
Hugo Peslier, Valérie Seegers and Pierre-Alban Dufour

34 Proton stereotactic centralized ablative radiation therapy for treating bulky tumor: a treatment plan study
Tengxiang Li, Xinsen Yao, Ruimin He, Xian Xue, Shuai Wang, Jinhu Chen, Qingtao Qiu, Yong Yin and Quan Tang

44 Evaluating the Implementation of fan-beam CT-guided online adaptive re-planning in definitive cervical cancer radiotherapy
Shuai Sun, Xinyue Gong, Yongguang Liang, Yuliang Sun, Dan Que, Yangchun Xie, Shumeng He, Lei He, Hao Liang, Yijun Wang, Xinyi Wu, Cheng Wang, Bo Yang, Jie Qiu, Ke Hu and Fuquan Zhang

56 The value of multi-phase CT based intratumor and peritumoral radiomics models for evaluating capsular characteristics of parotid pleomorphic adenoma
Qian Shen, Cong Xiang, Yongliang Han, Yongmei Li and Kui Huang

67 Analysis of the impact of rotation error on PTV margins in multiple brain metastases fractionated stereotactic radiotherapy based on single-isocenter multi-target technique
Yuhong Li, Rui Hua, Liling Dai, Wei Chen, Junyuan Zhang, Qian Wang, Yufeng Xu and Tingting Wang

80 Optimization method for determining vertices in lattice radiotherapy
Pan Ma, Yingjie Xu, Yuhe Yao, Ningning Lu and Jianrong Dai

91 Effect of physical parameter differences on the performance of a knowledge-based partial arc VMAT RapidPlan model for left breast cancer
Hai-liang Guo, Zeng-hong Lu, Jing-hua Zhong and Huai-wen Zhang

100 The evolution of FLASH radiotherapy: a bibliometric analysis
Shuokai Jia, Weige Wei, Yiwen He, Haichuan Yan, Shiru Zou, Yanmei Hao, Qing Xiao and Guangjun Li

117 Non-cancer effects after proton beam therapy for pediatric tumors- a narrative review
Anna Zając-Grabiec, Beata Biesaga, Monika Krzyżowska, Katarzyna Drosik-Rutowicz and Justyna Miszczyk

134 Application of the Monaco-serial biological function for cardiac dose constraints in DIBH-IMRT treatment planning for left-sided breast cancer
Haili Hu, Zhou Jueyi, Jiang Hao and Jianjun Lai

143 Dual regulation of the cGAS-STING pathway: new targets and challenges for subtype-specific immunotherapy in breast cancer
Hanchu Xiong, Rongxue Li, Lixian Yang, Yucheng Li and Xiao Ma

154 Dosimetric analysis of orthogonal collimator configuration in volumetric modulated arc therapy planning: a comparative study
Xin Huang, Chenlei Guo, Shuangtong Liu, Kuo Men and Hui Wang

166 Analysis of imaging signatures in ^{18}F-DOPA PET of glioblastoma treated with dose-escalated radiotherapy
Jing Qian, Deanna H. Pafundi, William G. Breen, Paul D. Brown, Christopher H. Hunt, Mark S. Jacobson, Derek R. Johnson, Timothy J. Kaufmann, Bradley J. Kemp, Sani H. Kizilbash, Val J. Lowe, Michael W. Ruff, Jann N. Sarkaria, Joon H. Uhm, Mark J. Zakhary, Maasa H. Seaberg, Hok Seum Wan Chan Tseung, Elizabeth S. Yan, Yan Zhang, Nadia N. Laack and Debra H. Brinkmann

178 Anesthesia is a potent determinant of ultra-high dose rate sparing in the murine total abdominal irradiation model
Armin D. Tavakkoli, William W. Daley, David I Hunter, Beverly A. Allen, Gretchen C. Carpenter, David J. Gladstone, Brian W. Pogue and P. Jack Hoopes

185 Dosimetric assessment of TomoDirect radiotherapy and TomoHelical radiotherapy in the clinical implementation of total skin irradiation
Haiyang Wang, Yifei Pi, Chunbo Liu, Panfeng Wang, Chengzhang Long, Yaping Qi, Fanyang Kong, Bin Han, Fangna Wang, Fei Jia, Lele Liu, Dandan Xu, Tengfei Ji, Huijuan Wu and Yuexin Guo

194 An innovative hippocampal-sparing whole-brain radiotherapy planning approach via the Halcyon system: achieving lower hippocampal doses
Ran Tang, Maoying Lan, Xingru Sun, Yue Luo, Anyan Gu, Qing Liu, Yingjing Li, Guozi Yang, Zhenyu Pan and Guanhua Deng

205 Case Report: Multimodal management of a rare pediatric astroblastoma using proton beam therapy and Gamma Knife radiosurgery—a case report and literature review
Xijia Zhang, Xinfa Wang, Weihai Ning, Jianfeng Liang, Yonglong Jin, Yuqian Nie, Jie Wang, Zishen Wang, Wei Wang, Jun Zhao, Jingjing Kong, Lu Yang, Dongxue Zhou, Yue Zou, Masashi Mizumoto and Shosei Shimizu

214 Mouse pancreatic tumor organoids reveal synergistic efficacy of low-dose anticancer drug and radiation combinations
Zachery Keepers, Aniketh Sharma, Sanjit Roy, Hurley Ryan, Binny Bhandary, Lei Ren, Narottam Lamichhane and Hem D. Shukla

224 Innovative patient-specific delivered-dose prediction for volumetric modulated arc therapy using lightweight Swin-Transformer
Yongqiang Zhou, Changfei Gong, Junming Jian and Yun Zhang

236 Dosimetric evaluations using cycle-consistent generative adversarial network synthetic CT for MR-guided adaptive radiation therapy
Gabriel L. Asher, Shiru Wang, Bassem I. Zaki, Gregory A. Russo, Gobind S. Gill, Charles R. Thomas, Temiloluwa O. Prioleau, Yuting Li, Rongxiao Zhang, Yue Yan and Brady Hunt

248 Strategy to select nasopharyngeal cancer patients for adaptive radiotherapy
Heleen Bollen, Elena Onorati, Annouschka Laenen, Anneleen Goedgebeur and Sandra Nuyts

258 Comparative impact of supine vs prone positioning on dose distribution, acute toxicity, and setup error in postoperative radiotherapy for cervical cancer: a multidimensional propensity-matched cohort study
Nanjie Xiao, Cuiyun Yuan, Tianshu Zhao, Tie Xu, Jiaomei Zhou, Junfang Liao, Miao Peng, Chenbin Liu, Zhijian Chen and Jing Jin

272 Innovative approaches in precision radiation oncology: advanced imaging technologies and challenges which shape the future of radiation therapy
Yue Yan, Daniel A. Alexander, Bryan P. Bednarz, Lawrence F. Bronk, Huixiao Chen, David J. Gladstone, Bin Han, Christopher M. Iannuzzi, Yuting Li, Ngoc Nguyen, Natasha Mulenga, Natalie N. Viscariello, Yuenan Wang, Joseph Weygand, Yana Zlateva and Fada Guan

305 Proton-boron capture interaction enhances killing of radiation resistant cancer cells
Dalong Pang, Mira Jung, Alfredo Velena, William Parke and Anatoly Dritschilo

frontiers | Frontiers in Medicine

TYPE Editorial
PUBLISHED 22 January 2026
DOI 10.3389/fmed.2026.1776567

Check for updates

OPEN ACCESS

EDITED AND REVIEWED BY
Giorgio Treglia,
Ente Ospedaliero Cantonale (EOC), Switzerland

*CORRESPONDENCE
Abdul K. Parchur
✉ aparchur@outlook.com;
✉ Abdul.Parchur@umm.edu
Poonam Yadav
✉ Poonam.Yadav@nm.org

RECEIVED 28 December 2025
ACCEPTED 05 January 2026
PUBLISHED 22 January 2026

CITATION
Parchur AK and Yadav P (2026) Editorial: Innovative approaches in precision radiation oncology. *Front. Med.* 13:1776567. doi: 10.3389/fmed.2026.1776567

COPYRIGHT
© 2026 Parchur and Yadav. This is an open-access article distributed under the terms of the Creative Commons Attribution License (CC BY). The use, distribution or reproduction in other forums is permitted, provided the original author(s) and the copyright owner(s) are credited and that the original publication in this journal is cited, in accordance with accepted academic practice. No use, distribution or reproduction is permitted which does not comply with these terms.

Editorial: Innovative approaches in precision radiation oncology

Abdul K. Parchur[1]* and Poonam Yadav[2]*

[1]Department of Radiation Oncology, University of Maryland School of Medicine, Baltimore, MD, United States, [2]Department of Radiation Oncology, Feinberg School of Medicine, Northwestern University, Chicago, IL, United States

KEYWORDS

adaptive radiotherapy, dosimetry and quality assurance, flash, imaging and verification, immuno-radiotherapy, precision radiation oncology, radiobiological modulation, treatment planning and delivery

Editorial on the Research Topic
Innovative approaches in precision radiation oncology

Radiation therapy remains a cornerstone of cancer care, with an estimated ∼50% of patients receiving radiotherapy at some point during their illness. Over the past decade, progress in image guidance, treatment delivery, computational modeling, and radiobiology has accelerated the shift toward precision radiation oncology, where treatment is increasingly adaptive, personalized, and data-driven. This Research Topic, *Innovative approaches in precision radiation oncology*, was developed to highlight multidisciplinary innovations that improve precision across the radiotherapy pipeline, from imaging and planning to delivery, biology, and clinical implementation. Following rigorous peer review, ∼50% of submitted manuscripts were accepted, resulting in a curated Research Topic of 25 articles authored by 212 contributors.

Treatment planning, delivery, and optimization

A substantial portion of the Research Topic focused on innovations in treatment planning, delivery techniques, and optimization strategies aimed at improving dose conformity, organ-at-risk (OAR) sparing, and clinical feasibility across diverse disease sites. Several studies addressed emerging paradigms for spatial dose modulation and high-precision delivery in challenging clinical scenarios.

Advancing spatially fractionated radiotherapy, Ma et al. introduced an optimization framework for determining vertex placement in lattice radiotherapy using closest packing combined with adaptive simulated annealing. Their method significantly increased the peak-to-valley dose contrast, with the optimized plans demonstrating a nearly six-fold improvement in peak-to-valley index compared with conventional packing approaches, highlighting a reproducible and automated strategy to enhance treatment precision for bulky tumors. Complementing this work on spatial dose modulation, Li et al. evaluated proton-based stereotactic centralized/core ablative radiation therapy (pSCART) in a treatment planning study of bulky tumors. By leveraging the physical dose advantages of protons, pSCART enabled higher prescription doses (24 Gy × 3 fractions) and improved high-dose central coverage while reducing dose spill at the tumor periphery and lowering mean doses to surrounding OARs compared with photon-based SCART techniques, supporting its potential for future clinical translation.

Also, contributions focused on optimization of volumetric modulated arc therapy (VMAT) planning parameters to improve OAR protection without compromising target coverage. Guo et al. demonstrated that careful adjustment of physical parameters in a knowledge-based partial-arc VMAT RapidPlan model for left-sided breast cancer significantly reduced doses to the heart, lungs, and contralateral breast, emphasizing the importance of aligning model configuration with delivery geometry to mitigate low-dose exposure and secondary cancer risk. In a related dosimetric study, Huang et al. showed that incorporating orthogonal collimator angles (0°/90°) in dual-arc VMAT improved conformity, dose gradient, and OAR sparing across head-and-neck, thoracic, and pelvic sites, with all plans maintaining high delivery accuracy, demonstrating a simple yet effective planning refinement applicable in routine practice. Optimization of biological and clinical dose constraints was further explored by Hu et al., who investigated the use of the Monaco serial biological function for cardiac dose optimization in deep-inspiration breath-hold IMRT for left-sided breast cancer. Their analysis identified an optimal K-value range (2–4) that achieved balanced reduction in mean and maximum cardiac and coronary artery doses while preserving target coverage, providing evidence-based guidance for biologically informed planning parameter selection. Innovations in system-specific planning were also highlighted. Tang et al. developed a hippocampal-sparing whole-brain radiotherapy planning approach using the Halcyon platform with coplanar dual-arc VMAT and target substructure segmentation. Compared with conventional systems, this strategy achieved improved dose homogeneity, reduced hippocampal dose and normal tissue complication probability, and high gamma passing rates, demonstrating that advanced planning techniques can enhance neurocognitive preservation without increasing workflow complexity. Furthermore, clinical feasibility of advanced planning and delivery workflows was reinforced by Sun et al., who evaluated fan-beam CT–guided online adaptive re-planning in definitive cervical cancer radiotherapy. Across 278 adaptive fractions, their approach consistently improved target coverage and OAR sparing with a mean gamma passing rate exceeding 99% and a clinically acceptable workflow duration of approximately 23 min, underscoring how optimized planning and delivery strategies can be successfully integrated into routine clinical practice. In the context of rare pediatric tumors, Zhang et al. reported a multimodal precision treatment strategy for MN1-altered astroblastoma, demonstrating how the tissue-sparing advantages of proton beam therapy can facilitate effective salvage Gamma Knife radiosurgery while maintaining durable local control and minimal toxicity.

Imaging, dosimetry, and verification

Advanced imaging, quantitative dosimetry, and rigorous verification are foundational to precision radiation oncology, enabling accurate target definition, reliable dose delivery, and safe clinical implementation of increasingly complex treatment techniques. Six contributions in this Research Topic addressed these themes across clinical, technical, and preclinical domains, highlighting how imaging and verification strategies directly influence treatment accuracy, toxicity, and translational reliability.

Several studies focused on dosimetric characterization and verification of complex delivery techniques. Wang et al. performed a comprehensive dosimetric and efficiency comparison between TomoDirect and TomoHelical radiotherapy for total skin irradiation. Their analysis demonstrated that TomoDirect plans using more than nine beams achieved target coverage, homogeneity, and organ-at-risk sparing comparable to TomoHelical delivery, while maintaining similar treatment times when appropriate auxiliary structure blocking was applied. These findings provide practical guidance for modality selection and protocol design in total skin irradiation, where large treatment volumes and delivery efficiency are critical. Quantitative assessment of dose delivery accuracy and verification was further advanced by Zhou et al., who developed a lightweight Swin-Transformer–based deep learning framework for patient-specific VMAT delivered-dose prediction. Their model achieved high structural similarity and gamma passing rates relative to ground truth dose distributions, while substantially reducing model complexity compared with existing transformer architectures. This work highlights the growing role of artificial intelligence in patient-specific quality assurance, offering a scalable and clinically viable alternative to labor-intensive measurement-based verification workflows. The role of imaging in refining dosimetric evaluation and treatment response assessment was addressed in multiple contributions. Qian et al. analyzed quantitative imaging features derived from ^{18}F-DOPA PET in glioblastoma patients treated with dose-escalated radiotherapy. Their results demonstrated that pre-treatment imaging signatures and early post-treatment changes could stratify survival outcomes in MGMT-unmethylated tumors and identify patients most likely to benefit from dose escalation. This study underscores the potential of functional imaging biomarkers to inform both dosimetric decision-making and adaptive treatment strategies. Similarly, Borowiec et al. evaluated the clinical value of extended baseline cross-sectional imaging in locally advanced high-risk breast cancer. By incorporating CT or PET-CT into initial staging, the authors showed that disease stage and radiation treatment planning were altered in a substantial proportion of patients, enabling highly customized dose delivery to surgically inaccessible nodal regions. Their findings emphasize that imaging choice at baseline can directly impact dosimetric strategy and treatment individualization. Geometric sensitivity and setup-related dose variation were examined by Xiao et al., who conducted a propensity-matched cohort study comparing supine and prone positioning in postoperative cervical cancer radiotherapy. While target coverage remained comparable, positioning significantly influenced organ dose distributions, setup error profiles, and acute toxicity patterns. This work highlights how verification of geometric and positional factors is integral to optimizing both dosimetry and clinical safety in pelvic radiotherapy. Finally, Tavakkoli et al. addressed verification and biological confounding factors in the preclinical evaluation of ultra-high dose-rate (FLASH) radiotherapy. Using a murine total abdominal irradiation model, they demonstrated that anesthetic-dependent tissue oxygenation critically determined the presence or absence of FLASH sparing. Their findings underscore the importance of rigorous control and reporting of physiological variables when

verifying dose-response relationships, particularly for emerging technologies poised for clinical translation.

Collectively, these studies demonstrate that precision radiation oncology relies not only on sophisticated planning and delivery techniques but also on robust imaging, dosimetric evaluation, and verification frameworks. By integrating quantitative imaging, advanced computational verification, and careful assessment of geometric and biological uncertainties, these contributions provide essential foundations for safe, accurate, and personalized radiotherapy.

Adaptive and online radiotherapy and clinical implementation

The transition from advanced treatment concepts to routine clinical practice represents a critical step in precision radiation oncology. Three contributions within this Research Topic focused on adaptive and online radiotherapy workflows, emphasizing real-time plan adaptation, clinical feasibility, and practical considerations for implementation in busy treatment environments.

Anchoring this theme, the technical feasibility of optimized planning and delivery was supported by Sun et al., who demonstrated high-accuracy fan-beam CT-guided online adaptive replanning in definitive cervical cancer radiotherapy, achieving consistent target coverage and organ-at-risk sparing across 278 fractions within a clinically acceptable workflow time**.** Building on this foundation, Asher et al. examined broader aspects of clinical implementation, focusing on workflow translation and operational considerations associated with adaptive radiotherapy adoption. Their study addressed practical challenges such as staffing, training, and integration of adaptive processes within existing clinical infrastructures, highlighting that successful implementation depends not only on technical capability but also on multidisciplinary coordination and institutional readiness. Complementing these perspectives, Pang et al. explored clinical adaptation strategies aimed at tailoring treatment delivery to patient-specific and time-varying anatomical changes. Their work emphasized decision-making frameworks for when and how to adapt treatment plans, underscoring the importance of balancing dosimetric benefit with workflow efficiency and clinical resource utilization.

Collectively, these studies demonstrate that adaptive radiotherapy has progressed beyond proof-of-concept, with emerging evidence supporting its safe and effective deployment in clinical practice (Yan et al.). By addressing real-time adaptation, workflow feasibility, and implementation strategy, these contributions provide a roadmap for translating adaptive radiotherapy technologies into routine patient care and advancing the clinical impact of precision radiation oncology.

Biological determinants of radiation response and therapeutic modulation

A defining challenge in precision radiation oncology is understanding how identical physical dose prescriptions can produce markedly different biological and clinical outcomes across patients. Several contributions in this Research Topic addressed this challenge by examining immune signaling pathways, tumor-microenvironment interactions, and biological predictors of treatment response, highlighting the importance of integrating molecular biology into radiation treatment paradigms.

Xiong et al. provided a comprehensive mini-review of the cGAS-STING signaling pathway as a central mediator linking radiation-induced DNA damage to innate and adaptive immune activation in breast cancer. The authors emphasized the dual and subtype-dependent roles of cGAS-STING signaling, demonstrating that acute pathway activation can enhance antitumor immunity and radiosensitization, whereas chronic or dysregulated activation may promote immunosuppression, regulatory T-cell expansion, and therapeutic resistance. By integrating molecular mechanisms with emerging translational and clinical considerations across luminal, HER2-positive, and triple-negative breast cancer subtypes, this work underscores the need for subtype-specific immune modulation strategies when designing radiation-immunotherapy combinations.

Complementing immune-centric mechanisms, Keepers et al. investigated biological response modulation using mouse pancreatic tumor organoids as a translational preclinical platform. Their study demonstrated that combining low-dose chemotherapy with fractionated radiation produced significantly greater tumor growth inhibition than either modality alone. This enhanced effect was associated with increased DNA damage signaling, elevated reactive oxygen species production, and suppression of mesenchymal markers, supporting the concept that biologically informed combination strategies can amplify radiation efficacy while potentially reducing treatment-related toxicity. The use of tumor-derived organoids further highlights the value of advanced biological models for evaluating radiation–drug interactions and guiding translational research.

Biological heterogeneity and target expression were further examined by Peslier et al. in a clinical study of patients with metastatic castration-resistant prostate cancer treated with ^{177}Lu-PSMA radioligand therapy. The authors identified clinical, biochemical, and PSMA PET-derived imaging factors associated with early treatment discontinuation and poor response, including markers of disease burden and reduced target expression. These findings emphasize that biological determinants of response play a critical role in radiopharmaceutical-based radiation treatments and reinforce the importance of biomarker-driven patient selection.

Finally, Zajac-Grabiec et al. reviewed non-cancer late effects following proton beam therapy in pediatric patients, focusing on neurocognitive, endocrine, cardiovascular, and brainstem toxicities. While proton therapy offers superior normal-tissue sparing compared with photon-based approaches, the review highlights that biological sensitivity of developing tissues remains a key determinant of long-term outcomes. This contribution underscores that precision radiation oncology must balance tumor control with age-dependent biological vulnerability when optimizing treatment strategies in pediatric populations.

These studies illustrate that precision radiation oncology extends well beyond technical optimization of dose delivery. Immune signaling pathways, tumor microenvironment biology, radiopharmaceutical target expression, and normal-tissue susceptibility all shape therapeutic response and toxicity. Integrating biological stratification, mechanistic insight, and biomarker-guided decision-making into radiation oncology practice will be essential for overcoming resistance, improving combination strategies, and advancing truly personalized radiation treatment.

Together, the contributions in this Research Topic demonstrate that precision radiation oncology extends beyond technical optimization of dose delivery to encompass imaging, adaptive workflows, biological modulation, and clinical implementation. By integrating advanced planning and verification, real-time adaptation, molecular and immune insights, and biomarker-guided decision-making, these studies collectively advance more effective, resilient, and truly personalized radiation treatment strategies.

Author contributions

AP: Writing – original draft, Writing – review & editing. PY: Writing – original draft, Writing – review & editing.

Conflict of interest

The author(s) declared that this work was conducted in the absence of any commercial or financial relationships that could be construed as a potential conflict of interest.

Generative AI statement

The author(s) declared that generative AI was not used in the creation of this manuscript.

Any alternative text (alt text) provided alongside figures in this article has been generated by Frontiers with the support of artificial intelligence and reasonable efforts have been made to ensure accuracy, including review by the authors wherever possible. If you identify any issues, please contact us.

Publisher's note

All claims expressed in this article are solely those of the authors and do not necessarily represent those of their affiliated organizations, or those of the publisher, the editors and the reviewers. Any product that may be evaluated in this article, or claim that may be made by its manufacturer, is not guaranteed or endorsed by the publisher.

frontiers | Frontiers in Oncology

TYPE Original Research
PUBLISHED 27 February 2025
DOI 10.3389/fonc.2025.1556122

Check for updates

OPEN ACCESS

EDITED BY
Abdul K Parchur,
Medical College of Wisconsin, United States

REVIEWED BY
Emran Saleh,
University of Aden, Yemen
Binod Manandhar,
Virginia Commonwealth University Health System, United States

*CORRESPONDENCE
Tomasz Borowiec
tomasz.borowiec@dcopih.pl

RECEIVED 06 January 2025
ACCEPTED 05 February 2025
PUBLISHED 27 February 2025

CITATION
Borowiec T, Matkowski R, Cybulska-Stopa B, Kuniej T, Kołodziejczyk A, Dupla D and Maciejczyk A (2025) Baseline cross-sectional imaging of locally advanced high-risk breast cancer facilitates highly customized radiation therapy in surgically inaccessible anatomical areas.
Front. Oncol. 15:1556122.
doi: 10.3389/fonc.2025.1556122

COPYRIGHT
© 2025 Borowiec, Matkowski, Cybulska-Stopa, Kuniej, Kołodziejczyk, Dupla and Maciejczyk. This is an open-access article distributed under the terms of the Creative Commons Attribution License (CC BY). The use, distribution or reproduction in other forums is permitted, provided the original author(s) and the copyright owner(s) are credited and that the original publication in this journal is cited, in accordance with accepted academic practice. No use, distribution or reproduction is permitted which does not comply with these terms.

Baseline cross-sectional imaging of locally advanced high-risk breast cancer facilitates highly customized radiation therapy in surgically inaccessible anatomical areas

Tomasz Borowiec[1]*, Rafał Matkowski[1,2], Bożena Cybulska-Stopa[1,3], Tomasz Kuniej[1], Andrzej Kołodziejczyk[1], Dorota Dupla[1] and Adam Maciejczyk[1,2]

[1]Lower Silesian Oncology, Pulmonology and Hematology Center, Wroclaw, Poland, [2]Department of Oncology, Wroclaw Medical University, Wroclaw, Poland, [3]Department of Hematology and Oncology, Faculty of Medicine, Wroclaw University of Science and Technology, Wrocław, Poland

Background: Routine medical imaging used for preliminary breast cancer workup, such as mammography (MMG) and ultrasound (US), has limited utility for radiation oncologists. We hypothesized that the inclusion of cross-sectional imaging (CT scan or PET-CT) prior to primary systemic therapy (PST) would improve clinical staging accuracy and facilitate customized postoperative radiation therapy planning. Therefore, this study aimed to compare the standard baseline imaging with extended radiological staging.

Methods: To assess our hypothesis, we performed a prospective, single-center study that included 132 participants who were recruited from October 2015 to March 2020. We quantified the value of cross-sectional imaging compared to those of MMG and US. Descriptive statistics, the Friedman and chi-square tests were performed, and $p < 0.05$ was considered significant.

Results: Patients were grouped into two cohorts: the CT scan cohort (n = 87) and the PET-CT cohort (n = 43). A comparison of the value of cross-sectional imaging with those of MMG and US revealed that staging and radiation planning were altered by this additional procedure. The originally determined disease stage changed in 36.8% and 51.2% of cases in the first and second groups, respectively. The consistency between the assessment of involved axillary lymph nodes using imaging (cN) and the postoperative pathology report (pN) were evaluated. In most cases, clinical and pathological evaluation were consistent, with $\chi2(1) = 18.98$; $p < 0.001$ for CT scan, and $\chi2(1) = 6.41$; $p = 0.03$ for PET-CT.

Conclusions: Cross-sectional imaging is recommended for patients with locally advanced high-risk breast cancer. A highly customized radiation therapy, including a dose boost, was administered in nine patients with affected lymph nodes that were surgically inaccessible. This procedure was facilitated by extended radiological staging.

KEYWORDS

breast cancer, high-risk patients, primary systemic therapy, pre-treatment imaging, treatment individualization

1 Introduction

Breast cancer is the most common malignancy among women worldwide. In the United States, over 290,000 new cases are diagnosed annually (1). The treatment of patients with breast cancer has evolved to a multidisciplinary approach. In the surgical treatment of breast cancer, breast-conserving therapy (BCT) is increasingly used. Extensive axillary node dissections are becoming less common. Two anatomical nodal areas seem to be particularly interesting. These are the supraclavicular region and the internal mammary (IM) nodes. Both of these are not routinely operated on. In case of involvement of IM nodes minimally invasive surgical techniques such as video-assisted thoracoscopic surgery (VATS) are safe, but there is a lack of data on whether patients actually benefit clinically from such a procedure (2). In patients with supraclavicular node involvement, radiotherapy alone seems to give better results than surgery combined with radiotherapy (3). Metastases in the IM nodes are usually not an isolated phenomenon but coexist with axillary nodes involvement. Based on the available knowledge, it is difficult to clearly recommend which imaging tests should be performed in in such cases (4).

Currently, initial systemic therapy is administered in most triple-negative breast cancer (TNBC) and HER2-positive cases to achieve pathological complete response (pCR). Irradiation is performed after surgical treatment to improve local control and overall survival in early and advanced breast cancer (5). When significant clinical response to systemic therapy is achieved, areas at risk of persistent disease (such as enlarged supraclavicular nodes) will not be evident on post-operative computed tomography (CT) scans that are used for treatment planning. Standard imaging techniques for diagnosis and staging of breast cancer, including mammography (MMG), ultrasound (US), and magnetic resonance imaging (MRI), have limited utility in personalizing radiation therapy (RT); therefore, planning systems are mainly based on CT images. MMG does not adequately visualize lymph nodes; moreover, it is more suitable for the evaluation of the primary foci in the low mammographic density breasts of postmenopausal women than in the glandular breasts of younger patients (6, 7), who are relatively frequently qualified for primary systemic therapy. Advanced RT techniques, such as intensity modulated radiation therapy (IMRT) require defining the desired dose to all target and non-target tissues on each slice of the planning CT. High-quality cross-sectional imaging that allows 3D visualizations, such as CT scans or positron emission tomography (PET-CT), are a necessary part of the procedure. Despite available data suggesting the utility of CT scan and PET-CT in breast cancer, they are not routinely performed (8–10). Cross-sectional imaging obtained before systemic therapy and surgery, followed by planning CT images, offers numerous possibilities for RT customization, such as increased dose in the non-operated anatomical area, especially where pathological lymph nodes were observed (e.g. supraclavicular region or internal mammary lymph nodes). Additionally, it can aid in diagnosing oligometastatic disease and can facilitate the application of stereotactic body radiation therapy (SBRT). Scans performed before cancer treatment and planning CT done postoperatively could be compared or superimposed on each other in a process referred to as image fusion, providing a tool for RT individualization (Figure 1). In our study, a radiation immobilization device was used to position patients during imaging (Figure 2). The aim of this single-center study was to compare standard baseline imaging with extended radiological staging in patients who are qualified for primary systemic therapy. Furthermore, we aimed to investigate whether CT scans and PET-CT can reliably visualize the primary focus in the breast as well as pathological lymph nodes in the axilla, and to determine whether the nodes that were recognized as being affected actually contained metastases by assessing the correlation between postoperative pathological reports and imaging results. Additionally, we analyzed whether extended radiological staging had an additional diagnostic value. The secondary objective of the study was to investigate how often the multidisciplinary team (MDT) modified the originally planned treatment strategy after receiving an additional examination result.

Abbreviations: CT scan, computed tomography scan, performed using intravenous contrast agent; CXR, chest X-ray; IMRT, intensity modulated radiation therapy; LDCT, low-dose computed tomography; MBC, metastatic breast cancer; MDT, multidisciplinary team; MMG, mammography; MRI, magnetic resonance imaging; NCCN, National Comprehensive Cancer Network; OS, overall survival; pCR, pathologic complete response; PET-CT, positron emission tomography; PFS, progression-free survival; planning CT, non-contrast-enhanced computer tomography performed in supine treatment position; PST, primary systemic therapy; RT, radiation therapy; TNBC, triple-negative breast cancer; US, ultrasound; 2-[18F] FDG, fluorodeoxyglucose.

2 Materials and methods

This was a prospective, cross-sectional, observational study. Data was collected from patients' medical records. Eligible patients comprised those aged ≥18 years with an established diagnosis of invasive breast adenocarcinoma after core needle biopsy. Assessment of histological grade and immunohistochemistry (IHC) evaluation of estrogen receptor (ER), progesterone receptor (PgR), Ki67, and human epidermal growth factor receptor 2 (HER2) status was required in the histopathology report. If the HER2 score was borderline, fluorescence *in situ* hybridization (FISH) was performed. Patients with an Eastern Co-operative Oncology Group Performance Status of 0–2, no distant metastases, and no clinically significant renal failure were recruited. All participants were selected for systemic preoperative therapy by a MDT at the Breast Unit of the Lower Silesian Oncology, Pulmonology, and Hematology Center in Wroclaw, Poland. After performing preliminary radiological staging according to the recommendations of the Polish Society of Clinical Oncology (bilateral MMG, breast US, and chest X-ray (CXR) regardless of the stage, abdominal cavity imaging using US and/or CT scan, and bone scintigraphy in CS III) (11), all eligible patients were offered an extended workup. The current Polish national recommendations indicate that additional imaging studies are optional; moreover, routine inclusion of chest cross-sectional imaging (CT scan or PET-CT) prior to primary systemic therapy (PST) is not commonly practiced. Considering the estimated risk of invasion and metastasis, the decision to perform one of the imaging modalities was made by the MDT. High-risk patients underwent PET-CT without strict criteria for selecting additional imaging modality. Two cohorts of patients were analyzed separately: a CT scan was performed in the first cohort, while a PET-CT was performed in the second. All imaging and treatment results used in the study were considered a part of the patients' diagnostic and

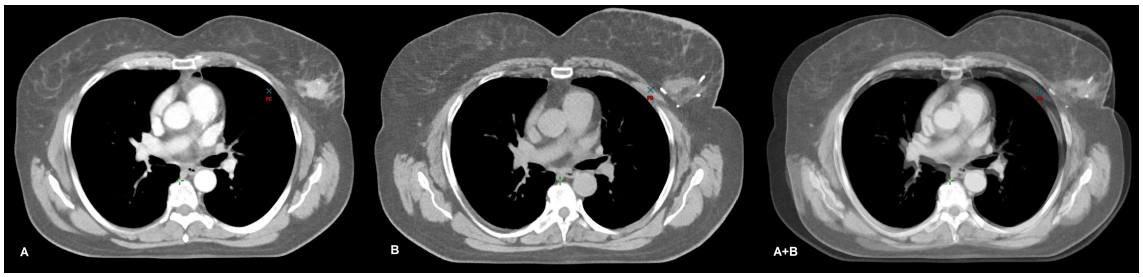

FIGURE 1
CT images of a participant in the CT scan cohort with cT2N0M0, G3 triple-negative breast cancer (TNBC) of the left breast. A contrast-enhanced focus is observed on the CT scan performed before systemic therapy **(A)**. The planning CT of the same patient demonstrates the breast tumor bed and tracers inserted by the surgeon **(B)**. Both images were taken in the same position. Although slight variations were observed in the respiratory phase, it does not affect the generation of fairly reliable fusion image by overlapping the two CT images (A+B). This approach may be facilitated while contouring the boost volume (increased irradiation dose).

therapeutic scheme. Overall, 132 participants were recruited between October 2015 and March 2020; however, after detailed verification, two patients were excluded. In one case, a surgical biopsy of the breast tumor eventually led to a tumorectomy, and the breast lesion could not be measured. In the other case, the assumed period of 2 weeks from the beginning of systemic therapy to the CT scan was exceeded. Further analyses included 130 participants (128 female and two male patients). All PET-CT examinations were performed before treatment, and a CT scan was allowed up to 2 weeks after starting systemic therapy, assuming that during this time there would be no significant tumor shrinkage in most patients. The recruitment process was interrupted during the COVID-19 pandemic, as participation required an additional clinic visit, which could increase the risk of coronavirus transmission. The last CT scan was performed on March 12, 2020, while the collection of COVID-19 statistics in Poland began on March 14, 2020 (according to the COVID-19 Data Repository of the Center for Systems Science and Engineering (CSSE) at Johns Hopkins University, there were 35 COVID-19 cases in Poland at that time). Thus, it can be concluded that CT scan and PET-CT results were unaffected by COVID-19 related bias, regarding both the lung parenchyma and potential vaccination-related lymphadenopathy (12). All scans were performed with the patient in the supine treatment position, were supervised by a radiation oncologist and experienced technicians; this position was also suited to the patient's anatomical structure. The prone position is not optimal if lymph node radiation is planned, and current guidelines and contouring atlases, which are helpful in daily practice, recommend the supine position (13–15). All CT scans were assessed by an experienced radiologist, and PET-CT were assessed by a nuclear medicine specialist. Measurements of tumor sizes were also made by the above-mentioned professionals. CT was performed using an intravenous contrast agent and PET-CT using fluorodeoxyglucose (2-[18F] FDG) as the radio-active tracer. The cross-sectional imaging result was attached to the patient's medical history and analyzed by the MDT.

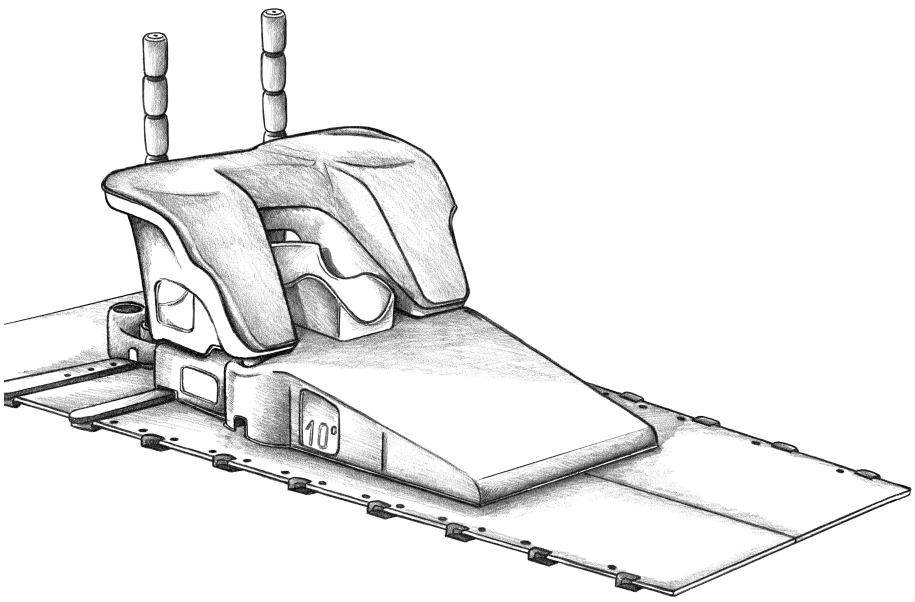

FIGURE 2
Orfit-AIO system was used for positioning. The layout can be customized based on various factors, such as anatomical conditions, breast size, and the patient's fitness. Most of the sets enable the selection of appropriate back support and adjustment of the location of the shoulder immobilization. The positional information can be easily stored for future reference, allowing for the recreation of the same body posture during subsequent CT scans or PET-CT.

Statistical analysis was performed using IBM SPSS Statistics 25.0 software (IBM Corp., Armonk, N.Y., USA). The Friedman test was used to evaluate the difference between the largest dimensions of the breast tumors in alternative medical imaging methods. Pairwise comparisons were performed using the *post-hoc* Dunn's test. The following descriptive statistics were considered: mean, standard deviation, median, minimum, maximum, and the first and third quartiles. The distribution of the analyzed variables was presented in detail. Pair collation was made based on the median. We compared the largest dimension of the largest breast tumor focus (T/mm), between the standard MMG, US, and CT scans, as well as between MMG, US, and PET-CT. Chi-square test was applied to estimate the distribution of the variables pN+ (involved axillary nodes based on the histopathology report) and cN+ (involved axillary nodes based on imaging). Consistency between the clinical assessment using imaging and the pathology report was estimated separately in the CT scan cohort and the PET-CT cohort. The rate of patients was calculated in terms of an additional diagnostic value of extended radiological staging, which resulted in a modification of the clinical stage or change in the management strategy. The level of statistical significance was set at $p < 0.05$.

3 Results

3.1 Patient demographics and tumor characteristics

The age of the participants was similar in CT scan and PET-CT cohorts, with a median of 51 and 50 years, respectively. High-grade G3 histologic tumors were the most common and have been confirmed in 55.1% of cases in the CT scan cohort and in 62.8% in the PET-CT cohort; the G1 grade was observed in only one participant. High Ki67 expression was predominant, with a median of 43.5 (7–90) in the CT scan cohort and 52.5 (2–90) in the PET-CT cohort (Table 1). Participants who qualified for PET-CT, according to the assessment of the MDT, had a higher risk of cancer spread and were, in several cases, originally non-operable. A cT4 clinical tumor stage was established in 39.5% of patients in this group. In the CT scan cohort, several patients (58.6%) had cT2 features. The most common subtype, based on the receptor profile and Ki67 rate, according to the St. Gallen surrogate classification for breast cancer (16), was luminal-B-like HER2 negative. Endocrine

TABLE 1 Patients' baseline characteristics.

		CT scan cohort (n=87)	PET-CT cohort (n=43)
Median age (years)		51 (25–80)	50 (24–74)
Sex	Women	85 (97.7%)	43 (100%)
	Men	2 (2.3%)	0
Clinical tumour stage (cT)	cT1	3 (3.4%)	0
	cT2	51 (58.6%)	16 (37.2%)
	cT3	25 (28.7%)	10 (23.3%)
	cT4	8 (9.2%)	17 (39.5%)
Clinical nodal stage (cN)	cN0	24 (27.6%)	7 (16.3%)
	cN1	26 (29.9%)	8 (18.6%)
	cN2	26 (29.9%)	14 (32.6%)
	cN3	11 (12.6%)	14 (32.6%)
Histologic grade	G1	0	1 (2.3%)
	G2	37 (42.5%)	14 (32.6%)
	G3	48 (55.1%)	27 (62.8%)
	not established	2 (2.3%)	1 (2.3%)
Median Ki67		43,5 (7–90)	52,5 (2–90)
St. Gallen surrogate classification for breast cancer	Luminal A-like	5 (5.7%)	4 (9.3%)
	Luminal B-like (HER2-negative)	34 (39.1%)	18 (41.9%)
	Luminal B-like (HER2-positive)	11 (12.6%)	9 (20.9%)
	HER2-positive (non-luminal)	8 (9.2%)	1 (2.3%)
	Triple-negative	29 (33.3%)	11 (25.6%)
Definitive surgery		82 (94.3%)	35 (81.4%)
No surgery		5 (5.7%)	8 (18.6%)
Pathologic complete response (pCR)		18 (22%)	8 (22.9%)
No pathologic complete response		64 (78%)	27 (77.1%)

Histologic grade rated on Scarf-Bloom-Richardson Grading System, Nottingham Modification. Abbreviations: CT, computed tomography; PET-CT, positron emission tomography.

therapy was rarely used as a form of preoperative treatment; however, it was used in three patients in the PET-CT cohort and in eight patients in the CT scan cohort. In 91.5% of the participants, PST was based on multi-drug chemotherapy. Anti-Her2 targeted therapy was administered when indicated. Optimal systemic therapy was selected by the MDT. The rate of pathologic complete response was rather low, slightly exceeding 22% in both cohorts, due to a high representation of patients with T4 and N3 features and the dominant subtype being Luminal B (HER2-negative) (17).

3.2 Tumor size measurements

The largest dimensions in millimeters (T/mm) of breast tumors measured using alternative medical imaging modalities were compared (Table 2). In cases of multifocal tumors, the largest lesion was assessed; the Friedman test was used to evaluate the differences. Only the dimensions evaluated using US were statistically significantly smaller ($p = 0.02$) than those evaluated using CT scan. However, in both cohorts, US and MMG were performed before the diagnosis was confirmed using biopsy, while CT scan was performed after the initial workup and evaluation by the MDT. Furthermore, disease progression over a period of several weeks may have occurred in some patients. In PET-CT cohort, the measurement of the focus in the breast was made in low-dose CT (LDCT), which is a component of the PET-CT scan. When the dimensions obtained from PET-CT were compared with those obtained from US and MMG, there was no statistically significant difference in the measurements ($p = 0.9$).

3.3 Baseline lymph node evaluation and consistency between the clinical assessment of lymph nodes with the postoperative pathology report

Unambiguous lymph node assessments were obtained using all imaging techniques, with clear differentiation between pathological (cN+) and non-involved (cN-) nodes as shown in Table 3. Following the exclusion of unoperated patients and those who reached pCR (both in the primary focus and in axillary nodes), the consistency between the clinical assessment of axillary lymph nodes (cN) using CT scan and US with the postoperative pathology report (pN) was evaluated (Table 4). This analysis is reliable because of the large cohort of participants with only a partial response, including 64 in the CT scan cohort and 27 in the PET-CT cohort. In 95.3% of node-positive cases, there were consistencies between microscopic and CT scan evaluations. In two cases (4.7%), lymph nodes were assessed on CT scan as not involved; however, histological examination revealed that they contained metastases. Similar results were obtained after comparing the clinical evaluation of lymph nodes using US and the postoperative pathology report. In 92.5% of node-positive cases, pathology reports and lymph node evaluations in US were consistent; however, in three cases (7.5%), lymph nodes were assessed as not involved using US but were found to contain metastases (Table 4). This suggests that the diagnostic values of CT scan and US are similar in terms of lymph node assessment. Chi-square test confirmed consistency between the clinical evaluation of

TABLE 3 Accuracy of imaging modalities in lymph node evaluation among patients without pathologic complete response.

No pathologic complete response	CT scan cohort (n=64)
Unequivocal lymph node evaluation by CT scan	60 (94%)
Dubious lymph node evaluation by CT scan	4 (6%)
Unequivocal lymph node evaluation by US	59 (92%)
Dubious lymph node evaluation by US	5 (8%)
No pathologic complete response	**PET-CT cohort (n=27)**
Unequivocal lymph node evaluation by PET-CT	26 (96%)
Dubious lymph node evaluation by PET-CT	1 (4%)
Unequivocal lymph node evaluation by US	26 (96%)
Dubious lymph node evaluation by US	1 (4%)

An unequivocal result was the one in which the nodes were recognized as pathological (cN+) or not involved (cN-). Results that reported suspicious or enlarged nodes were reckoned as dubious.
CT, computed tomography; PET-CT, positron emission tomography; US, ultrasound.

TABLE 2 Largest contiguous dimension of the tumour focus in alternative imaging methods.

CT scan cohort	M	Me	SD	Min	Max	Q1	Q3
T/mm MMG	40.79	37.5	21.88	10	130	25	51.25
T/mm US	38.51	38	13.95	11	75	29	46
T/mm CT scan	43.48	40	19.2	13	115	30	54
PET-CT cohort							
T/mm MMG	44.78	35	26.93	12	100	27	55
T/mm US	44.72	40	21.93	14	100	27	56
T/mm PET-CT	46.32	37.5	26.43	12	120	29.75	56

In case of multifocal tumours, the largest lesion (T) was taken into account. According to the criteria for determining T category in TNM Staging System For Breast Cancer, by American Joint Committee on Cancer (AJCC).
MMG, mammography; US, ultrasound; CT scan, computed tomography; PET-CT, positron emission tomography; M, mean; Me, median; SD, standard deviation; Min, minimum; Max, maximum; Q1, first quartile; Q3, third quartile.

TABLE 4 Consistency between clinical assessment of axillary lymph nodes (cN) by baseline CT scan, US, and the postoperative pathology report (pN).

Imaging vs pathology report	cN evaluated by CT scan			
	cN-(n = 11)		cN+ (n = 49)	
	n	%	n	%
pN- (n = 17)	9	52.9	8	47.1
pN+ (n = 43)	2	4.7	41	95.3
Imaging vs pathology report	cN evaluated by US			
	cN- (n = 16)		cN+ (n = 43)	
pN- (n = 19)	13	68.4	6	31.6
pN+ (n = 40)	3	7.5	37	92.5

Only patients with no pathologic complete response and unequivocal lymph node evaluation by imaging were included in this analysis (refer to Table 3).
CT, computed tomography; PET-CT, positron emission tomography; US, ultrasound.

involved lymph nodes using imaging (cN+) and the pathology report (pN+); for the CT scan cohort the result was $\chi2(1) = 18.98$; $p < 0.001$. All histopathological reports were analyzed postoperatively after the patients had received systemic treatment. It can be assumed that in some cases nodal pCR with a simultaneous lack of pCR in the primary focus had occurred. Moreover, node-only pCR occurs approximately twice as often as breast-only pCR (18). Migration of patients from the group cN+ to the pN- group is the expected effect of PST. Biopsy confirmation of lymph node metastases in all patients before systemic therapy is not routinely practiced. In cases of massive lymph node involvements that are visible on US and clinical examination (cN2 and cN3 patients), a biopsy is usually not justified. A small percentage of patients may also experience disease progression during systemic therapy. Therefore, assessments of false negative and false positive rates of axillary status were abandoned. Mirror analysis was also performed in the PET-CT cohort (Table 5). The clinical stage of patients who qualified for PET-CT was more advanced. Notably, there was no discordance between the nodes assessed as uninvolved by PET-CT and the postoperative pathology report. Although this cohort was smaller, the result of the Chi-square test confirmed the consistency between the clinical assessment of involved lymph nodes using imaging (cN+) and the pathology report (pN+), with $\chi2(1) = 6.41$; $p = 0.03$ for PET-CT.

TABLE 5 Consistency between clinical assessment of axillary lymph nodes (cN) by baseline PET-CT, US, and the postoperative pathology report (pN).

Imaging vs pathology report	cN evaluated by PET-CT			
	cN- (n = 3)		cN+ (n = 23)	
	n	%	n	%
pN- (n = 9)	3	33.3	6	66.7
pN+ (n = 17)	0	0	17	100
Imaging vs pathology report	cN evaluated by US			
	cN- (n = 5)		cN+ (n = 21)	
pN- (n = 8)	5	62.5	3	37.5
pN+ (n = 18)	0	0	18	100

Only patients with no pathologic complete response and unequivocal lymph node evaluation by imaging were included in this analysis (refer to the Table 3).
CT, computed tomography; PET-CT, positron emission tomography; US, ultrasound.

3.4 Added value of extended radiological staging

We also analyzed whether a CT scan or PET-CT had any additional diagnostic value compared to the standard initial workup. The results confirmed that in 49.4% of the participants, clinically significant information was obtained from CT scans. Internal mammary lymph node involvement was also detected in six patients. In two cases, the supraclavicular lymph nodes were found outside the anatomical boundaries suggested by the ESTRO guidelines for the delineation of lymph nodal areas. In one participant, CT scan findings aided in identifying a previously undiagnosed heart pathology (an interatrial thrombus). Involved lymph nodes in the mediastinum were found in one participant (M1 feature). In ten cases, CT scans revealed satellite foci within the involved breast, and in five cases, pectoral muscle infiltrations were identified. In the PET-CT cohort, one-fourth of the cases ended with modifications of the originally planned treatment strategy, and in 51.2% of cases, the originally determined disease stage changed. PET-CT confirmed the multifocal metastasis in seven patients and was helpful in diagnosing oligometastatic disease in two participants (Table 6).

4 Discussion

In malignancies that are highly sensitive to systemic therapy, such as nasopharyngeal cancer, it is difficult to consider modern RT planning without performing precise imaging before chemotherapy (19, 20). A thorough understanding of the original scope of the disease is required to determine the appropriate volume of irradiated tissues. The effectiveness of systemic therapy is increasing in patients with

TABLE 6 Impact of the CT scan and PET-CT on the multidisciplinary team's decision.

CT scan cohort (n=87)	n	%
Management strategy modification	9	10.3
Clinical stage shift	32	36.8
Other clinically significant findings	2	2.3
No added value of extended radiological staging	44	50.6
PET-CT cohort (n=43)	n	%
Management strategy modification	11	25.6
Clinical stage shift	22	51.2
No added value of extended radiological staging	10	23.3

Modification of the management strategy was understood as withdrawal of surgery or personalized radiation therapy (e.g., boost within the internal mammary lymph nodes or stereotactic body radiation therapy [SBRT] in oligometastatic disease).
CT, computed tomography; PET-CT, positron emission tomography.

breast cancer. Regarding HER2 positive and TNBC subtypes, pCR may be expected in nearly half of the treated population, even in patients with locally advanced diseases (21, 22). The NCCN guidelines allow for a supplemental RT boost to grossly involved or enlarged lymph nodes that have not been surgically resected (23); however, there are no recommendations on how to systematically diagnose such cases clinically. PET-CT is precise in evaluating breast cancer nodal involvement and was the basis for an anatomical atlas created in 2018 (24). A study published in 2012 demonstrated that a preoperative CT scan may facilitate and increase the precision of boost planning in the tumor bed (25). Experts in the field of adjuvant radiotherapy for breast cancer suggest the possibility of using PET-CT, especially in cases where a nodal boost is relevant, or to detect additional nodes in cases of extensive nodal involvement (26). Low avidity of 2-[18F]FDG PET-CT have been noticed in slow-proliferating tumors, including invasive lobular carcinoma; however, such cases are usually not qualified for PST. The Lucerne Toolbox 2, a multidisciplinary expert consensus published in 2023 states that the radiation oncologist should review the pre-treatment images of patients undergoing PST (27). For over 10 years, we have observed the usefulness of performing PET-CT during the basic staging in cases of advanced breast cancer. Fortunately, the current European Association of Nuclear Medicine/Society of Nuclear Medicine and Molecular Imaging (EANM/SNMMI) guidelines recommend performing 2-[18F]FDG PET-CT in patients with clinical stages IIB–IV (28). Recent experience in innovative imaging modalities, such as PET-prostate-specific membrane antigen (PSMA) in patients with prostate cancer, has led to the assumption that in some cases, nodal metastases could occur at sites beyond the typical locations mentioned in current contouring guidelines (29). In terms of the radiation dose for breast cancer, hypofractionated schedules are regarded as state-of-the-art (30). However, significantly less attention has been paid to complete radiation doses. Reportedly, an increased dose to the tumor bed doubles the local effectiveness of RT; however, the boost practice varies significantly in different cancer centers (31–33). For most neoplasms, a hard-to-question paradigm in which local control depends on the total dose seems true. Modern irradiation techniques enable safe and precise application of high doses. However, it has been proven in a small group of patients with breast cancer that IMRT is effective enough to be considered as an optional radical treatment, especially in those who decline surgery (34). Data on increased doses in areas other than the tumor bed are scarce; however, using a total dose higher than 60 Gy to involved lymph nodes improves local control (35–37). Particular attention should be paid to the internal mammary and supraclavicular nodes, because these are not routinely removed during surgical procedures (38). In the 130 patients in this study, a boost dose within the involved but unoperated lymph nodes was applied in nine patients, most often 63 Gy in 28 fractions. A boost was applied to the internal mammary lymph nodes in five patients (Figures 3–5), and to the pathological lymph nodes within the part of the axilla not covered surgically in four patients (Figure 6). Oligometastatic disease was diagnosed in two patients, and SBRT was administered.

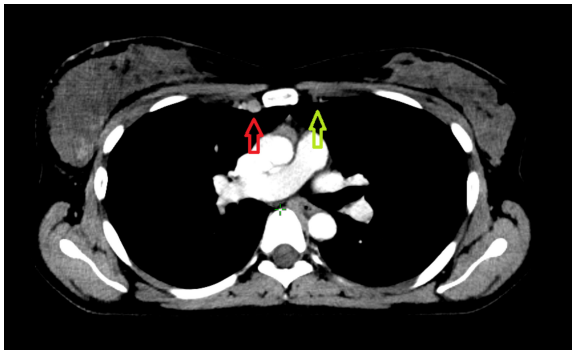

FIGURE 3
Involved internal mammary nodes, indicated by the red arrow, are difficult to visualize. For comparison, the internal mammary vessels on the contralateral uninvolved side are indicated by the green arrow.

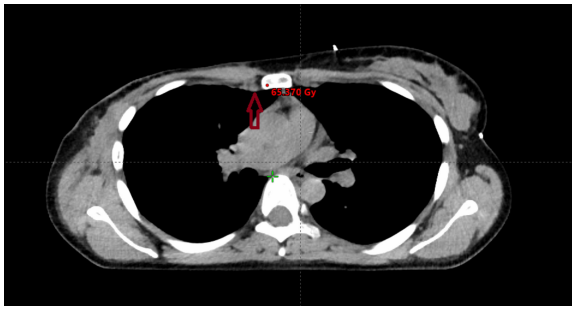

FIGURE 4
If primary systemic treatment (PST) is effective, remission will occur. On standard planning CT performed without intravenous contrast agent, the involved nodes may temporarily become almost invisible (dark red arrow). This image is from the same patient whose images are in the Figure 3 after systemic treatment and mastectomy.

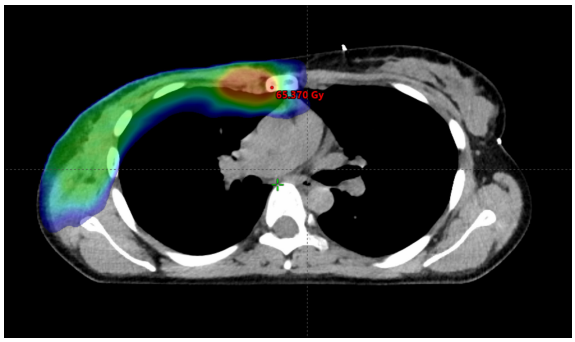

FIGURE 5
Modern radiotherapy techniques make it safe to boost the dose to the internal mammary lymph nodes. However, prior to implementing this approach, it is crucial to ascertain whether the internal mammary lymph nodes were involved and to determine the specific intercostal region affected. The irradiated volume is graphically represented, the area receiving a lower dose is in blue, while the boost area is in red.

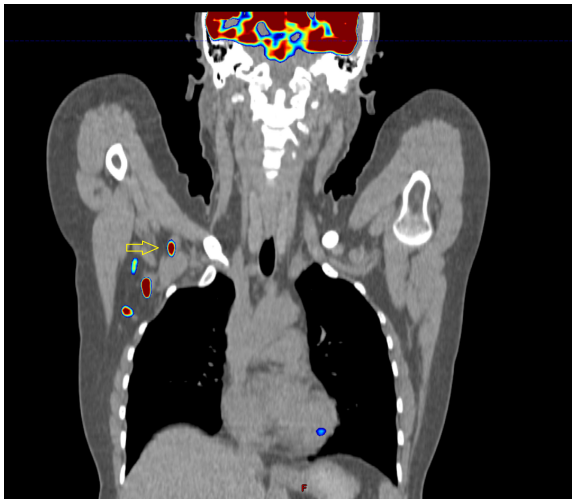

FIGURE 6
Images of a patient after axillary lymph node dissection, two out of eleven nodes contained metastases. Is this lymph node (yellow arrow) visible on baseline PET-CT operable? What has happened to the third node? It is very likely that it remained in the axilla, despite the surgeon's efforts.

In the future, apart from the tumor bed boost, the dose may also be modified, depending on the risk of anatomical area involvement. Such an approach is implemented in daily practice in RT for head and neck cancers, where one RT plan often involves three different doses to various areas: a gross disease dose to the volume of direct cancer infiltration, a high-risk subclinical disease dose to the areas that are the most common recurrence sites, and a low-risk dose to the elective lymph node areas (39). Similar methods may be used in the future for cases of breast cancer where high-quality imaging techniques are available.

This study has some limitations. First, it was not a randomized trial but an observational study; moreover, PET-CT may have been performed preferentially in the group of patients with an unfavorable prognosis. Therefore, it was not possible to compare the two additional imaging modalities. Second, the number of participants recruited was small; therefore, we could not analyze the impact of personalized RT on the progression-free survival (PFS) and overall survival (OS) of patients. Third, the anatomical scope of imaging modalities varied, as CT scans included the neck, chest, and upper part of the abdominal cavity, while PET-CT covered the entire body, which is a definite advantage of this technique and enables diagnosis of oligometastatic disease in some cases. On the other hand, CT scans are not time-consuming and easily available in virtually any modern radiation therapy facility. Despite these limitations, the results of our study are encouraging. The findings of this study are likely to be validated by a large, randomized, multicenter clinical trial in the future. The strength of our study is the fact that it concerns aggressive and advanced cases of breast cancer, qualified to PST. Among this group of patients, finding lymph nodes in areas not subjected to surgical treatment is highly probable.

A distinctive feature of our approach to breast cancer imaging was the use of radiation immobilization devices. This allows for very precise overlaying of the baseline and postoperative images. Modern oncology is complex; however, while performing a medical procedure, it is worth considering whether it can be

helpful in conducting the next one. Manual delineation during radiation treatment planning is subject to interobserver variability (IOV). Advances in artificial intelligence (AI) and other automation techniques are becoming helpful to radiation oncologists and radiologists. Moreover, studies have shown that these systems can be effective, provided the input data is of high quality (40, 41).

5 Conclusions

Our results indicate that both CT and PET-CT enable a detailed assessment of the location and size of primary tumors in the breast as well as pathological lymph nodes. Unlike MRI, which is most often performed in the prone position, which significantly affects anatomical features, both CT and PET-CT scans may be performed in the same layout as the therapeutic position. Furthermore, numerous researchers recommend performing CT or PET-CT in cases of suspected spread of the disease (42, 43). However, considering the capabilities of modern RT, routine and accurate imaging should be performed in a systematic way. In our opinion, adequate patient selection for preoperative systemic therapy should be performed by a MDT. This group of patients will benefit the most from extended radiological staging.

Data availability statement

The raw data supporting the conclusions of this article will be made available by the authors, without undue reservation.

Ethics statement

The studies involving humans were approved by Wroclaw Medical University, Plac Ludwika Hirszfelda 12, 53-413 Wroclaw, Poland. The studies were conducted in accordance with the local legislation and institutional requirements. The participants provided their written informed consent to participate in this study.

Author contributions

TB: Conceptualization, Data curation, Formal Analysis, Investigation, Methodology, Visualization, Writing – original draft, Writing – review & editing. RM: Conceptualization, Writing – review & editing. BC-S: Methodology, Writing – review & editing. TK: Writing – review & editing. AK: Writing – review & editing. DD: Writing – review & editing. AM: Supervision, Writing – review & editing.

Funding

The author(s) declare that no financial support was received for the research, authorship, and/or publication of this article.

Acknowledgments

We sincerely appreciate Michał Ordak for statistical elaboration and Izabela Pawińska for visualizations. We would like to express our deepest gratitude to Orit Kaidar-Person and Wendy A. Woodward for their brilliant suggestions and tips on academic writing.

Conflict of interest

The authors declare that the research was conducted in the absence of any commercial or financial relationships that could be construed as a potential conflict of interest.

Generative AI statement

The author(s) declare that no Generative AI was used in the creation of this manuscript.

Publisher's note

All claims expressed in this article are solely those of the authors and do not necessarily represent those of their affiliated organizations, or those of the publisher, the editors and the reviewers. Any product that may be evaluated in this article, or claim that may be made by its manufacturer, is not guaranteed or endorsed by the publisher.

Supplementary material

The Supplementary Material for this article can be found online at: https://www.frontiersin.org/articles/10.3389/fonc.2025.1556122/full#supplementary-material

References

1. Agostinetto E, Gligorov J, Piccart M. Systemic therapy for early-stage breast cancer: learning from the past to build the future. *Nat Rev Clin Oncol.* (2022) 19:763–74. doi: 10.1038/s41571-022-00687-1

2. Kawaguchi S, Tamura N, Suzuki S, Nishikawa A, Shibata A, Tanaka K, et al. Effectiveness of PET/CT and VATS for detecting and treating internal mammary lymph node metastasis: a case series. *Jpn J Clin Oncol.* (2023) 53:562–71. doi: 10.1093/jjco/hyad032

3. Song YC, Kong J, Li N, Liu XL, Li XH, Zhu LY, et al. Comparison of supraclavicular surgery plus radiotherapy versus radiotherapy alone in breast cancer patients with synchronous ipsilateral supraclavicular lymph node metastasis: A

multicenter retrospective study. *Radiother Oncol*. (2023) 183. doi: 10.1016/j.radonc.2023.109639

4. Eckert KM, Boughey JC, Piltin MA. Internal mammary lymphadenopathy in breast cancer: a narrative review and update. *Trans Breast Cancer Res*. (2024) 5:11–1. doi: 10.21037/tbcr-24-2

5. Poortmans PM, Weltens C, Fortpied C, Kirkove C, Peignaux-Casasnovas K, Budach V, et al. Internal mammary and medial supraclavicular lymph node chain irradiation in stage I–III breast cancer (EORTC 22922/10925): 15-year results of a randomised, phase 3 trial. *Lancet Oncol*. (2020) 21:1602–10. doi: 10.1016/S1470-2045(20)30472-1

6. Dialani V, James DF, Slanetz PJ. A practical approach to imaging the axilla. *Insights Into Imaging*. (2015) 6:217–29. doi: 10.1007/s13244-014-0367-8

7. Vinnicombe SJ. Breast density: why all the fuss? *Clin Radiol*. (2018) 73:334–57. doi: 10.1016/j.crad.2017.11.018

8. Sarno A, Mettivier G, Russo P. Dedicated breast computed tomography: Basic aspects. *Med Phys*. (2015) 42:2786–804. doi: 10.1118/1.4919441

9. Ahn SJ, Kim YS, Kim EY, Park HK, Cho EK, Kim YK, et al. The value of chest CT for prediction of breast tumor size: Comparison with pathology measurement. *World J Surg Oncol*. (2013) 11. doi: 10.1186/1477-7819-11-130

10. Koolen BB, van der Leij F, Vogel WV, Rutgers EJT, Vrancken Peeters MJTFD, Elkhuizen PHM, et al. Accuracy of 18F-FDG PET/CT for primary tumor visualization and staging in T1 breast cancer. *Acta Oncol (Madr)*. (2014) 53:50–7. doi: 10.3109/0284186X.2013.783714

11. Jassem J, Krzakowski Zespół autorski M, Krzakowski M, Bobek-Billewicz B, Duchnowska R, Jeziorski A, et al. WYTYCZNE POSTĘPOWANIA DIAGNOSTYCZNO-TERAPEUTYCZNEGO Rak piersi Breast cancer. *Oncol Clin Pract*. (2020) 16. doi: 10.5603/OCP.2020.0038

12. Wolfson S, Kim E, Plaunova A, Bukhman R, Sarmiento RD, Samreen N, et al. Axillary adenopathy after COVID-19 vaccine: no reason to delay screening mammogram. *Radiology*. (2022) 303:297–9. doi: 10.1148/radiol.213227

13. Fargier-Bochaton O, Wang X, Dipasquale G, Laouiti M, Kountouri M, Gorobets O, et al. Prone versus supine free-breathing for right-sided whole breast radiotherapy. *Sci Rep*. (2022) 12. doi: 10.1038/s41598-021-04385-3

14. Temme N, Hermann RM, Hinsche T, Becker JN, Sonnhoff M, Kaltenborn A, et al. Radiotherapy of Breast cancer in laterally tilted prone vs. supine position: what about the internal mammary chain? *J Pers Med*. (2022) 12:653. doi: 10.3390/jpm12040653

15. Offersen BV, Boersma LJ, Kirkove C, Hol S, Aznar MC, Biete Sola A, et al. ESTRO consensus guideline on target volume delineation for elective radiation therapy of early stage breast cancer. *Radiother Oncol*. (2015) 114:3–10. doi: 10.1016/j.radonc.2014.11.030

16. Vasconcelos I, Hussainzada A, Berger S, Fietze E, Linke J, Siedentopf F, et al. The St. Gallen surrogate classification for breast cancer subtypes successfully predicts tumor presenting features, nodal involvement, recurrence patterns and disease free survival. *Breast*. (2016) 29:181–5. doi: 10.1016/j.breast.2016.07.016

17. Zarotti C, Papassotiropoulos B, Elfgen C, Dedes K, Vorburger D, Pestalozzi B, et al. Biomarker dynamics and prognosis in breast cancer after neoadjuvant chemotherapy. *Sci Rep*. (2022) 12. doi: 10.1038/s41598-021-04032-x

18. Fayanju OM, Ren Y, Thomas SM, Greenup RA, Plichta JK, Rosenberger LH, et al. The clinical significance of breast-only and node-only pathologic complete response (PCR) after neoadjuvant chemotherapy (NACT): A review of 20,000 breast cancer patients in the National Cancer Data Base (NCDB). *Ann Surg*. (2018) 268:591–601. doi: 10.1097/SLA.0000000000002953

19. Xue F, Hu C, He X. Induction chemotherapy followed by intensity-modulated radiotherapy with reduced gross tumor volume delineation for stage T3–4 nasopharyngeal carcinoma. *Onco Targets Ther*. (2017) 10:3329–36. doi: 10.2147/OTT.S140420

20. De Felice F, Musio D, Tombolini V. Target volume delineation after induction chemotherapy in locally advanced head and neck cancer. *Oral Oncol*. (2015) 51:e81. doi: 10.1016/j.oraloncology.2015.09.005

21. Reina Sofi H, Gianni L, Pienkowski T, Im YH, Roman L, Tseng LM, et al. Effi cacy and safety of neoadjuvant pertuzumab and trastuzumab in women with locally advanced, infl ammatory, or early HER2-positive breast cancer (NeoSphere): a randomised multicentre, open-label, phase 2 trial. *Articles Lancet Oncol*. (2012) 13:25–32. www.thelancet.com/oncology.

22. Biswas T, Efird JT, Prasad S, Jindal C, Walker PR. The survival benefit of neoadjuvant chemotherapy and pCR among patients with advanced stage triple negative breast cancer(2017). Available online at: www.impactjournals.com/oncotarget.

23. Rashmi Kumar N, Berardi R, Abraham J, Aft R, Agnese D, Allison KH, et al. NCCN Guidelines Version 4.2022 Breast Cancer (2022). Available online at: https://www.nccn.

24. Borm KJ, Voppichler J, Düsberg M, Oechsner M, Vag T, Weber W, et al. FDG/PET-CT–based lymph node atlas in breast cancer patients. *Int J Radiat Oncol Biol Phys*. (2019) 103:574–82. doi: 10.1016/j.ijrobp.2018.07.2025

25. Boersma LJ, Janssen T, Elkhuizen PHM, Poortmans P, van der Sangen M, Scholten AN, et al. Reducing interobserver variation of boost-CTV delineation in breast conserving radiation therapy using a pre-operative CT and delineation guidelines. *Radiother Oncol*. (2012), 178–82. doi: 10.1016/j.radonc.2011.12.021

26. Kaidar-Person O, Offersen BV, Boersma L, Meattini I, Dodwell D, Wyld L, et al. Tricks and tips for target volume definition and delineation in breast cancer: Lessons learned from ESTRO breast courses. *Radiother Oncol*. (2021) 162:185–94. doi: 10.1016/j.radonc.2021.07.015

27. Kaidar-Person O, Pfob A, Gentilini OD, Borisch B, Bosch A, Cardoso MJ, et al. The Lucerne Toolbox 2 to optimise axillary management for early breast cancer: a multidisciplinary expert consensus. *eClinicalMedicine*. (2023) 61. doi: 10.1016/j.eclinm.2023.102085

28. Groheux D, Vaz SC, Ulaner GA, Cook GJR, Woll JPP, Mann RM, et al. Joint EANM-SNMMI guidelines on the role of 2-[18F]FDG PET/CT in no special type breast cancer: differences and agreements with European and American guidelines. *Eur J Nucl Med Mol Imaging*. (2024) 51:2701–5. doi: 10.1007/s00259-024-06694-x

29. Schiller K, Stöhrer L, Düsberg M, Borm K, Devecka M, Vogel MME, et al. PSMA-PET/CT-based lymph node atlas for prostate cancer patients recurring after primary treatment: clinical implications for salvage radiation therapy. *Eur Urol Oncol*. (2021) 4:73–83. doi: 10.1016/j.euo.2020.04.004

30. De Rose F, Fogliata A, Franceschini D, Iftode C, Navarria P, Comito T, et al. Hypofractionation with simultaneous boost in breast cancer patients receiving adjuvant chemotherapy: A prospective evaluation of a case series and review of the literature. *Breast*. (2018) 42:31–7. doi: 10.1016/j.breast.2018.08.098

31. Vrieling C, Van Werkhoven E, Maingon P, Poortmans P, Weltens C, Fourquet A, et al. Prognostic factors for local control in breast cancer after long-term follow-up in the EORTC boost vs no boost trial: A randomized clinical trial. *JAMA Oncol*. (2017) 3:42–8. doi: 10.1001/jamaoncol.2016.3031

32. Lee HH, Chen CH, Luo KH, Chuang HY, Huang CJ, Cheng YK, et al. Five-year survival outcomes of intensity-modulated radiotherapy with simultaneous integrated boost (IMRT-SIB) using forward IMRT or Tomotherapy for breast cancer. *Sci Rep*. (2020) 10. doi: 10.1038/s41598-020-61403-6

33. Krug D, Baumann R, Krockenberger K, Vonthein R, Schreiber A, Boicev A, et al. Adjuvant hypofractionated radiotherapy with simultaneous integrated boost after breast-conserving surgery: results of a prospective trial. *Strahlentherapie und Onkol*. (2021) 197:48–55. doi: 10.1007/s00066-020-01689-7

34. Shibamoto Y, Murai T, Suzuki K, Hashizume C, Ohta K, Yamada Y, et al. Definitive radiotherapy with SBRT or IMRT boost for breast cancer: Excellent local control and cosmetic outcome. *Technol Cancer Res Treat*. (2018) 17:1–7. doi: 10.1177/1533033818799355

35. Andring LM, Diao K, Sun S, Patel M, Whitman GJ, Schlembach P, et al. Locoregional management and prognostic factors in breast cancer with ipsilateral internal mammary and axillary lymph node involvement. *Int J Radiat Oncol Biol Phys*. (2022) 113:552–60. doi: 10.1016/j.ijrobp.2022.02.037

36. Purswani JM, Oh C, Teruel JR, Xiao J, Barbee DL, Maisonet OG, et al. Definitive radiation with nodal boost for patients with locally advanced breast cancer. *Pract Radiat Oncol*. (2023) 13:e103–14. doi: 10.1016/j.prro.2022.10.012

37. Diao K, Andring LM, Barcenas CH, Singh P, (Carisa)-Le-Petross H, Reed VK, et al. Contemporary outcomes after multimodality therapy in patients with breast cancer presenting with ipsilateral supraclavicular node involvement. *Int J Radiat Oncol Biol Phys*. (2022) 112:66–74. doi: 10.1016/j.ijrobp.2021.08.026

38. Yang K, Kim H, Choi DH, Park W, Noh JM, Cho WK. Optimal radiotherapy for patients with internal mammary lymph node metastasis from breast cancer. *Radiat Oncol*. (2020) 15. doi: 10.1186/s13014-020-1464-0

39. Wichmann J, Durisin M, Hermann RM, Merten R, Christiansen H. Moderately hypofractionated intensity-modulated radiotherapy with a simultaneous integrated boost for locally advanced head and neck cancer - do modern techniques fulfil their promise? *In Vivo (Brooklyn)*. (2021) 35:2801–8. doi: 10.21873/invivo.12566

40. Bayareh-Mancilla R, Medina-Ramos LA, Toriz-Vázquez A, Hernández-Rodríguez YM, Cigarroa-Mayorga OE. Automated computer-assisted medical decision-making system based on morphological shape and skin thickness analysis for asymmetry detection in mammographic images. *Diagnostics*. (2023) 13. doi: 10.3390/diagnostics13223440

41. Baroudi H, Brock KK, Cao W, Chen X, Chung C, Court LE, et al. Automated contouring and planning in radiation therapy: what is 'Clinically acceptable'? *Diagnostics*. (2023) 13. doi: 10.3390/diagnostics13040667

42. Barrett T, Bowden DJ, Greenberg DC, Brown CH, Wishart GC, Britton PD. Radiological staging in breast cancer: Which asymptomatic patients to image and how. *Br J Cancer*. (2009) 101:1522–8. doi: 10.1038/sj.bjc.6605323

43. Cardoso F, Kyriakides S, Ohno S, Penault-Llorca F, Poortmans P, Rubio IT, et al. Early breast cancer: ESMO Clinical Practice Guidelines for diagnosis, treatment and follow-up. *Ann Oncol*. (2019) 30:1194–220. doi: 10.1093/annonc/mdz173

frontiers | Frontiers in Medicine

TYPE Original Research
PUBLISHED 17 March 2025
DOI 10.3389/fmed.2025.1538507

Check for updates

OPEN ACCESS

EDITED BY
Abdul K. Parchur,
Medical College of Wisconsin, United States

REVIEWED BY
Akram Al-Ibraheem,
King Hussein Cancer Center, Jordan
Arutselvan Natarajan,
Stanford University, United States

*CORRESPONDENCE
Hugo Peslier
✉ hpeslier@yahoo.fr

RECEIVED 02 December 2024
ACCEPTED 27 February 2025
PUBLISHED 17 March 2025

CITATION
Peslier H, Seegers V and Dufour P-A (2025) Study of predictive factors for response to ^{177}LU-PSMA in patients with metastatic castration-resistant prostate cancer. *Front. Med.* 12:1538507. doi: 10.3389/fmed.2025.1538507

COPYRIGHT
© 2025 Peslier, Seegers and Dufour. This is an open-access article distributed under the terms of the Creative Commons Attribution License (CC BY). The use, distribution or reproduction in other forums is permitted, provided the original author(s) and the copyright owner(s) are credited and that the original publication in this journal is cited, in accordance with accepted academic practice. No use, distribution or reproduction is permitted which does not comply with these terms.

Study of predictive factors for response to ^{177}LU-PSMA in patients with metastatic castration-resistant prostate cancer

Hugo Peslier[1]*, Valérie Seegers[2] and Pierre-Alban Dufour[1]

[1]Department of Nuclear Medicine, Institut de Cancérologie de l'Ouest (ICO), Angers, France, [2]Research and Statistics Department, Institut de Cancérologie de l'Ouest (ICO), Angers, France

Introduction: Metastatic castration-resistant prostate cancer (mCRPC) is an aggressive disease with a poor prognosis and few therapeutic options. In recent years, ^{177}Lu-PSMA, a novel radioligand therapy, has shown promising results in patients who have failed conventional therapies. However, around 30% of patients do not respond adequately to this treatment. In this retrospective cohort study, we examined clinical, biological, and ^{68}Ga-PSMA PET/CT-derived factors associated with poor treatment response.

Materials and methods: We conducted a retrospective cohort study including 63 patients treated at ICO Angers for progressive mCRPC following Novel Hormonal Agents and taxane-based chemotherapy. The primary endpoint was early treatment discontinuation, defined as stopping therapy at or before the 4th cycle. Secondary endpoints included PSA response and overall survival.

Results: A total of 63 patients were included in the study. Factors associated with early treatment discontinuation included a BMI < 25 kg/m^2, PSA doubling time < 2 months, hemoglobin levels <10 g/dL, albumin levels <35 g/L, lactate dehydrogenase (LDH) levels >250 IU/L and alkaline phosphatase (ALP) levels >125 IU/L. On ^{68}Ga-PSMA PET/CT imaging, low SUL_{max}, high Total Tumor Volume, and a low PSG score were also linked to early treatment discontinuation.

Conclusion: This study identified several clinical, biological, and ^{68}Ga-PSMA PET/CT-derived factors associated with early treatment discontinuation. Patients with poor overall health, aggressive or extensive disease, or low PSMA expression are at higher risk of treatment failure.

KEYWORDS

^{177}Lu-PSMA, mCRPC, predictive factors, therapeutic response, SULmax, total tumor volume, PSG score

Introduction

According to the Global Cancer Observatory, prostate cancer is the second most common cancer and the fifth leading cause of cancer-related deaths in men worldwide in 2020, with an incidence rate of 30.7 per 100,000 and a mortality rate of 7.7 per 100,000 (1).

In France, according to 2018 data from INCA (Institut National du Cancer), prostate cancer is the most common cancer and the third leading cause of cancer-related deaths in men. The median age at diagnosis is 69 years. It is a condition with a favorable prognosis, with a 5-year survival rate of 93%. Indeed, 80% of cases are diagnosed at a localized stage, and the

stage of the disease at diagnosis is a major prognostic factor (2). Notably, the 5-year survival rate of *de novo* metastatic prostate cancer is around 30% (3).

In the natural evolution of untreated prostate cancer, initial localized disease slowly progresses to locoregional involvement, and subsequently to a metastatic stage with bone, lymph node or visceral metastases. Following definitive local therapy for localized forms through radical prostatectomy or external beam radiotherapy, recurrence is observed in 27–53% of patients (4).

At the metastatic castration-resistant stage defined by biochemical or radiological disease progression in an environment with very low serum testosterone concentration (< 50 ng/dL), prostate cancer is characterized by a poor prognosis and the available therapeutic options are currently limited to anti-hormonal deprivation therapy (ADT) in combination with novel hormonal agents (NHA) (e.g., enzalutamide, abiraterone) or taxane-based chemotherapies (e.g., docetaxel and cabazitaxel). For patients with metastatic castration-resistant prostate cancer (mCRPC) with alteration in BRCA 1 or 2, Olaparib can be considered after NHA (5).

For several decades, extensive research has sought to identify cellular targets for the development of novel targeted therapies in prostate cancer. In 1987, Horoszewicz et al. first described Prostate-Specific Membrane Antigen (PSMA) (6). This is a type II transmembrane protein involved in tumor proliferation and neoangiogenesis through the metabolism of glutamate and folates. PSMA is overexpressed in most prostate cancers, approximately 1,000 times more than in normal prostatic tissue, but is also physiologically expressed in various other tissues, particularly the salivary glands. Importantly, PSMA is not exclusive to prostate cancer; it is also present on endothelial cells of neovessels in other tumors, including colon adenocarcinoma, renal cell carcinoma, lung cancer, and melanoma. Studies have shown that PSMA expression correlates with tumor grade and the presence of metastatic disease, with higher levels associated with poorer prognosis.

In the field of nuclear medicine, several synthetic ligands of PSMA have been developed with the aim of creating radiopharmaceutical drugs both for imaging and therapy (7, 8). This refers to the concept of theranostics, a term derived from the combination of 'therapy' and 'diagnostics.' Theranostics involves using the same specific ligand for a cellular target, initially labeled with an isotope dedicated to imaging (e.g., ^{99m}Tc for SPECT imaging, or ^{68}Ga and ^{18}F for PET/CT imaging). In a subsequent step, the ligand is combined with an alpha or beta-emitting radioisotope capable of destroying the previously targeted tumor cells (for exemple ^{177}Lu wich is a beta- emitter, or ^{225}Ac wich is an alpha emitter) (9).

Among the radioisotopes suitable for therapy, ^{177}Lu is a beta-emitting radionuclide with a half-life of 6.65 days, a maximum β-particle energy of 497 keV and a maximum tissue penetration of 1.8 mm. This makes it particularly suitable for targeted treatment of prostate cancer tumors and their microenvironment, minimizing damage to surrounding healthy tissue. Gamma emission with 113 and 208 keV photons allows for whole-body scintigraphy after each treatment cycle to verify the proper uptake of the radiopharmaceutical drug to all tumor targets, ensure the absence of extravasation and to perform personalized dosimetry. Comparison of each post-therapy scintigraphy also allows tracking treatment efficacy and detecting any potential disease progression that would necessitate modification of the therapeutic approach (10, 11).

The international open-labeled phase 3 trial VISION involving 831 patients, investigating the efficacy and safety of ^{177}Lu-PSMA-617 (commercialized under the name PLUVICTO®), has shown significant promise in extending imaging-based progression-free survival (median: 8.7 vs. 3.4 months) and overall survival (median: 15.3 vs. 11.3 months) when administered alongside standard-care therapy in patients with advanced and progressive PSMA-positive mCRPC, ^{177}Lu-PSMA-617 was associated with a low incidence of serious adverse events. In this study, patients were required, among other criteria, to have previously received one NHA, at least one but no more than two taxane regimens, a positive ^{68}Ga-PSMA-11 PET-CET scan, an Eastern Cooperative Oncology Group (ECOG) Performance Status score of 0 through 2, a life expectancy >6 months and an adequate organ function. The positivity criteria for ^{68}Ga-PSMA PET/CT in the VISION study are presented below in Table 1 (12). Based on PSMA PET/CT criteria, patients who were classified as screen failures in the VISION trial had worse short-term outcomes than those who were classified as eligible (13).

In France, PLUVICTO® was first used in 2021 under a Temporary Authorization for Use. Since May 2023, it has been granted Marketing Authorization and is now routinely available for the treatment of adult patients with mCRPC who have progressive disease and are positive for PSMA, and who have been treated with androgen pathway inhibitor hormone therapy and taxane-based chemotherapy (14).

The initiation of treatment with PLUVICTO® is complex and requires the expertise of a nuclear medicine physician in collaboration with an oncologist. Joint recommendations have been issued by the European Association of Nuclear Medicine (EANM) and the Society of Nuclear Medicine and Molecular Imaging (SNMMI) (15).

Before starting treatment, several eligibility criteria must be confirmed. In a theranostic approach, a PET scan with ^{68}Ga-PSMA is required to identify PSMA-positive tumor targets and ensure there are no PSMA-negative lesions meeting the specified size criteria. Additionally, a standard biological assessment including a complete blood count, liver function tests and renal function tests must be conducted to rule out contraindications such as cytopenias or severe renal or hepatic insufficiency. A thorough evaluation of the patient's general health and comorbidities should be performed on a case-by-case basis during a pre-treatment consultation. Relative contraindications established by nuclear medicine societies include: a life expectancy of less than 3 months, an ECOG Performance Status of ≥3, uncontrollable urinary incontinence, acute urinary obstruction, severe comorbidities (e.g., psychiatric or cardiovascular conditions

TABLE 1 Interpretation criteria for ^{68}Ga-PSMA PET in the VISION study.

Positive ^{68}Ga-PSMA PET/CT	Négative ^{68}Ga-PSMA PET/CT
At least one PSMA-positive lesion *And* No PSMA-negative lesion	No PSMA-positive lesion *Or* Presence of at least one PSMA-negative lesion meeting the following size criteria: • a short axis ≥ 2.5 cm for lymph nodes • a short axis ≥ 1 cm for visceral or bone metastatic lesions
PSMA-positive lesion	**PSMA-negative lesion**
Lesion with uptake higher than that of the liver	Lesion with uptake equal or less than that of the liver

affecting hydration), severe renal or hepatic insufficiency (GFR < 30 mL/min, creatinine > twice the upper limit of normal, liver enzymes > five times the upper limit of normal), active infection, and significant cytopenias (WBC < 2.5 G/L, ANC < 1.5 G/L PLT < 75 G/L).

The standard treatment regimen consists of 6 cycles administered every 6 weeks, each involving an intravenous injection of 7.4 GBq of ^{177}Lu-PSMA-617. Due to the co-emission of a 208 keV gamma ray by ^{177}Lu, a whole-body scan is performed within 48 h after each injection to confirm proper radiopharmaceutical binding to tumor targets, check for tumor progression that might impact treatment continuation and ensure there is no extravasation at the injection site or contamination.

During and after PLUVICTO® administration, radioprotection measures must be implemented to prevent radioactive waste from contaminating the environment and to protect both healthcare staff and the patient's close contacts. Specifically, patients should be hospitalized for 6 to 24 h to collect their urine in decay containers. Radioprotection guidelines for home care can be adjusted based on dose rate measurements taken at the end of hospitalization.

Ongoing clinical and biological monitoring is essential during treatment, including assessing general health, screening for hematological and non-hematological toxicities and tracking PSA levels with tests conducted every 3 weeks. In cases of severe toxicity, adjustments to the dose, delays or discontinuation of treatment may be considered on an individual basis. Efficacy should be evaluated with Computed Tomography (CT) scans and bone scintigraphy every 12 weeks and at the end of the 6 treatment cycles. Indeed, as per the 2024 EAU – EANM – ESTRO – ESUR – SIOG Guidelines on Prostate Cancer, ^{68}Ga-PSMA PET/CT is not yet recommended as imaging modality for therapeutic assessment in clinical practice. The treatment regimen for ^{177}Lu-PSMA administered at ICO Angers is presented below in Figure 1.

Despite initial patient selection based on VISION study criteria, several retrospective studies indicate that approximately 30% of patients treated with ^{177}Lu-PSMA-617 do not respond favorably (PSA decline <50% during treatment), and there is limited knowledge regarding predictive factors for treatment success (16).

To prevent administering a complex, costly, and potentially side-effect-laden treatment to patients who are unlikely to benefit, it is crucial to identify the patient groups most likely to respond to ^{177}Lu-PSMA therapy. The aim of this study was to pinpoint clinical, biological and nuclear-imaging parameters in the pretherapeutic phase that are associated with a poor response to treatment.

Methods

Study design and population

We conducted a single-center, retrospective cohort including all consecutive patients treated at ICO Angers for mCRPC who received at least one cycle of ^{177}Lu-PSMA between February 2022 and December 2023.

Inclusion criteria encompassed the presence of mCRPC, progression following at least one line of taxane chemotherapy and second-generation hormone therapy, and a positive ^{68}Ga-PSMA PET/CT scan according to the VISION study criteria mentioned above.

Exclusion criteria included severe cytopenias and severe renal or hepatic insufficiency, as outlined in the PLUVICTO® product's Summary of Product Characteristics. Additionally, patients involved in clinical research protocols receiving experimental treatments during the ^{177}Lu-PSMA therapy period, and those who did not consent to the use of their health data for research purposes, were also excluded.

The following data were collected from the patient's electronic medical records: characteristics related to the initial disease and previously received treatments, clinical and biological characteristics at the start of ^{177}Lu-PSMA treatment, and characteristics of the ^{68}Ga-PSMA PET/CT scan before the first treatment cycle (C1).

Each treatment decision was made during a multidisciplinary tumor board meeting including oncologists and nuclear medicine physicians. During a pre-therapeutic consultation, patients were informed about the treatment modalities, expected benefits, and potential adverse effects. Written consent was systematically obtained. A consent form for the use of health data for research purposes was provided and completed by each patient who started treatment during the inclusion period. The study protocol was previously approved by an independent ethics committee.

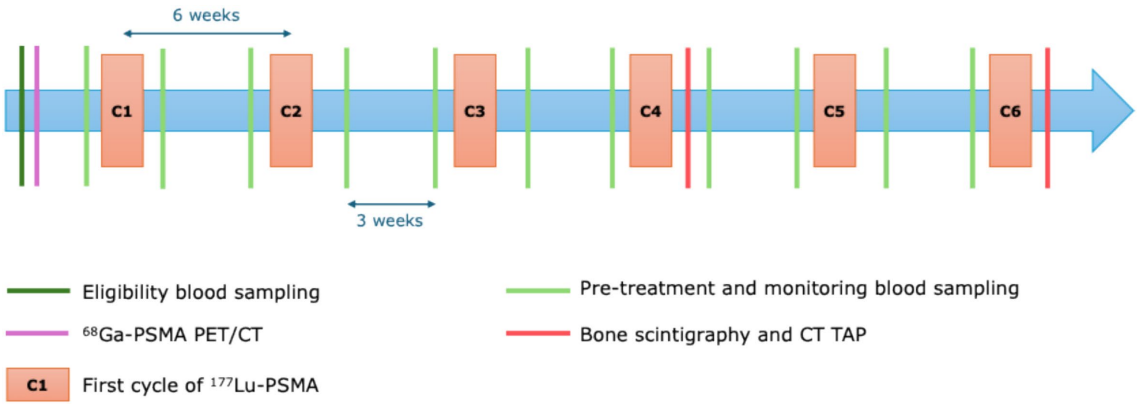

FIGURE 1
^{177}Lu-PSMA treatment regimen and monitoring at ICO Angers.

^{68}Ga-PSMA PET/CT and pre-treatment preparation

^{68}Ga-PSMA PET/CT scans were performed in accordance with the 2017 European Association of Nuclear Medicine and Society of Nuclear Medicine and Molecular Imaging (EANM and SNMMI) standard recommendations. The first 15 patients underwent their scans at the ICO site in Nantes: 7 on a 2019 Siemens Biograph Vision PET scanner and 8 on a 2020 Siemens Biograph Vision PET scanner. 1 patient had his scan at the Institut Gustave Roussy in Paris on a Siemens Biograph Vision 600 PET scanner, and 47 patients underwent their scans at ICO Angers: 24 on a Philips VEREOS PET scanner and 23 on a GE Discovery IQ PET scanner.

Each scan was interpreted by an experienced nuclear medicine physician on a Syngo.via platform (Siemens Healthineers, Erlangen, Germany), including both visual and quantitative analyses. Lesions were considered PSMA-positive if their uptake intensity was equal to or greater than that of healthy liver tissue.

Measurements of Maximum Standardized Uptake Value – Lean body mass (SUL_{max}) and Total Tumor Volume (TTV) were performed using the automatic segmentation module of the Syngo.via software, which allowed for automatic segmentation of all PSMA-positive lesions with a segmentation threshold of 41% of each lesion's SULmax (this threshold is the commonly used in the literature for lesion segmentation on PET images). To quantify the uptake of tumor lesions, we chose to use SUL_{max}, a semi-quantitative index that accounts for lean body mass, as opposed to SUV_{max} which is based on the total body weight. Indeed, due to significant differences in body morphotypes within the study population, the use of SUL_{max} allows for better interindividual comparability.

Patients were categorized into three groups based on the tracer uptake pattern for the definition of the PSG (PET Tumor-to-Salivary Gland) score, based on a visual analysis of the Maximum Intensity Projection image: patients whose more than 80% of lesions had higher uptake than the salivary glands were classified in the 'High' group; patients whose more than 80% of lesions had lower uptake than the salivary glands were classified in the 'Low' group; the remaining patients who did not fit into the first two categories were classified in the 'Intermediate' group. In an international multicenter retrospective study including 237 men, Hotta et al. demonstrated that this new visual score is predictive of the response to ^{177}Lu-PSMA treatment with better PSA reduction and longer overall survival for 'High' scores, and with a substantial interreader reproducibility (17).

^{177}Lu-PSMA therapy protocol

The ^{177}Lu-PSMA treatment protocol consisted of administering 6 cycles of 7,4 GBq, each spaced 6 weeks apart, in the context of day hospitalization. At the end of each cycle, whole-body scintigraphy was performed to verify the proper distribution of the radiopharmaceutical to the tumor targets, the absence of extravasation at the injection site or contamination, and the absence of new uptake sites that could suggest disease progression during treatment.

Regular clinical and biological monitoring was established, with laboratory tests performed within 7 days before each cycle and 3 weeks after each treatment cycle. These tests included PSA level measurement to track changes, complete blood counts, comprehensive liver and kidney function tests, and albumin levels to ensure the treatment's tolerability. Each patient was regularly consulted by both their treating oncologist and the nuclear medicine physician overseeing the treatment. In cases of severe adverse effects, such as cytopenias detected during monitoring, decisions regarding the spacing, postponement or permanent discontinuation of treatment cycles were made on a case-by-case basis by the multidisciplinary medical team.

At the end of the fourth cycle (C4) and the sixth cycle (C6), bone scintigraphy and CT scans of the thorax, abdomen, and pelvis (TAP) were performed to evaluate therapeutic efficacy. An earlier interim evaluation could be requested in case of suspected disease progression during treatment, before C4 or C6.

Outcomes

The primary endpoint was poor response to ^{177}Lu-PSMA, defined by early discontinuation of treatment between the first dose and post-C4 therapeutic assessment for any reason (e.g., progression objectively confirmed by CT or bone scan, or early treatment interruption due to severe hematological toxicity or deterioration in general condition, where continuing treatment was considered unreasonable). Secondary endpoints included a lack of treatment response as measured by PSA levels and the description of overall survival in treated patients. The lack of response based on PSA levels was defined as the proportion of patients who did not achieve a reduction of more than 50% from their baseline PSA level, as measured on the last biological assessment performed prior to C1.

Statistical analysis

Clinical and biological characteristics, disease extent at the start of ^{177}Lu-PSMA treatment, and prior treatments received are described for all patients included in this study, based on the nature of the variable studied, with the number of missing data presented where applicable. Quantitative or discrete data are summarized with median, 25^{th}-75^{th} percentiles, minimum, maximum, mean and standard deviation. Categorical and binary data are described by the number and percentage of data points for each modality.

Univariate analyses

To study the factors associated with early treatment discontinuation (primary endpoint), we distinguish between two groups of patients: those who were unable to receive more than 4 cycles and those who received 5 or 6 cycles of ^{177}Lu-PSMA. We compare characteristics related to initial disease and prior treatments, clinical characteristics at the start of ^{177}Lu-PSMA treatment and PET characteristics using ^{68}Ga-PSMA before the initiation of ^{177}Lu-PSMA treatment between these two groups using logistic regression models.

To investigate factors associated with progression or disease-related death, we used a semi-parametric Cox proportional hazards model to estimate the hazard ratios and associated *p*-values. In this model, time corresponds to the treatment regimen (C1 to C6). The

event of interest is disease progression or death related to cancer. Patients who complete all 6 cycles without progression are censored at C6. Patients who discontinue treatment before C6 without progression and without disease-related death are censored at the date of their last received cycle. Risk estimation and its 95% confidence interval are performed using the Kaplan–Meier method.

Multivariate analyses

All baseline variables are analyzed univariately first, and variables associated with survival with a p-value <0.2 are eligible for inclusion in the multivariate model. In cases of high correlation between two variables, the one most significantly associated with survival is preferred. Essential clinical characteristics for interpreting the multivariate analysis are also included in the model, regardless of their univariate significance.

For factors related to receiving 4 or fewer cycles, logistic regression models are employed. For factors associated with progression or disease-related death, Cox proportional hazards models are used.

Repeated PSA measurements

Characteristics of patients who experience a reduction in PSA levels of more than 50% after the start of treatment (compared to before treatment) are compared using logistic regression models. Individual PSA trajectories are graphically represented.

Analyses are conducted under the responsibility of the Clinical Research Department of ICO, Promotion Unit, using appropriate statistical software (R or SAS). No imputation of missing data is planned in the protocol. A p-value <0.05 is considered statistically significant. In this exploratory study, no correction for alpha inflation is planned.

Results

In this retrospective study, 63 patients were enrolled between February 2022 and December 2023. The average age at initial diagnosis was 62.2 ± 8.2 years and the average age at C1 was 71.8 ± 8.0 years.

At the time of diagnosis, 37 patients (58.7%) had metastatic disease, 16 patients (25.4%) had locally advanced disease and 10 patients (15.9%) had localized disease. A total of 34 patients (54%) had an ISUP (International Society of Urological Pathology) score of 4 or higher while 29 patients (46%) had an ISUP score below 4.

Before starting treatment, 56 patients (88.9%) had bone metastases, 35 patients (55.6%) had lymph node involvement, and 3 patients (7.9%) had visceral metastases (affecting the liver, lungs or brain). Of the group, 35 patients (55.6%) had received one line of NHA, 26 patients (41.3%) had received two lines, and 2 patients (3.2%) had received three lines. Additionally, 26 patients (41.3%) had undergone one line of taxane chemotherapy (Docetaxel only) while 37 patients (58.7%) had received two lines (Docetaxel followed by Cabazitaxel). The median initial PSA level was 67.7 ng/mL (95% CI: [19.8; 257.7]) and the median PSA doubling time before C1 was 2.2 months (95% CI: [1.4; 3.8]). On ^{68}Ga-PSMA PET/CT scans, the median SUL_{max} was 23.7 (95% CI: [18.5; 53.1]) and the median TTV was 82.2 mL (95% CI: [18.0; 251.8]). Among these patients, 18 (28.6%) had a high PSG score, 26 (41.3%) had an intermediate PSG score and 19 (30.2%) had a low PSG score.

The average time from initial diagnosis to the start of the first treatment cycle was 8.3 ± 5.8 years. The average time between the ^{68}Ga-PSMA PET/CT scan and the first treatment cycle was 1 ± 0.6 months. Resumed characteristics of the study population are presented in Table 2 and Appendix.

By the end of the study period, patients had received a median of 4 cycles of ^{177}Lu-PSMA therapy. Of these, 32 patients (50.7%) received between 1 and 4 cycles and 31 patients (49.2%) received 5 or 6 cycles. Among those who received one to four cycles, 26 discontinued treatment due to disease progression (objectively confirmed by imaging: CT or bone scan), while 6 stopped for other reasons: 3 due to hematotoxicity, 1 due to death related to heart failure, 1 due to severe hyponatremia and 1 patient who opted to discontinue despite a favorable therapeutic response.

Among patients who received five or six cycles, 4 (6.3%) experienced disease progression (objectively confirmed by imaging) and 4 were awaiting their C6. Overall, 38 patients (60.3%) saw a reduction in PSA levels of 50% or more during treatment.

Factors associated with early treatment discontinuation

In univariate analysis, the factors associated with early treatment discontinuation (four cycles or fewer) were as follows: a BMI < 25 vs. ≥ 25 kg/m^2 (OR: 3.85; 95% CI [1.30–11.11]; $p = 0.0148$), a PSA doubling time < 2 months vs. ≥ 2 months (OR: 3.57; 95% CI [1.22–10.00]; $p = 0.0206$), hemoglobin <10 g/dL vs. ≥ 10 g/dL (OR: 4.89; 95% CI [1.21–19.75]; $p = 0.0259$), albumin <35 g/L vs. ≥ 35 g/L (OR: 4.97; 95% CI [1.39–17.82]; $p = 0.0138$), LDH > 250 IU/L vs. ≤ 250 IU/L (OR: 5.96; 95% CI [1.99–17.86]; $p = 0.0014$), and ALP > 125 IU/L vs. ≤ 125 IU/L (OR: 4.07; 95% CI [1.42–11.7]; $p = 0.0091$). On ^{68}Ga-PSMA PET/CT, a lower SUL_{max} (per unit decrease: OR: 1.02; 95% CI [1.00–1.04]; $p = 0.0361$), a higher TTV compared to the median (OR: 4.62; 95% CI [1.60–13.35]; $p = 0.0047$) and a low vs. high PSG score (OR: 5.63; 95% CI [1.37–23.17]; $p = 0.0166$) were also associated with early treatment discontinuation. In multivariate analysis, BMI, PSA doubling time, PSG score, and TTV remained significantly associated with early treatment discontinuation.

The results of the statistical analyses are presented below in Tables 3, 4.

Additionally, aside from the PSG score, all these factors are significantly associated with disease progression and prostate cancer-specific mortality. This includes the presence of widespread bone involvement (HR: 2.34; 95% CI [1.14–4.78]; $p = 0.0198$) and pulmonary metastases (HR: 2.63; 95% CI [1.00–6.89]; $p = 0.0493$). In the multivariate analysis, BMI, PSA doubling time, albumin levels and TTV remain significant predictors. However, metastatic status at initial diagnosis (HR: 3.33; 95% CI [1.09–10.00]; $p = 0.0357$) and ECOG Performance Status ≥1 versus 0 (HR: 3.47; 95% CI [1.25–9.68]; $p = 0.0173$) also emerge as significant.

Detailed results are presented in the Appendix Tables 1, 2.

TABLE 2 Resumed characteristics of the study population.

Variable	Modality	4 cycles or less (n = 32 patients)	5 or 6 cycles (n = 31 patients)
Age at initial diagnosis	Min/Max	54.0/77.0	48.0/77.0
	Mean (std)	64.9 (5.8)	62.2 (8.2)
Age at first cycle of ^{177}Lu-PSMA	Min/Max	60.0/91.0	52.0/87.0
	Mean (std)	72.6 (7.5)	71.0 (8.6)
ISUP score	< 4	17 (53.1%)	12 (38.7%)
	≥ 4	15 (46.9%)	19 (61.3%)
Extent at diagnosis	Localized or locally advanced	14 (43.8%)	12 (38.7%)
	Metastatic	18 (56.2%)	19 (61.3%)
Number of previous NHA	1	16 (50.0%)	19 (61.3%)
	2	16 (50.0%)	10 (32.3%)
	3	0 (0%)	2 (6.5%)
Number of previous taxane	1	11 (34.4%)	15 (48.4%)
	2	21 (65.6%)	16 (51.6%)
Baseline PSA level	Min/Max	0.2/1032.4	0.01/1066.0
	Mean (std)	198.3 (240.3)	149.9 (242.9)
PSA doubling time (month)	≥ 2	14 (43.8%)	22 (73.3%)
	< 2	18 (56.2%)	8 (26.7%)
	NA	0	1
Time between initial diagnosis and first cycle of ^{177}Lu-PSMA	Min/Max	1.0/19.0	2.0/23.0
	Mean (std)	7.7 (5.6)	8.8 (6.0)
ECOG Performance Status	0	6 (18.8%)	11 (35.5%)
	≥ 1	26 (81.2%)	20 (64.5%)
Hb (g/dL)	≥ 10	21 (65.6%)	28 (90.3%)
	< 10	11 (34.4%)	3 (9.7%)
PLT (G/L)	> 150	29 (93.5%)	27 (87.1%)
	≤ 150	2 (6.5%)	4 (12.9%)
	NA	1	0
Albumin (g/L)	≥ 35	17 (56.7%)	26 (86.7%)
	< 35	13 (43.3%)	4 (13.3%)
	NA	2	1
Bone involvement	No	2 (6.2%)	5 (16.1%)
	Yes	30 (93.8%)	26 (83.9%)
Lymph node involvement	No	15 (46.9%)	13 (41.9%)
	Yes	17 (53.1%)	18 (58.1%)
Visceral metastases (liver, lung, brain)	No	25 (78.1%)	28 (90.3%)
	Yes	7 (21.9%)	3 (9.7%)

Min, Minimum; Max, Maximum; std, Standard Deviation; NA, Not Applicable; ^{177}Lu, lutetium-117; NHA, Novel Hormonal Agent; PSMA, prostate-specific membrane antigen; ISUP, International Society of Urological Pathology; ECOG, Eastern Cooperative Oncology Group; PSA: prostate-specific antigen; Hb, hemoglobin; PLT, Platelets; SUL_{max}, Maximum Standardized Uptake value – Lean body mass.

Factors associated with poor PSA response

In univariate analysis, the clinico-biological factors associated with a reduction in PSA of less than 50% during treatment were as follows: BMI < 25 vs. ≥ 25 kg/m^2 (OR: 3.85; 95% CI [1.30–11.11]; p = 0.0148), PSA doubling time < 2 vs. ≥ 2 months (OR: 3.54; 95% CI [1.21–10.30]; p = 0.0206), hemoglobin <10 g/dL vs. ≥ 10 g/dL (OR: 4.89; 95% CI [1.21–19.75]; p = 0.0259), albumin <35 g/L vs. ≥ 35 g/L (OR: 4.97; 95% CI [1.39–17.82]; p = 0.0138), LDH > 250 IU/L vs. ≤ 250 IU/L (OR: 5.96; 95% CI [1.99–17.86]; p = 0.0014), and ALP > 125 IU/L vs. ≤ 125 IU/L (OR: 4.07; 95% CI [1.42–11.7]; p = 0.0091). On ^{68}Ga-PSMA PET/CT, a higher SUL_{max} (per unit increase: OR = 0.98; 95% CI

TABLE 3 Risk of early treatment discontinuation – univariate analysis.

Variable	Modality	OR	OR_{inf}	OR_{sup}	*p* value
Age at initial diagnosis	1 more unit	1.06	0.98	1.14	0.1387
Age at first cycle of ^{177}Lu-PSMA	1 more unit	1.03	0.96	1.09	0.4281
ISUP score	≥ 4 vs. < 4	0.56	0.20	1.52	0.2528
Extent at diagnosis	Localized or locally advanced vs. metastatic	0.81	0.30	2.22	0.6847
	Locally advanced vs. localized	1.29	0.26	6.27	0.7560
	Metastatic vs. localized	0.95	0.23	3.83	0.9395
Initial treatment by radical prostatectomy	Yes vs. No	0.81	0.25	2.57	0.7144
Initial treatment by radiotherapy	Yes vs. No	0.73	0.27	1.98	0.5358
Enzalutamide	Yes vs. No	0.71	0.26	1.95	0.5032
Abiraterone	Yes vs. No	3.33	0.92	12.11	0.0674
Number of previous NHA	1 more unit	1.17	0.48	2.83	0.7316
Docetaxel	Yes vs. No	0.00	0.00	Inf	0.9915
Cabazitaxel	Yes vs. No	2.06	0.74	5.76	0.1672
Number of previous taxane based chemotherapy	1 more unit	1.79	0.65	4.93	0.2606
Baseline PSA	1 more unit	1.00	1.00	1.00	0.4278
PSA doubling time (month)	< 2 vs. ≥ 2	3.54	1.21	10.30	0.0206
Time between initial diagnosis and first cycle of ^{177}Lu-PSMA (years)	1 more unit	0.97	0.89	1.06	0.4537
	> 6 vs. ≤ 6	0.83	0.31	2.22	0.7070
Regular need of level 2 or 3 analgesics	Yes vs. No	2.06	0.74	5.76	0.1672
ECOG Performance Status	≥ 1 vs. 0	2.38	0.75	7.55	0.1398
BMI (kg/m^2)	≥ 25 vs. < 25	0.26	0.09	0.77	0.0148
Hb (g/dL)	< 10 vs. ≥ 10	4.89	1.21	19.75	0.0259
PLT (G/L)	≤ 150 vs. > 150	0.47	0.08	2.75	0.3989
WBC (G/L)	< 4 vs. ≥ 4	0.54	0.12	2.47	0.4259
Albumin (g/L)	< 35 vs. ≥ 35	4.97	1.39	17.82	0.0138
Corrected calcemia (mmol/L)	1 more unit	0.54	0.02	15.89	0.7180
LDH (U/L)	> 250 vs. ≤ 250	5.96	1.99	17.86	0.0014
ASAT (UI/L)	> 30 vs. ≤ 30	0.96	0.31	2.98	0.9414
ALAT (UI/L)	> 35 vs. ≤ 35	0.22	0.02	2.07	0.1844
gGT (UI/L)	> 45 vs. ≤ 45	1.47	0.51	4.21	0.4769
ALP (UI/L)	> 125 vs. ≤ 125	4.07	1.42	11.70	0.0091
SUL_{max}	1 more unit	0.98	0.96	1.00	0.0361
	Higher vs. Lower	0.38	0.14	1.05	0.0615
PSG score	Intermediate vs. High	3.03	0.84	10.99	0.0912
	Low vs. High	5.63	1.37	23.17	0.0166

(Continued)

TABLE 3 (Continued)

Variable	Modality	OR	OR_{inf}	OR_{sup}	*p* value
Total Tumor Volume	1 more unit	1.00	1.00	1.01	0.0475
	Higher vs. Lower	4.62	1.60	13.35	0.0047
Bone involvement	Yes vs. No	2.88	0.52	16.14	0.2279
	Single/oligometastatic vs. diffuse/widespread	0.56	0.17	1.91	0.3562
	No vs. diffuse/widespread	0.30	0.05	1.73	0.1775
Epiduritis	Yes vs. No	2.10	0.75	5.84	0.1553
Lymph node involvement	Yes vs. No	0.82	0.30	2.21	0.6934
Visceral metastases (liver, lung, brain)	Yes vs. No	2.61	0.61	11.21	0.1960
Time between ^{68}Ga-PSMA PET/CT and first cycle of ^{177}Lu-PSMA	1 more unit	1.23	0.50	3.06	0.6501

TABLE 4 Risk of early treatment discontinuation – multivariate analysis.

Variable	Modality	OR	OR_{inf}	OR_{sup}	Pr(>|t|)
Abiraterone	Yes vs. No	1.25	0.99	1.59	0.0703
PSA doubling time (month)	< 2 vs. ≥ 2	1.40	1.16	1.70	0.0013
BMI (kg/m^2)	≥ 25 vs. < 25	0.74	0.61	0.90	0.0042
Albumin (g/L)	< 35 vs. ≥35	1.25	0.97	1.61	0.0980
LDH (U/L)	> 250 vs. ≤ 250	1.24	1.00	1.53	0.0559
ALAT (UI/L)	> 35 vs. ≤ 35	0.78	0.54	1.14	0.2065
PSG score	Intermediate vs. High	1.09	0.85	1.39	0.5007
	Low vs. High	1.43	1.07	1.90	0.0182
Total Tumor Volume	Higher vs. lower	1.31	1.02	1.67	0.0373
Visceral metastases (liver, lung, brain)	Yes vs. No	0.86	0.63	1.18	0.3617
Extent at diagnosis	M1 vs. M0	0.85	0.64	1.13	0.2726
Time between initial diagnosis and first cycle of ^{177}Lu-PSMA (years)	> 6 vs. ≤ 6	0.84	0.63	1.12	0.2410

[0.96–1.00]; $p = 0.0361$), a higher TTV compared to the median (OR: 4.62; 95% CI [1.60–13.35]; $p = 0.0047$) and a low vs. high PSG score (OR: 5.63; 95% CI [1.37–23.17]; $p = 0.0166$) were associated with a reduction in PSA of less than 50%.

In multivariate analysis, BMI, PSA doubling time, LDH levels, and PSG score remained significantly associated with PSA response. However, ECOG Performance Status ≥1 vs. 0 (HR: 1.34; 95% CI [1.05–1.71]; $p = 0.0246$) also became significant.

The PSA level trends and detailed statistical analysis results are presented in Appendix Figure 1 and Appendix Tables 3, 4.

Overall survival from the first cycle of ^{177}Lu-PSMA

The median follow-up period was 13.7 months (95% CI: 10.5–20.9). A total of 34 deaths were observed in the cohort with a median overall survival of 12.8 months (95% CI: 9.4–18.1). The overall survival of the cohort is depicted in Figure 2.

Discussion

In this study, we assessed the impact of various clinico-biological factors and ^{68}Ga-PSMA PET/CT findings on the response to ^{177}Lu-PSMA treatment in patients with metastatic castration-resistant prostate cancer who had progressed after at least one line of taxane chemotherapy and NHA. We categorized the study population into two groups: patients who received 4 cycles or fewer of treatment versus those who received 5 to 6 cycles. We defined the group receiving 4 or fewer cycles as having a poor therapeutic response. This group also included 6 patients who discontinued treatment for reasons other than disease progression, allowing us to account for potential adverse effects of ^{177}Lu-PSMA, comorbidities, and practical management issues.

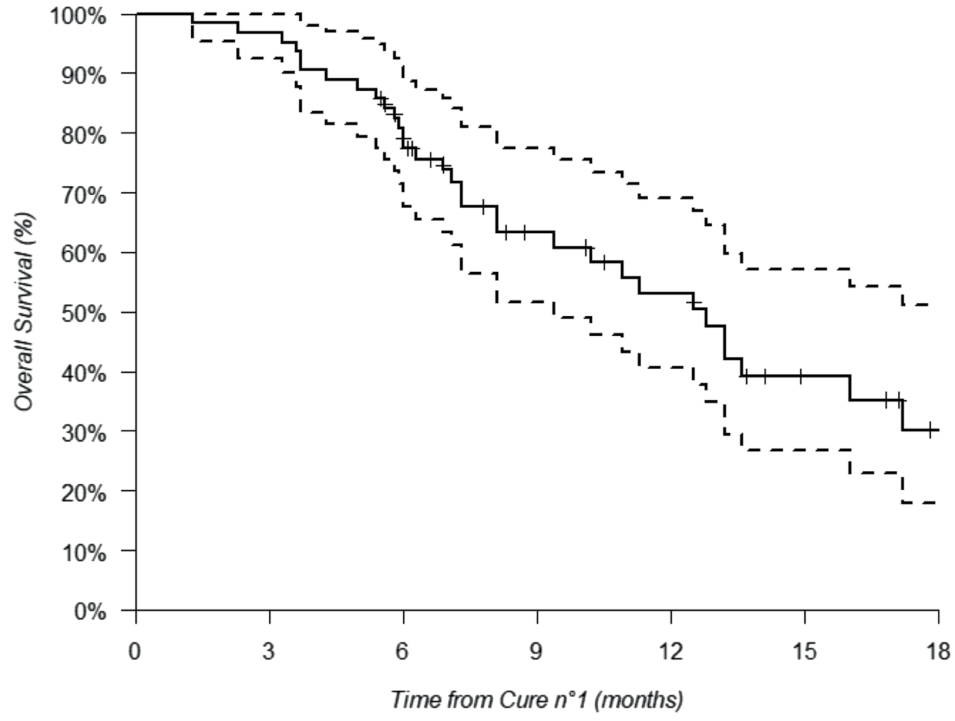

Number at risk

	n=63	n=61	n=48	n=26	n=20	n=10	n=5

Time (months)	n.risk	n.event	survival	lower 95% CI	upper 95% CI
3	61	2	0.968	0.926	1
6	48	12	0.774	0.676	0.886
9	26	7	0.632	0.517	0.774
12	20	4	0.53	0.406	0.692
15	10	5	0.391	0.268	0.571
18	5	2	0.302	0.179	0.511

FIGURE 2
Overall survival of the study population.

Impact of clinico-biological factors on response to ^{177}Lu-PSMA

Our analysis identified several clinico-biological factors associated with an early treatment discontinuation, early progression and low PSA response rate: BMI < 25 kg/m^2, short PSA doubling time, decreased hemoglobin and albumin level and increased LDH and ALP levels. While ECOG Performance Status ≥1 does not appear to be a predictor of early treatment discontinuation, it is associated with early progression and a poorer PSA response in multivariate analysis.

A low BMI, low serum albumin, and a high ECOG Performance Status generally reflect a state of malnutrition and are associated with a deterioration of the patient's overall condition. Cancer-associated malnutrition is known to impair response to chemotherapy (18–20). Based on our findings, we suggest that malnutrition may be linked to a poorer response to ^{177}Lu-PSMA. Further prospective studies are needed to confirm the impact of malnutrition on treatment outcomes with ^{177}Lu-PSMA. Nonetheless, close monitoring of patient's nutritional status before and during treatment is crucial. In cases of confirmed malnutrition, initiating a re-nutrition strategy could potentially improve therapeutic efficacy and survival.

Interestingly, higher BMI has been linked to better overall survival in cancer patients (21). This finding is paradoxical given that obesity is generally associated with increased all-cause mortality in the general population (22). This discrepancy might be due to one or more confounding factors, as BMI alone is not a reliable indicator of body composition or nutritional status. Body composition can vary widely by age and ethnicity, and individuals with the same BMI can have different distributions of lean and fat mass, which affects prognosis differently (23). For instance, a malnourished individual with sarcopenia but a normal BMI may have a worse prognosis compared to someone with a high BMI but without sarcopenia (24–26).

Additionally, our study did not consider recent weight loss before treatment, which could be another confounding factor (27, 28).

While metastatic versus non-metastatic status at initial diagnosis is not a predictor of early treatment discontinuation, it is associated with early progression in multivariate analysis. In a retrospective study, Francini et al. demonstrated improved overall survival in patients with metachronous versus synchronous hormone-sensitive metastatic prostate cancer (29). Similarly, Bajeot et al. reported that synchronous metastatic patients were more symptomatic and had a higher metastatic burden compared to their metachronous counterparts (30). This leads us to hypothesize that the synchronous metastatic patients in our cohort likely had a more aggressive disease, which may have adversely affected their therapeutic response.

PSA doubling time is a dynamic measure of PSA progression and is widely recognized as one of the most reliable biological markers of prostate cancer aggressiveness. In a prospective study of 1,804 men with localized prostate cancer, D'Amico et al. showed that a PSA velocity exceeding 2 ng/mL per year in the year before diagnosis was associated with a tenfold higher risk of prostate cancer-specific mortality compared to those with a PSA velocity of 2 ng/mL per year or less, following radical prostatectomy (31). Likewise, in a retrospective study of 8,669 patients treated with surgery or radiotherapy, D'Amico et al. demonstrated that a PSA doubling time of less than 3 months was linked to significantly shorter prostate cancer-specific survival after biochemical recurrence, with a Hazard Ratio of 19.6 (32). Consistent with our findings, other studies have shown a significant link between PSA doubling time and progression-free survival after ^{177}Lu-PSMA, with a short or negative doubling time predicting poor therapeutic response (33, 34). Based on our results and the existing literature, PSA doubling time also appears to reflect disease aggressiveness in the metastatic castration-resistant stage, with an impact on the response to ^{177}Lu-PSMA. However, the initial PSA level before ^{177}Lu-PSMA treatment does not appear to predict treatment response (35, 36).

In metastatic prostate cancer, elevated LDH levels are linked to shorter overall survival and poorer progression-free survival (PFS) (37). Similarly, in cases of bone metastatic prostate cancer, elevated ALP levels indicate increased osteoblastic activity and greater disease burden (38, 39), with a negative impact on overall survival (40). Other studies have confirmed that an elevation of these two markers is associated with a reduction in PFS after ^{177}Lu-PSMA (34, 36, 41–45). In our cohort, elevation of these two biological markers also predict a poor therapeutic response to ^{177}Lu-PSMA, as they are associated with earlier discontinuation of treatment. Thus, the elevation of these markers may also reflect aggressive metastatic disease.

A decrease in hemoglobin levels is frequently observed in cancer patients and is often due to multiple factors. These can include disease-related issues such as marrow infiltration, nutritional deficiencies, the inflammatory syndrome induced by the disease, or chemotherapy-induced toxicity affecting hematopoietic precursors. Low hemoglobin levels are known to be associated with reduced overall survival and lower treatment efficacy (46, 47). In our study, a hemoglobin level below 10 g/dL was strongly linked to early treatment discontinuation, early disease progression and a poorer PSA response with significant findings across all multivariate analyses. Therefore, investigating and addressing treatable causes of anemia may be beneficial for improving the response to ^{177}Lu-PSMA.

Contrary to several previous reports, we did not find a significant association between regular use of analgesics of levels 2 or 3 and early treatment discontinuation, early progression or PSA response (36, 48).

Lastly, we could not demonstrate a significant association between previous treatments received at the metastatic castration-resistant stage and response to ^{177}Lu-PSMA. However, the recent phase 3 clinical trial PSMAFore demonstrated that ^{177}Lu-PSMA-617 treatment prolonged radiographic PFS versus androgen receptor pathway inhibitor change in taxane-naïve mCRPC patients (49). Moreover, another phase 2 clinical trial, UpFrontPSMA, demonstrated that a sequential treatment including ^{177}Lu-PSMA followed by docetaxel resulted in a better therapeutic response based on PSA reduction compared to docetaxel alone (50). Finally, the TheraP clinical trial, which included 200 patients, found that ^{177}Lu-PSMA was more effective than Cabazitaxel in reducing PSA levels in progressive mCRPC patients eligible for Cabazitaxel. This suggests that earlier use of ^{177}Lu-PSMA before taxane chemotherapy failure may improve therapeutic response (51).

We were also unable to identify a significant link between initial disease characteristics at diagnosis (e.g., initial stage, histopathological grade), disease duration, type of local treatment (if any), and response to ^{177}Lu-PSMA.

Impact of metabolic factors on ^{68}Ga-PSMA PET/CT

In our analysis of ^{68}Ga-PSMA PET/CT, we identified that a low SUL_{max}, a low PSG score, and a high TTV are associated with a poorer therapeutic response.

SUL_{max} measures the maximum activity within the most intense tumor voxel on ^{68}Ga-PSMA PET/CT, adjusted for injected activity and the patient's lean body mass. This unitless value reflects the tumor's avidity for the tracer and thus the expression of membranous PSMA. Consequently, a lesion with high uptake of ^{68}Ga-PSMA results in intense binding and a high SUL_{max}. Other related measures include SUV_{max}, which quantifies the activity of the most intense voxel relative to total body weight, and SUV_{mean}, which measures the average activity within a segmented tumor volume, also relative to total body weight.

Our findings are consistent with those reported by Kuo et al. in their analysis of patients from the VISION study, which showed that high SUV_{mean} is associated with better PFS and overall survival (52). Similarly, Eisazadeh et al. found that a high SUL_{max} /Liver SUL_{mean} ratio was associated with longer PFS in patients treated with ^{177}Lu-PSMA I&T (53). Additionally, a prospective study by Emmett et al. which included 14 patients, demonstrated that high SUV_{max} or SUV_{mean} values correlate with a better PSA response (54).

Our results also confirm the predictive value of the PSG score, as described by Hotta et al., which considers the overall intensity of PSMA expression across all tumor lesions. An uptake higher than that of the salivary glands for most lesions predicts a better response to ^{177}Lu-PSMA. Conversely, an uptake lower than that of the salivary gland and, even more so, lower than that of the liver for most lesions predicts a poor response, with earlier treatment discontinuation and a less favorable PSA response (17). These results suggest that the intensity and homogeneity of lesions are key factors influencing the therapeutic response to ^{177}Lu-PSMA.

Furthermore, a high TTV is a predictive factor for poor response, associated with early treatment discontinuation, early progression and a worse PSA response. This finding corroborates Kuo et al.'s results in their analysis of VISION data (55) and Wang et al.'s findings, which showed an association between high tumor volume and poorer PSA response (56). In line with this, we also observed that diffuse osteomedullary infiltration on ^{68}Ga-PSMA PET/CT is associated with early progression.

In our study population, a low proportion of patients had undergone ^{18}F − FDG PET/CT in addition to ^{68}Ga-PSMA PET/CT before starting PLUVICTO® to detect dedifferentiated tumor lesions. Consequently, we were unable to assess the impact of the presence of FDG-avid and PSMA-low lesions (FDG+/PSMA−) on therapeutic response. Rosar et al. demonstrated in their retrospective study that the FDG SUV_{max} /PSMA SUV_{max} ratio calculated across multiple target lesions per patient was predictive of therapeutic response after 2 cycles of ^{177}Lu-PSMA. Specifically, an increase in this ratio (e.g., the presence of FDG+/PSMA− lesions) was associated with a poorer therapeutic response (57).

Several studies have demonstrated the adverse impact of visceral metastases, particularly hepatic involvement, on PFS and overall survival. A meta-analysis involving 1,504 patients indicated that the presence of visceral metastases is linked to both poorer biochemical response and shorter PFS and overall survival (58). We were unable to show this negative association in our cohort, likely due to limited statistical power: only 10 out of 63 patients had visceral involvement, and of these, only 3 received more than four cycles. However, we did find that pulmonary or pleural metastatic involvement was associated with early progression.

The observed overall survival in our study (median: 12.8 months) is lower than that reported in the VISION study (median: 15.3 months). This difference may be due to our more permissive inclusion criteria, which allowed us to include patients who were more severely impaired and had more extensive metastatic involvement. For instance, patients with a Superbonescan were excluded from the VISION study but were included in our cohort. Our study aimed to evaluate factors associated with the response to ^{177}Lu-PSMA in real-world conditions, which naturally differ from those in a clinical trial setting. Moreover, a higher proportion of patients in our cohort received Cabazitaxel (60.3% compared to 41.8% in the VISION study). Indeed, according to the prospective TheraP trial, prior treatment with Cabazitaxel is associated with poorer PFS when followed by ^{177}Lu-PSMA. Additionally, our study had a shorter median follow-up (13.7 months vs. 20.9 months), which could lead to an underestimation of overall survival. However, it is noteworthy that the proportion of patients achieving a PSA reduction of ≥50% during treatment was higher in our study compared to the VISION study (60.3% vs. 46.0%).

Additionally, it is interesting to note that the incidence of progression by C4 or earlier was higher among the initial patients treated in our cohort. This may be due to the overrepresentation of high tumor volumes and low PSG scores among these early patients. These patients also exhibited the most severe clinical and biological impairment. We can hypothesize that the latter patients were better selected, leading to more favorable therapeutic outcomes.

Main limitations of the study

The primary limitations of this study include its retrospective design, which may introduce recall bias, the small sample size that limits statistical power, and its monocentric nature, which could introduce selection bias and center-specific effects. Specifically, this cohort consists of patients treated at a center specialized in cancer care (Centre de Lutte Contre le Cancer - CLCC) with management practices that might differ from those at other hospital settings, including conventional hospitals.

Additionally, we were unable to investigate the impact of molecular biomarkers on treatment response due to their limited use in routine practice. For example, androgen receptor gene amplification, determined through blood sampling, is associated with reduced PFS in several studies (59–61). Moreover, there are rare cases of patients with lesions showing high ^{68}Ga-PSMA avidity and no FDG+/PSMA− lesions, who nevertheless exhibit a poor therapeutic response to ^{177}Lu-PSMA. Some data suggest that genomic alterations such as BRCA2 mutation or neuroendocrine differentiation, could play a key role in treatment resistance (62).

A summarized comparison of our results with those of the previously mentioned studies is available in Appendix Table 5.

Future perspectives

Currently, most studies focusing on predictive and prognostic factors associated with response to ^{177}Lu-PSMA have a low level of evidence due to their retrospective design, often monocentric nature, small sample sizes, and highly heterogeneous methodologies. Conducting prospective studies to validate the predictive value of already identified factors would be beneficial. Such studies could facilitate the development of nomograms that could be used in clinical practice to more objectively select patients who are most likely to benefit from treatment. For instance, Gafita et al. developed nomograms to predict response to ^{177}Lu-PSMA. However, this study is limited by its retrospective nature and the small size of the validation cohort (35).

Due to the high cost of treatment, its radiative nature, the complexity of its implementation, and potential adverse effects, patient selection is crucial.

This issue becomes even more significant considering that ^{177}Lu-PSMA could potentially be used at earlier stages of prostate cancer in the future, significantly increasing the number of patients who would require treatment. This raises the important question of how to select between ^{177}Lu-PSMA and other therapies based on the characteristics of the patients and their disease. Several clinical trials are currently investigating the efficacy of ^{177}Lu-PSMA in earlier stages of prostate cancer. For instance, the PSMAfore trial which included 468 patients demonstrated that ^{177}Lu-PSMA is superior to an androgen receptor pathway inhibitor change in taxane-naïve patients with mCRPC (63). Additionally, the ongoing PSMAddition trial is assessing the effectiveness of ^{177}Lu-PSMA combined with standard of care (SoC) versus SoC alone in patients with metastatic hormone-sensitive prostate cancer (64).

Similarly, new radiopharmaceuticals using alpha-emitting isotopes, such as actinium-225 (^{225}Ac − PSMA), have shown

promising results in patients who have progressed after ^{177}Lu-PSMA treatment (65).

Conclusion

Our study identifies several predictive factors associated with a poor response to ^{177}Lu-PSMA. Clinico-biologically, these factors include a body mass index (BMI) < 25 kg/m^2, a PSA doubling time < 2 months, hemoglobin levels <10 g/dL, albumin levels <35 g/L, LDH > 250 IU/L and ALP > 125 IU/L. These factors are associated with a reduced likelihood of achieving a satisfactory therapeutic response and an increased risk of early treatment discontinuation.

On ^{68}Ga-PSMA PET imaging, poor predictors include a low SUL_{max}, high tumor volume (TTV) and a low PSG score.

The study's findings underscore the importance of integrating clinico-biological parameters and advanced imaging results in the patient selection process for ^{177}Lu-PSMA therapy. These predictive factors can aid in identifying patients who are less likely to benefit from the treatment, thereby optimizing patient management and potentially guiding the use of alternative or additional therapeutic strategies.

Data availability statement

The raw data supporting the conclusions of this article will be made available by the authors, without undue reservation.

Ethics statement

The studies involving humans were approved by Comité d'Ethique - CHU Angers - 4, rue Larrey - 49933 Angers Cedex 9; comite-ethique@chu-angers.fr. The studies were conducted in accordance with the local legislation and institutional requirements. A consent form for the use of health data for research purposes was provided and completed by each patient who started treatment during the inclusion period. Written informed consent for participation was not required from the participants or the participants' legal guardians/next of kin in accordance with the national legislation and institutional requirements.

Author contributions

HP: Conceptualization, Data curation, Writing – original draft, Writing – review & editing. VS: Formal analysis, Methodology, Writing – original draft. P-AD: Supervision, Writing – original draft.

Funding

The author(s) declare that no financial support was received for the research and/or publication of this article.

Conflict of interest

The authors declare that the research was conducted in the absence of any commercial or financial relationships that could be construed as a potential conflict of interest.

Generative AI statement

The authors declare that no Gen AI was used in the creation of this manuscript.

Publisher's note

All claims expressed in this article are solely those of the authors and do not necessarily represent those of their affiliated organizations, or those of the publisher, the editors and the reviewers. Any product that may be evaluated in this article, or claim that may be made by its manufacturer, is not guaranteed or endorsed by the publisher.

Supplementary material

The Supplementary material for this article can be found online at: https://www.frontiersin.org/articles/10.3389/fmed.2025.1538507/full#supplementary-material

References

1. GCO. (2023). Cancer today. Available online at: http://gco.iarc.fr/today/home (Accessed November 29, 2023).

2. Institut National du Cancer. (2023). Panorama des cancers en France - édition 2023 - Ref: PANOKFR2023B. Available online at: https://www.e-cancer.fr/Expertises-et-publications/Catalogue-des-publications/Panorama-des-cancers-en-France-edition-2023 (Accessed November 29, 2023).

3. Siegel DA, O'Neil ME, Richards TB, Dowling NF, Weir HK. Prostate Cancer incidence and survival, by stage and race/ethnicity — United States, 2001–2017. *Morb Mortal Wkly Rep*. (2020) 69:1473–80. doi: 10.15585/mmwr.mm6941a1

4. Artibani W, Porcaro AB, De Marco V, Cerruto MA, Siracusano S. Management of biochemical recurrence after primary curative treatment for prostate Cancer: a review. *Urol Int*. (2017) 100:251–62. doi: 10.1159/000481438

5. Parker C, Castro E, Fizazi K, Heidenreich A, Ost P, Procopio G, et al. Prostate cancer: ESMO clinical practice guidelines for diagnosis, treatment and follow-up. *Ann Oncol*. (2020) 31:1119–34. doi: 10.1016/j.annonc.2020.06.011

6. Horoszewicz JS, Kawinski E, Murphy GP. Monoclonal antibodies to a new antigenic marker in epithelial prostatic cells and serum of prostatic cancer patients. *Anticancer Res*. (1987) 7:927–35.

7. Hawkey NM, Sartor AO, Morris MJ, Armstrong AJ. Prostate-specific membrane antigen–targeted Theranostics: past, present, and future approaches. *Clin Adv Hematol Oncol*. (2022) 20:227–38.

8. Shahrokhi P, Farahani AM, Tamaddondar M, Rezazadeh F. The utility of radiolabeled PSMA ligands for tumor imaging. *Chem Biol Drug Des*. (2022) 99:136–61. doi: 10.1111/cbdd.13946

9. Langbein T, Weber WA, Eiber M. Future of Theranostics: an outlook on precision oncology in nuclear medicine. *J Nucl Med*. (2019) 60:13S–9S. doi: 10.2967/jnumed.118.220566

10. IAEA. (2024). Livechart - Table of nuclides - nuclear structure and decay data. Available online at: https://www-nds.iaea.org/relnsd/vcharthtml/VChartHTML.html (Accessed January 20, 2024).

11. Sjögreen Gleisner K, Chouin N, Gabina PM, Cicone F, Gnesin S, Stokke C, et al. EANM dosimetry committee recommendations for dosimetry of ^{177}Lu-labelled somatostatin-receptor- and PSMA-targeting ligands. *Eur J Nucl Med Mol Imaging*. (2022) 49:1778–809. doi: 10.1007/s00259-022-05727-7

12. Sartor O, de Bono J, Chi KN, Fizazi K, Herrmann K, Rahbar K, et al. Lutetium-177-PSMA-617 for metastatic castration-resistant prostate Cancer. *N Engl J Med*. (2021) 385:1091–103. doi: 10.1056/NEJMoa2107322

13. Hotta M, Gafita A, Czernin J, Calais J. Outcome of patients with PSMA PET/CT screen failure by VISION criteria and treated with ^{177}Lu-PSMA therapy: a multicenter retrospective analysis. *J Nucl Med*. (2022) 63:1484–8. doi: 10.2967/jnumed.121.263441

14. Haute Autorité de Santé. (2024). PLUVICTO (lutécium (^{177}Lu) vipivotide tétraxétan) - Cancer de la prostate. Available online at: https://www.has-sante.fr/jcms/p_3443283/fr/pluvicto-lutecium-177lu-vipivotide-tetraxetan-cancer-de-la-prostate (Accessed August 14, 2024).

15. Kratochwil C, Fendler WP, Eiber M, Hofman MS, Emmett L, Calais J, et al. Joint EANM/SNMMI procedure guideline for the use of ^{177}Lu-labeled PSMA-targeted radioligand-therapy (^{177}Lu-PSMA-RLT). *Eur J Nucl Med Mol Imaging*. (2023) 50:2830–45. doi: 10.1007/s00259-023-06255-8

16. Rasul S, Hartenbach M, Wollenweber T, Kretschmer-Chott E, Grubmüller B, Kramer G, et al. Prediction of response and survival after standardized treatment with 7400 MBq ^{177}Lu-PSMA-617 every 4 weeks in patients with metastatic castration-resistant prostate cancer. *Eur J Nucl Med Mol Imaging*. (2021) 48:1650–7. doi: 10.1007/s00259-020-05082-5

17. Hotta M, Gafita A, Murthy V, Benz MR, Sonni I, Burger IA, et al. PSMA PET tumor–to–salivary gland ratio to predict response to [^{177}Lu]PSMA Radioligand therapy: an international multicenter retrospective study. *J Nucl Med*. (2023) 64:1024–9. doi: 10.2967/jnumed.122.265242

18. Gioulbasanis I, Baracos VE, Giannousi Z, Xyrafas A, Martin L, Georgoulias V, et al. Baseline nutritional evaluation in metastatic lung cancer patients: Mini nutritional assessment versus weight loss history. *Ann Oncol*. 22:835–41. doi: 10.1093/annonc/mdq440

19. Dewys WD, Begg C, Lavin PT, Band PR, Bennett JM, Bertino JR, et al. Prognostic effect of weight loss prior tochemotherapy in cancer patients. *Am J Med*. (1980) 69:491–7. doi: 10.1016/S0149-2918(05)80001-3

20. Andreyev HJN, Norman AR, Oates J, Cunningham D. Why do patients with weight loss have a worse outcome when undergoing chemotherapy for gastrointestinal malignancies? *Eur J Cancer*. (1998) 34:503–9. doi: 10.1016/S0959-8049(97)10090-9

21. Shachar SS, Williams GR. The obesity paradox in cancer – moving beyond BMI. *Cancer Epidemiol Biomark Prev*. (2017) 26:13–6. doi: 10.1158/1055-9965.EPI-16-0439

22. Flegal KM, Kit BK, Orpana H, Graubard BI. Association of all-cause mortality with overweight and obesity using standard body mass index categories: a systematic review and meta-analysis. *JAMA*. (2013) 309:71–82. doi: 10.1001/jama.2012.113905

23. Shah AD, Kandula NR, Lin F, Allison MA, Carr J, Herrington D, et al. Less favorable body composition and adipokines in south Asians compared with other US ethnic groups: results from the MASALA and MESA studies. *Int J Obes*. (2016) 40:639–45. doi: 10.1038/ijo.2015.219

24. Cruz-Jentoft AJ, Baeyens JP, Bauer JM, Boirie Y, Cederholm T, Landi F, et al. Sarcopenia: European consensus on definition and diagnosis: Report of the European Working Group on Sarcopenia in Older People. *Age and Ageing*. (2010) 39:412–23. doi: 10.1093/ageing/afq034

25. Cruz-Jentoft AJ, Landi F, Schneider SM, Zúñiga C, Arai H, Boirie Y, et al. Prevalence of and interventions for sarcopenia in ageing adults: a systematic review. Report of the international sarcopenia initiative (EWGSOP and IWGS). *Age Ageing*. (2014) 43:748–59. doi: 10.1093/ageing/afu115

26. Cruz-Jentoft AJ, Landi F, Topinková E, Michel JP. Understanding sarcopenia as a geriatric syndrome. *Curr Opin Clin Nutr Metab Care*. (2010) 13:1–7. doi: 10.1097/MCO.0b013e328333c1c1

27. Wallace JI, Schwartz RS. Involuntary weight loss in elderly outpatients: recognition, etiologies, and treatment. *Clin Geriatr Med*. (1997) 13:717–36. doi: 10.1016/S0749-0690(18)30146-0

28. Newman AB, Yanez D, Harris T, Duxbury A, Enright PL, Fried LP, et al. Weight change in old age and its association with mortality. *J Am Geriatr Soc*. (2001) 49:1309–18. doi: 10.1046/j.1532-5415.2001.49258.x

29. Francini E, Gray KP, Xie W, Shaw GK, Valença L, Bernard B, et al. Time of metastatic disease presentation and volume of disease are prognostic for metastatic hormone sensitive prostate cancer (mHSPC). *Prostate*. (2018) 78:889–95. doi: 10.1002/pros.23645

30. Bajeot AS, Roumiguié M, Rébillard X, Descotes JL, Duguet C, Lebret T, et al. Prise en charge des cancers de la prostate métastatiques synchrones et métachrones en France: étude observationnelle à partir des "RCP sentinelles" de l'AFU. *Prog En Urol*. (2022) 32:691–701. doi: 10.1016/j.purol.2022.04.013

31. D'Amico AV, Chen MH, Roehl KA, Catalona WJ. Preoperative PSA velocity and the risk of death from prostate Cancer after radical prostatectomy. *N Engl J Med*. (2004) 351:125–35. doi: 10.1056/NEJMoa032975

32. D'Amico AV, Moul JW, Carroll PR, Sun L, Lubeck D, Chen MH. Surrogate end point for prostate cancer–specific mortality after radical prostatectomy or radiation therapy. *JNCI J Natl Cancer Inst*. (2003) 95:1376–83. doi: 10.1093/jnci/djg043

33. Suman S, Parghane RV, Joshi A, Prabhash K, Bakshi G, Talole S, et al. Therapeutic efficacy, prognostic variables and clinical outcome of ^{177}Lu-PSMA-617 PRLT in progressive mCRPC following multiple lines of treatment: prognostic implications of high FDG uptake on dual tracer PET-CT Vis-à-Vis Gleason score in such cohort. *Br J Radiol*. (2019) 92:20190380. doi: 10.1259/bjr.20190380

34. Telli T, Tuncel M, Karabulut E, Aksoy S, Erman M, Akdogan B, et al. Prognostic factors of overall and prostate-specific antigen-progression-free survival in metastatic castration-resistant prostate cancer patients treated with ^{177}Lu-PSMA-617. A single-center prospective observational study. *Prostate*. (2023) 83:792–800. doi: 10.1002/pros.24518

35. Gafita A, Calais J, Grogan TR, Hadaschik B, Wang H, Weber M, et al. Nomograms to predict outcomes after ^{177}Lu-PSMA therapy in men with metastatic castration-resistant prostate cancer: an international, multicentre, retrospective study. *Lancet Oncol*. (2021) 22:1115–25. doi: 10.1016/S1470-2045(21)00274-6

36. Ferdinandus J, Eppard E, Gaertner FC, Kürpig S, Fimmers R, Yordanova A, et al. Predictors of response to Radioligand therapy of metastatic castrate-resistant prostate Cancer with ^{177}Lu-PSMA-617. *J Nucl Med*. (2017) 58:312–9. doi: 10.2967/jnumed.116.178228

37. Li F, Xiang H, Pang Z, Chen Z, Dai J, Chen S, et al. Association between lactate dehydrogenase levels and oncologic outcomes in metastatic prostate cancer: a meta-analysis. *Cancer Med*. (2020) 9:7341–51. doi: 10.1002/cam4.3108

38. Nishimori H, Ehata S, Suzuki HI, Katsuno Y, Miyazono K. Prostate Cancer cells and bone stromal cells mutually interact with each other through bone morphogenetic protein-mediated signals*. *J Biol Chem*. (2012) 287:20037–46. doi: 10.1074/jbc.M112.353094

39. Mundy GR. Metastasis to bone: causes, consequences and therapeutic opportunities. *Nat Rev Cancer*. (2002) 2:584–93. doi: 10.1038/nrc867

40. Heinrich D, Bruland Ø, Guise TA, Suzuki H, Sartor O. Alkaline phosphatase in metastatic castration-resistant prostate cancer: reassessment of an older biomarker. *Future Oncol*. (2018) 14:2543–56. doi: 10.2217/fon-2018-0087

41. Barber TW, Singh A, Kulkarni HR, Niepsch K, Billah B, Baum RP. Clinical outcomes of ^{177}Lu-PSMA Radioligand therapy in earlier and later phases of metastatic castration-resistant prostate Cancer grouped by previous Taxane chemotherapy. *J Nucl Med*. (2019) 60:955–62. doi: 10.2967/jnumed.118.216820

42. Heck MM, Tauber R, Schwaiger S, Retz M, D'Alessandria C, Maurer T, et al. Treatment outcome, toxicity, and predictive factors for Radioligand therapy with ^{177}Lu-PSMA-I&T in metastatic castration-resistant prostate Cancer. *Eur Urol*. (2019) 75:920–6. doi: 10.1016/j.eururo.2018.11.016

43. Rathke H, Holland-Letz T, Mier W, Flechsig P, Mavriopoulou E, Röhrich M, et al. Response prediction of ^{177}Lu-PSMA-617 Radioligand therapy using prostate-specific antigen, chromogranin a, and lactate dehydrogenase. *J Nucl Med*. (2020) 61:689–95. doi: 10.2967/jnumed.119.231431

44. Bräuer A, Grubert LS, Roll W, Schrader AJ, Schäfers M, Bögemann M, et al. ^{177}Lu-PSMA-617 radioligand therapy and outcome in patients with metastasized castration-resistant prostate cancer. *Eur J Nucl Med Mol Imaging*. (2017) 44:1663–70. doi: 10.1007/s00259-017-3751-z

45. Rahbar K, Ahmadzadehfar H, Kratochwil C, Haberkorn U, Schäfers M, Essler M, et al. German multicenter study investigating ^{177}Lu-PSMA-617 radioligand therapy in advanced prostate cancer patients. *J Nucl Med*. (2017) 58:85–90. doi: 10.2967/jnumed.116.183194

46. Zhang L, Zhou G, Li Y, Tang L, Mao Y, Lin A, et al. Combined prognostic value of pretreatment anemia and cervical node necrosis in patients with nasopharyngeal carcinoma receiving intensity-modulated radiotherapy: a large-scale retrospective study. *Cancer Med*. (2017) 6:2822–31. doi: 10.1002/cam4.1233

47. Caro JJ, Salas M, Ward A, Goss G. Anemia as an independent prognostic factor for survival in patients with cancer. *Cancer*. (2001) 91:2214–21. doi: 10.1002/1097-0142(20010615)91:12<2214::AID-CNCR1251>3.0.CO;2-P

48. Ahmadzadehfar H, Eppard E, Kürpig S, Fimmers R, Yordanova A, Schlenkhoff CD, et al. Therapeutic response and side effects of repeated radioligand therapy with ^{177}Lu-PSMA-DKFZ-617 of castrate-resistant metastatic prostate cancer. *Oncotarget*. (2016) 7:12477–88. doi: 10.18632/oncotarget.7245

49. Morris MJ, Castellano D, Herrmann K, de Bono JS, Shore ND, Chi KN, et al. ^{177}Lu-PSMA-617 versus a change of androgen receptor pathway inhibitor therapy for taxane-naive patients with progressive metastatic castration-resistant prostate cancer (PSMAfore): a phase 3, randomised, controlled trial [published correction appears in lancet]. *Lancet*. (2025) 404:2542. doi: 10.1016/S0140-6736(24)027168

50. Azad AA, Bressel M, Tan H, Voskoboynik M, Suder A, Weickhardt AJ, et al. Sequential [^{177}Lu]Lu-PSMA-617 and docetaxel versus docetaxel in patients with metastatic hormone-sensitive prostate cancer (UpFrontPSMA): a multicentre, open-label, randomised, phase 2 study. *Lancet Oncol*. (2024) 25:1267–76. doi: 10.1016/S1470-2045(24)00440-6

51. Hofman MS, Emmett L, Sandhu S, Iravani A, Joshua AM, Goh JC, et al. [^{177}Lu]Lu-PSMA-617 versus cabazitaxel in patients with metastatic castration-resistant prostate cancer (TheraP): a randomised, open-label, phase 2 trial. *Lancet*. (2021) 397:797–804. doi: 10.1016/S0140-6736(21)00237-3

52. Kuo P, Hesterman J, Rahbar K, Kendi AT, Wei XX, Fang B, et al. [68Ga]Ga-PSMA-11 PET baseline imaging as a prognostic tool for clinical outcomes to [^{177}Lu]Lu-PSMA-617 in patients with mCRPC: a VISION substudy. *J Clin Oncol*. (2022) 40:5002–2. doi: 10.1200/JCO.2022.40.16_suppl.5002

53. Eisazadeh R, Mirshahvalad SA, Schwieghofer-Zwink G, Hehenwarter L, Rendl G, Gampenrieder S, et al. Pre-treatment 68 Ga-PSMA-11 PET/CT prognostic value in predicting response to ^{177}Lu-PSMA-I&T therapy and patient survival. *Mol Imaging Biol*. (2024) 26:360–9. doi: 10.1007/s11307-024-01900-6

54. Emmett L, Crumbaker M, Ho B, Willowson K, Eu P, Ratnayake L, et al. Results of a prospective phase 2 pilot trial of ^{177}Lu–PSMA-617 therapy for metastatic castration-resistant prostate Cancer including imaging predictors of treatment response and patterns of progression. *Clin Genitourin Cancer*. (2019) 17:15–22. doi: 10.1016/j.clgc.2018.09.014

55. Kuo PH, Morris MJ, Hesterman J, Kendi AT, Rahbar K, Wei XX, et al. Quantitative 68Ga-PSMA-11 PET and clinical outcomes in metastatic castration-resistant prostate Cancer following ^{177}Lu-PSMA-617 (VISION trial). *Radiology*. (2024) 312:e233460. doi: 10.1148/radiol.233460

56. Wang G, Zang J, Jiang Y, Liu Q, Sui H, Wang R, et al. A single-arm, low-dose, prospective study of ^{177}Lu-EB-PSMA Radioligand therapy in patients with metastatic castration-resistant prostate Cancer. *J Nucl Med*. (2023) 64:611–7. doi: 10.2967/jnumed.122.264857

57. Rosar F, Burgard C, David S, Marlowe RJ, Bartholomä M, Maus S, et al. Dual FDG/PSMA PET imaging to predict lesion-based progression of mCRPC during PSMA-RLT. *Sci Rep*. (2024) 14:11271. doi: 10.1038/s41598-024-61961-z

58. Satapathy S, Mittal BR, Sood A. Visceral metastases as predictors of response and survival outcomes in patients of castration-resistant prostate Cancer treated with ^{177}Lu-labeled prostate-specific membrane antigen Radioligand therapy: a systematic review and Meta-analysis. *Clin Nucl Med*. (2020) 45:935–42. doi: 10.1097/RLU.0000000000003307

59. Vanwelkenhuyzen J, Van Bos E, Van Bruwaene S, Lesage K, Maes A, Üstmert S, et al. AR and PI3K genomic profiling of cell-free DNA can identify poor responders to Lutetium-^{177}-PSMA among patients with metastatic castration-resistant prostate Cancer. *Eur Urol Open Sci*. (2023) 53:63–6. doi: 10.1016/j.euros.2023.05.008

60. De Giorgi U, Sansovini M, Severi S, Nicolini S, Monti M, Gurioli G, et al. Circulating androgen receptor gene amplification and resistance to ^{177}Lu-PSMA-617 in metastatic castration-resistant prostate cancer: results of a phase 2 trial. *Br J Cancer*. (2021) 125:1226–32. doi: 10.1038/s41416-021-01508-5

61. Sun M, Thomas C, Orlando F, Sigouros M, Osborne J, Nauseef J, et al. 1390P circulating tumor DNA (ctDNA) and prognosis with PSMA-targeted radionuclide therapy (TRT). *Ann Oncol*. (2022) 33:S1179. doi: 10.1016/j.annonc.2022.07.1522

62. Moghrabi S, Al-Houwari R, Ruzzeh S, Al-Ibraheem A. Therapeutic challenges in metastatic castration-resistant prostate Cancer: a case study and review of prostate-specific membrane antigen-targeted therapy failures in highly prostate-specific membrane antigen-avid disease. *Cureus*. (2024) 16:e76224. doi: 10.7759/cureus.76224

63. Sartor O, Gauna DEC, Herrmann K, De BJS, Shore ND, Chi KNN, et al. LBA13 phase III trial of [^{177}Lu]Lu-PSMA-617 in taxane-naive patients with metastatic castration-resistant prostate cancer (PSMAfore). *Ann Oncol*. (2023) 34:S1324–5. doi: 10.1016/j.annonc.2023.10.085

64. Tagawa ST, Sartor AO, Saad F, Reid AH, Sakharova OV, Feng FY, et al. PSMAddition: a phase 3 trial to compare treatment with ^{177}Lu-PSMA-617 plus standard of care (SoC) and SoC alone in patients with metastatic hormone-sensitive prostate cancer. *J Clin Oncol*. (2023) 41:TPS5116–6. doi: 10.1200/JCO.2023.41.16_suppl.TPS5116

65. Sathekge MM, Lawal IO, Bal C, Bruchertseifer F, Ballal S, Cardaci G, et al. Actinium-225-PSMA radioligand therapy of metastatic castration-resistant prostate cancer (WARMTH act): a multicentre, retrospective study. *Lancet Oncol*. (2024) 25:175–83. doi: 10.1016/S1470-2045(23)00638-1

frontiers | Frontiers in Oncology

TYPE Original Research
PUBLISHED 20 March 2025
DOI 10.3389/fonc.2025.1474327

Check for updates

OPEN ACCESS

EDITED BY
Abdul K. Parchur,
Medical College of Wisconsin, United States

REVIEWED BY
Xiaowu Deng,
Sun Yat-sen University Cancer Center (SYSUCC), China
Nrusingh Biswal,
University of Maryland, United States

*CORRESPONDENCE
Quan Tang
tangquan528@sina.com
Qingtao Qiu
qiuqingt@126.com
Yong Yin
yinyongsd@126.com

†These authors share first authorship

RECEIVED 01 August 2024
ACCEPTED 27 February 2025
PUBLISHED 20 March 2025

CITATION
Li T, Yao X, He R, Xue X, Wang S, Chen J, Qiu Q, Yin Y and Tang Q (2025) Proton stereotactic centralized ablative radiation therapy for treating bulky tumor: a treatment plan study.
Front. Oncol. 15:1474327.
doi: 10.3389/fonc.2025.1474327

COPYRIGHT
© 2025 Li, Yao, He, Xue, Wang, Chen, Qiu, Yin and Tang. This is an open-access article distributed under the terms of the Creative Commons Attribution License (CC BY). The use, distribution or reproduction in other forums is permitted, provided the original author(s) and the copyright owner(s) are credited and that the original publication in this journal is cited, in accordance with accepted academic practice. No use, distribution or reproduction is permitted which does not comply with these terms.

Proton stereotactic centralized ablative radiation therapy for treating bulky tumor: a treatment plan study

Tengxiang Li[1,2†], Xinsen Yao[3†], Ruimin He[1,4], Xian Xue[5], Shuai Wang[6,7], Jinhu Chen[2], Qingtao Qiu[2*], Yong Yin[1,2*] and Quan Tang[1*]

[1]School of Nuclear Science and Technology, University of South China, Hengyang, China, [2]Department of Radiation Physics, Shandong Cancer Hospital and Institute, Shandong First Medical University and Shandong Academy of Medical Sciences, Jinan, China, [3]Department of Radiotherapy Center, Chenzhou NO.1 People's Hospital, Chenzhou, China, [4]Department of Oncology, The Second Affiliated Hospital, Hengyang Medical School, University of South China, Hengyang, China, [5]Institute of Radiation Protection and Nuclear Safety Medicine, Chinese Center for Disease Control and Prevention, Beijing, China, [6]Department of Radiation Oncology, The First Affiliated Hospital of USTC, Division of Life Sciences and Medicine, University of Science and Technology of China, Hefei, Anhui, China, [7]University of Science and Technology of China (USTC), School of Nuclear Science and Technology (SNST), Hefei, Anhui, China

Objective: Stereotactic centralized/core ablative radiation therapy (SCART) is a novel radiotherapy approach. This study investigates the potential benefits of proton-based SCART (pSCART) by leveraging the dosimetric advantages of protons and integrating them with the SCART technique.

Methods: Five clinical cases previously treated with conventional proton therapy were selected for this study. The pSCART plans utilized a relative biological effectiveness (RBE) prescription dose of 24 Gy (RBE) × 3 fractions, with each plan consisting of three to five fields. The prescribed dose for the CyberKnife SCART was the highest value meeting the organs-at-risk (OARs) dose limits and the tumor edge dose limits. The dose distributions of the CyberKnife-based SCART and pSCART plans were compared using five criteria: i) prescription dose; ii) 80% prescription dose volume, targets coverage at 80% and 20% dose levels, and the 80%/20% ratio; iii) volume receiving >5 Gy outside the tumor edge; iv) dose tolerance limits to OARs; and v) mean dose to OARs.

Results: pSCART can deliver a higher prescription dose of 24 Gy × 3 fractions versus SCART's 15 Gy × 2–3 fractions or 18 Gy × 2 fractions. Specifically, pSCART outperforms SCART in terms of the 80% prescription dose volume and 80% dose level coverage of stereotactic centralized/core target volumes (SCTV) achieving 69.77%–100.00% versus SCART's 43.6%–99.5%. The 20% dose level coverage for gross target volume (GTV) is slightly lower for pSCART, achieving 88.96%–98.64% versus SCART's 90.1%–99.9%. The maximum point dose outside the target volume is lower for pSCART at 4.58–6.19 Gy versus SCART's 4.78–6.67 Gy; additionally, the V_{5Gy} at the tumor edge is significantly smaller for pSCART at 5.93–23.72 cm^3 versus SCART's 6.85–151.66 cm^3. The average dose to most OARs in the pSCART plan is lower than in the SCART plan.

Conclusions: This work provides initial insights into evaluating treatment plans for bulky tumors using pSCART. Compared to the CyberKnife SCART, pSCART generates significantly higher prescription doses and larger high-dose regions within the GTV while delivering lower doses at the tumor edge, enhancing normal tissue sparing.

KEYWORDS

stereotactic, centralized/core ablative, proton, bulky tumor, radiation therapy

1 Introduction

Patients with bulky tumors often have a worse prognosis and frequently receive only palliative treatments (1, 2). A novel treatment approach termed stereotactic centralized/core ablative radiation therapy (SCART) has been developed for managing bulky or metastatic tumors. SCART is based on the principles of spatially fractionated radiation therapy (SFRT) (3, 4) and builds upon stereotactic body radiotherapy (SBRT) to optimize the high-dose region within the tumor core, aiming to achieve enhanced ablative effects, particularly in areas harboring cancer stem cells or highly resistant progenitors (5–7). Concurrently, low-dose radiation to the tumor periphery may mitigate some of the immunosuppressive effects associated with radiation at the tumor edge (8).

In a phase I study, SCART administration for recurrent or metastatic bulky tumors demonstrated favorable tolerability and safety, allowing for dose escalation up to the maximum tolerated dose (MTD) of 24 Gy delivered in 3 fractions (4). While the radiobiological mechanisms underlying this increased therapeutic index remain incompletely described, potential contributors include dose volume effects (9), bystander-like effects (10), differential vascular effects (11), inflammation and immunomodulatory effects (5, 12), and cell migration (13–15). By integrating the strong spatial dose modulation capability of SCART with the superior dose deposition characteristics of protons, the concept of proton-based SCART (pSCART) was proposed. This study investigates whether pSCART can achieve higher prescription doses, larger central/core high-dose regions, and reduced doses at the tumor edge.

This work evaluates the potential benefits of pSCART for treating bulky tumors such as soft tissue sarcomas, hepatic metastases, and pancreatic cancer. Specifically, it assesses the ability of pSCART technology to achieve the desired dose distribution pattern of SCART while ensuring effective protection of organs at risk (OARs) under high prescription doses. This research aims to guide future evaluations of pSCART clinical trials and facilitate its clinical implementation.

2 Materials and methods

2.1 Clinical case selection

Five clinical cases were selected from the patient database of our institution (Shandong Cancer Hospital and Institute, China): three sarcomas located in different anatomical regions—above the clavicle (Case 1), at the back (Case 2), and in the lower limb (Case 5)—as well as a pancreatic tumor (Case 3) and hepatic metastases (Case 4). The selection criteria included the following:

Tumor location: Cases encompassed commonly targeted sites for SBRT.

Target size: Lesions were measurable by computed tomography (CT) imaging, with maximum axial dimensions exceeding 5 cm [consistent with SCART trial criteria (4)].

Proximity to critical OARs.

The selected five cases in this study are described in Table 1.

All procedures adhered to institutional review board guidelines, and informed consent was waived for this retrospective planning study using fully anonymized CT datasets.

2.2 Treatment planning

CT acquisition protocol

Simulations were conducted using a SOMATOM Drive dual-source CT scanner (Siemens Healthineers AG, Forchheim, Germany) with a slice thickness of 1 mm. The scanning range extended at least 15 cm beyond the tumor margins in all directions.

CyberKnife-based SCART planning:

Delivery system: CyberKnife M6 C0521 (Accuray Inc., Sunnyvale, CA, USA);

Dose algorithm: finite-size pencil beam with side scatter (FSPB+); and

Dose recalculations: Monte Carlo recalculations with 1% statistical uncertainty.

Proton pSCART planning

Field set-up: Three to five fields were used, with a gantry angle interval of approximately 30° between adjacent fields. Non-coplanar fields can be adopted if necessary. Fields were positioned at appropriate angles near the tumor to avoid regions with significant density changes and the edge of the treatment couch. Each plan was completed by an experienced physicist from this institution who specializes in proton therapy.

TABLE 1 Tumor characteristics and treatment parameters.

	The site of tumor	Type	GTV vol. (cm^3)	SCTV vol. (cm^3)	SCTV vs. GTV
Case 1	Left supraclavicular	Sarcoma	80.76	3.71	4.59%
Case 2	Right back	Sarcoma	996.8	46.37	4.59%
Case 3	Abdomen	Pancreatic cancer	367.83	16.65	4.53%
Case 4	Abdomen	Hepatic metastases	694.46	33.84	4.87%
Case 5	Right leg	Sarcoma	559.33	26.16	4.68%

GTV, gross target volume; SCTV, stereotactic centralized/core target volumes.

Treatment planning system: RayStation V12.0.100.0 (RaySearch Laboratories, Stockholm, Sweden);

Beam model: Probeam™ TR3 proton therapy system (Varian Medical Systems, Palo Alto, CA, USA);

Dose algorithm: IonMonteCarlo with 1% statistical uncertainty;

Relative biological effectiveness (RBE): RBE = 1.1 per ICRU Report 78 recommendations (16); and

Robust optimization: accounts for ±3.5% range uncertainty and ±5 mm set-up errors.

Prescription dose schemes

The dose escalation framework was derived from the MTD trial of Dr. Yang et al. (4). The prescribed dose was based on the maximum dose to the gross target volume (GTV), as established in preclinical trials. The prescription dose was normalized to the maximum dose point within the treatment plan.

CyberKnife SCART

Prescription dose range: 15 Gy × 1 fraction to 24 Gy × 3 fractions;

Prescription dose determination: The fraction and prescribed dose of the SCART plan were determined based on OARs dose limits and the volumetric spillage (V_{5Gy} in non-target tissue per fraction).

Proton pSCART

Prescription dose: The highest dose of 24 Gy (RBE) × 3 fractions was utilized as determined in the MTD trial of Dr. Yang et al.

2.3 Dosimetric properties and metrics

The evaluation and comparison of SCART and pSCART considered three main points:

1. The target coverage in SCART and pSCART. SCART and pSCART plans considering an 80% prescribed dose coverage of stereotactic centralized/core target volumes (SCTV), with $V_{80}\% \geq 95\%$, and a 20% prescribed dose coverage of the GTV, with $V_{20}\% \geq 90\%$. Additionally, for SCART treatments, the ratio between the 80% and 20% prescribed doses ($V_{80}\%/V_{20}\%$) was computed, ensuring that this ratio exceeded 4.5% (4).
2. The extra-target dose distribution was quantified using two primary dosimetric indices: V_{5Gy}, the volume of non-target tissue receiving upper 5 Gy per fraction; and high-dose limit, the maximum dose to a specified volume outside the GTV. Both parameters were minimized through iterative optimization cycles.
3. The dose tolerance limits for OARs. For the SCART and pSCART plans, the dose distribution was similar to that of SBRT with an exceptionally high central dose. Consequently, existing SBRT dose limit values for OARs were employed to evaluate the pSCART plan. For normal organs like the bone, there were no strict and effective assessment indicators for tolerance to high-dose proton irradiation with fewer fractions. Therefore, dose limits for SCART were based on standard irradiation schemes (2 Gy per fraction). The normalized total dose (NTD) at 2 Gy-fractions, $NTD_{2.0}$, was computed using Equation 1.

$$NTD_{2.0} = n \cdot d\left(1 + \frac{d}{\alpha/\beta}\right)\left(1 + \frac{2Gy}{\alpha/\beta}\right)^{-1}. \quad (1)$$

The average dose to the femoral bone structures was converted to $NTD_{2.0}$, as the risk of radiation-induced complications was proportional to the mean dose of the organ (17). The biologically effective dose (BED) to OARs was computed using Equation 2.

$$BED = n \cdot d\left(1 + \frac{d}{\alpha/\beta}\right), \quad (2)$$

where the α/β values follow ICRU Report 91 recommendations (18). Radiation dose fractionation data for fractures in patients suggest an alpha/beta (α/β) ratio in the range of 1.8–2.8 Gy (19).

3 Results

The corresponding prescribed doses for the CyberKnife SCART and pSCART plans can be found in Table 2.

The fractions and prescribed doses of the CyberKnife SCART treatment were based on the MTD ranges used in the previous phase I clinical trial conducted by Dr. Yang (4), with the extra-target dose not exceeding 5 Gy (i.e., the volume of non-target tissue exposed to more than 5 Gy should be minimized), and the OARs dose limits.

TABLE 2 Treatment plans evaluated in this study.

	Equipment	Technique	Fractions	Prescribed dose (Gy)	Gantry angle (°)
Case 1	CyberKnife	SCART	2	36.0	Defined by TPS
	Proton	pSCART	3	72.0 (RBE)	330/0/70/135
Case 2	CyberKnife	SCART	2	30.0	Defined by TPS
	Proton	pSCART	3	72.0 (RBE)	180/270/305/340
Case 3	CyberKnife	SCART	2	30.0	Defined by TPS
	Proton	pSCART	3	72.0 (RBE)	280/310/340/10/40
Case 4	CyberKnife	SCART	3	45.0	Defined by TPS
	Proton	pSCART	3	72.0 (RBE)	180/260/300/320
Case 5	CyberKnife	SCART	3	45.0	Defined by TPS
	Proton	pSCART	3	72.0 (RBE)	180/235/280/330

The CyberKnife selects the best field combination from 3,600 discrete incident angles in the treatment planning system (TPS), enabling precise non-coplanar dose deposition. Proton therapy plans predominantly utilize coplanar field configurations; however, for specific anatomical sites (e.g., Case 1), non-coplanar fields are necessary to enhance dose conformity and sparing of organs at risk (OARs). In Case 1, a gantry angle of 135°combined with a couch angle of 315° was utilized.
SCART, stereotactic centralized/core ablative radiation therapy; pSCART, proton-based SCART; RBE, relative biological effectiveness.

3.1 Dose distributions of SCART and pSCART

In the pSCART plans, for Cases 1 and 2, where the organs at risk were located within or near the target volume with suboptimal dose gradients, inferior conformity was observed. In contrast, superior conformity was demonstrated in the remaining cases. The dose distributions of the pSCART plans for the five evaluated cases are illustrated in Figure 1.

The target dose distribution for the SCART plan delivered by the CyberKnife is presented in Figure 2.

Compared to conventional proton therapy plans, the pSCART plans require the generation of exceptionally high dose hot spots within the target area, resulting in a rapid dose falloff around the central region of the target volume. In Case 1, more stringent constraints were applied in the pSCART plan to protect the brachial plexus, leading to the formation of two distinct hot regions on either side of the brachial plexus. One region exhibits a maximum dose equivalent to the prescribed dose, while the other shows a lower dose. The differences in target dose distribution between pSCART and conventional proton therapy are illustrated in Figure 3.

3.2 Target coverage

The comparison of dosimetric indices defining target volume and coverage between SCART and pSCART is illustrated in Table 3.

In all instances except Case 1, the ratio of the 80% to 20% prescribed dose volume in the pSCART plan surpassed that in the SCART plan. According to the results in Table 3, the coverage of 80% of the prescribed dose to the GTV in all pSCART plans exceeded 4.5%. For Cases 2 to 5, the ratio of 80% to 20% of the prescribed dose was not only higher than 4.5% but also significantly greater than that observed in the CyberKnife SCART plans. This suggests that pSCART demonstrates a superior capability in generating central/core high-dose regions compared to the CyberKnife SCART and the linear accelerator with Volumetric Modulated Arc Therapy (VMAT) or Intensity-Modulated Radiotherapy (IMRT) technology used in the MTD trial of Dr. Yang et al.

3.3 Limit of high dose at tumor edge

The study compared dosimetric parameters for the generation of high-dose regions outside the target volume in the CyberKnife SCART and pSCART plans. The detailed parameters include two key indicators: volume and dose. Specifically, these parameters encompass the volume receiving a dose exceeding 5 Gy per fraction outside the target area, and the corresponding dose value for this high-dose volume should be minimized.

In the pSCART plans, these parameters were superior to those in the CyberKnife SCART plans, as illustrated in Table 4.

The prescribed dose in the CyberKnife SCART plan refers to the dose range from 15 Gy × 1 fraction to 24 Gy × 3 fractions and aims to minimize the high-dose region outside the target volume. For Case 1, both the CyberKnife SCART and pSCART plans achieved a smaller V_{5Gy} and lower dose outside the target area. Additionally, the pSCART plan for Case 4 also demonstrated this advantage. However, the remaining cases did not meet the requirement of maintaining doses outside the target area below 5 Gy per fraction, although the pSCART plan demonstrates better performance. Furthermore, the quality of the plan can be evaluated by restricting and assessing the volume size exceeding 5 Gy. In the pSCART plan, it was possible to achieve V_{5Gy} less than 20 cm^3, or close to 20 cm^3.

3.4 Assessment of dose tolerance limits

In Case 1, the maximum dose to the left brachial plexus was 27.25 Gy, exceeding the dose limits. However, only 0.78 cm^3

10.3389/fonc.2025.1474327

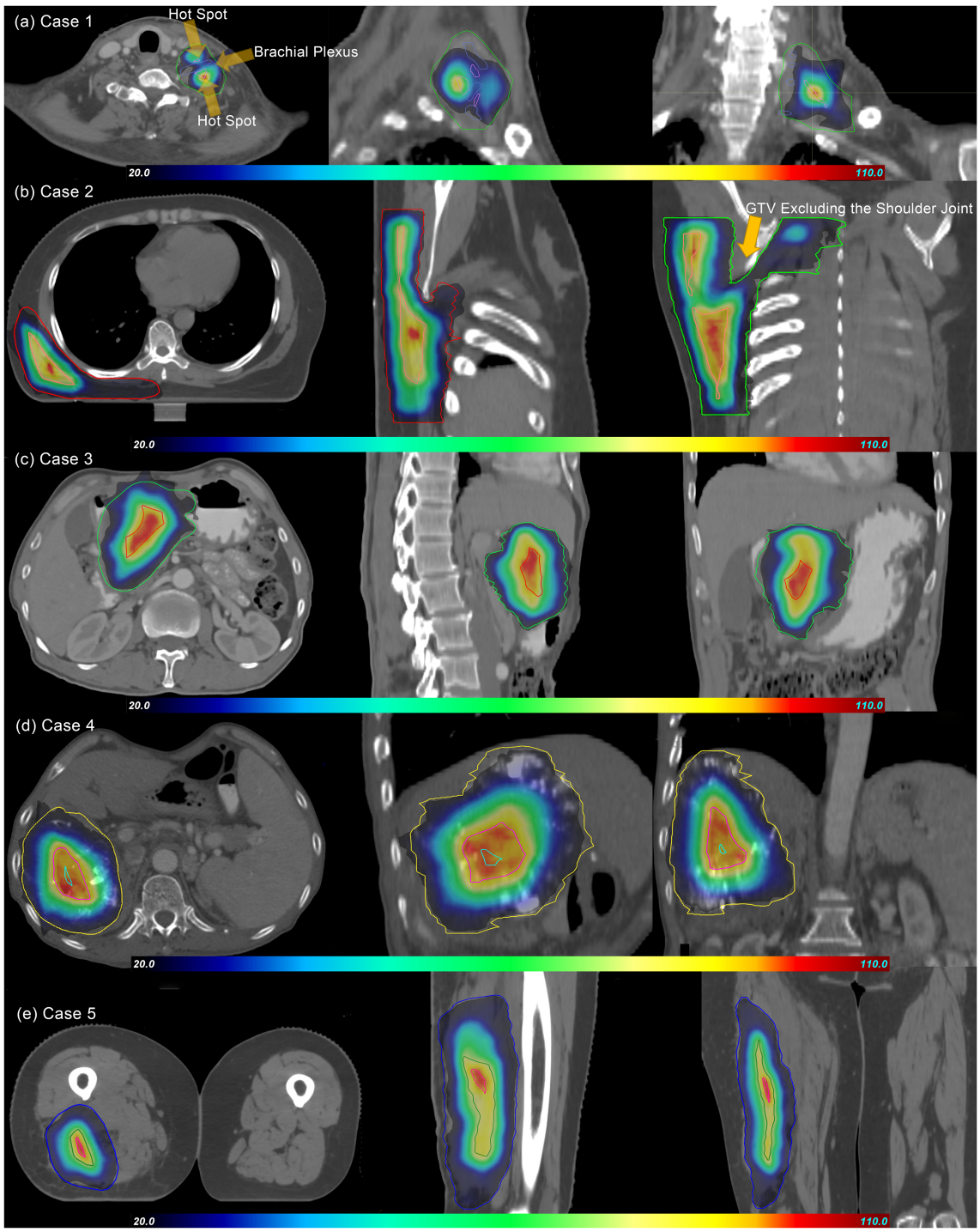

FIGURE 1
Dose distributions of pSCART treatments for the five cases. In the figure, GTV and SCTV are marked with contour lines of different colors. The dose gradient range is set from 20% to 110%, and the prescription dose is normalized with the maximum value of 100% as the benchmark. As shown in the figure, the dose volume spillage area outside GTV does not significantly exceed the 20% prescription dose threshold. Under the condition that functional imaging guidance is limited, the SCART technique theoretically should generate an SCTV with a regular geometric shape by uniformly shrinking GTV. However, in clinical practice, the areas overlapping with important serial organs like nerve plexuses (such as brachial plexus in Case 1), joint structures (such as shoulder joint in Case 2), digestive tracts, and major blood vessels, which are organs at risk (OARs), need to be excluded from SCTV to form the "SCTV-OARs" modified target area. This anatomical structure exclusion operation leads to the irregularity of SCTV in the pSCART plan. The research results show that the proton plan with active beam modulation is superior to the CyberKnife SCART plan in terms of SCTV coverage and conformity. This result is also verified by the "80% SCTV coverage" data in Table 3. SCART, stereotactic centralized/core ablative radiation therapy; pSCART, proton-based SCART; GTV, gross target volume; SCTV, stereotactic centralized/core target volumes.

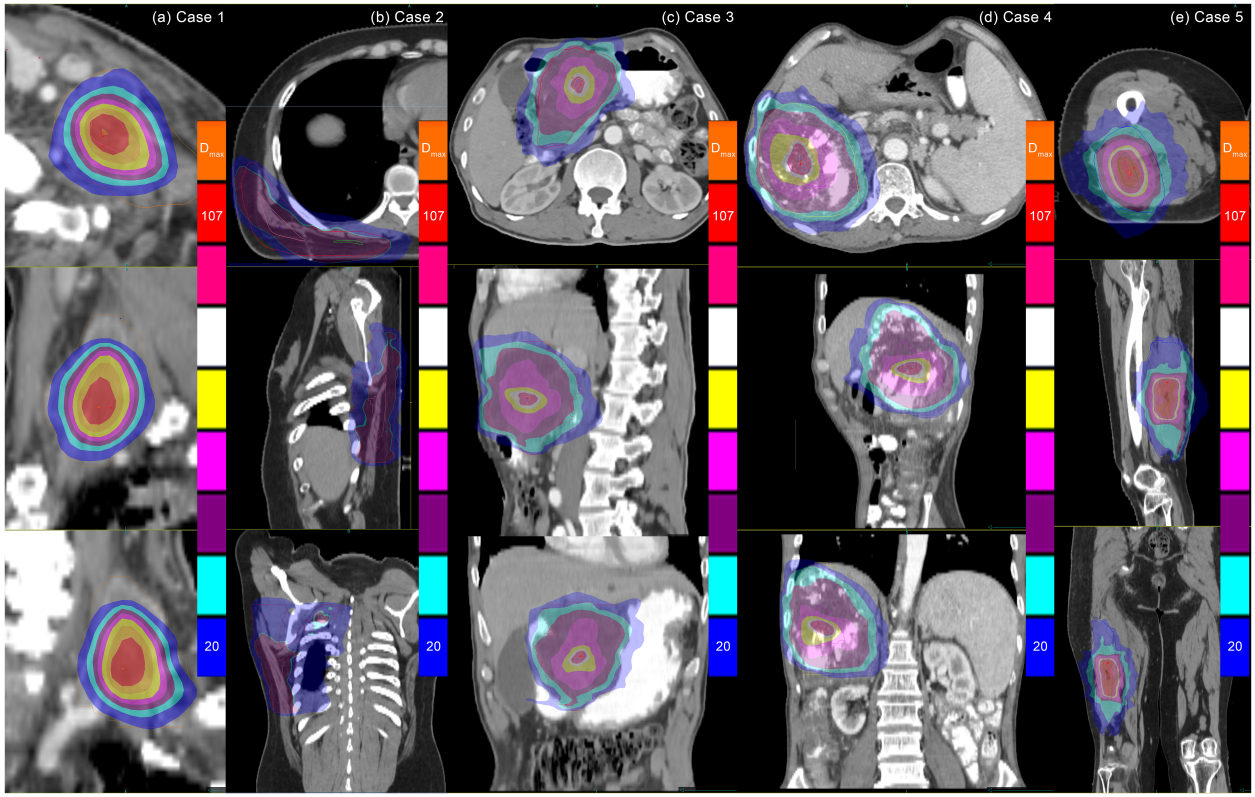

FIGURE 2
Dose distributions of CyberKnife SCART treatments for the five cases. Note: Dosimetric normalization to D_{max} resulted in gradient ranges of 20%–107%, with significant dose heterogeneity observed in GTV. While CyberKnife demonstrates enhanced plan design proficiency in meeting SCART clinical criteria, its inherent physical limitations hinder effective modulation of steep dose gradients between the high-dose regions of the SCTV and the low-dose regions adjacent to organs at risk (OARs). Quantitative analysis reveals compromised dosimetric performance for irregular target geometries (Cases 2 and 5) compared to regular-shaped targets. SCART, stereotactic centralized/core ablative radiation therapy; GTV, gross target volume.

received a dose of 20.4 Gy, meeting the requirement of at most 3 cm^3 at this dose level.

In Case 2, for the right lung, the spared volume from doses of 12.40 Gy was 1,410.76 cm^3; for all lungs, the spared volume was 2,490.4 cm^3 at 12.40 Gy and 2,489.33 cm^3 at 11.60 Gy, meeting the requirements of 1,000 and 1,500 cm^3, respectively. For the spinal cord, the maximum dose was 9.27 Gy, with no volume receiving doses of 18 or 12.3 Gy, while only 0.35 cm^3 received a dose of 8.63 Gy.

In Case 3, the duodenum received a maximum dose of 18.6 Gy, with 0.58 cm^3 at 16.5 Gy and 11.56 cm^3 at 11.4 Gy. For the right kidney, 66% of its volume received a dose of 0.48 Gy, with no volume receiving 16 Gy. The left kidney received no dose. For the liver, there was no volume receiving a dose of 19.2 Gy, indicating a spared volume of 1,318.74 cm^3 from doses of 19.2 Gy. For the stomach, the maximum dose was 15.26 Gy, with only 0.18 cm^3 receiving a dose of 16.5 Gy.

In Case 4, the duodenum showed no volume receiving a dose of 16.5 Gy, with only 0.59 cm^3 at 11.4 Gy and a maximum dose of 12.23 Gy. For the liver, the spared volume from doses of 19.2 Gy was 1,059.39 cm^3, and the maximum dose was 14.8 Gy.

In Case 5, the bone received a maximum dose of 9.64 Gy and a mean dose of 0.7 Gy. Using Formulas 1 and 2, the calculated $NTD_{2.0}$ (Equation 1) for the bone ranged from 10.46 to 10.88 Gy, significantly lower than the threshold of 40 Gy associated with femoral fracture (17).

The mean dose to the target to OARs was calculated, and the mean BED (Equation 2) of OARs is illustrated in Figures 4A–E.

4 Discussion

Patients afflicted with bulky tumors often face a poor prognosis (3). However, enhancing local disease control in bulky tumors can significantly improve both overall survival (OS) and quality of life (QOL). The substantial tumor size poses a significant challenge for conventional radiotherapy (1), as it increases the risk of collateral damage to surrounding tissues. To mitigate this risk, alternative approaches such as SFRT are required (20). SFRT, including techniques like GRID (21, 22), LATTICE (23, 24), and Mini-beam therapy (25–27), has demonstrated benefits in treating bulky tumors (20). Excessive doses can induce tumor cell death through vascular damage and antitumor immunity (28). The generation of multiple "hot spots" (in the form of strips or islands) to encompass the entirety of bulky tumors may need to limit the size of individual hot spots. Consequently, the total volume covered by these hot spots remains comparatively small compared to the overall volume of the bulky tumors (4, 8).

10.3389/fonc.2025.1474327

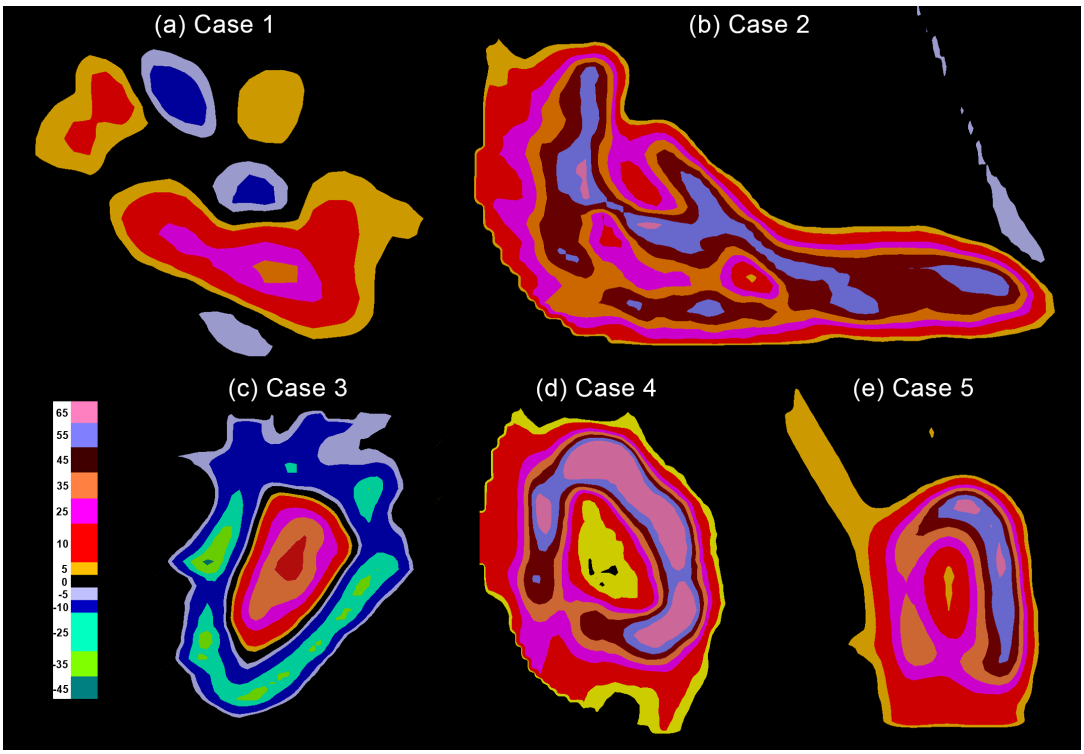

FIGURE 3
The target dose differences between pSCART and uniform dose proton plans. Note: Compared with proton therapy plans that employ uniform dose distribution, the pSCART technique achieves a dose escalation effect by increasing the dose at the center of the target volume. Dosimetric comparative analysis reveals that the pSCART plan exhibits a characteristic asymmetric dose distribution relative to the patient's original treatment plan. This spatial dose heterogeneity may enhance the biological response of SFRT through the radiation bystander effect; however, its dose–effect relationship requires systematic validation through animal and clinical trials. SCART, stereotactic centralized/core ablative radiation therapy; pSCART, proton-based SCART; SFRT, spatially fractionated radiation therapy.

SCART posits that increasing the proportion of the tumor's central core receiving ablative doses can enhance biological effects (6). This approach triggers the bystander effect and abscopal effect. In SCART, distinct high-dose central regions, low-dose peripheries, and intermediate-dose areas coexist within the GTV. High doses can achieve effective ablation, and expanding the high-dose region can further enhance ablation efficacy. Meanwhile, administering a lower dose at the tumor margins helps protect adjacent normal tissues.

TABLE 3 Dosimetric indexes of the target coverage in the CyberKnife SCART and proton-based SCART.

	Equipment	Technique	Vol. of 80% (cm^3)	80%/20%	80% cover of GTV	20% cover of GTV	80% cover of SCTV
Case 1	CyberKnife	SCART	7.22	6.06%	8.9%	90.1%	97.2%
	Proton	pSCART	0.46	0.74%	7.66%	94.16%	96.24%
Case 2	CyberKnife	SCART	31.11	1.59%	3.1%	96.6%	43.6%
	Proton	pSCART	48.28	5.28%	5.38%	91.53%	69.77%
Case 3	CyberKnife	SCART	15.44	2.07%	4.2%	99.9%	99.5%
	Proton	pSCART	39.00	11.11%	8.48%	92.86%	100.00%
Case 4	CyberKnife	SCART	38.09	5.55%	5.5%	98.4%	66.6%
	Proton	pSCART	59.05	9.95%	9.23%	88.96%	100.00%
Case 5	CyberKnife	SCART	67.57	5.37%	12.0%	98.4%	74.2%
	Proton	pSCART	40.10	7.17%	7.6%	98.64%	97.13%

The shaded area in gray indicates that the results of pSCART are lower in comparison.
GTV, gross target volume; SCTV, stereotactic centralized/core target volumes; SCART, stereotactic centralized/core ablative radiation therapy; pSCART, proton-based SCART.

10.3389/fonc.2025.1474327

TABLE 4 Dosimetric indices for high dose at tumor edge in SCART and pSCART.

	Equipment	Technique	V_{5Gy} (cm^3)	Gy/fractions
Case 1	CyberKnife	SCART	6.85	4.78
	Proton	pSCART	6.75	4.71
Case 2	CyberKnife	SCART	151.66	6.67
	Proton	pSCART	23.72	5.19
Case 3	CyberKnife	SCART	66.98	6.17
	Proton	pSCART	17.53	5.17
Case 4	CyberKnife	SCART	106.15	6.19
	Proton	pSCART	5.93	4.58
Case 5	CyberKnife	SCART	112.08	6.12
	Proton	pSCART	19.38	5.13

The results marked in gray indicate that the dose outside the target volume is less than 5 Gy/fraction or that the V_{5Gy} is less than 20 cm^3.
SCART, stereotactic centralized/core ablative radiation therapy; pSCART, proton-based SCART.

Previous SCART studies have shown that the high-dose region typically accounts for approximately 4.5% of the GTV (4, 8, 29). Protons delivered via spot-scanning technology offer superior dose modulation capabilities and reduce side effects. Consequently, this paper proposes pSCART treatment and investigates whether pSCART can achieve higher prescription doses, larger central/core high-dose regions, and lower doses at the tumor edge.

This study provides initial insight into the feasibility of treating bulky tumors with pSCART. Results demonstrate that the pSCART can achieve a prescription dose of 24 Gy × 3 fractions at the central high-dose region, with high-dose regions occupying a volume significantly greater than 4.5% of the GTV. The coverage rate of the high-dose area to the SCTV was relatively high. The volume outside the target area receiving a dose exceeding 5 Gy was smaller, and the extent of the high-dose region outside the target area was lower. Based on the results of the dose outside the target area, the following dose limit conditions for pSCART could be initially proposed: the dose volume outside the target area exceeding 5 Gy per fraction should be less than 20 cm^3.

Compared to CyberKnife-based SCART, pSCART can deliver a higher prescription dose and achieve comparable or superior tumor

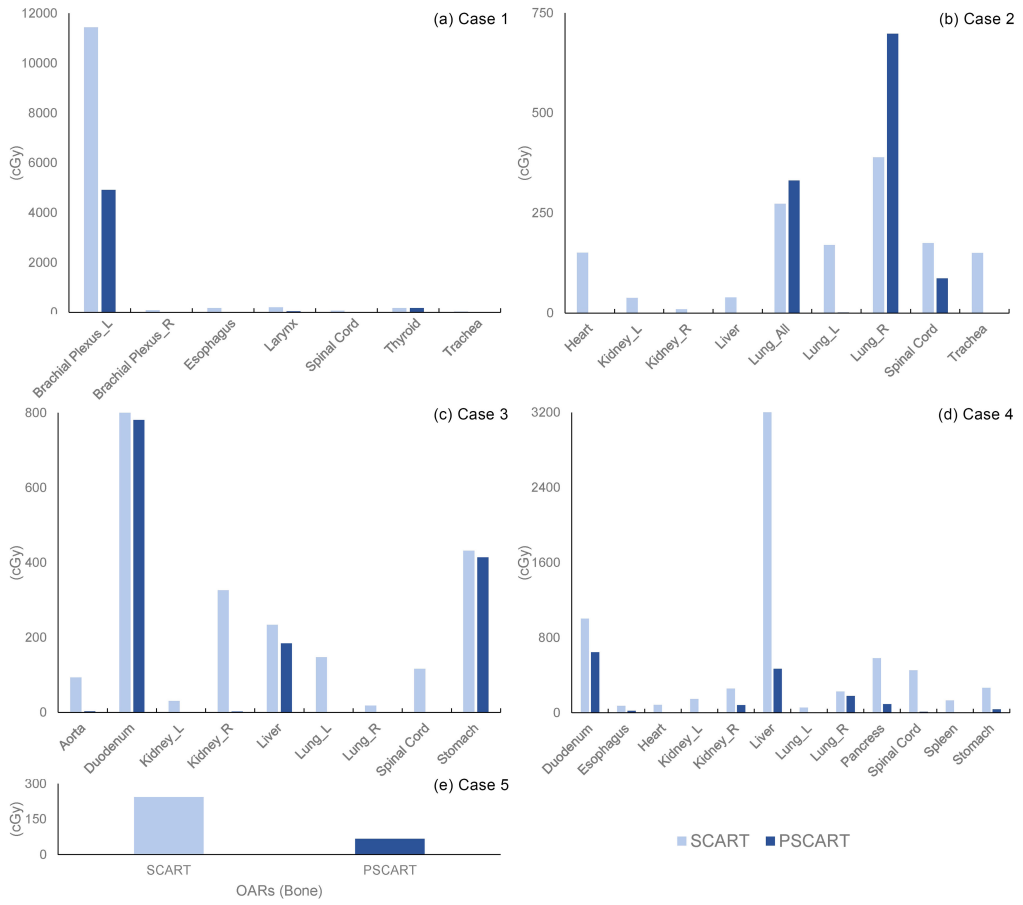

FIGURE 4
The average dosage of OARs in the CyberKnife SCART and pSCART plans. Note: The figure comparing the mean dose to OARs highlights the differences between SCART and pSCART plans. Except for the affected lung and total lungs in Case 2, the mean dose for all other cases in pSCART was lower than that in the SCART, with some OARs receiving no significant dose. It is important to note that mean dose has limitations in assessing serial organs, as it may not fully capture the potential damage to critical serial organs. Therefore, in the practical application of pSCART, it is recommended to emphasize the dose limits established for existing SBRT protocols. OARs, organs at risk; SCART, stereotactic centralized/core ablative radiation therapy; pSCART, proton-based SCART; SBRT, stereotactic body radiotherapy.

coverage while maintaining similar dose levels for OARs. The objective of SCART was not simply to administer a supra-high dose or a very large high-dose area but rather to adopt a balanced approach. Considering the protection of OARs as a premise, it may be necessary to adjust the prescription dose accordingly, potentially utilizing lower doses than those employed in this study. Compared to conventional proton radiotherapy, the pSCART plans deliver a high dose per fraction to the tumor (up to 72-Gy RBE total dose at the central region), particularly for targeting bulky lesions due to their ablative radiation dose nature. When not accounting for interplay effects and dose delivery errors due to respiratory motion, the pSCART plans based on active beam scanning (ABS) achieve more effective modulation of dose within the target volume. Daily patient set-up and tumor localization pose challenges due to organ movement relative to bony anatomy and inter-fraction organ deformation (30). Consequently, administering pSCART treatments in 3 fractions may reduce inter-fraction set-up uncertainties.

In the specific pSCART plans, the maximum dose received by the left brachial plexus in Case 1 and the dose of the volume at 11.4 Gy received by the duodenum in Case 3 did not meet the dose limit. Except for these two indicators, the remaining OARs in all cases conform to the prescribed dose limits for SBRT mentioned in AAPM TG101 reports (31). The brachial plexus in Case 1 was encompassed within the target volume, and the specific reduction of dose within the SCART target volume was unattainable. The pSCART plan yielded two distinct "hot spots" within the target volume, achieving the prescribed dose. In view of the lack of specific restrictions on bone dose in the existing dose limits for SBRT, in Case 5, the $NTD_{2.0}$ method was adopted for conversion to explore the possibility of comparison with dose limits that may lead to femoral fracture (17).

The assessment of toxicity to normal tissues anticipates that the Linear Quadratic (LQ) model will tend to overestimate the extent of damage, especially at doses exceeding 10 Gy per fraction (32). The approach to avoid femoral fracture by computing and evaluating the radiation dose to the bone using BED (Equation 1) and NTD (Equation 2) is conservative. Regarding the feasibility of delivering pSCART treatments in clinics, plans evaluated in this work are realizable using the experimental set-up already implemented for preclinical trials and treatment. The organ motion can be controlled as in current SBRT and common proton treatments. Further development of corresponding biological models and assessment parameters is still required for a more effective evaluation of the efficacy of pSCART.

5 Conclusions

This manuscript presents the first treatment plan evaluation of pSCART for treating sarcoma, pancreatic cancer, and liver cancer. Compared to the CyberKnife SCART, pSCART demonstrates superior dose prescription, larger central high-dose regions, and higher target coverage. Additionally, pSCART delivers lower doses at the tumor margins, reducing integral doses to OARs and enhancing normal tissue sparing. These advantages suggest an increased therapeutic index for bulky treatments. Phase I clinical trials are warranted to confirm these findings.

Data availability statement

The original contributions presented in the study are included in the article/supplementary material. Further inquiries can be directed to the corresponding authors.

Author contributions

TL: Resources, Writing – original draft, Writing – review & editing. XY: Writing – original draft, Writing – review & editing. JC: Project administration, Writing – original draft, Writing – review & editing. RH: Conceptualization, Investigation, Writing – review & editing. XX: Data curation, Formal analysis, Methodology, Writing – original draft. SW: Data curation, Formal analysis, Methodology, Writing – original draft. QQ: Data curation, Formal analysis, Methodology, Writing – original draft. QT: Conceptualization, Methodology, Project administration, Writing – original draft, Writing – review & editing. YY: Investigation, Resources, Supervision, Writing – review & editing.

Funding

The author(s) declare that financial support was received for the research and/or publication of this article. This project received funding from the Natural Science Foundation of China (Grant Nos. 82072094 and 12275162), Youth Foundation of National Natural Science Foundation of China (Grant No. 12305394) Natural Science Foundation of Shandong Province (Grant No. ZR2019LZL017), Taishan Scholars Project of Shandong Province (Grant No. ts201712098), Xinjiang Uygur Autonomous Region key research and development project (Grant No. 2022B03019-5), and Tumor precision radiotherapy peak plan (Grant No. 2021HZ81).

Conflict of interest

The authors declare that the research was conducted in the absence of any commercial or financial relationships that could be construed as a potential conflict of interest.

Publisher's note

All claims expressed in this article are solely those of the authors and do not necessarily represent those of their affiliated organizations, or those of the publisher, the editors and the reviewers. Any product that may be evaluated in this article, or claim that may be made by its manufacturer, is not guaranteed or endorsed by the publisher.

References

1. Johnson CR, Thames HD, Huang DT, Schmidt-Ullrich RK. The tumor volume and clonogen number relationship: tumor control predictions based upon tumor volume estimates derived from computed tomography. *Int J Radiat Oncol Biol Phys*. (1995) 33:281–7. doi: 10.1016/0360-3016(95)00119-j

2. Mohiuddin M, Curtis DL, Grizos WT, Komarnicky L. Palliative treatment of advanced cancer using multiple nonconfluent pencil beam radiation. *A Pilot Study Cancer*. (1990) 66:114–8. doi: 10.1002/1097-0142(19900701)66:1<114::aid-cncr2820660121>3.0.co;2-l

3. Tubin S. A partial tumor irradiation approach for complex bulky disease. *Semin Radiat Oncol*. (2024) 34:323–36. doi: 10.1016/j.semradonc.2024.04.005

4. Yang J, Lu Q, Qi W, Kolb RD, Wang L, Li Y, et al. Stereotactic central/core ablative radiation therapy: results of a phase I study of a novel strategy to treat bulky tumor. *Front Oncol*. (2024) 14:1364627. doi: 10.3389/fonc.2024.1364627

5. Luke JJ, Onderdonk BE, Bhave SR, Karrison T, Lemons JM, Chang P, et al. Improved survival associated with local tumor response following multisite radiotherapy and pembrolizumab: secondary analysis of a phase I trial. *Clin Cancer Res*. (2020) 26:6437–44. doi: 10.1158/1078-0432.Ccr-20-1790

6. Tubin S, Popper HH, Brcic L. Novel stereotactic body radiation therapy (Sbrt)-based partial tumor irradiation targeting hypoxic segment of bulky tumors (Sbrt-pathy): improvement of the radiotherapy outcome by exploiting the bystander and abscopal effects. *Radiat Oncol*. (2019) 14:21. doi: 10.1186/s13014-019-1227-y

7. Yan W, Khan MK, Wu X, Simone CB 2nd, Fan J, Gressen E, et al. Spatially fractionated radiation therapy: history, present and the future. *Clin Transl Radiat Oncol*. (2020) 20:30–8. doi: 10.1016/j.ctro.2019.10.004

8. Yan W, Mourad WF, Shi Z, Yang J, Lu Q, Qi W, et al. The safety and efficacy of scart for bulky metastatic or recurrent cancer, a phase I study. *Int J Radiat OncologyBiologyPhysics*. (2023) 117:e158. doi: 10.1016/j.ijrobp.2023.06.986

9. Hopewell JW, Morris AD, Dixon-Brown A. The influence of field size on the late tolerance of the rat spinal cord to single doses of X rays. *Br J Radiol*. (1987) 60:1099–108. doi: 10.1259/0007-1285-60-719-1099

10. Dilmanian FA, Qu Y, Feinendegen LE, Peña LA, Bacarian T, Henn FA, et al. Tissue-sparing effect of X-ray microplanar beams particularly in the cns: is a bystander effect involved? *Exp Hematol*. (2007) 35:69–77. doi: 10.1016/j.exphem.2007.01.014

11. Bouchet A, Serduc R, Laissue JA, Djonov V. Effects of microbeam radiation therapy on normal and tumoral blood vessels. *Phys Med*. (2015) 31:634–41. doi: 10.1016/j.ejmp.2015.04.014

12. Grass GD, Krishna N, Kim S. The immune mechanisms of abscopal effect in radiation therapy. *Curr Probl Cancer*. (2016) 40:10–24. doi: 10.1016/j.currproblcancer.2015.10.003

13. Dilmanian FA, Button TM, Le Duc G, Zhong N, Peña LA, Smith JA, et al. Response of rat intracranial 9l gliosarcoma to microbeam radiation therapy. *Neuro Oncol*. (2002) 4:26–38. doi: 10.1093/neuonc/4.1.26

14. Lee Y, Auh SL, Wang Y, Burnette B, Wang Y, Meng Y, et al. Therapeutic effects of ablative radiation on local tumor require cd8+ T cells: changing strategies for cancer treatment. *Blood*. (2009) 114:589–95. doi: 10.1182/blood-2009-02-206870

15. Garcia-Barros M, Paris F, Cordon-Cardo C, Lyden D, Rafii S, Haimovitz-Friedman A, et al. Tumor response to radiotherapy regulated by endothelial cell apoptosis. *Science*. (2003) 300:1155–9. doi: 10.1126/science.1082504

16. Wayne Newhauser, International Commission on Radiation Units and Measurements Report 78: Prescribing, Recording and Reporting Proton-beam Therapy, Radiation Protection Dosimetry. 133(1):60–2. doi: 10.1093/rpd/ncp005

17. Pak D, Vineberg KA, Griffith KA, Sabolch A, Chugh R, Ben-Josef E, et al. Dose–effect relationships for femoral fractures after multimodality limb-sparing therapy of soft-tissue sarcomas of the proximal lower extremity. *Int J Radiat Oncol Biol Phys*. (2012) 83:1257–63. doi: 10.1016/j.ijrobp.2011.09.047

18. Qi XS, Schultz CJ, Li XA. An estimation of radiobiologic parameters from clinical outcomes for radiation treatment planning of brain tumor. *Int J Radiat Oncol Biol Phys*. (2006) 64:1570–80. doi: 10.1016/j.ijrobp.2005.12.022

19. Hopewell JW. Radiation-therapy effects on bone density. *Med Pediatr Oncol*. (2003) 41:208–11. doi: 10.1002/mpo.10338

20. Zhang H, Wu X. Which modality of sfrt should be considered first for bulky tumor radiation therapy, grid or lattice? *Semin Radiat Oncol*. (2024) 34:302–9. doi: 10.1016/j.semradonc.2024.04.006

21. Gholami S, Nedaie HA, Longo F, Ay MR, Wright S, Meigooni AS. Is grid therapy useful for all tumors and every grid block design? *J Appl Clin Med Phys*. (2016) 17:206–19. doi: 10.1120/jacmp.v17i2.6015

22. Wang K, Marrufo JJ, Cothran CV, McClain PD, Lewis GD, Sabouri P, et al. Spatially fractionated radiotherapy grid for bulky tumor: A large single institution experience. *Int J Radiat OncologyBiologyPhysics*. (2024) 120:e284–e5. doi: 10.1016/j.ijrobp.2024.07.631

23. Iori F, Cappelli A, D'Angelo E, Cozzi S, Ghersi SF, De Felice F, et al. Lattice radiation therapy in clinical practice: A systematic review. *Clin Transl Radiat Oncol*. (2023) 39:100569. doi: 10.1016/j.ctro.2022.100569

24. Duriseti S, Kavanaugh J, Goddu S, Price A, Knutson N, Reynoso F, et al. Spatially fractionated stereotactic body radiation therapy (Lattice) for large tumors. *Adv Radiat Oncol*. (2021) 6:100639. doi: 10.1016/j.adro.2020.100639

25. Schneider T, De Marzi L, Patriarca A, Prezado Y. Advancing proton minibeam radiation therapy: magnetically focussed proton minibeams at a clinical centre. *Sci Rep*. (2020) 10:1384. doi: 10.1038/s41598-020-58052-0

26. Ortiz R, Belshi R, De Marzi L, Prezado Y. Proton minibeam radiation therapy for treating metastases: A treatment plan study. *Med Phys*. (2023) 50:2463–73. doi: 10.1002/mp.16203

27. Peucelle C, Nauraye C, Patriarca A, Hierso E, Fournier-Bidoz N, Martínez-Rovira I, et al. Proton minibeam radiation therapy: experimental dosimetry evaluation. *Med Phys*. (2015) 42:7108–13. doi: 10.1118/1.4935868

28. Song CW, Glatstein E, Marks LB, Emami B, Grimm J, Sperduto PW, et al. Biological principles of stereotactic body radiation therapy (Sbrt) and stereotactic radiation surgery (Srs): indirect cell death. *Int J Radiat Oncol Biol Phys*. (2021) 110:21–34. doi: 10.1016/j.ijrobp.2019.02.047

29. Yan W, Lu Q, Qi W, Yu F, Li Y, Li S, et al. SCART, a multi-center phase I trial of stereotactic central ablative radiation therapy for bulky tumor. *Cureus*. (2022) 14(2): a780.

30. Belikhin M, Shemyakov A, Ivanov D, Zavestovskaya I. Interplay effect in spot-scanning proton therapy with rescanning, breath holding, and gating: A phantom study. *Appl Sci*. (2024) 14:8473. doi: 10.3390/app14188473

31. Benedict SH, Yenice KM, Followill D, Galvin JM, Hinson W, Kavanagh B, et al. Stereotactic body radiation therapy: the report of aapm task group 101. *Med Phys*. (2010) 37:4078–101. doi: 10.1118/1.3438081

32. Brenner DJ. The linear-quadratic model is an appropriate methodology for determining isoeffective doses at large doses per fraction. *Semin Radiat Oncol*. (2008) 18:234–9. doi: 10.1016/j.semradonc.2008.04.004

frontiers | Frontiers in Oncology

TYPE Original Research
PUBLISHED 21 March 2025
DOI 10.3389/fonc.2025.1509619

Check for updates

OPEN ACCESS

EDITED BY
Abdul K. Parchur,
Medical College of Wisconsin, United States

REVIEWED BY
Tomasz Borowiec,
Lower Silesian Oncology Center, Poland
Silambarasan Anbumani,
Medical College of Wisconsin, United States

*CORRESPONDENCE
Ke Hu
huke8000@126.com
Fuquan Zhang
zhangfq@pumch.cn

†These authors have contributed equally to this work

RECEIVED 11 October 2024
ACCEPTED 03 March 2025
PUBLISHED 21 March 2025

CITATION
Sun S, Gong X, Liang Y, Sun Y, Que D, Xie Y, He S, He L, Liang H, Wang Y, Wu X, Wang C, Yang B, Qiu J, Hu K and Zhang F (2025) Evaluating the Implementation of fan-beam CT-guided online adaptive re-planning in definitive cervical cancer radiotherapy. *Front. Oncol.* 15:1509619. doi: 10.3389/fonc.2025.1509619

COPYRIGHT
© 2025 Sun, Gong, Liang, Sun, Que, Xie, He, He, Liang, Wang, Wu, Wang, Yang, Qiu, Hu and Zhang. This is an open-access article distributed under the terms of the Creative Commons Attribution License (CC BY). The use, distribution or reproduction in other forums is permitted, provided the original author(s) and the copyright owner(s) are credited and that the original publication in this journal is cited, in accordance with accepted academic practice. No use, distribution or reproduction is permitted which does not comply with these terms.

Evaluating the Implementation of fan-beam CT-guided online adaptive re-planning in definitive cervical cancer radiotherapy

Shuai Sun[1†], Xinyue Gong[1,2†], Yongguang Liang[1], Yuliang Sun[1], Dan Que[3], Yangchun Xie[4], Shumeng He[5], Lei He[1], Hao Liang[1], Yijun Wang[1], Xinyi Wu[6], Cheng Wang[7], Bo Yang[1], Jie Qiu[1], Ke Hu[1*] and Fuquan Zhang[1*]

[1]Department of Radiation Oncology, Peking Union Medical College Hospital, Chinese Academy of Medical Sciences and Peking Union Medical College, Beijing, China, [2]Eight-Year Program of Clinical Medicine, Peking Union Medical College, Chinese Academy of Medical Science and Peking Union Medical College, Beijing, China, [3]Department of Oncology, The Third Affiliated Hospital of Chongqing Medical University, Chongqing, China, [4]Department of Oncology, the Second Xiangya Hospital, Central South University, Changsha, Hunan, China, [5]United Imaging Research Institute of Intelligent Imaging, Radiotherapy (RT) Lab, Beijing, China, [6]Central Research Institute, United Imaging Healthcare Company, Shanghai, China, [7]Shanghai United Imaging Healthcare Co., Ltd, Radiotherapy (RT) Business Unit, Shanghai, China

Background: This study aims to investigate the feasibility of fan-beam computed tomography (FBCT)-guided online adaptive radiotherapy (oART) in radical radiotherapy for cervical cancer.

Methods: Ten patients who underwent radical radiotherapy for cervical cancer were enrolled in this study. All patients received external beam radiation therapy (EBRT) with a prescription dose of 50.4 Gy/28f, and daily oART with FBCT guidance was performed. Dosimetric analysis was conducted on 278 fractions, comparing the adaptive and scheduled plans. The γ passing rate was measured through *in-vivo* dose monitoring during treatment, using a 3%/3mm gamma criterion with an 88% threshold for alerts. The time invested in the oART workflow was recorded at each step. Acute toxicities were classified following the Common Terminology Criteria for Adverse Events (CTCAE) version 5.0.

Results: The adaptive plans demonstrated a dosimetric advantage in target coverage and/or organs at risk (OARs) sparing across all 278 fractions. Compared to the scheduled plan, the adaptive plan showed improved dose received by 95% (D95) of planning target volume (PTV), conformity index (CI), and homogeneity index (HI) ($P<0.001$). Among the three PTVs, the PTV of uterus (PTV_U) benefited most from dosimetric improvements in the adaptive plan, followed by the PTV of cervix, vagina, and parametrial tissues (PTV_C), while the PTV of lymph node (PTV_N) exhibited the least enhancement. For OARs, the adaptive plan achieved reductions in the dose to the most irradiated 2 cm^3 volume (D2cc) for the rectum, bladder, and small intestine ($P<0.001$). For patients with ovarian conservation, the dose to the 50% volume (D50) and the mean dose of the bilateral ovaries were decreased ($P<0.001$). The mean γ passing rate across all fractions was 99.24%. The mean duration of the oART workflow was 22.82 ± 3.61 min, with auto-segmentation & review (44.40%) and plan generation & evaluation (22.02%) being the most time-intensive steps. The incidence of Grade

1-2 acute non-hematological toxicity was 60%, with no cases of Grade 3 or higher observed.

Conclusions: The implementation of FBCT-guided oART in radical radiotherapy for cervical cancer was feasible. This approach has shown significant improvements in dose distribution and the potential to provide clinical benefits by reducing acute toxicity.

KEYWORDS

online adaptive radiotherapy (oART), cervical cancer, fan-beam computed tomography (FBCT), image-guided radiotherapy (IGRT), dosimetric distribution, acute toxicity

Introduction

Cervical cancer is among the most prevalent malignant neoplasms of the female reproductive system, exhibiting a global age-standardized incidence rate of 13.3 per 100,000 and a mortality rate of 7.2 per 100,000 in 2020, notably elevated in low and middle-income countries (1). Radiotherapy, particularly external beam radiotherapy (EBRT) followed by brachytherapy, plays a central role in the definitive management of locally advanced cervical cancer. The evolution of EBRT technology, along with the adoption of image-guided radiotherapy (IGRT), has resulted in better target conformity and reduced doses to organs at risk (OARs) (2, 3). However, dynamic changes in pelvic organ volume and position, such as bladder filling and intestinal gas variations, lead to significant inter-fractional motion of the target volume, making it challenging to deliver precise and effective radiation doses (4–6). Conventionally, inter-fractional motion has been managed by establishing sufficient margins from the clinical target volume (CTV) to the planning target volume (PTV), thereby ensuring adequate coverage. However, this approach increases radiation exposure to surrounding healthy tissues, elevating the risk of treatment-related toxicity. To mitigate these challenges, online adaptive radiotherapy (oART) has emerged as a promising approach to optimize dose delivery by adapting treatment plans to anatomical changes based on daily images (7). Recent advances in artificial intelligence (AI)-driven auto-segmentation and treatment planning have further enhanced the feasibility of oART (8).

Currently, clinical implementation of oART is guided by various imaging modalities, including cone-beam computed tomography (CBCT), magnetic resonance imaging (MRI), and fan-beam computed tomography (FBCT). CBCT is widely utilized for oART; however, its suboptimal image quality and the need for pseudo-CT generation for dose calculations may compromise treatment precision (9, 10). MR-guided radiotherapy has garnered attention for its superior soft-tissue contrast in adaptive workflows, but its widespread adoption is constrained by high cost, restricted availability, and prolonged treatment times (11). FBCT has emerged as a promising imaging modality for oART, offering a balance between high soft-tissue resolution and rapid image acquisition while enabling direct dose calculation on the acquired images. Despite these advantages, clinical research on FBCT-guided oART remains relatively limited.

This study aims to evaluate the implementation of FBCT-guided oART in definitive radiotherapy for cervical cancer. By comparing dosimetric outcomes, analyzing acute treatment-related toxicity and clinical response, as well as evaluating workflow processes, we seek to provide evidence supporting the wider clinical adoption of FBCT-guided adaptive strategies in cervical cancer.

Materials and methods

Patients

From May 2023 to August 2023, ten consecutive cervical cancer patients scheduled for undergo radical radiotherapy at Peking Union Medical College Hospital were enrolled in this study. Inclusion criteria included (1) confirmed diagnosis of cervical cancer through imaging and biopsy pathology; (2) indication for radical radiotherapy; (3) life expectancy of more than 6 months; (4) ECOG score of 0-2 and ability to remain lying flat for more than 30 minutes. Patients with a history of pelvic radiotherapy, contraindications to radiotherapy, or need for irradiation of the para-aortic or inguinal lymph node drainage regions were excluded. All patients received EBRT using volumetric modulated arc therapy (VMAT) followed by three-dimensional brachytherapy. All patients received 4-6 cycles of concurrent cisplatin-sensitizing chemotherapy, except one patient who was intolerant to platinum-based drugs. Treatment response was assessed at 1 and 3 months after radiotherapy using MRI and tumor markers. Squamous cell carcinoma antigen (SCC-Ag) was measured for squamous carcinoma, while carcinoembryonic antigen (CEA), cancer antigen 125 (CA125), and cancer antigen 19-9 (CA199) were analyzed for adenocarcinoma. Clinical complete response

(cCR) was defined as normal tumor marker levels and the absence of residual tumor or enlarged metastatic lymph nodes on pelvic MRI. Toxicities occurring during radiotherapy and within 3 months after its completion were defined as acute toxicities. These toxicities were graded and recorded according to the Common Terminology Criteria for Adverse Events version 5.0 (CTCAE 5.0).

CT simulation and reference plan generation

Patients were guided to empty their bladder and bowels 2 hours prior to both the CT simulation and each subsequent fraction. They were then instructed to consume 500 mL of water 1.5 hours before the treatment time and to refrain from urinating until after their session. Following fixation of the patient's position, a CT scan was conducted that covered an area extending from the superior boundary of the liver to 5 cm beneath the ischial tuberosity, with a scan slice thickness of 5 mm. The target volumes were delineated in accordance with Radiation Therapy Oncology Group consensus guidelines for definitive radiotherapy of cervical cancer (12, 13). The gross target volume of the lymph nodes (GTVnd) was defined as the metastatic lymph nodes visible on the CT/MRI/PET images. The CTV consisted of three parts, including the CTV of the lymph nodes (CTV_N), the CTV of the uterus (CTV_U), and the CTV of the cervix, vagina, and parametrial tissues (CTV_C). CTV_N encompassed the common iliac, internal iliac, external iliac, obturator, and presacral lymph node drainage regions. CTV_U was expanded isotropically by 10 mm to form the PTV of the uterus (PTV_U), while CTV_C and CTV_N were each expanded isotropically by 5 mm to generate the PTV of the cervix, vagina, and parametrial tissues (PTV_C) and the PTV of the lymph node (PTV_N), respectively. These three PTVs were then combined to form the overall PTV. GTVnd expanded a 5mm margin to create the PTV of the metastatic lymph nodes (PTVnd). The prescribed dose for the three PTVs was 50.4 Gy in 28 fractions, with a simultaneous boost of 60.2 Gy in 28 fractions to PTVnd. A dual-arc VMAT reference plan was created based on the clinical goal sheet (Supplementary Table S1) for treatment implementation, using a 2.5 mm dose grid spacing. All treatment plans in this study were generated using the United Treatment Planning System (uTPS, Shanghai United Imaging Healthcare Co., Ltd, Shanghai, China). The reference plan was manually designed using the Stochastic Platform Optimization (SPO) algorithm (14).

The workflow of daily oART

The oART for the definitive treatment of cervical cancer was performed using the uRT-linac 506c (Shanghai United Imaging Healthcare Co., Ltd, Shanghai, China), which is a 6-megavolt (MV) C-arm linear accelerator integrated with a diagnostic-quality kV FBCT. The X-ray linac and FBCT are co-axially equipped on the same bed, simultaneously realizing CT simulation, daily FBCT guidance, and beam delivery on the same platform. Detailed information about this machine has been previously reported (15).

As shown in Figure 1, the oART workflow mainly consisted of six steps: initial image acquisition, region of interest (ROI) auto-segmentation and review, adaptive plan generation, plan evaluation and selection, verification image acquisition, and treatment delivery. The oART workflow started with the initial FBCT acquisition. The FBCT scan covered an area extending more than 5 cm beyond the superior and inferior boundaries of the PTV volume with a scan slice thickness of 5 mm. The contours of the three CTVs were generated through deformable registration. The contours of all OARs were delineated using an AI-based auto-segmentation algorithm applied to daily FBCT images to account for inter-fractional anatomical changes. The auto-segmentation algorithm is based on a lightweight deep learning framework for radiotherapy treatment planning (RTP-Net). The algorithm supports whole-body OARs auto-segmentation with a level of accuracy comparable to, if not superior to, that of manual delineation, as evidenced by a mean Dice Similarity Coefficient (DSC) of 0.95. Furthermore, the algorithm facilitates real-time segmentation, with most tasks completed in under two seconds (16). Subsequently, the radiation oncologist reviewed and edited the ROI contours. Figure 2 shows the daily FBCT images of a representative patient. Compared with the simulation CT, the

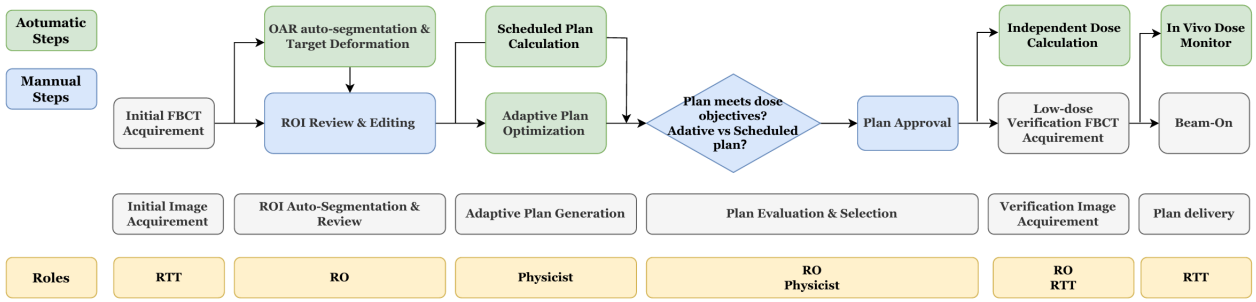

FIGURE 1
The workflow of FBCT-guided daily online adaptive radiotherapy. RO, radiation oncologist; RTT, radiotherapy technologist.

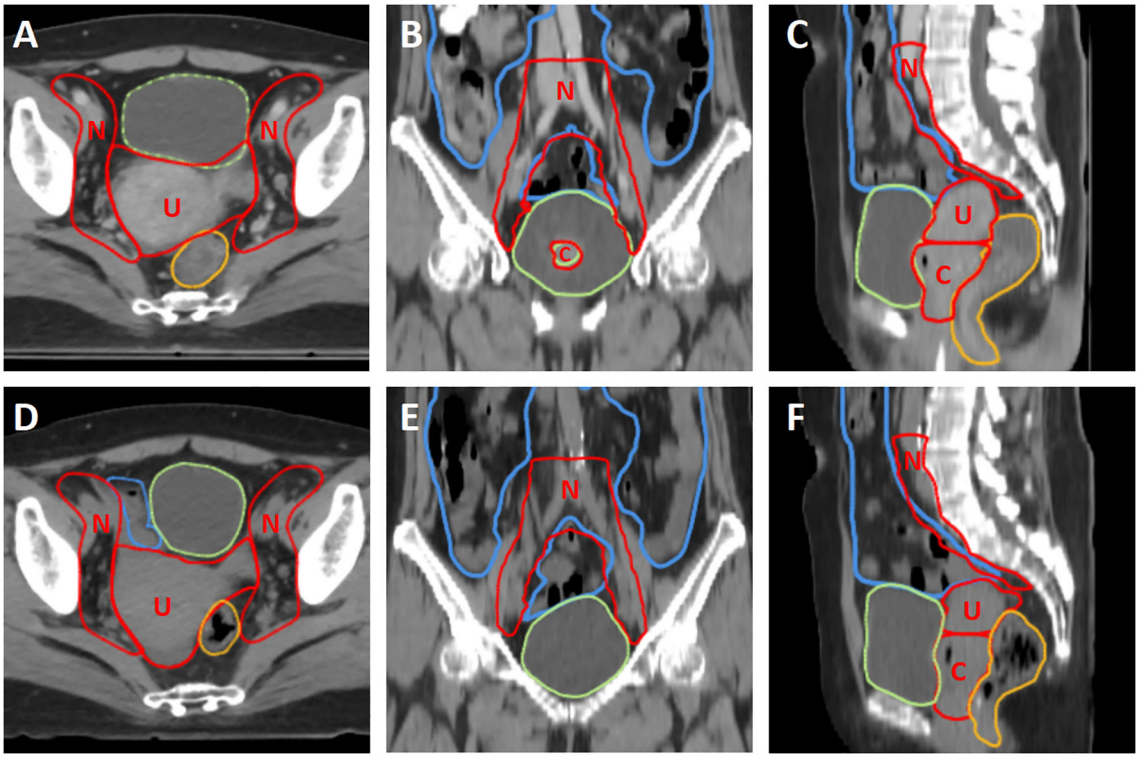

FIGURE 2
The comparison of simulation CT and daily kV FBCT of a representative patient. **(A–C)** The first row shows the simulation CT in axial, coronal, and sagittal planes, respectively. **(D–F)** The second row shows the daily kV FBCT in axial, coronal, and sagittal planes, respectively. The window level and window width are set to 40 and 400, respectively. Red contours represent the three CTVs (CTV_U, CTV_C, and CTV_N, labeled as U, C, and N), while green, yellow, and blue contours represent the bladder, rectum, and small intestine, respectively.

image quality remained consistent, whereas there were significant differences in the anatomical position of the CTV, which were attributed to variations in bladder filling and intestinal movement.

Once the contours review was completed, the adaptive plan was automatically created and optimized with the dose directly calculated on the daily kV FBCT images. This process utilized a fully automated algorithm that took the dose distribution of the reference plan and the clinical goal sheet as inputs. First, the clinical goal sheet was used to establish optimization constraints for the adaptive plan. Second, the dose-volume histograms (DVHs) of OARs were predicted by extracting the dose falloff features from the reference plan, which were used to update the optimization objectives. Third, target-related dosimetric parameters from the reference plan, including the conformity index (CI), dose at 2% and 98% volumes, and minimum and maximum doses, were extracted to guide the optimization process. Furthermore, the algorithm implemented various optimization strategies, including OAR dose reduction, dose conformity optimization, and hotspot removal, to ensure that the plan quality met the clinical requirements. Additionally, the scheduled plan was generated by mapping the reference plan to the daily kV FBCT images and recalculating the dose distribution.

Next, the workflow automatically proceeded to the plan evaluation and selection module. The radiation oncologist compares the clinical goals, dose distribution, and DVH of the adaptive and scheduled plans for evaluation and makes the final decision on plan selection manually. After plan approval, a validation FBCT was acquired using a low-dose protocol (one-third of the regular dose) to monitor intra-fractional changes. Meanwhile, the system automatically exported the selected plan to independent dose calculation software for online patient-specific quality assurance, which was conducted using a Monte Carlo-based independent dose calculation method tool uAssureTx.

During plan delivery, an electronic portal imaging device (EPID) was used to monitor the *in-vivo* doses of radiation fields. The transmission image was calculated using the Monte Carlo algorithm, taking into account the phase space of photons and electrons, detector response, and lateral scatter. The measured images were corrected before gamma comparison. To elaborate, geometry correction, dead pixel correction, dark current correction, and detector response correction were performed (17). Each patient underwent EPID *in vivo* monitoring for every fraction. A 3%/3mm gamma comparison between calculated transmission image and measured image is performed for every 30° of gantry rotation in real-time during delivery, and the passing rates are displayed on the treatment console. Based on previous studies and internal organ motion in real patient cases, we set the threshold of gamma passing rate to 88% (17, 18). If it falls below this threshold, the system alerts the therapist to assess treatment termination. The average passing rate overall delivered arc sections was calculated and reported for that fraction.

Statistical analysis

Mean and standard deviation (SD) were used for the analysis to describe continuous variables. Statistical tests with $P<0.05$ (two-sided) were considered significant. The Kolmogorov-Smirnov method was used to test the normality of the data. The dose difference between scheduled and adaptive plans was compared using the Wilcoxon signed-rank test for data with a non-normal distribution. The dose metrics were based on the addition of average value in the metrics across each delivered fraction (19). Boxplots showing the median value and interquartile range (IQR) were created with outliers outside 1.5 × IQR.

All statistical analyses were performed using SPSS version 26 (IBM Corp., Armonk, New York, USA) and R version 4.3.0 (R Core Team, R Foundation for Statistical Computing, Vienna, Austria), and GraphPad Prism 9 (GraphPad Software, La Jolla, California, USA).

Results

Patients characteristics

The clinical characteristics of the patients are summarized in Table 1. The average age of the enrolled patients was 54.7 ± 15.5 years. The FIGO stages ranged from IB3 to IIIC1, with squamous cell carcinoma being the predominant histological type, identified in 9 of 10 patients. Patients 3 and 10 underwent ovarian transposition surgery followed by ovarian-sparing radiotherapy. While all patients were scheduled for standard concurrent chemoradiotherapy, Patient 7 received immunotherapy with tislelizumab as a substitute for platinum-based chemotherapy due to intolerance. A total of 278 fractions were administered using oART technology. However, due to equipment maintenance or the absence of a radiation oncologist to delineate the target area, the remaining two treatments were conducted using the reference plan after confirming that the targets were not missed with FBCT.

Duration for the workflow of oART

The mean ± SD duration for the oART workflow was 22.82 ± 3.61min (Figures 3A–C), ranging from 15.58 to 38.45 minutes. The interquartile ranged from 20.39 to 24.63 minutes. The total time was recorded from the initial image acquisition to the completion of treatment delivery. The breakdown of the total time spent on the oART process is depicted in Figure 3C, including FBCT image acquisition and registration (2.25 ± 0.26min, 9.86%), ROI auto-segmentation & review (10.14 ± 2.81min, 44.40%), plan generation & evaluation (5.03 ± 1.41min, 22.02%), and beam-on (2.35 ± 0.21min, 10.31%). The remaining time (3.06 ± 1.74min, 13.41%) was allocated to transitional activities, including data transfer, equipment gantry adjustments, etc. The most time-intensive steps in the entire process were ROI auto-segmentation & review (44.40%) and plan generation & evaluation (22.02%), which exhibited the most significant variability among different patients and different treatment fractions.

TABLE 1 Clinical characteristics of 10 cervical cancer patients treated with the oART technique.

No.	Age	FIGO 2018 staging	Histopathology	Pelvic node boost	Ovarian Protection	Brachytherapy	Concurrent chemotherapy	Weight change (KG)	Acute toxicity grade*				Clinical Outcomes
									Rectum	UGI	Urinary	Hematologic	
1	55	IIIC1	Adeno	Yes	No	30Gy/5f	CDDP*6	+0.4	0	0	0	2	PR
2	58	IIA1	SCC	No	No	30Gy/5f	CDDP*5	-1.0	0	1	0	2	CR
3	30	IIB	SCC	No	Yes	30Gy/5f	CDDP*4	0	1	2	0	2	CR
4	57	IIIC1	SCC	Yes	No	30Gy/5f	CDDP*4	-5.3	0	2	0	3	CR
5	73	IIB	SCC	No	No	30Gy/5f	CDDP*4	-2.4	0	1	0	3	CR
6	53	IIIC1	SCC	Yes	No	30Gy/5f	CDDP*5	+0.1	0	0	0	3	CR
7	81	IIB	SCC	No	No	30Gy/5f	No	+1.0	0	0	0	3	CR
8	44	IB3	SCC	No	No	36Gy/6f	CDDP*5	+1.5	0	0	0	1	CR
9	60	IIB	SCC	No	No	30Gy/5f	CDDP*5	+1.6	0	1	0	2	CR
10	36	IIB	SCC	No	Yes	30Gy/5f	CDDP*5	-1.5	2	1	0	1	CR

FIGO, International Federation of Gynecology and Obstetrics; Adeno, adenocarcinoma; SCC, squamous cell carcinoma; CDDP, cis-diamminedichloroplatinum; UGI, upper gastrointestinal tract; CR, complete remission; PR, partial remission.
*Acute toxicity was graded by the CTCAE 5.0 version.

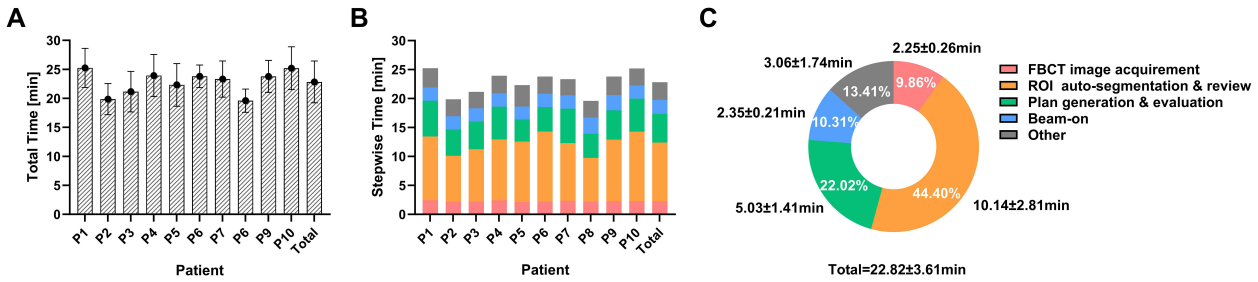

FIGURE 3
The duration for the workflow of oART. **(A)** Total duration of oART in each patient and overall. **(B, C)** Allocation of time within the various segments of oART in each patient and overall.

Comparison of dosimetric results between adaptive and scheduled plans

Table 2 and Figures 4A, B illustrate the dosimetric differences of the targets and OARs between the adaptive and scheduled plans.

For target dose distribution, the adaptive plan showed that the mean dose received by the 95% volume (D95) of PTV was 50.43 ± 0.13 Gy, which met the prescribed dose, in contrast to the scheduled plan's 47.49 ± 6.01 Gy (P<0.001). The adaptive plan offered significant improvements in the conformity index (CI) (0.90 vs. 0.82) and heterogeneity index (HI) (0.13 vs. 0.26) of the PTV compared to the scheduled plan (P<0.001). The adaptive plan also showed an increase in D95 of 6.74 Gy and 3.42 Gy for PTV_U and PTV_C, respectively (P<0.001), although the PTV_N D95 increased by only 0.15 Gy and was not statistically significant.

Regarding the dosimetric comparison for OARs, the adaptive plan yielded reductions in the dose to the most irradiated 2 cm3 volume (D2cc), the mean dose (Dmean), and the dose to the 50% of volume (D50) for the rectum by 0.10Gy, 0.12Gy, and 0.89Gy, respectively (P<0.05). For the bladder and small intestine, the adaptive plan showed a decrease in D2cc by 0.28Gy and 2.17Gy, respectively (P<0.001), although no significant dosimetric benefits were seen in the Dmean and D50 for these OARs. Furthermore, the dose to the 90% volume (D90) of bone marrow and the dose to the most irradiated 0.1 cm3 volume (D0.1cc) of spinal cord in the adaptive plan were significantly improved compared to the

TABLE 2 The difference in dosimetric parameters between adaptive plans and scheduled plans.

	Dosimetric Parameter (units)	Adaptive plans Mean ± SD	Scheduled plans Mean ± SD	Difference Mean ± SD	P-value
PTV	D95 (Gy)	50.43 ± 0.13	47.49 ± 6.01	2.94 ± 6.01	**<0.001***
	CI (%)	0.90 ± 0.03	0.82 ± 0.06	0.08 ± 0.07	**<0.001***
	HI (%)	0.13 ± 0.08	0.26 ± 0.18	-0.13 ± 0.19	**<0.001***
PTV_U	D95 (Gy)	50.58 ± 0.18	44.11 ± 9.77	6.47 ± 9.79	**<0.001***
PTV_C	D95 (Gy)	50.55 ± 0.17	47.14 ± 4.73	3.42 ± 4.72	**<0.001***
PTV_N	D95 (Gy)	50.54 ± 0.16	50.39 ± 1.67	0.15 ± 1.70	0.527
Rectum	D2cc (Gy)	52.22 ± 0.49	52.32 ± 1.62	-0.10 ± 1.68	**<0.001***
	Dmean (Gy)	35.17 ± 3.70	35.29 ± 5.99	-0.12 ± 5.71	**0.049***
	D50 (Gy)	38.36 ± 5.03	39.26 ± 9.51	-0.89 ± 9.81	**<0.001***
Bladder	D2cc (Gy)	53.39 ± 1.62	53.67 ± 1.79	-0.28 ± 1.15	**<0.001***
	Dmean (Gy)	36.05 ± 4.01	35.38 ± 7.15	0.68 ± 4.76	0.900
	D50 (Gy)	36.31 ± 6.16	36.34 ± 4.74	-0.03 ± 7.44	0.240
Small Intestine	D2cc (Gy)	52.70 ± 0.80	54.86 ± 1.91	-2.17 ± 1.57	**<0.001***
	Dmean (Gy)	17.59 ± 3.34	17.57 ± 3.52	0.02 ± 0.73	0.896
	D50 (Gy)	11.91 ± 6.05	11.91 ± 5.48	0.00 ± 1.71	0.973
Bone Marrow	D90 (Gy)	14.15 ± 1.63	15.04 ± 1.60	-0.89 ± 0.78	**<0.001***

(Continued)

TABLE 2 Continued

	Dosimetric Parameter (units)	Adaptive plans Mean ± SD	Scheduled plans Mean ± SD	Difference Mean ± SD	P-value
Left Femoral Head	D5 (Gy)	31.50 ± 3.11	31.16 ± 3.14	0.33 ± 2.32	0.286
Right Femoral Head	D5 (Gy)	31.28 ± 3.48	31.47 ± 3.58	0.19 ± 1.92	0.897
Spinal Cord	D0.1cc (Gy)	19.25 ± 4.28	22.74 ± 5.89	-3.49 ± 3.10	**<0.001***
Left Ovary	Dmean (Gy)	4.03 ± 0.36	7.01 ± 0.88	-2.97 ± 0.91	**<0.001***
	D50 (Gy)	3.93 ± 0.31	6.51 ± 0.60	-2.58 ± 0.65	**<0.001***
Right Ovary	Dmean (Gy)	3.96 ± 0.24	6.96 ± 2.01	-3.00 ± 1.95	**<0.001***
	D50 (Gy)	3.72 ± 0.24	6.46 ± 1.99	-2.73 ± 1.93	**<0.001***

*highlights significant p-values.
SD-standard deviation; PTV-planning target volume; CTV-clinical target volume; D95, D50, D5, D2cc, D0.1cc-the dose received by 95%, 50%, 5%, 2cc, 0.1cc of volumes; CI-conformity index = (Vt,ref/Vt)·(Vt,ref/Vref), Vt,ref is the target volume covered by the reference isodose line, Vt is the target volume, Vref is the total volume covered by the reference isodose line; HI-homogeneity index = (D2-D98)/D50.

scheduled plan (P<0.001). However, no dosimetric benefits for the bilateral femoral heads were observed in the adaptive plans. Notably, for the two patients undergoing ovarian-sparing radiotherapy, the adaptive plan halved the D50 and Dmean for bilateral ovaries to approximately 3-4 Gy (P<0.001).

According to Figure 4C, the DVH illustrates the dose disparities across the three treatment options. In terms of target dose distribution for PTV and PTVnd, the adaptive plan showed comparable results to the reference plan and notably superior results than the scheduled plan. The adaptive plan demonstrated an obvious improvement over the scheduled plan in terms of rectal dose distribution.

Analysis of target coverage alongside a priority 1 OAR constraint revealed a dosimetric benefit for the adaptive plans in

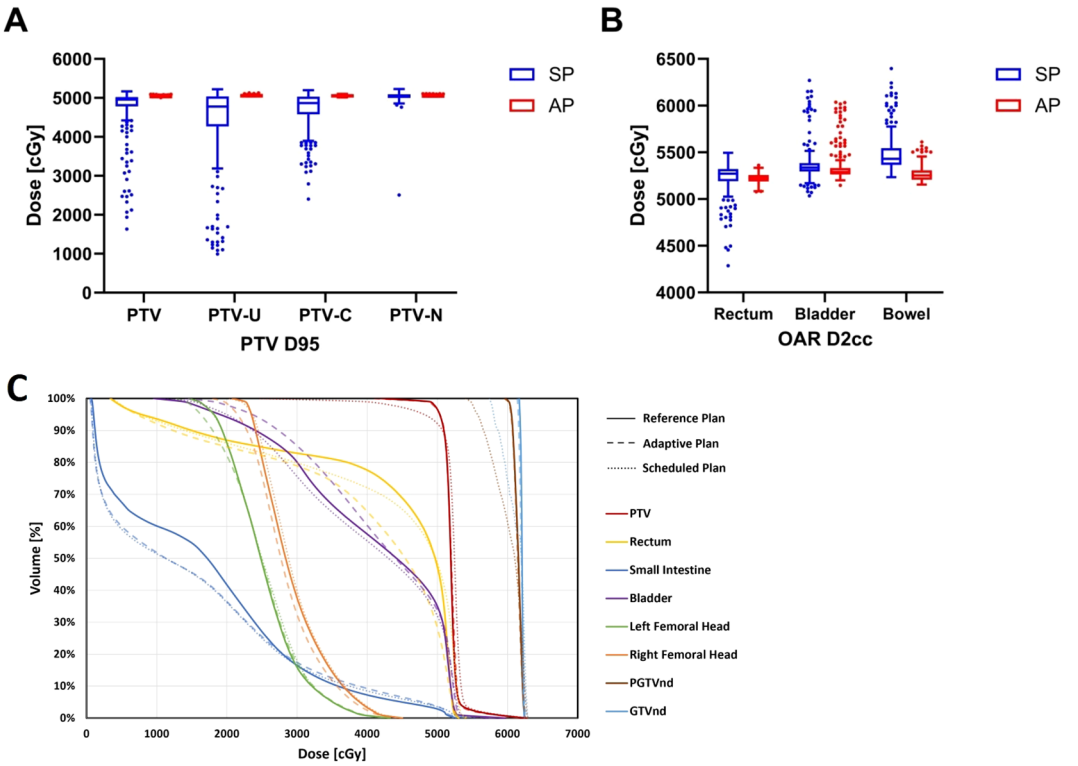

FIGURE 4
The differences in dosimetric parameters of targets and OARs between adaptive and scheduled plans: **(A)** PTV D95 **(B)** OARs D2cc **(C)** Dose-volume histograms of the three plans for a representative patient.

all 278 fractions. The adaptive plan demonstrated improvement in 222 fractions by providing enhanced target coverage and reduced small intestine D2cc exposure. In 2 fractions, it achieved superior target coverage with comparable small bowel D2cc to the scheduled plan. Meanwhile, in the remaining 54 fractions, the adaptive plan showed better performance in terms of protecting the small bowel D2cc, while both plans delivered a prescribed dose of at least 50.40 Gy to the PTV D95.

Independent dose verification and *in vivo* dose monitor

Independent dose verification revealed that out of 278 evaluations, the 3%/3mm γ passing rate was an exceptional 99.55 ± 0.29%. Notably, the lowest recorded γ passing rate was a remarkable 98.40%, comfortably surpassing the commonly accepted threshold for clinical requirements.

During plan delivery, EPID was used to monitor the *in-vivo* doses of radiation fields. Figure 5 illustrates that the implementation of two-dimensional *in vivo* dose monitoring during treatment administration yielded an average γ passing rate of 99.24 ± 1.35% across 278 fractions. All patients demonstrated a mean γ passing rate exceeding 99%, except for Patients 5, 6, and 10. Patients 5 and 10 had lower average gamma passing rates due to significant intestinal gas variations in some fractions. Patient 6 had a low gamma passing rate in the first four fractions because of insufficient CT scan range, but this issue was corrected in subsequent fractions.

Clinical outcomes and acute toxicities

The clinical outcomes and acute toxicities of the patients are presented in Table 1. The median follow-up time for all patients was 3.0 months (range: 3-4 months). At 3 months after radiotherapy, 90% of the patients achieved cCR. However, one patient showed persistent abnormal MRI signals, indicating residual tumor after treatment. The pathological type of this patient was gastric adenocarcinoma, which is known to be insensitive to radiotherapy.

In terms of acute toxicity, all patients experienced varying degrees of hematopoietic toxicity (Grade 1-3). The incidence of Grade 1-2 acute non-hematological toxicity in all patients was 60%, whereas no instances of Grade 3 or above acute non-hematological toxicity were observed. Upper gastrointestinal toxicity was common acute toxicity, with 2 cases of Grade 2 and 4 cases of Grade 1. Rectal toxicity mainly manifested as diarrhea, with 1 case of Grade 2 and 1 case of Grade 1. No patient experienced urinary toxicity. All patients fully recovered from acute toxicity at 3 months after the end of radiotherapy.

During radiotherapy, the patients' weight fluctuated slightly, with a mean weight change of -0.56 ± 2.11 Kg. Patient 4, however, experienced a significant weight loss of 5.4 Kg, which was attributed to poor appetite caused by Grade 2 upper gastrointestinal toxicity.

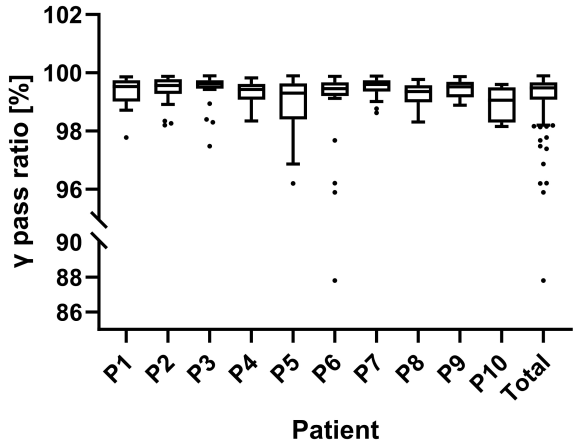

FIGURE 5
Results of *in-vivo* dose monitoring using an electronic portal imaging device (EPID). The γ passing rates for each patient and overall are shown. A 3%/3mm gamma criterion was used for real-time verification, with passing rates assessed every 30°of gantry rotation and an 88% threshold for alerts.

Discussion

Cervical cancer, due to the fact that it is significantly affected by physiological changes in the pelvic organs, is a typical disease that is suitable and necessary for oART (20). In this study, different from previous studies, diagnostic-quality FBCT was applied for oART image guidance. A comprehensive analysis was conducted on the workflow, dosimetry, and clinical outcomes associated with FBCT-guided daily oART in cervical cancer.

High-quality image guidance is a key foundation for implementing oART. The uRT-Linac 506c, utilized in this study, represents a CT-linac integration that combines kV FBCT with a 6-MV X-ray linac in a coaxial arrangement. This kV FBCT has been shown to achieve a spatial resolution of ≥15 line pairs per millimeter (lp/mm) and a low-contrast detectability of 2 mm (12). The acquired image sequence of FBCT shares a CT value-relative electron density conversion curve with the simulation CT, making it used directly for adaptive plan generation (15). While offering high spatial resolution, the imaging dose of FBCT is comparable to that of CBCT, alleviating concerns about increased patient radiation exposure with daily CT guidance. Currently, low-dose FBCT has already been adopted in clinics to reduce dosages further. Wei Gong et al. demonstrated that low-dose FBCT can achieve peripheral doses as low as 1.85mGy at the scanning field, highlighting its potential as a promising direction for future optimization (21, 22). In summary, FBCT offers a combination of high spatial resolution, direct usability for dose calculation and plan design, acceptable imaging radiation dose, and seamless integration with linear accelerators in a coaxial setup, making it a promising image guidance modality for oART.

The oART is a labor-intensive and time-consuming procedure; thus, minimizing the duration of the process is imperative for its

broader adoption in clinical practice. In this study, the average duration of the oART workflow was 22.82 ± 3.61min, similar to the reported average of 21-29 minutes in previous literature on daily oART for cervical cancer (20, 23, 24). In terms of the time composition, the ROI auto-segmentation & review was the most time-consuming step (44.40%), followed by the plan generation & evaluation (22.02%), which was also highlighted in the study by Shelley et al. (24). Considering the major speed-limiting steps in oART, further developments of AI-based deformable registration algorithms and dose optimization algorithms are crucial for enhancing oART efficiency (25). In addition, identifying the appropriate treatment fractions to trigger oART is an important approach to saving time and labor and maximizing clinical efficiency. Previous research has proposed various potential triggers, including weight loss, tumor shrinkage, changes in body shape, and significant deviations from dosimetric objectives for target coverage and OAR dose constraints, though the optimal timing for these triggers is still under investigation (26–28). Furthermore, there is growing interest in using machine learning and deep learning techniques to identify image features and develop predictive models for triggering oART, with relevant research conducted in pancreatic (29, 30) and lung cancers (31). The high-quality images provided by FBCT offer promising prospects for developing similar models for cervical cancer.

oART has obvious dosimetric advantages in cervical cancer radiotherapy and can deliver dose accurately. In this study, the adaptive plan achieved a mean PTV D95 exceeding the prescribed dose, ensuring superior conformity and homogeneity. In contrast, scheduled plans failed to meet the prescribed dose for mean PTV D95, potentially resulting in underdosed regions, or "cold spots," within the target volume, which could compromise tumor control. Notably, Figure 4A clearly illustrates the substantial variability in target coverage across different fractions in the scheduled plan, with numerous outliers in PTV D95. In contrast, the adaptive plan ensured that PTV D95 for nearly all fractions remained consistently close to the prescribed dose, demonstrating its robustness in ensuring treatment precision. Regarding normal tissue sparing, oART reduced radiation exposure to critical organs, including the small intestine, rectum, and bladder, though with modest absolute reductions. Notably, the ovarian dose was reduced by 50%, which could have significant clinical implications for ovarian function preservation. These findings align with previous studies that have demonstrated the dosimetric benefits of adaptive plans over scheduled plans (23, 24). Furthermore, EPID-based *in vivo* dose monitoring confirmed a mean γ passing rate above 98.5% for all patients, verifying the accuracy of dose delivery in FBCT-guided oART and further supporting its clinical feasibility.

Differential dosimetric advantages were observed within various sub-volumes of the target volumes. The PTV_U derived the most significant benefit from the adaptive plan, followed by PTV_C, whereas the PTV_N experienced the least improvement. This variation may be attributable to the uterus being more susceptible to movements from the adjacent rectum and bladder, while the position of lymph nodes remains relatively static. It is thus sensible to tailor the margins from CTV to PTV for different parts of the target volume, considering the distinct motion characteristics of various anatomical structures, to ensure adequate target coverage while minimizing exposure to surrounding healthy tissues. Based on our previous participation in an international multicenter study (32) and literature reports (33), we typically use a 15mm margin for CTV_U and CTV_C, and a 6-8mm margin for CTV_N in IGRT for cervical cancer in our hospital. There are no uniform conclusions regarding the PTV margins for daily oART of cervical cancer. However, previous studies on intra-fractional motion during radiotherapy for cervical cancer provide valuable insights that can guide margin selection. Guangyu Wang et al. investigated daily oART for postoperative cervical and endometrial cancer patients, finding that a uniform 5mm expansion ensured full coverage of the nodal CTV in 100% of fractions in the validation cohort. They further suggested that the margin could be reduced to 4 mm if >95% nodal CTV coverage was maintained (34). Extensive research on intra-fractional motion during adaptive radiotherapy for cervical cancer has consistently demonstrated that a 5mm margin is sufficient to achieve 95-98% CTV coverage (35, 36). However, the uterus, particularly at the fundus, exhibits substantial intra-fractional motion and is more susceptible to bladder filling variations (33). Given the high mobility of the uterine region, a CTV to PTV margin of 1cm has been recommended to ensure adequate coverage for the uterine fundus (37). In light of these findings, our study adopted a region-specific margin strategy to optimize target coverage while minimizing unnecessary dose exposure. A 5mm margin was applied to generate PTV_C and PTV_N, whereas a larger 10mm margin was used for PTV_U to compensate for the pronounced motion of the uterus.

The clinical benefits of the application of oART in cervical cancer in terms of reduction of treatment toxicity is currently unclear, and the available data on toxicity evaluation from previous studies are minimal. The incidence of Grade 1 and Grade 2 acute non-hematological toxicities (urinary, rectal, and upper gastrointestinal) was 60%, with no occurrences of Grade 3 or higher acute non-hematological toxicities. Comparing previous data from cervical cancer patients receiving IMRT at our medical center, Grade 1 and Grade 2 acute non-hematological toxicity occurred in 86.1% of patients (38), which is significantly higher than the incidence in patients receiving oART. Similar results were found in comparison with studies in other medical centers (39, 40). This preliminary evidence suggests the potential translation of dosimetric advantages of oART into clinical benefits, although robust support from large-sample clinical research data is still required.

To the best of our knowledge, this study represents the first prospective research to implement FBCT-guided daily oART for radical radiotherapy of cervical cancer. However, several limitations must be acknowledged. First, the study included only 10 cervical cancer patients with a short follow-up period, which limits the representativeness and statistical power of the findings. Consequently, we can only preliminarily conclude that FBCT-guided daily oART has the potential to reduce acute treatment-related toxicities in cervical cancer patients. Future large-scale, multicenter, randomized controlled trials are needed to further validate the clinical benefits of this technology. Second, patients with cervical cancer requiring radiotherapy in the para-aortic or inguinal lymphatic drainage areas were excluded due to the

additional time required for delineation in these regions. In future studies, a more diverse patient population, with varying individual and disease characteristics, should be included to explore whether FBCT-guided oART can offer efficient workflows and dose advantages in a broader range of patients. Third, this study did not conduct an in-depth analysis of anatomical changes in the target volume and OARs between pre- and post-treatment FBCT images. Consequently, there is a lack of investigation into the magnitude of intra-fractional motion and its influencing factors. As a result, the present study is unable to provide more specific recommendations regarding the optimal CTV-PTV margins in clinical applications of oART. Fourth, oART is both labor-intensive and time-consuming, and the default daily oART strategy in this study imposes a significant burden on the radiotherapy team. In future studies, identifying the appropriate treatment fractions for triggering oART is essential for conserving time and labor resources, which is critical for facilitating its broader clinical adoption.

Conclusion

The implementation of FBCT-guided oART in radical radiotherapy for cervical cancer was feasible. This approach has shown significant improvement in dose distribution and reliable dose delivery accuracy. Furthermore, it has been found to have an acceptable workflow time and the potential to provide clinical benefits by reducing acute toxicity. Further multicenter studies are essential to corroborate its clinical benefits. The popularization of this technology hinges on the refinement of the oART process and the development of a robust triggering model.

Data availability statement

The original contributions presented in the study are included in the article/supplementary material. Further inquiries can be directed to the corresponding authors.

Ethics statement

The studies involving humans were approved by Peking Union Medical College Hospital, Chinese Academy of Medical Sciences (Protocol number K2416). The studies were conducted in accordance with the local legislation and institutional requirements. The participants provided their written informed consent to participate in this study.

Author contributions

SS: Conceptualization, Data curation, Formal analysis, Writing – original draft, Writing – review & editing. XG: Formal analysis, Visualization, Writing – original draft. YL: Methodology, Writing – review & editing. YS: Methodology, Writing – review & editing. DQ: Data curation, Writing – review & editing. YX: Data curation, Writing – review & editing. SH: Software, Writing – review & editing. LH: Methodology, Writing – review & editing. HL: Methodology, Writing – review & editing. YW: Methodology, Writing – review & editing. XW: Software, Writing – review & editing. CW: Software, Writing – review & editing. BY: Supervision, Writing – review & editing. JQ: Supervision, Writing – review & editing. KH: Conceptualization, Project administration, Supervision, Writing – review & editing. FZ: Conceptualization, Project administration, Supervision, Writing – review & editing.

Funding

The author(s) declare that financial support was received for the research and/or publication of this article. This study was supported by the National High-Level Hospital Clinical Research Funding (No. 2022-PUMCH-B-127) and National Key R&D Program of China, Ministry of Science and Technology of the People's Republic of China (No. 2022YFC2407100, 2022YFC2407101, 2022YFC2407102).

Acknowledgments

We acknowledge the technical support from United Imaging Healthcare Company, for providing the oART equipment necessary to carry out the experiments described in this study.

Conflict of interest

Author XW was employed by United Imaging Healthcare Company. Author CW was employed by the company Shanghai United Imaging Healthcare Co., Ltd. Author SH was employed by the company United Imaging Research Institute of Intelligent Imaging.

The remaining authors declare that the research was conducted in the absence of any commercial or financial relationships that could be construed as a potential conflict of interest.

Generative AI statement

The author(s) declare that no Generative AI was used in the creation of this manuscript.

Publisher's note

All claims expressed in this article are solely those of the authors and do not necessarily represent those of their affiliated

organizations, or those of the publisher, the editors and the reviewers. Any product that may be evaluated in this article, or claim that may be made by its manufacturer, is not guaranteed or endorsed by the publisher.

Supplementary material

The Supplementary Material for this article can be found online at: https://www.frontiersin.org/articles/10.3389/fonc.2025.1509619/full#supplementary-material

References

1. Singh D, Vignat J, Lorenzoni V, Eslahi M, Ginsburg O, Lauby-Secretan B, et al. Global estimates of incidence and mortality of cervical cancer in 2020: a baseline analysis of the WHO Global Cervical Cancer Elimination Initiative. *Lancet Glob Health*. (2023) 11(2):e197–206. doi: 10.1016/S2214-109X(22)00501-0

2. Forrest J, Presutti J, Davidson M, Hamilton P, Kiss A, Thomas G. A dosimetric planning study comparing intensity-modulated radiotherapy with four-field conformal pelvic radiotherapy for the definitive treatment of cervical carcinoma. *Clin Oncol (R Coll Radiol)*. (2012) 24(4):e63–70. doi: 10.1016/j.clon.2011.06.008

3. Webster A, Appelt AL, Eminowicz G. Image-guided radiotherapy for pelvic cancers: A review of current evidence and clinical utilisation. *Clin Oncol (R Coll Radiol)*. (2020) 32(12):805–16. doi: 10.1016/j.clon.2020.09.010

4. Eminowicz G, Rompokos V, Stacey C, Hall L, McCormack M. Understanding the impact of pelvic organ motion on dose delivered to target volumes during IMRT for cervical cancer. *Radiother Oncol*. (2017) 122(1):116–21. doi: 10.1016/j.radonc.2016.10.018

5. Chen J, Liu P, Chen W, Bai P, Li J, Ni X, et al. Early changes of volume and sp*atial location in target and normal tissues caused by IMRT for cervical cancer*. *Tumori*. (2016) 102(6):610–3. doi: 10.5301/tj.5000413

6. Heijkoop ST, Langerak TR, Quint S, Mens JW, Zolnay AG, Heijmen BJ, et al. Quantification of intra-fraction changes during radiotherapy of cervical cancer assessed with pre- and post-fraction Cone Beam CT scans. *Radiother Oncol*. (2015) 117(3):536–41. doi: 10.1016/j.radonc.2015.08.034

7. Qiu Z, Olberg S, den Hertog D, Ajdari A, Bortfeld T, Pursley J. Online adaptive planning methods for intensity-modulated radiotherapy. *Phys Med Biol*. (2023) 68(10). doi: 10.1088/1361-6560/accdb2

8. Sibolt P, Andersson LM, Calmels L, Sjöström D, Bjelkengren U, Geertsen P, et al. Clinical implementation of artificial intelligence-driven cone-beam computed tomography-guided online adaptive radiotherapy in the pelvic region. *Phys Imaging Radiat Oncol*. (2021) 17:1–7. doi: 10.1016/j.phro.2020.12.004

9. Posiewnik M, Piotrowski T. A review of cone-beam CT applications for adaptive radiotherapy of prostate cancer. *Phys Med*. (2019) 59:13–21. doi: 10.1016/j.ejmp.2019.02.014

10. Liu H, Schaal D, Curry H, Clark R, Magliari A, Kupelian P, et al. Review of cone beam computed tomography based online adaptive radiotherapy: current trend and future direction. *Radiat Oncol*. (2023) 18(1):144. doi: 10.1186/s13014-023-02340-2

11. Otazo R, Lambin P, Pignol JP, Ladd ME, Schlemmer HP, Baumann M, et al. MRI-guided radiation therapy: an emerging paradigm in adaptive radiation oncology. *Radiology*. (2021) 298(2):248–60. doi: 10.1148/radiol.2020202747

12. Taylor A, Rockall AG, Reznek RH, Powell ME. Mapping pelvic lymph nodes: guidelines for delineation in intensity-modulated radiotherapy. *Int J Radiat Oncol Biol Phys*. (2005) 63(5):1604–12. doi: 10.1016/j.ijrobp.2005.05.062

13. Lim K, Small W Jr., Portelance L, Creutzberg C, Jürgenliemk-Schulz IM, Mundt A, et al. Consensus guidelines for delineation of clinical target volume for intensity-modulated pelvic radiotherapy for the definitive treatment of cervix cancer. *Int J Radiat Oncol Biol Phys*. (2011) 79(2):348–55. doi: 10.1016/j.ijrobp.2009.10.075

14. Huang S, Mai X, Liu H, Sun W, Zhu J, Du J, et al. Plan quality and treatment efficiency assurance of two VMAT optimization for cervical cancer radiotherapy. *J Appl Clin Med Phys*. (2023) 24(10):e14050. doi: 10.1002/acm2.v24.10

15. Yu L, Zhao J, Zhang Z, Wang J, Hu W. Commissioning of and preliminary experience with a new fully integrated computed tomography linac. *J Appl Clin Med Phys*. (2021) 22(7):208–23. doi: 10.1002/acm2.13313

16. Shi F, Hu W, Wu J, Han M, Wang J, Zhang W, et al. Deep learning empowered volume delineation of whole-body organs-at-risk for accelerated radiotherapy. *Nat Commun*. (2022) 13(1):6566. doi: 10.1038/s41467-022-34257-x

17. Feng B, Yu L, Mo E, Chen L, Zhao J, Wang J, et al. Evaluation of daily CT for EPID-based transit *in vivo* dosimetry. *Front Oncol*. (2021) 11:782263. doi: 10.3389/fonc.2021.782263

18. Ezzell GA, Burmeister JW, Dogan N, LoSasso TJ, Mechalakos JG, Mihailidis D, et al. IMRT commissioning: multiple institution planning and dosimetry comparisons, a report from AAPM Task Group 119. *Med Phys*. (2009) 36(11):5359–73. doi: 10.1118/1.3238104

19. Andersen ES, Noe K, Sørensen TS, Nielsen SK, Fokdal L, Paludan M, et al. Simple DVH parameter addition as compared to deformable registration for bladder dose accumulation in cervix cancer brachytherapy. *Radiother Oncol*. (2013) 107(1):52–7. doi: 10.1016/j.radonc.2013.01.013

20. Yock AD, Ahmed M, Ayala-Peacock D, Chakravarthy AB, Price M. Initial analysis of the dosimetric benefit and clinical resource cost of CBCT-based online adaptive radiotherapy for patients with cancers of the cervix or rectum. *J Appl Clin Med Phys*. (2021) 22(10):210–21. doi: 10.1002/acm2.v22.10

21. Gan G, Gong W, Jia L, Zhang W, Wang S, Zhou J, et al. Study of peripheral dose from low-dose CT to adaptive radiotherapy of postoperative prostate cancer. *Front Oncol*. (2023) 13:1227946. doi: 10.3389/fonc.2023.1227946

22. Gong W, Yao Y, Ni J, Jiang H, Jia L, Xiong W, et al. Deep learning-based low-dose CT for adaptive radiotherapy of abdominal and pelvic tumors. *Front Oncol*. (2022) 12:968537. doi: 10.3389/fonc.2022.968537

23. Peng H, Zhang J, Xu N, Zhou Y, Tan H, Ren T. Fan beam CT-guided online adaptive external radiotherapy of uterine cervical cancer: a dosimetric evaluation. *BMC Cancer*. (2023) 23(1):588. doi: 10.1186/s12885-023-11089-6

24. Shelley CE, Bolt MA, Hollingdale R, Chadwick SJ, Barnard AP, Rashid M, et al. Implementing cone-beam computed tomography-guided online adaptive radiotherapy in cervical cancer. *Clin Transl Radiat Oncol*. (2023) 40:100596. doi: 10.1016/j.ctro.2023.100596

25. Fan J, Cao X, Xue Z, Yap PT, Shen D. Adversarial similarity network for evaluating image alignment in deep learning based registration. *Med Image Comput Comput Assist Interv*. (2018) 11070:739–46. doi: 10.1007/978-3-030-00928-1_83

26. Yock AD, Ahmed M, Masick S, Morales-Paliza M, Kluwe C, Shinde A, et al. Triggering daily online adaptive radiotherapy in the pelvis: Dosimetric effects and procedural implications of trigger parameter-value selection. *J Appl Clin Med Phys*. (2023) 24(10):e14060. doi: 10.1002/acm2.v24.10

27. Figen M, Çolpan Öksüz D, Duman E, Prestwich R, Dyker K, Cardale K, et al. Radiotherapy for head and neck cancer: evaluation of triggered adaptive replanning in routine practice. *Front Oncol*. (2020) 10:579917. doi: 10.3389/fonc.2020.579917

28. Avgousti R, Antypas C, Armpilia C, Simopoulou F, Liakouli Z, Karaiskos P, et al. Adaptive radiation therapy: When, how and what are the benefits that literature provides? *Cancer Radiother*. (2022) 26(4):622–36. doi: 10.1016/j.canrad.2021.08.023

29. Nasief HG, Parchur AK, Omari E, Zhang Y, Chen X, Paulson E, et al. Predicting necessity of daily online adaptive replanning based on wavelet image features for MRI guided adaptive radiation therapy. *Radiother Oncol*. (2022) 176:165–71. doi: 10.1016/j.radonc.2022.10.001

30. Parchur AK, Lim S, Nasief HG, Omari EA, Zhang Y, Paulson ES, et al. Auto-detection of necessity for MRI-guided online adaptive replanning using a machine learning classifier. *Med Phys*. (2023) 50(1):440–8. doi: 10.1002/mp.16047

31. Ma C, Tian Z, Wang R, Feng Z, Jiang F, Hu Q, et al. A prediction model for dosimetric-based lung adaptive radiotherapy. *Med Phys*. (2022) 49(10):6319–33. doi: 10.1002/mp.v49.10

32. Khan A, Jensen LG, Sun S, Song WY, Yashar CM, Mundt AJ, et al. Optimized planning target volume for intact cervical cancer. *Int J Radiat Oncol Biol Phys*. (2012) 83(5):1500–5. doi: 10.1016/j.ijrobp.2011.10.027

33. Taylor A, Powell ME. An assessment of interfractional uterine and cervical motion: implications for radiotherapy target volume definition in gynaecological cancer. *Radiother Oncol*. (2008) 88(2):250–7. doi: 10.1016/j.radonc.2008.04.016

34. Wang G, Wang Z, Guo Y, Zhang Y, Qiu J, Hu K, et al. Evaluation of PTV margins with daily iterative online adaptive radiotherapy for postoperative treatment of endometrial and cervical cancer: a prospective single-arm phase 2 study. *Radiat Oncol*. (2024) 19(1):2. doi: 10.1186/s13014-023-02394-2

35. Yen A, Choi B, Inam E, Yeh A, Lin MH, Park C, et al. Spare the bowel, don't spoil the target: optimal margin assessment for online cone beam adaptive radiation therapy (OnC-ART) of the cervix. *Pract Radiat Oncol*. (2023) 13(2):e176–83. doi: 10.1016/j.prro.2022.10.009

36. Wang H, Li Z, Shi D, Yin P, Liang B, Zou J, et al. Assessing intra- and interfraction motion and its dosimetric impacts on cervical cancer adaptive radiotherapy based on 1.5T MR-Linac. *Radiat Oncol*. (2024) 19(1):176. doi: 10.1186/s13014-024-02569-5

37. Chan P, Dinniwell R, Haider MA, Cho YB, Jaffray D, Lockwood G, et al. Inter- and intrafractional tumor and organ movement in patients with cervical cancer

undergoing radiotherapy: a cinematic-MRI point-of-interest study. *Int J Radiat Oncol Biol Phys*. (2008) 70(5):1507–15. doi: 10.1016/j.ijrobp.2007.08.055

38. Sun S, Zhang F-q, Hu K, Hou X-r, Shen J, Lian X, et al. Clinical effect of concurrent chemotherapy and intensity-modulated radiotherapy in postoperative cervical cancer patients. *Chin J Radiat Oncol* (2013) 22(01):13–6. doi: 10.3760/cma.j.issn.1004-4221.2013.01.004

39. Hasselle MD, Rose BS, Kochanski JD, Nath SK, Bafana R, Yashar CM, et al. Clinical outcomes of intensity-modulated pelvic radiation therapy for carcinoma of the cervix. *Int J Radiat Oncol Biol Phys*. (2011) 80(5):1436–45. doi: 10.1016/j.ijrobp.2010.04.041

40. Akthar AS, Liao C, Eggener SE, Liauw SL. Patient-reported outcomes and late toxicity after postprostatectomy intensity-modulated radiation therapy. *Eur Urol*. (2019) 76(5):686–92. doi: 10.1016/j.eururo.2019.05.011

frontiers | Frontiers in Medicine

TYPE Original Research
PUBLISHED 22 April 2025
DOI 10.3389/fmed.2025.1566555

Check for updates

OPEN ACCESS

EDITED BY
Abdul K. Parchur,
Medical College of Wisconsin, United States

REVIEWED BY
Amanjot Kaur,
Mahatma Phule Charitable Trust Hospital, India
Mohamed Mekky,
Faculty of Dentistry Kafrelsheikh University, Egypt

*CORRESPONDENCE
Kui Huang
✉ huangk1990@qq.com
Yongmei Li
✉ lymzhang70@163.com

RECEIVED 25 January 2025
ACCEPTED 03 April 2025
PUBLISHED 22 April 2025

CITATION
Shen Q, Xiang C, Han Y, Li Y and Huang K (2025) The value of multi-phase CT based intratumor and peritumoral radiomics models for evaluating capsular characteristics of parotid pleomorphic adenoma.
Front. Med. 12:1566555.
doi: 10.3389/fmed.2025.1566555

COPYRIGHT
© 2025 Shen, Xiang, Han, Li and Huang. This is an open-access article distributed under the terms of the Creative Commons Attribution License (CC BY). The use, distribution or reproduction in other forums is permitted, provided the original author(s) and the copyright owner(s) are credited and that the original publication in this journal is cited, in accordance with accepted academic practice. No use, distribution or reproduction is permitted which does not comply with these terms.

The value of multi-phase CT based intratumor and peritumoral radiomics models for evaluating capsular characteristics of parotid pleomorphic adenoma

Qian Shen[1], Cong Xiang[2], Yongliang Han[3], Yongmei Li[3]* and Kui Huang[4]*

[1]Department of Radiology, The Affiliated Stomatology Hospital of Southwest Medical University, Luzhou, China, [2]School of Artificial Intelligence, Chongqing University of Technology, Chongqing, China, [3]Department of Radiology, The First Affiliated Hospital, Chongqing Medical University, Chongqing, China, [4]Department of Oral and Maxillofacial Surgery, The Affiliated Stomatology Hospital of Southwest Medical University, Luzhou, China

Objectives: Computed tomography (CT) imaging of parotid pleomorphic adenoma (PA) has been widely reported, nonetheless few reports have estimated the capsule characteristics of PA at length. This study aimed to establish and validate CT-based intratumoral and peritumoral radiomics models to clarify the characteristics between parotid PA with and without complete capsule.

Methods: In total, data of 129 patients with PA were randomly assigned to a training and test set at a ratio of 7:3. Quantitative radiomics features of the intratumoral and peritumoral regions of 2 mm and 5 mm on CT images were extracted, and radiomics models of Tumor, External2, External5, Tumor+ External2, and Tumor+External5 were constructed and used to train six different machine learning algorithms. Meanwhile, the prediction performances of different radiomics models (Tumor, External2, External5, Tumor+External2, Tumor+External5) based on single phase (plain, arterial, and venous phase) and multiphase (three-phase combination) were compared. The receiver operating characteristic (ROC) curve analysis and the area under the curve (AUC) were used to evaluate the prediction performance of each model.

Results: Among all the established machine learning prediction radiomics models, the model based on a three-phase combination had better prediction performance, and the model using a combination of intratumoral and peritumoral radiomics features achieved a higher AUC than the model with only intratumoral or peritumoral radiomics features, and the Tumor+External2 model based on LR was the optimal model, the AUC of the test set was 0.817 (95% CI = 0.712, 0.847), and its prediction performance was significantly higher ($p < 0.05$, DeLong's test) than that with the Tumor model based on LDA (AUC of 0.772), the External2 model based on LR (AUC of 0.751), and the External5 model based on SVM (AUC of 0.667). And the Tumor+External2 model based on LR had a higher AUC than the Tumor+External5 model based on LDA (AUC = 0.817 vs. 0.796), but no statistically significant difference ($P = 0.667$).

Conclusion: The intratumoral and peritumoral radiomics model based on multiphasic CT images could accurately predict capsular characteristics of parotid of PA preoperatively, which may help in making treatment strategies before surgery, as well as avoid intraoperative tumor spillage and residuals.

KEYWORDS

pleomorphic adenomas, radiomics, machine learning, capsular, computed tomography

1 Introduction

Pleomorphic adenoma (PA) is the most prevalent benign tumor of the parotid neoplasm, accounting for approximately 66.7% of all parotid tumors (1, 2). Although these slow-growing tumors are often considered low-risk, PAs still have a relatively high risk of malignant transformation and recurrence (1). Previous studies showed that capsular characteristics and surgical approach are the most likely reasons for recurrence (3, 4). The capsule characteristics refer to the appearance of the outer layer or capsule surrounding pleomorphic adenoma of the parotid gland. A well-defined capsule is necessary before surgery as it helps complete tumor removal during surgery, decreasing the rate of recurrence. Thus, accurate preoperative assessment of the capsular characteristics of parotid pleomorphic adenoma is essential for evaluating treatment decisions.

However, there is still no non-invasive, clinically applicable approach for preoperative assessment of capsular characteristics. Fine-needle aspiration cytology (FNAC) can not assess the capsular characteristics. Moreover, preoperative imaging for pleomorphic adenoma of the parotid glands includes ultrasound (US), computed tomography (CT) and magnetic resonance imaging (MRI). Due to US examination being easily affected by the adjacent bone and tumor location, its diagnostic efficacy is limited, so CT and MRI examinations are widely used in clinical practice (5, 6). Previous research has shown computed tomography (CT) imaging features and the histopathology of PAs were poor consistency, even by experienced radiologists to assess the capsular characteristics of PAs (7). And some studies have referred to the capsule of pleomorphic adenomas on MR imaging (8, 9), and indicated that a capsule completely surrounding the tumor has a high positive predictive value for the diagnosis of pleomorphic adenoma (8). However, in cases of pleomorphic adenomas with incomplete capsules, the margin of the lesion is unclear, which may lead to misdiagnosis. Therefore, there is an urgent need to develop more efficient and non-invasive assessments to aid in the preoperative evaluation of the capsular characteristics of parotid PAs.

Radiomics is a relatively new concept that analyzes and extracts quantitative data from medical images, which introduces a new way to mine valuable information contained in the images (10–12). And the feasibility of radiomics as a non-invasive approach has been demonstrated by its wide application in the early differential diagnosis and prognosis evaluation in multiple solid tumors (13, 14). Recently, due to its excellent performance in oncological applications, radiomics has been applied in preoperative identifying different pathological types of parotid tumors. However, those previous radiomics studies mainly focused on the primary tumor area alone (15–18), whereas little was known about the role of peritumoral radiomics features, which were likely to provide valuable but easily overlooked information about parotid tumors.

In this context, we hypothesized that peritumoral radiomics features may offer useful information for the possible infiltration of tumor toward normal tissue, which would be helpful for clinical decision. Thus, we aimed to explore the potential of radiomic features of the intratumoral and peritumoral radiomics features on CT images to preoperative predict the capsular characteristics of the parotid PA.

2 Materials and methods

2.1 Patients

This retrospective study was approved by the ethics committees of our hospital (approval number: K2023-414). The requirement for informed consent was waived owing to the retrospective nature of the study. The data of 129 patients with PA who underwent parotid surgery in our hospital from January 2014 to January 2023 were included in the Study. The inclusion criteria were as follows: (1) they were diagnosed with PA through surgical pathology; (2) they underwent plain CT and two-phase enhanced scans before receiving any treatment; (3) patients with primary PA. The exclusion criteria were as follows: (1) they were diagnosed with carcinoma ex PA; (2) images with severe noise or evident artifacts on CT images; (3) patients had previous parotid gland surgery. Figure 1 illustrates the workflow of our study.

2.2 The reference standard for capsular characteristics

The study divided patients into two groups: a complete capsule group and a incomplete capsule group. The incomplete capsule group included those patients with PAs who displayed any of the following capsular characteristics (19):

① “incomplete capsule” indicates partial absence of the encapsulation;
② “pseudopodia” indicates tumor nodules are separated by fibrous tissue but remain in contact with the main tumor capsule;

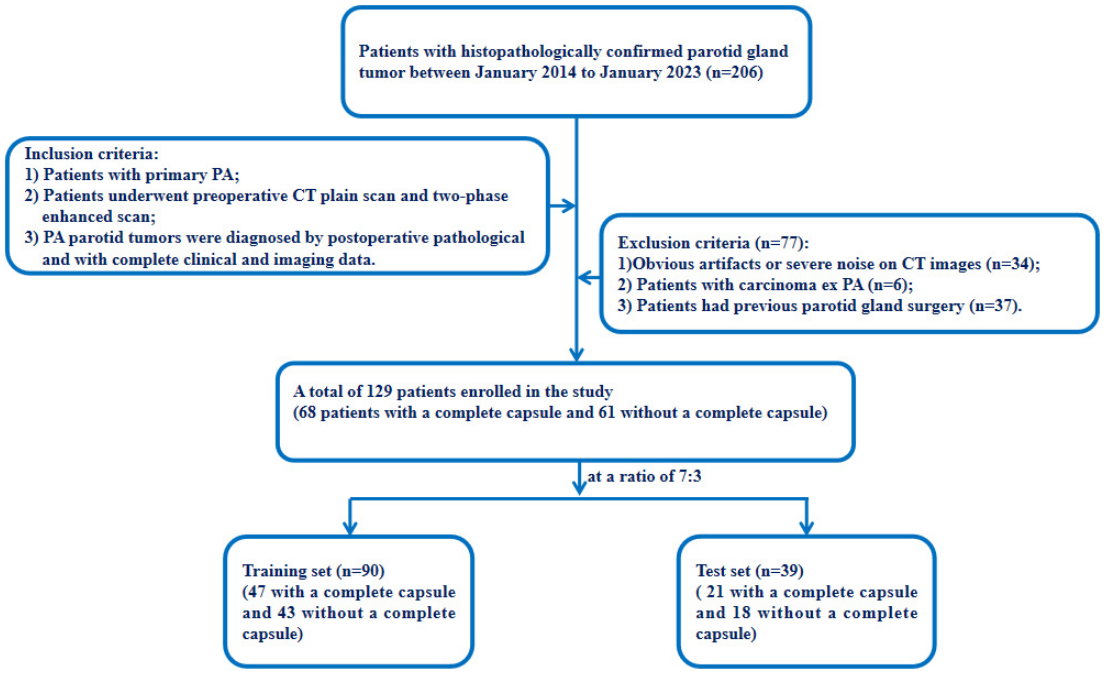

FIGURE 1
Flowchart for selecting the study population.

③ "capsule invasion" means that tumor tissue infiltration not separated from the main tumor mass;
④ "satellite nodules" indicates nodules separated from the main tumor by fat tissue or salivary gland, and they located adjacent to the main tumor mass but not connected to it.

All patients in this study underwent complete tumor resection. For the PA patients in the complete capsule group, the diagnosis was based on surgical and pathological reports. They were assigned to this group when the surgeon verified that they had well-defined borders, and the pathologist verified the integrity of the capsule. For patients in the incomplete capsule group, the diagnosis was made based on postoperative pathological results, which included the evaluation of its completeness as well as other capsular characteristics such as satellite nodules, pseudopodia, and capsule invasion.

2.3 Image acquisition

Using multi-slice spiral CT equipment, each patient underwent multi-phase scanning, including plain scanning phase, arterial scanning phase, and venous scanning phase. The CT images were stored in the Digital Imaging and Communications in Medicine (DICOM) format. The acquisition parameters of the above different devices are introduced in detail in Supplementary Table 1.

2.4 Image segmentation

The CT images of those patients were stored in DICOM format using standard soft tissue settings: window width of 400 HU and window level of 40 HU. Blinded to the histopathological results of the patients, two radiologists (with 3 and 5 years of clinical diagnostic experience) used the ITK-SNAP software (version 3.8.0[1]) to segment the region of interest (ROI) manually. The tumors were delineated along the margins layer-by-layer on axial multi-phase CT images, eliminating the vessels, bone, and normal adjacent tissue. When multiple lesions were found in the parotid gland, the largest lesion with a confirmed pathology was selected for analysis. The intra- and inter-observer reproducibility were evaluated by the intraclass correlation coefficient (ICC). The segmentation was executed independently by radiologist-A and radiologist-B during the same period to evaluate inter-observer agreement of extracted radiomics features. Radiologist-A then repeated the same case procedure 1 month later, and an ICC greater than 0.75 indicated good consistency.

After manual tumor segmentation, 2 mm and 5 mm peritumoral regions were automatically segmented using Python (version 3.7.12[2]) (Figure 2). Next, the bone and air were filtered from the delineation by setting the maximum (400 HU) and minimum (−200 HU) thresholds, and the final ROI border (peritumoral regions) was manually adjusted (20, 21).

2.5 Radiomics feature extraction and selection

PyRadiomics in Python was used for feature extraction. In order to reduce the impact of different scanning devices, all CT

1 http://www.itksnap.org/
2 http://www.python.org

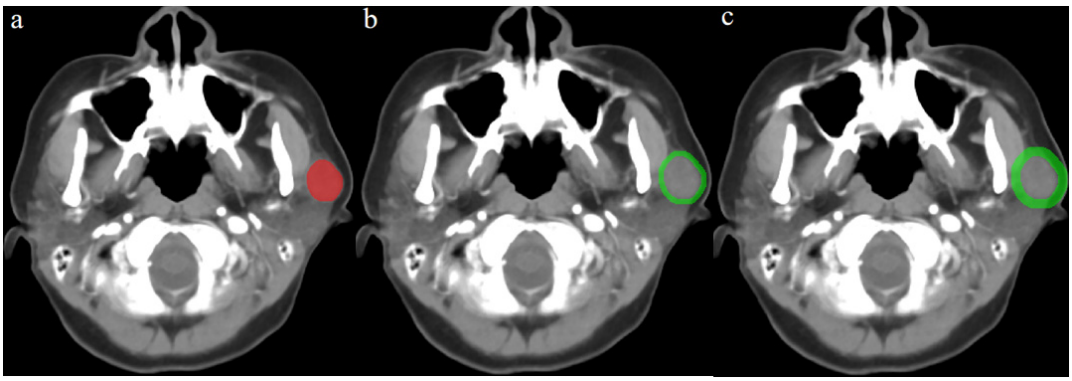

FIGURE 2
Contrast-enhanced computed tomography (CT) image from a pleomorphic adenoma patient, highlighted regions represent the primary tumor **(a)** and peritumoral region of 2 mm **(b)** and 5 mm **(c)**.

images were resampled to a voxel spacing of $1 \times 1 \times 1$ mm^3, and standardization and resampling techniques were applied to preprocess the images and data to ensure the consistency of the CT images between patients. Feature extraction was conducted from five different ROIs—Tumor, External2, External5, Tumor+External2, and Tumor+External5— for each patient using the PyRadiomics Radiomics Feature Extractor toolbox. Each segmented region obtained 1,288 radiomic features, including the first-order (252), gray-level co-occurrence matrix (308), gray-level run-length matrix (224), and gray-level size zone matrix (224), gray-level dependence matrix (196) and neighboring gray-tone difference matrix (70). These algorithms for obtaining radiomics features were referenced from the image biomarker standardization initiative (IBSI) (22).

The radiomics features dimensionality reduction and selection in the training set were as follows: firstly, analysis of variance (ANOVA) was performed on the extracted features to select statistically significant features with ICC scores > 0.9. Secondly, We decreased the dimensionality of the feature space by assessing the similarity of each feature pair and removing one of the features if the Pearson correlation coefficient (PCC) value was higher than 0.95. Ultimately, features with non-zero coefficients were selected using the least absolute shrinkage and selection operator (LASSO) regression model with 10-fold cross-validation, which was described in Supplementary Appendix 1.

2.6 Model construction and evaluation

Based on the radiomics features extracted from the plain scan, arterial and venous phase CT images, our study built and validated six machine learning algorithms, including support vector machine (SVM), logistic regression (LR), extreme gradient boosting (XGBoost), linear discriminant analysis (LDA), random forest (RF) and decision tree (DT). For each region (Tumor, External2, External5, Tumor+External2, and Tumor+External5), by combining each machine learning algorithm with 15 different feature sets, 90 models were established. And 10-fold cross-validation on the training set was used to identify the hyperparameters of each model.

We evaluated the diagnostic performance of those models by comparing the area under the curve (AUC) of the receiver operating characteristic curve (ROC), accuracy, positive prediction value (PPV), sensitivity, specificity, and negative prediction value (NPV). Then, the best radiomics model and scanning phase were obtained.

2.7 Statistical analysis

All statistical analyses were performed using PyRadiomics in Python (version 3.7.12; see text footnote 2), and SPSS (version 26.0; IBM, Armonk, NY, United States) software. Comparisons between sets were performed using the Student's t-test or the Mann–Whitney U test for continuous variables and the χ^2 or Fisher exact test for categorical variables. Besides, the "sklearn" packages were used for plotting the curves of the ROC. Two-sided $p < 0.05$ was deemed statistically significant for all statistical tests.

3 Results

3.1 The population and radiological features of patients

The details of the patient's clinical and radiological characteristics are shown in Table 1. No significant statistical differences in characteristics were found between the training and test sets in terms of sex, age, smoking, drinking, symptom, shape, margin, density, cystic areas, enhanced uniformity, except for the max diameter, whose p-value in the test set were < 0.05. Furthermore, univariate and multivariate logistic regression were used to select the independent clinical predictors of patients, however, we found no significant clinical predictors in this study.

3.2 Radiomic signature models and performances

A total of 1,288 radiomics features were extracted from each region; therefore, 6,440 radiomics features were extracted

TABLE 1 Clinical and computed tomography (CT) morphological characteristics of patients in the training and test sets.

Variables	Training set (n = 90)			Test set (n = 39)		
	PA with complete capsule (n = 43)	PA without complete capsule (n = 47)	P	PA with complete capsule (n = 43)	PA without complete capsule (n = 47)	P
Age[b] (years)	44.65 ± 16.32	45.96 ± 12.88	0.67	44.27 ± 18.76	48.25 ± 16.57	0.47
Max-diameter[b] (cm)	2.1 ± 60.68	2.21 ± 0.71	0.71	2.31 ± 0.57	1.67 ± 0.49	< 0.01*
Sex[a] (F/M)	25/18	30/17	0.58	9/9	7/14	0.29
Smoking[a] (yes/no)	14/29	9/38	0.15	5/13	8/13	0.50
Drinking[a] (Yes/No)	7/36	13/43	0.20	4/14	9/12	0.18
Symptoms[a] (with/without)	5/38	7/40	0.65	1/17	1/20	0.91
Shape[a] (round/non-round)	9/34	15/32	0.24	3/15	6/15	0.38
Margin[a] (clear/unclear)	40/3	46/1	0.29	17/1	20/1	0.91
Density[a] (homogeneous/heterogeneous)	20/23	29/18	0.15	11/7	12/9	0.80
Cystic areas[a] (with/without)	16/27	19/28	0.75	3/15	8/13	0.15
Enhancement degree[a] (slight/moderate/obvious)	1/12/30	4/22/21	0.02*	1/10/7	4/10/7	0.37
Enhanced uniformity[a] (yes/no)	18/25	15/32	0.33	9/9	8/13	0.46

*Represents $p < 0.05$. [a]Categorical data are presented as numbers (n). [b]Quantitative data are presented as means (standard deviations) or medians (quartiles), p-value was calculated using the independent samples t-test or Mann–Whitney U test. p-value was calculated with the χ^2 or Fisher's exact test. PA, pleomorphic adenoma; F, female; M, male.

from images of each scanning phase. Then, five radiomics signatures were established based on Tumor, External2, External5, Tumor+External2, and Tumor+External5. Then, six machine learning methods were used to establish 120 radiomics models in the arterial phase, venous phase, and plain phase, as well as a three-phase combination. The results of different feature screening methods in each phase are shown in Supplementary Tables 2–4.

Among all the established machine learning prediction radiomics models, the model based on a three-phase combination had better prediction performance, and the model using a combination of intratumoral and peritumoral radiomics features achieved a higher AUC than the model with only intratumoral or peritumoral radiomic features, which was presented in Table 2. The 14 selected features in the Tumor+External2 model were shown in Figure 3. And the Tumor+External2 model based on LR was the optimal model, the AUC of the test set was 0.817 (95% CI = 0.712, 0.847), and its prediction performance was significantly higher than that with the Tumor model based on LDA (AUC = 0.772, P = 0.004), the External2 model based on LR (AUC = 0.751, P = 0.032), and the External5 model based on SVM (AUC = 0.667, P = 0.018). And the Tumor+External2 model based on LR had a higher AUC than the Tumor+External5 model based on LDA (AUC = 0.817 vs. 0.796), but no statistically significant difference (P = 0.667). Figure 4 depicts the ROC curves of the top performing models based on three-phase combination in the training set (a) and test sets (b). The Calibration curves (a) and DCA curves (b) of the top performing models based on three-phase combination in the test set are shown in Figure 5.

For single phase, the performance of models based on the arterial and venous scan phases were generally better than that in the plain scan phase. Tumor+External2 model based on the venous phase has the highest prediction performance: in the test set (when using the LR classifier), the AUC was 0.785 (95% CI = 0.713, 0.857). The AUC values of the five models using six different machine learning algorithm-based models in the test sets are shown in Figures 6a–d represent plain phase, arterial phase, venous phase and three-phase combination phase, respectively.

4 Discussion

In this study, we established and evaluated the ability of multiphasic enhanced CT imaging features from Tumor, External2, External5, Tumor+External2, and Tumor+External5 radiomics features to accurately predict capsular characteristics of PA. We found that regardless of the size of the peritumoral region, radiomics features including the peritumoral signatures were more accurate indicators in the test sets. Specifically, the performance of the Tumor+External2 radiomics model based on the three-phase combination achieved the best performance among all radiomics models in the test sets, with AUC of 0.817 (95% CI = 0.712, 0.847). And the radiomics model based on the LR classifier was superior to the model based on other machine learning algorithms.

Previous radiomics research on PAs has mostly concentrated on the tumor parenchyma, ignoring the tumor-surrounding tissue, while it can reflect the important biological information about the tumor, including its potential for malignant behavior and its interactions with surrounding tissues. Furthermore, the value of tumor-adjacent tissues has been confirmed in recent studies, demonstrating their potential capacity in predicting treatment response, characterizing tumor behavior and evaluating the risk of recurrence (13, 23, 24). However, the application of the peritumoral region in pleomorphic adenoma of the parotid gland has not yet been explored. Besides, the definitions of peritumoral regions

TABLE 2 Diagnostic performance of different feature screening methods in venous phase.

Model/classifiers	Cohort	AUC (95% CI)	Accuracy	Sensitivity	Specificity	NPV	PPV
Three-phase combination							
SVM							
Tumor	Training	0.975 (0.950–0.986)	0.944	0.884	1.000	1.000	0.904
	Test	0.720 (0.643–0.779)	0.641	0.611	0.667	0.611	0.667
External2	Training	0.964 (0.949–0.986)	0.967	0.953	0.979	0.976	0.958
	Test	0.614 (0.567–0.688)	0.513	0.500	0.524	0.474	0.550
External5	Training	0.982 (0.928–0.974)	0.911	0.907	0.915	0.907	0.915
	Test	0.677 (0.571–0.700)	0.590	0.556	0.619	0.556	0.619
Tumor+External2	Training	0.940 (0.922–0.969)	0.944	0.977	0.915	0.913	0.977
	Test	0.807 (0.722–0.841)	0.744	0.722	0.762	0.722	0.762
Tumor+External5	Training	0.979 (0.951–0.988)	0.978	0.977	0.979	0.977	0.979
	Test	0.757 (0.662–0.828)	0.564	0.556	0.571	0.526	0.600
LR							
Tumor	Training	0.958 (0.890–0.945)	0.900	0.884	0.915	0.905	0.896
	Test	0.749 (0.573–0.793)	0.539	0.444	0.619	0.500	0.565
External2	Training	0.937 (0.916–0.963)	0.900	0.907	0.894	0.886	0.913
	Test	0.751 (0.602–0.780)	0.641	0.667	0.619	0.600	0.684
External5	Training	0.937 (0.867–0.926)	0.867	0.837	0.894	0.878	0.857
	Test	0.606 (0.484–0.656)	0.436	0.556	0.333	0.417	0.467
Tumor+External2	Training	0.942 (0.876–0.935)	0.911	0.930	0.894	0.889	0.933
	Test	0.817 (0.712–0.847)	0.722	0.760	0.762	0.643	0.640
Tumor+External5	Training	0.937 (0.911–0.957)	0.889	0.884	0.894	0.884	0.894
	Test	0.762 (0.672–0.819)	0.667	0.611	0.714	0.647	0.682
LDA							
Tumor	Training	0.909 (0.845–0.939)	0.889	0.884	0.894	0.884	0.894
	Test	0.772 (0.567–0.786)	0.692	0.556	0.810	0.714	0.680
External2	Training	0.916 (0.853–0.955)	0.878	0.873	0.915	0.900	0.860
	Test	0.683 (0.534–0.751)	0.615	0.500	0.714	0.600	0.625
External5	Training	0.873 (0.836–0.912)	0.844	0.791	0.894	0.872	0.824
	Test	0.616 (0.472–0.658)	0.513	0.389	0.619	0.467	0.542
Tumor+External2	Training	0.871 (0.858–0.919)	0.844	0.860	0.830	0.822	0.867
	Test	0.815 (0.698–0.857)	0.641	0.756	0.714	0.625	0.652
Tumor+External5	Training	0.908 (0.840–0.930)	0.844	0.884	0.809	0.809	0.884
	Test	0.796 (0.626–0.814)	0.692	0.611	0.762	0.688	0.696
XGBoost							
Tumor	Training	0.937 (0.884–0.959)	0.956	0.930	0.979	0.976	0.939
	Test	0.743 (0.468–0.753)	0.590	0.556	0.619	0.556	0.619
External2	Training	0.927 (0.906–0.972)	0.956	0.953	0.957	0.953	0.957
	Test	0.632 (0.505–0.657)	0.538	0.556	0.524	0.500	0.579
External5	Training	0.950 (0.891–0.971)	0.967	0.977	0.957	0.955	0.978
	Test	0.646 (0.424–0.634)	0.487	0.278	0.667	0.417	0.519
Tumor+External2	Training	0.921 (0.873–0.956)	0.933	0.953	0.915	0.911	0.956
	Test	0.712 (0.607–0.757)	0.667	0.611	0.714	0.647	0.682
Tumor+External5	Training	0.945 (0.908–0.982)	1.000	1.000	1.000	1.000	1.000
	Test	0.725 (0.571–0.801)	0.462	0.389	0.524	0.412	0.500

(Continued)

TABLE 2 (Continued)

Model/classifiers	Cohort	AUC (95% CI)	Accuracy	Sensitivity	Specificity	NPV	PPV
RF							
Tumor	Training	0.806 (0.739–0.883)	0.844	0.814	0.872	0.854	0.837
	Test	0.608 (0.436–0.705)	0.615	0.722	0.524	0.565	0.688
External2	Training	0.905 (0.779–0.888)	0.822	0.814	0.830	0.814	0.830
	Test	0.548 (0.416–0.658)	0.436	0.778	0.143	0.438	0.429
External5	Training	0.834 (0.771–0.872)	0.800	0.860	0.745	0.755	0.854
	Test	0.414 (0.320–0.624)	0.487	0.500	0.476	0.450	0.526
Tumor+External2	Training	0.820 (0.754–0.873)	0.822	0.814	0.830	0.814	0.830
	Test	0.716 (0.481–0.756)	0.590	0.611	0.571	0.550	0.632
Tumor+External5	Training	0.925 (0.756–0.894)	0.889	0.884	0.894	0.884	0.894
	Test	0.659 (0.479–0.741)	0.462	0.444	0.476	0.421	0.500
DT							
Tumor	Training	0.789 (0.694–0.811)	0.778	0.814	0.745	0.745	0.814
	Test	0.507 (0.371–0.697)	0.539	0.389	0.667	0.500	0.560
External2	Training	0.832 (0.708–0.839)	0.822	0.744	0.894	0.865	0.792
	Test	0.574 (0.372–0.692)	0.513	0.444	0.571	0.471	0.545
External5	Training	0.803 (0.730–0.845)	0.844	0.884	0.809	0.809	0.884
	Test	0.474 (0.346–0.644)	0.462	0.500	0.429	0.429	0.500
Tumor+External2	Training	0.788 (0.697–0.831)	0.800	0.930	0.681	0.727	0.914
	Test	0.509 (0.441–0.714)	0.692	0.722	0.667	0.650	0.737
Tumor+External5	Training	0.853 (0.712–0.849)	0.844	0.930	0.766	0.784	0.923
	Test	0.566 (0.426–0.696)	0.564	0.556	0.571	0.526	0.800

AUC, area under curve; CI, confdence interval; NPV, negative predictive value; PPV, positive predictive value; SVM, support vector machine; LR, logistic regression; LDA, linear discriminant analysis; XGBoost, extreme gradient boosting; RF, random forest; DT, decision tree.

have been explored in many previous studies, including distances ranging from 5 mm to 30 mm for lung nodules, 5 mm to 10 mm for breast cancer and 10 mm to 30 mm for malignant brain tumor (13, 25, 26). According to the findings of these studies, the peritumoral area nearest the tumor issue usually provides the highest predictive accuracy.

Unlike previous studies on patients with PAs, which mainly concentrated on intratumoral features and estimated radiomics signatures, we expanded the distance of 2 mm and 5 mm around the tumor and established five radiomic models based on multiphasic enhanced CT imaging to compare their predictive performance. The results indicated that the features extracted from the Tumor+External2 model exhibited the best performance in accurately predicting capsular characteristics of PA, consistent with the results of Li (2). The capsule features appear at the edge of the tumor, and the satellite nodules are more common within a range of 2 mm from the central mass (27), which may contribute to this result. Furthermore, we found that the AUC of the Tumor+External2 model to clarify the capsular characteristics of the parotid PA was higher than that of the Tumor+External5 model. However, there was no statistical significance in this finding. This may suggest that the peritumoral region tissues within 5 mm of the tumor contain valuable information that could identify the encapsulates of PAs.

In addition, our investigation found that the most of the remaining discriminative radiomics features in the Tumor+External2 model were texture features, and this result was consistent with those of previous studies (2, 19), texture features could quantify the inter-voxel relationships in an image and describe microscopic characteristics in CT images of PA. Texture features can reflect the capsular characteristics of the variations in the micro-structures and contain part of pathological characteristics related to the capsule of parotid gland tumor. Furthermore, we applied univariate and multivariate logistic regression to select the independent clinical predictors of patients; however, we found no significant clinical predictors. These results were further evidence that radiomics model was effective and accurate tool for preoperative identification of capsular characteristics of parotid PA.

However, our study faces some limitations. Firstly, the magnetic resonance imaging (MRI) has excellent resolution of the soft tissues, may provide more valuable information compared to CT images. It may be beneficial to explore the potential of MRI-based radiomics features in future studies. Secondly, although the reliability and reproducibility of radiomics feature extraction were satisfactory between the two observers, intratumoral regions were drawn manually to execute image segmentation. Despite using an automatic technique for peritumoral region segmentation, we prefer a fully automatic method that may improve stability

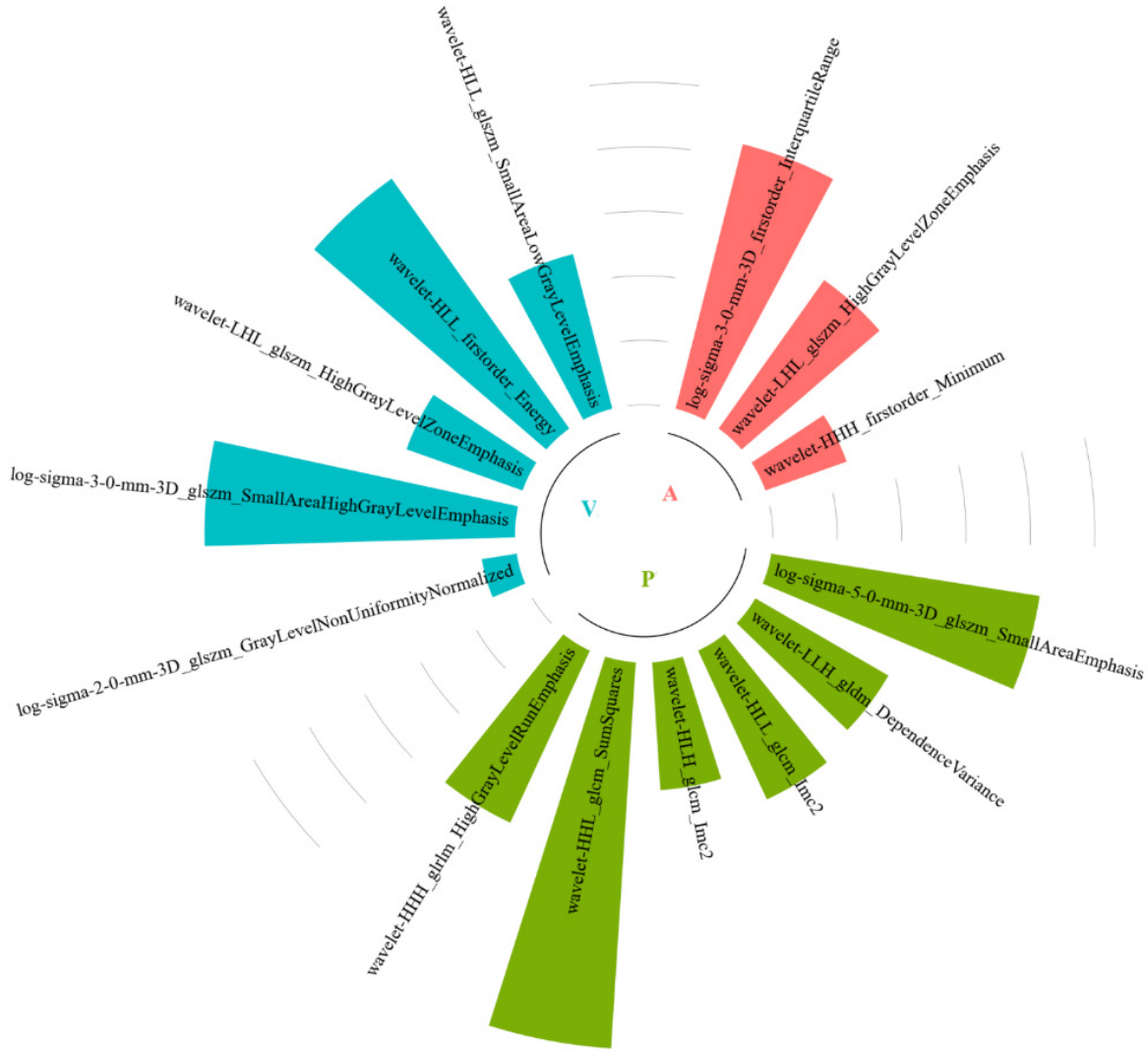

FIGURE 3
Radiomics feature selection results.

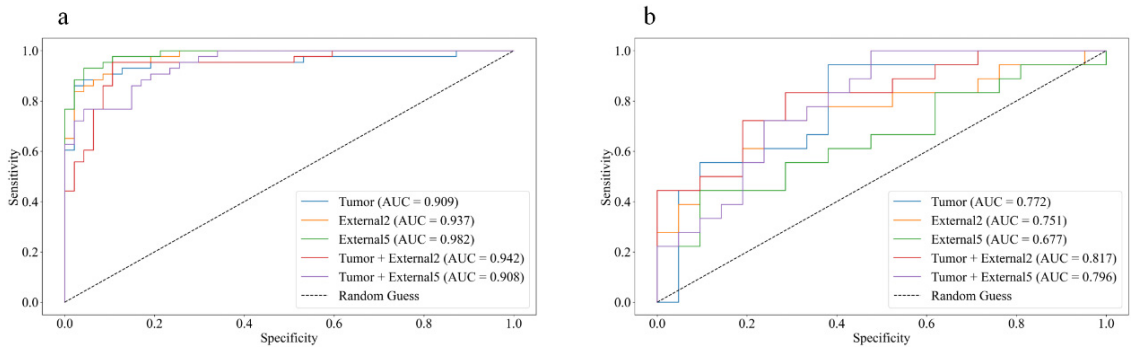

FIGURE 4
The receiver operating characteristic (ROC) curves of the top performing models based on three-phase combination in the training set **(a)** and test sets **(b)**.

and could be applied in future studies. Finally, the sample size in our study was small, and we did not use an independent external validation cohort in this study, thus restricting the generalization ability of our models; thus, larger cohorts, multicentric and external validation are needed for further research and validation.

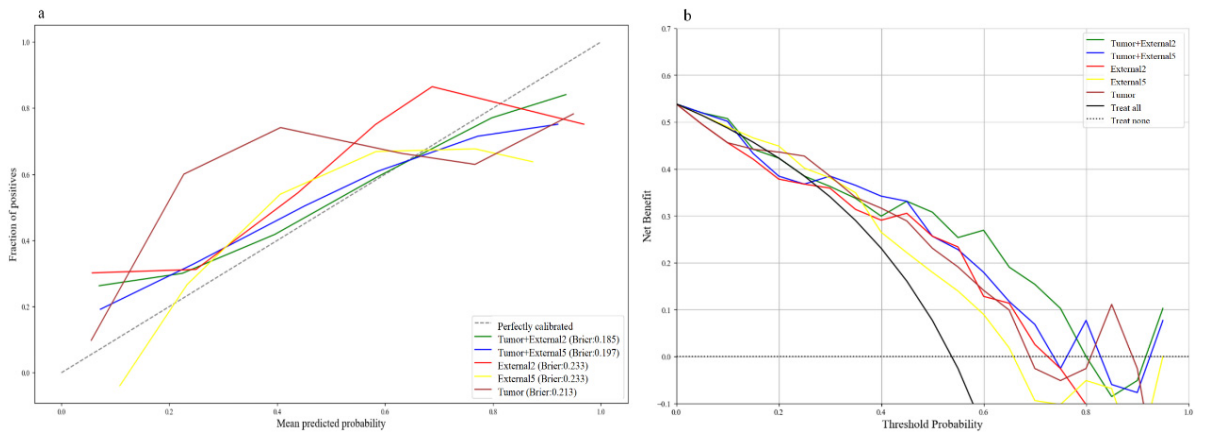

FIGURE 5
The calibration curves **(a)** and DCA curves **(b)** of the top performing models based on three-phase combination in the test set.

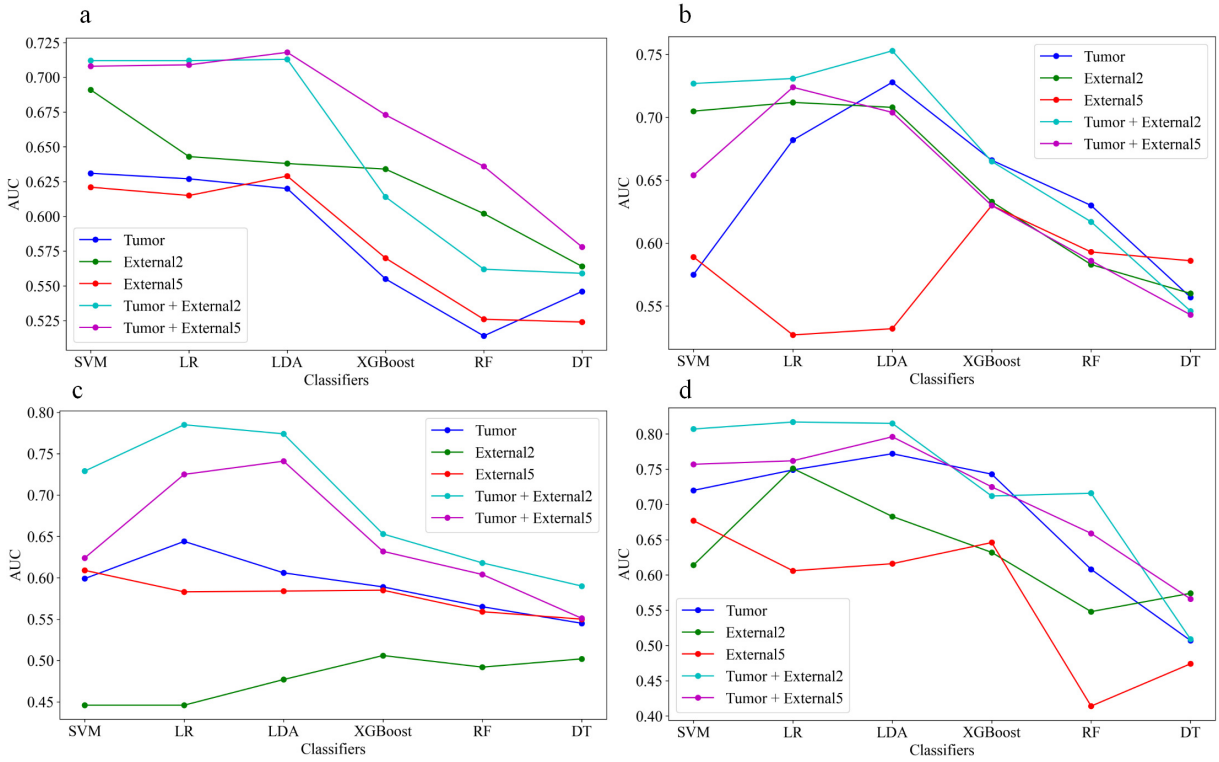

FIGURE 6
The area under the curve (AUC) values of the five models using six different machine learning algorithm-based models in the test sets, **(a–d)** represent plain phase, arterial phase, venous phase and three-phase combination phase, respectively.

5 Conclusion

In conclusion, CT radiomics features integrating both peritumoral and intratumoral regions could accurately predict capsular morphological characteristics of parotid PA via machine learning models, with obvious advantages compared with conventional image diagnosis, which may provide a valuable tool for preoperative clinical decision-making of patients with parotid PA.

Data availability statement

The raw data supporting the conclusions of this article will be made available by the authors, without undue reservation.

Ethics statement

The studies involving humans were approved by the Institutional Review Board of the First Affiliated Hospital of

Chongqing Medical University. The studies were conducted in accordance with the local legislation and institutional requirements. The institutional review board waived the requirement of written informed consent for participation due to the retrospective nature of the study.

Author contributions

QS: Data curation, Investigation, Methodology, Software, Writing – original draft. CX: Data curation, Software, Writing – original draft. YH: Data curation, Investigation, Writing – original draft. YL: Funding acquisition, Methodology, Supervision, Writing – review and editing. KH: Funding acquisition, Methodology, Supervision, Writing – review and editing, Software.

Funding

The author(s) declare that financial support was received for the research and/or publication of this article. This study was supported by the Key Project of Technological Innovation and Application Development of Chongqing Science and Technology Bureau (No. CSTC2021 jscx-gksb-N0008), the Sichuan Science and Technology Innovation and Entrepreneurship Seedling Project (24MZGC0077), the Doctoral Initiation Program of the Affiliated Stomatological Hospital of Southwest Medical University (0802304002), and the Youth Researcher Climbing Program of the Affiliated Stomatological Hospital of Southwest Medical University (0802304018).

Acknowledgments

We would like to thank ShanXiong Chen for constructive criticism of this manuscript.

Conflict of interest

The authors declare that the research was conducted in the absence of any commercial or financial relationships that could be construed as a potential conflict of interest.

Generative AI statement

The authors declare that no Generative AI was used in the creation of this manuscript.

Publisher's note

All claims expressed in this article are solely those of the authors and do not necessarily represent those of their affiliated organizations, or those of the publisher, the editors and the reviewers. Any product that may be evaluated in this article, or claim that may be made by its manufacturer, is not guaranteed or endorsed by the publisher.

Supplementary material

The Supplementary Material for this article can be found online at: https://www.frontiersin.org/articles/10.3389/fmed.2025.1566555/full#supplementary-material

References

1. Andreasen S, Therkildsen M, Bjørndal K, Homøe P. Pleomorphic adenoma of the parotid gland 1985-2010: A Danish nationwide study of incidence, recurrence rate, and malignant transformation. *Head Neck.* (2016) 38:1364–9. doi: 10.1002/hed.24228

2. Li S, Su X, Ning Y, Zhang S, Shao H, Wan X, et al. CT based intratumor and peritumoral radiomics for differentiating complete from incomplete capsular characteristics of parotid pleomorphic adenoma: A two-center study. *Discov Oncol.* (2023) 14:76. doi: 10.1007/s12672-023-00665-8

3. Witt R, Eisele D, Morton R, Nicolai P, Poorten V, Zbären P. Etiology and management of recurrent parotid pleomorphic adenoma. *Laryngoscope.* (2015) 125:888–93. doi: 10.1002/lary.24964

4. Lopes M, Barroso K, Henriques ÁCG, Dos Santos JN, Martins MD, de Souza LB. Pleomorphic adenomas of the salivary glands: retrospective multicentric study of 130 cases with emphasis on histopathological features. *Eur Arch Otorhinolaryngol.* (2017) 274:543–51. doi: 10.1007/s00405-016-4253-5

5. Prasad R. Parotid gland imaging. *Otolaryngol Clin North Am.* (2016) 49:285–312. doi: 10.1016/j.otc.2015.10.003

6. Liu Y, Li J, Tan Y, Xiong P, Zhong L. Accuracy of diagnosis of salivary gland tumors with the use of ultrasonography, computed tomography, and magnetic resonance imaging: A meta-analysis. *Oral Surg Oral Med Oral Pathol Oral Radiol.* (2015) 119:238–45. doi: 10.1016/j.oooo.2014.10.020

7. Kim H, Kim S, Kim Y, et al. Correlation between computed tomography imaging and histopathology in pleomorphic adenoma of parotid gland. *Auris Nasus Larynx.* (2018) 45:783–90. doi: 10.1016/j.anl.2017.09.013

8. Alibek S, Zenk J, Bozzato A, Lell M, Grunewald M, Anders K, et al. The value of dynamic MRI studies in parotid tumors. *Acad Radiol.* (2007) 14:701–10. doi: 10.1016/j.acra.2007.03.004

9. Okahara M, Kiyosue H, Hori Y, Matsumoto A, Mori H, Yokoyama S. Parotid tumors: MR imaging with pathological correlation. *Eur Radiol.* (2003) 13:25–33. doi: 10.1007/s00330-003-1999-0

10. Park J, Kim H. Radiomics as a quantitative imaging biomarker: Practical considerations and the current standpoint in neuro-oncologic studies. *Nucl Med Mol Imaging.* (2018) 52:99–108. doi: 10.1007/s13139-017-0512-7

11. Liu Z, Wang S, Dong D, Wei J, Fang C, Zhou X, et al. The applications of radiomics in precision diagnosis and treatment of oncology: Opportunities and challenges. *Theranostics.* (2019) 9:1303–22. doi: 10.7150/thno.30309

12. Riesterer O, Pruschy M, Bender S, Sharma A, Bogowicz M, Tanadini-Lang S, et al. Consolidation cetuximab after concurrent triplet radiochemotherapy+cetuximab in patients with advanced head and neck cancer: A randomized phase II study. *Radiother Oncol.* (2020) 150:62–9. doi: 10.1016/j.radonc.2020.06.011

13. Beig N, Khorrami M, Alilou M, Prasanna P, Braman N, Orooji M, et al. Perinodular and intranodular radiomic features on lung CT images distinguish adenocarcinomas from Granulomas. *Radiology.* (2019) 290:783–92. doi: 10.1148/radiol.2018180910

14. Langlotz C, Allen B, Erickson B, Kalpathy-Cramer J, Bigelow K, Cook T, et al. A roadmap for foundational research on artificial intelligence in medical imaging: From the 2018 NIH/RSNA/ACR/ The academy workshop. *Radiology.* (2019) 291:781–91. doi: 10.1148/radiol.2019190613

15. Zheng Y, Li J, Liu S, Cui J, Zhan J, Pang J, et al. MRI-Based radiomics nomogram for differentiation of benign and malignant lesions of the parotid gland. *Eur Radiol.* (2021) 31:4042–52. doi: 10.1007/s00330-020-07483-4

16. Al Ajmi E, Forghani B, Reinhold C, Bayat M, Forghani R. Spectral multi-energy CT texture analysis with machine learning for tissue classification: An investigation using classification of benign parotid tumours as a testing paradigm. *Eur Radiol.* (2018) 28:2604–11. doi: 10.1007/s00330-017-5214-0

17. Zhang D, Li X, Lv L, Yu J, Yang C, Xiong H, et al. A preliminary study of CT texture analysis for characterizing epithelial tumors of the parotid gland. *Cancer Manag Res.* (2020) 12:2665–74. doi: 10.2147/CMAR.S245344

18. Zheng Y, Zhou D, Liu H, Wen MCT-. based radiomics analysis of different machine learning models for differentiating benign and malignant parotid tumors. *Eur Radiol.* (2022) 32:6953–64. doi: 10.1007/s00330-022-08830-3

19. Mai W, Tan J, Zhang L, Wang L, Zhang D, Shi C, et al. Predicting high-risk capsular features in pleomorphic adenoma of the parotid gland through a nomogram model based on ADC imaging. *Acad Radiol.* (2024) 31:4408–18. doi: 10.1016/j.acra.2024.06.003

20. Keek S, Sanduleanu S, Wesseling F, de Roest R, van den Brekel M, van der Heijden M, et al. Computed tomography-derived radiomic signature of head and neck squamous cell carcinoma (peri)tumoral tissue for the prediction of locoregional recurrence and distant metastasis after concurrent chemo-radiotherapy. *PLoS One.* (2020) 15:e0232639. doi: 10.1371/journal.pone.0232639

21. Lin C, Yan J, Yap W, Kang C, Chang Y, Tsai T, et al. Prognostic value of interim CT-based peritumoral and intratumoral radiomics in laryngeal and hypopharyngeal cancer patients undergoing definitive radiotherapy. *Radiother Oncol.* (2023) 189:109938. doi: 10.1016/j.radonc.2023.109938

22. Fornacon-Wood I, Mistry H, Ackermann C, Blackhall F, McPartlin A, Faivre-Finn C, et al. Reliability and prognostic value of radiomic features are highly dependent on choice of feature extraction platform. *Eur Radiol.* (2020) 30:6241–50. doi: 10.1007/s00330-020-06957-9

23. Wu X, Dong D, Zhang L, Fang M, Zhu Y, He B, et al. Exploring the predictive value of additional peritumoral regions based on deep learning and radiomics: A multicenter study. *Med Phys.* (2021) 48:2374–85. doi: 10.1002/mp.14767

24. Akinci D'Antonoli T, Farchione A, Lenkowicz J, Chiappetta M, Cicchetti G, Martino A, et al. CT radiomics signature of tumor and peritumoral lung parenchyma to predict nonsmall cell lung cancer postsurgical recurrence risk. *Acad Radiol.* (2020) 27:497–507. doi: 10.1016/j.acra.2019.05.019

25. Mao N, Shi Y, Lian C, Wang Z, Zhang K, Xie H, et al. Intratumoral and peritumoral radiomics for preoperative prediction of neoadjuvant chemotherapy effect in breast cancer based on contrast-enhanced spectral mammography. *Eur Radiol.* (2022) 32:3207–19. doi: 10.1007/s00330-021-08414-7

26. Liu D, Chen J, Ge H, Hu X, Yang K, Liu Y, et al. Differentiation of malignant brain tumor types using intratumoral and peritumoral radiomic features. *Front Oncol.* (2022) 12:848846. doi: 10.3389/fonc.2022.848846

27. Iro A, Agaimy A, Müller S, Sievert M, Iro H, Mantsopoulos K, et al. Satellite nodules in pleomorphic adenomas of the parotid gland: A nightmare for less invasive parotid surgery? *Oral Oncol.* (2021) 115:105218. doi: 10.1016/j.oraloncology.2021.105218

frontiers | Frontiers in Oncology

TYPE Original Research
PUBLISHED 25 April 2025
DOI 10.3389/fonc.2025.1564126

Check for updates

OPEN ACCESS

EDITED BY
Poonam Yadav,
Northwestern University, United States

REVIEWED BY
Edwin Quashie,
Indiana University, United States
Nahid Gorjizadeh,
Tehran University of Medical Sciences, Iran

*CORRESPONDENCE
Tingting Wang
blue72000@126.com
Yufeng Xu
2568248835@qq.com

†These authors have contributed equally to this work

RECEIVED 21 January 2025
ACCEPTED 03 April 2025
PUBLISHED 25 April 2025

CITATION
Li Y, Hua R, Dai L, Chen W, Zhang J, Wang Q, Xu Y and Wang T (2025) Analysis of the impact of rotation error on PTV margins in multiple brain metastases fractionated stereotactic radiotherapy based on single-isocenter multi-target technique. *Front. Oncol.* 15:1564126. doi: 10.3389/fonc.2025.1564126

COPYRIGHT
© 2025 Li, Hua, Dai, Chen, Zhang, Wang, Xu and Wang. This is an open-access article distributed under the terms of the Creative Commons Attribution License (CC BY). The use, distribution or reproduction in other forums is permitted, provided the original author(s) and the copyright owner(s) are credited and that the original publication in this journal is cited, in accordance with accepted academic practice. No use, distribution or reproduction is permitted which does not comply with these terms.

Analysis of the impact of rotation error on PTV margins in multiple brain metastases fractionated stereotactic radiotherapy based on single-isocenter multi-target technique

Yuhong Li[1†], Rui Hua[1†], Liling Dai[2†], Wei Chen[1], Junyuan Zhang[1], Qian Wang[3], Yufeng Xu[1*] and Tingting Wang[1*]

[1]Department of Radiation Oncology, Affiliated Cancer Hospital of Nanjing Medical University, Jiangsu Cancer Hospital, Jiangsu Institute of Cancer Research, Nanjing, Jiangsu, China, [2]Department of Science and Technology, Affiliated Cancer Hospital of Nanjing Medical University, Jiangsu Cancer Hospital, Jiangsu Institute of Cancer Research, Nanjing, Jiangsu, China, [3]Department of Thoracic Surgery, Affiliated Cancer Hospital of Nanjing Medical University, Jiangsu Cancer Hospital, Jiangsu Institute of Cancer Research, Nanjing, Jiangsu, China

Background: Rotational error cannot be overlooked in single-isocenter multi-target (SIMT) stereotactic radiotherapy. This retrospective study aimed to evaluate the treatment accuracy of linear accelerator-based fractionated stereotactic radiotherapy (FSRT) using SIMT non-coplanar volumetric modulated arc therapy (VMAT) in patients with multiple brain metastases. We explored the impact of rotational error on planning target volume (PTV) margins, providing clinical evidence for the selection of appropriate PTV margin values.

Methods: A total of 161 patients with multiple brain metastases (733 treatments; actual clinical PTV margins ranged from 1~2 mm) were included. Theoretical PTV margins were calculated based on the Van Herk and Jenghwa Chang formulas. We analyzed the influence of the distance from each target to the treatment isocenter, rotational errors, and PTV margin on treatment outcomes. Additionally, individualized PTV margins for each patient were calculated using the Jenghwa Chang formula and patients were divided into subgroups according to a 2-mm threshold for further analysis.

Results: The mean residual translational setup errors ranged from −0.04~0.01 mm, and rotational setup errors ranged from 0.15°~0.49°, both within acceptable limits. According to the Van Herk formula, required margins in posterior-anterior, superior-inferior, and right-left directions were 1.44 mm, 1.68 mm, and 1.78 mm, respectively. By incorporating both translational and rotational errors using the Jenghwa Chang formula, the comprehensive margin ranged from 1.69~1.79 mm (calculated based on the 95% confidence interval of distances from targets to isocenter). Additionally, when the mean distance from all targets to their respective treatment isocenters was 30.62 mm, the required margin calculated solely for translational errors using the Jenghwa Chang formula was 1.23 mm; if rotational errors were neglected, target coverage probability would decrease from 95% to 73%. Further subgroup analysis showed that 25 patients whose

individualized theoretical margins exceeded 2 mm tended to experience worse outcomes compared to others, including intracranial local failure (ILF, defined as lesion progression within the previously irradiated intracranial region during follow-up; 32.00% vs. 22.29%, *P = 0.32*), one-year local control (64.00% vs. 65.44%, *P = 0.89*), and one-year intracranial progression-free survival (iPFS, 44.00% vs. 51.45%, *P = 0.85*). However, these differences did not reach statistical significance.

Conclusion: This study confirms that the SIMT non-coplanar VMAT technique ensures treatment accuracy for FSRT in multiple brain metastases. Rotational errors reduce dose coverage, and a minimum safety margin of 1.79 mm is recommended to ensure tumor coverage and reduce local failure, providing a basis for future treatment optimization.

KEYWORDS

single-isocenter multi-target, fractionated stereotactic radiotherapy, volumetric modulated arc therapy, multiple brain metastases, rotational errors, planning target volume margin expansion

1 Introduction

It is estimated that approximately 30% of cancer patients will develop brain metastases during the course of their disease, and with the optimization of cancer treatment methods in recent years, the incidence of brain metastases continues to rise (1). Among these, more than half of the brain metastases are multiple lesions (the number of lesions ≥ 2) (2). For multiple lesions, especially when the cumulative volume of the metastases is large, an increasing number of studies suggest using fractionated stereotactic radiotherapy (FSRT) for treatment (3, 4). FSRT is characterized by a single high-dose fraction and a steep dose gradient at the tumor boundary, making precise localization during treatment particularly crucial. Even small positioning errors can alter the overall dose distribution in the target area, significantly reducing the conformity of the dose to the target and thereby affecting treatment outcomes (5). Although FSRT based on linear accelerators, combined with image-guided technologies such as KV cone-beam computed tomography (KV-CBCT) and six-degree-of-freedom (6-DOF) treatment couch, can effectively correct initial setup errors to the maximum extent possible, residual setup errors may still result in decreased target dose coverage, which in turn increases the risk of tumor recurrence (6–9).

In the past, FSRT for multiple brain metastases typically employed a multi-isocenter approach, where each target was treated individually, resulting in treatment durations of several hours per session. To improve treatment efficiency, the single-isocenter multiple-target (SIMT) non-coplanar volumetric modulated arc therapy (VMAT) technique has been increasingly applied in FSRT for multiple brain metastases. Unlike the multi-isocenter approach, the SIMT technique uses a single isocenter located at the geometric center of the total planning target volume (PTV), allowing for the treatment of multiple targets simultaneously. This approach not only reduces patient imaging doses but also achieves similar dosimetric effects to the former method (10, 11). However, the implementation of SIMT technology may introduce additional rotational errors that affect the dose distribution. Correcting these errors across all target areas simultaneously using KV-CBCT and a 6-DOF treatment couch is challenging (6–8). The International Commission on Radiation Units and Measurements Report 50 recommends increasing the expansion margin to ensure adequate dose coverage for the tumor target area, thus generating the PTV. Traditionally, the formula proposed by Van Herk et al. has been widely used for quantitatively analyzing the expansion margin required for the gross tumor volume (GTV) or clinical target volume (12). Additionally, some studies have suggested increasing the expansion margin by 0~3 mm on the basis of GTV to accommodate setup errors (13). However, given the technical differences across various radiation therapy centers, and the fact that the Van Herk formula does not account for the adverse effects of rotational errors in SIMT techniques, there is currently no consensus in the field regarding the exact definition of the expansion margin. In recent years, several research teams have explored the expansion margin from GTV to PTV (14–18). Jenghwa Chang, using a statistical modeling approach, proposed a new formula for calculating the expansion margin, which takes both translational and rotational errors into account. The resulting value ensures that the probability of GTV being included within the corresponding PTV region is greater than the pre-set coverage probability (15, 16, 19).

Based on the aforementioned background, this study aims to retrospectively analyze the application of FSRT for multiple brain

metastases in our center, utilizing a linear accelerator and SIMT non-coplanar VMAT technology, and to assess its treatment accuracy. Differences in PTV margins calculated by the Van Herk and Jenghwa Chang formulas were compared, and the impacts of distances from targets to the treatment isocenter, rotational errors, and PTV margins on patient outcomes were analyzed to provide guidance for selecting clinical PTV margins in our center.

2 Materials and methods

2.1 Patient cohort and treatment characteristics

This study retrospectively analyzed patients with multiple brain metastases who underwent FSRT at Jiangsu Cancer Hospital from January 2021 to December 2023. The study was approved by the Ethics Committee of Jiangsu Cancer Hospital. Inclusion criteria were as follows: (1) FSRT was performed on all patients using the Varian TrueBeam linear accelerator equipped with the HyperArc system; (2) non-coplanar radiation fields and SIMT-VMAT were used; (3) patients had more than one brain metastasis; (4) patients were able to undergo follow-up every 2~3 months via telephone, outpatient visits, or hospitalization. Exclusion criteria included: (1) brainstem or leptomeningeal metastases; (2) primary pathology of small cell lung cancer; (3) treatment interruption; (4) failure to adhere to KV-CBCT imaging verification and 6-DOF treatment couch correction protocols.

All patients were immobilized in a supine position using a No.1 carbon fiber baseplate (model: Q-Fix Pro-Lok, dose attenuation rate <0.5%) combined with an Orfit integrated head fixation system. The fixation system included a thermoplastic head mask anchored at three points (forehead and bilateral temporal regions; thickness: 3.5 mm; repositioning accuracy ≤ 0.5 mm) and an adjustable-angle S-shaped headrest (sagittal deviation ≤ 1.0 mm; tilt angle range: –10° to +30°). After initial positioning, the treatment isocenter was marked on the mask using a laser positioning system to ensure daily reproducibility. Contrast-enhanced computed tomography (CT) (range: from cranial vertex to C4 vertebra, 512 × 512 matrix, slice thickness: 1 mm, spiral pitch: 0.8) and 3.0T magnetic resonance imaging with T1-weighted contrast-enhanced sequences (TR/TE = 500/15 ms, slice thickness: 1 mm, FOV: 240 × 240 mm) were fused using a mutual-information rigid registration algorithm (mean squared error < 0.8 mm), verified independently by two radiation oncologists. The GTV was delineated on fused images, defined as clearly identifiable tumor areas (lesions unclear on planning images were excluded). The PTV was created by expanding the GTV by 1~2 mm. A multileaf collimator with leaf width of 2.5 mm (dynamic positioning accuracy ≤ 0.5 mm verified daily by electronic portal imaging device) and maximum collimator diameter of 1.7 cm was employed. Cone-beam computed tomography (CBCT)-guided setup verification with 6-DOF corrections (bone and soft-tissue dual-mode registration) was conducted before each treatment; residual errors were required to be ≤ 2 mm (translation) and ≤ 3° (rotation). An optical surface monitoring system tracked forehead landmarks in real-time during treatment, automatically pausing irradiation upon displacement exceeding 1.0 mm. Treatment utilized 6 MeV-X rays in flattening filter-free mode with a maximum dose rate of 2400 MU/min. Dosimetric verification employed an ArcCHECK phantom (passing criteria: ≥ 95% for 3%/2 mm) and ion-chamber point-dose measurements (deviation ≤ ± 2%). The treatment plan required that over 95% of the PTV area receive the prescribed dose, with the dose distribution approximating a Gaussian curve. The low dose outside the PTV should be uniformly distributed around the target, and the dose fall-off should be controlled at greater than 10% per 3 mm. Additionally, the dose in the region outside the PTV should not exceed the prescribed dose. The 10 Gy isodose lines of two adjacent target volumes should not overlap. Dose limits for critical organs followed the RTOG9005 guidelines (20).

2.2 Data collection and processing

All treatment plans were generated using the Eclipse planning system with the Acuros dose algorithm. With the treatment isocenter as the origin of a three-dimensional coordinate system, the coordinates (x, y, z) of the geometric center of each patient's targets were recorded, and distances (d) from the isocenter to each target were calculated using the Euclidean formula (Equation 1). Subsequently, the mean distance of all targets to the isocenter for each patient ($\bar{d}$) was calculated using Equation 2. Additionally, the overall mean distance (D) for all patients was obtained using Equation 3. Residual setup errors in six directions were recorded for each treatment: rotational errors R_{Roll}, R_{Pitch}, and R_{Yaw} correspond to roll, pitch, and yaw directions, respectively; translational errors T_{IS}, T_{RL} and T_{PA} correspond to superior–inferior, right–left, and posterior–anterior directions, respectively. The total translational error (T_{total}, in mm) for each treatment session was calculated using Equation 4, for subsequent error analysis.

$$d = \sqrt{x^2 + y^2 + z^2} \tag{1}$$

$$\bar{d} = \frac{1}{n}\sum_{i=1}^{n}\sqrt{x_i^2 + y_i^2 + z_i^2} \tag{2}$$

In Equation 2, (x_i, y_i, z_i) represents the three-dimensional coordinates of the geometric center of the i-th brain metastasis relative to the treatment isocenter for each patient, and n represents the number of brain metastases for that patient.

$$D = \frac{1}{N}\sum_{j=1}^{N} d_j \tag{3}$$

In Equation 3, d_j denotes the distance between the geometric center of the j-th brain metastasis and its respective treatment isocenter, and N denotes the total number of lesions across all patients enrolled in the study.

$$T_{total} = \sqrt{T_{IS}{}^2 + T_{RL}{}^2 + T_{PA}{}^2} \tag{4}$$

In addition, based on the error angles of the patient in the three rotational directions (R_{Roll}, R_{Pitch}, R_{Yaw}) during each treatment, the corresponding rotation matrix $\mathcal{R}$ was constructed:

$$\boldsymbol{R} = \mathcal{R}_{\boldsymbol{x}}(R_{Roll})\mathcal{R}_{\boldsymbol{y}}(R_{Pitch})\mathcal{R}_{\boldsymbol{z}}(R_{Yaw}) \tag{5}$$

Where $\mathcal{R}_{\boldsymbol{x}}(R_{Roll})$, $\mathcal{R}_{\boldsymbol{y}}(R_{Pitch})$, $\mathcal{R}_{\boldsymbol{y}}(R_{Yaw})$ represent the rotation matrices for the rotation angles R_{Roll}, R_{Pitch} and R_{Yaw} (in °) around the x-axis, y-axis, and z-axis, respectively. Subsequently, the rotation matrix $\mathcal{R}$ was converted into a rotation vector $\mathcal{V}$ using Rodrigues' rotation formula Equation 6. The direction of $\mathcal{V}$ denotes the rotation axis, represented by the unit vector $\mathcal{U}$ Equation 7, and its magnitude corresponds to the total rotation angle R_{total} (in °):

$$\mathcal{V} = \frac{1}{2\sin(R_{total})}\begin{bmatrix} \mathcal{R}_{32} - \mathcal{R}_{23} \\ \mathcal{R}_{13} - \mathcal{R}_{31} \\ \mathcal{R}_{21} - \mathcal{R}_{12} \end{bmatrix} \tag{6}$$

$$\mathcal{V} = R_{totol}\mathcal{U} \tag{7}$$

$$R_{total} = \cos^{-1}\left(\frac{trace(\mathcal{R})-1}{2}\right) \tag{8}$$

Where $trace(\mathcal{R})$ is the trace of the rotation matrix $\mathcal{R}$, and $\mathcal{R}_{\mathbf{ij}}$ is the element at the i-th row and j-th column of the rotation matrix $\mathcal{R}$.

Using Equations 5~8, the rotational errors from each treatment fraction were integrated into a single comprehensive rotational angle (R_{total}) for subsequent analysis of the PTV margin.

2.3 Calculation of PTV margin expansion

According to Van Herk et al., in order to ensure that at least 90% of patients' PTVs receive 95% of the prescribed dose, the margin expansion is calculated as follows (12):

$$M_{Van\ Herk} = 2.5\Sigma + 0.7\sigma \tag{9}$$

where $M_{Van\ Herk}$ represents the calculated margin, Σ (in mm) is the population systematic error, and σ (in mm) is the population random error. Given the limited fractions per patient and relatively small inter-individual variations, the group mean of the random error standard deviation (SD) is typically used to compute σ (Equation 11). The calculations of Σ and σ are as follows:

$$\sum = \sqrt{\frac{P}{N(P-1)}\sum_{p=1}^{P}F_p(m_p - \bar{m})^2} \tag{10}$$

$$\begin{aligned}\sigma &= \sqrt{\frac{1}{N-P}\sum_{p=1}^{P}(F_p - 1)\cdot\sigma_p^2} \\ &= \sqrt{\frac{1}{N-P}\sum_{p=1}^{P}\sum_{f=1}^{Fp}(x_{pf} - m_p)^2}\end{aligned} \tag{11}$$

where N is the total number of fractions, P is the total number of patients, F_p is the number of fractions for patient p, x_{pf} (in mm) is the translational error along the x-axis for patient p in fraction f, σ_p (in mm) is the SD of random errors for patient p, m_p (in mm) is the mean translational error (systematic error) for patient p, and $\bar{m}$ (in mm) is the mean systematic error across all patients.

Jenghwa Chang's method accounts for rotational uncertainties, assuming random errors in translation and rotation that follow independent three-dimensional normal distributions (15, 16, 19). Using Chang's approach, the comprehensive PTV margin considering both translational and rotational uncertainties ($M_{trans+rot}$) was calculated for all 161 patients as follows:

$$\begin{aligned}M_{trans+rot} &= \sqrt{M_{trans}^2 + M_{rot}^2} \\ &= \sqrt{(\chi_\alpha\cdot\sigma_{T_{total}})^2 + (\chi_\alpha\cdot\sigma_{r_{total}})^2} \\ &= \chi_\alpha\sqrt{\sigma_{T_{total}}^2 + \sigma_{r_{total}}^2} \\ &= \chi_\alpha\sqrt{\sigma_{T_{total}}^2 + (0.01424\cdot\bar{d}\cdot\sigma_{R_{total}})^2}\end{aligned} \tag{12}$$

Where M_{trans} and M_{rot} represent the PTV margin expansions required to accommodate translational and rotational errors, respectively Equation 12. χ_α represents the value corresponding to the probability that the GTV is covered by the PTV. When the probability of the GTV being within the PTV is at least 95%, χ_α is set to 2.795. $\sigma_{T_{total}}$ is the standard deviation of the total translational error (T_{total}) for all 733 treatments across all patients (The calculation of T_{total} is shown in Equation 4). $\sigma_{r_{total}}$ (in mm) represents the rotational uncertainty for all 733 treatments, and $\sigma_{R_{total}}$ (in °) represents the standard deviation of the total rotation error (R_{total}) for all 733 treatments.

2.4 Grouping and endpoints

Considering individual differences, the study calculated individualized PTV margin expansion for each patient using the Jenghwa Chang formula, denoted as $M'_{trans+rot}$, with the following calculation process:

$$M'_{trans+rot} = \chi_\alpha\sqrt{(\sigma'_{T_{total}})^2 + (0.01424\cdot\bar{d}\cdot\sigma'_{R_{total}})^2} \tag{13}$$

Where $\sigma'_{T_{total}}$ represents the standard deviation of the total translational error (T_{total}) across all treatment fractions for each patient. $\sigma'_{R_{total}}$ (in °) represents the standard deviation of the total rotation error (R_{total}) across all treatment fractions for each patient.

Actual margins applied in this study ranged from 1~2 mm. Patients were divided into two groups based on whether their calculated personalized margin ($M'_{trans+rot}$) exceeded 2 mm. This grouping enabled exploration of the prognostic impact of margins smaller than the theoretically required value when rotational errors were considered. Additionally, referencing previously reported threshold values (21–24), subgroup analyses were conducted using of $\bar{d}$ 30 mm as the cutoff to investigate the effect of target-isocenter distance on tumor control under rotational errors within ±3°.

Primary endpoints were intracranial progression-free survival (iPFS) and local control (LC), with secondary endpoints including intracranial local failure (ILF) and overall survival (OS). iPFS was

defined as the duration from FSRT initiation until intracranial lesion progression or the last follow-up. LC was defined as the absence of intracranial progression in irradiated regions throughout follow-up or until death. ILF was defined as lesion progression within irradiated regions during follow-up. OS was defined as the time from FSRT initiation to death or last follow-up if still alive. Disease progression was evaluated using the Response Evaluation Criteria in Solid Tumors version 1.1 criteria (25).

2.5 Statistical analysis

Analyses were performed using SPSS v26.0 and R v4.4.2. Continuous variables were reported as mean ± SD for normally distributed data, median and range for non-normally distributed data, and categorical variables were presented as frequencies and percentages. Comparisons utilized the t-test, Wilcoxon rank-sum test, or chi-square test as appropriate. Kaplan–Meier survival curves and log-rank tests compared iPFS and OS. Spearman correlation assessed variable relationships. Cox proportional hazards regression analyzed prognostic factors for iPFS and OS. Logistic regression explored relationships between target-isocenter distances, rotational errors, LC, and ILF. Multivariate linear regression assessed independent impacts of metastasis characteristics and treatment parameters on rotational errors and PTV margins. Statistical significance was defined as $P < 0.05$.

3 Results

3.1 Patient characteristics and plan statistics

This retrospective study analyzed patients with multiple brain metastases treated by linear accelerator-based FSRT at Jiangsu Cancer Hospital from January 2021 to December 2023. A total of 161 patients with 391 lesions were included, undergoing 733 treatments. As detailed in Table 1, the mean age was 61.42 ± 9.57 years; 88 patients (54.66%) were male, and 73 (45.34%) were female. The median Karnofsky Performance Status (KPS) was 80 (range: 60~100). The primary tumor was predominantly lung cancer (75.78%, n=122), with a median of two brain metastases per patient (range: 2-8), a median maximum lesion diameter of 16.1 mm (range: 3~70.6 mm), and a median lesion volume of 2.98 cm^3 (range: 0.11~188.24 cm^3). Patients underwent a median of 3 fractions (range: 2~15). Regarding treatment planning, the median Conformity Index (CI) was 1.03 (range: 0.92~1.89), mean Homogeneity Index (HI) was 0.13 ± 0.06, median $D_{2\%}$ (the minimum dose delivered to the hottest 2% of the volume) was 34.78 Gy (range: 20.45~68.66 Gy), median $D_{50\%}$ (the minimum dose delivered to the hottest 50% of the volume) was 32.75 Gy (range: 20.29~64.09 Gy), and median $D_{98\%}$ (the minimum dose delivered to the hottest 98% of the volume) was 29.83 Gy (range: 19.94~59.45 Gy). The average distance from lesion geometric centers to the isocenter was 30.62 ± 11.04 mm (95% confidence interval (95% CI): 28.91~32.34 mm; Figure 1).

TABLE 1 Patient Baseline Characteristics.

Characteristic	Value
Gender, NO (%)	
Female	73 (45.34)
Male	88 (54.66)
Age, years, mean ± SD	61.42 ± 9.57
KPS, percentages, median (range)	80 (60~100)
Primary Site, NO (%)	
Esophagus	9 (5.59)
Lung	122 (75.78)
Breast	14 (8.70)
Other	16 (10)
Number of BM, NO, median (range)	2 (2~8)
Maximum Diameter of BM, mm, median (range)	16.1 (3.0~70.6)
Volume of BM, cm^3, median (range)	2.98 (0.11~188.24)
CI, median (range)	1.03 (0.92~1.89)
HI, mean ± SD	0.13 ± 0.06
$D_{2\%}$, Gy, median (range)	34.78 (20.45~68.66)
$D_{50\%}$, Gy, median (range)	32.75 (20.29~64.09)
$D_{98\%}$, Gy, median (range)	29.83 (19.94~59.45)
Fractions, NO, median (range)	3 (2~15)
$\bar{d}$, mm, mean ± SD	30.62 ± 11.04

NO, number; SD, standard deviation; KPS, karnofsky performance status; BM, brain metastases; CI, conformity index; HI, homogeneity index; Gy, gray. $D_{2\%}$ represents the minimum dose received by the hottest 2% of the target volume the dose. $D_{50\%}$ represents the minimum dose received by the hottest 50% of the target volume the dose. $D_{98\%}$ represents the minimum dose received by the hottest 98% of the target volume the dose. $\bar{d}$ represents the average distance from each patient's target volume geometric center to the treatment isocenter.

3.2 Geometric accuracy

In this study, the six-dimensional residual setup error data for 733 treatments after KV-CBCT correction are presented in Figure 2. In the translational directions (Figure 2A), the average residual errors were as follows: posterior-anterior direction: 0.01± 0.59 mm; superior-inferior direction: – 0.04 ± 0.68 mm); right-left direction: – 0.001 ± 0.75 mm). In the rotational directions (Figure 2B), the average residual errors were as follows: yaw: 0.30° ± 1.05°); pitch: 0.15° ± 1.17°); roll: 0.49° ± 1.48°). Inter-group comparisons for the three rotational directions (Wilcoxon rank-sum test) revealed significant differences between roll and both yaw and pitch ($P < 0.001$) (Figure 2B). Further analysis showed a significant positive correlation between R_{total} and T_{total} ($P < 0.01$), though the

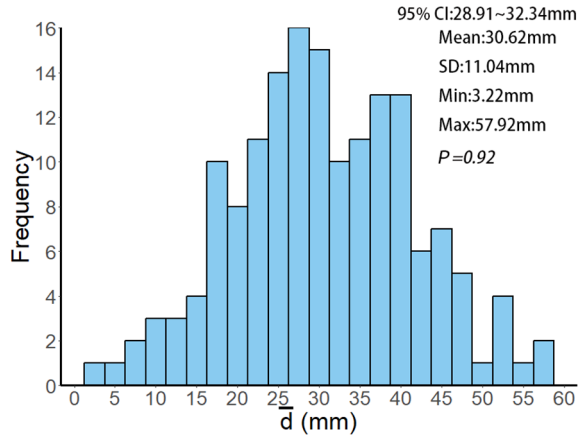

FIGURE 1
Histogram of the frequency distribution of $\bar{d}$ values among 161 patients. $\bar{d}$ represents the average distance of each patient's target volume geometric center to the treatment isocenter, calculated using Equations 1~2. 95% CI, SD, Min and Max represent the 95% confidence interval, standard deviation, minimum value and maximum value of the $\bar{d}$ values, respectively. *P = 0.92* indicates that the Kolmogorov-Smirnov test, used to analyze the $\bar{d}$ values of all patients, confirms the data follows a normal distribution (*P = 0.92 > 0.05*).

correlation coefficient (*r = 0.19*) suggests a weak association between the two (Figure 3).

Further analysis (Table 2) examined correlations between setup errors (rotational and translational) and lesion number, maximum diameter, cumulative volume, and fractions. Spearman correlation analyses revealed weak positive correlations between rotational errors and cumulative lesion volume (r = 0.20, *P = 0.01*) and maximum diameter (r = 0.24, *P < 0.01*), and between cumulative lesion volume and translational errors (r = 0.16, *P = 0.04*). Multivariate linear regression confirmed maximum lesion diameter as an independent predictor of rotational error (Beta = 0.24, 95% CI: 0.02~0.27, *P = 0.02*); other factors (fraction number, cumulative volume, lesion number) showed no significant independent effects (*P = 0.24, 0.96*, and *0.62*, respectively). No factors showed statistical significance in predicting translational errors (diameter, *P = 0.07*; fractions, *P = 0.12*; volume, *P = 0.59*; lesion number, *P = 0.28*).

3.3 Margin calculation results

In this study, the random errors σ of the six-dimensional residual setup errors (including posterior-anterior, superior-inferior, right-left, yaw, pitch, and roll directions) for 161 patients were 0.54 mm, 0.54 mm, 0.64 mm, 0.79°, 0.80°, and 1.14°, respectively. The system errors Σ were 0.42 mm, 0.52 mm, 0.53 mm, 0.84°, 0.97°, and 1.15° (Table 3). Using Van Herk formula (Equations 9~11), the PTV margin expansion values for the three translational directions (posterior-anterior, superior-inferior, right-left) were calculated to be 1.44 mm, 1.68 mm, and 1.78 mm, respectively. Furthermore, the results (Table 3) show that the standard deviations of the T_{total} and R_{total} for all patients, after processing with KV-CBCT and the 6-DOF treatment couch, were 0.44 mm and 1.02°, respectively. When both translational and rotational factors are considered, the combined PTV margin expansion $M_{trans+rot}$ calculated using the Jenghwa Chang formula is 1.74 mm with $\bar{d}$ at its mean value (i.e., 30.62 mm, see Equation 3). When $\bar{d}$ is considered within the 95% CI (i.e., 28.91~32.34 mm), the corresponding $M_{trans+rot}$ values range from 1.69~1.79 mm (Table 3).

Potential influencing factors for PTV margin were explored (Table 2). Spearman correlation analysis showed a weak positive correlation between fraction number and PTV margin (r = 0.25, *P < 0.01*) and a weak negative correlation with lesion number (r = –0.21, *P = 0.01*). Multivariate regression analysis, including lesion diameter, fraction number, cumulative volume, and lesion number, revealed no statistically significant independent predictors of PTV margin (diameter *P = 0.22*, fractions *P = 0.14*, volume *P = 0.28*, lesion number *P = 0.10*).

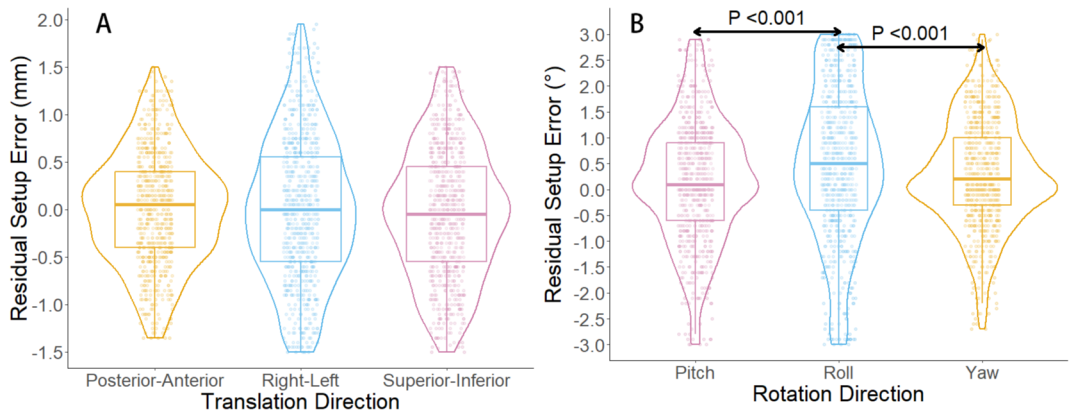

FIGURE 2
Boxplot and violin plot of residual setup errors in six directions. **(A)** shows the distribution of residual setup errors in three translational directions. **(B)** displays the distribution of residual setup errors in three rotational directions. In **(B)**, significant differences are observed in the residual setup errors between the roll direction and the yaw and pitch directions (*P < 0.001*, Wilcoxon rank-sum test).

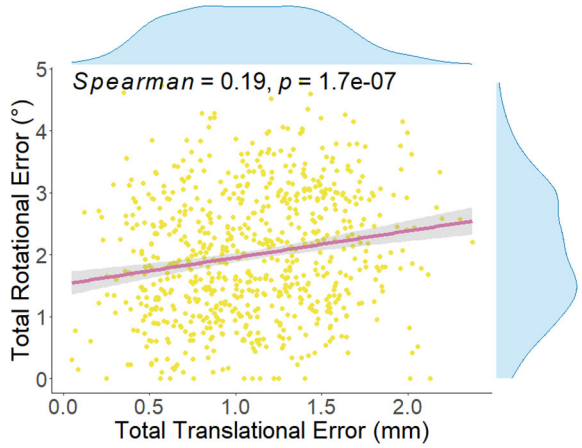

FIGURE 3
Spearman correlation analysis between total translational error and total rotation error for each treatment. The correlation coefficient (*Spearman = 0.19, P = 1.7e-0.7*) indicates a statistically significant relationship between the two. The total translational error for each treatment is calculated using Equation 4, while the total rotation error is calculated using Equations 5~8.

3.4 Prognostic outcomes

As of December 2024, the median follow-up was 16.87 months, with an ILF rate of 24.23% and a 1-year LC rate of 65.22%. Median iPFS was 12.87 months, median OS was not reached, with 1-year cumulative iPFS and OS at 50.92% and 70.80%, respectively.

Given the combined impact of rotational errors and target-isocenter distance on dose distribution, subgroup analyses were conducted based on a distance cutoff of 30 mm ($\bar{d}$ ≤30 mm, n = 77; $\bar{d}$ >30 mm, n = 84). Results (Table 4) showed no significant differences in ILF rates (23.34% vs. 25.00%, *P = 0.81*) or 1-year local control rates (71.43% vs. 59.52%, *P = 0.11*). Kaplan-Meier analysis revealed no significant differences between groups in cumulative 1-year iPFS (50.62% vs. 49.97%, *P = 0.80*) or OS (66.18% vs. 73.81%, *P = 0.38*). Further analysis (Table 5) showed rotational errors did not significantly impact iPFS, OS, ILF, or local control rates (all *P > 0.05*).

Considering rotational errors, personalized margins ($M'_{trans+rot}$) were calculated (Equation 13), identifying 25 patients (15.53%) needing >2 mm margins. Comparing outcomes between patients requiring margins ≤2 mm vs. >2 mm revealed no statistically significant differences in 1-year cumulative iPFS (51.45% vs. 44.00%, *P = 0.85*), OS (69.84% vs. 71.78%, *P = 0.87*), ILF rates (22.79% vs. 32.00%, *P = 0.32*), or 1-year local control rates (65.44% vs. 64.00%, *P = 0.89*).

TABLE 2 Spearman correlation analysis between tumor and treatment parameters versus setup errors and PTV margins.

Variables	$\bar{R}_{total}$		$\bar{T}_{total}$		$M'_{trans+rot}$	
	r	*P*	r	*P*	r	*P*
Number of BM	0.07	0.37	−0.05	0.53	−0.21	0.01
Volume of BM	0.20	0.01	0.16	0.04	−0.01	0.91
Maximum Diameter of BM	0.24	< 0.01	0.14	0.07	0.01	0.90
Fractions	−0.12	0.12	−0.12	0.12	0.25	< 0.01

$\bar{R}_{total}$ denotes the average of R_{total} across all treatment fractions per patient, where R_{total} represents the overall rotational error per treatment calculated using Equations 5-8. $\bar{T}_{total}$ denotes the average of T_{total} across all treatment fractions per patient, where T_{total} represents the overall translational error per treatment calculated using Equation 4. $M'_{trans+rot}$ indicates the individualized PTV margin per patient derived from the Jenghwa Chang model, as detailed in Equation 13. BM, brain metastases. R, correlation coefficient.

4 Discussion

In the current medical field, radiation therapy for multiple brain metastases has become a significant challenge in cancer treatment. In recent years, the application of SIMT non-coplanar VMAT technology for treating multiple brain metastases has been evaluated in numerous studies (10, 11, 23, 26). VMAT provides highly conformal dose distribution for multiple brain metastases by adjusting the intensity of beams, dose rates, and gantry rotation speed. Compared to coplanar VMAT, non-coplanar VMAT significantly improves the dose conformity and dose gradient of the PTV of brain metastases, especially when the lesions are close to each other (11). Furthermore, studies have shown that SIMT non-coplanar VMAT technology can reduce the total treatment time by nearly half while maintaining a high level of local control rate (10, 11). However, SIMT technology still faces several challenges in practical application, particularly with the introduction of rotational errors. As the distance from the target to the isocenter increases, the impact of rotational uncertainty on lesion dose coverage becomes more pronounced (5, 23, 26, 27). Roper et al. reported that when the distance between the isocenter and the target increases, a rotational error exceeding 1°can significantly lower the expected dose coverage of the target (5). Moreover, Sagawa et al. found that in multiple brain metastases, as the rotational error increased, the V_{10Gy} (the volume receiving at least 10 Gy) to V_{16Gy} (the volume receiving at least 16 Gy) values for the brain significantly increased, indicating that rotational errors may elevate the risk of tumor recurrence and normal brain tissue damage (27). These findings emphasize the necessity of controlling and correcting rotational errors when using SIMT technology to ensure the precision and safety of treatment.

Based on this background, the present study systematically analyzed residual six-dimensional setup errors. As shown in Table 3, average translational residual errors ranged from −0.04~0.01 mm, and rotational residual errors ranged from 0.15° ~0.49°. According to the AAPM Task Group 142 report, residual setup errors after KV-CBCT correction and 6DOF couch adjustment should be within 1 mm and 0.5° (28). Recently, several studies have advocated even stricter criteria (14, 29). For instance, Carminucci et al. reported average residual translational errors of 1.67, 0.73, and 0.75 mm in posterior-anterior, superior-inferior, and right-left directions, respectively, and average rotational errors of 0.73°, 1.44°, and 0.76° in pitch, roll, and yaw

TABLE 3 Planning target volume margins calculation.

	Margin with Translational Errors						Margin with Translational & Rotational Errors	
	T_{PA} (mm)	T_{IS} (mm)	T_{RL} (mm)	R_{Yaw} (°)	R_{Pitch} (°)	R_{Roll} (°)		
Mean	0.01	−0.04	−0.001	0.30	0.15	0.49	$\sigma_{T_{total}}$(mm)	0.44
SD	0.59	0.68	0.75	1.05	1.17	1.48	95% CI for $\bar{d}$ (mm)	28.91~32.34
σ	0.54	0.54	0.64	0.79	0.80	1.14	$\sigma_{R_{total}}$ (°)	1.02
Σ	0.42	0.52	0.53	0.84	0.97	1.15	χ_α	2.795
$M_{Van\ Herk}$ (mm)	1.44	1.68	1.78	/	/	/	$M_{trans+rot}$ (mm)	1.69~1.79

The standard deviation of the total translational error ($\sigma_{T_{total}}$) represents the standard deviation of the total translational error (T_{total}) for all 733 treatments across the 161 patients (T_{total} is calculated using Equation 4). T_{PA}, T_{IS}, T_{RL}, R_{Yaw}, R_{Pitch}, R_{Roll} represent the residual setup errors in the posterior-anterior, superior-inferior, right-left, yaw, pitch, and roll directions, respectively. SD refers to the standard deviation. σ represents the group random error, calculated using Equation 11. Σ represents the group systematic error, calculated using Equation 10. $M_{Van\ Herk}$ represents the planning target volume (PTV) margin expansion calculated using Van Herk's formula for the 161 patients, considering only the residual setup error in the translational directions. T_{total} represents the total translational error for each patient before every treatment. $\sigma_{T_{total}}$ is the standard deviation of T_{total} for all 733 treatments across 161 patients. "95% CI for $\bar{d}$" denotes the 95% confidence interval of $\bar{d}$, which is the average distance from each patient's target volume geometric center to the treatment isocenter. R_{total} represents the total rotational error for each patient before each treatment, calculated using formulas Equations 5~8, and $\sigma_{R_{total}}$ is the standard deviation of R_{total} for all 733 treatments across the 161 patients. χ_α represents the value corresponding to the probability of the gross tumor volume (GTV) being covered by the PTV. When the probability of GTV being inside the PTV is at least 95%, χ_α is set to 2.795. $M_{trans+rot}$ represents the combined PTV margin expansion for the 161 patients, considering both rotational and setup errors, calculated using Jenghwa Chang formula.

directions during stereotactic radiotherapy (29). Compared to these studies, our results demonstrated superior setup accuracy for FSRT based on the SIMT non-coplanar VMAT technique, surpassing those commonly required in traditional whole brain radiotherapy (WBRT). Previous reports have indicated WBRT systematic translational errors ranging from –0.63 mm to 0.73 mm, with random errors of 0.75~1.39 mm (30). Such comparisons underscore FSRT's distinct suitability for treating multiple brain metastases in the era of precision radiotherapy. Notably, the present study found significantly larger setup errors in the roll direction compared to pitch and yaw (Figure 2B). This observation aligns with previous literature and clinical experience, reflecting the greater practical difficulty in controlling roll rotations (31). Furthermore, we observed a statistically significant positive correlation between R_{total} and T_{total} (r = 0.19, $P < 0.01$; Figure 3). Although the correlation is relatively weak, it suggests an upward trend in translational errors with increasing rotational deviations. This finding corroborates earlier research (32, 33); Keeling et al. reported a close relationship between translational uncertainty and couch rotation angles in stereotactic radiotherapy (32).

TABLE 4 Analysis of the impact of distance from lesion to treatment isocenter on patient prognosis.

Endpoints	$\bar{d}$ ≤ 30 mm Group (N = 77)	$\bar{d}$ >30 mm Group (N = 84)	*P*
one-year LC rates, %	71.43	59.52	0.11
ILF rates, %	23.34	25.00	0.81
1-year cumulative iPFS, %	50.62	49.97	0.80
1-year cumulative OS, %	66.18	73.81	0.38

$\bar{d}$ denotes the average distance from each patient's lesion geometrical center to the treatment isocenter, calculated by Equation 2. LC, local control. ILF, intracranial local failure. iPFS, intracranial progression-free survival. OS, overall survival; N, number.

The mechanisms underlying setup errors are complex, involving multiple contributing factors. Previous studies have identified several elements that may exacerbate these errors. Firstly, during the image guidance and registration process for multiple brain metastases, the relative motion between lesions can make it difficult for the 6-DOF treatment couch with CBCT to effectively correct all positioning uncertainties (6–8). Secondly, image registration and correction may lead to extended treatment times, which could increase the uncertainty of intrafraction motion (26, 34). Tarnavski et al. found that when the treatment duration exceeds 10 minutes, the probability of patient movement greater than 2 mm or 2 ° significantly increases (34). Furthermore, Schmidhalter et al. pointed out that, in non-frame fixation systems, some positioning inaccuracies may be related to weight loss in patients during radiotherapy, leading to increased movement space within the mask (35). This study did not analyze the impact of intrafraction motion. Although previous studies have suggested using CBCT before and after treatment to reduce the impact of setup errors, this measure was not implemented in our center due to economic and time constraints (36). To further elucidate potential causes of setup errors, we analyzed the influence of factors such as lesion count, maximum diameter, cumulative tumor volume, and number of treatment fractions (Table 2). The results indicated that cumulative tumor volume and maximum lesion diameter showed a weak but significant positive correlation with setup errors, particularly rotational errors, with lesion diameter demonstrating a significant independent association ($P = 0.02$). This suggests that larger lesions are more prone to increased setup and registration errors. A plausible explanation is that tumors undergoing radiation-induced necrosis or volume reduction may shift their relative position with respect to the skull, thereby affecting the accuracy of target registration, especially when employing bone-based alignment methods. This phenomenon is particularly pronounced with larger tumors or larger cumulative volumes (37). In summary,

TABLE 5 Analysis of the impact of rotational errors on patient prognosis.

Endpoints	$R_{total} \leq 1°$ vs. $1° < R_{total} \leq 2°$		$R_{total} \leq 1°$ vs. $R_{total} > 2°$	
	HR/OR (95% CI)	*P*	HR/OR (95% CI)	*P*
one-year LC rates	1.82(0.35~9.40)	0.48	2.04(0.40~10.52)	0.39
ILF	1.25(0.24~6.52)	0.79	1.01(0.19~5.31)	0.99
iPFS	2.10(0.84~5.27)	0.12	1.93(0.77~4.84)	0.16
OS	1.65(0.51~5.36)	0.41	1.44(0.44~4.72)	0.55

The effects of rotational errors on iPFS and OS were evaluated using Cox proportional hazards regression models, while effects on intracranial local failure rate and 1-year local control rate were analyzed using logistic regression. R_{total} denotes the overall rotational error per treatment calculated using Equations 5~8. LC, local control. ILF, intracranial local failure. iPFS, intracranial progression-free survival. OS: overall survival. HR, hazard ratio. OR, odds ratio; 95%; CI, 95% confidence interval.

although overall setup errors in our study were within an acceptable range, a trend toward increased errors was observed in patients with larger lesions. Clinically, this highlights the necessity of more stringent monitoring and correction of setup errors for such patients, to ensure precise radiation dose delivery.

For FSRT based on SIMT and non-coplanar VMAT frame-free fixation techniques, some studies strongly recommend that radiation therapy centers define dedicated margins around metastatic lesions to minimize the negative impact of setup errors (38). Many studies, based on different considerations, have proposed various formulas for calculating PTV margin expansion (12, 14–18). Among these, the formula proposed by Van Herk is widely used for calculating PTV margin expansion based on translational errors (12). This formula aims to ensure that at least 90% of patients receive 95% of the prescribed dose coverage and has become a standard practice in clinical settings. In this study, the random error σ for the translational directions of 161 patients across 733 treatments ranged from 0.54~0.64 mm, with system errors Σ ranging from 0.42~0.53 mm (Table 3). Using the Van Herk formula, the PTV margin expansions for the posterior-anterior, superior-inferior, and right-left directions were 1.44 mm, 1.68 mm, and 1.78 mm, respectively, which aligns with results from previous studies (7, 39, 40). However, because the Van Herk formula does not fully account for rotational errors, it may underestimate the actual required PTV margin expansion in the application of SIMT technology (12). To overcome the limitations of the Van Herk formula, Jenghwa Chang proposed a statistical model-based method that integrates both translational and rotational errors to derive a PTV margin expansion formula that ensures the probability of the GTV being within the PTV region exceeds the predefined coverage probability (15, 16, 19). This formula provides a more accurate and universally applicable calculation for the expansion margin by considering factors such as the distance from the target volume to the isocenter, the confidence corresponding to the probability of GTV being covered by the PTV, and the six-dimensional setup errors, thereby improving upon the Van Herk formula (15, 16, 19). In this study, when $\bar{d}$ lies within its 95% CI (28.91~32.34 mm), the PTV margin expansion determined by Jenghwa Chang formula ranges from 1.69~1.79 mm. It is noteworthy that when $\bar{d}$ is taken as the average distance between all targets and the treatment isocenter for all patients (i.e., the D value, see Equation 3), according to the results in Table 3, with $\sigma_{T_{total}} = 0.44$ mm and a required GTV coverage probability of 95%, the initial translational margin M_{trans} without considering rotation errors is 1.23 mm (i.e., $M_{trans} = \sqrt{(\chi_\alpha \times \sigma_{T_{total}})^2} = \sqrt{(2.795 \times 0.44)^2} = 1.23\,mm$). If rotation errors are not considered, the GTV coverage probability drops to 73% when the rotational uncertainty $\sigma_{r_{total}}$ is 0.44 mm (i.e., $\sigma_{r_{total}} = 0.01424 \times D \times \sigma_{R_{total}} = 0.44\,mm$), as $\chi_\alpha = \frac{M_{trans}}{\sqrt{(\sigma^2_{T_{total}} + \sigma^2_{r_{total}})}} = \frac{1.23}{\sqrt{(0.44^2 + 0.44^2)}} = 1.977$, which corresponds to approximately 73% GTV coverage probability according to Jenghwa Chang's study (15). When considering the rotational error ($\sigma_{r_{total}} = 0.44\,mm$), an additional 0.51 mm error compensation (i.e., $\Delta M = \chi_\alpha \sqrt{\sigma^2_{T_{total}} + \sigma^2_{r_{total}}}) - M_{trans} = 2.795 \sqrt{(0.44^2 + 0.44^2)} - 1.23 = 0.51\,mm$) can prevent a reduction in the GTV coverage probability. The study revealed that when rotational errors are considered, the combined margin expansions, the combined margin $M_{trans+rot}$ ranging from 1.69 mm to 1.79 mm encompass most of the recommended values derived from the Van Herk formula, particularly aligning closely with its maximum recommended value of 1.78 mm in the right-left direction (Table 3). From a clinical standpoint, adopting a single, unified margin expansion is more practical and can improve consistency in both treatment planning and quality assurance. Therefore, taking both translational and rotational errors into account, this study proposes using the 95% CI's upper bound derived from the Jenghwa Chang formula (1.79 mm) as the minimum safety reference for PTV margins in FSRT for multiple brain metastases at our center, thereby accommodating most patient setup errors and ensuring sufficient tumor dose coverage. It is noteworthy that the recommended PTV margin of 1.79 mm in our study contrasts significantly with the larger margins commonly used in WBRT, typically around 5 mm (41, 42). WBRT employs larger margins to ensure coverage of all potential metastatic sites, inevitably increasing radiation exposure to normal brain tissue and potentially causing long-term cognitive impairments (43). In contrast, our proposed FSRT margins substantially reduce the radiation dose to healthy brain tissue, simultaneously enhancing local control through precise dose delivery. This clearly underscores the clinical value and unique advantages of SIMT-based FSRT in treating multiple brain metastases.

Jenghwa Chang's study points out that: 1. When the distance from the isocenter is small, the required compensatory margin for rotation errors increases slowly as the rotation error grows; however, when the isocenter distance significantly increases, the

impact of rotation errors on dose deviation shows an "amplification effect," leading to a steeper increase in the required margin expansion (19). 2. When the margin required to compensate for translational errors (M_{trans}) is small, the impact of rotation errors and isocenter distance on the combined margin expansion ($M_{trans+rot}$) becomes more significant (14). Taken together, these findings indicate the necessity and complexity of integrating both rotation uncertainty and isocenter distance into the determination of appropriate PTV margins for multiple brain metastases. Several other studies have also explored this nonlinear relationship between isocenter distance and rotation errors leading to off-target effects. For instance, Calmels et al. demonstrated that for very small targets (PTV margin: 2 mm, volume < 1 cm^3), a rotational error of 1° at distances beyond 3 cm from the isocenter caused up to a 2.0% median decrease in GTV $D_{95\%}$ (21). Prentou et al. further proposed that, with a 1° rotational error, the distance from target to isocenter should be strictly limited to within 4 cm to prevent clinically relevant deterioration (>5%) in coverage, CI, and $D_{95\%}$ (22). Tsui et al. recommended restricting the isocenter distance to within 3.6~3.7 cm for rotational errors up to ±2° to maintain stable dose distribution (23). Additionally, Nakano et al. developed a geometric coverage loss model indicating that to limit geometric coverage loss due to rotational errors within 5%, lesions located beyond 7.6 cm from the isocenter should not be treated using SIMT techniques (24). They also emphasized an interaction effect between lesion size and isocenter distance, recommending a maximum isocenter-to-PTV distance of 5.5 cm for 1.5-mm lesions with a rotation error of 0.5°, and an even stricter limitation (3 cm) for lesions smaller than 2 cm^3. Our study's median lesion volume was 2.98 cm^3, with rotation errors within ±3.0° and a mean distance from the lesion center to the isocenter of 30.62 mm, closely aligning with the recommended 3~4 cm threshold from the aforementioned studies (21–23). Collectively, these findings indicate that our study's current isocenter distance effectively balances geometric precision and dose coverage requirements. Furthermore, caution should be exercised for lesions closely spaced (e.g., edge-to-edge distance <3 cm), as this might lead to overlapping dose hotspots (44). Given these considerations, we conducted subgroup analyses using 30 mm as a distance threshold. The results showed a consistent trend toward inferior clinical outcomes in tumor control for the subgroup with a distance greater than 30 mm ($\bar{d}$ >30 mm) (see Table 4). Although the statistical significance between isocenter distance and clinical prognosis was not achieved, the observed dose-outcome trends corresponded well with the dose degradation patterns described by Calmels and Nakano et al. (21, 24). These observations suggest that with SIMT, when rotational errors are below 3°, isocenter distances greater than 3 cm may enter a region of dose coverage degradation, thereby necessitating stricter error management beyond this range. Furthermore, we explored the relationship between rotational errors and clinical outcomes but did not find statistically significant results (Table 5). Possible explanations include: (1) Substantial patient heterogeneity possibly masking the potential impact of rotational errors and isocenter distance on prognosis, considering the multifactorial nature of outcomes in brain metastases influenced by lesion volume, prescribed dose, KPS scores, systemic therapies, and primary tumor histology (45, 46). (2) Our standardized use of 1~2 mm PTV margins was adequate for the majority of patients, as theoretical calculations based on the Jenghwa Chang formula indicated that only 15.53% of patients required margins greater than 2 mm. This likely provided sufficient dose coverage for most patients under current margin strategies, diminishing the potential prognostic influence of geometric errors.

To comprehensively evaluate potential factors influencing the PTV margin, we further explored associations between lesion number, maximum lesion diameter, cumulative lesion volume, and the number of treatment fractions with PTV margins. The analysis revealed a weak positive correlation between treatment fractions and PTV margins and a weak negative correlation between lesion number and PTV margins (Table 2). However, subsequent multivariate regression analysis did not confirm independent effects of these factors, suggesting that the determination of PTV margins might be influenced by a combination of multiple factors. As previously mentioned, the impact of isocenter distance and setup errors may have greater significance. Additionally, although several studies have demonstrated the influence of target size on margin expansion (5, 21, 23), our study did not find a statistically significant correlation between lesion size and $M'_{trans+rot}$ ($P = 0.91$). We speculate that using the average isocenter distance across all targets for individualized PTV margin calculation might have masked individual variations in lesion size, thus weakening the statistical correlation between the two variables. To further investigate the clinical applicability of the Jenghwa Chang formula, we divided patients based on the individualized $M'_{trans+rot}$ value, using a cutoff of 2 mm. Although the differences between the two groups did not reach statistical significance, the group with $M'_{trans+rot}$ > 2 mm demonstrated a higher ILF rate (32.0% vs. 22.8%), lower 1-year cumulative iPFS rate (44.00% vs. 51.45%), and slightly lower 1-year LC rate (64.00% vs. 65.44%). Clinically, most radiation oncology centers typically adopt PTV margins ranging from 0~2 mm (13). A survey from the Japanese Radiation Oncology Study Group also indicated 2 mm as the most commonly used margin (47). However, our study identified 25 patients whose theoretical margins exceeded 2 mm when rotational errors were considered, yet the clinical margins remained at 1~2 mm, potentially indicating a risk of suboptimal long-term local control. Previous research suggests that excessively large margins can increase the risk of radiation necrosis (36, 48), while insufficient margins may inadequately compensate for rotational errors, compromising local dose coverage. Given the observed adverse trends in ILF rates, 1-year LC, and cumulative iPFS for the $M'_{trans+rot}$ > 2 mm group, We hypothesize that for patients with significant rotational errors, continuing to use an expansion margin within 2 mm may leave a risk of target miss, potentially leading to a decline in local control rates during follow-up. Based on this, this study suggests that for some patients with high rotational errors or excessively large distances from the isocenter, the expansion margin

should be slightly increased to ensure the stability of local tumor control while balancing the risk of radiation necrosis.

This study, being a retrospective analysis, still has some limitations. Firstly, the study primarily relies on residual error data corrected by KV-CBCT and does not comprehensively quantify the dynamic movement of patients within fractions, which may lead to an underestimation of the true error. Previous studies that conducted CBCT scans before and after treatment have shown that the average intra-fraction motion in the translational direction ranges from 0.07 mm to 0.1 mm, and in the rotational direction, the average intra-fraction motion is between 0.027 ° and 0.109 °. This suggests that future research at our center could consider real-time imaging monitoring or multiple CBCT scans to obtain a more comprehensive error evaluation (31). Secondly, the Jenghwa Chang formula assumes that the target volume is nearly spherical and applies uniform margin expansions in all directions. However, in clinical practice, the shapes of multiple lesions and the distances from the target volumes to the isocenter vary, which may lead to differences in the sensitivity of different target volumes to rotational errors. Although some studies have explored non-uniform margin strategies based on different target shapes and distances, the challenge remains to implement personalized margin expansions within the treatment planning system (14, 18). Finally, the results of this study, which incorporate rotational error into margin analysis, are based on theoretical models and single-center data, lacking validation through multi-center or prospective trials. Therefore, the generalizability and applicability of the conclusions drawn from this study need to be further verified with a larger sample size and longer follow-up periods.

5 Conclusion

Through retrospective analysis of SIMT-based non-coplanar VMAT for patients with multiple brain metastases, this study demonstrated acceptable geometric accuracy with residual translational setup errors ranging from –0.04~0.01 mm and rotational errors between 0.15°~0.49°. This indicates that the technique ensured high precision and dose consistency within our center. According to the Van Herk formula, required margins for posterior-anterior, superior-inferior, and right-left directions were 1.44 mm, 1.68 mm, and 1.78 mm, respectively. However, when accounting for rotational errors using the Jenghwa Chang formula, the comprehensive margins based on the 95% CI for isocenter distances ranged between 1.69~1.79 mm. Using the average distance of all lesions to their respective isocenters (30.62 mm), the Jenghwa Chang formula calculated a translational-only margin of 1.23 mm, with rotational uncertainty $\sigma_{r_{total}}$ at 0.44 mm. Ignoring rotational errors decreased the target coverage probability from 95% to 73%. Further subgroup analysis indicated that while differences in ILF rates, 1-year LC, and cumulative iPFS between patients with $M'_{trans+rot}$ > 2 mm and ≤ 2 mm were not statistically significant, the former demonstrated unfavorable trends (higher ILF, lower LC and iPFS). This suggests that the current margin range (1~2 mm) may be inadequate to maintain long-term local control in patients with significant rotational errors. Moreover, subgrouping by average isocenter distance (30 mm threshold) indicated that patients with lesions situated over 3 cm from the isocenter might be at increased risk of compromised dose coverage when rotational errors were within ±3.0°, potentially affecting tumor control. In summary, this study recommends a minimum safe margin of 1.79 mm for SIMT-based non-coplanar VMAT FSRT in treating multiple brain metastases, ensuring sufficient coverage in most clinical scenarios and providing a basis for future treatment optimization.

Data availability statement

The raw data supporting the conclusions of this article will be made available by the authors, without undue reservation.

Ethics statement

The studies involving humans were approved by the Ethics Committee of Jiangsu Cancer Hospital. The studies were conducted in accordance with the local legislation and institutional requirements. The participants provided their written informed consent to participate in this study.

Author contributions

YL: Conceptualization, Data curation, Investigation, Software, Validation, Writing – original draft. RH: Conceptualization, Formal analysis, Investigation, Software, Supervision, Writing – original draft. LD: Conceptualization, Formal analysis, Methodology, Resources, Software, Writing – original draft. WC: Conceptualization, Data curation, Formal analysis, Resources, Software, Writing – original draft. JZ: Resources, Software, Supervision, Validation, Visualization, Writing – original draft, Writing – review & editing. QW: Funding acquisition, Investigation, Methodology, Project administration, Resources, Writing – review & editing. YX: Data curation, Formal analysis, Funding acquisition, Investigation, Methodology, Project administration, Writing – original draft, Writing – review & editing. TW: Conceptualization, Data curation, Funding acquisition, Project administration, Supervision, Visualization, Writing – original draft, Writing – review & editing.

Funding

The author(s) declare that financial support was received for the research and/or publication of this article. This work was supported

by the National Natural Science Foundation of China (grant numbers: 8200102414).

Acknowledgments

We also appreciate the technical support from the Jiangsu Institute of Cancer Research.

Conflict of interest

The authors declare that the research was conducted in the absence of any commercial or financial relationships that could be construed as a potential conflict of interest.

Generative AI statement

The author(s) declare that no Generative AI was used in the creation of this manuscript.

Publisher's note

All claims expressed in this article are solely those of the authors and do not necessarily represent those of their affiliated organizations, or those of the publisher, the editors and the reviewers. Any product that may be evaluated in this article, or claim that may be made by its manufacturer, is not guaranteed or endorsed by the publisher.

References

1. Suh JH, Kotecha R, Chao ST, Ahluwalia MS, Sahgal A, Chang EL. Current approaches to the management of brain metastases. *Nat Rev Clin Oncol*. (2020) 17:279–99. doi: 10.1038/s41571-019-0320-3

2. Starkweather CK, Choi BD, Alvarez-Breckenridge C, Brastianos PK, Oh K, Wang N, et al. Initial approach to the patient with multiple newly diagnosed brain metastases. *Neurosurgery Clinics North America*. (2020) 31:505–13. doi: 10.1016/j.nec.2020.05.002

3. Minniti G, Scaringi C, Paolini S, Lanzetta G, Romano A, Cicone F, et al. Single-fraction versus multifraction (3 × 9 gy) stereotactic radiosurgery for large (>2 cm) brain metastases: A comparative analysis of local control and risk of radiation-induced brain necrosis. *Int J Radiat OncologyBiologyPhysics*. (2016) 95:1142–8. doi: 10.1016/j.ijrobp.2016.03.013

4. Thomsen BJ, Soliman H. The modern management of untreated large (>2 cm) brain metastases: a narrative review. *Chin Clin Oncol*. (2022) 11:16–6. doi: 10.21037/cco-21-136

5. Roper J, Chanyavanich V, Betzel G, Switchenko J, Dhabaan A. Single-isocenter multiple-target stereotactic radiosurgery: risk of compromised coverage. *Int J Radiat OncologyBiologyPhysics*. (2015) 93:540–6. doi: 10.1016/j.ijrobp.2015.07.2262

6. Xu H, Brown S, Chetty IJ, Wen N. A systematic analysis of errors in target localization and treatment delivery for stereotactic radiosurgery using 2D/3D image registration. *Technol Cancer Res Treat*. (2017) 16:321–31. doi: 10.1177/1533034616664425

7. Infusino E, Trodella L, Ramella S, D'Angelillo RM, Greco C, Iurato A, et al. Estimation of patient setup uncertainty using BrainLAB Exatrac X-Ray 6D system in image-guided radiotherapy. *J Appl Clin Med Physics*. (2015) 16:99–107. doi: 10.1120/jacmp.v16i2.5102

8. Gevaert T, Verellen D, Tournel K, Linthout N, Bral S, Engels B, et al. Setup accuracy of the novalis exacTrac 6DOF system for frameless radiosurgery. *Int J Radiat OncologyBiologyPhysics*. (2012) 82:1627–35. doi: 10.1016/j.ijrobp.2011.01.052

9. Ramakrishna N, Rosca F, Friesen S, Tezcanli E, Zygmanszki P, Hacker F. A clinical comparison of patient setup and intra-fraction motion using frame-based radiosurgery versus a frameless image-guided radiosurgery system for intracranial lesions. *Radiotherapy Oncology*. (2010) 95:109–15. doi: 10.1016/j.radonc.2009.12.030

10. Ruggieri R, Naccarato S, Mazzola R, Ricchetti F, Corradini S, Fiorentino A, et al. Linac-based VMAT radiosurgery for multiple brain lesions: comparison between a conventional multi-isocenter approach and a new dedicated mono-isocenter technique. *Radiat Oncol (London England)*. (2018) 13:38. doi: 10.1186/s13014-018-0985-2

11. Clark GM, Popple RA, Young PE, Fiveash JB. Feasibility of single-isocenter volumetric modulated arc radiosurgery for treatment of multiple brain metastases. *Int J Radiat OncologyBiologyPhysics*. (2010) 76:296–302. doi: 10.1016/j.ijrobp.2009.05.029

12. Van Herk M, Remeijer P, Rasch C, Lebesque JV. The probability of correct target dosage: dose-population histograms for deriving treatment margins in radiotherapy. *Int J Radiat OncologyBiologyPhysics*. (2000) 47:1121–35. doi: 10.1016/S0360-3016(00)00518-6

13. Grimm J, ML B, Jackson A. High dose per fraction, hypofractionated treatment effects in the clinic (HyTEC): an overview. *J Int J Radiat Oncol Biol Phys*. (2021) 110:1–10. doi: 10.1016/j.ijrobp.2020.10.039

14. Miao J, Xu Y, Tian Y, Liu Z, Dai J. A study of nonuniform CTV to PTV margin expansion incorporating both rotational and translational uncertainties. *J Appl Clin Med Phys*. (2019) 20:78–86. doi: 10.1002/acm2.12763

15. Chang J. A statistical model for analyzing the rotational error of single isocenter for multiple targets technique. *Med Phys*. (2017) 44:2115–23. doi: 10.1002/mp.12262

16. Chang J. Statistical analysis of the rotation error for single-isocenter technique. *Int J Radiat OncologyBiologyPhysics*. (2016) 96:E655. doi: 10.1016/j.ijrobp.2016.06.2269

17. Rojas-López JA, Venencia CD, Chesta MÁ, Tamarit F. Assessment of PTV margin adequacy for single isocenter multiple brain metastases using genetic algorithms. *Biomed Phys Eng Express*. (2023) 9:045028. doi: 10.1088/2057-1976/acdde5

18. Yock AD, Grees B, Luo G. Innovative margin design and optimized isocenter to minimize the normal tissue in target volumes for single-isocenter multi-target stereotactic radiosurgery. *Phys Med Biol*. (2023) 68:195025. doi: 10.1088/1361-6560/acf751

19. Chang J. Incorporating the rotational setup uncertainty into the planning target volume margin expansion for the single isocenter for multiple targets technique. *Pract Radiat Oncology*. (2018) 8:475–83. doi: 10.1016/j.prro.2018.04.011

20. Shaw E, Scott C, Souhami L, Dinapoli R, Kline R, Loeffler J, et al. Single dose radiosurgical treatment of recurrent previously irradiated primary brain tumors and brain metastases: final report of RTOG protocol 90-05. *Int J Radiat OncologyBiologyPhysics*. (2000) 47:291–8. doi: 10.1016/S0360-3016(99)00507-6

21. Calmels L, Blak Nyrup Biancardo S, Sibolt P, Nørring Bekke S, Bjelkengren U, Wilken E, et al. Single-isocenter stereotactic non-coplanar arc treatment of 200 patients with brain metastases: multileaf collimator size and setup uncertainties. *Strahlentherapie und Onkologie: Organ der Deutschen Rontgengesellschaft. [et al]*. (2022) 198:436–47. doi: 10.1007/s00066-021-01846-6

22. Prentou G, Pappas EP, Logothetis A, Koutsouveli E, Pantelis E, Papagiannis P, et al. Dosimetric impact of rotational errors on the quality of VMAT-SRS for multiple brain metastases: Comparison between single- and two-isocenter treatment planning techniques. *J Appl Clin Med Phys*. (2020) 21:32–44. doi: 10.1002/acm2.12815

23. Tsui SSW, Wu VWC, Cheung JSC. Comparison of dosimetric impact of intra-fractional setup discrepancy between multiple- and single-isocenter approaches in linac-based stereotactic radiotherapy of multiple brain metastases. *J Appl Clin Med Phys*. (2022) 23:e13484. doi: 10.1002/acm2.13484

24. Nakano H, Tanabe S, Yamada T, Utsunomiya S, Takizawa T, Sakai M, et al. Maximum distance in single-isocenter technique of stereotactic radiosurgery with rotational error using margin-based analysis. *Radiological Phys technology*. (2021) 14:57–63. doi: 10.1007/s12194-020-00602-2

25. Schwartz LH, Litière S, De Vries E, Ford R, Gwyther S, Mandrekar S, et al. RECIST 1.1—Update and clarification: From the RECIST committee. *Eur J Cancer*. (2016) 62:132–7. doi: 10.1016/j.ejca.2016.03.081

26. Eder MM, Reiner M, Heinz C, Garny S, Freislederer P, Landry G, et al. Single-isocenter stereotactic radiosurgery for multiple brain metastases: Impact of patient misalignments on target coverage in non-coplanar treatments. *Z fur medizinische Physik*. (2022) 32:296–311. doi: 10.1016/j.zemedi.2022.02.005

27. Sagawa T, Ohira S, Ueda Y, Akino Y, Mizuno H, Matsumoto M, et al. Dosimetric effect of rotational setup errors in stereotactic radiosurgery with HyperArc for single and multiple brain metastases. *J Appl Clin Med physics*. (2019) 20:84–91. doi: 10.1002/acm2.12716

28. Klein EE, Hanley J, Bayouth J, Yin F, Simon W, Dresser S, et al. Task Group 142 report: Quality assurance of medical acceleratorsa). *Med Phys*. (2009) 36:4197–212. doi: 10.1118/1.3190392

29. Carminucci A, Nie K, Weiner J, Hargreaves E, Danish SF. Assessment of motion error for frame-based and noninvasive mask-based fixation using the Leksell Gamma Knife Icon radiosurgery system. *J Neurosurgery*. (2018) 129:133–9. doi: 10.3171/2018.7.GKS181516

30. Park JW, Yea JW, Park J, Oh SA. Setup uncertainties and appropriate setup margins in the head-tilted supine position of whole-brain radiotherapy (WBRT). *PloS One*. (2022) 17:e0271077. doi: 10.1371/journal.pone.0271077

31. Liu RJ, Yang SX, Neylon J, Hall MD, Dandapani S, Vora N, et al. Residual setup errors in cranial stereotactic radiosurgery without six degree of freedom robotic couch: Frameless versus rigid immobilization systems. *J Appl Clin Med physics*. (2020) 21:87–93. doi: 10.1002/acm2.12828

32. Keeling V, Hossain S, Jin H, Algan O, Ahmad S, Ali I. Quantitative evaluation of patient setup uncertainty of stereotactic radiotherapy with the frameless 6D ExacTrac system using statistical modeling. *J Appl Clin Med physics*. (2016) 17:111–27. doi: 10.1120/jacmp.v17i3.5959

33. Lee SK, Huang S, Zhang L, Ballangrud AM, Aristophanous M, Cervino Arriba LI, et al. Accuracy of surface-guided patient setup for conventional radiotherapy of brain and nasopharynx cancer. *J Appl Clin Med physics*. (2021) 22:48–57. doi: 10.1002/acm2.13241

34. Tarnavski N, Engelholm SA, Af Rosenschold PM. Fast intra-fractional image-guidance with 6D positioning correction reduces delivery uncertainty for stereotactic radiosurgery and radiotherapy. *J Radiosurg SBRT*. (2016) 4:15–20.

35. Schmidhalter D, Malthaner M, Born EJ, Pica A, Schmuecking M, Aebersold DM, et al. Assessment of patient setup errors in IGRT in combination with a six degrees of freedom couch. *Z für Medizinische Physik*. (2014) 24:112–22. doi: 10.1016/j.zemedi.2013.11.002

36. Faccenda V, Panizza D, Pisoni V, Trivellato S, Daniotti MC, Bianchi SP, et al. Single-isocenter linac-based radiosurgery for brain metastases with coplanar arcs: A dosimetric and clinical analysis. *Cancers*. (2023) 15:4496. doi: 10.3390/cancers15184496

37. Ohtakara K, Hoshi H. Target volume geometric change and/or deviation from the cranium during fractionated stereotactic radiotherapy for brain metastases: potential pitfalls in image guidance based on bony anatomy alignment. *J Med Imaging Radiat oncology*. (2014) 58:729–36. doi: 10.1111/1754-9485.12194

38. Hanna SA, Mancini A, Dal Col AH, Asso RN, Neves-Junior WFP. Frameless image-guided radiosurgery for multiple brain metastasis using VMAT: A review and an institutional experience. *Front Oncol*. (2019) 9:703. doi: 10.3389/fonc.2019.00703

39. Tanaka Y, Oita M, Inomata S, Fuse T, Akino Y, Shimomura K. Impact of patient positioning uncertainty in noncoplanar intracranial stereotactic radiotherapy. *J Appl Clin Med physics*. (2020) 21:89–97. doi: 10.1002/acm2.12820

40. Oh SA, Yea JW, Kang MK, Park JW, Kim SK. Analysis of the setup uncertainty and margin of the daily exacTrac 6D image guide system for patients with brain tumors. *PloS One*. (2016) 11:e0151709. doi: 10.1371/journal.pone.0151709

41. Miura K, Kurosaki H, Utsumi N, Sakurai H. Use of a head-tilting baseplate during tomotherapy to shorten the irradiation time and protect the hippocampus and lens in hippocampal sparing-whole brain radiotherapy. *Technol Cancer Res Treat*. (2021) 20:1533033820986824. doi: 10.1177/1533033820986824

42. Shimizu H, Sasaki K, Aoyama T, Tachibana H, Tanaka H, Koide Y, et al. Examination of the best head tilt angle to reduce the parotid gland dose maintaining a safe level of lens dose in whole-brain radiotherapy using the four-field box technique. *J Appl Clin Med Phys*. (2021) 22:49–57. doi: 10.1002/acm2.13151

43. Gondi V, Bauman G, Bradfield L, Burri SH, Cabrera AR, Cunningham DA, et al. Radiation therapy for brain metastases: an ASTRO clinical practice guideline. *Pract Radiat Oncology*. (2022) 12:265–82. doi: 10.1016/j.prro.2022.02.003

44. Yu X, Wang Y, Yuan Z, Yu H, Song Y, Zhao L, et al. Benefit of dosimetry distribution for patients with multiple brain metastases from non-small cell lung cancer by a Cyberknife stereotactic radiosurgery (SRS) system. *BMC Cancer*. (2020) 20:1144. doi: 10.1186/s12885-020-07624-4

45. Ribeiro LM, Bomtempo FF, Rocha RB, Telles JPM, Neto EB, Figueiredo EG. Development and adaptations of the Graded Prognostic Assessment (GPA) scale: a systematic review. *Clin Exp Metastasis*. (2023) 40:445–63. doi: 10.1007/s10585-023-10237-3

46. Berger A, Mullen R, Bernstein K, Alzate JD, Silverman JS, Sulman EP, et al. Extended survival in patients with non–small-cell lung cancer–associated brain metastases in the modern era. *Neurosurgery*. (2023) 93:50–9. doi: 10.1227/neu.0000000000002372

47. Gevaert T, Steenbeke F, Pellegri L, Engels B, Christian N, Hoornaert MT, et al. Evaluation of a dedicated brain metastases treatment planning optimization for radiosurgery: a new treatment paradigm? *Radiat Oncol*. (2016) 11:13. doi: 10.1186/s13014-016-0593-y

48. Barnes MP, Greer PB. Evaluation of the TrueBeam machine performance check (MPC) beam constancy checks for flattened and flattening filter-free (FFF) photon beams. *J Appl Clin Med Phys*. (2017) 18:139–50. doi: 10.1002/acm2.12016

frontiers | Frontiers in Oncology

TYPE Original Research
PUBLISHED 30 April 2025
DOI 10.3389/fonc.2025.1582402

Check for updates

OPEN ACCESS

EDITED BY
Poonam Yadav,
Northwestern University, United States

REVIEWED BY
Edwin Quashie,
Indiana University, United States
Xin Tong,
University of Kansas Medical Center,
United States

*CORRESPONDENCE
Pan Ma
mpsophia@163.com
Ningning Lu
ningninglu09@163.com

RECEIVED 24 February 2025
ACCEPTED 09 April 2025
PUBLISHED 30 April 2025

CITATION
Ma P, Xu Y, Yao Y, Lu N and Dai J (2025) Optimization method for determining vertices in lattice radiotherapy.
Front. Oncol. 15:1582402.
doi: 10.3389/fonc.2025.1582402

COPYRIGHT
© 2025 Ma, Xu, Yao, Lu and Dai. This is an open-access article distributed under the terms of the Creative Commons Attribution License (CC BY). The use, distribution or reproduction in other forums is permitted, provided the original author(s) and the copyright owner(s) are credited and that the original publication in this journal is cited, in accordance with accepted academic practice. No use, distribution or reproduction is permitted which does not comply with these terms.

Optimization method for determining vertices in lattice radiotherapy

Pan Ma*, Yingjie Xu, Yuhe Yao, Ningning Lu* and Jianrong Dai

Department of Radiation Oncology, National Cancer Center/National Clinical Research Center for Cancer/Cancer Hospital, Chinese Academy of Medical Sciences and Peking Union Medical College, Beijing, China

Purpose: This study presents an optimization method for arranging lattice radiotherapy (LRT) targets to enhance the contrast between peak and valley doses, aiming to improve the treatment effectiveness and precision.

Materials and methods: The LRT target comprises multiple sphere-like vertices generated using the optimization method, which involves four steps: 1) generating a volume for vertex arrangement, 2) determining initial positions and size of packing units, 3) determining initial positions and size of all the vertices and 4) optimizing the final vertex positions by using adaptive simulated annealing (ASA). Volumetric modulated arc therapy plans were retrospectively regenerated using the initial vertices produced by closest packing (Plan_Clo) and vertices obtained after ASA optimization (Plan_Opt). The peak-to-valley index (PVI) that characterizes the difference between peak and valley doses was introduced to evaluate the performance.

Results: A statistically significant difference was observed in the average PVI between Plan_Clo and Plan_Opt ($p = 0.000$). The average PVI ratio for Plan_Opt compared to Plan_Clo was 5.95 ± 4.87 (range: 1.24–16.80).

Conclusion: The proposed optimization method for determining LRT target vertices has been validated, demonstrating a significant improvement in the PVI. ASA optimization, combined with closest packing, effectively enhanced the peak-to-valley dose difference in LRT, showcasing its potential for advancing treatment planning.

KEYWORDS

optimization, adaptive simulated annealing, closest packing, lattice, peak-to-valley index

1 Introduction

Spatially fractionated radiotherapy (SFRT) involves delivering highly nonuniform tumor dose distributions, substantially differing from regular radiotherapy that seeks the highest possible dose homogeneity (1–3). SFRT was first demonstrated in 1909 by Alban Köhler, a pioneering German radiologist who developed grid radiotherapy (4). Over more than a century of development, four main types of SFRT techniques have emerged: grid (5–7), lattice (2, 8–10), microbeam (11) and minibeam (12). The grid and lattice techniques are clinically used, particularly for treating bulky tumors, showing significant and sometimes drastic palliative tumor responses with minimal toxicity (13–21). Grid radiotherapy using multi-leaf collimators is more widely available and offers improved dosimetry compared with radiotherapy using physical grid blocks. However, two-dimensional grid radiotherapy remains challenging, as normal tissues are exposed to high radiation doses, with the highest doses being delivered to superficial tissues outside the target volume.

Introduced as a modern 3D SFRT technique, lattice radiotherapy (LRT) offers flexibility to achieve the intended SFRT goals by generating desired nonuniform dose distributions using an inverse planning approach. LRT planning defines high dose vertices as inverse optimization targets consisting of sphere-like sub-volumes (i.e., vertices) with diameters of approximately 1 cm and separation between dose vertex centers of approximately 2–5 cm (2, 14, 22).

In LRT, no rigorous requirements are imposed for either the symmetry of placing high dose vertices or the uniformity of their size and shapes. Instead, the number of high dose vertices depends on the size and shape of the tumor volume as well as the resolution of beam apertures.

The prescription of an LRT plan requires specifying the peak, valley, and tumor peripheral (i.e., normal tissue) doses. The peak dose is prescribed to cover 95% of the high dose vertices, and the normal tissue dose specifies the maximum allowable dose around the tumor margin to control toxicity. While meeting the prescription requirements of the high dose vertex and normal tissue doses, planning is aimed at minimizing the valley dose and increasing the difference between the peak and valley doses.

Currently, oncologists arrange vertices manually using simple geometric tools, such as distance measurement, available in treatment planning systems (TPSs) (14, 22). This kind manual method is time-consuming, error-prone, inaccurate, and poorly reproducible. In addition, it hinders data traceability and auditing, and it fails to suitably handle complexity. During the placement of vertices, several key issues need to be addressed, such as determining the initial vertex positions inside the gross tumor volume (GTV), optimizing the angle for arranging a layer of vertices on the axial plane, and selecting the appropriate diameter and spacing of vertices.

Tucker et al. (23) employed a script to automatically generate SFRT spheres by rotating the vertices of the lattice grid about the craniocaudal axis in 10° increments up to 90° and then translating in 2–3 mm increments along 3 cm on the axial planes of a computed tomography (CT) scan, notably enhancing the positioning efficiency. Similarly, Zhang et al. (24, 25) optimized vertex positions considering the peak-to-valley dose and organ at risk sparing as optimization objectives.

The closest packing of equally sized spheres in three-dimensional space is achieved through face-centered cubic (FCC) or hexagonal close packing (HCP) arrangements, both occupying approximately 74% of the space (26). In these configurations, each sphere is surrounded by 12 neighboring spheres, resulting in a coordination number of 12. Duriseti et al. (14)applied this method to the target volume delineation in SFRT.

In this study, we adopted the closest packing method along with an optimization method to automatically determine vertices in LRT, aiming to increase the difference between the peak and valley doses.

2 Materials and methods

The considered LRT target comprises multiple sphere-like vertices generated using HCP closest packing and an optimization method. Closest packing involves three steps: 1) contracting the GTV inward to generate the volume for vertex arrangement, 2) determining the initial positions and size of packing units (PUs), and 3) determining initial positions and size of all the vertices. Next, the optimization method adds a step of 4) optimizing the final vertex positions.

2.1 Volume for vertex arrangement

To obtain radiotherapy data, medical imaging techniques such as CT, magnetic resonance imaging, ultrasound, and positron emission tomography/CT are commonly used to create images of normal tissues and tumors. By analyzing the relative positions of normal tissues and tumors, the volume for placing LRT vertices (VPV) can be generated. As SFRT delivers a high dose, the arrangement of high dose LRT vertices should remain sufficiently distant from normal tissues to ensure protection. The corresponding distance is related to the GTV, and the boundary is determined by contracting the GTV inward by margin m_{inward} derived from fitting data in Ref. (2) as follows (Equation 1):

$$m_{inward} = \begin{cases} 1, & V < 200, \\ 0.00125V + 0.75, & 200 \le V < 1000, \\ 2, & V \ge 1000, \end{cases} \quad (1)$$

where V is the GTV in cubic centimeters.

2.2 Initial position and size of vertices

2.2.1 Closest packing

We adopt HCP packing to arrange the sphere-like vertices for LRT planning. The sphere arrangement can be visualized as a stack

of close-packed layers, with each layer containing spheres arranged in a hexagonal pattern. The layers are arranged such that the spheres in one layer fit perfectly into the spaces between the spheres in the surrounding layers, resulting in a very efficient packing. The layers in HCP stacking are arranged as ABAB…, where A layers contain spheres at the corners and B layers contain vertices at the face centers. Then, the sequence of A and B layers repeats.

The three-layer spheres, i.e., the PUs, are arranged using HCP packing as illustrated in Figure 1a. The sphere contours through the plane of the center of the outermost layer are shown in Figure 1b, with the middle circle being tangent to the surrounding six circles and indicating closest packing. In closest packing, each sphere is surrounded by up to 12 spheres.

2.2.2 Initial position and size of vertices

To determine the centers of all the PUs, closest packing involves two steps: 1) determining the center of the first PU and 2) stacking the remaining PUs around the first PU. For convenience, the first PU center is located at the geometric center, $(x_0,\ y_0,\ z_0)$, of the VPV. The PU diameter d in centimeters is calculated using Equation 2 and derived from fitting data in Ref. (2):

$$d = \begin{cases} 2, & V < 50, \\ 0.002V + 1.9, & 50 \le V < 1000, \\ 4, & V \ge 1000. \end{cases} \tag{2}$$

The number of rows, columns, and layers of the remaining PUs are related to the VPV, (x, y, z), and the center of the first sphere, $(x_0,\ y_0,\ z_0)$, as follows (Equations 3–8):

$$\begin{aligned} LineNum_1 &= \left\lceil \frac{|\max(x) - x_0|}{\frac{\sqrt{3}}{2}d} \right\rceil + 2, LineNum_2 \\ &= \left\lceil \frac{|\min(x) - x_0|}{\frac{\sqrt{3}}{2}d} \right\rceil + 2, \end{aligned} \tag{3}$$

$$\begin{aligned} RowNum_1 &= \left\lceil \frac{|\max(y) - y_0|}{d} \right\rceil + 2,\ RowNum_2 \\ &= \left\lceil \frac{|\min(y) - y_0|}{d} \right\rceil + 2, \end{aligned} \tag{4}$$

$$\begin{aligned} LayerNum_1 &= \left\lceil \frac{|\max(z) - z_0|}{\frac{\sqrt{3}}{2}d} \right\rceil + 2, LayerNum_2 \\ &= \left\lceil \frac{|\min(z) - z_0|}{\frac{\sqrt{3}}{2}d} \right\rceil + 2, \end{aligned} \tag{5}$$

where $Line\ Num_1$, $Line\ Num_2$, $Row\ Num_1$, $Row\ Num_2$, $Layer\ Num_1$, and $Layer\ Num_2$ are the number of columns, rows, and layers in the left, right, anterior, posterior, superior, and inferior directions, respectively, expressed a coordinate system with respect to the patient. The PUs have spatial repetition every two layers, and 2 is used to ensure a complete search space for subsequent optimization.

The coordinates of the center, $(x_i,\ y_i,\ z_i)$, of packed sphere i can be calculated as follows:

$$x_i = \begin{cases} x_0 + (i-1)d, & 1 \le i \le LineNum_1 \\ x_0 + (i+1)d, & -1 \le i \le -LineNum_2 \end{cases}, \tag{6}$$

$$y_i = \begin{cases} y_0 + (i-1)d, & 1 \le i \le RowNum_1 \\ y_0 + (i+1)d, & -1 \le i \le -RowNum_2 \end{cases}, \tag{7}$$

$$z_i = \begin{cases} z_0 + (i-1)d, & 1 \le i \le LayerNum_1 \\ z_0 + (i+1)d, & -1 \le i \le -LayerNum_2 \end{cases}. \tag{8}$$

LRT planning involves sphere-like vertices similar to the PUs. Hence, the sphere centers obtained by closest packing are the sphere-like vertex centers in the positions of the vertices, as shown in Figure 2.

The size of the vertices is determined by the size of the tumor, whose diameter is calculated based on data fitting in Ref. (2) as follows:

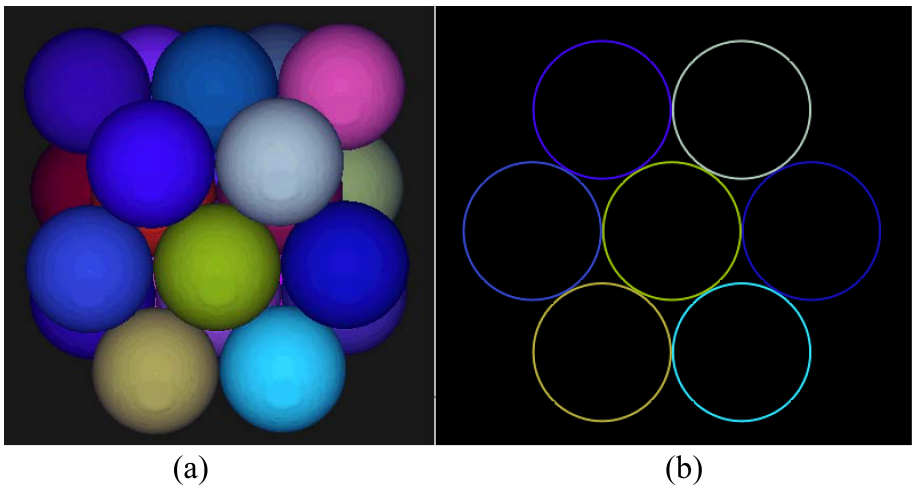

FIGURE 1
The three-layer spheres arranged using the HCP packing method **(a)** and the sphere contour drawn through the plane of the center of the outermost layer **(b)**.

$$d' = \begin{cases} 0.5, & V < 50, \\ 0.001V + 0.4258, & 50 \le V < 1000, \\ 1.5, & V \ge 1000, \end{cases} \quad (9)$$

where d' is the diameter of the sphere-like vertices in centimeters. The vertex layer is parallel or perpendicular to the transverse plane of the patient image. If the total volume of vertices calculated within the VPV using Equation 9 is less than V_0 (V_0 is 1% of the GTV in this study), d' can be incrementally adjusted, for example, by 1 mm, until the total vertex volume reaches V_0. This method determines the initial vertex diameter.

2.3 Final positions of vertices

2.3.1 Adaptive simulated annealing

For optimization, adaptive simulated annealing (ASA), a variant of conventional simulated annealing, is adopted owing to its three key advantages: 1) different parameters can employ distinct cooling schedules, enabling faster annealing compared with Boltzmann annealing; 2) a reannealing feature enables adaptive sensitivity changes in a multidimensional solution space; 3) over 100 options are available for tuning various classes of nonlinear stochastic systems (27). These advantages, along with a publicly available source code (http://www.ingber.com), make ASA applicable to numerous scientific fields, including radiotherapy.

We apply ASA to optimize the vertex positions for LRT planning. This method adjusts the initial positions of the vertices by translating and rotating the vertices while maintaining a constant total volume. The optimization objective is increasing the distance between vertices to maximize the difference between peak and valley doses.

The distance to be optimized is expressed as (Equation 10)

$$\max \ d(x', y', z', \alpha, \beta, \gamma), \quad (10)$$

where (x', y', z') represents the positions of the first PU and (α, β, γ) represent the angles of the closest packing layer.

The closest packing arrangement exhibits repeatability in its pattern, ensuring that the vertices can be rotated and translated within a certain range to achieve the optimal solution. The following constraints are considered (Equations 11–13):

$$(x_i, \ y_i, \ z_i) \in \text{VPV}, \quad (11)$$

$$-180° \le \alpha, \ \beta, \ \gamma \in \le 180°, \quad (12)$$

$$V = 0.01 V_{GTV}, \quad (13)$$

where (x_i, y_i, z_i) represents the coordinates of the points within vertex i, and V and V_{GTV} are the total volume of all the vertices and GTV, respectively.

2.3.2 Optimization procedure

ASA optimization comprises the following eight steps (Figure 3):

1. Input data of VPV, center position $(x_0, \ y_0, \ z_0)$, initial diameter d_0 of first PU, and diameter d' of vertices;
2. Set n to 1;
3. Calculate diameter of PU for step n as $d_n = d_0 + 0.1(n-1)$;
4. Apply HCP closest packing to generate initial positions of vertices and calculate initial volume V_0;
5. Using ASA, adjust the temperature parameters to control the probability distribution of random numbers within the domain defined by $\Delta x \in (-\sqrt{3}d_n, \sqrt{3}d_n)$, $\Delta y \in (-d_n, d_n)$, $\Delta z \in (-\sqrt{3}d_n, \sqrt{3}d_n)$, $\Delta\alpha \in (-\pi, \pi)$, $\Delta\beta \in (-\pi, \pi)$, and $\Delta\gamma \in (-\pi, \pi)$. Randomly generate displacement $(\Delta x, \Delta y, \Delta z, \Delta\alpha, \Delta\beta, \Delta\gamma)$ of vertex $(x_i, \ y_i, \ z_i)$;
6. Calculate optimal target volume V_n;
7. If V_n is greater than or equal to V_0, go to step 8. Otherwise, go to step 5;

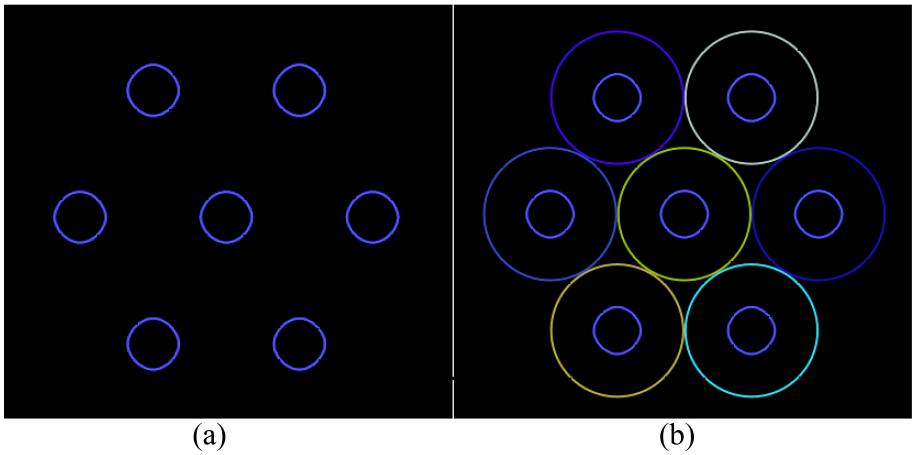

FIGURE 2
The initial arrangement of the vertices **(a)** generated by placing a vertex at the center of each PU **(b)**.

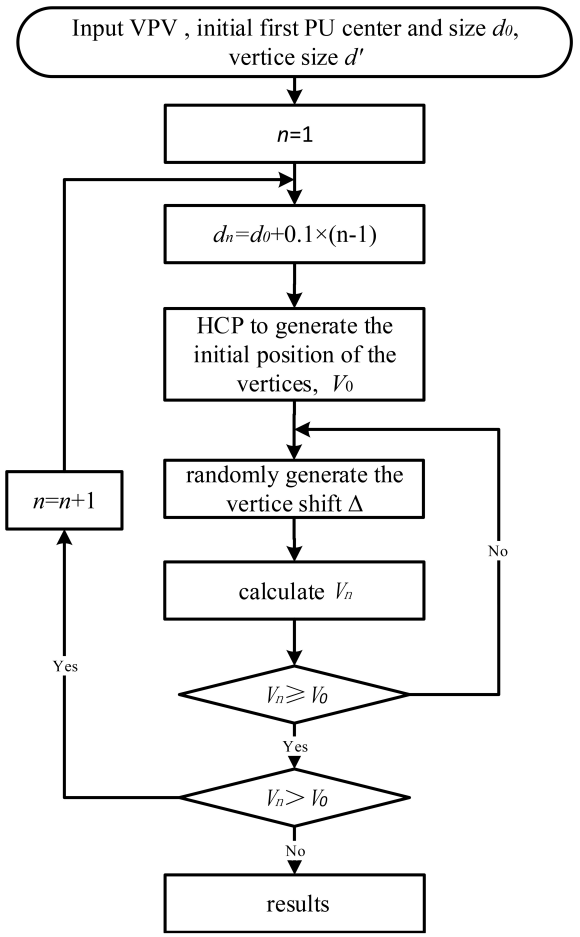

FIGURE 3
The flow chart of the adaptive simulated annealing optimization method.

8. If V_n is greater than V_0, set n to $n + 1$ and go to step 3. Otherwise, return the position of vertices (x_i, y_i, z_i) and terminate.

If a portion of a sphere-like vertex lies outside the VPV, the volume of that portion is subtracted, resulting in vertices that are not entirely spherical. Any volume less than 0.065 cm^3, which is equivalent to a sphere with a diameter less than 0.5 cm, is discarded to avoid generating excessively small subfields that cannot be implemented in practice.

2.4 LRT planning

In this study, we considered 17 patients for retrospective LRT replanning using the Pinnacle3 TPS (version 9.16; Philips Healthcare, Andover, MA, USA), which was commissioned according to the TG-119 recommendations. The GTV and critical structures were contoured and reviewed during a chart round by radiation oncologists. For each patient, volumetric modulated arc therapy plans were designed using the initial vertices obtained from closest packing (Plan_Clo) and the final vertices after ASA optimization (Plan_Opt).

The total volume of the vertices was 1% of the GTV, and d' was defined accordingly.

The flattening filter-free photon beam energy for all plans was set to 6 MV for delivery using a Varian Edge linear accelerator (Varian Medical Systems, Palo Alto, CA, USA) equipped with 80 pairs of leaves, with leaf widths of 2.5 mm within the central 10 cm range and 5 mm for the remaining leaves. The dose grid resolution was 0.2 × 0.2 × 0.2 cm. Volumetric modulated arc therapy plans were generated using from three to six coplanar partial arcs (28). The delivery time was not limited. The continuous gantry motion, dose-rate variation, and multileaf collimator motion were approximated by optimizing individual beams at 3°–4° gantry angle increments.

The same dose–volume constraints were applied to all the plans during inverse planning optimization. The final dose distributions were calculated using adaptive convolution. Planning was intended to deliver a prescribed dose of 15 Gy to at least 95% of the vertices in one fraction, and the dose uniformity requirement ranged from −5% to 30%. Rings 1, 2, and 3 at distances of 5, 10, and 15 mm from the vertices were respectively generated to enhance the dose gradient and minimize the penumbra region. Additional spheres between the vertices were created to reduce the dose in the valley region. Optimization for a specific patient aimed to minimize the dose to the normal tissue outside the GTV while maintaining the maximum peak dose and minimum valley dose.

2.5 Evaluation measure

The valley dose, not the peak dose, has been closely associated with increased survival when compared with controls (9, 29). Although white papers are currently being defined for both grid therapy and LRT, additional advanced measures of the dose heterogeneity are needed (2, 3, 30).

The contrast between peak and valley doses is a key in SFRT planning. However, existing definitions vary: ① D_{95}^{valley} (31) defines the dose covering 95% of the valley region, derived from the GTV minus the vertices with a non-uniform margin, which approximates the minimum dose of the valley region; ②$VPDR_{90/10}$ (32)uses the $D_{10\%}/D_{90\%}$ thresholds, but it trends to underestimate the true peak doses; ③$VPDR_{Median}$ (33) calculates the dose ratios between adjacent vertices' D1% peaks and their corresponding midpoint valleys, offering a more accurate representation of spatial configurations. The absence of standardized metrics impedes inter-study comparisons and clinical optimization of therapeutic ratios between tumor control and normal tissue sparing. The absence of standardized metrics hinders meaningful comparisons across studies.

As illustrated in the Figure 4, the maximum and minimum doses in the red and green profile curves are identical despite the varying dose gradients. Notably, the valley region is the distinctive feature between various SFRT techniques, with a larger volume

indicating a greater ability to widen the dose gap between peaks and valleys.

To precisely characterize the dose peaks and valleys, we conducted a quantitative evaluation of the dose distributions. Defining regions above 80% as peaks, those below 20% as valleys, and those between 80% and 20% as penumbra regions in the dose profile between the centers of adjacent spheres facilitated the evaluation. Large peak and valley areas along with small penumbra areas yielded more pronounced dose peaks and valleys (blue curve in extreme scenario of Figure 4). Accordingly, we defined the peak-to-valley index (PVI) as

$$PVI = \frac{S_{\text{peak}} S_{\text{valley}}}{S_{\text{penumbra}}}, \tag{14}$$

where S_{peak}, S_{valley}, and $S_{penumbra}$ are the areas of the peak, valley, and penumbra regions, respectively. A higher PVI indicates more pronounced dose peaks and valleys.

For evaluation, every vertex and its closest neighbors formed a pair of dose peak and valley, and the PVI was calculated. If a vertex had multiple neighbors, the average PVI was considered. Each plan contained multiple vertices, and the average PVI across all the vertices in the plan was computed to evaluate the plan PVI. Owing to the relative high valley doses in the LRT plans, the peak and valley dose thresholds were set to 80% and 50%, respectively. The PVI from Plan_Opt was compared with that from Plan_Clo to evaluate the optimization effectiveness.

The mean dose to the GTV and dose to 1 cm^3 of normal tissue (NT_{1cc}) were used to evaluate the differences in the internal and external doses of the GTV. Normal tissue was determined by subtracting the GTV from the patient contour outline on the GTV plane.

The Wilcoxon matched-pairs and signed-rank tests for nonparametrically distributed data were applied to compare Plan_Clo with Plan_Opt, respectively. Statistical significance was considered for $p < 0.05$ (two-tailed). All the statistical analyses were performed using SPSS Version 13.0 (SPSS, Chicago, IL, USA).

3 Results

3.1 Representative patient

Figure 5 shows the distribution of vertices in three-dimensional space (first row) and isodose distributions on the axial planes (next three rows) for a representative patient under Plan_Clo (left) and Plan_Opt (right). The red, blue, and magenta contours represent the GTV, VPV, and organ at risk (bladder), respectively, and the green shaded area represents the vertices.

The patient's GTV was 1407.00 cm^3, and the VPV was 320.15 cm^3. The vertex volumes were 15.11 and 15.29 cm^3, accounting for 1.07% and 1.09% of the GTV for 11 and 11 vertices in Plan_Clo and Plan_Opt, respectively. The vertex spacings were 36 and 41 mm for Plan_Clo and Plan_Opt, respectively. The two plans provided a vertex diameter of 15 mm.

After optimization, the PVI for Plan_Opt showed a 16-fold increase, achieving significant benefit. This result suggested that when the GTV had a more complex geometry, optimization was more effective for planning.

As shown in the three-dimensional images, the vertices for Plan_Opt were placed where the VPV shape changed considerably (e.g., vertices at the top of the images). Owing to the different vertex distribution planes in the three plans, a direct comparison of the corresponding layers was not possible; thus, only representative layers were depicted.

3.2 All patients

As shown in Figure 6, the average GTV and VPV were 1225.46 ± 858.81 cm^3 (range, 545.64–4113 cm^3) and 395.33 ± 355.70 cm^3 (range, 151.98–654.31 cm^3). The average number of vertices per patient was 11 ± 6 (range, 7–32) for Plan_Clo and 12 ± 6 (range, 6–32) for Plan_Opt.

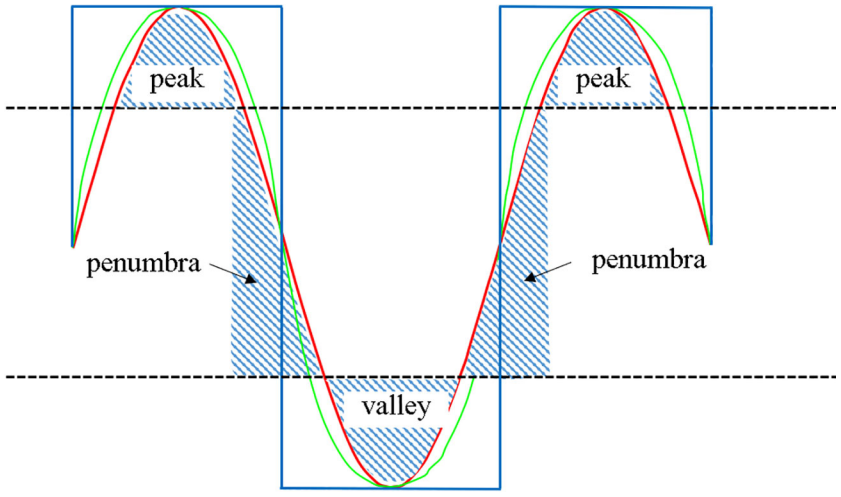

FIGURE 4
Diagram illustrating definitions of peak region, valley region, and penumbra region.

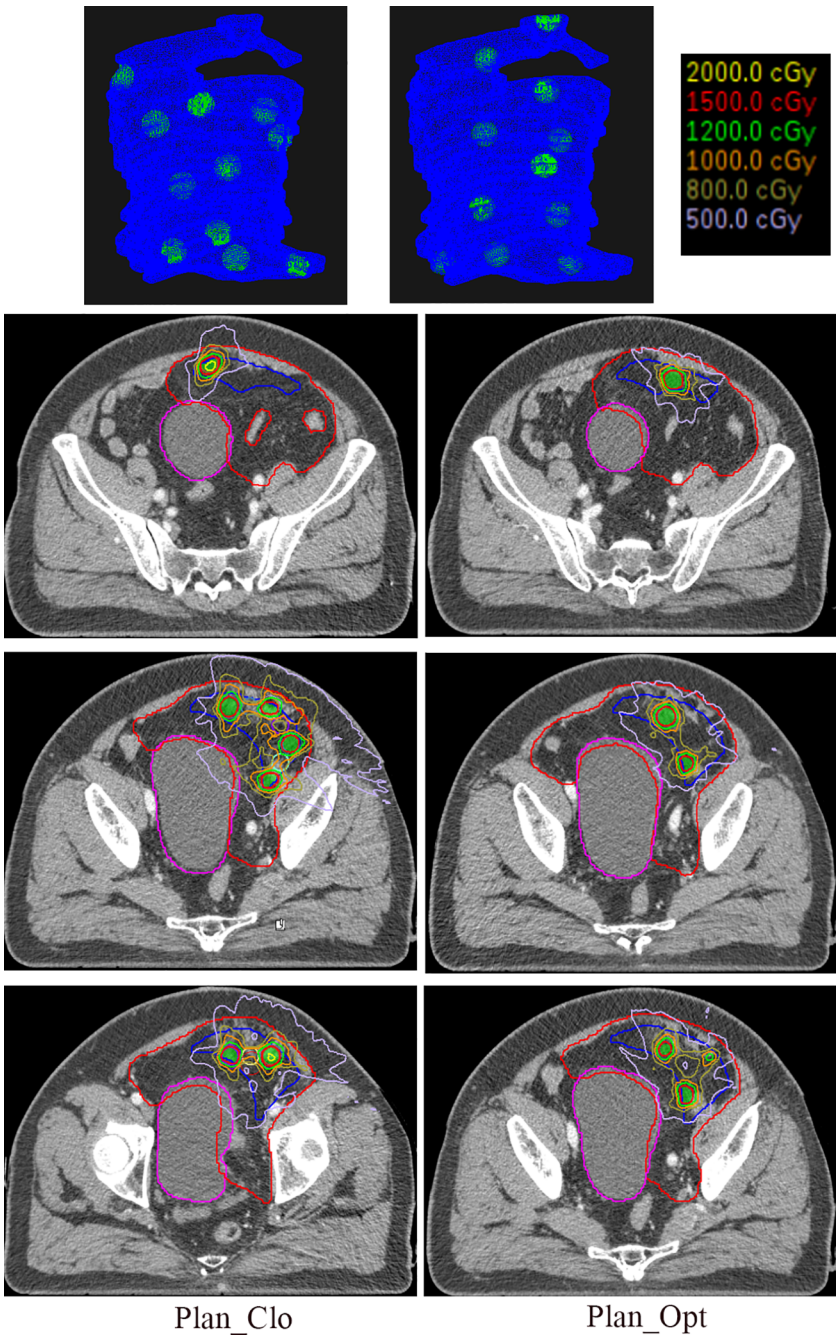

FIGURE 5
The first row of the figure illustrates the three-dimensional distribution of vertices, with the blue region indicating the VPV and the green region denoting the vertices. The remaining three rows show the isodose distributions in the central axial planes for one representative patient in Plan_Clo (left) and Plan_Opt (right). The red line represents the GTV, the blue line represents the VPV, the magenta line represents the organ at risk, bladder, and the green shaded area represents the vertices. Plan_Clo and Plan_Opt were generated using initial vertices from closest packing and optimized vertices from adaptive simulated annealing, respectively.

For Plan_Clo and Plan_Opt, the distance between vertices per patient varied, with average distances of 34.15 ± 5.79 mm (range, 20.00–40.00 mm) and 37.86 ± 6.40 mm (range, 23.00–45.00 mm) across the 17 patients, respectively.

The average volume of the vertices was 12.68 ± 8.76 cm^3 (range, 3.4–41.81 cm^3) for Plan_Clo and 12.66 ± 8.84 cm^3 (range, 3.41–42.39 cm^3) for Plan_Opt. The average total volume of the vertices showed no significant difference between Plan_Opt and Plan_Clo ($p = 0.820$). The vertex diameters were consistent across the two plans for every patient. For the 17 patients, the average diameter was 13.14 ± 2.32 mm (range, 7.5–15 mm). Table 1 provided a clear summary of the key data extracted from Figure 6, making it easier for comparison and analysis.

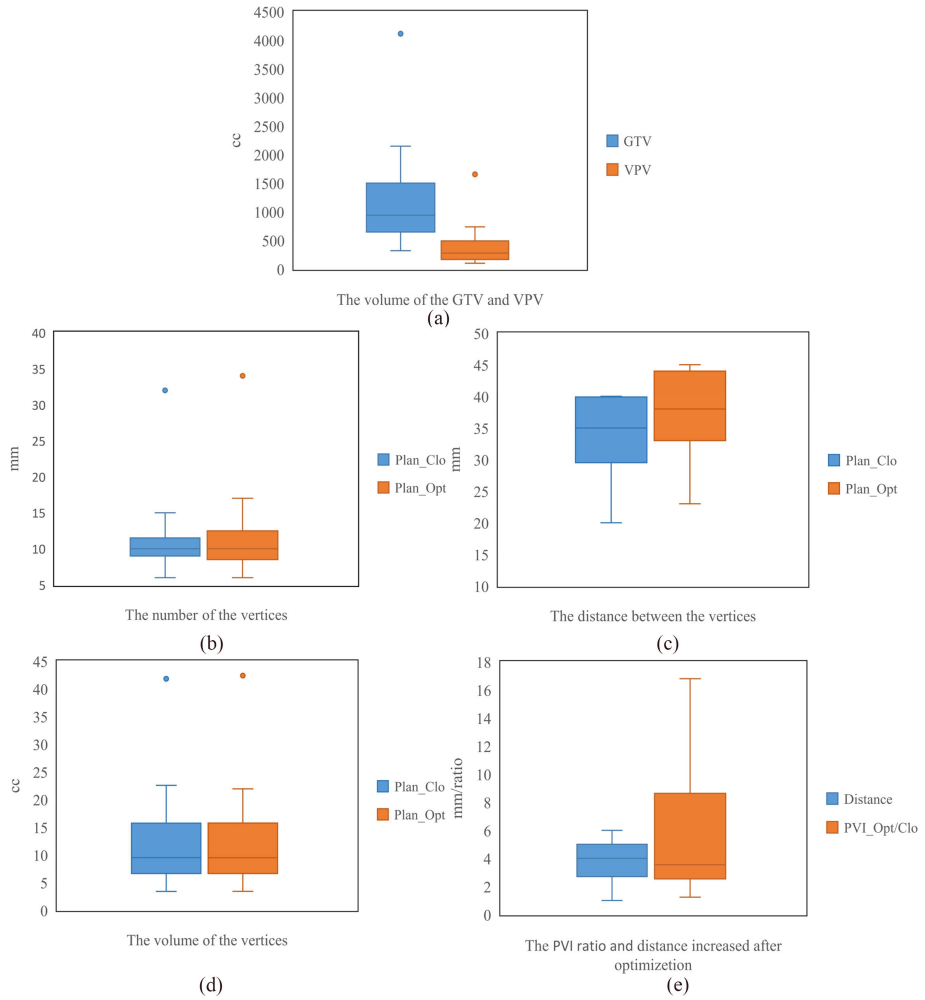

FIGURE 6
The statistics for seventeen patients, including the volumes of GTV and VPV **(a)**, the number of vertices **(b)**, the distance between vertices **(c)**, the volume of vertices **(d)**, and the *PVI* and increase in distance between vertices **(e)**. Plan_Clo and Plan_Opt were generated using initial vertices from closest packing and optimized vertices from adaptive simulated annealing, respectively.

3.3 Performance of optimization method

The average increase in distance d between vertices was 3.7 ± 1.3 mm. The maximum increase (5 mm) was from 36 to 41 mm, and the minimum increase (1 mm) was from 40 to 41 mm.

PVI ratio was used to compare the PVI difference between Plan_Opt and Plan_Clo, for which the average PVI across the 17 patients showed a statistically significant difference (p = 0.000). As shown in Figure 6e, the average PVI ratio (PVI_Opt/Clo) between Plan_Clo and Plan_Che was 5.95 ± 4.87 (range, 1.24–16.80). After optimizing the vertex positions, the distances between the vertices increased and the PVI improved.

The average NT_{1cc} values were 27.81 and 24.88 Gy across the 17 patients for Plan_Clo and Plan_Opt, respectively, with no statistically significant difference (p = 0.332). The mean doses to GTV averaged 13.86 and 15.50 Gy across 17 patients for Plan_Clo and Plan_Opt, respectively, showing a statistically significant difference (p = 0.02).

Within the GTV, the optimized plan had a higher mean dose because vertices of the same volume were more dispersed throughout the GTV after optimization. Constraints on normal tissue were set through the objective function. Thus, the maximum dose to 1 cm^3 of normal tissue showed no statistically significant difference between plans.

4 Discussion

In this study, we considered the vertices in LRT to have a sphere-like shape. If a cylinder is considered, the vertices can be automatically generated using our method, with only one plane being required to set the vertex regions. The vertex positions were also optimized while maintaining the total volume of the vertices to increase both the distance between vertices and PVI. While maintaining the total volume of the vertices, their sizes could be reduced, thereby increasing the difference between peak and valley doses.

10.3389/fonc.2025.1582402

TABLE 1 Summary of box plot statistics from Figure 6 for GTV, VPV, vertices, and PVI optimization.

Data Category		Min Value	Q1 (First Quartile)	Median	Q3 (Third Quartile)	Max Value
Volume (cc)	GTV	319.23	658.09	938.38	1419.41	4113.00
	VPV	99.69	175.57	277.26	414.78	1654.03
Number of Vertices	Plan_Clo	6	10	11	13	31
	Plan_Opt	6	9	10	12	34
Distance Between Vertices (mm)	Plan_Clo	20	30	35	39	40
	Plan_Opt	23	34	38	44	45
Volume of the Vertices (cc)	Plan_Clo	3.4	6.96	9.49	15.26	41.81
	Plan_Opt	3.41	6.96	9.47	15.39	42.39
PVI Ratio and Distance(Ratio/mm)	PVI_Opt/Clo	1.24	2.57	3.55	6.49	16.80
	Distance	1	3	4	5	6

The automatic arrangement of LRT targets allows to eliminate suboptimal arrangements by discarding individual oncologist's preferences and ensure consistent target placement across patients, thus contributing to homogeneity across clinical trials. Manually adjusting the vertex positions is based solely on intuition, which alters the distances between the adjusted vertex and its neighboring vertices, further affecting the PVI. Introducing manual adjustments increases the influence of human factors, thereby introducing unintended plan heterogeneity. However, if a clinician determines that a particular sphere is too close to a critical organ and cannot provide adequate protection, manual adjustments may still be made. With the increasing clinical experience in applying the method proposed in this study, we aim to improve its robustness in generating vertices by refining the inward boundary adjustment during the VPV generation process, thereby minimizing the need for manual vertex adjustments.

Increasing evidence indicates that tumors exhibit large heterogeneity, leading to high variability in their dose response to radiotherapy, which can drastically impact the clinical outcomes (34–36). Generating spatially heterogeneous treatment doses that account for the dose response variability of individual tumors has clinical significance. Therefore, an alternative approach with scientific rigor and accuracy may involve positioning vertices based on metabolic data. This concept, known as metabolic-guided LRT, was explored by Ferini et al. (29). It involves targeting the locations with high 18F-FDG uptake, corresponding to areas of increased metabolic activity, to administer higher doses to the more active tumor regions. During optimization of LRT target arrangement, clinical information of this nature may be incorporated for assigning high weights to ensure that the LRT vertices are positioned in metabolically active regions.

Compared with the Tucker method (23), our approach utilizes closest packing and optimization introducing two additional rotational directions. Moreover, our method achieves higher precision in step size and rotation, providing a greater scope for finding the optimal solution. In this study, we used a computer equipped with an Intel(R) Core (TM) i7–8700 processor at 3.20 and 3.19 GHz and 24 GB of random-access memory, achieving an average optimization time of approximately 5 min. For clinical implementation, acceleration by graphics processing units may reduce the processing time.

A potential area for improving optimization is the uniformity of spacing between vertex regions. In radiotherapy, especially for techniques like SFRT that require nonuniform dose distribution, a more relaxed approach might be beneficial. In these cases, the tumor region can be partitioned into multiple sections, and within each section, vertex regions can be arranged with flexible spacing, allowing for small variations in inter-vertex distance. This relaxed approach could help achieve a better overall solution by making small compromises in certain areas, leading to larger dosimetric improvements elsewhere in the treatment volume. Such flexibility could improve the dosimetric outcomes, addressing both geometrical and clinical objectives, which are often constrained in radiotherapy optimization. Incorporating these aspects would allow for a more comprehensive treatment planning method, potentially improving treatment effectiveness by considering the underlying biological objectives, such as tumor control probability and normal tissue complication probability.

The implementation and creation of LRT fields and heterogeneous dose distributions have been facilitated by modern multileaf collimators and advanced TPSs. However, current TPSs do not fully support the creation of LRT targets or provide adequate evaluation tools for SFRT fields and plans (37). The introduction of two additional rotational directions in this study would allow a conventional TPS to assess the dose distribution only on the axial plane. Modifying the TPS to include the evaluation of dose distributions on the plane of close-packed layers as well as the PVI calculation may enable a more intuitive assessment of dose distributions in LRT planning.

5 Conclusion

The proposed optimization method for determining LRT target vertices has been validated, demonstrating a significant improvement in the PVI. ASA optimization, combined with closest packing, effectively enhanced the peak-to-valley dose difference in LRT, showcasing its potential for advancing treatment planning.

Data availability statement

The raw data supporting the conclusions of this article will be made available by the authors, without undue reservation.

Ethics statement

The studies involving humans were approved by National Cancer Center/Cancer hospital, Chinese Academy of Medical Sciences and Peking Union Medical College. The studies were conducted in accordance with the local legislation and institutional requirements. Written informed consent for participation was not required from the participants or the participants' legal guardians/next of kin in accordance with the national legislation and institutional requirements.

Author contributions

PM: Conceptualization, Formal Analysis, Methodology, Resources, Software, Validation, Writing – original draft. YX: Methodology, Resources, Writing – review & editing. YY: Data curation, Methodology, Writing – review & editing. NL: Data curation, Investigation, Project administration, Resources, Supervision, Writing – original draft. JD: Conceptualization, Formal Analysis, Investigation, Methodology, Project administration, Writing – review & editing.

Funding

The author(s) declare financial support was received for the research and/or publication of this article. This work was supported by the CAMS Innovation Fund for Medical Sciences (CIFMS) (2023-I2M-C&T-B-089) and National Natural Science Foundation of China (82003244).

Acknowledgments

A patent was applied for the method and system for optimizing the arrangement of spatially fractionated radiotherapy targets in China (Patent application number 202310175605.3).

Conflict of interest

The authors declare that the research was conducted in the absence of any commercial or financial relationships that could be construed as a potential conflict of interest.

Generative AI statement

The author(s) declare that no Generative AI was used in the creation of this manuscript.

Publisher's note

All claims expressed in this article are solely those of the authors and do not necessarily represent those of their affiliated organizations, or those of the publisher, the editors and the reviewers. Any product that may be evaluated in this article, or claim that may be made by its manufacturer, is not guaranteed or endorsed by the publisher.

References

1. Prezado Y. Divide and conquer: spatially fractionated radiation therapy. *Expert Rev Mol Med*. (2022) 24):e3. doi: 10.1017/erm.2021.34

2. Wu X, Perez NC, Zheng Y, Li X, Guha C. The technical and clinical implementation of LATTICE radiation therapy (LRT). *Radiat Res*. (2020) 6:737–46. doi: 10.1667/RADE-20-00066.1

3. Zhang H, Wu X, Zhang X, Chang SX, Mayr NA. Photon GRID radiation therapy: A physics and dosimetry white paper from the radiosurgery society (RSS) GRID/LATTICE, microbeam and FLASH radiotherapy working group. *Radiat Res*. (2020) 6:665–77. doi: 10.1667/RADE-20-00047.1

4. Laissue JA, Blattmann H, Slatkin DN. Alban Köhler (1874-1947): Inventor of grid therapy. *Med Phys*. (2012) 2:90–9. doi: 10.1016/j.zemedi.2011.07.002

5. Mohiuddin M, Fujita M, Regine WF, Megooni AS, Ibbott GS, Ahmed MM. High-dose spatially-fractionated radiation (GRID): a new paradigm in the management of advanced cancers. *Int J Radiat Oncol*. (1999) 45:721-7. doi: 10.1016/S0360-3016(99)00170-4

6. Mohiuddin M, Stevens JH, Reiff JE, Huq MS, Suntharalingam N. Spatially fractionated (GRID) radiation for palliative treatment of advanced cancer. *Radiat Oncol Invest*. (1996) 4:41–7. doi: 10.1002/(SICI)1520-6823(1996)4:1<41::AID-ROI7>3.0.CO;2-M

7. Sathishkumar S, Dey S, Meigooni AS, Regine WF, Kudrimoti MS, Ahmed MM, et al. The impact of TNF-alpha induction on therapeutic efficacy following high dose spatially fractionated (GRID) radiation. *Technol Cancer Res Treat*. (2002) 1):141–47. doi: 10.1177/153303460200100207

8. Blanco Suarez JM, Amendola BE, Perez N, Amendola M, Wu X. The use of lattice radiation therapy (LRT) in the treatment of bulky tumors: A case report of a large metastatic mixed mullerian ovarian tumor. *Cureus*. (2015) 11:e389. doi: 10.7759/cureus.389

9. Rivera JN, Kierski TM, Kasoji SK, Abrantes AS, Dayton PA, Chang SX. Conventional dose rate spatially-fractionated radiation therapy (SFRT) treatment response and its association with dosimetric parameters-A preclinical study in a Fischer 344 rat model. *PloS One*. (2020) 6:e0229053. doi: 10.1371/journal.pone.0229053

10. Wu X, Ahmed MM, Pollack A. On modern technical approaches of 3D high-dose lattice radiotherapy (LRT). *Cureus*. (2010) 3:e9. doi: 10.7759/cureus.9

11. Slatkin DN, Spanne P, Dilmanian FA, Sandborg M. Microbeam radiation therapy. *Med Phys*. (1992) 6:1395–400. doi: 10.1118/1.596771

12. Prezado Y, Fois GR. Proton-minibeam radiation therapy: a proof of concept. *Med Phys*. (2013) 3:031712. doi: 10.1118/1.4791648

13. Amendola BE, Perez NC, Wu X, Amendola MA, Qureshi IZ. Safety and efficacy of lattice radiotherapy in voluminous non-small cell lung cancer. *Cureus*. (2019) 3: e4263. doi: 10.7759/cureus.4263

14. Duriseti S, Kavanaugh J, Goddu S, Price A, Knutson N, Reynoso F, et al. Spatially fractionated stereotactic body radiation therapy (Lattice) for large tumors. *Adv Radiat Oncol*. (2021) 3:100639. doi: 10.1016/j.adro.2020.100639

15. Iori F, Cappelli A, D'Angelo E, Cozzi S, Ghersi SF, De Felice F, et al. Lattice Radiation Therapy in clinical practice: A systematic review. *Clin Transl Radiat Oncol*. (2023) 39):100569. doi: 10.1016/j.ctro.2022.100569

16. Kavanaugh JA, Spraker MB, Duriseti S, Basarabescu F, Price A, Goddu M, et al. LITE SABR M1: Planning design and dosimetric endpoints for a phase I trial of lattice SBRT. *Radiother Oncol*. (2022) 167):172–78. doi: 10.1016/j.radonc.2021.12.003

17. Mohiuddin M, Curtis DL, Grizos WT, Komarnicky L. Palliative treatment of advanced cancer using multiple nonconfluent pencil beam radiation. *A pilot study Cancer*. (1990) 1:114–8. doi: 10.1002/1097-0142(19900701)66:1<114::aid-cncr2820660121>3.0.co;2-l

18. Mohiuddin M, Miller T, Ronjon P, Malik U. Spatially fractionated grid radiation (SFGRT): A novel approach in the management of recurrent and unresectable soft tissue sarcoma. *Int J Radiat Oncol*. (2009) 3:S526–S26. doi: 10.1016/j.ijrobp.2009.07.1200

19. Neuner G, Mohiuddin MM, Walde NV, Goloubeva O, Regine WF. High-dose spatially fractionated GRID radiation therapy (SFGRT): a comparison of treatment outcomes with Cerrobend vs. MLC SFGRT. *Int J Radiat Oncol Biol Phys*. (2011) 5:1642–49. doi: 10.1016/j.ijrobp.2011.01.065

20. Peñagarícano JA, Moros EG, Ratanatharathorn V, Yan Y, Corry P. Evaluation of spatially fractionated radiotherapy (GRID) and definitive chemoradiotherapy with curative intent for locally advanced squamous cell carcinoma of the head and neck: initial response rates and toxicity. *Int J Radiat Oncol Biol Phys*. (2010) 5:1369–75. doi: 10.1016/j.ijrobp.2009.03.030

21. Pollack A, Chinea FM, Bossart E, Kwon D, Abramowitz MC, Lynne C, et al. Phase I trial of MRI-guided prostate cancer lattice extreme ablative dose (LEAD) boost radiation therapy. *Int J Radiat Oncol Biol Phys*. (2020) 2:305–15. doi: 10.1016/j.ijrobp.2020.01.052

22. Grams MP, Owen D, Park SS, Petersen IA, Haddock MG, Med EBJ, et al. VMAT grid therapy: A widely applicable planning approach. *Pract Radiat Oncol*. (2020) 11: e339–e47. doi: 10.1016/j.prro.2020.10.007

23. Tucker WW, Mazur TR, Schmidt MC, Hilliard J, Badiyan S, Spraker MB, et al. Script-based implementation of automatic grid placement for lattice stereotactic body radiation therapy. *Phys Imaging Radiat Oncol*. (2024) 29):100549. doi: 10.1016/j.phro.2024.100549

24. Zhang W, Li W, Lin Y, Wang F, Chen RC, Gao H. TVL1-IMPT: optimization of peak-to-valley dose ratio via joint total-variation and L1 dose regularization for spatially fractionated pencil-beam-scanning proton therapy. *Int J Radiat Oncol Biol Phys*. (2023) 3:768–78. doi: 10.1016/j.ijrobp.2022.09.064

25. Zhang W, Lin Y, Wang F, Badkul R, Chen RC, Gao H. Lattice position optimization for LATTICE therapy. *Med Phys*. (2023) 12:7359–67. doi: 10.1002/mp.16572

26. Hales T, Adams M, Bauer G, Dang DT, Harrison J, Hoang TL, et al. A formal proof of the Kepler conjecture. *Mathematics*. (2015) 3:47–58. doi: 10.48550/arXiv.1501.02155

27. Ingber L. Adaptive simulated annealing (ASA): Lessons learned. *Control and Cybernetics* (2000) 25:33-54. doi: 10.48550/arXiv.cs/0001018

28. Xu Y, Xu Y, Men K, Xiao J, Dai J. Application of piecewise VMAT technique to whole-brain radiotherapy with simultaneous integrated boost for multiple metastases. *Radiat Oncol (London England)*. (2022) 1:86. doi: 10.1186/s13014-022-02059-6

29. Fernandez-Palomo C, Chang S, Prezado Y. Should peak dose be used to prescribe spatially fractionated radiation therapy?-A review of preclinical studies. *Cancers (Basel)*. (2022) 15:3909. doi: 10.3390/cancers14153625

30. Zhang H, Mayr NA. Spatially Fractionated, Microbeam and FLASH Radiation Therapy. In: Zhang H, Mayr NA, editors. *A physics and multi-disciplinary approach*. IOP Publishing, IOP Publishing, Bristol, UK (2023).

31. Yang D, Wang W, Hu J, Hu W, Zhang X, Wu X, et al. Feasibility of lattice radiotherapy using proton and carbon-ion pencil beam for sinonasal Malignancy. *Ann Trans Med*. (2022) 8:467. doi: 10.21037/atm-21-6631

32. Murphy NL, Philip R, Wozniak M, Lee BH, Donnelly ED, Zhang H. A simple dosimetric approach to spatially fractionated GRID radiation therapy using the multileaf collimator for treatment of breast cancers in the prone position. *J Appl Clin Med Phys*. (2020) 11:105–14. doi: 10.1002/acm2.13040

33. Prado A, Martí J, García de Acilu P, Zucca D, Ángel de la Casa M, García J, et al. Dosimetrical and geometrical parameters in single-fraction lattice radiotherapy for the treatment of bulky tumors: Insights from initial clinical experience. *Physica medica: PM: an Int J devoted to Appl Phys to Med biology: Off J Ital Assoc Biomed Phys (AIFB)*. (2024) 123):103408. doi: 10.1016/j.ejmp.2024.103408

34. Bedard PL, Hansen AR, Ratain MJ, Siu LL. Tumour heterogeneity in the clinic. *Nature*. (2013) 7467:355–64. doi: 10.1038/nature12627

35. Heppner GH. Tumor heterogeneity. *Cancer Res*. (1984) 6:2259–65.

36. Meacham CE, Morrison SJ. Tumour heterogeneity and cancer cell plasticity. *Nat Biotechnol*. (2013) 7467:328–37. doi: 10.1038/nature12624

37. Li H, Mayr NA, Griffin RJ, Zhang H, Pokhrel D, Grams M, et al. Overview and recommendations for prospective multi-institutional spatially fractionated radiation therapy clinical trials. *Int J Radiat Oncol Biol Phys*. (2024) 3:737–49. doi: 10.1016/j.ijrobp.2023.12.013

frontiers | Frontiers in Oncology

TYPE Original Research
PUBLISHED 13 May 2025
DOI 10.3389/fonc.2025.1589270

Check for updates

OPEN ACCESS

EDITED BY
Poonam Yadav,
Northwestern University, United States

REVIEWED BY
Phillip Prior,
Medical College of Wisconsin, United States
Vibhay Pareek,
All India Institute of Medical Sciences, India

*CORRESPONDENCE
Huai-wen Zhang
1761580890@qq.com

RECEIVED 07 March 2025
ACCEPTED 22 April 2025
PUBLISHED 13 May 2025

CITATION
Guo H-l, Lu Z-h, Zhong J-h and Zhang H-w (2025) Effect of physical parameter differences on the performance of a knowledge-based partial arc VMAT RapidPlan model for left breast cancer. *Front. Oncol.* 15:1589270. doi: 10.3389/fonc.2025.1589270

COPYRIGHT
© 2025 Guo, Lu, Zhong and Zhang. This is an open-access article distributed under the terms of the Creative Commons Attribution License (CC BY). The use, distribution or reproduction in other forums is permitted, provided the original author(s) and the copyright owner(s) are credited and that the original publication in this journal is cited, in accordance with accepted academic practice. No use, distribution or reproduction is permitted which does not comply with these terms.

Effect of physical parameter differences on the performance of a knowledge-based partial arc VMAT RapidPlan model for left breast cancer

Hai-liang Guo[1], Zeng-hong Lu[1], Jing-hua Zhong[1] and Huai-wen Zhang[2*]

[1]Department of Oncology, the First Affiliated Hospital of Gannan Medical University, Jiangxi Clinical Research Center for Cancer, First Clinical Medical College, Gannan Medical University, Ganzhou, China, [2]Department of Radiation Oncology, Jiangxi Cancer Hospital & Institute, Jiangxi Clinical Research Center for Cancer, The Second Affiliated Hospital of Nanchang Medical College, Nanchang, China

Objective: To optimize the protection of organs at risk (OARs) in left breast cancer radiotherapy, this study investigated how physical parameter adjustments affect the performance of a Rapidplan-based dose-volume histogram (DVH) prediction model.

Methods: Twenty patients who underwent left breast-conserving surgery were enrolled. Partial arc volumetric modulated arc therapy (VMAT) plans were designed per patient, with X-direction field width set to half-beam and right breast (Breast-R) contoured as an avoidance structure to generate Rapidplan model. The model was used to predict and generate three plans: AP_partial arc (avoidance structure prioritized), RP_partial arc (no avoidance structure), and FP_partial arc (expanded field width). Dosimetric comparisons against the original plan evaluated the impact of parameter selection.

Results: AP_partial arc reduced mean doses of Breast-R, Heart, Lung-L, and Lung-R by 7.7 cGy, 9.8 cGy, 16.7 cGy, and 1.1 cGy, respectively ($p < 0.05$). Conversely, RP_partial arc increased mean dose of Breast-R by 66.3 cGy ($p < 0.05$). FP_partial arc raised V5 of Lung-L, V5 of Heart, and mean dose of Lung-L by 4.01%, 2.25%, and 36 cGy ($p < 0.05$).

Conclusion: The knowledge-based partial arc model for rapid planning of left breast cancer accurately predicts the DVH of OARs. However, before performing dose prediction, physical parameters such as radiation field width and planned avoidance structures should be considered to reduce the risk of low-dose exposure volume to OARs and secondary cancer.

KEYWORDS

left breast cancer, DVH, RapidPlan, partial arc VMAT, dosimetry

1 Introduction

Breast cancer is a common malignant tumor in women (1). After breast-conserving surgery, most patients need radiotherapy to reduce the local recurrence rate. Three-dimensional conformal radiotherapy (3D-CRT), intensity-modulated radiotherapy (IMRT), and volume-rotating intensity-modulated radiotherapy (VMAT) have been used to treat breast cancer. Many studies have confirmed that VMAT irradiation technology has significant dosimetric advantages in the treatment of breast cancer (2, 3). However, full or half arc VMAT plans usually increase the low-dose exposure volume of the contralateral lung and breast, which may increase the risk of secondary cancer (4–6). Previous studies compared 50–60° partial arc VMAT with full-arc or half-arc VMAT. Their research results showed that partial arc technology reduced the radiation dose and volume of radiation to OARs on the contralateral side (7). Fogliata et al. conducted a risk assessment of VMAT and 3D-CRT radiotherapy technology for secondary cancer of the contralateral breast. The results showed that partial arc VMAT was as good as 3D-CRT in avoiding parts, and the acute and late NTCP levels of the affected organs were reduced (8). Even if partial arcs are used for VMAT planning and design, extensive planning design time is needed, and the consistency of the dose distribution quality is poor.

RapidPlan (Varian Medical Systems, USA) is a knowledge-based planning (KBP) solution that builds a predictive model by extracting historical planning information (9). These models can prospectively estimate the DVH of all OARs contained in the training model according to the anatomical characteristics of any new patient. The RapidPlan was reported to reduce the radiation dose to OARs and also improve the efficiency of the plan design (10–12). RapidPlan has been commercially promoted and has been extensively tested in many clinical cases (including VMAT of the breast cancer) (13, 14). The Varian RapidPlan model trained on VMAT and supine orientation can be used for other techniques and orientations (15, 16). The RapidPlan model configurations can be shared and implemented across multiple centers with simple adaptations to local protocols (17, 18). A VMAT KBP model driven by plans performed on a conventional linear accelerator (LINAC) with 6 MV flattening filter (FF) beams was reported to provide high-quality plans performed with 6 MV flattening filter-free (FFF) beams on the new Halcyon© LINAC (19).

However, mismatched physical parameters between the optimization scheme and the RapidPlan model may result in deviations of the final dose distribution from the initial prediction. Yusuke Sakai et al. (20) developed a knowledge-based RapidPlan model using 32 TrueBeam SI-VMAT plans (1 full arc + 3 non-coplanar partial arcs). When validating the model on the Halcyon system, significant DVH deviations were observed in low-dose regions (<9 Gy), with differences in gradient index, conformity index, and normal brain volumes receiving ≥12 Gy, ≥18 Gy, and ≥27 Gy. Similarly, Cagni et al. (21) reported discrepancies between RapidPlan-predicted and RapidArc-achieved DVHs when applying a tomotherapy-trained model to arc-based plans, particularly for Spinal cord doses. Fogliata et al. (22) further highlighted that inconsistent avoidance sector settings in breast cancer models led to systematic overestimation of contralateral breast and contralateral lung doses.

Although a lot of evidence that physical parameters (avoidance structures, collimator field width) critically influence breast cancer dose distributions (23–25), existing RapidPlan models rarely integrate these factors during prediction. To address this challenge, this study developed a left breast cancer partial arc VMAT RapidPlan model and evaluated how to adjust to avoid the impact of structure and field width on OAR dose prediction. The results of this study aim to guide the selection of clinical parameters to reduce the exposure dose to breast-R, heart, lung-L, and lung-R.

2 Methods

This retrospective study included 20 consecutive patients with early-stage breast cancer (pathological stage T1N0M0) on the left side who underwent breast-conserving surgery between January 2023 and December 2024. Inclusion criteria: a pathologically confirmed diagnosis of T1N0M0 left breast cancer, ipsilateral breast CTV volume ≤1000cm^3, age 18-70 years, and irradiation only to the whole breast and tumor bed. Exclusion criteria: previous chest radiotherapy or active systemic diseases (such as coronary artery disease, connective tissue disease), radiotherapy contraindications (such as pregnancy, pacemaker implantation), and the need for additional regional lymph node irradiation. The study protocol was approved by the institutional ethics committee (number: LLSC-2024067).

The patient was fixed in the breast bracket and vacuum negative pressure pad (model R610-DCF1, Klarity Company, China), the head was centered, and the rod was lifted and held with both hands. Computed tomography (CT) scanning was performed in the free-breathing mode. OARs, such as the left lung (Lung-L), Heart, right breast (Breast-R), right lung (Lung-R), Spinal cord, and trachea, were contoured. The clinical target volume (CTV) was the total volume of breast tissue measured on CT with the help of line markers placed around the palpable breast tissue. PTV was expanded 5 mm on the basis of the CTV but did not include the Heart. PTV and CTV were retracted 5 mm from the skin and restricted backward to the anterior edge of the intercostal space.

The partial arc VMAT plan (partial arc plan) for each patient was optimized on a Varian VitalBeam LINAC with a 6-MV FF photon energy beam, Millennium 120 leaf MLC, and jaw tracking mode. A dose rate of 600 MU/min was used to deliver 42.56 Gy to the PTV in 16 fractions. The VMAT plan was optimized using the photon optimization (PO) mode with Eclipse 15.5 3D planning system, and dose calculation was performed using the Acros XB algorithm with a calculation grid of 2.5 mm. The isocenter of the radiation field was placed on the midpoint of the line between the medial boundary and the lateral boundary of the PTV in the median transverse section CT image of each patient's PTV, according to a report by Boman et al. (26). Field width in the X direction used a half-beam to reduce the effect of the beam divergence angle on the healthy lung and breast.

Four partial arcs were used to design each plan. The first partial arcs were rotated 160°–165° to 95°–100counterclockwise and the arcs were reversed, and the second partial arcs were rotated 280°–285° to 350°–355°clockwise and the arcs were reversed, with a collimator at an angle of 0–10° to ensure that the bottom edge of the jaw was parallel to the sternum alignment to reduce radiation to the ipsilateral lung. Breast-R was defined as the avoidance structure to reduce exposure. A 10 mm virtual bolus was used in the optimization design to open the MLC leaf in the air outside the target volume to compensate for reductions in the dose coverage in the target area caused by the patient's respiratory movement, breast edema, or breast deformation, according to the method proposed by Rossi et al. (27). The virtual bolus was removed during the final dose calculation.

The RapidPlan optimization component consisted of three main parts: a modeling and training engine, an automatic constraint prediction module, and a new VMAT/IMRT optimization objective based on the quality of the historical data used for training. During the extraction phase, several anatomical and dosimetric features were obtained from the patient's anatomical structures and plan. Each OAR was divided into sub-volumes based on its position relative to the field and target. During the training phase, principal component analysis was performed on the OAR volume within the field to identify the geometric features most correlated with a dosimetric principal component score of 1. A regression model using these two components was applied to obtain the regression between anatomical/geometric features and dosimetric features. The OAR region that did not belong to the "in-field" was modeled using a simple model as the mean and standard deviation to estimate the dose. The final estimated DVH was based on the combination of different subvolume partitioned parts. In model evaluation, the goodness of fit (regression) was determined by the coefficient of determination R2 and the mean chi-squared x2. Potential outliers were also evaluated.

We used 20 partial arc plans created earlier to generate a fast-planning model, called the partial arc model, which considered radiation-endangered organs, including the Heart, Lung-L, Lung-R, and Breast-R. The selection of optimization objectives is shown in Table 1. Based on the guidelines provided by the manufacturer, this study observed various statistical charts to identify and classify possible geometric shapes, dose outliers, and points with strong influence in the fitted model after training. The thresholds for the modified Z-score (mZ), studentized residual (SR), and Cook's distance (CD) were set at 3.5, 3.0, and 10.0, respectively. No samples exceeded these thresholds. Then, the model was used to generate dose distributions for 20 patients undergoing the optimization process, with the optimize goal determined by the model without any human modifications or interactions. This plan was called the RP_ partial arc plan. Then, the above operations were repeated, but Breast-R was set as the avoidance structure before optimization. This plan was called the AP_ partial arc plan. Finally, the width of the X-direction field was increased to 14 cm, and Breast-R was set as the avoidance structure. Then, the model was used to generate dose distributions on 20 patients during the optimization process, with the optimize goal determined by the model. This plan was named the FP_ partial arc plan, as shown in Figure 1.

TABLE 1 Optimization objectives in the RapidPlan model.

Structure	Parameter type	Objective	Priority
PTV	Upper Objective	$D_{max,0\%}$<102% of prescription	120
	Lower Objective	$D_{min,97\%}$>100% of prescription	120
	Lower Objective	$D_{min,100\%}$>99% of prescription	120
Breast-R	Line Objective	Generated	Generated
Heart	Line Objective	Generated	Generated
Lung-L	Line Objective	Generated	Generated
Lung-R	Line Objective	Generated	Generated
Spinal Cord	Line Objective	Generated	Generated

Finally, the output three plans of the RapidPlan model were compared with the original plan used to train the RapidPlan module of the left breast cancer. The comparison included various dose volume indicators, such as V95%, V107%, and D98% of PTV, and the mean dose of the Lung-L,Heart, Breast-R and Lung-R, V20 and V5 of Lung-L, V5 of Heart.

The dosimetric data were obtained through DVH. All of the DVH data were statistically analyzed using SPSS 16.0 software. The Shapiro-Wilk test was used to test the normality of the data, and the Levene test was used to verify the homogeneity of variance. The quantitative data are expressed as the mean ± standard deviation ($\bar{x} \pm s$). The two related samples were compared via repeated measurement data analysis of variance. A p-value of < 0.05 indicated a statistically significant difference.

3 Results

3.1 partial arc VMAT RapidPlan model

Table 2 reports the dosimetric characteristics of the partial arc plans used to generate the RapidPlan model. Table 3 summarizes the model training results from the configuration information in terms of goodness-of-fit (coefficient of determination R^2, chi-square x^2, and outliers). All of the cases were accepted, and none was considered a true outlier. The regression plots and residual plots related to the four OARs are shown in Figure 2. Only Lung-R showed a large standard deviation and a large variance (dashed line). Other regression plots and residual plots had a clear slope, and the standard deviation and variance were small.

3.2 Comparison

Figures 3A–C shows the predicted DVH range and automatic objectives in the RapidPlan model based on KBP and the three sets of plans, as well as the predicted DVH difference between the actual and model-predicted DVH for patient 11.

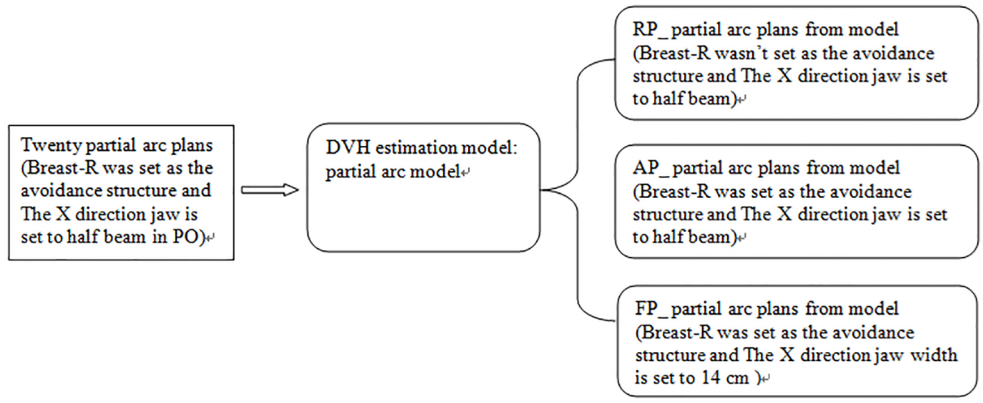

FIGURE 1
Diagram of the model and plans.

Figure 4 shows a DVH comparison of the original plan and the partial arc Model output three kinds of plans for Patient 11. The Breast-R DVH curve in the RP_ partial arc plan without Breast-R as an avoidance structure moved forward significantly. The Low-dose region of the Lung-L DVH curve in the FP_ partial arc plan moved forward, but Lung-R moved backward. The other cases in the cohort presented features similar to those of patient 11.

Table 4 shows the comparison of doses to PTV and OARs between the original plan and the other three output plans. All three plans output by the partial arc model met the clinical prescription dose requirements and showed no difference from the original plan ($p > 0.05$). The AP_partial arc plan significantly reduced the average doses to breast-R, heart, lung-L, and lung-R, by 7.7 cGy, 9.8 cGy, 16.7 cGy, and 1.1 cGy, respectively ($p < 0.05$). Aligning the physical parameter settings with the RapidPlan model configuration improved the preservation of OARs compared to the original clinical plan. The study results showed that the RP_partial arc plan reduced the V5 values for lung-L and heart, but increased the average dose to breast-R to 66.3 cGy ($p < 0.05$). An increase in breast-R dose may increase the risk of secondary malignancies, such as contralateral breast cancer, by approximately 1.5% per Gy. The FP_partial arc plan resulted in an increase of 4.01%, 2.25%, and 36 cGy in V5 for lung-L, V5 for heart, and average dose to lung-L, respectively ($p < 0.05$). However, V5 of lung-L is one of the key indicators for predicting radiation pneumonitis, and an increase in low-dose (V5) volume may lead to an increased probability of radiation pneumonitis.

TABLE 2 Dose characteristics of the partial arc plans selected for model input.

Structure	Dosimetric goal	partial arc plans
PTV	D98%>95%[%]	97.70 ± 0.00[%]
	V107%<10%[%]	4.68 ± 2.30[%]
	V110%<1%[%]	0.14 ± 0.17[%]
Breast-R	Mean<400cGy[cGy]	71 ± 54[cGy]
Heart	Mean<500cGy[cGy]	213 ± 95[cGy]
	V_{5Gy}<50%[%]	6.08 ± 3.98[%]
Lung-L	Mean<1000cGy[cGy]	576 ± 118[cGy]
	V_{5Gy}<40%[%]	21.89 ± 4.16[%]
	V_{20Gy}<20%[%]	10.36 ± 2.97[%]
Lung-R	V_{5Gy}<20%[%]	0.00 ± 0.00[%]
	Mean<100cGy[cGy]	16 ± 8[cGy]

4 Discussion

In the RapidPlan model established through the partial arc VMAT in this study, regression plots of four organs showed correlations between geometric and dosimetric features (Figure 2). Although Lung-R showed a large regression standard deviation and residual, the average dose to Lung-R was less than 20 cGy, and the data fluctuations were not clinically significant. All three sets of plans generated by the RapidPlan model met the clinical requirements ($p > 0.05$).

Most studies on the performance of the RapidPlan model utilize historical patient data to construct the RapidPlan model and employ it to re-optimize the MLC sequence while retaining other parameters such as field geometry and photon energy, subsequently comparing it with manual artificial plans (28). Unlike traditional methods, this study specifically focuses on two under-researched physical parameters—avoidance structure definition and collimator field width—to evaluate their impact on the performance of the

TABLE 3 Model training results.

Index	Breast-R	Heart	Lung-L	Lung-R
coefficients of determination R^2	0.818	0.9	0.843	0.401
Chi-square x^2	1.193	1.141	1.25	1.118
outliers	3	2	3	0

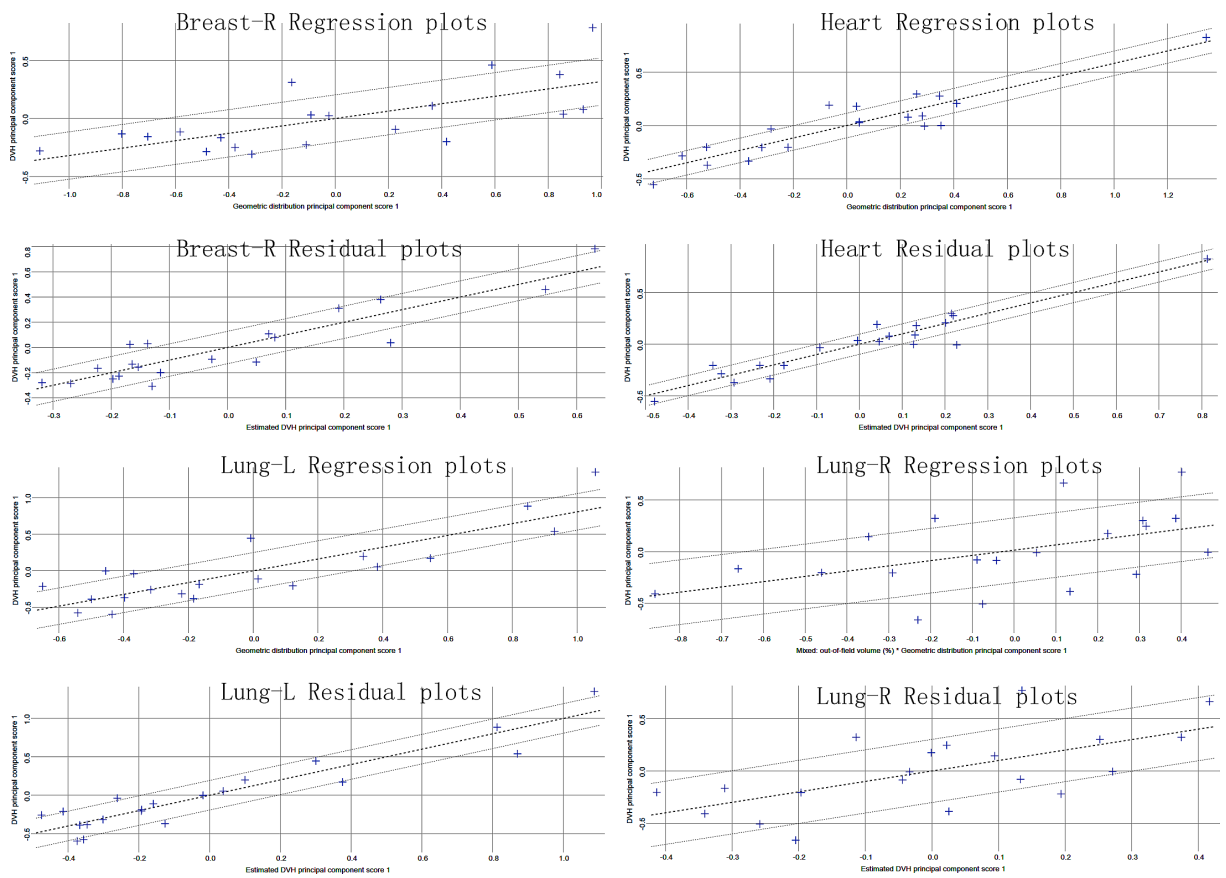

FIGURE 2
Regression and residual plots of the partial arc VMAT RapidPlan model.

RapidPlan model in left breast VMAT planning. The AP_partial arc plan replicates the physical parameters of the model training data, including Breast-R as an avoidance structure. When the structure is positioned before the target in the beam's-eye-view or projected into the beam's-eye-view in the Eclipse photon optimizer (as a different option), the closed MLC shields the avoidance structure, thereby reducing the dose received by the avoidance structure. Compared to manual plans, the AP_partial arc plan significantly reduces OAR doses (such as Dmean for the heart: 9.8 cGy, Dmean for Breast-R: 7.7 cGy, V20 for Lung-L: 0.36%, Dmean for Lung-L: 16.7 cGy) ($p < 0.05$). These findings indicate that RapidPlan's ability in OAR protection is comparable to or even superior to manual planning, aligning with previous research results (14, 29) and supporting its clinical application in standardized left breast VMAT. Notably, the average doses for Lung-R and Breast-R in this study (Lung-R: 14.9 cGy; Breast-R: 63.3 cGy) were 15-20% lower than values reported in similar RapidPlan breast studies (30, 31). This may primarily be attributed to the synergistic effects of the partial arc VMAT geometry (limiting contralateral exposure) and strict avoidance structure implementation.

Radiation exposure to the contralateral breast is a recognized risk factor for secondary cancer during or after radiotherapy (32, 33). For women aged <40 years who received a contralateral breast dose >1.0 Gy, the long-term risk of secondary cancer was increase in a dose-dependent manner, which is inversely correlated with the age at exposure (34). In the RP_partial arc protocol, the average dose to Breast-R reached 1.37 Gy, exceeding the 1 Gy threshold associated with an increased risk of secondary cancer in younger patients. Compared to the original plan, the average dose to Breast-R increased by 66 cGy was potentially increasing the risk of secondary cancer in the contralateral breast by approximately 2.0%. This dose increase may be due to the fact that Breast-R was not considered as an avoidance structure during the optimization process. Although the partial arc rapid planning model generated automatic optimization targets, the lack of explicit Breast-R avoidance constraints resulted in unintended dose spillover. Figure 3A also shows that the actual dose volume histogram (DVH) cut-off dose for Breast-R is higher than the model prediction. This discrepancy reflects a mismatch between the avoidance structure configuration in the clinical plan and the parameters embedded in the rapid planning model, impairing its ability to perform contralateral breast avoidance. Antonella et al. (22) emphasized that model training requires strict alignment between the clinical plan and the avoidance structure defined in the RapidPlan configuration. Differences in these parameters will inevitably lead to systematic deviations between the predicted dose volume histogram (DVH) and the actual obtained DVH. Our research results also confirm this viewpoint, highlighting the

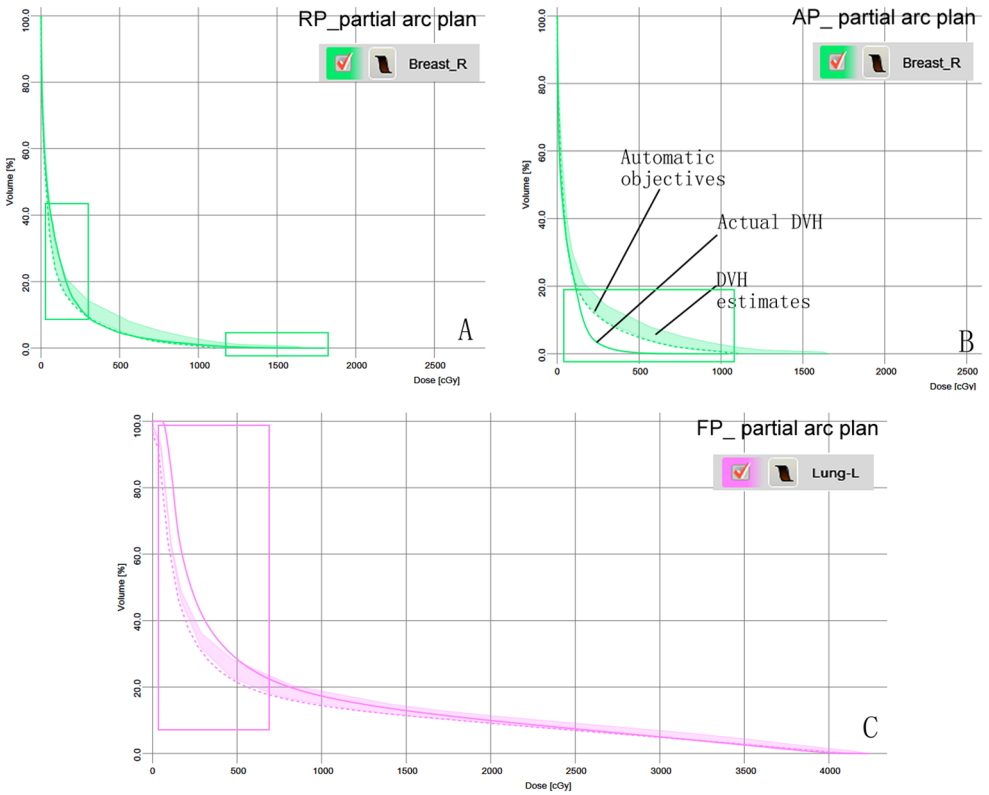

FIGURE 3
Model-based predictive objectives with the estimation range, automatic objectives (line objectives), and the actual DVH of patient 11 in the three plans. **(A)** Breast-R in the RP_ partial arc plan. **(B)** Breast-R in the AP_ partial arc plan. **(C)** Lung-L in the FP_ partial arc plan. The rectangular area represents the difference between the actual DVH and the predicted DVH.

necessity of coordinating the physical parameter settings (avoidance structure) with the model training framework to ensure reliable dose prediction and OAR protection.

The Eclipse treatment planning system employs jaw tracking technology in VMAT, where the jaw dynamically follows the MLC position to minimize inter-leaf leakage and reduce scatter dose to adjacent OARs (35). Different jaw widths significantly affect the dosimetry and complexity of VMAT plans. To balance modulation efficiency and delivery accuracy, it is generally recommended to set the starting position of the jaw as the target volume for automatic conformal, or to limit the jaw width in the X direction to ≤14 cm (36, 37). The original model training plan uses half-beam blocks in the X direction to minimize the impact of beam divergence on contralateral lung and breast tissue. In the FP_partial arc plan, the field width in the X direction is expanded to 14 cm while retaining the breast-R as an avoidance structure. Compared to the original plan, there was no significant change in the average dose of breast-R or lung-R. However, the V5 of lung-L increased by 4.01%, and the average dose of lung-L increased by 36 cGy ($p < 0.05$), which may be due to the following three factors: (1) the RapidPlan model may not accurately predict leakage outside the main beam, (2) increased MLC leaf travel distance leads to increased MLC leakage dose, and (3) prolonged MLC leaf travel time leads to prolonged beam on time. Yilmaz et al. (38) noted that the V5 of lung was an important predictor of radiation pneumonitis, and low-dose high-volume lung radiation causes greater damage to lung function than high-dose low-volume lung radiation. Recht A et al. studied radiation-induced lung injury caused by breast cancer radiotherapy and reported that the risk of radiation pneumonitis caused by relatively low-dose lung volume (V5) exposure after radiotherapy is significant (39). Rodrigues et al. also proposed that the Dmean of the ipsilateral lung is an important parameter for predicting radiation pneumonitis after radiotherapy (40). The FP_partial arc plan increases the V5 and Dmean of lung-L by 4% and 36 cGy, respectively, which may increase the probability of patients developing radiation pneumonitis. Similarly, an increase in the V5 and average dose of the heart (2.1%, 24 cGy) may lead to long-term cardiac toxicity. Darby et al. demonstrated that a 1 Gy increase in major coronary artery events linearly increases by 7.4% (41), emphasizing the need to minimize cardiac exposure even at low doses. Overall, these results highlight that deviations in field width settings and model training parameters can compromise its ability to limit low-dose exposure to critical organs, especially the heart and ipsilateral lung.

Breast radiotherapy dose distribution is influenced by various factors, including the angle/number of rotational arcs, collimator angle, breast CTV shape/size, and non-coplanar field configuration. This study focuses solely on the impact of avoidance structures and field width on the performance of the RapidPlan model. This study is based on data from 20 patients at a single center, and the field width was fixed during the training of the KBP model, which limits

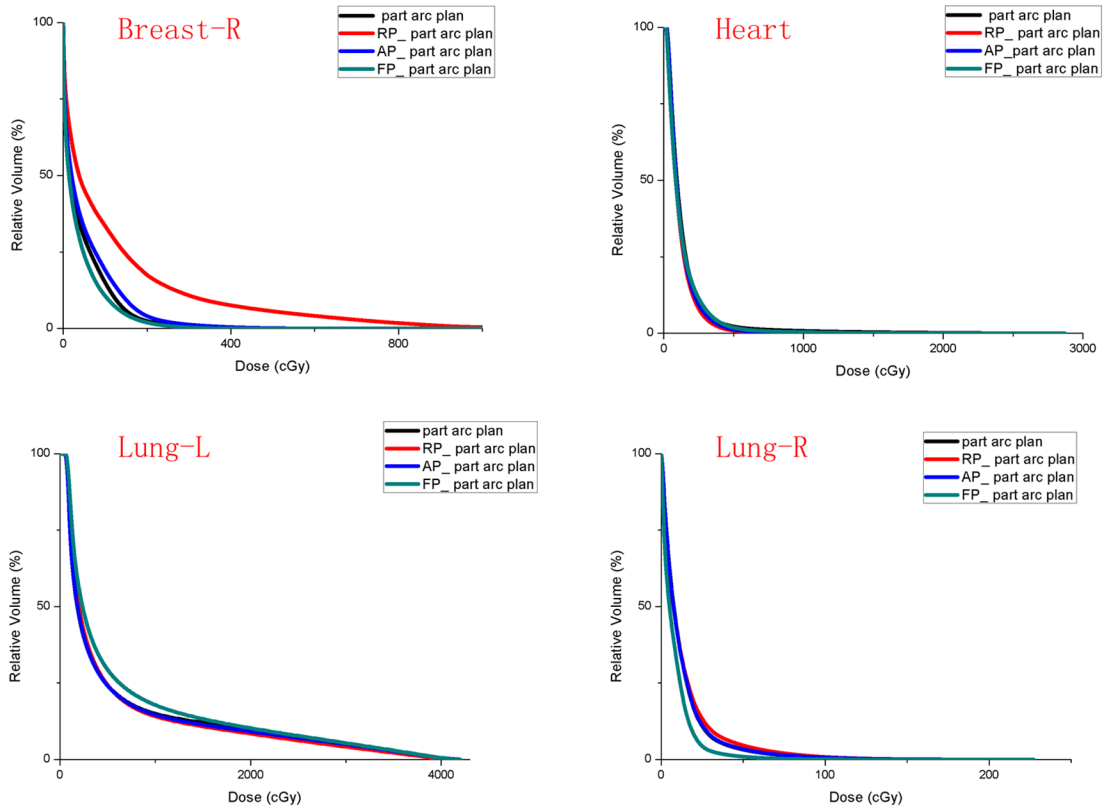

FIGURE 4
DVH of OARs comparison for patient 11 in the original plan and three plans generate by model.

our ability to study the model's generalization performance, especially for patients with larger breast volumes (>1000 cm^3) or complex geometric shapes. In future research, we will expand the KBP training dataset by collecting data from breast cancer patients at multiple radiotherapy centers, while fully considering changes in arc angles (e.g., 180°–300°), collimator rotation (15°–45°), breast CTV volume (500–1500 cm^3), and the definition of avoidance structures to enhance the model's adaptability to heterogeneous physical parameters. Referring to Baroudi et al., a hybrid AI architecture can be explored: the nnU-Net model can autonomously optimize the gantry angle and field shape based on the spatial relationship between breast CTV/OAR, while RapidPlan generates dose targets (42). This integration will standardize plan quality by reducing operator-dependent variability.

TABLE 4 Dose comparison of the PTV and OARs in the original plan and three plans generate by model.

Structure	Index	partial arc plan	RP_ partial arc plan	AP_ partial arc plan	FP_ partial arc plan
PTV	V95% (%)	99.3 ± 0.2	99.3 ± 0.2	99.2 ± 0.3	99.2 ± 0.2
	V107% (%)	4.8 ± 2.8	4.3 ± 2.6	4.3 ± 2.5	4.1 ± 2.6
	D98% (cGy)	4161.3 ± 13	4162 ± 13.8	4159.9 ± 15.8	4159.4 ± 15.6
Breast-R	mean dose (cGy)	71 ± 54	137.3 ± 113.0 *	63.3 ± 47.1 *	61.1 ± 44
Heart	mean dose (cGy)	213 ± 95	191.3 ± 92.6*	203.2 ± 96*	237.1 ± 101.4
	V5 (%)	6.08 ± 3.98	5.3 ± 3.8*	5.7 ± 3.9*	8.3 ± 5.5*
Lung-L	mean dose (cGy)	576 ± 118	543.3 ± 104.6*	559.3 ± 115.6*	612 ± 128.4*
	V5 (%)	21.89 ± 4.16	21.7 ± 3.8*	21.8 ± 4.2*	25.9 ± 5.6*
	V20 (%)	10.36 ± 2.97	9.4 ± 2.8*	10 ± 3*	10.3 ± 3.0*
Lung-R	mean dose (cGy)	16 ± 8	15.3 ± 8.5	14.9 ± 7. 0*	15.5 ± 7.7

*Statistically significant difference ($p < 0.05$) in pairwise comparisons compared to the partial arc plan.

5 Conclusions

The knowledge-based partial arc model for rapid planning of left breast cancer accurately predicts the DVH of OARs. However, before performing dose prediction, physical parameters such as radiation field width and planned avoidance structures should be considered to reduce the risk of low-dose exposure to OARs and secondary cancer.

Data availability statement

The original contributions presented in the study are included in the article/supplementary material. Further inquiries can be directed to the corresponding author.

Author contributions

HG: Conceptualization, Data curation, Methodology, Writing – original draft, Writing – review & editing. ZL: Data curation, Formal analysis, Resources, Writing – original draft, Writing – review & editing. JZ: Data curation, Formal analysis, Methodology, Writing – original draft, Writing – review & editing. HZ: Conceptualization, Formal analysis, Writing – original draft, Writing – review & editing.

Funding

The author(s) declare that no financial support was received for the research and/or publication of this article.

Conflict of interest

The authors declare that the research was conducted in the absence of any commercial or financial relationships that could be construed as a potential conflict of interest.

Generative AI statement

The author(s) declare that no Generative AI was used in the creation of this manuscript.

Publisher's note

All claims expressed in this article are solely those of the authors and do not necessarily represent those of their affiliated organizations, or those of the publisher, the editors and the reviewers. Any product that may be evaluated in this article, or claim that may be made by its manufacturer, is not guaranteed or endorsed by the publisher.

References

1. Medical Policy and Administration Agency and National Health Commission of the People's Republic of China. Breast cancer treatment guidelines (2022 edition). *Chin J Oncol.* (2023) 45:803–33. doi: 10.3760/cma.j.cn112152-20230706-00281

2. Zhang Y, Huang Y, Ding S, Yuan X, Shu Y, Liang J, et al. A dosimetric and radiobiological evaluation of VMAT following mastectomy for patients with left-sided breast cancer. *Radiat Oncol.* (2021) 16:171. doi: 10.1186/s13014-021-01895-2

3. Zhang J, Jing S, Jing B, Sun W, Wang Q, Wang J, et al. Automatic VMAT on the left side Intensity-modulated radiotherapy planning. *Chin J Cancer Prev Treat.* (2021) 28:753–8. doi: 10.16073/j.cnki.cjcpt.2021.10.07

4. Feng X, Zhang Y, Yue Q, Xiao B, Zhang Y, Li R, et al. Dosimetry study of three radiotherapy methods in whole milk, upper and lower clavicle and inner milk lymph node region after left breast conserving surgery. *Chin J Clin Oncol.* (2020) 47:397–401. doi: 10.3969/j.issn.1000-8179.2020.08.405

5. Xu B, Cao Y, Li J. Dosimetry comparison between H-IMRT technique and H-VMAT technique in post-operative radiotherapy for breast adenocarcinoma. *J Pract Oncol.* (2021) 35:511–6. doi: 10.11904/j.issn.1002-3070.2021.06.005

6. Gao Y, Zhong H, Li Z, Zhang G, Li L, Shi Y, et al. Meta-analysis of the dose ratio between intensity modulated arc therapy and intensity modulated radiotherapy after modified radical surgery for breast cancer. *Chin J Radiat Oncol.* (2021) 30:1159–66. doi: 10.3760/cma.j.cn113030-20200818-00429

7. Virén T, Heikkilä J, Myllyoja K, Koskela K, Lahtinen T, Seppälä J. Tangential volumetric modulated arc therapy technique for left-sided breast cancer radiotherapy. *Radiat Oncol.* (2015) 10:79. doi: 10.1186/s13014-015-0392-x

8. Fogliata A, De Rose F, Franceschini D, Stravato A, Seppälä J, Scorsetti M, et al. Critical appraisal of the risk of secondary cancer induction from breast radiation therapy with volumetric modulated arc therapy relative to 3D conformal therapy. *Int J Radiat Oncol Biol Phys.* (2018) 100:785–93. doi: 10.1016/j.ijrobp.2017.10.040

9. Tang C, Gong C, Liu B, Guo H, Dai Z, Yuan J, et al. Feasibility and dosimetric evaluation of single- and multi-isocentre stereotactic body radiation therapy for multiple liver metastases. *Front Oncol.* (2023) 13:1144784. doi: 10.3389/fonc.2023.1144784

10. Inoue E, Doi H, Monzen H, Tamura M, Inada M, Ishikawa K, et al. Dose-volume histogram analysis of knowledge-based volumetric-modulated arc therapy planning in postoperative breast cancer irradiation. *In Vivo.* (2020) 34:1095–101. doi: 10.21873/invivo.11880

11. Lou CY, Cheng Y, Lei HC, Zhu W, Wang X, Wang X, et al. The Eclipse application interface combined with RapidPlan's automated plan design approach for clinical practice. *Chin J Radiat Oncol.* (2022) 31:49–54. doi: 10.3760/cma.j.cn113030-20210201-00057

12. Apaza Blanco OA, Almada MJ, Garcia Andino AA, Zunino S, Venencia D. Knowledge-based volumetric modulated arc therapy treatment planning for breast cancer. *J Med Phys.* (2021) 46:334–40. doi: 10.4103/jmp.JMP_51_21

13. Gui JL, Zhou XY. Application of Rapidplan optimization module in intensity modulated radiotherapy after left breast cancer surgery. *Chongqing Med.* (2022) 009:051. doi: 10.3969/j.issn.1671-8348.2022.09.016

14. Frederick A, Roumeliotis M, Grendarova P, Quirk S. Performance of a knowledge-based planning model for optimizing intensity-modulated radiotherapy plans for partial breast irradiation. *J Appl Clin Med Phys.* (2022) 23:e13506. doi: 10.1002/acm2.13506

15. Kang Z. Using dose volume histogram (DVH) predictions to improve the plan quality of helical tomotherapy (HT). *Med Dosim.* (2024) 49:363–71. doi: 10.1016/j.meddos.2024.05.002

16. Hirashima H, Nakamura M, Mukumoto N, Ashida R, Fujii K, Nakamura K, et al. Reducing variability among treatment machines using knowledge-based planning for head and neck, pancreatic, and rectal cancer. *J Appl Clin Med Phys.* (2021) 22:245–54. doi: 10.1002/acm2.13316

17. Roach D, Wortel G, Ochoa C, Jensen HR, Damen E, Vial P, et al. Adapting automated treatment planning configurations across international centres for prostate radiotherapy. *Phys Imaging Radiat Oncol.* (2019) 10:7–13. doi: 10.1016/j.phro.2019.04.007

18. Tudda A, Castriconi R, Benecchi G, Cagni E, Cicchetti A, Dusi F, et al. Knowledge-based multi-institution plan prediction of whole breast irradiation with tangential fields. *Radiother Oncol.* (2022) 175:10–6. doi: 10.1016/j.radonc.2022.07.012

19. Costa E, Richir T, Robilliard M, Bragard C, Logerot C, Kirova Y, et al. Assessment of a conventional volumetric-modulated arc therapy knowledge-based planning model applied to the new Halcyon© O-ring linac in locoregional breast cancer radiotherapy. *Phys Med.* (2021) 86:32–43. doi: 10.1016/j.ejmp.2021.05.022

20. Sakai Y, Kubo K, Matsumoto K, Hosono M, Monzen H. Feasibility of coplanar VMAT for brain metastases using halcyon with knowledge-based planning from non-coplanar plan. *In Vivo*. (2025) 39:894–901. doi: 10.21873/invivo.13893

21. Cagni E, Botti A, Micera R, Galeandro M, Sghedoni R, Orlandi M, et al. Knowledge-based treatment planning: An inter-technique and inter-system feasibility study for prostate cancer. *Phys Med*. (2017) 36:38–45. doi: 10.1016/j.ejmp.2017.03.002

22. Fogliata A, Parabicoli S, Paganini L, Reggiori G, Lobefalo F, Cozzi L, et al. Knowledge-based DVH estimation and optimization for breast VMAT plans with and without avoidance sectors. *Radiat Oncol*. (2022) 17:200. doi: 10.1186/s13014-022-02172-6

23. Kim H, Jung J, Jung H, Jeong J, Lee D, Jeong HW, et al. Comparison of jaw mode and field width for left-breast cancer using tomoDirect three-dimensional conformal radiation therapy: A phantom study. *Healthcare (Basel)*. (2022) 10:2431. doi: 10.3390/healthcare10122431

24. Zhang Y, Fu W, Brandner E, Percinsky S, Moran M, Huq MS. Minimizing normal tissue low dose bath for left breast Volumetric Modulated Arc Therapy (VMAT) using jaw offset. *J Appl Clin Med Phys*. (2024) 25:e14365. doi: 10.1002/acm2.14365

25. Billaudeau A, Costa E, Vu-Bezin J. Scripting a planning avoidance structure to perform simultaneous integrated boost breast on Halcyon linear accelerators. *Med Dosim*. (2024) 49:328–31. doi: 10.1016/j.meddos.2024.04.003

26. Boman E, Rossi M, Haltamo M, Skyttä T, Kapanen M. A new split arc VMAT technique for lymph node positive breast cancer. *Phys Med*. (2016) 32:S1120–1797(16)30954-1. doi: 10.1016/j.ejmp.2016.10.012

27. Rossi M, Virén T, Heikkilä J, Seppälä J, Boman E. The robustness of VMAT radiotherapy for breast cancer with tissue deformations. *Med Dosim*. (2021) 46:86–93. doi: 10.1016/j.meddos.2020.09.005

28. Wu H, Jiang F, Yue H, Li S, Zhang Y. A dosimetric evaluation of knowledge-based VMAT planning with simultaneous integrated boosting for rectal cancer patients. *J Appl Clin Med Phys*. (2016) 17:78–85. doi: 10.1120/jacmp.v17i6.6410

29. Castriconi R, Esposito PG, Tudda A, Mangili P, Broggi S, Fodor A, et al. Replacing manual planning of whole breast irradiation with knowledge-based automatic optimization by virtual tangential-fields arc therapy. *Front Oncol*. (2021) 11:712423. doi: 10.3389/fonc.2021.712423

30. Redapi L, Rossi L, Marrazzo L, Penninkhof JJ, Pallotta S, Heijmen B. Comparison of volumetric modulated arc therapy and intensity-modulated radiotherapy for left-sided whole-breast irradiation using automated planning. *Strahlenther Onkol*. (2022) 198:236–46. doi: 10.1007/s00066-021-01817-x

31. Waheed A, Butt S, Ishtiaq A, Mehreen S, Raza M, Yousaf M. Dosimetric comparison of whole breast radiotherapy using field-in-field and volumetric modulated arc therapy techniques in left-sided breast cancer patients. *Cureus*. (2021) 13:e15732. doi: 10.7759/cureus.15732

32. Grantzau T, Mellemkjær L, Overgaard J. Second primary cancers after adjuvant radiotherapy in early breast cancer patients: a national population based study under the Danish Breast Cancer Cooperative Group (DBCG). *Radiother Oncol*. (2013) 106:42–9. doi: 10.1016/j.radonc.2013.01.002

33. Ramin C, Veiga LHS, Vo JB, Curtis RE, Bodelon C, Aiello Bowles EJ, et al. Risk of second primary cancer among women in the Kaiser Permanente Breast Cancer Survivors Cohort. *Breast Cancer Res*. (2023) 25:50. doi: 10.1186/s13058-023-01647-y

34. Stovall M, Smith SA, Langholz BM, Boice JD Jr, Shore RE, Andersson M, et al. Dose to the contralateral breast from radiotherapy and risk of second primary breast cancer in the WECARE study. *Int J Radiat Oncol Biol Phys*. (2008) 72:1021–30. doi: 10.1016/j.ijrobp.2008.02.040

35. Jung S, Kim JI, Park JM, Shin KH, Kim JH, Choi CH. Comparison of treatment plans between static jaw and jaw tracking techniques in postmastectomy intensity-modulated radiation therapy. *Phys Eng Sci Med*. (2022) 45:181–7. doi: 10.1007/s13246-022-01100-y

36. Su J, Dong Y, Zhu Y, Wei X, Huang X. Design VMAT plan of left breast cancer postoperative radiotherapy based on TrueBeam platform. *Chin J Cancer Prev Treat*. (2022) 29:1746–52. doi: 10.16073/j.cnki.cjcpt.2022.24.05

37. Kuo LC, Ballangrud ÅM, Ho AY, Mechalakos JG, Li G, Hong L. A VMAT planning technique for locally advanced breast cancer patients with expander or implant reconstructions requiring comprehensive postmastectomy radiation therapy. *Med Dosim*. (2019) 44:150–4. doi: 10.1016/j.meddos.2018.04.006

38. Yilmaz U, Koylu M, Savas R, Alanyali S. Imaging features of radiation-induced lung disease and its relationship with clinical and dosimetric factors in breast cancer patients. *J Cancer Res Ther*. (2023) 19:S0. doi: 10.4103/jcrt.jcrt_442_21

39. Recht A, Ancukiewicz M, Alm El-Din MA, Lu XQ, Martin C, Berman SM, et al. Lung dose-volume parameters and the risk of pneumonitis for patients treated with accelerated partial-breast irradiation using three-dimensional conformal radiotherapy. *J Clin Oncol*. (2009) 27:3887–93. doi: 10.1200/JCO.2008.20.0121

40. Rodrigues G, Lock M, D'Souza D, Yu E, Van Dyk J. Prediction of radiation pneumonitis by dose - volume histogram parameters in lung cancer–a systematic review. *Radiother Oncol*. (2004) 71:127–38. doi: 10.1016/j.radonc.2004.02.015

41. Darby SC, Ewertz M, McGale P, Bennet AM, Blom-Goldman U, Brønnum D, et al. Risk of ischemic heart disease in women after radiotherapy for breast cancer. *N Engl J Med*. (2013) 368:987–98. doi: 10.1056/NEJMoa1209825

42. Baroudi H, Che Fru L, Schofield D, Roniger DL, Nguyen C, Hancock D, et al. An automated treatment planning portfolio for whole breast radiotherapy. *Med Phys*. (2025) 52:1779–88. doi: 10.1002/mp.17588

frontiers | Frontiers in Oncology

TYPE Systematic Review
PUBLISHED 15 May 2025
DOI 10.3389/fonc.2025.1580848

Check for updates

OPEN ACCESS

EDITED BY
Poonam Yadav,
Northwestern University, United States

REVIEWED BY
Hisashi Nakano,
Niigata University, Japan
Andreas Antzoulas,
General University Hospital of Patras, Greece
Suresh Yadav,
Gandhi Medical College Bhopal, India

*CORRESPONDENCE
Guangjun Li
gjnick829@sina.com

†These authors have contributed equally to this work

RECEIVED 21 February 2025
ACCEPTED 22 April 2025
PUBLISHED 15 May 2025

CITATION
Jia S, Wei W, He Y, Yan H, Zou S, Hao Y, Xiao Q and Li G (2025) The evolution of FLASH radiotherapy: a bibliometric analysis. *Front. Oncol.* 15:1580848. doi: 10.3389/fonc.2025.1580848

COPYRIGHT
© 2025 Jia, Wei, He, Yan, Zou, Hao, Xiao and Li. This is an open-access article distributed under the terms of the Creative Commons Attribution License (CC BY). The use, distribution or reproduction in other forums is permitted, provided the original author(s) and the copyright owner(s) are credited and that the original publication in this journal is cited, in accordance with accepted academic practice. No use, distribution or reproduction is permitted which does not comply with these terms.

The evolution of FLASH radiotherapy: a bibliometric analysis

Shuokai Jia[1,2†], Weige Wei[1,2†], Yiwen He[2], Haichuan Yan[2], Shiru Zou[2], Yanmei Hao[1,2], Qing Xiao[1,2] and Guangjun Li[1,2*]

[1]Department of Radiation Oncology, Cancer Center, West China Hospital, Sichuan University, Chengdu, Sichuan, China, [2]Department of Radiotherapy Physics & Technology, West China Hospital, Sichuan University, Chengdu, Sichuan, China

Introduction: FLASH radiotherapy (FLASH-RT) represents a groundbreaking technique, characterized by its ultra-high dose rate and its remarkable ability to spare normal tissues from damage. Numerous studies on FLASH-RT have been conducted worldwide. However, to date, no comprehensive bibliometric analysis has been performed in this field. This study aims to provide an overview of the advancements in FLASH-RT and identify potential future research directions through bibliometric analysis.

Method and materials: The research team performed a literature search in the Web of Science Core Collection (WOSCC), covering the period from 1967 to 2024, and identified 461 publications relevant to the field of interest. Visualization tools, including VOSviewer, CiteSpace, and Bibliometrix, were employed to analyze countries, institutions, authors, journals, references, and keywords, thereby uncovering research frontiers and hotspots within the field.

Results: In recent years, a considerable number of publications on FLASH-RT have emerged. The United States has the highest number of publications (n=208). The institution with the highest publication count is "Lausanne University Hospital" (n=39). The author with the most citations is "Vozenin, M" (n=31), while the author with the most co-citations is "Montay-Gruel, P" (n=812). Medical Physics is the journal with the highest number of both publications and co-citations, whereas Radiotherapy and Oncology has the highest number of citations. The paper titled "Ultrahigh dose-rate FLASH irradiation increases the differential response between normal and tumor tissue in mice" has the highest number of both citations and co-citations. The most frequently co-occurring keywords is "FLASH radiotherapy" (n=379).

Conclusions: Our bibliometric analysis of FLASH-RT explores key dimensions of the field, including publication trends, international collaborations, influential

journals and authors, and keyword evolution. It assesses FLASH-RT's historical development, current global status, and recent progress in biological mechanisms, equipment, and clinical translation, aiming to offer researchers a comprehensive overview.

KEYWORDS

FLASH radiotherapy (FLASH-RT), ultra-high dose rate (UHDR), biological mechanisms, device, preclinical and clinical trials, bibliometric analysis

1 Introduction

In recent years, cancer has become a major global health challenge, with over half of all patients requiring radiation therapy during treatment (1, 2). This approach utilizes high-energy radiation, including photons, electrons, protons and heavy ions, to damage the DNA of cancer cells, thereby inhibiting their growth and survival (3, 4). However, radiation may also affect surrounding healthy tissues, potentially causing toxicity and long-term complications, highlighting the need for careful management to minimize these risks (5).

For decades, the primary goal of radiotherapy has been to maximize tumor control while minimizing damage to normal tissues, thereby reducing radiation-induced complications. High-energy radiation at conventional dose rates causes damage to tumors while also causing injury to normal tissues. In recent years, advancements in technologies such as Intensity-Modulated Radiation Therapy, Image-Guided Radiation Therapy, particle therapy, and Stereotactic Body Radiation Therapy (SBRT) have considerably improved the therapeutic outcomes (6, 7). Current research is increasingly focused on the development of innovative treatment modalities, with FLASH radiotherapy (FLASH-RT) emerging as one of the most promising techniques (8).

FLASH-RT, characterized by its ultra-high dose rate (UHDR) delivery within an extremely short duration, is believed to induce the "FLASH effect", which enhances normal tissue tolerance while maintaining high therapeutic doses to tumors (9, 10). Numerous studies have demonstrated that FLASH-RT can mitigate toxicity to normal tissues while achieving therapeutic outcomes comparable to conventional radiotherapy (11–14).

The advantages of FLASH-RT have drawn significant scientific interest, sparking global discussions and expanding research efforts. These studies highlight current trends, key characteristics, and the challenges to its sustainable development. Identifying key studies that guide FLASH-RT, support its clinical implementation, and predict future research trends is crucial for advancing this promising modality.

Abbreviations: e-beam, Electron Beam; FLASH-RT FLASH, Radiotherapy; PBS, Pencil Beam Scanning; SBRT, Stereotactic Body Radiation Therapy; SCI-E, Science Citation Index Expanded; UHDR, Ultra-High Dose Rate; VHEE, Very High Energy Electron; WOSCC, Web of Science Core Collection.

Previous retrospective studies have summarized FLASH-RT development, often focusing on specific aspects like radiobiological mechanisms, beam type development, or historical milestones (15–17). Bibliometric analysis, using quantitative methods to identify patterns in knowledge dissemination, offers a scientific approach to exploring trends and future directions within a field. This systematic research approach has been widely applied in radiotherapy. Currently, researchers have conducted bibliometric studies on several radiotherapy techniques, such as proton therapy (18) and SBRT (19). Additionally, bibliometric analyses related to radiotherapy focusing on specific cancer sites, including nasopharyngeal carcinoma (20) and rectal cancer (21). However, to the best of our knowledge, no dedicated bibliometric analysis focusing specifically on FLASH-RT has been reported to date. As the first comprehensive bibliometric study on FLASH-RT, this research aims to map its mechanisms, technological advancements, and clinical translation, providing valuable insights to guide its development and future investigations.

2 Materials and methods

2.1 Data source search strategy

The Web of Science Core Collection (WOSCC) serves as a crucial database for accessing a comprehensive range of global academic information. Highly regarded within the academic community, this database acts as a wealth of academic resources for researchers. For this analysis, the Science Citation Index Expanded (SCI-E) database was chosen as the main data source. On September 23, 2024, a comprehensive search and update of references was performed within the SCI-E, which is particularly well-suited for bibliometric analysis (22). Literature retrieval was completed within one day to avoid citation fluctuations caused by the rapid update of publications.

The key search terms included "FLASH", "ultra-high dose rate", "radiation therapy", "radiotherapy", "clinical trials", "clinical translation", "LINAC", "dose delivery", "proton therapy", and "particle therapy". We have arranged and combined these search terms to develop a rigorous search strategy. We searched and retrieved data on FLASH-RT from the past few decades (from

1967 to 2024), obtaining 1,124 publications. Only publications in the English language were included in this study (n=1111). Our study included only "articles" and "review" (n=677). "Meeting Abstract", "Proceeding Paper", "Editorial Material", "Early Access", "Letter", "Correction", and other types of publications were not considered. Then, we read the titles, abstracts, and even full texts of these publications to screen out papers that were closely related to our research topic, ensuring the purity of the data. Ultimately, only 461 publications were included in the bibliometric analysis. A detailed description of the search strategy can be found in the Supplementary Material, while the screening methodology is outlined in Figure 1.

2.2 Data analysis and visualization

In this research, we utilized VOSviewer (1.6.20), CiteSpace (5.7.R2), and Bibliometrix (4.4.1) to analyze and visualize 461 academic articles. Data on authors, nationalities, affiliations, article titles, journals, citation counts, and keywords were collected for comprehensive analysis.

VOSviewer, a free and open-source software, is highly effective in visualizing bibliometric networks, including relationships between keywords, authors, and publications (23). The counting method adopts "Full counting". The normalization method uses the option "Association strength". The visualization layout employs the "Force Atlas 2 algorithm" to achieve optimal cluster formation. In the results of visual analysis: the color of nodes represents different clusters, the size of nodes indicates the weight of the node, and the thickness of lines represents the strength of the relationship.

CiteSpace identifies research hotspots, emerging trends, and knowledge structures through co-citation and citation burst analyses. We employed the g-index as the literature selection criterion. The network scale was controlled by setting the parameter k=25 in the selection criteria. For burst detection analysis, we adjusted the "Minimum Duration" to 1 to capture emerging trends while maintaining sensitivity to short-term scholarly attention. We adjust the γ parameter (gamma value) to keep the number of "Burst Items" within a reasonable range. For the visualization analysis of CiteSpace, the red bar graph represents the frequent occurrence of keywords, while the blue bar graph indicates infrequent occurrence of keywords. The greater the intensity of the bar graph, the higher the frequency of occurrence.

Bibliometrix, an R-based software, offers extensive bibliometric analysis capabilities, including performance metrics and science mapping across various databases (24). The retrieved 461 articles were exported in BibTeX format to R environment. The exported files contained citation metadata including authors, titles, journals, institutions, etc. Bibliometric diagrams were generated using the bibliometrix R package. The "summary()" function was employed to analyze the most relevant source and country scientific production. The visualization analysis results presented by Bibliometrix indicate that countries marked in blue represent those with national scientific output. The depth of the blue color is proportional to the national scientific output, with darker blue signifying higher national scientific output.

3 Results

3.1 Publication outputs and time trend

The publication trend of FLASH-RT from 1967 to 2024 can be divided into two distinct phases. Initial reports on FLASH date back

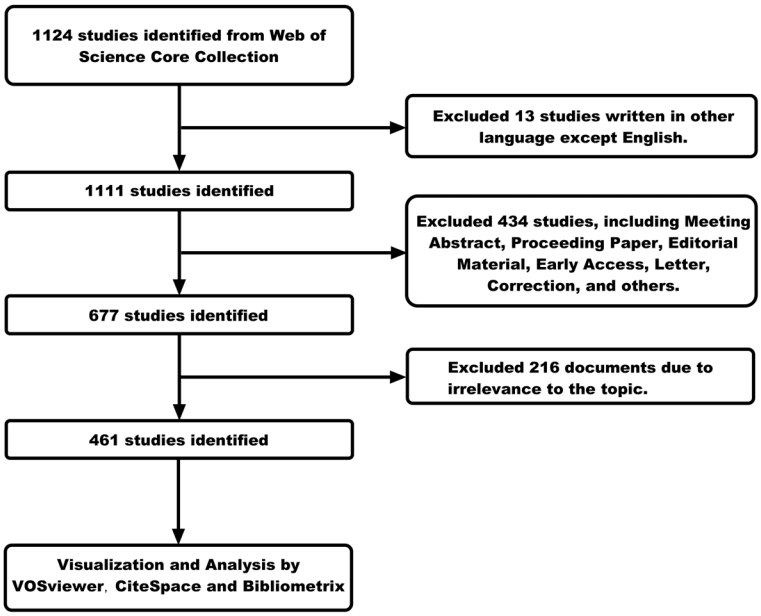

FIGURE 1
Publications screening flowchart.

to 1967. Between 1967 and 2017, publications were sporadic, with a fragmented distribution and several years without relevant articles. In contrast, a marked increase in annual publications has been observed from 2017 to 2024 (Figure 2). To analyze this recent surge, a mathematical model was applied to fit the publication trend. The mathematical model employed in our analysis is $y = 9.5292x^2 - 40.309x + 59.119$ ($R^2 = 0.9973$, $P<0.001$) (Figure 2). Data collection was completed on September 23, 2024, and it is anticipated that the actual number of publications for 2024 will surpass the number reported in the literature.

3.2 Distribution of country and institution

A total of 40 countries have contributed to FLASH-RT from 1967 to 2024. Global scientific productivity was analyzed with Bibliometrix, revealing that the United States exhibits the highest level of scientific output in this area (Figure 3A). An analysis of international collaborations, conducted through VOSviewer, identified two distinct clusters of countries. One cluster, centered around the United States, includes close collaborations with China, Germany, and Switzerland. The other cluster, led by the United Kingdom, is closely associated with France, Italy, and Sweden (Figure 3B). The top five countries by publication volume are the United States (n=208), Switzerland (n=69), China (n=56), Germany (n=53), and the United Kingdom (n=52).

We also mapped the network of collaborations among institutions involved in FLASH-RT research. A total of 700 institutions worldwide contribute to this field, with 74 organizations publishing five or more articles. After excluding two isolated nodes, the remaining 72 institutions were grouped into five clusters (Figure 3C). "Lausanne Univ Hosp" has the highest number of publications (n=39) and exhibits the strongest co-authorship relationships with other institutions. Additionally, we plotted the average age of these institutions based on their years of publication activity, revealing a trend towards increasing institutional engagement in this research area over time (Figure 3D).

3.3 Co-authorship and co-citation between authors

A total of 2,322 authors contributed to the field during the study period. We visualized the co-authorship relationships among authors with more than five publications (Figures 4A, B). After excluding a few isolated nodes, the co-authorship network of 124 authors was revealed, grouped into 11 clusters. The top five authors with the highest publication counts are Vozenin, M (n=31), Petersson, K (n=28), Bailat, C (n=24), Bourhis, J (n=20), and Zhang, R (n=19), all of whom have made significant contributions and exert considerable influence in the field. The co-authorship relationships within each cluster are strong, and there are also significant collaborative links between authors across different clusters.

The analysis of co-citations among authors is equally important. Among the 5,785 authors with co-citation relationships, 50 authors had a significantly higher co-citation count, each exceeding 60. A visual analysis of the co-citation relationships among these authors was conducted (Figure 5). The five authors with over 200 co-citations are Montay-Gruel, P (n=812), Vozenin, M (n=532), Favaudon, V (n=464), Bourhis, J (n=412), and Diffenderfer, E (n=217). These authors play a central role in the field, as evidenced by their high co-citation frequencies.

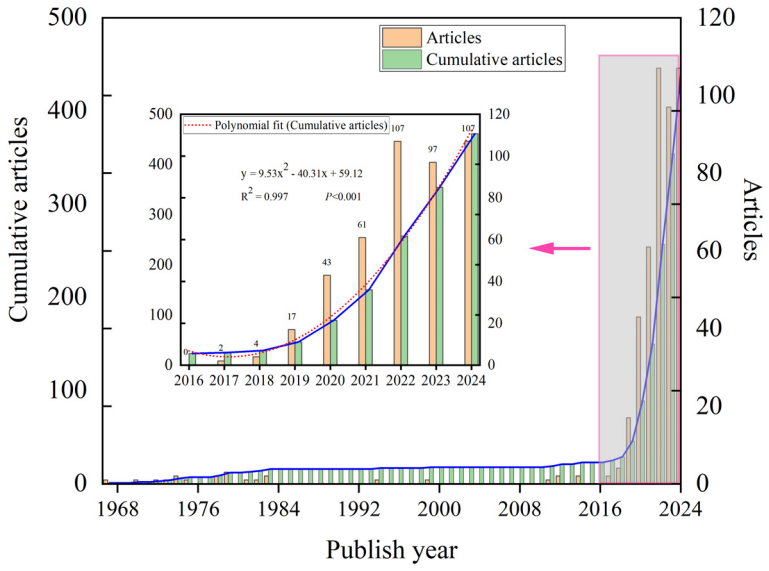

FIGURE 2
Global publication trends on FLASH-RT.

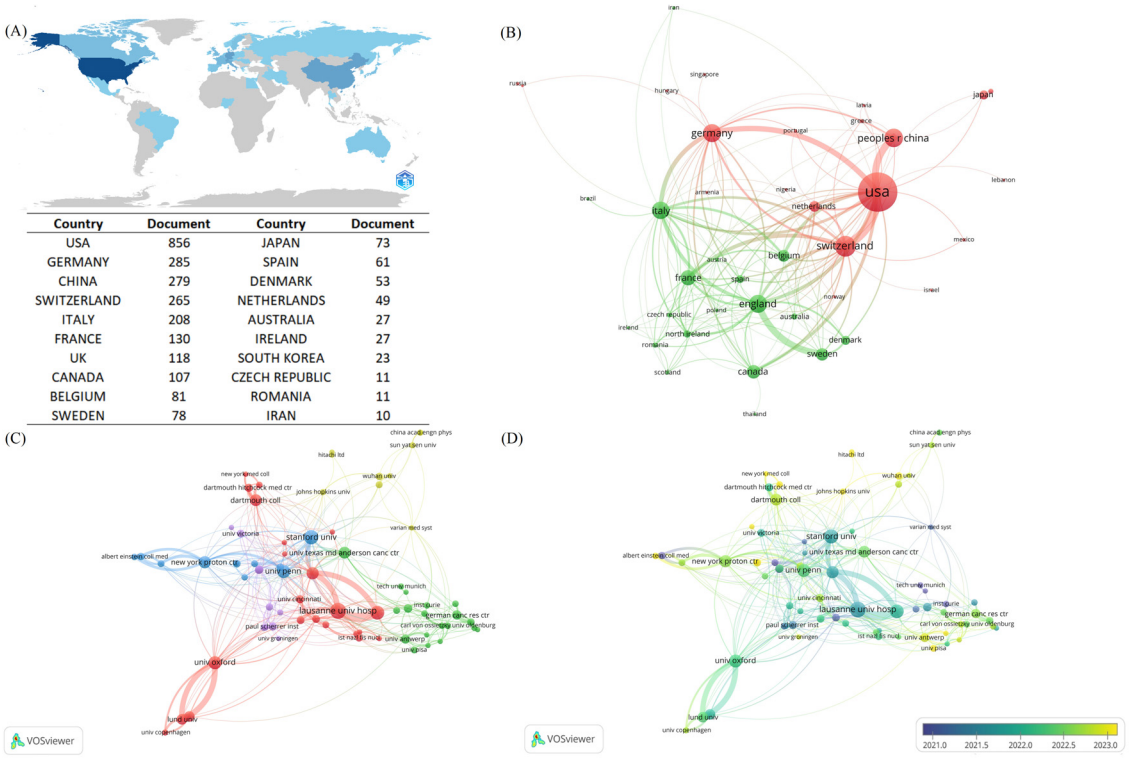

Country	Document	Country	Document
USA	856	JAPAN	73
GERMANY	285	SPAIN	61
CHINA	279	DENMARK	53
SWITZERLAND	265	NETHERLANDS	49
ITALY	208	AUSTRALIA	27
FRANCE	130	IRELAND	27
UK	118	SOUTH KOREA	23
CANADA	107	CZECH REPUBLIC	11
BELGIUM	81	ROMANIA	11
SWEDEN	78	IRAN	10

FIGURE 3
Contributions and co-operative relations between countries and institution. **(A)** Countries marked in blue in the figure represent countries with national scientific production in the FLASH-RT neighborhood, and the degree of blue is proportional to national scientific production, with darker blue representing higher national scientific production. Specific national science production values are also presented in this figure. **(B)** Map of country co-operation. Different colors represent different clusters. A node represents a country, the larger the node the greater the number of publications for that country. The lines between countries represent the co-operation between countries, the thicker the line the stronger the co-operation between countries. **(C)** Institutional co-authorship relationship map. Different colors represent different clusters. The size of the nodes is proportional to the number of publications of the institutions. The thicker the connecting line between the nodes indicates the closer the co-authorship between the two institutions. **(D)** Chart of average year of institutional issuance. Yellower colors indicate a later average year of institutional issuance.

3.4 Visualization and analysis of journals

We also conducted a visual analysis of the journals publishing in the FLASH-RT field. The ten journals with the highest number of articles in this area were identified (Figure 6A). Medical Physics has the most publications (n=89). Additionally, the top five journals based on citation and co-citation counts are presented in Table 1. Radiotherapy and Oncology has the highest number of citations, while Medical Physics leads in co-citations. A co-citation analysis of the journals was also performed (Figure 6B). From a total of 2,375 journals analyzed, only those with more than 30 co-citations were included, resulting in 32 journals being classified into three distinct clusters.

3.5 Citation and co-citation analysis of publications

Among the cited literature, we identified the top 20 most frequently referenced documents (Table 2). These documents were ranked in descending order based on citation count, and their average citations per year were also calculated. A visual analysis of the co-citation relationships among these documents was conducted (Figure 7A). A total of 8,312 documents exhibited co-citation relationships, with 39 documents receiving more than 60 co-citations. These 39 documents were analyzed and categorized into three broad clusters. Additionally, a citation burst analysis was performed, highlighting the 25 documents with the highest citation burst intensity (Figure 7B). One prominent document published in 2014, titled “Ultrahigh Dose-Rate FLASH Irradiation Increases the Differential Response Between Normal and Tumor Tissue in Mice”, stands out with the highest number of citations and co-citations. Following this, we conducted another citation burst analysis, focusing on the publication date of this key document (Figure 7C). This series of analyses clearly identifies the literature that has significantly influenced the FLASH-RT field, providing guidance for future research. It also helps us determine which documents are frequently used together, serving as a theoretical foundation for subsequent studies.

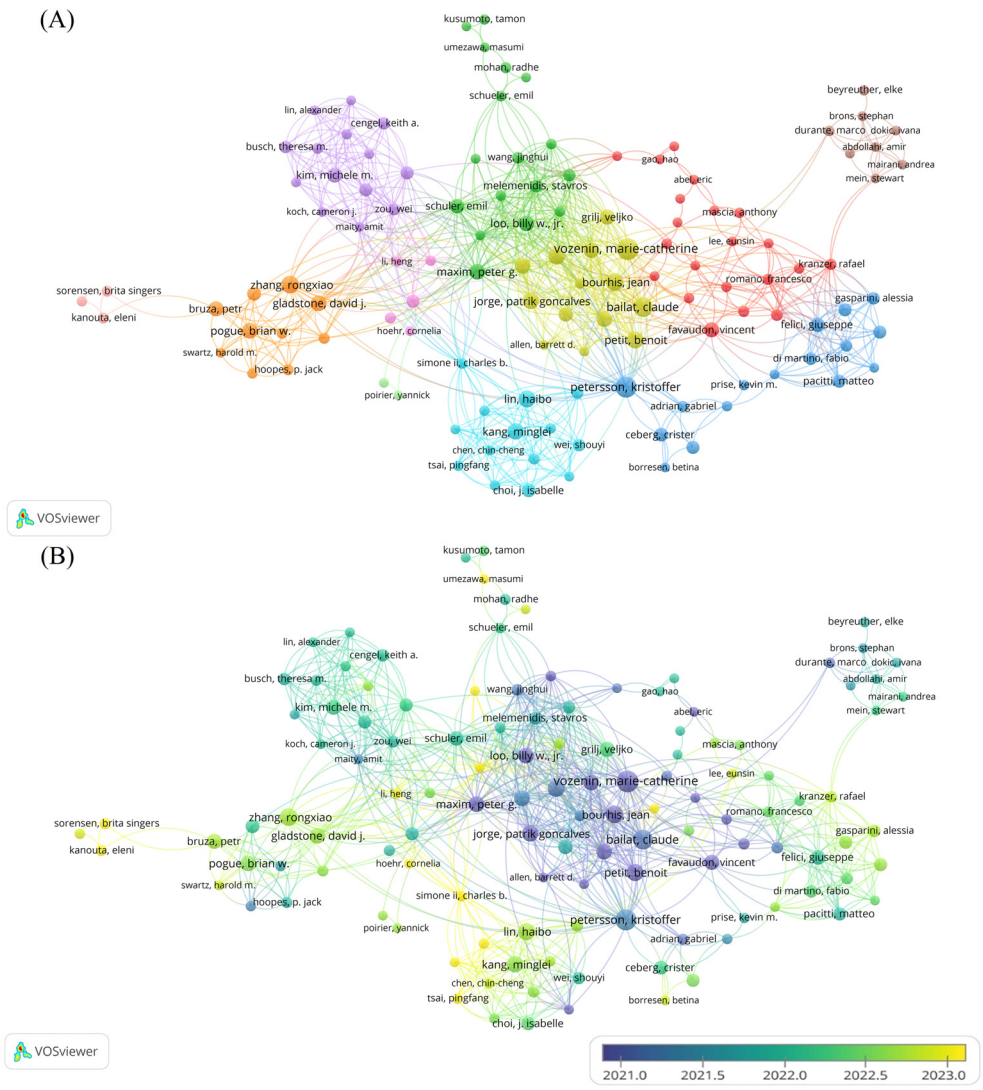

FIGURE 4
Analysis of the characteristics of the author's posting. **(A)** Co-authorship between authors. Different colors represent different clusters. Each node represents an author, the larger the node, the more publications the author has. The line between authors represents the co-authorship relationship between authors, the thicker the line, the stronger the co-authorship relationship between authors. **(B)** Graph of the average number of years authors have been posting. Different colors represent different years of posting.

3.6 Visualization and analysis of keywords

We conducted a visual analysis of the keywords in the included articles. First, we generated a co-occurrence map of the keywords, along with a keyword average age map (Figures 8A, B). This analysis focused on 54 keywords, each appearing at least eight times. The keywords were grouped into three clusters to highlight their relationships. The five keywords with the highest co-occurrence counts are "flash radiotherapy" (n=379), "ultra-high dose rate" (n=86), "dosimetry" (n=77), "cells" (n=74), and "dose rates" (n=72). The average age of the keywords reveals shifts in focus over time, with "survival" being replaced in recent years by terms like "flash effect" and "ultra-high dose rate". Additionally, a burst analysis of keywords was performed, identifying the 50 keywords with the highest burst intensity (Figure 8C). The keyword "mammalian cell" exhibited the highest burst intensity.

4 Discussion and critical review

4.1 In-depth analyses of the results sections

In the previous section, we observed a growing body of research on FLASH-RT by scholars in recent years. Among the 461 publications included in our analysis, the overwhelming majority were original articles (n=417). A substantial proportion of these publications appeared in high-impact journals within the fields of

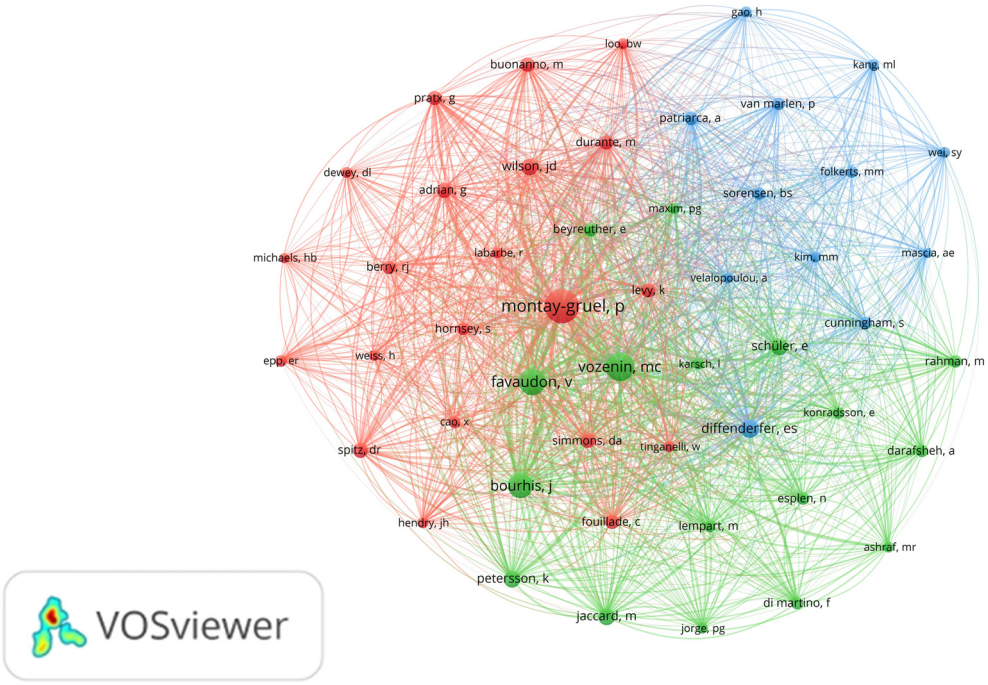

FIGURE 5
Co-citation analysis between authors. Different colors represent different clusters. Each node represents an author, and the larger the node, the more co-citations the author has. A line between different authors represents a co-citation relationship between authors, the thicker the line, the more co-citations between two authors.

radiation oncology and medical physics. Unlike previous reviews that provided in-depth summaries of specific FLASH-RT topics, this review uses bibliometrics to offer a comprehensive overview of the entire field. Existing bibliometric analyses in radiation therapy have involved FLASH-RT. Song, G et al. highlighted proton FLASH as an upcoming research hotspot, which aligns with our findings (18). Our study further enriches this discourse by providing a comprehensive examination of FLASH-RT's development and status. We employed bibliometric analysis to assess the full spectrum of research methods used in these publications, yielding noteworthy results. These results can largely be attributed to three key factors: the mechanisms underlying the FLASH effect remain unclear and are the focus of extensive research; the devices and equipment utilized for FLASH-RT are not widely accessible and have been rapidly evolving in recent years and the clinical transition of FLASH-RT presents a challenge that awaits resolution (40–42).

Since 2017, FLASH-RT publications have experienced exponential growth, likely attributable to several key factors. The FLASH concept was first proposed in 2014 (10). Its impact was immediate, yet related research efforts took time to develop. The middle three years were occupied with experiment design, equipment preparation, and the writing and approval of papers. The 2017 publications that observed the FLASH effect marked a turning point (13). The successful replication of the FLASH effect and its scientific potential are the primary reasons for the subsequent surge in publications.

While 40 countries contributed to this field, the predominant countries accounted for the vast majority of publications. The United States leads in FLASH-RT publications due to government funding, exemption policies, equipment for generating UHDR beams, and the FLASH Alliance. The National Institutes of Health, the largest global public funder of biomedical research, supports many scientific projects. In June 2022, the U.S. Food and Drug Administration approved the Investigational Device Exemption for the FAST-02 human clinical trial, advancing FLASH-RT research. The U.S. also has equipment infrastructure as the largest proton therapy market with the most operating proton centers. American firms, such as Varian, offer crucial technological support. Varian's ProBeam proton therapy system was designed with the capability to deliver UHDR proton beams incorporated from the outset. Varian formed the FlashForward consortium in 2018, uniting thirteen institutions on UHDR proton therapy for cancer. Similar alliances exist in Europe, like the FLASHKNiFE alliance announced by PMB, bringing together top European institutions. These alliances promote international cooperation. Concurrently, we posit that inter-institutional co-authorship is somewhat shaped by inter-country cooperation. We observe that in the institutional co-authorship graph, institutions within the same cluster originate from different countries, further illustrating the concept of national co-authorship. For instance, the institutions in the red cluster represent seven different countries: Switzerland, the United Kingdom, the United States, Sweden, Italy, Denmark, and Germany.

The co-authorship clusters are also characterized by a tendency for different clusters to focus on specific types of FLASH; the more similar the types, the closer the clusters are to each other, resulting in a

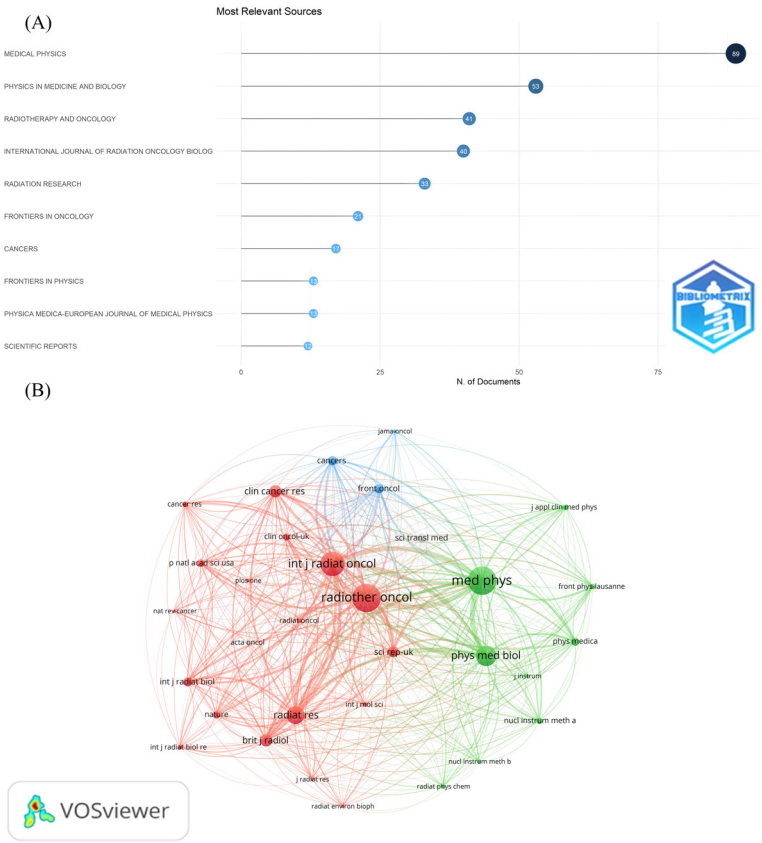

FIGURE 6
Visual analysis of journal publications. **(A)** The most relevant journals. The Y-axis labels the name of the journal and the X-axis indicates the number of publications in the corresponding journal. **(B)** Journal co-citation relationship mapping. Different colors represent different clusters. Each node represents a journal, and the larger the node, the more co-cited the journal is. The line between the nodes indicates the co-citation relationship between journals, and the thicker the line, the closer the co-citation relationship.

higher degree of integration. Vozenin, Marie-Catherine's cluster concentrates on the biological effects of FLASH. Zhang, Rongxiao's cluster is centered around the mechanisms underlying FLASH effect. The cluster related to Zhang, Rongxiao emphasizes the mechanisms of the FLASH effect. The co-citation relationships among the authors highlight the overlap of their research interests and their influence within the FLASH-RT field. An author's co-citation count is influenced by the number of high-impact articles and the total number of publications in their related field, and there exists a positive correlation between the two. We analyzed the publication patterns of the three most influential authors in FLASH-RT research. They entered the field early and gained prominence through high-impact reviews, experiments observing the FLASH effect, or new mechanisms that caused widespread repercussions.

Several factors contribute to the findings of the co-citation analysis of the journals. The journals in the red cluster feature articles on FLASH research with a broader focus, exemplified by Radiotherapy and Oncology (n=2259) and International Journal of Radiation Oncology Biology Physics (n=1748). Conversely, the journals in the green cluster primarily focus on research devices and techniques related to FLASH. Medical Physics (n=2292) and Physics in Medicine and Biology (n=1310) are among the core

TABLE 1 Top five journals for citations and co-citations.

Rank	Top 5 popular journals	Citations (n)	Top 5 cited journals	Co-citations (n)
1	Radiotherapy and Oncology	2945	Medical Physics	2292
2	Medical Physics	1611	Radiotherapy and Oncology	2259
3	International Journal of Radiation Oncology Biology Physics	1535	International Journal of Radiation Oncology Biology Physics	1748
4	Clinical Cancer Research	823	Physics in Medicine and Biology	1310
5	Radiation Research	750	Radiation Research	1056

TABLE 2 The 20 documents with the highest number of citations.

Paper	DOI	Total Citations	Normalized TC
FAVAUDON V, 2014, SCI TRANSL MED (10)	10.1126/scitranslmed.3008973	803	1.82
VOZENIN MC, 2019, CLIN CANCER RES (25)	10.1158/1078-0432.CCR-17-3375	462	2.59
MONTAY-GRUEL P, 2017, RADIOTHER ONCOL (13)	10.1016/j.radonc.2017.05.003	423	1.42
BOURHIS J, 2019, RADIOTHER ONCOL-a (26)	10.1016/j.radonc.2019.06.019	400	2.24
MONTAY-GRUEL P, 2019, PROC NATL ACAD SCI U S A (27)	10.1073/pnas.1901777116	326	1.83
VOZENIN MC, 2019, CLIN ONCOL (28)	10.1016/j.clon.2019.04.001	316	1.77
WILSON JD, 2020, FRONT ONCOL (29)	10.3389/fonc.2019.01563	305	4.33
BOURHIS J, 2019, RADIOTHER ONCOL (9)	10.1016/j.radonc.2019.04.008	300	1.68
DIFFENDERFER ES, 2020, INT J RADIAT ONCOL BIOL PHYS (30)	10.1016/j.ijrobp.2019.10.049	283	4.01
MONTAY-GRUEL P, 2018, RADIOTHER ONCOL (12)	10.1016/j.radonc.2018.08.016	245	1.67
SPITZ DR, 2019, RADIOTHER ONCOL (31)	10.1016/j.radonc.2019.03.028	182	1.02
PATRIARCA A, 2018, INT J RADIAT ONCOL BIOL PHYS (32)	10.1016/j.ijrobp.2018.06.403	180	1.23
BUONANNO M, 2019, RADIOTHER ONCOL (33)	10.1016/j.radonc.2019.02.009	177	0.99
SCHULER E, 2017, INT J RADIAT ONCOL BIOL PHYS (34)	10.1016/j.ijrobp.2016.09.018	171	0.58
SIMMONS DA, 2019, RADIOTHER ONCOL (35)	10.1016/j.radonc.2019.06.006	163	0.91
FOUILLADE C, 2020, CLIN CANCER RES (36)	10.1158/1078-0432.CCR-19-1440	161	2.28
DURANTE M, 2018, BR J RADIOL (37)	10.1259/bjr.20170628	161	1.10
ESPLEN N, 2020, PHYS MED BIOL (38)	10.1088/1361-6560/abaa28	159	2.26
MONTAY-GRUEL P, 2021, CLIN CANCER RES (11)	10.1158/1078-0432.CCR-20-0894	155	4.64
ADRIAN G, 2020, BR J RADIOL (39)	10.1259/bjr.20190702	144	2.04

journals, contributing significantly to the volume of articles with high co-citation counts. In contrast, the blue section is dedicated to examining the feasibility of FLASH applications for treating specific clinical diseases, though it currently holds less influence in the FLASH-RT field.

The five keywords with the most co-occurrences center around the radiotherapy domain, suggesting that the FLASH technique, characterized by UHDR, is broadly acknowledged within this field. The remaining keywords, concerning both biological mechanisms and devices, emphasize the implementation of FLASH-RT in clinical practice. The term "mammalian cell" exhibits the highest explosive frequency, attributed to continuous preclinical and clinical trials conducted from the 1970s to the present day.

4.2 Biological mechanisms of FLASH-RT

So far, the biological mechanism of FLASH-RT is not clear, but some popular viewpoints have emerged. In the previous keyword clustering analysis, we can see "hypoxia" (n=12), "depletion" (n=12), "oxygen" (n=22), "kinetics" (n=11) and "oxygen depletion" (n=41). This is closely related to the oxygen depletion hypothesis of FLASH-RT. The frequent occurrence of related keywords depends on the controversy and discussion caused by this hypothesis.

As early as 1959, studies revealed that increasing the radiation dose rate could diminish the radiation susceptibility of Salmonella and enhance its survival (43). Subsequent experiments on mammalian cells have yielded similar results, with MILL et al. demonstrating that mammalian cells can repair sub-lethal DNA damage following irradiation at UHDR (44). Early researchers postulated that the decreased radiosensitivity induced by high dose rates was associated with a low oxygen environment (45).

The oxygen depletion hypothesis was the first proposed mechanism for the FLASH effect (28). It initially gained traction due to two factors. First, *in vitro* cell experiments from the last century directly implicated oxygen in radiation responses. Second, it aligns with traditional radiobiological views that hypoxic cells or tissues are more radiation-resistant (39, 46). While this hypothesis initially explained the FLASH effect, numerous studies have since shown it cannot fully account for the phenomenon. Hu et al.'s computer model demonstrated that the hypoxic environment from UHDR irradiation of normal tissues does not reach radiation-resistance levels (47). Moreover, under the same dose conditions, oxygen consumption by tissues from UHDR irradiation is even less than from conventional radiotherapy (48, 49). Research on reactive oxygen species, free radical recombination, and tissue antioxidant systems also challenges the oxygen depletion hypothesis (50, 51). The interaction mechanisms between particle orbits proposed by

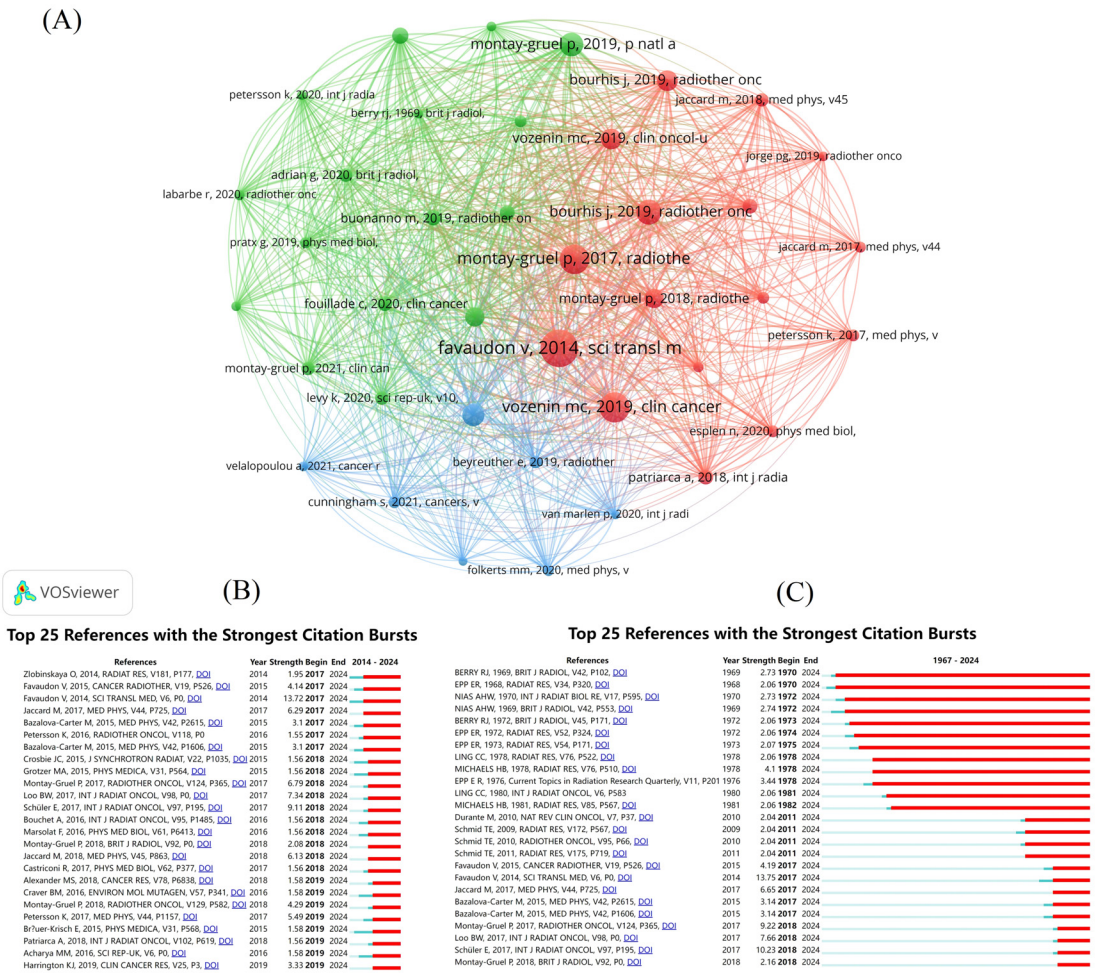

FIGURE 7
Visual analysis of publications. **(A)** Literature co-citation analysis mapping. Different colors represent different clusters. A node represents a piece of literature, and the larger the node is, the more co-citations the literature has. The line between the nodes represents the co-citation relationship between the documents, and the thicker the line, the stronger the co-citation relationship between the documents. **(B)** Citation explosion graphs for literature from 1967-2024. **(C)** Citation explosion graphs for literature from 2014-2024.

researchers further support these alternative theories (52, 53). Collectively, these findings suggest that oxygen depletion is just one factor contributing to the FLASH effect.

The immune hypothesis presents another widely accepted perspective on the biological mechanism of FLASH-RT. Although its number of relevant studies is far less than that of the oxygen depletion hypothesis, some results have been achieved. This hypothesis posits that UHDR elicit a distinct immune response within the immune system, subsequently triggering the FLASH effect. In 2020, Jin et al. were pioneers in proposing the explicit hypothesis that UHDR significantly diminishes the cytotoxic effects on circulating immune cells (54). The significance of the inflammatory response in the FLASH effect has been acknowledged in relatively early research (55). Additionally, there have been advancements in studies that specifically target immune cells within the circulatory system. The researchers employed two distinct modeling approaches to examine the effects of continuous partial body irradiation and pulsed irradiation on the levels of surviving blood lymphocytes. They concluded that human blood lymphocyte populations recovered more rapidly from continuous partial irradiation at UHDR compared to conventional dose rates (56, 57). Research on the immunological hypothesis of FLASH-RT is limited, with few comprehensive reviews such as high-quality meta-analyses or biosignal analyses. The number of studies on immunological mechanisms is small, and several critical issues need addressing. Previous research has not clearly identified the specific immune response mechanisms activated by UHDR irradiation. Given that only a small fraction of immune cells are in the circulating blood pool, the mechanism by which this triggers the FLASH effect remains unclear. The FLASH effect induced by UHDR irradiation should be clearly linked to irradiation parameters and the quantity of irradiated immune cells. Resolving these issues will deepen the impact of the immunological hypothesis.

Beyond the two primary hypotheses, there are additional perspectives. For instance, one question is whether the tumor microenvironment influences the FLASH effect (58, 59). Collectively, the exploration of biological mechanisms associated

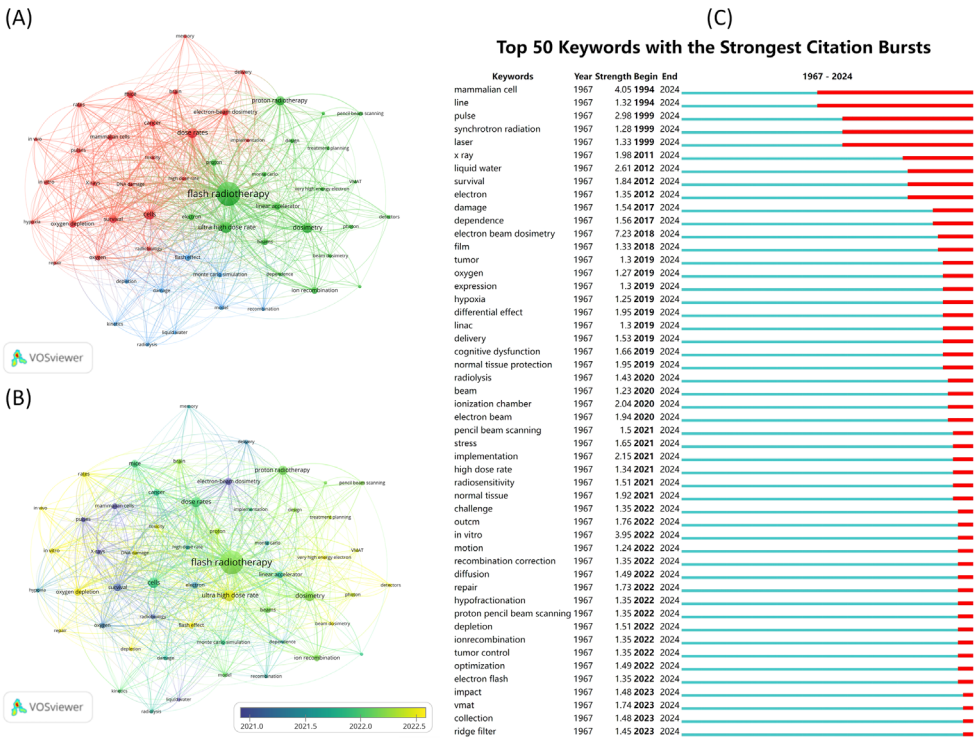

FIGURE 8
Visual analysis of keywords. **(A)** Keyword co-occurrence analysis. Different colors represent different clusters. Each node represents a keyword, and the larger the node, the higher the frequency of this keyword. The line between the nodes indicates a co-occurrence relationship between the keywords, and the thicker the line, the more frequent the co-occurrence of the two. **(B)** Keyword average year graph. Shows the average year in which keywords appear. **(C)** Keyword eruption chart.

with FLASH is thorough and profound. Although new questions continually emerge from the latest research findings, this is an essential process for the future advancement of FLASH-RT.

4.3 Device basis for the realization of UHDR

In order to attain UHDR for application in tumor therapy, appropriate device support is crucial. Devices can be categorized into four types according to the radiation type: electrons, protons, X-rays, and heavy ions. Combined with the results of the bibliometric analysis, the current status of the development of FLASH-RT for the four ray types is different.

4.3.1 Current status of development of electronic FLASH-RT

The keywords “electron” (n=26), “electron-beam dosimetry” (n=37) and “very high energy electron” (n=12) are related to electron FLASH-RT. Evidently, Electronic FLASH-RT has evolved more rapidly and there are more studies on it.

The availability of UHDR the electron-beam (e-beam) surpasses that of the other three radiation types, making their transition from preclinical experiments to clinical applications a logical priority. UHDR electron beams can be generated using specialized miniaturized accelerators or modified medical linear electron accelerators (60, 61). In early 2014, the Oriatron eRT6 linear accelerator, developed by PMB-Alcen, was installed at the University Hospital of Lausanne. This accelerator fulfills the demand for UHDR and high precision radiotherapy equipment for FLASH-RT and represents the first model specifically designed for e-beam FLASH-RT (62). Following this, SIT Sordina developed the ElectronFLASH accelerator, specifically dedicated to research in electron FLASH-RT (63). Modifications and upgrades to existing clinical accelerators can also effectively yield the UHDR e-beam, as illustrated by Garty et al.’s adaptation of a decommissioned Varian Clinac to deliver such beams (64). Successful modifications were also made to two clinical accelerators produced by Medtec (Elekta Precise, Elekta AB) (65). This year, Sloop et al. proposed a design approach that would allow Clinacs to switch between conventional and UHDR modes (66). The enhancement of the classical e-beam accelerator Mobetron has also shown progress in the delivery of the UHDR e-beam (67).

Unfortunately, the penetration depth of the e-beam is quite limited, which may constrain their future applications. Intraoperative radiotherapy represents a promising development for e-beam FLASH-RT, allowing for e-beam therapy in suitable cases of breast, rectal, and pancreatic cancers (68). Very high energy electron (VHEE) beams show potential for treating deep tumors, but they encounter significant challenges (69). As of now, there are no VHEE beams devices available for clinical application, and related studies primarily utilize Monte Carlo techniques for beam modeling (70).

Accurate dose measurement is crucial for the advancement of radiotherapy. The frequency with which the term "detectors" (n=10) appears reflects the progress of FLASH-RT in this area. Initially, Gafchromic EBT-XD films and Advanced Markus parallel plate ionization chambers were employed for the dosimetry of electron beam FLASH (71, 72). Following this, researchers have developed several new devices for e-beam FLASH dosimetry, particularly including: e-beam current transformers, silicon carbide detectors, and diamond detectors (73–75). In developing new equipment, existing dose and detection tools are sometimes employed to assess the accuracy of the new devices in dose monitoring. Gafchromic EBT-XD film and flashDiamond detectors are utilized as comparison standards in the development of new devices (76, 77).

4.3.2 Current status of proton FLASH-RT

Proton radiotherapy is an advanced technique characterized by its unique "Bragg peak" dose deposition, which maximally delivers doses to tumor tissue while minimizing exposure to normal tissues (78). Due to the unique physical properties of proton beams, it is anticipated that they will be capable of treating deep tumors in the future, thereby bridging the gap left by electronic FLASH-RT. In clinical applications of proton radiotherapy, achieving complete tumor coverage requires the diffusion of the original Bragg peak to create an Spread-out Bragg Peak. "Proton" (n=27), "proton radiotherapy" (n=57) and "pencil beam scanning" (n=13), the frequency of these keywords related to proton FLASH-RT reflects its rapid development and the large number of related studies.

In 2020, numerous studies on proton FLASH-RT were conducted. Diffenderfer et al. developed a novel radiotherapy device that employs double-scattered protons to deliver FLASH proton beams guided by computed tomography, and conducted dosimetric verification (30). Darafsheh, A et al. laid the groundwork for preclinical studies by modifying the clinical Mevion HYPERSCAN(R) synchrotron to deliver UHDR proton beams (79). Pencil beam scanning (PBS) is a high-precision, low-side-effect, personalized proton therapy technology with extensive applications and significant therapeutic potential, capable of generating qualified UHDR proton beams (80, 81). Folkerts et al. devised a method for calculating proton field dose rate distributions for PBS, further advancing the research and potential applications of PBS FLASH-RT. Following their research, there has been a continuous stream of enhancements to the original technique along with the creation of new methods (82). In 2021, Nesteruk et al. adapted a clinical PBS to allow for the delivery of proton beams with dose rates ranging from 1 to 9000 Gy/s (83). The synchrotron, essential for the realization of proton FLASH-RT, has also undergone improvements (84, 85). In 2022, Zhang et al. designed and optimized a ridge filter, which is one of the most promising methods for achieving proton FLASH-RT. The ridge filter is an innovative beam modulation device capable of rapidly modulating the proton beam at a single energy, producing a dose distribution closely resembling that of intensity-modulated proton therapy. This rapid beam modulation capability enables proton FLASH-RT to be administered in a very short time, thereby satisfying the timing requirements for FLASH-RT (86, 87). In 2023, Ding et al. introduced a method to attain UHDR proton beams: spot-scanning proton arc therapy combined with FLASH. They provided the first voxel-based treatment that achieves UHDR while maintaining high dose consistency in proton beam therapy. This technique may also streamline the clinical process by removing the necessity for standardized ridge filters (88).

Devices for dose verification and monitoring in proton FLASH-RT are rapidly advancing as well. Faraday cups, capable of dosimetry and characterization of beam properties, provide real-time monitoring and feedback and are unaffected by dose rate; thus, they are anticipated to be used as dose verification devices for proton FLASH-RT (89, 90). High-resolution 2D transmission ionization chambers have been validated for monitoring dosimetric parameters related to the proton penumbral beam under FLASH conditions (8, 91). Besides the two types of dose monitoring equipment noted above, scintillator detectors, films (EBT3, EBT-XD and OC-1), parallel plate ionization chambers, and amorphous silicon detectors have also shown distinct advantages and potential (92–95).

4.3.3 Current status of development of X-ray FLASH-RT

X-rays are currently the most commonly used type of radiation in radiotherapy. Furthermore, X-rays have been shown to induce the FLASH effect (12). The keywords "X-rays" (n=19) and "Volumetric-Modulated Arc Therapy (n=8)" are related to photon radiotherapy. It can be seen that the number of studies related to X-ray FLASH-RT is low compared to electrons and protons.

Several platforms offer UHDR from high-energy X-rays. However, most are still in the research phase or lack relevant biological evidence (96, 97). A well-established platform for X-ray FLASH research, referred to as "partner", is described below. In 2022, Gao et al. assessed the partner platform developed at the Chengdu Terahertz Free Electron Laser Facility. They achieved promising results, confirming that the partner platform can deliver UHDR X-rays and induce the FLASH effect (98). The platform was subsequently re-evaluated by Yiwei Yang et al., yielding consistent results. Following dose verification using devices such as the EBT3 radiochromic film and a fast current transformer, the experimental platform demonstrated the ability to deliver high-energy X-rays at dose rates exceeding 1000 Gy/s.

The primary types of relevant dose detection equipment include silicon-based sensors, scintillator detectors, color-changing films, and thermoluminescent dosimeters (99–101). Effective thermal management of the X-ray tube is essential because of the high current needed to produce UHDR high-energy X-rays (102). Besides the aforementioned related devices, research on collimators has also been undertaken. The experimentation and optimization of decoupled ring collimators and GRID collimators have yielded potentially effective engineering solutions for X-ray FLASH-RT, while also identifying several parameters that may influence the dose rate (103, 104).

4.3.4 Current status of development of heavy ion FLASH-RT

As a state-of-the-art tumor treatment technology in the 21st century, heavy ion radiotherapy has seen significant development and application globally in recent years. As heavy ion radiotherapy is an emerging technology, the associated equipment base is relatively underdeveloped. But there has been some progress in research related to heavy ion FLASH-RT (105).

In 2023, Yagi et al. proposed that UHDR carbon ion beams could be generated using a medical synchrotron, while also highlighting the potential risk of damage to monitoring devices (106). In 2024, Lang et al. developed a FLASH ionization chamber designed for dosimetry of carbon ion FLASH-RT under low-pressure conditions, using a Faraday cup to confirm its dose-rate dependence (107). A specialized dose detector for UHDR carbon ion beams was also created, capable of measuring dose, dose rate, and dose profile. This development offers insights for the future advancement of related devices: employing large plane-parallel ionization chambers with small electrode spacing may enable more accurate monitoring of the dose in heavy-ion FLASH (108).

While FLASH-RT equipment is rapidly evolving, its development and clinical application face technical barriers. Triggering the FLASH effect requires numerous specific conditions, many of which differ from conventional radiotherapy parameters. A key requirement is an UHDR (40Gy/s), far exceeding existing clinical radiotherapy equipment capabilities. This poses a severe challenge to current accelerator technology. Achieving such a high dose rate demands extremely high beam intensity and stability from accelerators, as well as precise radiation energy delivery to target tissue in an extremely short time. Operating under these high beam conditions exceeds conventional accelerator capabilities, and also imposes higher demands on accelerator scattering performance (109). Additionally, FLASH-RT has stringent requirements for the fine temporal structure of beam dose delivery. Parameters such as pulse dose rate, pulse duration, pulse interval time, number of pulses, total irradiation time, and average dose rate can all potentially affect the FLASH effect (110). These parameters also challenge dose monitoring devices. Traditional dosimetry equipment cannot be directly applied to FLASH-RT. For example, UHDR beams may cause detector saturation and ion recombination, compromising measurement accuracy (111). Furthermore, detectors must be able to resolve the beam's time structure. The ability to characterize in real-time the temporal and spatial structure of the transmission beam, and measure physical parameters under UHDR beam conditions, represents new requirements that FLASH-RT imposes on dose detection equipment (112, 113).

4.4 Evaluation of relevant preclinical and clinical trials

The advancement of FLASH-RT is fundamentally rooted in extensive preclinical and clinical experiments. In the previous keyword analysis, "cells" (n=74), "mice" (n=41), "mammalian cells" (n=24), "brain" (n=21), "*in vitro*" (n=19), "*in vivo*" (n=9), "memory" (n=9) and other keywords reflect to some extent the clinical transformation of FLASH.

Preclinical experiments in FLASH-RT can be generally categorized into two main types: cellular experiments and live animal experiments. To our knowledge, the cells utilized in preclinical experiments include dried Artemia eggs, tumor cells, normal human lung fibroblasts, zebrafish embryos, clonally derived CHO-KI cells, and cryptic nematode embryos (33, 114–117). Cellular experiments are typically conducted under *in vitro* conditions and are often used to investigate some basic metrics. For instance, researchers often examine whether there are differences in survival rates after irradiation with conventional radiotherapy compared to FLASH-RT, and whether any FLASH effect is observed. Numerous animal types are also suitable for preclinical experiments. In 2019, Vozenin et al. conducted UHDR irradiation on minipigs and cats, yielding evidence of the benefits of FLASH-RT and strongly advocating for further evaluation of FLASH-RI in human patients (25). Subsequently, minipigs and cats have been studied as larger vertebrate models to validate the protective effects of FLASH (118). In 2021, Konradsson et al. conducted a study on treating superficial malignancies using the FLASH e-beam in canine patients, assessing the feasibility and safety of the approach (119). Following this, Gjaldbaek et al. also investigated the efficacy of FLASH-RT on canine tumors. There is no doubt that among all animal models, the mouse is the most commonly used and effective model. Researchers have noted protective effects on brain tissue, lungs, skin, heart, esophagus, and intestines in mice subjected to UHDR (120–124). Similar design thinking and depth of exploration are evident in mouse experiments. For instance, in 2020, Allen et al. utilized a mouse model to elucidate the protective effects of FLASH-RT on brain tissue. They propose that FLASH-RT may safeguard the vascular system in mice without causing damage to the blood-brain barrier (125). In 2021, Montay-Gruel et al. employed dose-fractionated therapy to simultaneously validate the neuroprotective effects of FLASH-RT in mice and optimize tumor therapy (11). Mouse experiments likewise reveal potential future clinical applications. Radiotherapy is a critical treatment for glioblastoma, and in 2022, Liljedahl et al. conducted experiments on mice, concluding that FLASH was equally effective in fully immunocompetent animals with glioblastoma, a finding that could be advantageous for glioblastoma treatment (126).

Existing FLASH-RT clinical studies have yielded relatively positive results. The treatment of the first patient receiving FLASH-RT was reported in 2019. Bourhis et al. administered electron beam FLASH-RT at the University Hospital of Lausanne for a 75-year-old patient with cutaneous lymphoma. The results were encouraging: the patient exhibited a sustained anti-tumor response and experienced fewer radiation-related side effects than initially anticipated (26). This human trial confirmed the feasibility and safety of FLASH-RT for clinical applications. It was followed by two clinical trials involving proton FLASH-RT. In 2023, Mascia et al. conducted a non-randomized trial of palliative FLASH-RT for limb bone metastases in participants treated at the Cincinnati Children's/University of California Health Proton Therapy

Center. In this non-randomized trial, metrics concerning clinical workflow, treatment efficacy, and safety data demonstrated that UHDR proton FLASH-RT is clinically feasible (127). In 2024, Daugherty et al. evaluated treatment toxicity and pain relief in study participants with painful sternal metastases who were treated with FLASH-RT, along with assessing workflow metrics in a clinical setting (128). Undoubtedly, the clinical research on FLASH-RT is confronted with challenges. The scarcity of clinical studies and slow progress can be attributed to several factors. The biological mechanisms underlying FLASH-RT remain unclear, and the lack of specialized equipment further hampers clinical investigation. Selecting appropriate patients based on tumor characteristics such as type, location, and stage is also a formidable task (14). Although preclinical studies have yielded promising results, the substantial anatomical and physiological differences between animal models and human models cast doubt on the direct applicability of these findings to clinical safety and efficacy (129). Moreover, the involvement of high-energy radiation introduces complex ethical and regulatory issues (130). These factors collectively contribute to the certain obstacles faced in advancing FLASH-RT clinical research. In summary, the clinical translation process of FLASH-RT relies on advanced accelerator equipment as well as dose detection devices and treatment planning systems that complement it. At the same time, support from relevant policies also promotes the clinical translation process. Researchers can also consider introducing advanced technologies from traditional radiation therapy (such as image-guided and adaptive radiotherapy) and processes (such as quality assurance) into FLASH-RT. This is beneficial for the development of FLASH-RT.

5 Limitation

The data for this study is sourced from the WOSCC database, which does not encompass all the literature in this field. The lack of cross-validation with other datasets introduces risks of both dataset selection bias and overfitting. Therefore, the results may not fully represent the current status of the entire FLASH-RT domain. Related research in this field has advanced rapidly in recent years, and this econometric analysis can only partially reflect the current state of development based on the literature included. Furthermore, as co-citation frequency is time-dependent, high-quality literature published in recent years may exhibit lower co-citation frequencies because of their shorter publication periods, leading to a discrepancy with the actual situation. When employing VOSviewer and CiteSpace for data visualization and analysis, there is no standardized reference for the time division, thresholding, and cropping methods applied to the data, which may introduce bias.

6 Conclusion

Our bibliometric analysis of FLASH-RT delves into several key dimensions of the field. We systematically examined publication trends to identify growth patterns and pivotal moments in research output. Our analysis also mapped international collaborations, revealing the global network of institutions and countries contributing to FLASH-RT advancements. We further identified influential journals and authors who have significantly shaped the discourse through high-impact contributions. Additionally, we analyzed keyword evolution to trace shifting research priorities and emerging focal points within the field. Additionally, it examines recent progress in biological mechanisms, equipment, and clinical translation. This analysis aims to offer researchers a comprehensive overview of the field.

Data availability statement

Research data are stored in an institutional repository and will be shared upon request to the corresponding author.

Author contributions

SJ: Data curation, Formal analysis, Methodology, Writing – original draft. WW: Writing – review & editing, Software. YWH: Data curation, Visualization, Writing – original draft. HY: Visualization, Writing – original draft, Validation. SZ: Writing – original draft, Methodology, Software. YMH: Conceptualization, Data curation, Investigation, Visualization, Writing – review & editing, Writing – original draft. QX: Conceptualization, Investigation, Writing – review & editing. GL: Investigation, Writing – review & editing, Supervision.

Funding

The author(s) declare that financial support was received for the research and/or publication of this article. This work was supported by the National Natural Science Foundation of China (Grant No.12475348 and No.12205209).

Conflict of interest

The authors declare that the research was conducted in the absence of any commercial or financial relationships that could be construed as a potential conflict of interest.

Generative AI statement

The author(s) declare that no Generative AI was used in the creation of this manuscript.

Publisher's note

All claims expressed in this article are solely those of the authors and do not necessarily represent those of their affiliated

organizations, or those of the publisher, the editors and the reviewers. Any product that may be evaluated in this article, or claim that may be made by its manufacturer, is not guaranteed or endorsed by the publisher.

Supplementary material

The Supplementary Material for this article can be found online at: https://www.frontiersin.org/articles/10.3389/fonc.2025.1580848/full#supplementary-material

References

1. Bray F, Laversanne M, Sung H, Ferlay J, Siegel RL, Soerjomataram I, et al. Global cancer statistics 2022: globocan estimates of incidence and mortality worldwide for 36 cancers in 185 countries. *CA Cancer J Clin*. (2024) 74:229–63. doi: 10.3322/caac.21834

2. Pereira S, Orlandi E, Deneuve S, Barcellini A, Chalaszczyk A, Behm-Ansmant I, et al. The normal, the radiosensitive, and the ataxic in the era of precision radiotherapy: A narrative review. *Cancers*. (2022) 14:6252. doi: 10.3390/cancers14246252

3. Fabbrizi MR, Parsons JL. Radiotherapy and the cellular DNA damage response: current and future perspectives on head and neck cancer treatment. *Cancer Drug Resistance*. (2020) 3:775–90. doi: 10.20517/cdr.2020.49

4. Huang R-X, Zhou P-K. DNA damage response signaling pathways and targets for radiotherapy sensitization in cancer. *Signal Transduction Targeted Ther*. (2020) 5:60. doi: 10.1038/s41392-020-0150-x

5. Badiyan SN, Puckett LL, Vlacich G, Schiffer W, Pedersen LN, Mitchell JD, et al. Radiation-induced cardiovascular toxicities. *Curr Treat Options Oncol*. (2022) 23:1388–404. doi: 10.1007/s11864-022-01012-9

6. Lühr A, von Neubeck C, Pawelke J, Seidlitz A, Peitzsch C, Bentzen SM, et al. Radiobiology of proton therapy": results of an international expert workshop. *Radiother Oncol*. (2018) 128:56–67. doi: 10.1016/j.radonc.2018.05.018

7. Marcu L, Bezak E, Allen BJ. Global comparison of targeted alpha vs targeted beta therapy for cancer: *in vitro*, *in vivo* and clinical trials. *Crit Rev Oncology/Hematol*. (2018) 123:7–20. doi: 10.1016/j.critrevonc.2018.01.001

8. Rahman M, Trigilio A, Franciosini G, Moeckli R, Zhang R, Böhlen TT. Flash radiotherapy treatment planning and models for electron beams. *Radiother Oncol*. (2022) 175:210–21. doi: 10.1016/j.radonc.2022.08.009

9. Bourhis J, Montay-Gruel P, Gonçalves Jorge P, Bailat C, Petit B, Ollivier J, et al. Clinical translation of flash radiotherapy: why and how? *Radiother Oncol*. (2019) 139:11–7. doi: 10.1016/j.radonc.2019.04.008

10. Favaudon V, Caplier L, Monceau V, Pouzoulet F, Sayarath M, Fouillade C, et al. Ultrahigh dose-rate flash irradiation increases the differential response between normal and tumor tissue in mice. *Sci Trans Med*. (2014) 6:245ra93. doi: 10.1126/scitranslmed.3008973

11. Montay-Gruel P, Acharya MM, Jorge PG, Petit B, Petridis IG, Fuchs P, et al. Hypofractionated flash-rt as an effective treatment against glioblastoma that reduces neurocognitive side effects in mice. *Clin Cancer Res*. (2021) 27:775–84. doi: 10.1158/1078-0432.Ccr-20-0894

12. Montay-Gruel P, Bouchet A, Jaccard M, Patin D, Serduc R, Aim W, et al. X-rays can trigger the flash effect: ultra-high dose-rate synchrotron light source prevents normal brain injury after whole brain irradiation in mice. *Radiother Oncol*. (2018) 129:582–8. doi: 10.1016/j.radonc.2018.08.016

13. Montay-Gruel P, Petersson K, Jaccard M, Boivin G, Germond JF, Petit B, et al. Irradiation in a Flash: Unique Sparing of Memory in Mice after Whole Brain Irradiation with Dose Rates above 100gy/S. *Radiother Oncol*. (2017) 124:365–9. doi: 10.1016/j.radonc.2017.05.003

14. Vozenin MC, Bourhis J, Durante M. Towards clinical translation of flash radiotherapy. *Nat Rev Clin Oncol*. (2022) 19:791–803. doi: 10.1038/s41571-022-00697-z

15. Hageman E, Che PP, Dahele M, Slotman B, Sminia P. Radiobiological aspects of flash radiotherapy. *Biomolecules*. (2022) 12:18. doi: 10.3390/biom12101376

16. Lin BW, Gao F, Yang YW, Wu D, Zhang Y, Feng G, et al. Flash radiotherapy: history and future. *Front Oncol*. (2021) 11:644400. doi: 10.3389/fonc.2021.644400

17. Nesteruk KP, Psoroulas S. Flash irradiation with proton beams: beam characteristics and their implications for beam diagnostics. *Appl Sciences-Basel*. (2021) 11:11. doi: 10.3390/app11052170

18. Song G, Zheng Z, Zhu Y, Wang Y, Xue S. A review and bibliometric analysis of global research on proton radiotherapy. *Med (Baltimore)*. (2024) 103:e38089. doi: 10.1097/MD.0000000000038089

19. Liu Y, Li J, Cheng X, Zhang X. Bibliometric analysis of the top-cited publications and research trends for stereotactic body radiotherapy. *Front Oncol*. (2021) 11:795568. doi: 10.3389/fonc.2021.795568

20. Guan Y, Yu B-B, Liu S, Luo H-Y, Huang S-T. Research trends of radiation induced temporal lobe injury in patients with nasopharyngeal carcinoma from 2000 to 2022: A bibliometric analysis. *Radiat Oncol*. (2023) 18:151. doi: 10.1186/s13014-023-02345-x

21. Xiao Y, Qiu M, Huang W, Hu S, Tan C, Nan F, et al. Global status of research on radiotherapy for rectal cancer: A bibliometric and visual analysis. *Front Public Health*. (2022) 10:962256. doi: 10.3389/fpubh.2022.962256

22. Aggarwal A, Lewison G, Idir S, Peters M, Aldige C, Boerckel W, et al. The state of lung cancer research: A global analysis. *J Thoracic Oncol*. (2016) 11:1040–50. doi: 10.1016/j.jtho.2016.03.010

23. van Eck NJ, Waltman L. Software survey: vosviewer, a computer program for bibliometric mapping. *Scientometrics*. (2009) 84:523–38. doi: 10.1007/s11192-009-0146-3

24. Aria M, Cuccurullo C. Bibliometrix: an R-tool for comprehensive science mapping analysis. *J Informetrics*. (2017) 11:959–75. doi: 10.1016/j.joi.2017.08.007

25. Vozenin MC, De Fornel P, Petersson K, Favaudon V, Jaccard M, Germond JF, et al. The advantage of flash radiotherapy confirmed in mini-pig and cat-cancer patients. *Clin Cancer Res*. (2019) 25:35–42. doi: 10.1158/1078-0432.Ccr-17-3375

26. Bourhis J, Sozzi WJ, Jorge PG, Gaide O, Bailat C, Duclos F, et al. Treatment of a first patient with flash-radiotherapy. *Radiother Oncol*. (2019) 139:18–22. doi: 10.1016/j.radonc.2019.06.019

27. Montay-Gruel P, Acharya MM, Petersson K, Alikhani L, Yakkala C, Allen BD, et al. Long-term neurocognitive benefits of FLASH radiotherapy driven by reduced reactive oxygen species. *Proc Natl Acad Sci*. (2019) 116:10943–10951. doi: 10.1073/pnas.1901777116

28. Vozenin MC, Hendry JH, Limoli CL. Biological benefits of ultra-high dose rate flash radiotherapy: sleeping beauty awoken. *Clin Oncol*. (2019) 31:407–15. doi: 10.1016/j.clon.2019.04.001

29. Wilson JD, Hammond EM, Higgins GS, Petersson K. Ultra-High Dose Rate (FLASH) Radiotherapy: Silver Bullet or Fool's Gold? *Front Oncol*. (2020) 9:1563. doi: 10.3389/fonc.2019.01563

30. Diffenderfer ES, Verginadis II, Kim MM, Shoniyozov K, Velalopoulou A, Goia D, et al. Design, implementation, and *in vivo* validation of a novel proton flash radiation therapy system. *Int J Radiat Oncol Biol Phys*. (2020) 106:440–8. doi: 10.1016/j.ijrobp.2019.10.049

31. Spitz DR, Buettner GR, Petronek MS, St-Aubin JJ, Flynn RT, Waldron TJ, et al. An integrated physico-chemical approach for explaining the differential impact of FLASH versus conventional dose rate irradiation on cancer and normal tissue responses. *Radiother Oncol*. (2019) 139:23–27. doi: 10.1016/j.radonc.2019.03.028

32. Patriarca A, Fouillade C, Auger M, Martin F, Pouzoulet F, Nauraye C, et al. Experimental Set-up for FLASH Proton Irradiation of Small Animals Using a Clinical System. *Int J Radiat Oncol Biol Phys*. (2018) 102:619–626. doi: 10.1016/j.ijrobp.2018.06.403

33. Buonanno M, Grilj V, Brenner DJ. Biological effects in normal cells exposed to flash dose rate protons. *Radiother Oncol*. (2019) 139:51–5. doi: 10.1016/j.radonc.2019.02.009

34. Schüler E, Trovati S, King G, Lartey F, Rafat M, Villegas M, et al. Experimental Platform for Ultra-high Dose Rate FLASH Irradiation of Small Animals Using a Clinical Linear Accelerator. *Int J Radiat Oncol Biol Phys*. (2017) 97:195–203. doi: 10.1016/j.ijrobp.2016.09.018

35. Simmons DA, Lartey FM, Schüler E, Rafat M, King G, Kim A, Ko R, et al. Reduced cognitive deficits after FLASH irradiation of whole mouse brain are associated with less hippocampal dendritic spine loss and neuroinflammation. *Radiother Oncol*. (2019) 139:4–10. doi: 10.1016/j.radonc.2019.06.006

36. Fouillade C, Curras-Alonso S, Giuranno L, Quelennec E, Heinrich S, Bonnet-Boissinot S, et al. FLASH Irradiation Spares Lung Progenitor Cells and Limits the Incidence of Radio-induced Senescence. *Clin Cancer Res*. (2020) 26:1497–1506. doi: 10.1158/1078-0432.CCR-19-1440

37. Durante M, Bräuer-Krisch E, Hill M. Faster and safer? FLASH ultra-high dose rate in radiotherapy. *Br J Radiol*. (2018) 91:20170628. doi: 10.1259/bjr.20170628

38. Esplen N, Mendonca MS, Bazalova-Carter M. Physics and biology of ultrahigh dose-rate (FLASH) radiotherapy: a topical review. *Phys Med Biol*. (2020) 65:23TR03. doi: 10.1088/1361-6560/abaa28

39. Adrian G, Konradsson E, Lempart M, Bäck S, Ceberg C, Petersson K. The flash effect depends on oxygen concentration. *Br J Radiol*. (2020) 93:6. doi: 10.1259/bjr.20190702

40. Ma JJ, Lin YT, Tang M, Zhu YN, Gan GN, Rotondo RL, et al. Simultaneous dose and dose rate optimization via dose modifying factor modeling for flash effective dose. *Med Phys*. (2024) 51:5190–203. doi: 10.1002/mp.17251

41. Orobeti S, Sima LE, Porosnicu I, Diplasu C, Giubega G, Cojocaru G, et al. First *in vitro* cell co-culture experiments using laser-induced high-energy electron flash irradiation for the development of anti-cancer therapeutic strategies. *Sci Rep*. (2024) 14:14866. doi: 10.1038/s41598-024-65137-7

42. Poulsen PR, Johansen JG, Sitarz MK, Kanouta E, Kristensen L, Grau C, et al. Oxygen enhancement ratio-weighted dose quantitatively describes acute skin toxicity variations in mice after pencil beam scanning proton flash irradiation with changing doses and time structures. *Int J Radiat Oncol Biol Phys*. (2024) 120:276–86. doi: 10.1016/j.ijrobp.2024.02.050

43. Dewey DL, Boag JW. Modification of the oxygen effect when bacteria are given large pulses of radiation. *Nature*. (1959) 183:1450–1. doi: 10.1038/1831450a0

44. Mill AJ. Recovery of cultured mammalian-cells from sublethal damage when irradiated at ultrahigh dose-rates. *Nuclear Instruments Methods*. (1979) 163:577–81. doi: 10.1016/0029-554x(79)90152-6

45. Weiss H, Epp ER, Heslin JM, Ling CC, Santomasso A. Oxygen Depletion in Cells Irradiated at Ultrahigh Dose-Rates and at Conventional Dose-Rates. *Int J Radiat Biol*. (1974) 26:17–29. doi: 10.1080/09553007414550901

46. Petersson K, Adrian G, Butterworth K, McMahon SJ. A quantitative analysis of the role of oxygen tension in flash radiation therapy. *Int J Radiat Oncol Biol Phys*. (2020) 107:539–47. doi: 10.1016/j.ijrobp.2020.02.634

47. Hu AK, Qiu R, Wu Z, Zhang H, Li WB, Li JL. A computational model for oxygen depletion hypothesis in flash effect. *Radiat Res*. (2022) 197:175–83. doi: 10.1667/rade-20-00260.1

48. El Khatib M, Van Slyke AL, Velalopoulou A, Kim MM, Shoniyozov K, Allu SR, et al. Ultrafast tracking of oxygen dynamics during proton flash. *Int J Radiat Oncol Biol Phys*. (2022) 113:624–34. doi: 10.1016/j.ijrobp.2022.03.016

49. Van Slyke AL, El Khatib M, Velalopoulou A, Diffenderfer E, Shoniyozov K, Kim MM, et al. Oxygen monitoring in model solutions and *in vivo* in mice during proton irradiation at conventional and flash dose rates. *Radiat Res*. (2022) 198:181–9. doi: 10.1667/RADE-21-00232.1

50. Koch CJ, Kim MM, Wiersma RD. Radiation-chemical oxygen depletion depends on chemical environment and dose rate: implications for the flash effect. *Int J Radiat Oncol Biol Phys*. (2023) 117:214–22. doi: 10.1016/j.ijrobp.2023.04.001

51. Labarbe R, Hotoiu L, Barbier J, Favaudon V. A physicochemical model of reaction kinetics supports peroxyl radical recombination as the main determinant of the flash effect. *Radiother Oncol*. (2020) 153:303–10. doi: 10.1016/j.radonc.2020.06.001

52. Boscolo D, Scifoni E, Durante M, Krämer M, Fuss MC. May oxygen depletion explain the flash effect? A chemical track structure analysis. *Radiother Oncol*. (2021) 162:68–75. doi: 10.1016/j.radonc.2021.06.031

53. Thompson SJ, Prise KM, McMahon SJ. Investigating the potential contribution of inter-track interactions within ultra-high dose-rate proton therapy. *Phys Med Biol*. (2023) 68:17. doi: 10.1088/1361-6560/acb88a

54. Jin JY, Gu AX, Wang WL, Oleinick NL, Machtay M, Kong FM. Ultra-high dose rate effect on circulating immune cells: A potential mechanism for flash effect? *Radiother Oncol*. (2020) 149:55–62. doi: 10.1016/j.radonc.2020.04.054

55. Zhu HY, Xie DH, Yang YW, Huang SM, Gao XW, Peng YL, et al. Radioprotective effect of X-ray abdominal flash irradiation: adaptation to oxidative damage and inflammatory response may be benefiting factors. *Med Phys*. (2022) 49:4812–22. doi: 10.1002/mp.15680

56. Cucinotta FA, Smirnova OA. Effects of partial-body, continuous/pulse irradiation at dose rates from flash to conventional rates on the level of surviving blood lymphocytes: modeling approach. *I. Continuous Irradiation Radiat Res*. (2024) 201:535–45. doi: 10.1667/rade-23-00222.1

57. Cucinotta FA, Smirnova OA. Effects of partial-body, continuous/pulse irradiation at dose rates from flash to conventional rates on the level of surviving blood lymphocytes: modeling approach ii. *Two- Multiple-Pulse Irradiation Radiat Res*. (2024) 201:546–57. doi: 10.1667/rade-23-00221.1

58. Jay-Gerin JP. Ultra-high dose-rate (Flash) radiotherapy: generation of early, transient, strongly acidic spikes in the irradiated tumor environment. *Cancer Radiotherapie*. (2020) 24:332–4. doi: 10.1016/j.canrad.2019.11.004

59. Kim YE, Gwak SH, Hong BJ, Oh JM, Choi HS, Kim MS, et al. Effects of ultra-high doserate flash irradiation on the tumor microenvironment in lewis lung carcinoma: role of myosin light chain. *Int J Radiat Oncol Biol Phys*. (2021) 109:1440–53. doi: 10.1016/j.ijrobp.2020.11.012

60. Kanouta E, Poulsen PR, Kertzscher G, Sitarz MK, Sorensen BS, Johansen JG. Time-resolved dose rate measurements in pencil beam scanning proton flash therapy with a fiber-coupled scintillator detector system. *Med Phys*. (2023) 50:2450–62. doi: 10.1002/mp.16156

61. Lempart M, Blad B, Adrian G, Bäck S, Knöös T, Ceberg C, et al. Modifying a clinical linear accelerator for delivery of ultra-high dose rate irradiation. *Radiother Oncol*. (2019) 139:40–5. doi: 10.1016/j.radonc.2019.01.031

62. Jorge PG, Grilj V, Bourhis J, Vozenin MC, Germond JF, Bochud F, et al. Validation of an ultrahigh dose rate pulsed electron beam monitoring system using a current transformer for flash preclinical studies. *Med Phys*. (2022) 49:1831–8. doi: 10.1002/mp.15474

63. Di Martino F, Del Sarto D, Bass G, Capaccioli S, Celentano M, Coves D, et al. Architecture, flexibility and performance of a special electron linac dedicated to flash radiotherapy research: electronflash with a triode gun of the centro pisano flash radiotherapy (Cpfr). *Front Phys*. (2023) 11:1268310. doi: 10.3389/fphy.2023.1268310

64. Garty G, Obaid R, Deoli N, Royba E, Tan YW, Harken AD, et al. Ultra-high dose rate flash irradiator at the radiological research accelerator facility. *Sci Rep*. (2022) 12:22149. doi: 10.1038/s41598-022-19211-7

65. Konradsson E, Wahlqvist P, Thoft A, Blad B, Bäck S, Ceberg C, et al. Beam control system and output fine-tuning for safe and precise delivery of flash radiotherapy at a clinical linear accelerator. *Front Oncol*. (2024) 14:1342488. doi: 10.3389/fonc.2024.1342488

66. Sloop A, Ashraf MR, Rahman M, Sunnerberg J, Dexter CA, Thompson L, et al. Rapid switching of a C-series linear accelerator between conventional and ultrahigh-dose-rate research mode with beamline modifications and output stabilization. *Int J Radiat Oncol Biol Phys*. (2024) 119:1317–25. doi: 10.1016/j.ijrobp.2024.01.215

67. Dai TY, Sloop AM, Ashraf MR, Sunnerberg JP, Clark MA, Bruza P, et al. Commissioning an ultra-high-dose-rate electron linac with end-to-end tests. *Phys Med Biol*. (2024) 69:165028. doi: 10.1088/1361-6560/ad69fc

68. Calvo FA, Serrano J, Cambeiro M, Aristu J, Asencio JM, Rubio I, et al. Intraoperative electron radiation therapy: an update of the evidence collected in 40 years to search for models for electron-flash studies. *Cancers*. (2022) 14:3693. doi: 10.3390/cancers14153693

69. Ronga MG, Cavallone M, Patriarca A, Leite AM, Loap P, Favaudon V, et al. Back to the future: very high-energy electrons (Vhees) and their potential application in radiation therapy. *Cancers*. (2021) 13:4942. doi: 10.3390/cancers13194942

70. Maxim PG, Tantawi SG, Loo BW. Phaser: A platform for clinical translation of flash cancer radiotherapy. *Radiother Oncol*. (2019) 139:28–33. doi: 10.1016/j.radonc.2019.05.005

71. Giuliano L, Franciosini G, Palumbo L, Aggar L, Dutreix M, Faillace L, et al. Characterization of ultra-high-dose rate electron beams with electronflash linac. *Appl Sciences-Basel*. (2023) 13:631. doi: 10.3390/app13010631

72. Gómez F, Gonzalez-Castaño DM, Fernández NG, Pardo-Montero J, Schüller A, Gasparini A, et al. Development of an ultra-thin parallel plate ionization chamber for dosimetry in flash radiotherapy. *Med Phys*. (2022) 49:4705–14. doi: 10.1002/mp.15668

73. Oesterle R, Jorge PG, Grilj V, Bourhis J, Vozenin MC, Germond JF, et al. Implementation and validation of a beam-current transformer on a medical pulsed electron beam linac for flash-rt beam monitoring. *J Appl Clin Med Phys*. (2021) 22:165–71. doi: 10.1002/acm2.13433

74. Rinati GV, Felici G, Galante F, Gasparini A, Kranzer R, Mariani G, et al. Application of a novel diamond detector for commissioning of flash radiotherapy electron beams. *Med Phys*. (2022) 49:5513–22. doi: 10.1002/mp.15782

75. Romano F, Milluzzo G, Di Martino F, D'Oca MC, Felici G, Galante F, et al. First characterization of novel silicon carbide detectors with ultra-high dose rate electron beams for flash radiotherapy. *Appl Sciences-Basel*. (2023) 13:2986. doi: 10.3390/app13052986

76. Bedogni R, Russo L, Calamida A, Castro-Campoy AI, Fontanilla A, Dashdondog D, et al. Unbalanced core detector (Ucd): A novel direct-reading dosimeter for flash radiotherapy. *Eur Phys J Plus*. (2024) 139:563. doi: 10.1140/epjp/s13360-024-05356-z

77. Cayley J, Tan YRE, Petasecca M, Cutajar D, Breslin T, Rosenfeld A, et al. Moskin dosimetry for an ultra-high dose-rate, very high-energy electron irradiation environment at peer. *Front Phys*. (2024) 12:1401834. doi: 10.3389/fphy.2024.1401834

78. Newhauser WD, Zhang R. The physics of proton therapy. *Phys Med Biol*. (2015) 60:R155–209. doi: 10.1088/0031-9155/60/8/r155

79. Darafsheh A, Hao Y, Zwart T, Wagner M, Catanzano D, Williamson JF, et al. Feasibility of proton flash irradiation using a synchrocyclotron for preclinical studies. *Med Phys*. (2020) 47:4348–55. doi: 10.1002/mp.14253

80. Kang ML, Wei SY, Choi JI, Simone CB, Lin HB. Quantitative assessment of 3d dose rate for proton pencil beam scanning flash radiotherapy and its application for lung hypofractionation treatment planning. *Cancers*. (2021) 13:3549. doi: 10.3390/cancers13143549

81. Wei SY, Lin HB, Choi JI, Simone CB, Kang ML. A novel proton pencil beam scanning flash rt delivery method enables optimal oar sparing and ultra-high dose rate delivery: A comprehensive dosimetry study for lung tumors. *Cancers*. (2021) 13:5790. doi: 10.3390/cancers13225790

82. Folkerts MM, Abel E, Busold S, Perez JR, Krishnamurthi V, Ling CC. A framework for defining flash dose rate for pencil beam scanning. *Med Phys*. (2020) 47:6396–404. doi: 10.1002/mp.14456

83. Nesteruk KP, Togno M, Grossmann M, Lomax AJ, Weber DC, Schippers JM, et al. Commissioning of a clinical pencil beam scanning proton therapy unit for ultra-high dose rates (Flash). *Med Phys*. (2021) 48:4017–26. doi: 10.1002/mp.14933

84. Shi Y, Zhang MZ, Ou-Yang LH, Chen ZL, Li XF, Li DM. Design of a rapid-cycling synchrotron for flash proton therapy. *Nuclear Sci Techniques*. (2023) 34:145. doi: 10.1007/s41365-023-01283-3

85. Titt U, Yang M, Wang XC, Iga K, Fredette N, Schueler E, et al. Design and validation of a synchrotron proton beam line for flash radiotherapy preclinical research experiments. *Med Phys*. (2022) 49:497–509. doi: 10.1002/mp.15370

86. Chan TY, Cho IC, Farooq A, Fan KH, Tsai YT, Chao TC, et al. Mini-ridge filter designs for conformal flash proton therapy. *Radiat Phys Chem*. (2024) 224:112017. doi: 10.1016/j.radphyschem.2024.112017

87. Zhang GL, Gao WC, Peng H. Design of static and dynamic ridge filters for flash-impt: A simulation study. *Med Phys*. (2022) 49:5387–99. doi: 10.1002/mp.15717

88. Liu G, Zhao LW, Li XQ, Zhang S, Dai SY, Lu XL, et al. A novel ultrahigh-dose-rate proton therapy technology: spot-scanning proton arc plus flash (Splash). *Int J Radiat Oncol Biol Phys*. (2023) 117:730–7. doi: 10.1016/j.ijrobp.2023.05.012

89. Togno M, Nesteruk KP, Schäfer R, Psoroulas S, Meer D, Grossmann M, et al. Ultra-high dose rate dosimetry for pre-clinical experiments with mm-small proton fields. *Physica Medica-European J Med Phys*. (2022) 104:101–11. doi: 10.1016/j.ejmp.2022.10.019

90. Winterhalter C, Togno M, Nesteruk KP, Emert F, Psoroulas S, Vidal M, et al. Faraday cup for commissioning and quality assurance for proton pencil beam scanning beams at conventional and ultra-high dose rates. *Phys Med Biol*. (2021) 66:124001. doi: 10.1088/1361-6560/abfbf2

91. Zou W, Diffenderfer ES, Ota K, Boisseau P, Kim MM, Cai YL, et al. Characterization of a high-resolution 2d transmission ion chamber for independent validation of proton pencil beam scanning of conventional and flash dose delivery. *Med Phys*. (2021) 48:3948–57. doi: 10.1002/mp.14882

92. Kanouta E, Johansen JG, Kertzscher G, Sitarz MK, Sorensen BS, Poulsen PR. Time structure of pencil beam scanning proton flash beams measured with scintillator detectors and compared with log files. *Med Phys*. (2022) 49:1932–43. doi: 10.1002/mp.15486

93. Lee E, Lourenço AM, Speth J, Lee N, Subiel A, Romano F, et al. Ultrahigh dose rate pencil beam scanning proton dosimetry using ion chambers and a calorimeter in support of first in-human flash clinical trial. *Med Phys*. (2022) 49:6171–82. doi: 10.1002/mp.15844

94. Villoing D, Koumeir C, Bongrand A, Guertin A, Haddad F, Métivier V, et al. Proton beam dosimetry at ultra-high dose rates (Flash): evaluation of gafchromic™ (Ebt3, ebt-xd) and orthochromic (Oc-1) film performances. *Med Phys*. (2022) 49:2732–45. doi: 10.1002/mp.15526

95. Wyrsch N, Antognini L, Ballif C, Braccini S, Casolaro P, Dunand S, et al. Amorphous silicon detectors for proton beam monitoring in flash radiotherapy. *Radiat Measurements*. (2024) 177:107230. doi: 10.1016/j.radmeas.2024.107230

96. Liu FC, Shi JR, Zha H, Li GH, Li A, Gu WH, et al. Development of a compact linear accelerator to generate ultrahigh dose rate high-energy X-rays for flash radiotherapy applications. *Med Phys*. (2023) 50:1680–98. doi: 10.1002/mp.16199

97. Sampayan SE, Sampayan KC, Caporaso GJ, Chen YJ, Falabella S, Hawkins SA, et al. Megavolt bremsstrahlung measurements from linear induction accelerators demonstrate possible use as a flash radiotherapy source to reduce acute toxicity. *Sci Rep*. (2021) 11:17104. doi: 10.1038/s41598-021-95807-9

98. Gao F, Yang YW, Zhu HY, Wang JX, Xiao DX, Zhou Z, et al. First demonstration of the flash effect with ultrahigh dose rate high-energy X-rays. *Radiother Oncol*. (2022) 166:44–50. doi: 10.1016/j.radonc.2021.11.004

99. Cecchi DD, Therriault-Proulx F, Lambert-Girard S, Hart A, Macdonald A, Pfleger M, et al. Characterization of an X-ray tube-based ultrahigh dose-rate system for *in vitro* irradiations. *Med Phys*. (2021) 48:7399–409. doi: 10.1002/mp.15234

100. Miles D, Sforza D, Wong JH, Rezaee M. Dosimetric characterization of a rotating anode X-ray tube for flash radiotherapy research. *Med Phys*. (2024) 51:1474–83. doi: 10.1002/mp.16609

101. Vignati A, Giordanengo S, Fausti F, Villarreal OAM, Milian FM, Mazza G, et al. Beam monitors for tomorrow: the challenges of electron and photon flash rt. *Front Phys*. (2020) 8:375. doi: 10.3389/fphy.2020.00375

102. Winter J, Dimroth A, Roetzer S, Zhang YZ, Krämer KL, Petrich C, et al. Heat management of a compact X-ray source for microbeam radiotherapy and flash treatments. *Med Phys*. (2022) 49:3375–88. doi: 10.1002/mp.15611

103. Clements N, Bazalova-Carter M, Esplen N. Monte carlo optimization of a grid collimator for preclinical megavoltage ultra-high dose rate spatially-fractionated radiation therapy. *Phys Med Biol*. (2022) 67:185001. doi: 10.1088/1361-6560/ac8c1a

104. Lyu QH, Neph R, O'Connor D, Ruan D, Boucher S, Sheng K. Road: rotational direct aperture optimization with a decoupled ring-collimator for flash radiotherapy. *Phys Med Biol*. (2021) 66:035020. doi: 10.1088/1361-6560/abcbd0

105. Weber UA, Scifoni E, Durante M. Flash radiotherapy with carbon ion beams. *Med Phys*. (2022) 49:1974–92. doi: 10.1002/mp.15135

106. Yagi M, Shimizu S, Minami K, Hamatani N, Tsubouchi T, Takashina M, et al. Ultra-high dose-rate carbon-ion scanning beam with a compact medical synchrotron contributing to further development of flash irradiation. *Anticancer Res*. (2023) 43:581–9. doi: 10.21873/anticanres.16194

107. Lang XL, Hu ZG, Zhao ZL, Zhou K, Xu ZG, Li M, et al. Preliminary study of low-pressure ionization chamber for online dose monitoring in flash carbon ion radiotherapy. *Phys Med Biol*. (2024) 69:025008. doi: 10.1088/1361-6560/ad13d0

108. Yagi M, Shimizu S, Hamatani N, Miyoshi T, Nomura T, Toyoda T, et al. Development and characterization of a dedicated dose monitor for ultrahigh-dose-rate scanned carbon-ion beams. *Sci Rep*. (2024) 14:11574. doi: 10.1038/s41598-024-62148-2

109. Chaikh A, Edouard M, Huet C, Milliat F, Villagrasa C, Isambert A. Towards clinical application of ultra-high dose rate radiotherapy and the flash effect: challenges and current status. *Cancer Radiother*. (2024) 28:463–73. doi: 10.1016/j.canrad.2024.07.001

110. Beddok A, Lahaye C, Calugaru V, De Marzi L, Fouillade C, Salvador S, et al. A comprehensive analysis of the relationship between dose rate and biological effects in preclinical and clinical studies, from brachytherapy to flattening filter free radiation therapy and flash irradiation. *Int J Radiat Oncol Biol Phys*. (2022) 113:985–95. doi: 10.1016/j.ijrobp.2021.02.009

111. Boag JW, Hochhauser E, Balk OA. The effect of free-electron collection on the recombination correction to ionization measurements of pulsed radiation. *Phys Med Biol*. (1996) 41:885–97. doi: 10.1088/0031-9155/41/5/005

112. Romano F, Bailat C, Jorge PG, Lerch MLF, Darafsheh A. Ultra-high dose rate dosimetry: challenges and opportunities for flash radiation therapy. *Med Phys*. (2022) 49:4912–32. doi: 10.1002/mp.15649

113. Zou W, Zhang R, Schuler E, Taylor PA, Mascia AE, Diffenderfer ES, et al. Framework for quality assurance of ultrahigh dose rate clinical trials investigating flash effects and current technology gaps. *Int J Radiat Oncol Biol Phys*. (2023) 116:1202–17. doi: 10.1016/j.ijrobp.2023.04.018

114. Auer S, Hable V, Greubel C, Drexler GA, Schmid TE, Belka C, et al. Survival of tumor cells after proton irradiation with ultra-high dose rates. *Radiat Oncol*. (2011) 6:139. doi: 10.1186/1748-717x-6-139

115. Beyreuther E, Brand M, Hans S, Hideghéty K, Karsch L, Lessmann E, et al. Feasibility of proton flash effect tested by zebrafish embryo irradiation. *Radiother Oncol*. (2019) 139:46–50. doi: 10.1016/j.radonc.2019.06.024

116. Iwasaki T, Kato Y, Antoku S. Study of biological effectiveness of high-energy electrons at ultrahigh dose-rates using dry eggs of artemia. *Radiat Res*. (1974) 57:195–206. doi: 10.2307/3573827

117. Schoenauen L, Stubbe FX, Van Gestel D, Penninckx S, Heuskin ACC. Elegans: A potent model for high-throughput screening experiments investigating the flash effect. *Clin Trans Radiat Oncol*. (2024) 45:100712. doi: 10.1016/j.ctro.2023.100712

118. Bley CR, Wolf F, Jorge PG, Grilj V, Petridis I, Petit B, et al. Dose- and volume-limiting late toxicity of flash radiotherapy in cats with squamous cell carcinoma of the nasal planum and in mini pigs. *Clin Cancer Res*. (2022) 28:3814–23. doi: 10.1158/1078-0432.Ccr-22-0262

119. Konradsson E, Arendt ML, Jensen KB, Borresen B, Hansen AE, Bäck S, et al. Establishment and initial experience of clinical flash radiotherapy in canine cancer patients. *Front Oncol*. (2021) 11:658004. doi: 10.3389/fonc.2021.658004

120. Alaghband Y, Cheeks SN, Allen BD, Montay-Gruel P, Doan NL, Petit B, et al. Neuroprotection of radiosensitive juvenile mice by ultra-high dose rate flash irradiation. *Cancers*. (2020) 12:1671. doi: 10.3390/cancers12061671

121. Kim K, Kim MM, Skoufos G, Diffenderfer ES, Motlagh SAO, Kokkorakis M, et al. Flash proton radiation therapy mitigates in fl ammatory and fibrotic pathways and preserves cardiac function in a preclinical mouse model of radiation-induced heart disease. *Int J Radiat Oncol Biol Phys*. (2024) 119:1234–47. doi: 10.1016/j.ijrobp.2024.01.224

122. Levy K, Natarajan S, Wang JH, Chow S, Eggold JT, Loo PE, et al. Abdominal flash irradiation reduces radiation-induced gastrointestinal toxicity for the treatment of ovarian cancer in mice. *Sci Rep*. (2020) 10:21600. doi: 10.1038/s41598-020-78017-7

123. Ren WT, Hou L, Zhang K, Chen H, Feng X, Jiang ZM, et al. The sparing effect of ultra-high dose rate irradiation on the esophagus. *Front Oncol*. (2024) 14:1442627. doi: 10.3389/fonc.2024.1442627

124. Soto LA, Casey KM, Wang JH, Blaney A, Manjappa R, Breitkreutz D, et al. Flash irradiation results in reduced severe skin toxicity compared to conventional-dose-rate irradiation. *Radiat Res*. (2020) 194:618–24. doi: 10.1667/rade-20-00090

125. Allen BD, Acharya MM, Montay-Gruel P, Jorge PG, Bailat C, Petit B, et al. Maintenance of tight junction integrity in the absence of vascular dilation in the brain of mice exposed to ultra-high-dose-rate flash irradiation. *Radiat Res*. (2020) 194:625–35. doi: 10.1667/rade-20-00060.1

126. Liljedahl E, Konradsson E, Gustafsson E, Jonsson KF, Olofsson JK, Ceberg C, et al. Long-term anti-tumor effects following both conventional radiotherapy and flash in fully immunocompetent animals with glioblastoma. *Sci Rep*. (2022) 12:12285. doi: 10.1038/s41598-022-16612-6

127. Mascia AE, Daugherty EC, Zhang YB, Lee E, Xiao ZY, Sertorio M, et al. Proton flash radiotherapy for the treatment of symptomatic bone metastases the fast-01 nonrandomized trial. *JAMA Oncol*. (2023) 9:62–9. doi: 10.1001/jamaoncol.2022.5843

128. Daugherty EC, Zhang Y, Xiao Z, Mascia AE, Sertorio M, Woo J, et al. Flash radiotherapy for the treatment of symptomatic bone metastases in the thorax (Fast-02): protocol for a prospective study of a novel radiotherapy approach. *Radiat Oncol*. (2024) 19:34. doi: 10.1186/s13014-024-02419-4

129. Noval Rivas M, Arditi M. Kawasaki disease: pathophysiology and insights from mouse models. *Nat Rev Rheumatol*. (2020) 16:391–405. doi: 10.1038/s41584-020-0426-0

130. Sheehan M, Timlin C, Peach K, Binik A, Puthenparampil W, Lodge M, et al. Position statement on ethics, equipoise and research on charged particle radiation therapy. *J Med Ethics*. (2014) 40:572–5. doi: 10.1136/medethics-2012-101290

frontiers | Frontiers in Oncology

TYPE Systematic Review
PUBLISHED 30 May 2025
DOI 10.3389/fonc.2025.1554765

Check for updates

OPEN ACCESS

EDITED BY
Poonam Yadav,
Northwestern University, United States

REVIEWED BY
Ariana Pritha,
University of New Mexico Health Sciences Center, United States
Utpal Gaikwad,
Krupamayi Hospitals Pvt Ltd, India

*CORRESPONDENCE
Anna Zając-Grabiec
anna.zajac-grabiec@ifj.edu.pl

RECEIVED 02 January 2025
ACCEPTED 12 May 2025
PUBLISHED 30 May 2025

CITATION
Zając-Grabiec A, Biesaga B, Krzyżowska M, Drosik-Rutowicz K and Miszczyk J (2025) Non-cancer effects after proton beam therapy for pediatric tumors- a narrative review. *Front. Oncol.* 15:1554765. doi: 10.3389/fonc.2025.1554765

COPYRIGHT
© 2025 Zając-Grabiec, Biesaga, Krzyżowska, Drosik-Rutowicz and Miszczyk. This is an open-access article distributed under the terms of the Creative Commons Attribution License (CC BY). The use, distribution or reproduction in other forums is permitted, provided the original author(s) and the copyright owner(s) are credited and that the original publication in this journal is cited, in accordance with accepted academic practice. No use, distribution or reproduction is permitted which does not comply with these terms.

Non-cancer effects after proton beam therapy for pediatric tumors- a narrative review

Anna Zając-Grabiec[1]*, Beata Biesaga[1,2], Monika Krzyżowska[1], Katarzyna Drosik-Rutowicz[3] and Justyna Miszczyk[1]

[1]Department of Medical Physics, Cyclotron Centre Bronowice, Institute of Nuclear Physics Polish Academy of Sciences, Krakow, Poland, [2]Department of Medical Biology, Faculty of Medicine, Andrzej Frycz Modrzewski Krakow University, Krakow, Poland, [3]Ist Department of Radiotherapy and Chemotherapy Oncology, Maria Sklodowska-Curie National Research Institute of Oncology, Gliwice, Poland

Introduction: Radiation therapy can cause serious complications and side effects, especially in children. Proton beam therapy is considered as safer and more effective than traditional photon therapy because this type of modality offers precise radiation dose delivery to cancer cells while minimizing irradiation dose to adjacent normal tissue. Moreover, pediatric patients undergoing PBT may also experience a range of non-cancer late effects, including brainstem injury, cognitive dysfunctions, and side effects from endocrine or cardiovascular systems. The present type and frequency of non-cancer effects in children after proton therapy.

Methods: Therefore, this review aims to analyze publications addressing the occurrence of side effects from proton therapy in pediatric patients, excluding those related to the induction of secondary malignancies. We used data from two publicly available databases for this review: the U.S. National Library of Medicine's ClinicalTrials.gov (https://clinicaltrials.gov) for the analysis of clinical trials and PubMed, utilizing iCite (https://iCite.od.nih.gov)/Office of Portfolio Analysis, NIH, Bethesda, MD), a web-based application providing access to bibliometric information on publications.

Results: The review of the literature shows that PBT reduces the risk of cognitive, neuroendocrine, and cardiovascular dysfunctions concerning those observed after PT. Contradictory results were observed for brain stem injury. The majority of studies found cumulative incidence (CI) of brainstem injury at a relatively low level (0.7% – 5.0%) after PBT, as compared to PT.

Discussion: However, some authors underlie a higher rate of brainstem injury in children irradiated due to tumors localized in PF. Therefore, further studies, especially prospective ones, are needed to accurately describe the incidence and risk of late toxicity of proton beam therapy in children.

KEYWORDS

proton beam therapy (PBT), late toxicity, pediatric tumors, non-cancer effects, photon therapy (PT)

Highlights

- Brain cancer stem injuries, cognitive dysfunctions, neuroendocrine and cardiovascular damage are the most frequent non-cancer late effects after proton beam therapy (PBT) in children.
- The majority of findings analyzing the risk of late toxicity after proton beam therapy in children found it decreased after PBT in relation to photon therapy (PT).
- A few studies indicated that children with tumors located in the posterior fossa (PF) or subjected to craniospinal irradiation are more susceptible to brainstem injury and cognitive dysfunctions.
- The majority of studies concerning late toxicity after proton therapy in children were conducted in small groups of patients and there are mostly retrospective studies. Further prospective studies are needed in a large group of patients, which will also allow for the analysis of factors related to radiotherapy outcomes after proton irradiation in longer follow-up studies.

Introduction

In 2019, a total of 291,319 new cases of malignant cancers in children and 98,834 deaths due to childhood cancers were documented globally (1). The most common pediatric cancers, which also account for the majority of cancer-related deaths, include leukemia, brain and central nervous system (CNS) tumors, and non-Hodgkin lymphoma (2, 3). Generally, the cure rate for childhood cancers is approximately 85% (3). This high survival rate, particularly in developed countries, is attributed to advancements in the treatment of pediatric malignancies. Such treatment is typically a multidisciplinary approach, encompassing surgery, chemotherapy, and radiotherapy (RT) (3). Unfortunately, both the disease itself and the treatments carry the risk of long-term complications, potentially affecting all organs and systems. The severity of these complications depends on many factors like the type of cancer, its stage at diagnosis, the age at onset (children under 5 years old are particularly vulnerable), as well as the therapeutic methods used, and their intensity. The Childhood Cancer Survivor Study (CCSS) revealed that about one in five childhood cancer survivors died by the age of 30, and one in ten of these deaths was directly attributed to treatment-related factors (3, 4). Additionally, the CCSS identified specific treatment-related risk factors for late mortality, with the highest relative risk (RR) associated with radiotherapy (RR = 2.9), followed by epipodophyllotoxins (RR = 2.3) and alkylating agents (RR = 2.2) (4).

Radiotherapy is a fundamental component of treatment for many children and adolescents with malignant diseases. In pediatric patients, RT is a part of a comprehensive treatment plan and is frequently used in combination with chemotherapy and/or surgery. However, the use of RT in children requires special caution due to the increased sensitivity of developing tissues to ionizing radiation and the potential for long-term side effects in growing organisms. Secondary malignancies, neurocognitive deficits, increased risk of vascular complications such as stroke and heart disease, hormonal deficiencies, impairments in bone and soft tissue growth, vision and hearing issues, and failures in sexual and reproductive function, are among the most common late-side effects of RT in children (3, 4).

Given that the use of T in children poses a significant risk for late side effects, PBT is gaining increasing interest in the treatment of certain pediatric malignancies. Due to the Bragg peak, PBT is an advanced form of RT that allows for precise radiation dose delivery to cancer cells while minimizing exposure to normal tissues. This advantage is based on the fundamental physical principle of: its ability to control the depth at which protons release their energy within the body.

This characteristic enables physicians to precisely target tumors located deep within the body without unnecessarily irradiating surrounding normal tissues. Hence, PBT is particularly suitable for treating cancers in children, whose bodies are still growing and maturing. PBT is also preferred in childhood malignancies due to longer survivorship and a higher therapeutic ratio of protons.

PBT is divided into the modern pencil beam scanning (PBS) technique the passive scattering (PS) techniqueode (5). In this article, in addition to comparing PBT with PT, we would also like to draw attention to the determination of the type of PBT in the individual non-tumor effects after proton beam therapy for childhood cancers. However, few studies have compared the effect of PT

Nowadays, PBT is used in the treatment of pediatric brain, spinal cord, eye, soft tissue tumors, and lymphoma of the mediastinum (6). Treatment outcomes after PBT in children appear more promising compared to PT (6, 7). However, as with any medical intervention, PBT can cause potential adverse consequences and risks. In recent years, the potential for secondary tumors developing as a consequence of PBT has become an increasingly important complication. Single-center evaluations and analyses using the National Cancer Database suggest that the risk of secondary malignancies after PBT in children may be lower than with PT, especially with advanced modalities of proton therapy like pencil beam scanning that reduces neutron production (7, 8). The types of secondary cancers observed after PBT are similar to those seen after conventional radiation treatments (7–9). The most commonly reported were sarcomas, central nervous system tumors, leukemia, thyroid, and skin cancers. While the risk is reduced after PBT, it is not eliminated. Children may be at a slightly higher risk of developing secondary cancers due to their longer life expectancy after radiotherapy, which also allows more time for potential malignant transformation (10).

Besides the risk of secondary malignancies, pediatric patients undergoing PBT may experience also a range of non-cancer late effects, which can vary based on factors such as the type of tumor, the patient's age, the radiation dose, and the specific areas targeted (11). Some potential non-cancer effects that have been explored include brainstem injury, cognitive functions, and side effects from cardiovascular or endocrine systems. Our focus was to allow for a more precise and homogenous analysis, as broader radiation therapy complications inclusion would have introduced

heterogeneity in both endpoints and reporting across studies. Reported outcomes vary widely depending on i.e. tumor type, treatment protocol, radiation dose, patient age, and the anatomical areas exposed to radiation. Due to the unique physical properties of proton beam therapy and its shorter clinical history compared to photon radiotherapy, long-term data collection is still ongoing, and these results should be subject to further verification. Furthermore, to our knowledge, there are only a few published articles, including one from 2020, that discussed in one paragraph the existing literature on non-cancer-related late side effects of proton therapy in children (11). Therefore, this review aims to analyze publications addressing the occurrence of side effects from proton therapy in pediatric patients, excluding those related to the induction of secondary malignancies. We used data from two publicly available databases for this review: the U.S. National Library of Medicine's ClinicalTrials.gov (https://clinicaltrials.gov) for the analysis of clinical trials and PubMed, utilizing iCite (https://iCite.od.nih.gov)/Office of Portfolio Analysis, NIH, Bethesda, MD), a web-based application providing access to bibliometric information on publications. During the search process, we applied a combination of carefully selected keywords and Boolean operators to ensure a focused yet inclusive approach. Keywords included: *"pediatric"*, *"children"*, *"adolescents"*, *"side effects"*, *"adverse effects"*, *"toxicity"*, *"non-cancer effects"*, and *"quality of life"*. To maintain a clear scope, we excluded results related to *"secondary malignancies"* or *"secondary cancer"*. The search was conducted in English and included all articles regardless of publication year. A simplified diagram explaining the inclusion and exclusion criteria, the databases searched, the number of studies identified, and the selection process is shown on Figure 1.

The central nervous system tumors, alongside leukemia, represent the most common malignant neoplasms in childhood and adolescence. CNS tumors frequently arise in the PF of the skull. Their most common histological types are medulloblastoma, ependymoma, and atypical teratoid rhabdoid tumor (ATRT). Due to the frequent location of these tumors in the PF, irradiated patients are at risk of brainstem damage, potentially resulting in cranial nerve deficits, loss of motor control, impaired respiration, or even death (10, 12). Regarding photon radiation, the brainstem necrosis rate has been reported to range between 2.5% to 6.7% (12).

The present data show that PBT represents an important and preferred approach in the therapeutic management of children with brain tumors (12). The number of children receiving PBT is steadily increasing (13). Importantly, a narrative literature review

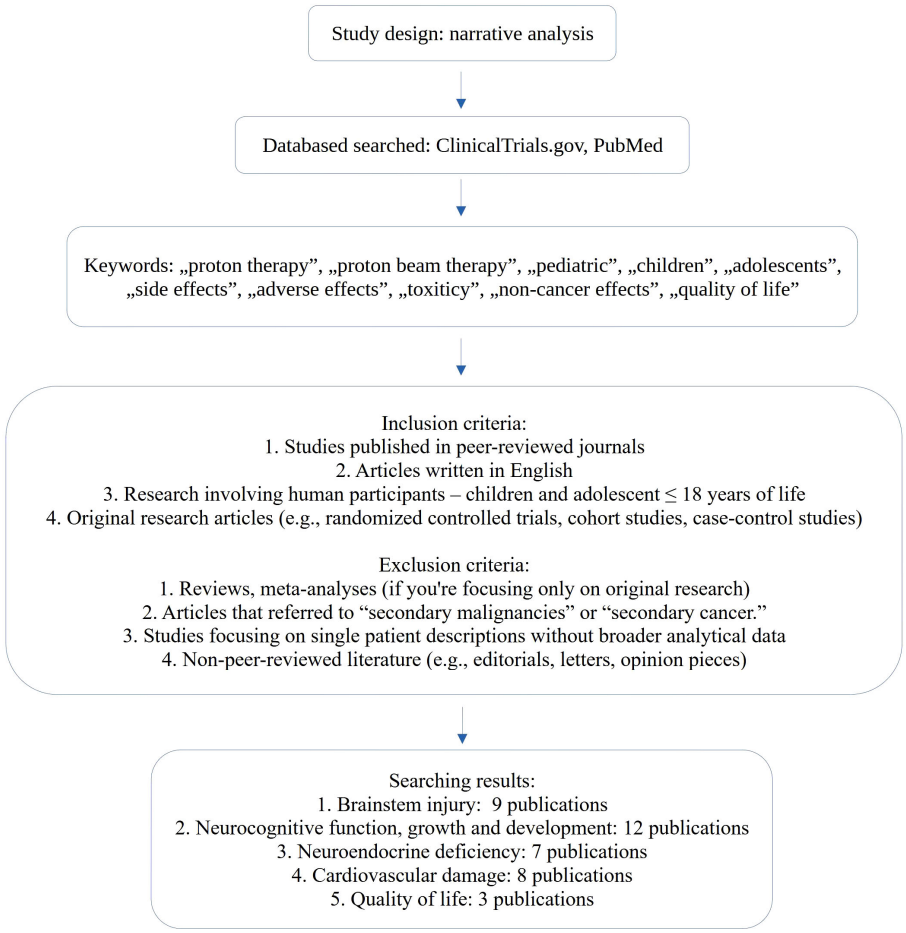

FIGURE 1
Narrative analysis.

concerning children after PBT suggests that the cumulative incidence (CI) of brainstem injury is relatively low (0.7% (14) – 5.0% (15)), and slightly lower compared to photon therapy (see Table 1). However, it is worth noting the findings of some authors (15, 19, 21), who analyzed CI or the rate of brainstem injury in children with pediatric tumors and reported significantly higher values. These findings highlight, among others, the importance of differences in linear energy transfer (LET) and consequently in relative biological effectiveness (RBE) within the spread-out Bragg peak (SOBP). Both LET and RBE are elevated at the distal ends of the SOBP (22). These observations might be elaborated by studies from Giantsoudie et al. (18). Performing a retrospective analysis of 111 children treated with PT for medulloblastoma, these researchers calculated dose and LET distribution for therapy plans (using the Monte Carlo system) and estimated RBE (based on published LET models) (18). They found higher LET levels in the subgroup of symptomatic patients with CNS injury compared to asymptomatic patients. However, no clear correlation was observed between injury sites and elevated RBE. Notable, the authors discussed limitations of the study like a small sample size and the need for further research on this topic (18).

Currently, LET and RBE variability within the SOBP are not considered in proton therapy planning (13, 18). Therefore, more conservative approaches to brainstem irradiation are being emphasized (13). For this reason, the Children's Oncology Group has introduced changes to the ACNS0831 protocol for ependymoma, imposing stricter proton dose constraints on the brainstem (13) (see Table 1). In contrast to the aforementioned results regarding the CI of brainstem injury, other authors have reported much lower CI rates (0.7% – 2.3%) in groups of children with primary PF tumors (13, 14, 16, 17). Several factors influence the development of brainstem injury, including total proton dose, irradiated brainstem volume, adjuvant chemotherapy treatment, and the interval between surgery and RT (13–17, 19, 21). Regarding dose and irradiated volume, Gentile et al. (16) found that among five patients with brainstem injury after PBT, four had a brainstem in the highest dose quartile (>55.8 Gy), and the V_{55} volume in the highest tertile (>6.0). On the contrary, Gunther et al. (19) reported a higher median D_{50} (≥54 Gy RBE) for patients with radiographic changes compared to those without them. Some studies have also shown that adjuvant chemotherapy (16, 18, 21) is associated with an increased risk of brainstem injury, likely due to its radiosensitizing effect (23). This result may be explained by insufficient tissue healing following resection. However, the effect of patient age on the risk of PBT-induced brainstem injury remains unclear. Some studies identify younger age as a risk factor (19, 20), while others suggest that older age (>5 years (16)) at diagnosis is associated with a higher incidence of imaging changes. It is also important to consider the varied definitions of brainstem injury used in reviewed studies. Some authors define this effect based on MRI changes coupled with new neurological symptoms unrelated to tumor progression (16, 18), while others include only MRI using previously published scales (19), or the CTCAE scale (13, 15, 20). an overestimation of clinically significant injury, as some imaging abnormalities might be transient, subclinical, or unrelated to functional impairment. In contrast, MRI diagnostics enable differential diagnosis of changes in nervous tissue resulting from either active neoplastic infiltration or additionally, intrinsic radiation sensitivity likely plays a role, although little is known about genetic or other factors influencing increased pediatric brainstem injury related to PBT (see Table 1).

To summarize the data on the incidence of brainstem injuries in children after PBT, further studies, especially prospective ones are needed to precisely describe the incidence and risk of brainstem necrosis in children. The PBS. At the same time, it is necessary to ensure that the risk of recurrence is not increased in the photon and proton cohorts with a longer period of clinical and imaging follow up.

Neurocognitive dysfunctions

Children treated with cranial radiation therapy for brain tumors are at an increased risk of neurocognitive impairment, affecting both overall intellectual functioning (expressed, for example, by full-scale IQ - FSIQ) and specific cognitive domains such as executive functions, attention, memory, processing speed, and control (24). Preclinical studies have identified white matter and hippocampal substructures as critical areas involved in radiation-induced cognitive impairment (25). For decades, the late cognitive and academic effects observed in patients treated with conventional photon-based radiotherapy have been studied. Following this type of RT, declines in global IQ1–3 and specific cognitive domains (e.g., executive functions, attention, language, and fine motor control) have been commonly reported (26). Furthermore, survivors experience poorer academic performance, particularly in academic fluency (i.e., the ability to quickly perform basic tasks in reading, writing, and mathematics) compared to their peers. However, it remains unclear whether newer approaches, such as proton radiotherapy, pose an increased risk of neurocognitive impairment. A potential advantage of PBT over PT is its ability to reduce the exposure of healthy tissue surrounding the target area, potentially mitigating its harmful effects on neurocognitive outcomes. In line with this observation, most studies [27-35] have not demonstrated an increased incidence of neurocognitive impairment (see Table 2). However, the Child et al. publication (29) analyzing a total of 88 children who underwent PBT (58 patients) or PT (30 patients) reported a decline in neurocognitive function in all cognitive domains assessed after RT. All groups were significantly below the population mean on processing speed and motor coordination. On all other cognitive measures, the PBT focal group did not differ significantly from the population mean. In contrast, the PT group scored significantly below the population mean on all cognitive measures except for the attention tasks. Both the PT and PBT groups scored significantly below the population mean on the FSIQ. In terms of academic proficiency, all groups scored significantly below the standards on measures of mathematical fluency and writing (most $p < 0.01$). The PT group performed worse than the PBT group on cognitive and academic measures (29).

TABLE 1 Summary of data concerning brainstem injury in children after proton therapy.

Authors	Patients	Median age [years]	Cancer Type	Type of PBT	Medium dose [Gy]	CHT	Post-PRT observation time [years]	Cumulative incidence of toxicity
Vogel et al. (2019) (14)	166	10	Astrocytoma Ependymoma	PBS	55.4	±	19.6	General - 0.7%
Haas- Kogan et al. (2018) (13)	671	5.4	Medulloblastoma – 57% Ependymoma –27%s, Glimas and ATRT – 14%	PBS	55 Gy		3.0	Grade 2+ - 2.38%. Grade 3+ - 1.3% FBI– 0.4%
Gentile et al. (2018) (16)	198	6.6	Medulloblastoma – 71.3% Ependymoma – 25.9% ATRT – 2.8%	–	54 Gy	±	4.2	General - 2.3% Medulloblastoma – 1.9% Ependymoma – 3.6% ATRT – 0.0%
Indelicato et al. (2018) (15)	179	3.5	Ependymoma (65% located in PF)	PS	54 Gy ≤3 y/o 59.4 GY >3 y/o	±	4.4	Grade2+ - 5.0% PF sites – 8.4%
Ares et al. (2016) (17)	50	2.6	Ependymoma	PBS	59.4	±	3.6	CIT – 2.8% Grade3 +-
Giantsoudi et al. (2015) (18)			Medulloblastoma	–		+	4.2	General - 3.6% Grade 3+ - 2.7%
Gunther et al. (2015) (19)	37	4.4	Ependymoma	–	59.4%	±	0,3	43%*
Indelicato et al. (2014) (20)	313	5.9	Ependymoma -23.4% Medulloblastoma – 12.1% Other - 64.5%	PS	54.0 CGE	±	2.0	General– 3.8% PE – 10.7% Grade 2 - 2.2% Grade 3 – 0.3 Grade 3- 0.3% Grade 4 – 0.6% Grade 5 – 0.3% Grade3+ – 2.1%
McGovern et al. (2014) (19)	31	1.6	ATRT	PBS	54.0 Gy – 17 pts 24 Gy – 7 pts 30,6 Gy – 7 pts	±	2.0	General - 16%* PF – 9.7%

ATRT, atypical teratoid/rhabdoid tumors; CHT, chemotherapy; CIT, cumulative incidence of toxicity; FBI, fatal brainstem injury; PF, posterior fossa; PBS, PS.

10.3389/fonc.2025.1554765

TABLE 2 The potential non-cancer effects of proton therapy, such as neurocognitive function, growth and development, and quality of life in pediatric patients.

Author	Patients	PRT initiation age [yrs]	Cancer type	Type of PBT	Medium dose [Gy]	CRT	Post-PRT observation time [yrs]	Incidence of neurocognitive impairment
Mash et al. (2023) (27)	12	4.6	Low-Grade Glioma Embryonal tumor Ependymoma	–	53.55	±	8.9	No incidence of neurocognitive impairment: No changes in white matter integrity.
Ali et al. (2021) (28)	41	2.0	Glioma-42.3% Medulloblastoma/ PNET-7.7% Ependymoma-19.2% Atypical teratoid rhabdoid tumor Primitive neuroectodermal tumor Germinoma – 11.52% Other-15.4%	–	nd	+	2.3	No incidence of neurocognitive impairment
Child et al. (2021) (29)	58	7.7	Glioma-25.9% Medulloblastoma/ PNET-32.7% Ependymoma-13.9% Germ Cell Tumor-17.2% Other-10.3%	PS	F: 50.4 CSI: 54.0	nd	6.1	Variable - F *vs* CSI: FSIQ - 13.3% *vs* 28.6%) VCI - 3.3% *vs* 28.6% PRI – 10% *vs* 17.9%), WMI - 10% (F), 17.9% PSI – 30% *vs* 46.4% Fine Motor – 26.7% *vs* 60.7 Switching (Verbal) - 26.7% *vs* 17.9% Switching (Graphomotor) – 30% *vs* 46.4% Inhibition/Switching – 23.3% *vs* 32.1% Verbal Learning – 20% *vs* 32.1% Verbal Memory *vs*16.7% *vs* 21.4% Visual Learning 10% *vs* 25% Visual Memory 13.3% *vs* 14.3% Attention 13.3% *vs* 17.9% Omissions 3.3% *vs* 10.7% Reading fluency 23.3% *vs* 42.9% Writing fluency 26.7% *vs* 53.6% Math Fluency 33.3% *vs* 42.9%
Weusthof et al. (2021) (30)	26	9.4	Glioma-42.3% Medulloblastoma/ PNET-7.7% Ependymoma-19.2% Craniopharyngioma – 3.8* Germinoma – 11.52% Other-15.4%	–	51.3	±	3.5	No incidence of neurocognitive impairment
Yip et al. (2020) (31)	14		Medulloblastoma – 36.0%	–	nd	nd	4.3	No incidence of neurocognitive impairment

(Continued)

10.3389/fonc.2025.1554765

TABLE 2 Continued

Author	Patients	PRT initiation age [yrs]	Cancer type	Type of PBT	Medium dose [Gy]	CRT	Post-PRT observation time [yrs]	Incidence of neurocognitive impairment
Kahalley et al. (2020) (32)	37	8.6	Medulloblastoma	PBS	54.0		10	No incidence of neurocognitive impairment
Gross et al. (2019) (33)	58	7.4	Craniopharyngioma - 8.6% Medulloblastoma/PNET - 44.8% Ependymoma –8.6% Germinoma -15.5% Glioma -15.5% Other - 6.9%	–	nd	±	2.6	No incidence of neurocognitive impairment
Peterson et al. (2019) (34)	22	10.0	nd	–	nd	nd	nd	No incidence of neurocognitive impairment
Yang et al. (2018) (35)	4	5.9	Atypical meningioma Retinoblastoma Ependymoma	PBS	nd	+	nd	No incidence of neurocognitive impairment
Pulsifer et al. (2018) (36)	60	12.3	Medulloblastoma – 38.3% Gliomas – 18.3% Craniopharyngioma – 15.0% Ependymoma – 11.7% Other – 16.7%	PBS	52.2	±	3.6	FSIQ – 40% Processing Speed – 35%
Kahalley et al. (2016) (37)	90	9.2	Glioma – 22.2% Medulloblastoma/PNET – 37.8% Ependymoma – 4.4% Germ cell tumor – 18.9% Other – 16.7%	90% PS 10% PBS	54		5	No incidence of neurocognitive impairment

CRT, conformal radiotherapy; CSI, craniospinal irradiation; F, focal; FSIQ, Full Scale Intelligence Quotient; nd, no data; PRI, Perceptual Reasoning Index; PSI, Processing Speed Index; VCI, Verbal Comprehension Index; WMI, Working Memory Index.; PBS, PS.

10.3389/fonc.2025.1554765

Overall, the results indicated that patients who received focal PBT achieved results that were within the norm on most cognitive and academic measures compared to children who received PT. The results of patients who received PBT were generally comparable to normative results for typically developing children. Even the weaknesses in processing speed, fine motor skills, and academic abilities fell slightly below the average range, indicating clinically mild challenges in these areas for this group. Similarly, Pulsifer et al. (36) demonstrated that patients under 6 years of age and those receiving craniospinal irradiation (CSI) were particularly vulnerable to IQ loss. Importantly, adaptive functioning did not worsen, and processing speed remained within normal limits (i.e., standard score ≥ 90) in both the focal and CSI PBT groups (36).

Several studies have also directly compared neurocognitive function following PBT and PT (see Table 3). These comparisons indicated that the subgroup of children receiving CSI PT was associated with the highest risk of neurocognitive decline. In this subgroup, particularly low cognitive functioning was observed, with 76% of individuals showing significant reductions in global intellectual functioning, and 53–88% experiencing difficulties across all tasks related to cognitive and academic fluency (except for a computerized attention task). The CSI PBT group also demonstrated lower scores in overall intellectual functioning and cognitive domains sensitive to radiotherapy (e.g. working memory, processing speed, fine motor skills, executive functions, and memory). Nonetheless, a smaller percentage of this group fell into the impaired range compared to the CSI PT (38). Pediatric patients with brain tumors who received PBRT scored significantly higher on most of the neurocognitive outcomes than those who received XRT (38).

It is also important to note that many factors, both related and unrelated to radiotherapy, influence neurocognitive outcomes. During RT, particular attention should be paid to the percentage of CSI use and the increased dose administered to specific brain regions such as the temporal lobes, hippocampus, and frontal lobes, as these areas may have a more detrimental effect on cognitive and

TABLE 3 Comparison of children's neurocognitive dysfunction between proton beam therapy and photon irradiation.

RT				PBT		
Authors	Patients	Total radiation dose [Gy]	Main results	Patients	Total radiation dose [Gy]	Main results
Mash et al. (2023) (27)	10	T: 53.4	Reduction of white matter integrity Relative significantly lower of cognitive and motor functions (FSIQ, VCI, PRI, WMI) F group: relative significantly lower overall intelligence, verbal reasoning, visual-motor skills, motor coordination	12	53.5	No reduction of white matter integrity. No decrease in cognitive and motor functions (FSIQ, VCI, PRI, WMI) F group: no change in respect to overall intelligence, verbal reasoning, visual-motor skills, motor coordination
Child et al. (2021) (29)	30	F: 54.0 CSI: 54.0	F group: significant decrease concerning FSIQ, verbal and graphomotor switching, math, reading and writing fluency, processing spin, fine motor coordination CSI: significant impairments in motor skills, processing speed, attention and interpersonal relations, math, reading and writing fluency, processing spin, fine motor coordination	58	F: 50.4 CSI: 54.0	F group: math and writing fluency, processing spin, fine motor coordination CSI: significant decrease concerning FSIQ, verbal and graphomotor switching, math, reading and writing fluency, processing spin, fine motor coordination
Kahalley et al. (2020) (32)	42	T: 55.8 CSI: 23.4	Significant decrease in global IQ, working memory, and processing speed	37	T: 54.0 CSI: 23.4	Stable intellectual outcomes in most domains (IQ, perceptual reasoning, working memory),(even in the context of CSI) Processing speed: decrease over time
Gross et al. (2019) (33)	67	F: CSI:	Relative lower full-scale IQ and processing speed, higher verbal IQ, and general adaptive function F group: relatively lower PSI CSI: relative lower VIQ, FSIQ/GAI	58	F: CSI:	Relative higher full-scale IQ and processing speed, higher verbal IQ, and general adaptive functions F group: relatively higher PSI CSI: relative higher VIQ, FSIQ/GAI
Pulsifer et al. (2018) (36)	60		Processing speed and working memory skills were significantly lower at follow-up for patients treated with CSI, regardless of age.	90	52.2	Motor, social interaction, personal living, community living - no significant change in adaptive functioning was found after PRT, regardless of age or radiation field
Kahalley et al. (2016) (37)	60	T: 54.0 CSI: 23.4	IQ decreased by 1.1 points per year in the RT group. IQ was lower in the RT group (by 12.5 points) compared to the PBT group.	90	T: 54.0 CSI: 23.4	No change in IQ over time.

CSI, craniospinal irradiation; F, focal; FSIQ, Full Scale Intelligence Quotient; GAI, General Ability Index; PRI, Perceptual Reasoning Index; PSI, Processing Speed Index; T, total; VCI, Verbal Comprehension Index; WMI, Working Memory Index.

social functioning compared to other brain regions (39, 40). In the study by Kahalley et al. (37), the majority of patients treated with PB. Additionally, the longer follow-up period available for photon-treated patients should be considered (33, 37). Other factors include chemotherapy exposure (41) and age at diagnosis (22, 24, 26, 42).

Non-treatment-related factors include pre-existing comorbidities (such as seizure disorders, stroke, hydrocephalus, or the need for VP shunts) and genetic factors. It has also been demonstrated that chemotherapy and surgery may have a potential negative impact on neurocognitive outcomes independently of radiotherapy (43, 44). Furthermore, attention should be given to the tests measuring overall neurocognitive abilities, such as processing speed (an index assessed in Wechsler-based evaluations like WISC-IV and WAIS-IV IQ). Although these parameters are most affected by radiotherapy, they are not considered in abbreviated IQ tests such as Estimated IQ, WASI-II, or the General Ability Index. Therefore, some authors recommend avoiding these tests in prospective studies to prevent the potential underestimation of cognitive decline (11).

Neuroendocrine dysfunctions

Neuroendocrine dysfunctions, alongside neurocognitive impairment, are one of the most frequently reported late effects of radiation therapy in children treated for brain tumors. These dysfunctions are directly related to damage to the hypothalamic-pituitary axis (HPA). CSI, through its impact on the HPA, can also affect organs beyond the central nervous system (CNS), including the thyroid, heart, lungs, liver, pancreas, kidneys, gonads, and bones, including spinal growth abnormalities (45). Therefore, children receiving CSI are at risk of multiple endocrinopathies, including growth hormone deficiency (GHD), hypothyroidism, adrenal insufficiency, and abnormal sex hormone production manifesting as hypogonadism or precocious puberty. These long-term deficiencies are a significant cause of morbidity among brain tumor survivors, affecting up to 80% of this population and being associated with an increased risk of various other medical conditions, necessitating chronic treatment and leading to high healthcare costs. The extent of radiation-induced endocrinopathies appears to be dose-dependent (46). The most common endocrinopathies are considered to be growth hormone deficiency and hypothyroidism. In the cohort treated with photon irradiation, the prevalence of adrenal insufficiency, precocious puberty, and sex hormone deficiency was 8%, 16%, and 19%, while for it was 5%, 18% and 3%, respectively (47).

Proton beam radiotherapy reduces radiation exposure to normal tissues, such as the hypothalamus and pituitary gland (10). Theoretically, this type of radiation method may prevent the development of neuroendocrine dysfunction. Multiple dosimetric comparative studies have demonstrated the potential to reduce the radiation dose received by the HPA when compared to 3D photon therapy or intensity-modulated photon therapy (48, 49). Based on PBT dosimetric advantage, modeling studies have suggested that proton therapy compared to photon therapy is associated with a reduced risk of late endocrinological effects (50).

A narrative literature review has identified that PBT was also associated with an increased risk of neuroendocrine dysfunction (see Table 4). In the cited studies, the incidence of growth hormone deficiency (GHD) ranged from 37.5% (51) to 60% (55). However, the lowest percentage observed in the analysis performed by Yip et al. (51) was noticed for the entire cohort included in the study, regardless of whether the children received CSI or not. Importantly, the follow-up period was 4.4 years. Of note, most endocrinopathies can manifest within the subsequent 6 years following cancer treatment, as endocrine complications have been reported decades later (58). Therefore, the incidence of endocrine disorders in patients with a follow-up period of less than 5 years may be underestimated. Another frequently occurring neuroendocrine dysfunction after PBT is hypothyroidism, with the incidence ranging between 17.7% (51) to 47.5% (55). Other neuroendocrinopathies were reported at significantly lower rates. Aldrich et al. (52) in univariate analyses showed no clinical or demographic factors to be associated with the occurrence of any endocrinopathy, except for moderate differences in GHD between treatment protocols (see Table 4).

Several studies have directly compared the incidence of neuroendocrine dysfunctions between PBT and PT. Yip et al. (51) found that proton therapy is associated with a lower risk of hypothyroidism (29% for PT vs. 19% for PB

Yinuo Li et al. (57) analyzed the late effects of proton therapy (PBT) in children with malignant tumors. The kidney is frequently irradiated in radiotherapy for childhood malignant tumors, such as childhood neuroblastoma and rhabdomyosarcoma. In all cases, the kidney was irradiated through the primary lesion. In the irradiated and contralateral control kidneys, the median volume changes were 5.63 and 5.23 mL/year; and the median % volume changes at 1 year were 8.55% and 9.53%, respectively. The median relative volume change of the irradiated kidneys at 1 year was 16.42% compared with the control kidneys. The larger the irradiated volume, the greater the loss of renal volume. The volume reduction was significantly greater in patients aged 4–7 years than in patients aged 2–3 years. The results suggest that kidneys exposed to PBT for the treatment of childhood malignancies show continued atrophy during follow-up. The degree of atrophy increases with increasing radiation dose, larger irradiated volume, and older age. However, with growth and maturation, the contralateral kidney becomes progressively larger and less radiosensitive (57).

Summarized, reviewed studies support the observation that proton therapy is associated with a lower incidence of hypothyroidism, thyroid protection, and sex hormone deficiency compared to conventional X-ray therapy. These findings highlight the potential benefits of PBT application, especially in minimizing endocrine sequelae in patients undergoing treatment for medulloblastoma. Further investigation into growth hormone deficiency and non-hormonal growth changes in patients treated with both protons and photons is necessary to establish comprehensive treatment protocols.

TABLE 4 The narrative review of endocrine deficiency after proton beam therapy in children.

Author	Patients	PBT initiation age [yrs]	Cancer type	Medium dose [Gy]	CRT	Post-PBT observation time [yrs]	Incidence of endocrine deficiency
Yip et. al. (2022) (51)	32		Medulloblastoma - 38%	54.0	±	4.4	Growth hormone deficiency – 37.5% *vs* 50.0% (CSI) Hypothyroidism - 19%. *vs* 17.7% (CSI) Sex Hormone Deficiency- 6.3% vs 0.0% (CSI) Hormone Replacement Therapy 37.5% vs 50.0% (CSI)
Aldrich et al. (2021) (52)	64	7.6	Medulloblastoma	CSI< 30 Gy- 63.5 (n=40) CSI≥30 (n=23)	nd	5.6	Primary Hypothyroidism- 28% Growth hormone deficiency – 52.5% Adrenal insufficiency- 5% Endocrine replacement therapy- 55.0% Sex Hormone Deficiency-2.5% Precocious puberty- 17.5%
Bielamowicz et al. (2018) (53)	41		Meduloblastoma		nd	3.8	Hypothyroidism – 19.0% Primary hypothyroidism - 7.3% Central hypothyroidism – 9.8%
Eaton et al. (2016) (54)	40	6.2	Medulloblastoma	TB – 60 (n=24) PF – 30 (n=12) PF → TBa – 10 (n = 4)	+	5.8	Hypothyroidism- 22.5% Growth hormone deficiency- 52.5% Adrenal insufficiency- 5% Sex Hormone Deficiency-2.5% Precocious puberty- 17.5%
Greenberger et al. (2014) (55)	29	11.0	Low-grade gliomas of the brain or spinal cordOther-15.4%	52.2	±	7.6	Growth hormone deficiency – 60.0% Hypothyroidism – 47.5% Cortisol insufficiency – 22.5% Testosterone deficiency – 16.0% Elevated prolactin – 12.5% Diabetes Insipidus – 9.0% Precocious Puberty – 6.0%
Viswanathan et al. (2011) (56)	31	11.9	Craniopharyngioma - 7 Medulloblastoma - 6 Glioma- 4 Other – 14	F: 50.4 CSI: 54.0	±	1.8	Growth hormone deficiency (n = 6), TSH deficiency (n = 4), ACTH deficiency (n = 4), and hypogonadotropic hypogonadism (n = 4).
Yinuo Li et al. (2023) (57)	11	8	Rhabdomyosarcoma - 2 Neuroblastoma- 8 Osteosarcoma- 1		±	2,04	The median relative change in irradiated kidney volume was 16.42% compared to the control group after 1 year.

CRT, conformal radiotherapy; CSI, craniospinal irradiation; nd, no data.

10.3389/fonc.2025.1554765

Cardiovascular damage

Increased cardiovascular morbidity and mortality are well-documented late toxicities following mediastinal radiotherapy in patients with Hodgkin lymphoma (HL) (59). Although HL is a rare malignancy in the general population, a significant percentage of cases occur in adolescents and young adults (60), which makes it the most common malignancy among individuals aged 15 to 19 years. Hodgkin lymphoma is characterized by a high probability of long-term survival, which allows sufficient time for latent radiation-induced damage to manifest, ultimately affecting both quality of life and, in some cases, life expectancy. Cardiovascular disease (CVD) is viewed as the most common non-malignant cause of death among HL survivors (61).

RT targeting the cranial or craniospinal regions for brain tumors or leukemia can damage the hypothalamic-pituitary-thyroid axis, especially with doses exceeding 20 Gy (62–64). This damage may disrupt metabolic processes and hormone regulation, thereby increasing CVD risk factors such as obesity, dyslipidemia, insulin resistance, and diabetes (63–66). Chemotherapy agents, particularly anthracyclines, cyclophosphamide, cytarabine, cisplatin, and ifosfamide, often administered in combination with radiotherapy, can also adversely affect the cardiovascular system by impairing myocardial function or causing peripheral damage (64). Post-radiation myocardial toxicity is associated with diffuse interstitial fibrosis, microvascular damage, and valvular fibrosis (64). In the vascular system, chronic inflammation induced by radiation has increased the risk of atherosclerosis development (64, 65).

Studies evaluating whole-heart dosimetric parameters concerning late cardiotoxicity have shown that increased cardiotoxicity correlates with higher whole-heart dose, greater intracardiac dose inhomogeneity, male sex, and increasing age (65–67). As a result, hematologists and oncologists may accept higher relapse rates and salvage therapies in exchange for omitting radiotherapy to reduce late toxicities (68). With the growing number of proton therapy centers, more young HL patients have received PBT (69). Several studies have compared cardiovascular toxicity following proton beam therapy and photon radiotherapy. Zhang et al. (70) analyzed 17 pediatric patients with medulloblastoma treated with either passively scattered protons (PS) therapy or craniospinal irradiation using field-in-field photons. They compared the risk of lifetime attributable risk (RLAR) and relative risk (RRs had a significantly higher RLAR for cancer mortality than boys. In earlier work published by the same authors (71), comparisons of cardiac toxicity risks in pediatric patients with Hodgkin's disease (HD) and medulloblastoma (MB) showed that PS therapy reduced predicted cardiac toxicity risks compared to photon therapy, particularly in the MB patient cohort. Hoppe et al. (72) conducted a study on 13 pediatric and adolescent HL patients, comparing three-dimensional conformal radiotherapy (3DCRT), intensity-modulated radiotherapy (IMRT), and proton therapy (PBT) for involved node radiotherapy (INRT). The authors found that proton therapy significantly reduced average heart doses compared to 3DCRT and IMRT, lowering radiation exposure to all major heart subunits. Consequently, as the authors suggested proton therapy reduced the risk of cardiac toxicity. Similarly, Lautenschlaeger et al. (73) showed that in a cohort of young adult HL patients, PBT provided significant dose-sparing benefits to the lungs, coronary arteries, and heart valves compared to photon-based plans.

Summarized, these studies suggest that proton vs. photon therapy may reduce the risk of cardiac toxicity and secondary cancer incidence in pediatric patients with Hodgkin's lymphoma and medulloblastoma. The extent of these benefits is influenced by many factors including cancer type, patient age, and specific treatment protocols.

Quality of life

The Childhood Cancer Survivor Study found that among young adult survivors of childhood cancer diagnosed between 1970 and 1986, at least 1 of 6 health status domains (general health, mental health, functional status, activity limitations, cancer-related pain, and cancer-related anxiety) deteriorated moderately or severely in 44% (74). Currently, the cumulative incidence of chronic disease recorded 30 years after cancer diagnosis is 73%, with a cumulative incidence of 42% for severe, disabling, or life-threatening conditions or death attributable to chronic disease (75). Concerning PBT, Garcia-Marqueta et al. (76) evaluated the quality of life in a group of 207 patients with intracranial meningioma treated with pencil-beam scanning proton beam therapy proton therapy was assessed using the PEDQOL questionnaires, evaluating physical, emotional, social, and school functioning domains. The study demonstrated an estimated 5-year local control and overall survival rates of 19.4% and 100.0%, respectively. Except for one patient who developed a cataract requiring surgery, no grade ≥3 late toxicities were reported. During the first year after PBT, one child required educational support, one needed to attend a special school, one had social difficulties, and three children required assistance with daily basic activities (DBA). Three years post-PBT, only one child continued to require assistance for DBA. Proton therapy, delivered mode BT therefore has a clear advantage in the treatment of brain tumors, especially in children. In fact, an improvement in neuropsychological outcomes has been observed in pediatric patients with brain tumors after PBT (76).

There are also studies comparing health-related quality of life (HRQoL) after PBT and PT. These studies assessed the parameter known as health-related quality of life (HRQoL). Kaltahau et al. (77) investigated HRQoL in a group of 142 pediatric patients aged 2–18 years with intracranial tumors treated with proton radiotherapy at Massachusetts General Hospital, followed for six years post-treatment. The authors demonstrated a significant correlation between lower full-scale IQ (FSIQ) and poorer HRQoL outcomes. Additionally, the use of craniospinal irradiation (CSI) and chemotherapy was associated with worse HRQoL outcomes. A study performed by Yock et al. (78) focused on comparing HRQoL outcomes in this patient group as reported by parent-proxies. Three years after treatment, the proton cohort scored 10 points higher in the overall baseline HRQoL score, and this

difference was statistically significant (78). This prospective study of children with brain tumors treated with PBT shows the influence of disease type and treatment intensity on HRQoL. Worse HRQoL scores were 19 shown in the domains of anxiety, communication, and worry, suggesting that increased support from psychiatrists, psychologists, and medical staff may also improve HRQoL scores.

Results of the above-mentioned studies emphasize the long-term benefits of PBT in reducing late toxicities and improving QoL outcomes in pediatric oncology patients.

Summary, conclusions, and future directions

Proton radiotherapy is considered an effective and precise cancer treatment method causing minimal side effects. We conducted a narrative review of the published literature on the non-cancer effects after PBT, but we did not perform a meta-analysis due to considerable variability between studies. In published articles, there are multiple sources of heterogeneity, some of which include differences in cancer types, population characteristics, study methodologies, type of radiotherapy used, and fractionation schedule. radiotherapy (79–81). Compared to photons, the LET which is the predominant factor that influences the RBE increases rapidly with depth along the SOBP reaching a maximum value at the distal edge of the Bragg peak (82). This potentially can increase the radiation DNA damage to healthy tissue and may influence outcomes. Several pre-clinical and clinical studies have investigated the LET and RBE distributions, however, much is still unknown about the mechanism by which LET affects RBE for healthy tissue compared to cancer cells (82). In a recently published study, the authors report on the association of LET and dose which may contribute to greater radiation risk of necrosis after pencil beam scanning proton therapy in 33 pediatric patients with posterior fossa tumors (83). On the other hand, in 36 pediatric brain tumor patients treated with passive scattering proton therapy, the authors highlighted that the elevated LET could be a minor contributor to the observed brainstem toxicity, but a very minor trend towards higher LET and increased RBE-weighted dose was seen in patients with brainstem toxicity (84). Therefore, the individual assessment of LET and RBE in preclinical and clinical studies for pediatric tumors should be explored further.

The other sources of heterogeneity that limit the presented review studies are the applied two alternative modes of PT delivery. for highly conformal dose distribution, PS (85). The clinical significance for pediatrics of the differences between the two alternative proton modes is not well understood. The information about treatment modes like PBS or PS has been identified in our review but future studies will be necessary to better compare the two treatment modalities on treatment outcomes after proton beam therapy for pediatric tumors.

Limitations of the narrative review also include the exclusion of unpublished manuscripts and abstracts from conference proceedings.

The majority of findings analyzing the risk of late toxicity after proton beam therapy in children found a decrease in this risk after PBT in relation to. The analysis indicates that PBT generally reduces the risks of cognitive, neuroendocrine, and cardiovascular complications compared to conventional In the study by Michael T et al. (86), proton beam therapy has been shown to be the preferred radiotherapy modality for childhood cancers, which are rare and heterogeneous diseases. Radiation to the head and neck region is associated with a range of radiotherapy complications affecting vision, hearing, feeding, and growth. Support for proton therapy comes from risk modeling and a limited number of cohort series (86). We compared the efficacy and expected toxicity of proton and photon radiotherapy for childhood cancers and examined the benefits of proton radiotherapy in reducing acute and late radiation toxicities, including the risk of secondary malignancies, vision, and cognition. Proton therapy demonstrated few acute and late radiotherapy toxicities and provided similar rates of locoregional control in pediatric patients with head and neck cancer. In addition, Masashi Mizumoto et al. (87) valuated the long-term benefits of PBT in cancer survivors. Retrospective observational study of 62 pediatric patients who received PBT for 5 or more years. Analysis showed that the irradiated site (head and neck, brain) was significantly associated with late toxicities. No malignant secondary tumors occurred in the irradiated field. Data suggest that PBT has the potential to reduce the risk of late mortality and secondary malignancy (87). However, even with its advantages, non-cancer effects can arise, which vary depending on the treatment site, dose, and age of the child.

Our findings generally support a lower incidence of certain late toxicities following PBT in comparison to photon therapy, especially in pediatric patients. However, the evidence remains inconclusive in several key areas. Some studies suggest that children treated for posterior fossa tumors or undergoing craniospinal irradiation may still be at risk of brainstem injury or neurocognitive decline. Moreover, many published reports are retrospective, based on small sample sizes, and suffer from inconsistent definitions and reporting of toxicity outcomes.

Different childhood cancers exhibit varying degrees of radiosensitivity and associated risk of late toxicity. The above studies have shown that patients with medulloblastoma treated with PBT had cognitive deficits and endocrine dysfunction compared with photon therapy. Patients with ependymoma treated with PBT have comparable tumor control with potentially fewer neurocognitive side effects, similar to children with rhabdomyosarcoma. s can be seen in Tables 1–4, age at the time of treatment seems to be a factor influencing susceptibility to radiation-induced side effects. Children under 5 years of age are particularly susceptible to neurocognitive disorders due to ongoing brain development. Analysis may provide a more structured and comprehensive understanding of the effects of PBT in different pediatric populations. This stratified approach may also guide future research and clinical decision-making by ensuring that treatment protocols and of each subgroup.

Given these limitations, it is evident that future research must move beyond retrospective analyses and isolated institutional experiences. There is a pressing need for large-scale, prospective studies conducted across multiple centers, with harmonized

methodologies and long-term follow-up. Such studies should not only assess clinical endpoints but also include comprehensive evaluations of patient-reported outcomes and neuropsychological functioning, particularly in pediatric populations where subtle cognitive deficits may emerge years after treatment. Furthermore, the role of biological and treatment-related modifiers—such as age at exposure, anatomical site, and individual radiosensitivity—requires further exploration to identify patients at higher risk of adverse effects.

Another critical direction for future studies is the comparative evaluation of proton and photon therapies through controlled clinical trials, where feasible, or well-designed observational studies employing matched cohorts and robust statistical methods. These investigations should focus not only on dosimetric advantages but also on long-term functional outcomes and quality of life. At the same time, international collaboration and the creation of shared databases or registries could greatly enhance the power and generalizability of findings, allowing researchers to pool data and identify meaningful patterns that may not be apparent in single-center studies. Additionally, the incorporation of novel biomarkers—including imaging-based and molecular indicators—holds promise for more precise risk stratification and individualized treatment planning. As the field of radiogenomics evolves, future research should aim to integrate these tools into clinical protocols to better predict and mitigate the risk of late toxicity.

In conclusion, while PBT appears to offer significant benefits in reducing late adverse effects, particularly among children, the current evidence base is not yet sufficient to draw definitive conclusions (Figure 2). A more coordinated, methodologically rigorous, and multidimensional research agenda is essential to fully understand and optimize the long-term safety and

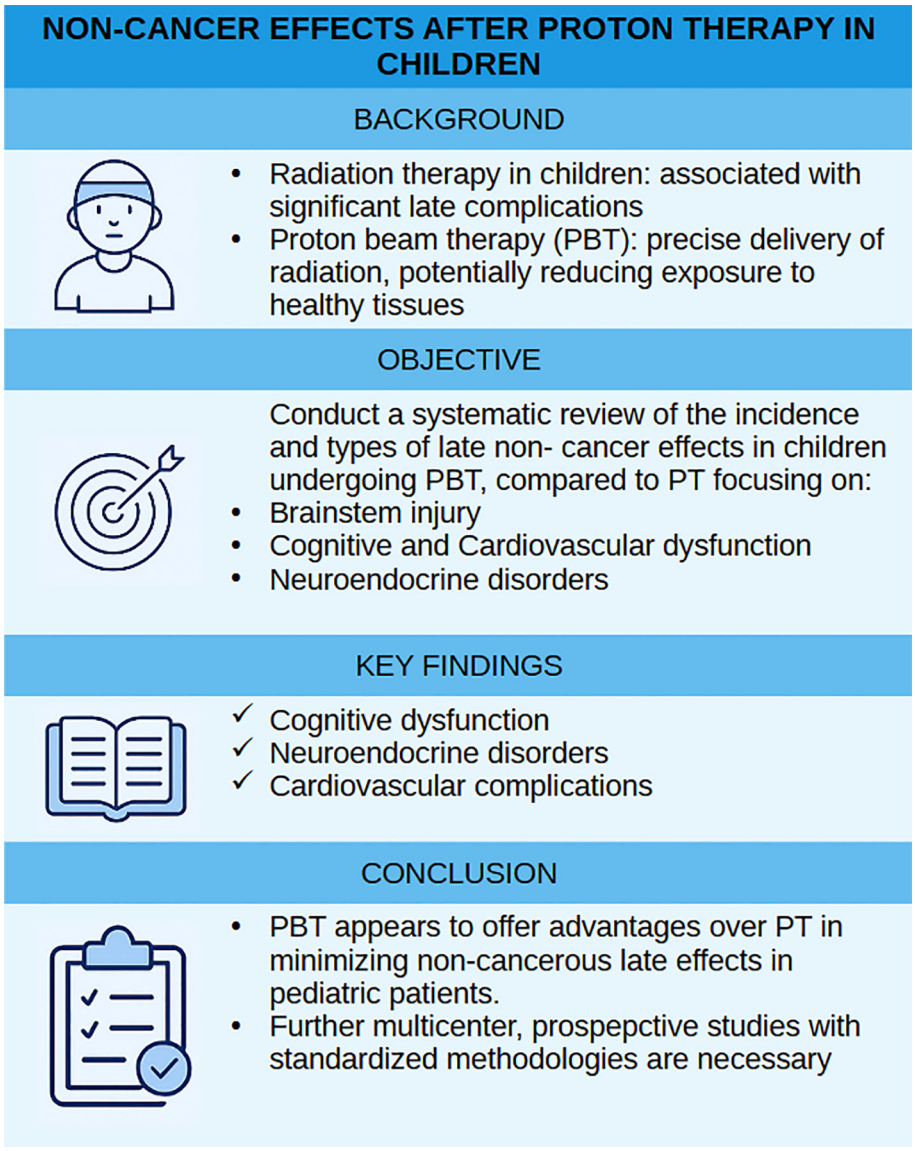

FIGURE 2
Summary figure.

effectiveness of proton therapy. The risk of these non-cancer effects underscores the importance of long-term follow-up for children who undergo proton therapy. Regular monitoring and early interventions can help mitigate these impacts and improve the quality of life for pediatric patients. Therefore, to advance our understanding of the key determinants of non-cancer effects, further prospective studies are needed in large groups of patients, which will also allow for the analysis of factors related to proton radiotherapy.

Author contributions

AZ-G: Writing – original draft, Writing – review & editing, Funding acquisition, Investigation, Methodology. BB: Investigation, Methodology, Writing – review & editing. MK: Investigation, Methodology, Writing – review & editing. KD-R: Investigation, Methodology, Writing – review & editing. JM: Conceptualization, Funding acquisition, Supervision, Writing – review & editing.

Funding

The author(s) declare that financial support was received for the research and/or publication of this article. The research and publication were financed from the state budget under the Ministry of Education and Science (Poland) program entitled Science for Society II, No. NdS-II/SP/0295/2023/01 (project title "The importance of proton radiotherapy in the treatment of patients with central nervous system tumors"), total project amount 1 mln PLN.

Acknowledgments

AZ-G acknowledges the project Miniatura 8, No. 2024/08/X/NZ7/00625 entitled "Combination of modern, complex multi-drug chemotherapy with radiotherapy (proton or photon) as a new strategy for the treatment of glioblastoma multiforme" founded by the National Science Centre, Poland for initial review performed about toxicity for study planning.

Conflict of interest

The authors declare that the research was conducted in the absence of any commercial or financial relationships that could be construed as a potential conflict of interest.

Generative AI statement

The author(s) declare that no Generative AI was used in the creation of this manuscript.

Publisher's note

All claims expressed in this article are solely those of the authors and do not necessarily represent those of their affiliated organizations, or those of the publisher, the editors and the reviewers. Any product that may be evaluated in this article, or claim that may be made by its manufacturer, is not guaranteed or endorsed by the publisher.

References

1. Wu Y, Deng Y, Wei B, Xiang D, Hu J, Zhao P, et al. Global, regional, and national childhood cancer burden, 1990-2019: An analysis based on the Global Burden of Disease Study 2019. *J Adv Res*. (2022) 40:233–47. doi: 10.1016/j.jare.2022.06.001

2. Jemal A, Siegel R, Xu J, Ward E. Cancer statistics, 2010. *CA Cancer J Clin*. (2010) 60:277–300. doi: 10.3322/caac.20073

3. Palmer JD, Tsang DS, Tinkle CL, Olch AJ, Kremer LCM, Ronckers CM, et al. Late effects of radiation therapy in pediatric patients and survivorship. *Pediatr Blood Cancer*. (2021) 68:e28349. doi: 10.1002/pbc.28349

4. Armstrong GT, Liu Q, Yasui Y, Neglia JP, Leisenring W, Robison LL, et al. Late mortality among 5-year survivors of childhood cancer: a summary from the Childhood Cancer Survivor Study. *J Clin Oncol*. (2009) 10;27:2328–38. doi: 10.1200/JCO.2008.21.1425

5. Mishra MV, Khairnar R, Bentzen SM, Larson G, Tsai H, Sinesi C, et al. Proton beam therapy delivered using pencil beam scanning vs. passive scattering/uniform scanning for localized prostate cancer: Comparative toxicity analysis of PCG 001-09. *Clin Transl Radiat Oncol*. (2019) 19:80–6. doi: 10.1016/j.ctro.2019.08.006

6. Leroy R, Benahmed N, Hulstaert F, Van Damme N, De Ruysscher D. Proton therapy in children: A systematic review of clinical effectiveness in 15 pediatric cancers. *Int J Radiat Oncol Biol Phys*. (2016) 95(1):267-278. doi: 10.1016/j.ijrobp.2015.10.025

7. Indelicato DJ, Bates JE, Mailhot Vega RB, Rotondo RL, Hoppe BS, Morris CG, et al. Second tumor risk in children treated with proton therapy. *Pediatr Blood Cancer*. (2021) 68:e28941. doi: 10.1002/pbc.28941

8. Xiang M, Chang DT, Pollom EL. Second cancer risk after primary cancer treatment with three-dimensional conformal, intensity-modulated, or proton beam radiation therapy. *Cancer*. (2020) 126:3560–8. doi: 10.1002/cncr.32938

9. Chung CS, Yock TI, Nelson K, Xu Y, Keating NL, Tarbell NJ. Incidence of second Malignancies among patients treated with proton versus photon radiation. *Int J Radiat Oncol Biol Phys*. (2013) 87:46–52. doi: 10.1016/j.ijrobp.2013.04.030

10. Upadhyay R, Yadav D, Venkatesulu BP, Singh R, Baliga S, Raval RR, et al. Risk of secondary Malignant neoplasms in children following proton therapy vs. photon therapy for primary CNS tumors: A systematic review and meta-analysis. *Front Oncol*. (2022) 12:893855. doi: 10.3389/fonc.2022.893855

11. Greenberger BA, Yock TI. The role of proton therapy in pediatric Malignancies: Recent advances and future directions. *Semin Oncol*. (2020) 47:8–22. doi: 10.1053/j.seminoncol.2020.02.002

12. Devine CA, Liu KX, Ioakeim-Ioannidou M, Susko M, Poussaint TY, Huisman TAGM, et al. Brainstem injury in pediatric patients receiving posterior fossa photon radiation. *Int J Radiat Oncol Biol Phys*. (2019) 105:1034–42. doi: 10.1016/j.ijrobp.2019.08.039

13. Haas-Kogan D, Indelicato D, Paganetti H, Esiashvili N, Mahajan A, Yock T, et al. National Cancer Institute Workshop on Proton Therapy for Children: considerations regarding brainstem injury. *Int J Radiat Oncol Biol Phys*. (2018) 101:152–68. doi: 10.1016/j.ijrobp.2018.01.013

14. Vogel J, Grewal A, O'Reilly S, Lustig R, Kurtz G, Minturn JE, et al. Risk of brainstem necrosis in pediatric patients with central nervous system Malignancies after pencil beam scanning proton therapy. *Acta Oncol*. (2019) 58:1752–6. doi: 10.1080/0284186X.2019.1659996

15. Indelicato DJ, Bradley JA, Rotondo RL, Nanda RH, Logie N, Sandler ES, et al. Outcomes following proton therapy for pediatric ependymoma. *Acta Oncol*. (2018) 57:644–8. doi: 10.1080/0284186X.2017.1413248

16. Gentile MS, Yeap BY, Paganetti H, Goebel CP, Gaudet DE, Gallotto SL, et al. Brainstem injury in pediatric patients with posterior fossa tumors treated with proton beam therapy and associated dosimetric factors. *Int J Radiat Oncol Biol Phys* (2018) 100:719–29. doi: 10.1016/j.ijrobp.2017.11.026

17. Ares C, Albertini F, Frei-Welte M, Bolsi A, Grotzer MA, Goitein G, et al. Pencil beam scanning proton therapy for pediatric intracranial ependymoma. *J Neurooncol*. (2016) 128:137–45. doi: 10.1007/s11060-016-2090-4

18. Giantsoudi D, Sethi RV, Yeap BY, Eaton BR, Ebb DH, Caruso PA, et al. Incidence of CNS injury for a cohort of 111 patients treated with proton therapy for medulloblastoma: LET and RBE associations for areas of injury. *Int J Radiat Oncol Biol Phys*. (2016) 95:287–96. doi: 10.1016/j.ijrobp.2015.09.015

19. Gunther JR, Sato M, Chintagumpala M, Ketonen L, Jones JY, Allen PK, et al. Imaging changes in pediatric intracranial ependymoma patients treated with proton beam radiation therapy compared to intensity modulated radiation therapy. *Int J Radiat Oncol Biol Phys*. (2015) 93:54–63. doi: 10.1016/j.ijrobp.2015.05.01

20. Indelicato DJ, Flampouri S, Rotondo RL, Bradley JA, Morris CG, Aldana PR, et al. Incidence and dosimetric parameters of pediatric brainstem toxicity following proton therapy. *Acta Oncol*. (2014) 53:1298–304. doi: 10.3109/0284186X.2014.957414

21. McGovern SL, Okcu MF, Munsell MF, Kumbalasseriyil N, Grosshans DR, McAleer MF, et al. Outcomes and acute toxicities of proton therapy for pediatric atypical teratoid/rhabdoid tumor of the central nervous system. *Int J Radiat Oncol Biol Phys*. (2014) 90:1143–52. doi: 10.1016/j.ijrobp.2014.08.354

22. Horendeck D, Walsh KD, Hirakawa H, Fujimori A, Kitamura H, Kato TA. High LET-like radiation tracks at the distal side of accelerated proton bragg peak. *Front Oncol*. (2021) 11:690042. doi: 10.3389/fonc.2021.690042

23. Ruben JD, Dally M, Bailey M, Smith R, McLean CA, Fedele P. Cerebral radiation necrosis: incidence, outcomes, and risk factors with emphasis on radiation parameters and chemotherapy. *Int J Radiat Oncol Biol Phys*. (2006) 65:499–508. doi: 10.1016/j.ijrobp.2005.12.002

24. Monje ML, Mizumatsu S, Fike JR, Palmer TD. Irradiation induces neural precursor-cell dysfunction. *Nat Med*. (2002) 8:955–62. doi: 10.1038/nm749

25. Greene-Schloesser D, Robbins ME. Radiation-induced cognitive impairment—from bench to bedside. *Neuro Oncol*. (2012) 14:iv37–44. doi: 10.1093/neuonc/nos196

26. Hopewell JW, van der Kogel AS. Pathological mechanisms leading to the development of late radiation-induced damage to the central nervous system. *Front Radiat Ther Oncol*. (1999) 33:265–75. doi: 10.1159/000061239

27. Mash LE, Kahalley LS, Raghubar KP, Goodrich-Hunsaker NJ, Abildskov TJ, De Leon LA, et al. Cognitive sparing in proton versus photon radiotherapy for pediatric brain tumor is associated with white matter integrity: an exploratory study. *Cancers (Basel)*. (2023) 15:1844. doi: 10.3390/cancers15061844

28. Ali JS, Ashford JM, Swain MA, Harder LL, Carlson-Green BL, Miller JM, et al. Predictors of cognitive performance among infants treated for brain tumors: findings from a multisite, prospective, longitudinal trial. *J Clin Oncol*. (2021) 39:2350–8. doi: 10.1200/JCO.20.01687

29. Child AE, Warren EA, Grosshans DR, Paulino AC, Okcu MF, Ris MD, et al. Long-term cognitive and academic outcomes among pediatric brain tumor survivors treated with proton versus photon radiotherapy. *Pediatr Blood Cancer*. (2021) 68:: e29125. doi: 10.1002/pbc.29125

30. Weusthof K, Lüttich P, Regnery S, König L, Bernhardt D, Witt O, et al. Neurocognitive outcomes in pediatric patients following brain irradiation. *Cancers (Basel)*. (2021) 13:3538. doi: 10.3390/cancers13143538

31. Yip ATT, Huynh-Le MP, Crawford J, Kaner R, MacEwan I, Hattangadi-Gluth JA. Comparing endocrine and neurocognitive outcomes in pediatric brain tumor patients treated with proton vs photon radiation. *Int J Radiat Oncol Biol Phys*. (2020) 108:E237–8. doi: 10.1016/j.ijrobp.2020.07.1518

32. Kahalley LS, Peterson R, Ris MD, Janzen L, Okcu MF, Grosshans DR, et al. Superior intellectual outcomes after proton radiotherapy compared with photon radiotherapy for pediatric medulloblastoma. *Clin Oncol*. (2020) 38:454–61. doi: 10.1200/JCO.19.01706

33. Gross JP, Powell S, Zelko F, Hartsell W, Goldman S, Fangusaro J, et al. Improved neuropsychological outcomes following proton therapy relative to X-ray therapy for pediatric brain tumor patients. *Neuro Oncol*. (2019) 21:934–43. doi: 10.1093/neuonc/noz070

34. Mash RK, Katzenstein JM. Working memory and processing speed among pediatric brain tumor patients treated with photon or proton beam radiation therapy. *Childrens Health Care*. (2019) 48:131–41. doi: 10.1080/02739615.2018.1510330

35. Yang CC, Lin SY, Tseng CK. Maintenance of multidomain neurocognitive functions in pediatric patients after proton beam therapy: a prospective case-series study. *Appl Neuropsychol Child*. (2019) 8:389–95. doi: 10.1080/21622965.2018.1471996

36. Pulsifer MB, Duncanson H, Grieco J, Evans C, Tseretopoulos ID, MacDonald S, et al. Cognitive and adaptive outcomes after proton radiation for pediatric patients with brain tumors. *Int J Radiat Oncol Biol Phys*. (2018) 102:391–8. doi: 10.1016/j.ijrobp.2018.05.069

37. Kahalley LS, Ris MD, Grosshans DR, Okcu MF, Paulino AC, Chintagumpala M, et al. Comparing intelligence quotient change after treatment with proton versus photon radiation therapy for pediatric brain tumors. *J Clin Oncol*. (2016) 34:1043–9. doi: 10.1200/JCO.2015.62.1383

38. Lassaletta Á, Morales JS, Valenzuela PL, Esteso B, Kahalley LS, Mabbott DJ, et al. Neurocognitive outcomes in pediatric brain tumors after treatment with proton versus photon radiation: a systematic review and meta-analysis. *World J Pediatr*. (2023) 19:727–40. doi: 10.1007/s12519-023-00726-6

39. Zureick AH, Evans CL, Niemierko A, Grieco JA, Nichols AJ, Fullerton BC, et al. Left hippocampal dosimetry correlates with visual and verbal memory outcomes in survivors of pediatric brain tumors. *Cancer*. (2018) 124:2238–45. doi: 10.1002/cncr.31143

40. Merchant TE, Schreiber JE, Wu S, Lukose R, Xiong X, Gajjar A. Critical combinations of radiation dose and volume predict intelligence quotient and academic achievement scores after craniospinal irradiation in children with medulloblastoma. *Int J Radiat Oncol Biol Phys*. (2014) 90:554–61. doi: 10.1016/j.ijrobp.2014.06.058

41. Ris MD, Walsh K, Wallace D, Armstrong FD, Holmes E, Gajjar A, et al. Intellectual and academic outcome following two chemotherapy regimens and radiotherapy for average-risk medulloblastoma: COG A9961. *Pediatr Blood Cancer*. (2013) 60:1350–7. doi: 10.1002/pbc.24496

42. Calvo W, Hopewell JW, Reinhold HS, Yeung TK. Time- and dose-related changes in the white matter of the rat brain after single doses of X rays. *Br J Radiol*. (1988) 61:1043–52. doi: 10.1259/0007-1285-61-731-1043

43. Krull KR, Hardy KK, Kahalley LS, Schuitema I, Kesler SR. Neurocognitive outcomes and interventions in long-term survivors of childhood cancer. *J Clin Oncol*. (2018) 36:2181–9. doi: 10.1200/JCO.2017.76.4696

44. Beebe DW, Ris MD, Armstrong FD, Fontanesi J, Mulhern R, Holmes E, et al. Cognitive and adaptive outcome in low-grade pediatric cerebellar astrocytomas: evidence of diminished cognitive and adaptive functioning in National Collaborative Research Studies (CCG 9891/POG 9130). *J Clin Oncol*. (2005) 23:5198–204. doi: 10.1200/JCO.2005.06.117

45. Vatner RE, Niemierko A, Misra M, Weyman EA, Goebel CP, Ebb DH, et al. Endocrine deficiency as a function of radiation dose to the hypothalamus and pituitary in pediatric and young adult patients with brain tumors. *J Clin Oncol*. (2018) 36:2854–62. doi: 10.1200/JCO.2018.78.1492

46. Ramanauskienė E, Labanauskas L, Verkauskienė R, Sileikienė R. Early development of endocrine and metabolic consequences after treatment of central nervous system tumors in children. *Medicina (Kaunas)*. (2014) 50:275–80. doi: 10.1016/j.medici.2014.10.006

47. Young S, Phaterpekar K, Tsang DS, Boldt G, Bauman GS. Proton radiotherapy for management of medulloblastoma: A systematic review of clinical outcomes. *Adv Radiat Oncol*. (2023) 8:101189. doi: 10.1016/j.adro.2023.101232

48. Lee CT, Bilton SD, Famiglietti RM, Riley BA, Mahajan A, Chang EL, et al. Treatment planning with protons for pediatric retinoblastoma, medulloblastoma, and pelvic sarcoma: how do protons compare with other conformal techniques? *Int J Radiat Oncol Biol Phys*. (2005) 63:362–72. doi: 10.1016/j.ijrobp.2005.01.060

49. St Clair WH, Adams JA, Bues M, Fullerton BC, La Shell S, Kooy HM, et al. Advantage of protons compared to conventional X-ray or IMRT in the treatment of a pediatric patient with medulloblastoma. *Int J Radiat Oncol Biol Phys*. (2004) 58:727–34. doi: 10.1016/S0360-3016(03)01574-8

50. Pérez-Andújar A, Newhauser WD, Taddei PJ, Mahajan A, Howell RM. The predicted relative risk of premature ovarian failure for three radiotherapy modalities in a girl receiving craniospinal irradiation. *Phys Med Biol*. (2013) 58:3107–23. doi: 10.1088/0031-9155/58/10/3107

51. Yip AT, Yu JD, Huynh-Le MP, Salans M, Unnikrishnan S, Qian AS, et al. Post-treatment neuroendocrine outcomes among pediatric brain tumor patients: Is there a difference between proton and photon therapy? *Clin Transl Radiat Oncol*. (2022) 34:37–41. doi: 10.1016/j.ctro.2022.02.010

52. Aldrich KD, Horne VE, Bielamowicz K, Sonabend RY, Scheurer ME, Paulino AC, et al. Comparison of hypothyroidism, growth hormone deficiency, and adrenal insufficiency following proton and photon radiotherapy in children with medulloblastoma. *J Neurooncol*. (2021) 155:93–100. doi: 10.1007/s11060-021-03847-y

53. Bielamowicz K, Okcu MF, Sonabend R, Paulino AC, Hilsenbeck SG, Dreyer Z, et al. Hypothyroidism after craniospinal irradiation with proton or photon therapy in patients with medulloblastoma. *Pediatr Hematol Oncol*. (2018) 35:257–67. doi: 10.1080/08880018.2018.1471111

54. Eaton BR, Esiashvili N, Kim S, Patterson B, Weyman EA, Thornton LT, et al. Endocrine outcomes with proton and photon radiotherapy for standard risk medulloblastoma. *Neuro Oncol*. (2016) 18:881–7. doi: 10.1093/neuonc/nov302

55. Greenberger BA, Pulsifer MB, Ebb DH, MacDonald SM, Jones RM, Butler WE, et al. Clinical outcomes and late endocrine, neurocognitive, and visual profiles of proton radiation for pediatric low-grade gliomas. *Int J Radiat Oncol Biol Phys*. (2014) 89:1060–8.

56. Viswanathan V, Pradhan KR, Eugster EA. Pituitary hormone dysfunction after proton beam radiation therapy in children with brain tumors. *Endocr Pract*. (2011) 17:891–6. doi: 10.4158/EP10391.OR

57. Li Y, Mizumoto M, Oshiro Y, Nitta H, Saito T, Iizumi T, et al. A retrospective study of renal growth changes after proton beam therapy for pediatric Malignant tumor. *Curr Oncol*. (2023) 30:1560–70. doi: 10.3390/curroncol30020120

58. Clement SC, Meeteren AY, Kremer LC, van Trotsenburg AS, Caron HN, van Santen HM. High prevalence of early hypothalamic-pituitary damage in childhood brain tumor survivors: need for standardized follow-up programs. *Pediatr Blood Cancer.* (2014) 61:2285–9. doi: 10.1002/pbc.25176

59. Lipshultz SE, Adams MJ, Colan SD, Constine LS, Herman EH, Hsu DT, et al. Long-term cardiovascular toxicity in children, adolescents, and young adults who receive cancer therapy: pathophysiology, course, monitoring, management, prevention, and research directions: a scientific statement from the American Heart Association. *Circulation.* (2013) 128:1927–95. doi: 10.1161/CIR.0b013e3182a88099

60. Gallicchio L, Daee DL, Rotunno M, Barajas R, Fagan S, Carrick DM, et al. Epidemiologic research of rare cancers: trends, resources, and challenges. *Cancer Epidemiol Biomarkers Prev.* (2021) 30:1305–11. doi: 10.1158/1055-9965.EPI-20-1796

61. Frankart AJ, Nagarajan R, Pater L. The impact of proton therapy on cardiotoxicity following radiation treatment. *J Thromb Thrombolysis.* (2021) 51:877–83. doi: 10.1007/s11239-020-02303-4

62. Yang EH, Marmagkiolis K, Balanescu DV, Hakeem A, Donisan T, Finch W, et al. Radiation-induced vascular disease-A state-of-the-art review. *Front Cardiovasc Med.* (2021) 8:652761. doi: 10.3389/fcvm.2021.652761

63. Mansour A, Trefi A, Mansour M, Shekho A, Salloum S. The complexities of treating brain and spinal cord tumors: a review of current approaches. *Ann Med Surg (Lond).* (2023) 85:4969–72. doi: 10.1097/MS9.0000000000001213

64. Perez IE, Taveras Alam S, Hernandez GA, Sancassani R. Cancer therapy-related cardiac dysfunction: an overview for the clinician. *Clin Med Insights Cardiol.* (2019) 13:1179546819866445. doi: 10.1177/1179546819866445

65. Hahn E, Jiang H, Ng A, Bashir S, Ahmed S, Tsang R, et al. Late cardiac toxicity after mediastinal radiation therapy for hodgkin lymphoma: contributions of coronary artery and whole heart dose-volume variables to risk prediction. *Int J Radiat Oncol Biol Phys.* (2017) 98:1116–23. doi: 10.1016/j.ijrobp.2017.03.026

66. Mu X, Björk-Eriksson T, Nill S, Oelfke U, Johansson KA, Gagliardi G, et al. Does electron and proton therapy reduce the risk of radiation induced cancer after spinal irradiation for childhood medulloblastoma? A comparative treatment planning study. *Acta Oncol.* (2005) 44:554–62. doi: 10.1080/02841860500218819

67. van Nimwegen FA, Schaapveld M, Cutter DJ, Janus CPM, Krol ADG, Hauptmann M, et al. Radiation dose-response relationship for risk of coronary heart disease in survivors of Hodgkin Lymphoma. *JCO.* (2016) 34:235–43. doi: 10.1200/JCO.2015.63.4444

68. Tseng YD, Cutter DJ, Plastaras JP, Parikh RR, Cahlon O, Chuong MD, et al. Evidence-based review on the use of proton therapy in lymphoma from the particle therapy cooperative group (PTCOG) lymphoma subcommittee. *Int J Radiat Oncol Biol Phys.* (2017) 99:825–42. doi: 10.1016/j.ijrobp.2017.05.004

69. Ho CK, Flampouri S, Hoppe BS. Proton therapy in the management of lymphoma: the. *Cancer J.* (2014) 20:387–92. doi: 10.1097/PPO.0000000000000076

70. Zhang R, Howell RM, Taddei PJ, Giebeler A, Mahajan A, Newhauser WD. A comparative study on the risks of radiogenic second cancers and cardiac mortality in a set of pediatric medulloblastoma patients treated with photon or proton craniospinal irradiation. *Radiother Oncol.* (2014) 113:84–8. doi: 10.1016/j.radonc.2014.07.003

71. Zhang R, Howell RM, Homann K, Giebeler A, Taddei PJ, Mahajan A, et al. Predicted risks of radiogenic cardiac toxicity in two pediatric patients undergoing photon or proton radiotherapy. *Radiat Oncol.* (2013) 8:184. doi: 10.1186/1748-717X-8-184

72. Hoppe BS, Flampouri S, Su Z, Latif N, Dang NH, Lynch J, et al. Effective dose reduction to cardiac structures using protons compared with 3DCRT and IMRT in mediastinal Hodgkin lymphoma. *Int J Radiat Oncol Biol Phys.* (2012) 84:449–55. doi: 10.1016/j.ijrobp.2011.12.034

73. Lautenschlaeger S, Iancu G, Flatten V, Baumann K, Thiemer M, Dumke C, et al. Advantage of proton-radiotherapy for pediatric patients and adolescents with Hodgkin's disease. *Radiat Oncol.* (2019) 14:157. doi: 10.1186/s13014-019-1360-7

74. Hudson MM, Mertens AC, Yasui Y, Hobbie W, Chen H, Gurney JG, et al. Health status of adult long-term survivors of childhood cancer: a report from the Childhood Cancer Survivor Study. *JAMA.* (2003) 290:1583–92. doi: 10.1001/jama.290.12.1583

75. Oeffinger KC, Mertens AC, Sklar CA, Kawashima T, Hudson MM, Meadows AT, et al. Chronic health conditions in adult survivors of childhood cancer. *N Engl J Med.* (2006) 355:1572–82. doi: 10.1056/NEJMsa060185

76. García-Marqueta M, Vázquez M, Krcek R, Kliebsch UL, Baust K, Leiser D, et al. Quality of life, clinical, and patient-reported outcomes after pencil beam scanning proton therapy delivered for intracranial grade WHO 1–2 meningioma in children and adolescents. *Cancers (Basel).* (2023) 15:4447. doi: 10.3390/cancers15184447

77. McMahon SJ, Paganetti H, Prise KM. LET-weighted doses effectively reduce biological variability in proton radiotherapy planning. *Phys Med Biol.* (2018) 63:225009. doi: 10.1088/1361-6560/aae8a5

78. Hahn C, Ödén J, Dasu A, Vestergaard A, Fuglsang Jensen M, Sokol O, et al. Towards harmonizing clinical linear energy transfer (LET) reporting in proton radiotherapy: a European multi-centric study. *Acta Oncol.* (2022) 61:206–14. doi: 10.1080/0284186X.2021.1992007

79. Paganetti H, 2nd SCB, Bosch WR, Haas-Kogan D, Kirsch DG, Li H, et al. NRG oncology white paper on the relative biological effectiveness in proton therapy. . *Int J Radiat Oncol Biol Phys.* (2025) 121:202–17. doi: 10.1016/j.ijrobp.2024.07.2152

80. Sørensen BS, Pawelke J, Bauer J, Burnet NG, Dasu A, Hřyer M, et al. Does the uncertainty in relative biological effectiveness affect patient treatment in proton therapy? *Radiother Oncol.* (2021) 163:177–84. doi: 10.1016/j.radonc.2021.08.016

81. Wang JH, Oglesby R, Tran A, Guryildirim M, Miller M, Sheikh K, et al. The association of linear energy transfer and dose with radiation necrosis after pencil beam scanning proton therapy in pediatric posterior fossa tumors. *Int J Radiat Oncol Biol Phys.* (2025) 121:1219–28. doi: 10.1016/j.ijrobp.2024.11.086

82. Fjæra LF, Indelicato DJ, Handeland AH, Ytre-Hauge KS, Lassen-Ramshad Y, Muren LP, et al. A case-control study of linear energy transfer and relative biological effectiveness related to symptomatic brainstem toxicity following pediatric proton therapy. *Radiother Oncol.* (2022) 175:47–55. doi: 10.1016/j.radonc.2022.07.022

83. Fukumitsu N, Kubota H, Demizu Y, Suzuki T, Hasegawa D, Kosaka Y, et al. Comparison of passive-scattered and intensity-modulated proton beam therapy of craniospinal irradiation with proton beams for pediatric and young adult patients with brain tumors. *Jpn J Radiol.* (2024) 42:182–9. doi: 10.1007/s11604-023-01499-8

84. Kuhlthau KA, Pulsifer MB, Yeap BY, Morales DR, Delahaye J, Hill KS, et al. Prospective study of health-related quality of life for children with brain tumors treated with proton radiotherapy. *J Clin Oncol.* (2012) 30:2079–86. doi: 10.1200/JCO.2011.37.0577

85. Yock TI, Bhat S, Szymonifka J, Yeap BY, Delahaye J, Donaldson SS, et al. Quality of life outcomes in proton and photon treated pediatric brain tumor survivors. *Radiother Oncol.* (2014) 113:89–94. doi: 10.1016/j.radonc.2014.08.017

86. Spiotto MT, McGovern SL, Gunn GB, Grosshans D, McAleer MF, Frank SJ, et al. Proton radiotherapy to reduce late complications in childhood head and neck cancers. *Int J Part Ther.* (2021) 8:155–67. doi: 10.14338/IJPT-20-00069.1

87. Mizumoto M, Murayama S, Akimoto T, Demizu Y, Fukushima T, Ishida Y, et al. Long-term follow-up after proton beam therapy for pediatric tumors: a Japanese national survey. *Cancer Sci.* (2017) 108:444–7. doi: 10.1111/cas.13140

Glossary

AI	Adrenal Insufficiency
ATRT	Atypical Teratoid Rhabdoid Tumor
CCSS	Childhood Cancer Survivor Study
CI	Cumulative Incidence
CNS	Central Nervous System
CSI	Craniospinal Irradiation
CVD	Cardiovascular Disease
DBA	Daily Basic Activities
FSIQ	Full-Scale IQ
GHD	Growth Hormone Deficiency
HD	Hodgkin's Disease
HL	Hodgkin Lymphoma
HPA	Hypothalamic-Pituitary Axis
HRQoL	Health-Related Quality Of Life;
IMRT	Intensity-Modulated Radiotherapy
INRT	Involved Node Radiotherapy
LET	Linear Energy Transfer
MB	Medulloblastoma
PBS	Pencil Beam Scanning
PBT	Proton Beam Therapy
PF	Posterior Fossa
PS	Passive Scattering
PT	Photon Therapy
QoL	Quality of Life
RBE	Relative Biological Effectiveness
RLAR	Risk of Lifetime Attributable Risk;
RR	Relative Risk
Radiotherapy	SHD Hormone Deficiency
SOBP	Spread-Out Bragg peak
3DCRT	Three-Dimensional Conformal Radiotherapy.

frontiers | Frontiers in Oncology

TYPE Original Research
PUBLISHED 09 June 2025
DOI 10.3389/fonc.2025.1610980

Check for updates

OPEN ACCESS

EDITED BY
Poonam Yadav,
Northwestern University, United States

REVIEWED BY
Jia-Ming Wu,
Wuwei Cancer Hospital of Gansu Province, China
Elham Khakshour,
Sabzevar University of Medical Sciences, Iran

*CORRESPONDENCE
Jianjun Lai
385806945@qq.com

RECEIVED 13 April 2025
ACCEPTED 15 May 2025
PUBLISHED 09 June 2025

CITATION
Hu H, Jueyi Z, Hao J and Lai J (2025) Application of the Monaco-serial biological function for cardiac dose constraints in DIBH-IMRT treatment planning for left-sided breast cancer. *Front. Oncol.* 15:1610980. doi: 10.3389/fonc.2025.1610980

COPYRIGHT
© 2025 Hu, Jueyi, Hao and Lai. This is an open-access article distributed under the terms of the Creative Commons Attribution License (CC BY). The use, distribution or reproduction in other forums is permitted, provided the original author(s) and the copyright owner(s) are credited and that the original publication in this journal is cited, in accordance with accepted academic practice. No use, distribution or reproduction is permitted which does not comply with these terms.

Application of the Monaco-serial biological function for cardiac dose constraints in DIBH-IMRT treatment planning for left-sided breast cancer

Haili Hu[1,2], Zhou Jueyi[3], Jiang Hao[2] and Jianjun Lai[4,5]*

[1]Zhejiang Chinese Medical University, Hangzhou, Zhejiang, China, [2]Zhejiang Hospital, Hangzhou, Zhejiang, China, [3]Lishui People's Hospital, Lishui, Zhejiang, China, [4]Hangzhou Cancer Hospital, Hangzhou, Zhejiang, China, [5]Affiliated Hangzhou First People's Hospital, School of Medicine, Westlake University, Hangzhou, China

Background: The Serial function in the Monaco treatment planning system is essential for cardiac dose optimization in left breast cancer radiotherapy; however its optimal K-value for deep-inspiration breath-hold intensity-modulated radiotherapy (DIBH-IMRT) has not been established. This study aims to determine the evidence-based K-value configuration for clinical implementation.

Methods: 41 left breast cancer patients undergoing DIBH-IMRT were retrospectively analyzed. Plans were stratified by Monaco-Serial K-values: Group A (K=1), B ($2 \leq K \leq 4$), and C (K>4). Dosimetric parameters (heart, LAD, Lung-L) and dose-volume reduction rates (Groups B/C vs A) were compared. Correlations between K-values and DIBH-induced anatomical changes (Lung-L volume increment rate, Lung-L/Heart volume ratio, and Heart-Breast Distance increment) were assessed

Results: All plans satisfied target coverage. Group B achieved optimal cardiac protection: mean heart dose (273.9 $\pm$ 91.0 cGy), max heart dose (2676.2 $\pm$ 1380.7 cGy), and LAD doses (mean: 411.3 cGy; max: 1483.3 $\pm$ 736.3 cGy) significantly decreased versus Group A. Lung-L V500cGy in Group B increased marginally but within clinical tolerance. Correlation analysis confirmed that Group B achieved balanced control of mean/maximum heart doses, aligning with the expected effects of anatomical variations induced by the DIBH technique.

Conclusions: Adjusting Monaco-Serial K-value to $2 \leq K \leq 4$ provides optimal dose constraints for the heart and substructures while ensuring target coverage, making it the optimal parameter setting for left breast cancer DIBH-IMRT.

KEYWORDS

breast cancer, radiotherapy planning, biological optimization, monte carlo, equivalent biological dose

1 Introduction

Breast cancer is the most common malignancy among women worldwide, with radiotherapy serving as a critical adjunctive treatment (1, 2). However, due to the anatomical proximity of the breast to the heart, radiation exposure during treatment is strongly associated with an increased risk of radiation-induced heart disease, particularly in left-sided breast cancer (3). Modern radiotherapy planning systems, utilizing inverse intensity-modulated radiotherapy (IMRT) and dose optimization algorithms, effectively limit radiation exposure to organs at risk (OARs) while ensuring adequate target dose coverage, and have become a standard in clinical practice (4–6). To further reduce cardiac dose, the deep inspiration breath-hold (DIBH) technique has emerged as an essential approach in recent breast cancer radiotherapy (7, 8). DIBH increases lung volume, expanding the distance between the target and the heart, which enhances dose attenuation in the target area and minimizes radiation exposure to the heart (9, 10). The combination of DIBH with IMRT dose optimization algorithms has been shown to significantly reduce radiation to the heart and its substructures, thereby lowering the risk of radiation-induced heart disease (11).

The Monaco treatment planning system (TPS), which uses the Monte Carlo dose calculation algorithm, is one of the most widely employed systems in clinical practice, providing highly accurate dose optimization results that closely reflect actual radiation-induced damage (12). The system's Serial function is a key biological optimization tool, especially for dose constraints applied to the heart and its substructures. In Monaco-Serial, a K value of 1 is commonly used for setting average dose constraints to the heart and its substructures in left breast cancer free-breathing IMRT (FB-IMRT) (13, 14). However, with DIBH-IMRT, significant anatomical changes, such as the increased distance between the heart and the target, can render previous settings suboptimal, and to date, there is a lack of studies addressing this issue.

This study aims to identify the optimal K value setting for Monaco-Serial in DIBH-IMRT for left-sided breast cancer by retrospectively analyzing 41 patients who underwent DIBH-IMRT. Radiotherapy plans were designed using different Monaco-Serial K values, and dosimetric comparisons were made. Furthermore, the correlation between changes in dose-volume parameters of OARs and anatomical variations post-DIBH was explored. The goal is to provide data-driven insights for optimizing Monaco-Serial settings in left-sided breast cancer DIBH-IMRT, thus supporting the clinical application of the Monaco system in designing DIBH-IMRT treatment plans.

2 Materials and methods

This study was approved by the Ethics Committee of the researchers' hospital (Approval No. 2024-145K) and prospectively registered at ClinicalTrials (identifier NO.NCT06796257), adhering to ICMJE guidelines. It included 41 patients with left-sided breast cancer who underwent breast-conserving surgery followed by whole-breast radiotherapy between August 2022 and December 2024, with a mean age of 43.3 years (range: 29–72 years). All participants demonstrated good compliance and successfully completed the entire DIBH treatment protocol. The study workflow is outlined in Figure 1, which encompasses CT simulation and positioning under both free-breathing (FB) and DIBH conditions, radiotherapy plan design and evaluation, as well as the analysis of anatomical changes and dose reduction rates following DIBH.

2.1 CT simulation and target delineation

All patients were positioned and immobilized using a vacuum bag combined with a single-board system (R612, Klarity, China).

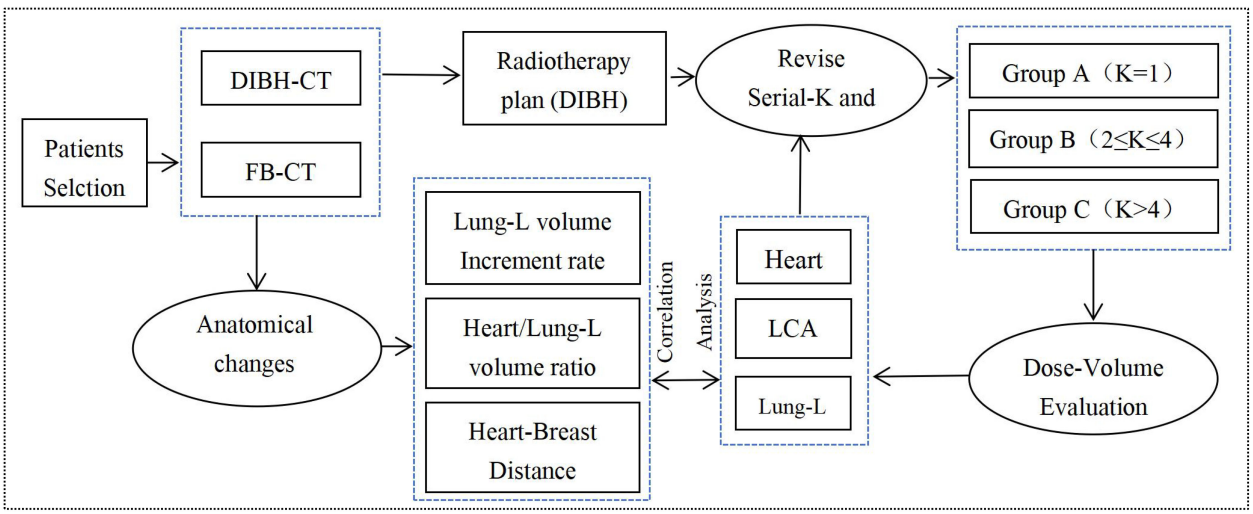

FIGURE 1
Flow chart of the radiotherapy treatment planning.

CT simulation images were acquired with a CT scanner (Somatom, Siemens, Germany), covering the scan range from the inferior margin of the mandible to the inferior margin of the liver. Immediately after completing the CT scan in the FB position, each patient underwent a chest-breathing DIBH CT scan. Prior to the DIBH scan, patients received breathing training and were required to achieve breath-holding for more than 20 seconds in three consecutive attempts. Those who met this criterion were deemed eligible for DIBH CT scanning. Breathing gating during DIBH was performed using a laser-based surface scanner (Sentinel, C-RAD AB, Sweden), with the gating point monitored at the mid-sternum. The CT scan was conducted at a voltage of 110 kV, with a slice thickness of 3 mm. For the DIBH scan, an iodinated contrast agent was administered to enhance image quality. Both DIBH-CT and FB-CT images were subsequently transferred to the radiotherapy planning system (Monaco 6.0, Elekta, Sweden).

On the DIBH-CT images, radiation oncologists reviewed and contoured the OARs and target volumes. The Gross Tumor Volume (GTV), Clinical Target Volume (CTV) and OARs were defined according to Radiation Therapy Oncology Group (RTOG) standards (15), while the Planning Target Volume (PTV) and Planning Gross Tumor Volume (PGTV) were generated by expanding the CTV and GTV by 10 mm and contracting the subcutaneous volume by 5 mm. The heart, left lung, right lung, and body contour were auto-contoured using an automatic segmentation tool (AccContour, China), with manual adjustments made by the radiation oncologist. The left anterior descending artery (LAD) was manually contoured by the radiation oncologist. All OARs and target delineations were reviewed and approved by senior radiation oncology experts.

2.2 Radiotherapy plan design

All patients received a prescribed dose of 5000 cGy in 25 fractions for the PTV. Postoperative breast-conserving surgery patients received an additional boost to the PGTV, totaling 5750 cGy in 25 fractions. Target volume coverage adhered to ICRU recommendations, ensuring that the maximum dose did not exceed 107%, and the 95% isodose line covered the PTV/PGTV. The DIBH radiotherapy plans for all patients were designed by the same radiation therapy physicist using 6MV-FFF photon energy with 6 tangential IMRT fields based on the DMLC technique. All dose calculations were performed using the Monte Carlo algorithm on Monaco 6.0, with a 3 mm calculation grid and a statistical uncertainty of 1%.

During radiotherapy planning, the dose limits for OARs followed the guidelines for breast cancer radiotherapy (Chinese Medical Association, 2020 edition) (16). The dose-volume objectives, optimization functions, and parameter settings are summarized in Table 1. Three different radiotherapy plans were designed for each patient based on varying Monaco-Serial K values for cardiac dose constraints: Group A (K=1), Group B (2≤K ≤ 4), and Group C (K>4). For heart dose constraints, the Equivalent Uniform Dose (EUD) was adjusted according to dose optimization principles, with modifications made in response to changes in K values. For the lung (Lung-L), LAD, and spinal cord dose constraints, EUD, MOD (Mean Organ Damage), and Maximum Dose values were fine-tuned to minimize OARs dose-volume while maintaining adherence to dose optimization principles, as outlined in Table 1. All three radiotherapy plans were reviewed and approved by the same senior radiation oncologist before undergoing dosimetric analysis. Additionally, the plans were independently verified using the 3D dose verification system (Evolution, IBA, Germany), ensuring consistency and accuracy. The verification criterion required a gamma passing rate (2mm/3%) of over 95%.

2.3 Measurement and calculation of anatomical structure changes

The following three anatomical change parameters after DIBH were measured and calculated for all patients using CT images from both FB and DIBH:

(1) Lung-L volume increment rate = (DIBH Lung-L volume - FB Lung-L volume)/FB Lung-L volume; (2) Heart/Lung-L volume ratio = DIBH Heart volume/DIBH Lung-L volume; (3) Heart-breast distance increment = DIBH Heart-breast distance - FB Heart-breast distance. The measurement method for the Heart-breast distance in both FB and DIBH is illustrated in Figure 2, which is provided in the supplementary materials. The CT slice used for this measurement is the transverse cross-section at the midline of the breast in the head-foot direction.

2.4 Dosimetric and correlation analysis

The dosimetric differences in three OARs—Heart, LAD, and Lung-L—were statistically analyzed and compared across the radiotherapy plans of Groups A, B and C. Group A served as the

TABLE 1 Dose-volume constraints for OARs and the optimization functions and parameters used in this study.

Target Volume	Dose-Volume Target	Constraint Functions and Parameter Settings
Lung-L	Dmean ≤ 1500 cGy (1200 cGy), V3000 cGy ≤ 20% (15%), V2000 cGy ≤ 30% (25%), V500 cGy ≤ 50% (50%)	Parallel: ①EUD=2800 cGy/MOD=16%; K=3 ②EUD=1800 cGy/MOD=25%; K=3 ③EUD=480 cGy/MOD=48%; K=3 Serial: EUD=1000~1400 cGy; K=1
Lung-R	Dmean ≤ 500 cGy (300 cGy)	Serial: EUD=500 cGy; K=1
Heart	Dmean ≤ 800 cGy (400 cGy)	Serial: EUD=300~1000 cGy; Group A: K=1; Group B: 2≤K ≤ 4; Group C: K>4
LAD	Dmean ≤ 2500 cGy (1000 cGy)	Serial: EUD=400~1000 cGy; K=1
Spinal cord	Dmax ≤ 4000 cGy (3000 cGy)	Maximum Dose: 3000 cGy

In the "Dose-Volume Target" column, values outside the parentheses are the guideline-recommended values, and values inside the parentheses represent the experience values from our center for left breast DIBH radiotherapy plans. EUD, Equivalent Uniform Dose; MOD, Mean Organ Damage; K, Value of Power Law Exponent.

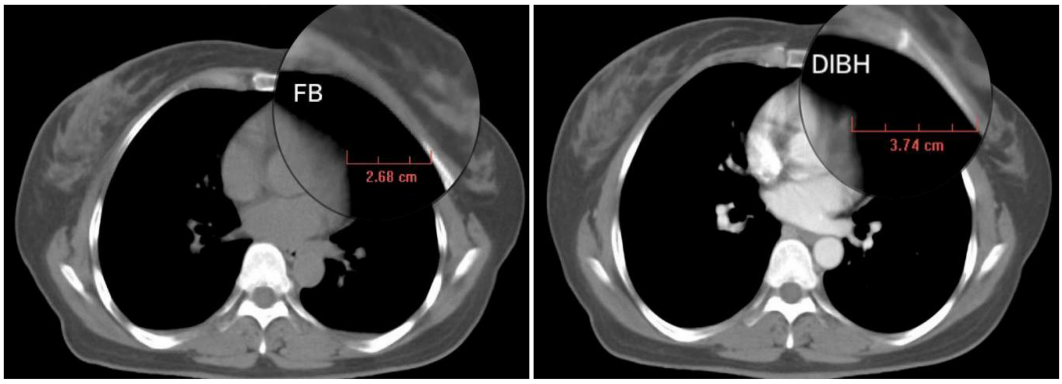

FIGURE 2
Example of the measurement method for heart-breast distance under FB and DIBH conditions.

reference, and the dose-volume reduction rates for the three OARs in Groups B and C were calculated after adjusting the K value. Additionally, the dose-volume reduction rates for OARs in Groups B and C were correlated with DIBH-related anatomical changes: Lung-L volume increment rate, Heart/Lung-L volume ratio, and Heart-breast distance increment.

2.5 Statistical analysis

Data were first tested for non-normal distribution using the Shapiro-Wilk test. The Mann-Whitney U test was applied to analyze differences between two groups, while the Kruskal-Wallis H test was used for comparisons among multiple groups. When significant differences were detected among groups, pairwise comparisons were performed with Bonferroni correction to adjust for multiple testing. Pearson correlation analysis was performed to investigate the relationship between dose-volume reduction rates of OARs and anatomical indicators. All statistical analyses were conducted using SPSS 27.0, with a p-value of < 0.05 considered statistically significant unless otherwise specified after correction.

3 Results

3.1 Dosimetric statistics for All DIBH-IMRT treatment plans

3.1.1 Dose-volume results of OARs in the three radiotherapy plans

Table 2 and Figure 3 summarize the dose-volume data for the heart, LAD, and ipsilateral lung under the three treatment plans: Group A, Group B, and Group C. Compared to Group A, both Group B and Group C demonstrated reductions in the average and maximum doses to the Heart and LAD, with Group B showing better dose control than Group C. In Group B, the average dose to the Heart and LAD decreased to 273.9 ± 91.0 cGy and 411.3 ± 127.8 cGy ($p < 0.05$), respectively, while the maximum dose decreased to 2676.2 ± 1380.7 cGy and 1483.3 ± 736.3 cGy ($p < 0.05$), respectively.

For the ipsilateral lung (Lung-L), the V500 cGy in Group A was 44.2 ± 6.2% ($p < 0.05$), with an average dose of 1033.1 ± 162.8 cGy, which was the lowest among the three groups. In Group B, although the V500 cGy and average dose for Lung-L showed a slight increase, the values remained within an acceptable range.

In summary, adjusting the Serial-K value for the Heart to the Group B range ($2 \leq K \leq 4$) significantly optimized the dose constraints for the heart and its substructures, while only causing a minimal increase in the dose-volume to the ipsilateral lung.

3.1.2 Dose-volume reduction rates of major OARs after adjusting the cardiac serial-K value

The dose-volume reduction rate was calculated using the following formula: Dose-volume Reduction Rate = ((Adjusted Dose - Original Dose)/Original Dose) * 100%. Table 3 summarizes the dose-volume reduction rates for the three OARs—Heart, LAD, and Lung-L—in Group B and Group C compared to Group A. Figure 4 displays the density distribution curves of the dose-volume reduction rates for OARs in Group B and Group C relative to Group A. As shown in Table 3, compared to Group A, Group B demonstrated an average reduction rate of 29.4% ± 14.2% for the Heart and 18.7% ± 15.5% for the LAD, with maximum dose reduction rates of 29.3% ± 38.0% and 24.0% ± 13.4%, respectively. For Lung-L, the average reduction rate for V500 cGy in Group B compared to Group A was -8.6 ± 15.3% and -15.6 ± 17.5%, respectively. Figure 4 further illustrates that Group B significantly outperformed Group C in terms of dose reduction rates for both the Heart and LAD.

In conclusion, these results underscore that adjusting the Serial-K value for the Heart to the Group B range ($2 \leq K \leq 4$) not only optimized dose constraints for the heart and its substructures, but also led to only a slight increase in Lung-L V500 cGy.

3.2 Anatomical parameter measurements and calculation results after DIBH

The study results demonstrated significant anatomical changes following DIBH compared to the FB state in 41 patients. The Lung-

TABLE 2 Summary of treatment planning data for OARs, for the 41 left breast cancer patients included in this study, with DIBH, different Serial-K value ranges and 6 fields tIMRT.

Dose-Volume for OARs	Group A (K=1)	Group B (2≤K ≤ 4)	Group C (K>4)	*p*
Heart mean Dose(cGy)	423.4 ± 213	**273.9 ± 91.0**	312.7 ± 110.2	<0.05
Heart max Dose(cGy)	3980.0 ± 1038.0	**2676.2 ± 1380.7**	2856.1 ± 1440.9	<0.05
LAD mean Dose(cGy)	530.3 ± 197.6	**411.3 ± 127.8**	440.6 ± 134.0	<0.05
LAD max Dose(cGy)	2012.9 ± 1008.0	**1483.3 ± 736.3**	1537.3 ± 755.6	<0.05
Lung-L mean Dose(cGy)	1033.1 ± 162.8	1042.0 ± 165.4	1126.9 ± 183.0	=0.09
Lung-L V500cGy(%)	**44.2 ± 6.2**	46.7 ± 7.2	49.7 ± 8.2	<0.05
Lung-L V2000cGy(%)	17.5 ± 4.1	17.5 ± 4.3	18.7 ± 4.4	=0.32
Lung-L V3000cGy(%)	12.1 ± 3.6	11.4 ± 3.6	12.7 ± 4.0	=0.56

The dose-volume parameters for OARs are presented as mean values ± one standard deviation. Most favourable value was marked in bold.

L volume increment rate was 81.7 ± 36.2%, the Heart/Lung-L volume ratio was 0.03 ± 0.09, and the Heart-breast distance increment was 1.0 ± 0.5 cm. These measurements indicate significant anatomical changes after DIBH compared to the FB state.

3.3 Correlation analysis results between anatomical and dosimetric parameters

Figure 5 shows the correlation between the dose-volume reduction rates of the Heart, LAD, and Lung-L in Group B (2≤K ≤

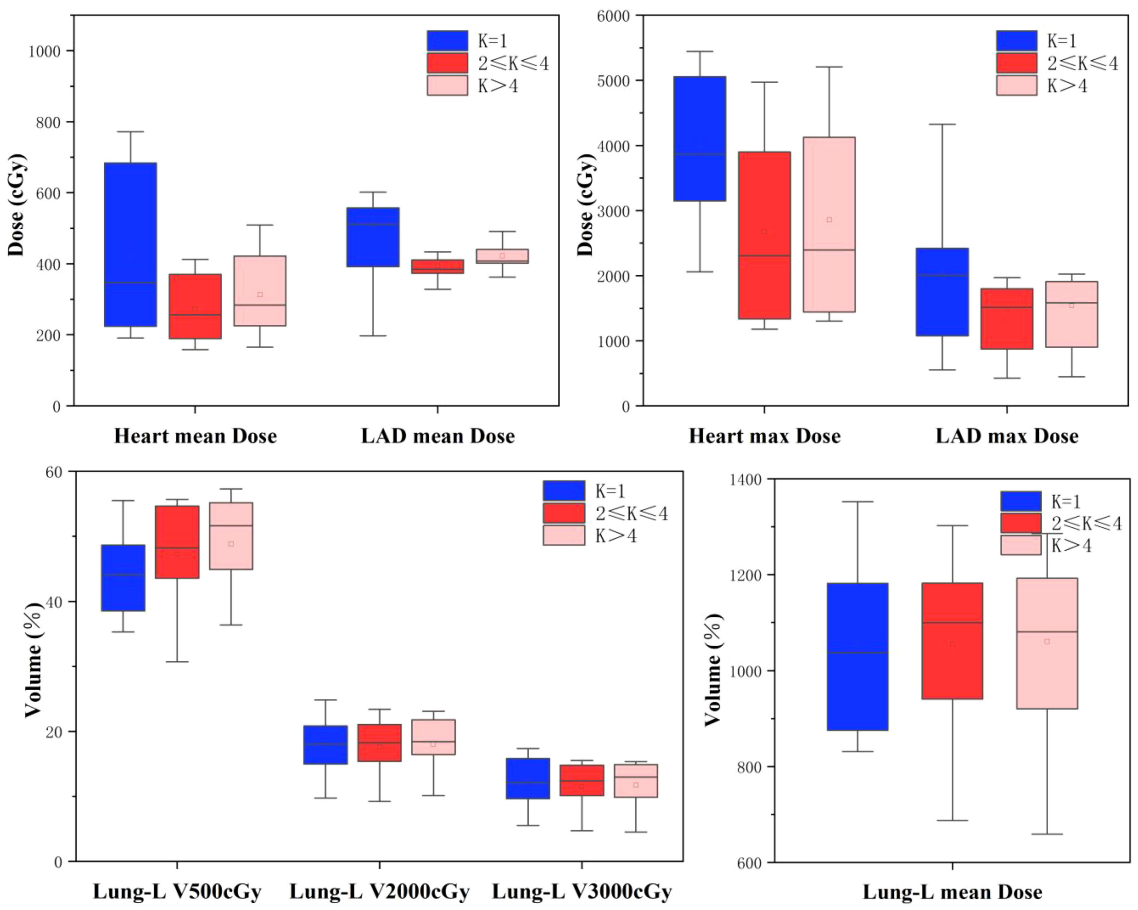

FIGURE 3
Boxplots of treatment planning data for OARs, for the 41 left breast cancer patients included in this study, with DIBH, different serial-K value ranges and 6 fields tIMRT.

TABLE 3 Summary of reduction rates in dose-volume of OARs after treatment plan optimization by varying Serial-K values (two groups: B、C), relative to treatment plan optimization with Group A, for the 41 patients with left breast cancer included in this study, with DIBH and 6 tIIMRT fields.

Dose-Volume for OARs	Group B (2≤K ≤ 4, %)	Group C (K>4, %)	*p*
Heart mean Dose(cGy)	**29.4 ± 14.2**	20.1 ± 16.0	<0.05
Heart max Dose(cGy)	**29.3 ± 38.0**	24.5 ± 40.1	<0.05
LAD mean Dose(cGy)	**18.7 ± 15.5**	12.7 ± 17.0	<0.05
LAD max Dose(cGy)	**24.0 ± 13.4**	21.1 ± 14.1	<0.05
Lung-L mean Dose(cGy)	-1.1 ± 8.3	-8.7 ± 7.1	<0.05
Lung-L V500cGy(%)	-8.6 ± 15.3	-15.6 ± 17.5	<0.05
Lung-L V2000cGy(%)	0.1 ± 11.0	-7.4 ± 11.5	<0.05
Lung-L V3000cGy(%)	5.9 ± 9.8	-4.8 ± 9.5	<0.05

Reduction rates in dose-volume of OARs are shown as mean values with one standard deviation for OARs. Most favourable value was marked in bold.

4) and Group C (K>4) compared to Group A (K=1), after adjusting the Monaco-Serial K value for constraining the heart, and the three anatomical parameters: Heart/Lung-L volume ratio, Heart/breast Distance Increment, and Lung-L volume Increment rate.

As shown in Figure 5, in Group B (2≤K ≤ 4), the Heart/breast Distance is strongly positively correlated with both the average and maximum heart dose reduction rates. The Heart/Lung-L volume ratio is strongly negatively correlated with these dose reduction

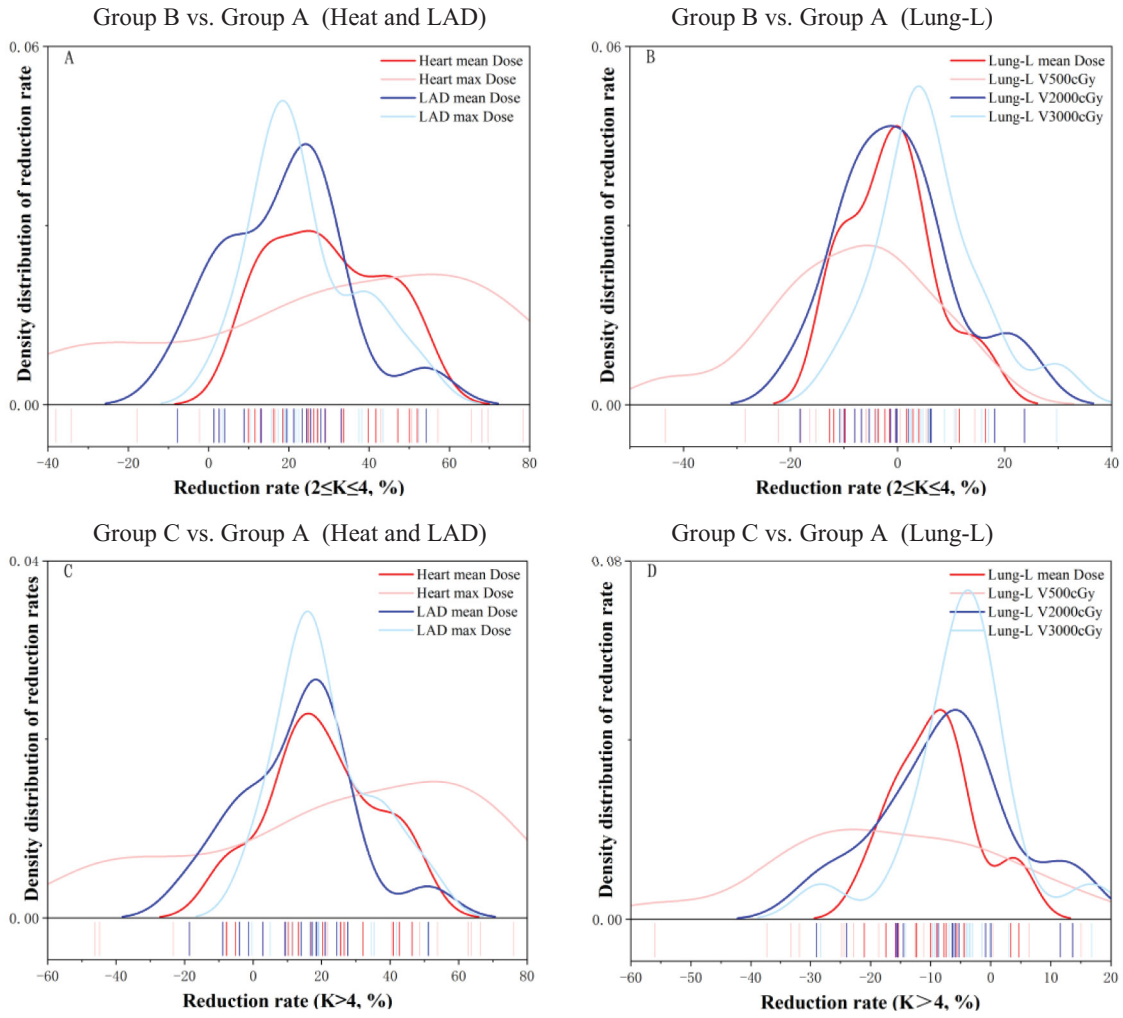

FIGURE 4
This figure displays the density distribution curves of dose-volume reduction rates for OARs after optimization of radiotherapy plans using different serial-K values (divided into two Groups: B、C), relative to Group A.

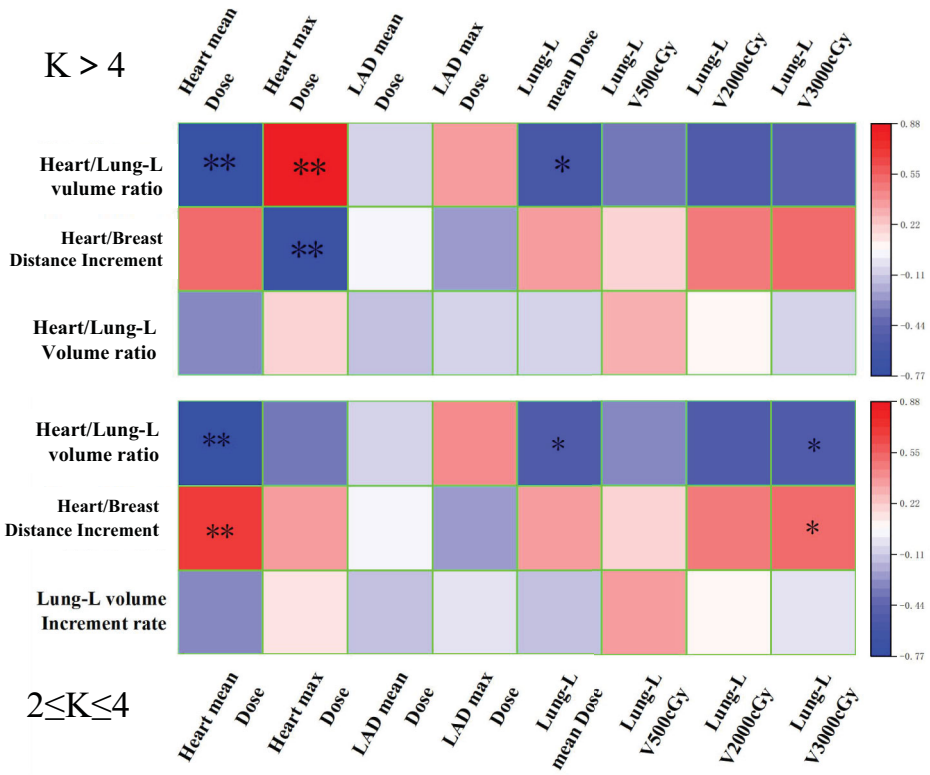

FIGURE 5
The correlation heatmap shows the pearson's correlation between the reduction rates in dose-volume of OARs (compared to Group A), and the modifications in anatomical structures (after DIBH) from radiotherapy planning for different Serial-K values (Group B and C). ** Significant correlation at the 0.01 level. * Significant correlation at the 0.05 level.

rates. After DIBH, the changes in these two anatomical parameters enabled Group B (2≤K ≤ 4) to effectively constrain both the average and maximum heart doses, with a more significant effect observed on the average dose, which aligns with the expected effects of anatomical variations induced by the DIBH technique. In contrast, Group C (K>4) did not achieve optimal constraints for either the average or maximum doses.

Therefore, the correlation analysis indicates that adjusting the Monaco-Serial K value for heart constraint to the Group B (2≤K ≤ 4) range results in the best correlation between anatomical parameters and heart and substructure doses. This further confirms that Group B (2≤K ≤ 4) is the optimal range for the Monaco-Serial K value in DIBH radiotherapy plans for left-sided breast cancer.

4 Discussion

In breast cancer radiotherapy, the risk of cardiac injury is primarily linked to the mean dose to the heart, which increases linearly with radiation dose. Studies have demonstrated that for every 100 cGy increase in the mean radiation dose to the heart, the likelihood of adverse coronary events rises by 7.4%, with the risk potentially persisting for decades (3). Since radiotherapy implementation is based on treatment plan design, radiation-induced heart damage is closely associated with the optimized dose distribution in radiotherapy plans (17–19).

With current photon radiotherapy technology, combining DIBH with IMRT dose optimization algorithms can effectively limit radiation exposure to the heart and its substructures, potentially significantly reducing the risk of radiation-induced heart disease. In IMRT dose optimization, traditional physical optimization functions fail to fully account for the true biological response of different tissues or organs to radiation during treatment (20). However, Niemierko introduced the EUD function, which incorporates bological parameters to quantify tissue responses to radiation and optimize the dose distribution in radiotherapy plans by considering the biological characteristics of organs and the dose-response relationship. This results in a more accurate reflection of the biological effects of radiation on tissues and organs, thus improving treatment precision and safety (21, 22). Numerous studies have confirmed that the EUD function can effectively control the dose to OARs in breast cancer radiotherapy, reducing radiation-induced damage to structures like the heart (23, 24). For example, Lee et al. (23) compared the quality and performance of dose-volume (DV) plans and DV-EUD plans in breast cancer radiotherapy. Their results showed that DV-EUD plans provided better protection for OARs, reducing lung and heart doses compared to standard DV plans. Similarly, Mihailidis et al. (24) found that EUD-based plans offered superior protection for OARs while maintaining target coverage. Consequently, the use of EUD-based biological

optimization functions has become widely accepted and applied in clinical research (25–29).

In this study, we employed the Monaco TPS, which supports advanced biological optimization models such as the Lyman-Kutcher-Burman (LKB) model. Among these, the Monaco-Serial function is a biological optimization model for serial organs based on the concept of EUD. A key parameter in this model is K—typically ranging from 1 to 20—which modulates the organ's sensitivity to different dose distributions. A lower K value indicates greater sensitivity to the mean dose. Previous studies have successfully applied a K value of 1 in free-breathing IMRT plans for left-sided breast cancer to achieve effective optimization of heart dose-volume constraints. However, the optimal K value for DIBH-IMRT planning remains uncertain and warrants further investigation (30–32). In this study, when applying Monaco-Serial to optimize the heart dose in left-sided breast cancer DIBH-IMRT, adjusting the Serial-K from K=1 to the range of $2 \leq K \leq 4$ (Group B) achieved the best dose constraints for the heart and its substructures, with only a slight increase in Lung-L V500 cGy (still <50%). This finding differs from previous studies and experiences with FB-IMRT. Research by Tanguturi et al. (33) noted that changes in lung volume between FB and DIBH significantly affect heart dose optimization. Cao et al. (34) found that the increased distance between the heart and the chest wall in DIBH significantly impacted heart dose optimization. Thus, the improved heart dose constraints observed in our study, with Serial-K adjusted to $2 \leq K \leq 4$, may be attributed to anatomical changes induced by DIBH compared to FB.

To further explore the impact of anatomical changes after DIBH on the optimal K value, we analyzed the correlation between anatomical structure changes and the dose-volume reduction rates of OARs with increased K values. The study found that after DIBH, as the Heart/Lung-L volume ratio and Heart/breast Distance Increment increased, a modest increase in K (within the $2 \leq K \leq 4$ range) effectively constrained both the mean and maximum heart doses, with the most significant effect on mean dose constraints. These results align with previous studies and clinical expectations (22, 23). However, for Group C (K>4), further increases in K led to stronger constraints on the maximum dose, which impacted the dose distribution of the target area. This caused a shift in the balance between the heart dose constraint function and the target optimization function, ultimately limiting the optimization effect on the heart and its substructures. This further supports the conclusion that the optimal K value range for left-sided breast cancer DIBH-IMRT is $2 \leq K \leq 4$.

5 Conclusion

This study is the first to report the application of the Monaco-Serial biological optimization function in left-sided breast cancer DIBH-IMRT radiotherapy plans. The results demonstrate that adjusting the Serial-K value to the range of $2 \leq K \leq 4$ enables more effective constraints on both the mean and maximum heart doses while maintaining target dose coverage, significantly reducing the risk of radiation-induced heart damage. This finding provides valuable data to support clinical radiotherapy plan design. However, this study only focused on integer values of K. Future research will further investigate the impact of fractional K values (e.g., K=1.1, 1.2, 2.1, 2.2) on plan quality to optimize the application of the Monaco-Serial biological function. Additionally, the results may be influenced by factors such as the dose calculation algorithm, grid resolution, and dose smoothing techniques in the Monaco system, and future studies should further explore the impact of these technical parameters.

Data availability statement

The raw data supporting the conclusions of this article will be made available by the authors, without undue reservation.

Ethics statement

The studies involving humans were approved by the Ethics Committee of Zhejiang hospital (Approval No. 2024-145K). The studies were conducted in accordance with the local legislation and institutional requirements. Written informed consent for participation was not required from the participants or the participants' legal guardians/next of kin because This study is a retrospective analysis based on patients' prior imaging data, and ethical review has granted a waiver of informed consent.

Author contributions

HH: Writing – original draft. ZJ: Writing – review & editing. JH: Conceptualization, Writing – review & editing. JL: Conceptualization, Writing – review & editing.

Funding

The author(s) declare that financial support was received for the research and/or publication of this article. This work was supported in part by the Lishui Science and Technology Project under Grant 2024SJZC127, the Zhejiang Medical and Health Science and Technology Project under Grant 2025KY003, and the Zhejiang Province Natural Science Foundation under Grant LMS25H280007.

Conflict of interest

The authors declare that the research was conducted in the absence of any commercial or financial relationships that could be construed as a potential conflict of interest.

Publisher's note

All claims expressed in this article are solely those of the authors and do not necessarily represent those of their affiliated organizations, or those of the publisher, the editors and the reviewers. Any product that may be evaluated in this article, or claim that may be made by its manufacturer, is not guaranteed or endorsed by the publisher.

References

1. Kaklamani VG, Arteaga CL. Breast cancer: The good, the bad, and an important call to effective risk reduction strategies. *CA-CANCER J Clin*. (2024) 74:471–4. doi: 10.3322/caac.21867

2. Wu J, Fan D, Shao Z, Xu B, Ren G, Jiang Z, et al. CACA guidelines for holistic integrative management of breast cancer. *Holist Integr Oncol*. (2022) 1:7. doi: 10.1007/s44178-022-00007-8

3. Darby SC, Ewertz M, McGale P, Bennet AM, Blom-Goldman U, Brønnum D, et al. Risk of ischemic heart disease in women after radiotherapy for breast cancer. *N Engl J Med*. (2013) 368:987–98. doi: 10.1056/NEJMoa1209825

4. Zaynutdinov N, Abdujapparov A, Djuraev F, Vakhabov I. 28P One-week ultra-hypofractionated partial breast RT in early breast cancer: 3DCRT vs IMRT. *Ann Oncol*. (2023) 34:S1477. doi: 10.1016/j.annonc.2023.10.160

5. Tang LL, Guo R, Zhang N, Deng B, Chen L, Cheng ZB, et al. Effect of radiotherapy alone vs radiotherapy with concurrent chemoradiotherapy on survival without disease relapse in patients with low-risk nasopharyngeal carcinoma: A randomized clinical trial. *JAMA-J Am Med Assoc*. (2022) 328:728–36. doi: 10.1001/jama.2022.13997

6. Coles CE, Earl H, Anderson BO, Barrios CH, Bienz M, Bliss JM, et al. The lancet breast cancer commission. *Lancet*. (2024) 403:1895–950. doi: 10.1016/S0140-6736(24)00747-5

7. Yeh H, Lin J. The impact of the deep inspiration breath-hold (DIBH) technique in the heart and other organ-at-risk (OAR) dose sparing in the postoperative radiotherapy to the left early breast cancer. *Ann Oncol*. (2022) 33:S1435. doi: 10.1016/j.annonc.2022.10.021

8. Garcia Alvarez M, Peraza Fernandez C, Rodrigues C, Mateos Dominguez M, Montijano Linde M, Marrone I, et al. 118P Should DIBH (deep inspiration breath-hold) be the standard of care in LBC (left breast cancer)? *Ann Oncol*. (2020) 31:S55. doi: 10.1016/j.annonc.2020.03.221

9. Huijskens S, Granton P, Fremeijer K, van Wanrooij C, Offereins-van Harten K, Schouwenaars-van den Beemd S, et al. Clinical practicality and patient performance for surface-guided automated VMAT gating for DIBH breast cancer radiotherapy. *Radiother Oncol*. (2024) 195:110229. doi: 10.1016/j.radonc.2024.110229

10. Zhang G. Evaluating the use of SGRT on left breast DIBH: target accuracy and cardiac reproducibility. *Int J Radiat Oncol*. (2021) 111:e228. doi: 10.1016/j.ijrobp.2021.07.783

11. Nissen HD, Appelt AL. Improved heart, lung and target dose with deep inspiration breath hold in a large clinical series of breast cancer patients. *Radiother Oncol*. (2012) 106:28–32. doi: 10.1016/j.radonc.2012.10.016

12. Zhang R, Fleckenstein J. EP-2181: Modeling and comparison the dosimetric impact of two couch model of iBEAM evo 415 in Monaco. *TPS Radiother Oncol*. (2018) 127:S1205. doi: 10.1016/s0167-8140(18)32490-3

13. El Ouardy K, Zerfaoui M, Oulhouq Y, Bahhous K, Rrhioua A, Bakari D. A comparative study of boost dose delivery techniques in breast cancer radiotherapy optimising efficacy and minimising toxicity. *Radiat Prot Dosim*. (2024) 200:459–66. doi: 10.1093/rpd/ncad328

14. Kargar N, Zeinali A, Molazadeh M. Impact of dose calculation algorithms and radiobiological parameters on prediction of cardiopulmonary complications in left breast radiation therapy. *J BioMed Phys Eng*. (2024) 14:129–40. doi: 10.31661/jbpe.v0i0.2305-1616

15. Li XA, Tai A, Arthur DW, Buchholz TA, Macdonald S, Marks LB, et al. Variability of target and normal structure delineation for breast cancer radiotherapy: an RTOG multi-institutional and multiobserver study. *Int J Radiat Oncol Biol Phys*. (2009) 73:944–51. doi: 10.1016/j.ijrobp.2008.10.034

16. Chinese Medical Association Radiation Oncology Physician Branch. Guidelines for radiotherapy of breast cancer (Chinese medical association, 2020 edition). *Chin J Radiat Oncol*. (2021) 30:321–42. doi: 10.3760/cma.j.cn113030-20210107-00010

17. Lestuzzi C, Cosei I, Navarria F, Viel E, Ravasel A, Fumagalli A, et al. Safety of heart radiotherapy for Malignant cardiac tumors: a short and long term study. *Eur Heart J*. (2022) 43:2. doi: 10.1093/eurheartj/ehac544.1803

18. Taylor C, McGale P, Brønnum D, Correa C, Cutter D, Duane FK, et al. Cardiac structure injury after radiotherapy for breast cancer: cross-sectional study with individual patient data. *J Clin Oncol*. (2018) 36:2288–96. doi: 10.1200/JCO.2017.77.6351

19. Wu C, Lin D, Ma F, Jiang F, Wang Y. New progress in elucidating the relationship between cancer therapy and cardiovascular toxicity. *Biosci Trends*. (2021) 15:211–8. doi: 10.5582/bst.2021.01278

20. Mukherjee S, Hong L, Deasy JO, Zarepisheh M. Integrating soft and hard dose-volume constraints into hierarchical constrained IMRT optimization. *Med Phys*. (2019) 47:414–21. doi: 10.1002/mp.13908

21. Niemierko A. Reporting and analyzing dose distributions: a concept of equivalent uniform dose. *Med Phys*. (1997) 24:103–10. doi: 10.1118/1.598063

22. Wu Q, Djajaputra D, Wu Y, Zhou J, Liu HH, Mohan R. Intensity-modulated radiotherapy optimization with gEUD-guided dose-volume objectives. *Phys Med Biol*. (2003) 48:279–91. doi: 10.1088/0031-9155/48/3/301

23. Lee TF, Ting HM, Chao PJ, Wang HY, Shieh CS, Horng MF, et al. Dosimetric advantages of generalised equivalent uniform dose-based optimisation on dose-volume objectives in intensity-modulated radiotherapy planning for bilateral breast cancer. *Brit J Radiol*. (2012) 85:1499–506. doi: 10.1259/bjr/24112047

24. Mihailidis DN, Plants B, Farinash L, Harmon M, Whaley L, Raja P, et al. Superiority of equivalent uniform dose (EUD)-based optimization for breast and chest wall. *Med Dosim*. (2009) 35:67–76. doi: 10.1016/j.meddos.2009.03.002

25. Raturi VP, Motegi A, Zenda S, Nakamura N, Hojo H, Kageyama SI, et al. Comparison of a Hybrid IMRT/VMAT technique with non-coplanar VMAT and non-coplanar IMRT for unresectable olfactory neuroblastoma using the RayStation treatment planning system-EUD, NTCP and planning study. *J Radiat Res*. (2021) 62:540–8. doi: 10.1093/jrr/rrab010

26. Liu L, Qiao H, Xiao Y, Tang J, Liu R. Clinical application of equivalent uniform dose in intensity-modulated rotational radiotherapy based on eclipse TPS. *Zhongguo Yi Liao Qi Xie Za Zhi*. (2024) 48:533–8. doi: 10.12455/j.issn.1671-7104.240118

27. Söhn M, Yan D, Liang J, Meldolesi E, Vargas C, Alber M. Incidence of late rectal bleeding in high-dose conformal radiotherapy of prostate cancer using equivalent uniform dose-based and dose-volume-based normal tissue complication probability models. *Int J Radiat Oncol*. (2007) 67:1066–73. doi: 10.1016/j.ijrobp.2006.10.014

28. Tao C, Liu B, Li C, Zhu J, Yin Y, Lu J. A novel knowledge-based prediction model for estimating an initial equivalent uniform dose in semi-auto-planning for cervical cancer. *Radiat Oncol*. (2022) 17:151. doi: 10.1186/s13014-022-02120-4

29. Senthilkumar K, Maria Das KJ. Comparison of biological-based and dose volume-based intensity-modulated radiotherapy plans generated using the same treatment planning system. *J Cancer Res Ther*. (2019) 15:S33–8. doi: 10.4103/jcrt.JCRT_956_16

30. Shan Z. Dosimetric comparison of the lung dose on the affected side in radiotherapy after breast cancer breast-conserving therapy based on two subfield optimization methods in Monaco planning system. *JCMR*. (2021) 2:3. doi: 10.32629/jcmr.v2i2.362

31. Virén T, Heikkilä J, Myllyoja K, Koskela K, Lahtinen T, Seppälä J. Tangential volumetric modulated arc therapy technique for left-sided breast cancer radiotherapy. *Radiat Oncol*. (2015) 10:79. doi: 10.1186/s13014-015-0392-x

32. Bellala R, Kuppusamy A, Bellala VM, Tyagi T, Manoharan S, Gangarapu G, et al. Review of clinical applications and challenges with surface-guided radiation therapy. *J Cancer Res Ther*. (2023) 19:1160–9. doi: 10.4103/jcrt.JCRT_1147_21

33. Tanguturi SK, Lyatskaya Y, Chen Y, Catalano PJ, Chen MH, Yeo WP, et al. Prospective assessment of deep inspiration breath-hold using 3-dimensional surface tracking for irradiation of left-sided breast cancer. *Pract Radiat Oncol*. (2015) 5:358–65. doi: 10.1016/j.prro.2015.06.002

34. Cao N, Kalet AM, Young LA, Fang LC, Kim JN, Mayr NA, et al. Predictors of cardiac and lung dose sparing in DIBH for left breast treatment. *Phys Medica*. (2019) 67:27–33. doi: 10.1016/j.ejmp.2019.09.240111

frontiers | Frontiers in Oncology

TYPE Mini Review
PUBLISHED 10 June 2025
DOI 10.3389/fonc.2025.1619097

Check for updates

OPEN ACCESS

EDITED BY
Poonam Yadav,
Northwestern University, United States

REVIEWED BY
Aishwarya Guha,
Chittaranjan National Cancer Institute (CNCI), India

*CORRESPONDENCE
Xiao Ma
maxiao7525308@126.com

†These authors have contributed equally to this work

RECEIVED 27 April 2025
ACCEPTED 15 May 2025
PUBLISHED 10 June 2025
CORRECTED 11 June 2025

CITATION
Xiong H, Li R, Yang L, Li Y and Ma X (2025) Dual regulation of the cGAS-STING pathway: new targets and challenges for subtype-specific immunotherapy in breast cancer. *Front. Oncol.* 15:1619097. doi: 10.3389/fonc.2025.1619097

COPYRIGHT
© 2025 Xiong, Li, Yang, Li and Ma. This is an open-access article distributed under the terms of the Creative Commons Attribution License (CC BY). The use, distribution or reproduction in other forums is permitted, provided the original author(s) and the copyright owner(s) are credited and that the original publication in this journal is cited, in accordance with accepted academic practice. No use, distribution or reproduction is permitted which does not comply with these terms.

Dual regulation of the cGAS-STING pathway: new targets and challenges for subtype-specific immunotherapy in breast cancer

Hanchu Xiong†, Rongxue Li†, Lixian Yang, Yucheng Li and Xiao Ma*

Cancer Center, Department of Radiation Oncology, Zhejiang Provincial People's Hospital, Affiliated People's Hospital, Hangzhou Medical College, Hangzhou, Zhejiang, China

Research on immune regulation mechanisms in breast cancer is crucial for breaking through therapeutic bottlenecks. This paper comprehensively reviews the dual roles of the cGAS-STING pathway in Luminal, HER2+, and triple-negative breast cancer (TNBC): its activation can enhance antitumor immunity, but chronic activation may lead to immunosuppression. By integrating molecular mechanisms, clinical translation, and subtype-specific strategies, it provides new directions for precision immunotherapy.

KEYWORDS

cGAS, STING, breast cancer, tumor microenvironment, innate immunity

1 Introduction

Breast cancer, the most frequently occurring malignant tumor among women globally, poses a serious threat to patients' health and quality of life and is also one of the leading causes of cancer-related deaths (1, 2). Its complexity lies in its heterogeneity, being composed of different subtypes with varying biological behaviors, morphological characteristics, and treatment responses. Based on molecular features, breast cancer is mainly divided into four subtypes: Luminal type (60-70%): including Luminal A (HR+/HER2-/low Ki-67) and Luminal B (HR+/high Ki-67); HER2+ type (20%): driven by HER2 overexpression leading to aggressive growth; Triple-negative breast cancer (TNBC) (10-15%): ER/PR/HER2-negative, with a high risk of recurrence and metastasis (3, 4). According to the NCCN treatment guidelines, endocrine therapy is a common treatment for ER-positive breast cancer patients, and anti-HER2 targeted therapy is recommended for HER2-positive patients (5). However, there is currently no specific targeted therapy for TNBC. Despite significant progress in diagnosis and treatment, including multi-modal strategies such as surgery, chemotherapy, radiotherapy, endocrine therapy, and targeted therapy, 20%-30% of patients may still develop metastatic disease (6, 7). Recently, immune checkpoint inhibitors (e.g., anti-PD-1/PD-L1) have achieved breakthroughs in TNBC, with the KEYNOTE-355 trial showing that pembrolizumab combined with chemotherapy

extended progression-free survival (PFS) from 5.6 to 9.7 months in advanced TNBC patients (6, 8, 9). However, immune therapy still faces significant challenges. The tumor microenvironment varies greatly among subtypes, with high T-cell infiltration but strong immunosuppression in TNBC; HER2+ type has STING pathway inhibition leading to trastuzumab resistance, and the Luminal type has AKT1 overactivation weakening immune response; systemic immune activation may also trigger cytokine storms or autoimmune reactions (10–12). However, due to tumor heterogeneity and the development of drug resistance, the long-term effects of these treatments are often limited. Therefore, identifying new therapeutic targets and developing effective strategies for metastatic breast cancer is crucial for improving patient prognosis and survival rates.

Immunotherapy has made significant strides in cancer treatment. Immune checkpoint inhibitors targeting PD-1/PD-L1 show promise across multiple malignancies (13, 14). As tumor immunotherapy gains precision and efficacy, interest in developing new approaches is rising. The cancer-immune system interaction is intricate and dynamic. While the immune system can combat tumors by identifying and eliminating abnormal cells, tumors can evade this response through mechanisms like PD-L1 upregulation and Treg recruitment (15, 16). cGAS is a cytosolic innate immune sensor of double-stranded DNA (dsDNA), which interacts with the sugar-phosphate backbone of dsDNA via positively charged amino acid residues, a process further facilitated by a conserved zinc ribbon (17). Activated cGAS synthesizes cGAMP using ATP and GTP, inducing conformational changes in the endoplasmic reticulum-resident STING protein and promoting its trafficking from the endoplasmic reticulum to the Golgi apparatus (18). The most common mechanism by which STING enhances antitumor immune function is through the induction of interferon and inflammatory cytokine production, thereby activating cytotoxic CD8+ T cells to promote adaptive immune responses (19). The cGAS-STING pathway, linking DNA damage to immune responses, plays a dual role in breast cancer (20). It can both enhance antitumor immunity and, when chronically activated, potentially drive immunosuppression (21). STING agonists can enhance antitumor immune responses, their combination with radiotherapy can boost complete response rates in TNBC (22). In HER2+ breast cancer, STING activation reverses trastuzumab resistance, and combination therapy with DS-8201 can extend median progression-free survival (mPFS). In the Luminal subtype, STING expression correlates with macrophage infiltration, yet chronic activation may expand Tregs, blunting therapeutic effects (23, 24).

cGAS-STING activation begins when cGAS detects cytosolic dsDNA, such as damage from radiotherapy or chemotherapy. This triggers a cascade: cGAS produces cGAMP, which activates STING, leading to IRF3 and NF-κB-driven expression of type I interferons and pro-inflammatory factors (25, 26). Beyond the classical cGAS-STING pathway characterized by IFN-I and other cytokine expression, non-canonical STING activation pathways should also be noted. STING can directly activate autophagy independently of TBK1-IRF3 and classical autophagy signaling molecules (27). When activated STING translocates to the endoplasmic reticulum-Golgi intermediate compartment (ERGIC), it acts as a potential autophagy receptor, using ERGIC as the primary membrane source to promote the lipidation of microtubule-associated LC3, inducing autophagy to eliminate invading pathogens and cytosolic DNA (28) (Figure 1). Several STING agonists are now in clinical trials, showing potential in breast cancer. For example, in a phase I trial (NCT03937141) targeting advanced/metastatic solid tumors or lymphomas, researchers explored the combined therapeutic effects of the STING agonist ADU-S100 (MIW815) and the PD-1 inhibitor pembrolizumab. Results showed that this combination therapy could significantly enhance antitumor immune responses in certain patients, as evidenced by an increase in tumor-infiltrating lymphocytes (TILs) (30). MK-1454 in a phase II trial for HER2+ breast cancer extended mPFS by 3.1 months when combined with trastuzumab and chemotherapy, though with a 18% incidence of grade 3+ febrile neutropenia (31). These findings indicate that combining STING agonists with existing therapies may overcome resistance but require further safety optimization. By finely tuning cGAS-STING activity, we can enhance breast cancer immunogenicity and the efficacy of immune checkpoint inhibitors, offering more effective strategies for patients. Moreover, the link between cGAS-STING activation and genetic instability in breast cancer opens new avenues for personalized treatment strategies tailored to specific genetic backgrounds (Figure 2).

This review systematically summarizes the pivotal roles of the cGAS-STING signaling pathway in breast cancer initiation, progression, drug resistance, and therapeutic responses, as well as its profound impact on tumor advancement and microenvironmental remodeling. The article delves into the intricate interplay between the activation status of the cGAS-STING pathway and the tumor immune microenvironment across distinct breast cancer subtypes, elucidating how these interactions may lead to divergent clinical outcomes—either beneficial or detrimental. Furthermore, the review critically examines current research directions and challenges associated with the cGAS-STING axis in breast cancer, while emphasizing recent breakthroughs in cGAS-STING-related studies. By integrating these insights, this work aims to deepen the mechanistic understanding of researchers and clinicians regarding the dual roles of cGAS-STING in breast cancer pathogenesis, ultimately paving the way for novel precision therapeutic strategies tailored to the molecular heterogeneity of the disease.

2 The cGAS-STING pathway and breast cancer

Breast cancer encompasses major subtypes, including Luminal, HER2+, and TNBC, each of which exhibits significant differences in response to treatment. The cGAS-STING pathway activates antitumor immunity by detecting cytoplasmic DNA, but its effects vary among subtypes. In the pathogenesis of breast cancer, the activation of the cGAS-STING signaling pathway plays a crucial role in enhancing antitumor immune responses, thereby suppressing the progression and metastasis of breast cancer, offering new potential strategies for immunotherapy in breast cancer (33). Cancer immunotherapy (ICI) is a key and rapidly evolving treatment modality that stands alongside surgical intervention, cytotoxic chemotherapy, radiotherapy, and

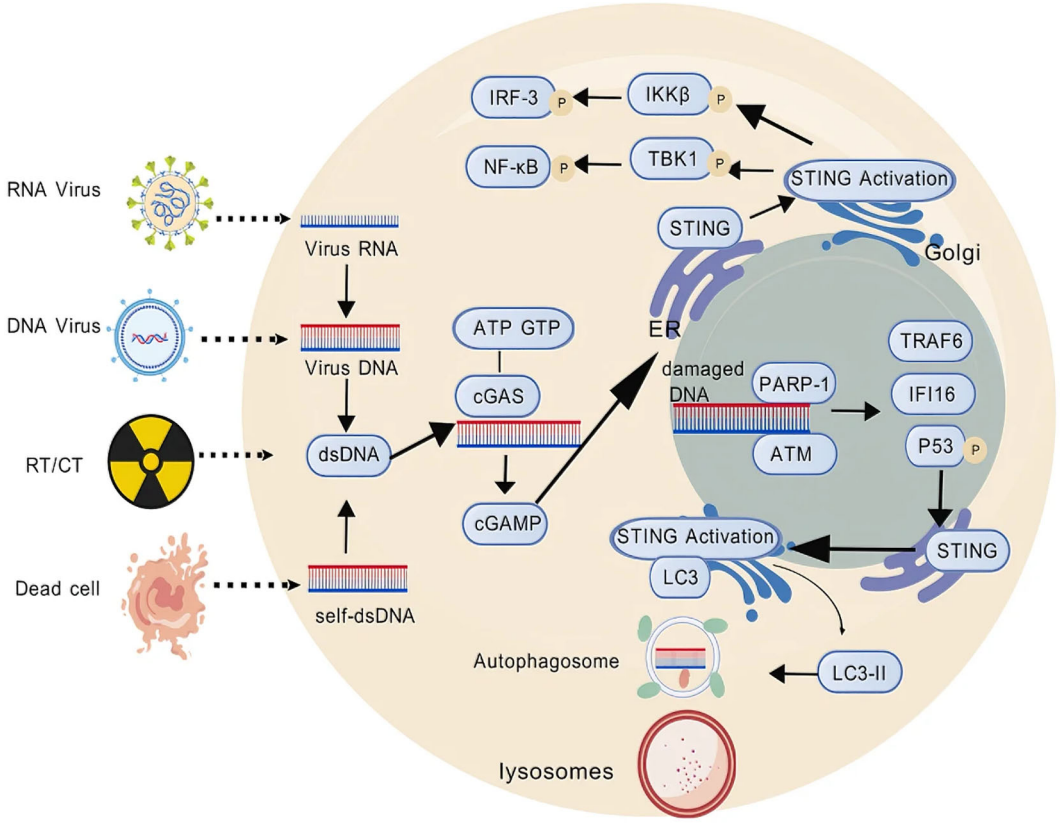

FIGURE 1
Schematic of the cGAS–STING pathway. cGAS-dependent STING pathway: dsDNA activates cGAS, which catalyzes the synthesis of cGAMP, subsequently leading to IRF3 and NF-κB-driven expression of type I interferons and pro-inflammatory factors. cGAS-independent STING pathway: damaged DNA-induced PARP-1 and ATM are recruited and promote the assembly of a STING signaling complex comprising P-p53, IFI16 and TRAF6, which acts as a potential autophagy receptor to promote the lipidation of microtubule-associated LC3, inducing autophagy to eliminate invading pathogens and cytosolic DNA. This figure was generated by GDP (29).

targeted therapy (34). Thus, it represents the fifth pillar of cancer management. As our understanding of the molecular mechanisms and roles of the cGAS-STING pathway in breast cancer deepens, the development of new immunotherapeutic approaches is likely to benefit.

In recent years, research on the cGAS-STING pathway in breast cancer has made significant progress, and its regulatory mechanisms and clinical significance have become increasingly clear. Chen et al. systematically analyzed the prognostic value of cGAS-STING related genes (CSRG) in breast cancer patients by obtaining 1,087 breast cancer samples and 179 normal breast tissue samples from The Cancer Genome Atlas (TCGA) and Genotype Tissue Expression (GTEX) databases, identifying 35 CSRGs. Further refinement using Cox regression identified 11 differentially expressed genes (DEGs) associated with prognosis, constructing a machine learning-based risk assessment and prognostic model. The study results indicate that this risk model can effectively predict the survival and prognosis of breast cancer patients, with patients having a low-risk score showing significantly better overall survival (OS) compared to those with a high-risk score (35).

Additionally, the study found a significant correlation between the risk score and tumor-infiltrating immune cells, immune checkpoints, and responses to immunotherapy, providing a new perspective for precision treatment and prognostic evaluation of breast cancer. The expression of the STING protein is closely related to the tumor microenvironment in breast cancer. In breast cancer tissues, the expression levels of STING are positively correlated with the infiltration of tumor-associated macrophages (TAMs), indicating that STING may affect tumor progression by regulating the infiltration of TAMs (36). Ka et al. showed that in breast cancer, NR1D1 promotes the accumulation of dsDNA fragments induced by DNA damage, activating the cGAS-STING signaling pathway, thereby increasing the production of type I IFN and downstream chemokines CCL5 and CXCL10 (37). Totis et al. have indicated that radiotherapy can trigger the activation of the cGAS-STING axis through the induction of cytoplasmic dsDNA fragments (38). The activation of cGAS-STING initiates type I interferon-mediated innate immune signaling, which is instrumental in eradicating malignant tumors (18). These findings reveal the potential of cGAS-STING pathway activation for anti-tumor immunity. Recently, there has been a growing interest in the activation of the cGAS-STING pathway through nanomaterials, providing new strategies for immunotherapy in breast cancer. However, Qin and others have shown that even in the presence of cytoplasmic DNA

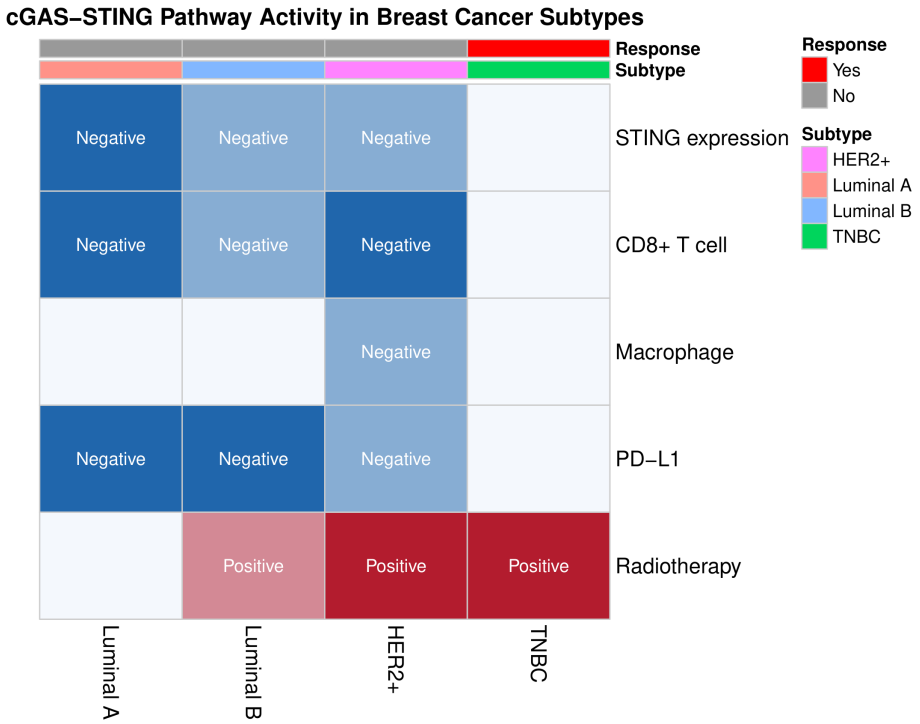

FIGURE 2
Heatmap of key immunological biomarkers (e.g., STING expression, CD8+ T cell infiltration, macrophage infiltration, PD-L1 expression) and immunotherapy responses in different subtypes of breast cancer. TNBC shows higher radiotherapy sensitivity (marked in red) and unique potential for immunotherapy, contrasting with the suppressed STING pathway activity (marked in blue) in Luminal subtypes. This figure was generated by the R package "ggplot2" (32).

accumulation, hypoxia can induce an immunosuppressive phenotype in tumor cells (39). The mechanisms by which tumor cells suppress the activation of the cGAS-STING pathway induced by hypoxia to evade immunity are largely unclear. Research has shown that hypoxia stimulates JNK1/2-mediated phosphorylation of phosphoenolpyruvate carboxykinase 1 (PCK1) at S151, a phosphorylation that triggers the interaction between PCK1 and cGAS. PCK1 associated with cGAS competitively consumes GTP, a substrate shared by PCK1 and cGAS. Consequently, PCK1 inhibits GTP-dependent cGAS activation and subsequent STING-promoted immune cell infiltration and activation in the tumor microenvironment, thereby promoting tumor growth in mice. Blocking PCK1 function in combination with anti-PD-1 antibody therapy exhibits an additive therapeutic effect on tumor growth (39). Furthermore, PCK1 S151 phosphorylation is negatively correlated with cGAS-STING activation and patient survival rates in human breast cancer specimens.

These findings reveal the complex mechanisms of the cGAS-STING pathway in breast cancer, showing both anti-tumor potential and the possibility of promoting tumor progression and drug resistance under certain conditions. Further exploration is needed to clarify the specific roles of the cGAS-STING pathway in different breast cancer subtypes and to develop targeted therapeutic strategies. In particular, modulating the cGAS-STING pathway to overcome immune suppression and drug resistance will be an important direction for breast cancer immunotherapy.

2.1 The role of the cGAS-STING pathway in luminal breast cancer

Luminal-type breast cancer, defined by molecular traits and hormone receptor expression, is linked to a better prognosis (4). It's divided into Luminal A and B subtypes based on ER, PR levels and HER2 status. Characterized by high ER and PR expression and low or negative HER2 expression, these cancers often respond well to hormone therapy due to the presence of ER and PR. They typically have lower proliferation rates and slower progression compared to HER2-positive or TNBC subtypes (40, 41). However, Luminal-type patients still face recurrence and metastasis risks, especially early after treatment, and may develop endocrine resistance, limiting therapeutic efficacy (42). The cGAS-STING pathway's role and regulatory mechanisms in Luminal breast cancer are a hot research topic. Recent studies indicate it significantly impacts tumor immunoregulation and drug resistance, with a dual role in the Luminal subtype (43, 44). Thus, in addition to endocrine therapy, combining other treatments like chemotherapy, radiotherapy, targeted therapy, and immunotherapy may be needed to enhance outcomes and survival rates in Luminal-type breast cancer patients.

In Luminal breast cancer, the activation status of the cGAS-STING pathway has a complex interplay with the tumor immune microenvironment (45). As analyzed by Liu et al., analyzing STING and CD68 expression in breast cancer tissues reveals links between their expression and immune cell infiltration. Results show a significant correlation between positive STING expression, HER2

positivity, and the Luminal subtype. Notably, in Luminal A and B breast cancer patients, STING expression correlates positively with macrophage infiltration (46). Macrophages, key immune cells in the tumor microenvironment, are closely related to tumor immune responses and prognosis. These findings offer new insights into understanding the immune microenvironment and treatment responses in breast cancer. In ER+HER2- breast cancer, the abnormal inactivation of the cGAS-STING pathway is linked to endocrine therapy resistance. Zhang's team found that in drug-resistant cells, over-activation of AKT1 kinase hinders the formation of the TBK1/STING/IRF3 complex, reducing cytoplasmic DNA sensing and suppressing cGAS-STING activation (47). Notably, cGAS-STING inhibition and AKT1 activation form a positive feedback loop, worsening drug resistance. Animal experiments show that combining AKT1 inhibitors with STING agonists can disrupt this cycle. This approach activates innate (e.g., dendritic cells) and adaptive immunity (e.g., cytotoxic T cells), significantly curbing tumor growth and offering a new strategy to reverse drug resistance.

While cGAS-STING activation may enhance antitumor immunity, sustained activation can pose tumorigenic risks. For example, STING signaling can promote the expansion of regulatory T cells (Tregs) by inducing the secretion of immunosuppressive factors like IL-6, ultimately leading to immune evasion (48, 49). This dual-edged effect suggests the need for precise pathway regulation. On one hand, restoring its normal function in drug-resistant patients is required to enhance immune surveillance. On the other hand, over-activation induced immunosuppressive microenvironments must be avoided (50, 51). It's crucial to deeply understand the spatiotemporal specific regulatory mechanisms of the cGAS-STING pathway in the Luminal subtype. Research priorities should include: dynamic changes in pathway activity in different molecular subtypes (Luminal A/B), how tumor-stromal cell crosstalk affects pathway function, developing combination therapies based on pathway status such as sequential STING agonist and immune checkpoint inhibitor or AKT inhibitor use.

In summary, precise cGAS-STING pathway activity regulation is key for balancing immune activation and suppression. Future research should further explore its specific mechanisms in Luminal breast cancer and drug-based optimization of its antitumor effects.

2.2 The role of the cGAS-STING pathway in HER2+ breast cancer

HER2+ breast cancer is characterized by the overexpression of HER2, and targeted therapies (e.g., trastuzumab, DS-8201) have significantly improved patient prognoses (52, 53). However, drug resistance and an immunosuppressive tumor microenvironment remain clinical challenges. Recent studies indicate that abnormal regulation of the cGAS-STING pathway interacts with HER2 signaling, jointly influencing treatment responses and immune evasion (54).

Recent studies have shown that HER2-targeted therapy resistance is associated with pathway inhibition. Cai et al. found that the tumor microenvironment in HER2+ breast cancer patients with resistance shows significant immunosuppression, which is closely related to reduced activity of the cGAS-STING pathway (55). The immune-related prognostic index (IRPI) they constructed shows that patients with high IRPI scores have poorer prognoses, further confirming that cGAS-STING pathway inhibition is a key mechanism driving immune evasion in trastuzumab-resistant breast cancer. Notably, combining STING agonists with DS-8201 can reverse the immunosuppressive phenotype and significantly inhibit the progression of resistant tumors in preclinical models (56). Wu et al. found that HER2 overexpression can weaken antitumor immune responses by disrupting cGAS-STING signaling in Colorectal cancer. Anti-HER2 therapies (e.g., trastuzumab) may partially restore cGAS-STING pathway function, activating the tumor-killing activity of CD8+ T cells and NK cells. This suggests a synergistic effect between HER2-targeted therapy and immune modulation (57).

2.3 The role of the cGAS-STING pathway in TNBC

TNBC is a unique breast cancer type, lacking ER, PR, and HER2 expression. It accounts for 10-15% of breast cancer cases and is highly aggressive, metastatic, and associated with a poor prognosis (58, 59). Due to the lack of effective targeted therapies, TNBC patients face a higher risk of recurrence (60). Recent studies indicate that the cGAS-STING pathway plays a dual role in TNBC by modulating immune responses and the tumor microenvironment (61). Nanotechnology is emerging as a new approach for precise regulation of this pathway (62, 63).

In TNBC, immunological activation is linked to therapeutic enhancement. When cytosolic DNA (e.g., from radiotherapy/chemotherapy-induced damage) activates the cGAS-STING pathway, it triggers type I interferon signaling via the STING-TBK1-IRF3 axis, recruiting CD8+ T cells and NK cells to enhance antitumor immunity (64, 65). Preclinical studies show that TNBC patients with high STING expression have a prolonged progression-free survival by 6 months compared to those with low expression, indicating its potential as a prognostic biomarker. For example, Liu et al. found that radiotherapy - induced DNA damage significantly inhibits tumor growth in TNBC mouse models by activating the cGAS-STING pathway (66). Xu et al. pointed out that activating the cGAS-STING pathway can enhance the immunogenicity of TNBC cells and improve the efficacy of immune checkpoint inhibitors (67). They developed a ruthenium(II) arene complex C5 based on ferritin and constructed a C5-AFt nanoparticle delivery system, which inhibits the growth and metastasis of TNBC by inducing ferroptosis via mitochondrial damage and activating the cGAS-STING pathway. On the other hand, the cGAS-STING pathway can promote tumor immune evasion under microenvironmental stress. For instance, in triple-negative breast cancer cells, when there is an

error in chromosome segregation, the cGAS-STING signaling pathway is activated. The activation of this pathway further triggers the non-classical NF-κB signaling pathway, leading to the release of IL-6 and activating the IL-6/STAT3 signaling pathway, ultimately promoting the survival and development of drug resistance of triple-negative breast cancer cells (68).

In recent years, nanomaterials have become a research hotspot in the treatment of TNBC due to their precise delivery and multifunctional characteristics. Many studies have been committed to the activation of the cGAS-STING pathway based on nanotechnology. The core challenge in TNBC treatment lies in overcoming the immunosuppressive microenvironment and enhancing drug penetration, and the precise delivery and multifunctional characteristics of nanomaterials provide a breakthrough direction for this. The oxygen self-supplying nanoradiosensitizer ALFM developed by Wang et al. enhances the antitumor immune response and improves radioimmunotherapy for TNBC by activating immunogenic cell death (ICD) and the cGAS-STING signaling pathway (69). The study by Kim et al. has shown that cannabidiol (CBD) can stimulate PD-L1 expression in TNBC cells and significantly activate the cGAS-STING pathway (70). The combination of CBD and anti-PD-L1 antibodies enhances the antitumor immune response. These two examples both illustrate that the activation of the cGAS-STING pathway enhances immunogenicity. Moreover, the activation of the cGAS-STING pathway is also associated with the remodeling of the tumor microenvironment and the enhancement of drug penetration. For example, the study by Zhou et al. developed a zinc-copper bimetallic nanoplatform coated with polydopamine (CZP NPs), which can effectively induce photothermal-enhanced copper deposition and activate the cGAS-STING signaling pathway, thereby reversing the immunosuppressive tumor microenvironment in TNBC (71). Photothermal therapy significantly enhances these effects, and the combination of CZP NPs with αPD-L1 markedly boosts antitumor immunity and suppresses tumor growth. Some researchers have combined losartan, a STING agonist, and a PD-L1 inhibitor to form an intelligent nanosystem. Losartan is released in the tumor microenvironment, where it degrades the extracellular matrix to enhance the penetration of immunotherapeutic drugs (72). Subsequently, the reactive oxygen species generated by photosensitizers ensure the targeted release of drugs, activate the cGAS-STING pathway, and enhance the immune response.

With the rapid development of nanotechnology and biomaterials science, new materials are constantly emerging, bringing more opportunities for the treatment of TNBC. In the field of TNBC, many materials have demonstrated antitumor efficacy by activating the cGAS-STING pathway. Specifically, these materials can influence the growth of TNBC cells. For instance, under growth-restricted conditions, activation of the cGAS-STING pathway helps breast cancer cells survive, while inhibition of this pathway triggers autophagy-dependent cell death mechanisms. Additionally, these materials can modulate the tumor microenvironment. For example, by promoting photothermal-enhanced copper deposition and activating the cGAS-STING signaling pathway, they can alter the immunosuppressive state of TNBC, enhance antitumor immune responses, and inhibit tumor growth. Moreover, they can activate immune responses, such as enhancing the immunogenicity of TNBC cells and improving the therapeutic efficacy of immune checkpoint inhibitors by activating the cGAS-STING pathway. This ultimately brings more effective treatment options for TNBC patients. Looking to the future, the in-depth integration of materials science with immunotherapy and other multidisciplinary fields is expected to provide more efficient and precise treatment options for TNBC patients. On one hand, new materials can achieve precise drug delivery, increasing the concentration of drugs in tumor tissues and reducing toxicity to normal tissues. On the other hand, through rational design and functional modification, materials can possess multiple functions, such as simultaneously activating the cGAS-STING pathway, modulating the tumor microenvironment, and enhancing immune responses, to maximize the synergistic antitumor effect.

2.4 Involvement of cGAS-STING pathway in stemness, metastasis and drug resistance of breast cancer

In Luminal breast cancer, the inactivation of the cGAS-STING pathway and the overactivity of AKT kinase form a vicious cycle, which is a significant cause of endocrine therapy resistance and metastasis in patients (47). Team Dengrong from Sun Yat-sen University has found that the cGAS-STING pathway activity is significantly reduced in Luminal breast cancer cells, while AKT kinase is abnormally active. AKT directly interferes with the key molecule TBK1 downstream of STING, causing the STING-IRF3 signaling pathway to "malfunction," thereby inhibiting the immune system's ability to produce type I interferons and allowing tumor cells to evade immune attacks, ultimately rendering drugs (such as tamoxifen) gradually ineffective (47). For this mechanism, Team Dengrong confirmed that combination therapy strategies have shown significant potential: STING agonists (such as ADU-S100) can reactivate immune surveillance functions, while AKT inhibitors (such as Capivasertib) can block the abnormal signaling of the enzyme, and their synergistic effect not only reverses drug resistance but also transforms immune "cold tumors" into "hot tumors," enhancing T cell infiltration. Meanwhile, another Team Ang Zheng found that SNORA47 affected stemness and chemotherapy sensitivity of Luminal breast cancer cells via EBF3/RPL11/c-Myc axis, providing a new direction for precision therapy of Luminal breast cancer patients (73).

Studies have shown that resistance to HER2-targeted therapies in HER2+ BC is often associated with the abnormal activation of mesenchymal HER2+ cancer stem cells, Team Serenella M Pupa found that a consistent enrichment of CD36 in HER2+ breast cancer stem cells from all tested resistant cell models that mechanistically occurs via Wnt signaling pathway activation (74). Consistently, dual blockade of CD36 and HER2 increased the efficacy of anti-HER2 drugs favoring the transition of stem cells into therapy-sensitive epithelial state. In addition, other preclinical experiments have shown

that the combination of STING agonists (such as ADU-S100) with HER2-targeted drugs (such as trastuzumab or DS-8201) can significantly reduce the proportion of cancer stem cells and inhibit the clonogenic ability of drug-resistant cells, suggesting that STING activation may reverse resistance by remodeling the TME and regulating stem cell properties (75).

In TNBC, the abnormal regulation of the cGAS-STING pathway is closely related to tumor immune evasion and therapeutic drug resistance. Researchers have found that TNBC cells activate the phosphorylation of the metabolic enzyme ADSL under hypoxic conditions, promoting the abnormal accumulation of its metabolic product, fumarate (48). Fumarate can directly bind to and inhibit the activity of the STING protein, blocking the cGAMP-mediated STING-IRF3 signal transduction, leading to a decrease in the secretion of type I interferons, thereby weakening the anti-tumor immune response and causing drug resistance to immune therapies (48). Since Mn^{2+} has great potential for activating the cGAS-STING signaling pathway to generate antitumor immune responses, Team Haisheng reported that microneedles loaded with sparfloxacin and Zinc-Manganese sulfide nanoparticles could significantly suppress tumor growth, thereby significantly enhancing the tumor infiltration and cytotoxic effects of CD4+/CD8+ T cells and strongly inhibiting the lung metastasis of TNBC cells (76).

3 Conclusion

After reviewing and organizing a large number of relevant studies, we have gained a comprehensive understanding of the role of the cGAS-STING pathway in different breast cancer subtypes (Table 1). Overall, this pathway plays a crucial role throughout the course of breast cancer, with its activation state closely linked to the tumor immune microenvironment. On one hand, activation of the pathway can enhance antitumor immune responses, opening new avenues for breast cancer immunotherapy. On the other hand, its sustained activation in certain contexts may lead to immunosuppression and drug resistance, negatively impacting treatment outcomes (Figure 3). Specifically, in Luminal breast cancer hyperactivation of AKT kinase inhibits the formation of the STING-IRF3 complex by binding to TBK1, blocking IFN-I secretion and impairing immune surveillance. Concurrently, STING signaling inactivation further promotes AKT phosphorylation, forming a vicious cycle that drives endocrine therapy resistance. Endocrine resistance in Luminal breast cancer (particularly

TABLE 1 Overview of the mechanisms andfunctions of cGAS-STING in breast cancer.

First author	year	Breast cancer subtypes	Model	Targets	cGAS/STING pathway status	Conclusion
Zhang et al. (47)	2024	luminal	Human breast cancer cell lines, Nude mouse models	cGAS-STING pathway, AKT1	Inactivated	Inactivated cGAS-STING signaling contributes to endocrine resistance through a positive feedback loop with AKT1.
Cai et al. (55)	2024	HER2+	HER2+ breast cancer cell lines Human HER2+ BC samples, Humanized mouse models	STING, IRF3	Inactivated	Silencing of cGAS-STING pathway is a key determinant of immune escape in Herceptin-resistant BC.
Wang et al. (69)	2024	TNBC	Oxygen-supplying nano-radiosensitizer	FePt alloy, MnO nanocrystals	Activated	Oxygen-supplying nano-radiosensitizer enhances TNBC radioimmunotherapy by activating cGAS-STING.
Xu et al. (67)	2024	TNBC	C5-AFt NPs	cGAS-STING	Activated	C5-AFt NPs inhibit TNBC growth and metastasis via ferroptosis and cGAS-STING activation.
Kim et al. (70)	2024	TNBC	Human TNBC cells	CBD, cGAS-STING	Activated	CBD enhances PD-L1 expression and Atezolizumab efficacy via cGAS-STING activation.
Zhong et al. (72)	2023	TNBC	Mouse breast cancer cell lines	GSDME, cGAS-STING	Activated	Nanodrug induces pyroptosis and activates cGAS-STING for enhanced TNBC therapy.
Zhou et al. (71)	2025	TNBC	Cu-ZnO2@PDA nanoplatforms	cGAS-STING	Activated	Zinc-copper nanoplatform enhances TNBC immunotherapy via cGAS-STING activation.
Liu et al. (66)	2022	TNBC	Human TNBC cell lines	cGAS-STING	Activated	cGAS-STING promotes TNBC cell survival under stress, offering new treatment opportunities.
Chen et al. (45)	2024	TNBC	Primary breast cancer samples (n=380), TCGA and METABRIC cohorts	STING, pTBK1, pSTAT1	Activated	cGAS-STING pathway is highly expressed in TNBC and is associated with genomic instability and immune cell infiltration.

(Continued)

TABLE 1 Continued

First author	year	Breast cancer subtypes	Model	Targets	cGAS/STING pathway status	Conclusion
Zhang et al. (51)	2025	BRCA	TAMs cell lines, Mouse models	cGAS, STING, TBK1, IRF3	Activated/Inactivated	Targeting cGAS-STING pathway for reprogramming TAMs shows promise in enhancing anti-tumor immunotherapy.
Ka et al. (37)	2023	BRCA	MMTV-PyMT mouse model, Breast cancer cell lines (MDA-MB-231, SKBR3)	NR1D1, cGAS, STING, IFN	Activated	NR1D1 enhances anti-tumor immunity via activating cGAS-STING pathway and promoting CD8+ T-cell responses.
Totis et al. (38)	2024	BRCA	An *in vitro* 4T1 breast cancer model	dsDNA、IFN-β	Activated	Carbon ions induce higher yields of cytoplasmic dsDNA fragments per unit dose compared to photons, and the release of interferon-β increases with increasing radiation dose.
Liu et al. (36)	2024	BRCA	83 breast cancer patients	STING, CD68	STING expression is lower in breast cancer tissue than in adjacent tissue	STING and CD68 are linked to breast cancer progression. STING activation may enhance TAMs function. STING agonists could improve immune therapy response.
Qin et al. (39)	2025	BRCA	Breast cancer cell lines and mouse models	PCK1, cGAS-STING	Inhibited by PCK1	PCK1 suppresses cGAS-STING activation, promoting immune evasion. Blocking PCK1 combined with anti-PD-1 therapy is effective. PCK1 S151 phosphorylation correlates negatively with patient survival.

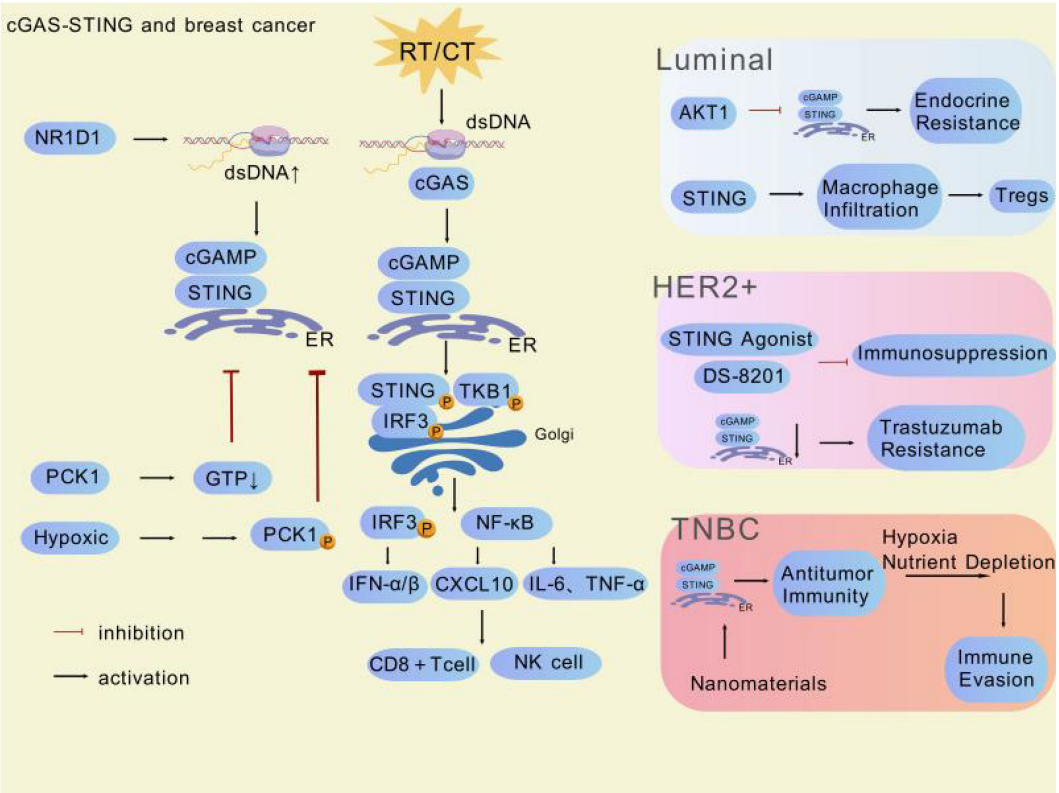

FIGURE 3
Multiple factors and potentially clinically valuable drugs are involved in regulating the cGAS-STING pathway in different subtypes of breast cancer. This figure was generated by GDP (29).

the ER+/HER2- subtype) remains a major research focus. Deng Rong's team validated through clinical samples and humanized mouse models that combining STING agonists (e.g., ADU-S100) with AKT inhibitors (e.g., Capivasertib) breaks this cycle, significantly suppressing resistant tumor growth and promoting CD8+ T-cell infiltration, thereby converting "cold tumors" into "hot tumors". However, chronic STING activation may upregulate PD-L1 expression via the IRF3 signaling axis and induce regulatory T-cell expansion, leading to an immunosuppressive microenvironment. The resistance mechanisms of STING agonists in Luminal breast cancer are complex, involving signaling pathway imbalances, metabolic abnormalities, and immune microenvironment remodeling, necessitating further research. In HER2-positive breast cancer, STING agonists (e.g., ADU-S100) activate the cGAS-STING pathway to promote IFN-I secretion, enhancing APC maturation and cross-presentation. However, PI3K/AKT pathway hyperactivity driven by PIK3CA mutations inhibits STING signaling by disrupting TBK1-STING interactions, blocking IFN-β secretion and enabling immune evasion. Preclinical studies in trastuzumab-resistant models demonstrate that combining STING agonists (e.g., ADU-S100) with HER2-targeted antibody-drug conjugates (e.g., DS-8201) significantly reduces the proportion of CD44+/CD24− cancer stem cells and enhances dendritic cell cross-presentation to promote CD8+ T-cell infiltration. The therapeutic challenges of TNBC stem from its high heterogeneity and immunosuppressive microenvironment. Current research focuses on manganese-based nanoagonists (e.g., BMP-Au), which activate the cGAS-STING pathway by inducing mitochondrial DNA release and synergize with radiotherapy to enhance immunogenic cell death, promoting CD8+ T-cell infiltration and significantly inhibiting TNBC lung metastasis. Combined with radiotherapy, this approach downregulates PD-L1 expression in the TME, reduces immunosuppressive myeloid-derived suppressor cells, and enhances antitumor immune responses. Additionally, GSH-responsive manganese oxide nanocubes activate both AMPK and STING pathways, inducing ferroptosis and immune responses to overcome chemoresistance. Mn^{2+}release further activates the cGAS-STING pathway, promoting IFN-I secretion and APC function. However, studies also reveal that STING agonists may induce expansion of PD-$L1^{high}$ monocytes via the IRF3-IFN-I axis, fostering an immunosuppressive microenvironment. TLR2 agonist pretreatment reprograms STING signaling by inducing K63 ubiquitination of STING, promoting its interaction with TRAF6, suppressing the IRF3-IFN-I axis, and activating the NF-κB pathway, thereby converting monocytes into PD-$L1^{low/-}$ antitumor phenotypes. In breast cancer mouse models, combined TLR2/STING agonist therapy significantly inhibits tumor growth and induces systemic antitumor immunity. This mechanism has been validated in TNBC models (e.g., 4T1 breast cancer), where the combined strategy improves tumor suppression rates by over threefold and reduces lung metastasis. Nevertheless, hypoxia-induced metabolic reprogramming (e.g., ADSL-mediated fumarate accumulation) competitively inhibits cGAS activity, blocking STING signaling, while protective autophagy further weakens chemosensitivity by lysosomal degradation of STING protein. Future research should focus on exploring the specific mechanisms of the cGAS-STING pathway in different breast cancer subtypes, developing precise biomarkers and diagnostic tools, optimizing modulator development and application strategies, investigating multidisciplinary comprehensive treatment models, and identifying effective ways to overcome tumor heterogeneity and drug resistance. This will provide more precise and effective treatment options for breast cancer patients, improve their prognosis, and enhance survival rates and quality of life.

Author contributions

HX: Writing – original draft. RL: Writing – original draft. LY: Writing – review & editing. YL: Writing – review & editing. XM: Writing – review & editing, Methodology, Conceptualization, Validation.

Funding

The author(s) declare that financial support was received for the research and/or publication of this article. The work was supported by the National Natural Science Foundation of China (82102814), Zhejiang Provincial Natural Science Foundation of China under grants (LQ22H160053), Zhejiang Provincial People's Hospital Scientific Research Foundation for The Excellent Youth (ZRY2020B007), Zhejiang Provincial Project for Medical and Health Science and Technology (2025691521).

Conflict of interest

The authors declare that the research was conducted in the absence of any commercial or financial relationships that could be construed as a potential conflict of interest.

Generative AI statement

The author(s) declare that no Generative AI was used in the creation of this manuscript.

Correction note

This article has been corrected with minor changes. These changes do not impact the scientific content of the article.

Publisher's note

All claims expressed in this article are solely those of the authors and do not necessarily represent those of their affiliated organizations, or those of the publisher, the editors and the reviewers. Any product that may be evaluated in this article, or claim that may be made by its manufacturer, is not guaranteed or endorsed by the publisher.

References

1. Abedian Kasgri K, Abazari M, Tehrani H, Yazdani Charati J, Momeni Badeleh S, Momeni Badeleh K, et al. A systematic review for evaluation of specialized programs for addressing young women with breast cancer problems. *Oncol Res Treat*. (2022) 45:504–24. doi: 10.1159/000525413

2. Ablasser A, Gulen MF. Erratum: Global cancer statistics 2018: GLOBOCAN estimates of incidence and mortality worldwide for 36 cancers in 185 countries. *CA: A Cancer J Clinicians*. (2020) 68:394–424. doi: 10.3322/caac.21609

3. Feng Y, Spezia M, Huang S, Yuan C, Zeng Z, Zhang L, et al. Breast cancer development and progression: Risk factors, cancer stem cells, signaling pathways, genomics, and molecular pathogenesis. *Genes Dis*. (2018) 5:77–106. doi: 10.1016/j.gendis.2018.05.001

4. Ignatiadis M, Sotiriou C. Luminal breast cancer: from biology to treatment. *Nat Rev Clin Oncol*. (2013) 10:494–506. doi: 10.1038/nrclinonc.2013.124

5. Gradishar W, Salerno KE. NCCN guidelines update: breast cancer. *J Natl Compr Cancer Network*. (2016) 14:641–4. doi: 10.6004/jnccn.2016.0181

6. Edechi CA, Ikeogu N, Uzonna JE, Myal Y. Regulation of immunity in breast cancer. *Cancers*. (2019) 11:1080. doi: 10.3390/cancers11081080

7. Kong X, Zhang J, Chen S, Wang X, Xi Q, Shen H, et al. Immune checkpoint inhibitors: breakthroughs in cancer treatment. *Cancer Biol Med*. (2024) 39:1577–87. doi: 10.20892/j.issn.2095-3941.2024.0055

8. Cortes J, Cescon DW, Rugo HS, Nowecki Z, Im S-A, Yusof MM, et al. Pembrolizumab plus chemotherapy versus placebo plus chemotherapy for previously untreated locally recurrent inoperable or metastatic triple-negative breast cancer (KEYNOTE-355): a randomised, placebo-controlled, double-blind, phase 3 clinical trial. *Lancet*. (2020) 396:1817–28. doi: 10.1016/s0140-6736(20)32531-9

9. Hattori M, Masuda N, Takano T, Tsugawa K, Inoue K, Matsumoto K, et al. Pembrolizumab plus chemotherapy in Japanese patients with triple-negative breast cancer: Results from KEYNOTE-355. *Cancer Med*. (2023) 12:10280–93. doi: 10.1002/cam4.5757

10. Kim NI, Park MH, Cho N, Lee JS. Comparison of the clinicopathologic features and T-cell infiltration of B7-H3 and B7-H4 expression in triple-negative breast cancer subtypes. *Appl Immunohistochemistry Mol Morphology*. (2022) 30:246–56. doi: 10.1097/pai.0000000000001001

11. Ong L-T, Lee WC, Ma S, Oguz G, Niu Z, Bao Y, et al. IFI16-dependent STING signaling is a crucial regulator of anti-HER2 immune response in HER2+ breast cancer. *Proc Natl Acad Sci United States America*. (2022) 119:e2201376119. doi: 10.1073/pnas.2201376119

12. Zhang A, Miao K, Sun H, Deng C-X. Tumor heterogeneity reshapes the tumor microenvironment to influence drug resistance. *Int J Biol Sci*. (2022) 18:3019–33. doi: 10.7150/ijbs.72534

13. Aden D, Zaheer S, Sureka N, Trisal M, Chaurasia JK, Zaheer S. Exploring immune checkpoint inhibitors: Focus on PD-1/PD-L1 axis and beyond. *Pathol - Res Pract*. (2025) 269:155864. doi: 10.1016/j.prp.2025.155864

14. Ai L, Chen J, Yan H, He Q, Luo P, Xu Z, et al. Research status and outlook of PD-1/PD-L1 inhibitors for cancer therapy. *Drug Design Dev Ther*. (2020) 14:3625–49. doi: 10.2147/dddt.s267433

15. Ishida Y, Agata Y, Shibahara K, Honjo T. Induced expression of PD-1, a novel member of the immunoglobulin gene superfamily, upon programmed cell death. *EMBO J*. (1992) 11:3887-95. doi: 10.1002/j.1460-2075.1992.tb05481.x

16. Zaidi N, Jaffee EM. Immunotherapy transforms cancer treatment. *J Clin Invest*. (2018) 129:46–7. doi: 10.1172/jci126046

17. Kwon J, Bakhoum SF. The cytosolic DNA-sensing cGAS-STING pathway in cancer. *Cancer Discov*. (2020) 10:26–39. doi: 10.1158/2159-8290.Cd-19-0761

18. Zheng J, Mo J, Zhu T, Zhuo W, Yi Y, Hu S, et al. Comprehensive elaboration of the cGAS-STING signaling axis in cancer development and immunotherapy. *Mol Cancer*. (2020) 19:133. doi: 10.1186/s12943-020-01250-1

19. Parkes EE, Savage KI, Lioe T, Boyd C, Halliday S, Walker SM, et al. Activation of a cGAS-STING-mediated immune response predicts response to neoadjuvant chemotherapy in early breast cancer. *Br J Cancer*. (2022) 126:247–58. doi: 10.1038/s41416-021-01599-0

20. Ablasser A, Gulen MF. The role of cGAS in innate immunity and beyond. *J Mol Med*. (2016) 94:1085–93. doi: 10.1007/s00109-016-1423-2

21. Ferrarelli LK. The two faces of cGAS in cancer and immunity. *Sci Signaling*. (2018) 11. doi: 10.1126/scisignal.aaw0850

22. Geyer CE Jr, Untch M, Prat A, Rastogi P, Niikura N, Mathias E, et al. Abstract OT1-02-03: Trastuzumab deruxtecan (T-DXd; DS-8201) vs trastuzumab emtansine (T-DM1) in high-risk patients with HER2-positive, residual invasive early breast cancer after neoadjuvant therapy: A randomized, phase 3 trial (DESTINY-Breast05). *Cancer Res*. (2022) 82:OT1-02-03.

23. Hines JB, Kacew AJ, Sweis RF. The development of STING agonists and emerging results as a cancer immunotherapy. *Curr Oncol Rep*. (2023) 25:189–99. doi: 10.1007/s11912-023-01361-0

24. Jungles KM, Holcomb EA, Pearson AN, Jungles KR, Bishop CR, Pierce LJ, et al. Updates in combined approaches of radiotherapy and immune checkpoint inhibitors for the treatment of breast cancer. *Front Oncol*. (2022) 12:1022542. doi: 10.3389/fonc.2022.1022542

25. Yue B, Gao W, Lovell JF, Jin H, Huang J. The cGAS-STING pathway in cancer immunity: dual roles, therapeutic strategies, and clinical challenges. *Essays Biochem*. (2025) 69:EBC20253006. doi: 10.1042/ebc20253006

26. Zhang Z, Zhang C. Regulation of cGAS–STING signalling and its diversity of cellular outcomes. *Nat Rev Immunol*. (2025). doi: 10.1038/s41577-024-01112-7

27. Shen M, Jiang X, Peng Q, Oyang L, Ren Z, Wang J, et al. The cGAS–STING pathway in cancer immunity: mechanisms, challenges, and therapeutic implications. *J Hematol Oncol*. (2025) 18:40. doi: 10.1186/s13045-025-01691-5

28. Gui X, Yang H, Li T, Tan X, Shi P, Li M, et al. Autophagy induction via STING trafficking is a primordial function of the cGAS pathway. *Nature*. (2019) 567:262–6. doi: 10.1038/s41586-019-1006-9

29. Jiang S, Li H, Zhang L, et al. Generic Diagramming Platform (GDP): a comprehensive database of high-quality biomedical graphics. *Nucleic Acids Res*. (2025) 53(D1):D1670-6. doi: 10.1093/nar/gkae973

30. Meric-Bernstam F, Sweis RF, Kasper S, Hamid O, Bhatia S, Dummer R, et al. Combination of the STING agonist MIW815 (ADU-S100) and PD-1 inhibitor spartalizumab in advanced/metastatic solid tumors or lymphomas: an open-label, multicenter, phase ib study. *Clin Cancer Res*. (2022) 29:110–21. doi: 10.1158/1078-0432.ccr-22-2235

31. Wang B, Yu W, Jiang H, Meng X, Tang D, Liu D. Clinical applications of STING agonists in cancer immunotherapy: current progress and future prospects. *Front Immunol*. (2024) 15:1485546. doi: 10.3389/fimmu.2024.1485546

32. Gómez-Rubio V. ggplot2 - Elegant Graphics for Data Analysis (2nd Edition). *J Stat Software, Book Rev*. (2017) 77, 2:1–3. doi: 10.18637/jss.v077.b02

33. Samson N, Ablasser A. The cGAS–STING pathway and cancer. *Nat Cancer*. (2022) 3:1452–63. doi: 10.1038/s43018-022-00468-w

34. Basak U, Mukherjee S, Chakraborty S, Sa G, Dastidar SG, Das T. In-silico analysis unveiling the role of cancer stem cells in immunotherapy resistance of immune checkpoint-high pancreatic adenocarcinoma. *Sci Rep*. (2025) 15:10355. doi: 10.1038/s41598-025-93924-3

35. Chen C, Wang J, Dong C, Lim D, Feng Z. Development of a risk model to predict prognosis in breast cancer based on cGAS-STING-related genes. *Front Genet*. (2023) 14:1121018. doi: 10.3389/fgene.2023.1121018

36. Liu H, Hu J, Peng J, Hu Z. Expression and clinical significance of STING and CD68 in breast cancer. *J Bengbu Medical College*. (2024) 49:307–12. doi: 10.13898/j.cnki.issn.1000-2200.2024.03.006

37. Ka N-L, Park MK, Kim S-S, Jeon Y, Hwang S, Kim SM, et al. NR1D1 stimulates antitumor immune responses in breast cancer by activating cGAS-STING signaling. *Cancer Res*. (2023) 83:3045–58. doi: 10.1158/0008-5472.can-23-0329

38. Totis C, Averbeck NB, Jakob B, Schork M, Volpi G, Hintze DF, et al. Induction of cytoplasmic dsDNA and cGAS-STING immune signaling after exposure of breast cancer cells to X-rays or high energetic carbon ions. *Adv Radiat Oncol*. (2024) 10:101783. doi: 10.1016/j.adro.2025.101783

39. Qin W, Duan Y, Hu Z, Hou Y, Wen T, Ouyang Y, et al. PCK1 inhibits cGAS-STING activation by consumption of GTP to promote tumor immune evasion. *J Exp Med*. (2025) 222:e20240902. doi: 10.1084/jem.20240902

40. Han Y, Xu S, Colditz GA, Toriola AT. Trends in breast cancer mortality according to molecular subtypes: A population-based study. *J Clin Oncol*. (2021) 39:572. doi: 10.1200/jco.2021.39.15_suppl.572

41. Li J, Chen Z, Su K, Zeng J. Clinicopathological classification and traditional prognostic indicators of breast cancer. *Int J Clin Exp Pathol*. (2015) 8:8500–5.

42. Selli C, Dixon JM, Sims AH. Accurate prediction of response to endocrine therapy in breast cancer patients: current and future biomarkers. *Breast Cancer Res*. (2016) 18:118. doi: 10.1186/s13058-016-0779-0

43. Chen Y, Yue S, Yu L, Cao J, Liu Y, Deng A, et al. Regulation and function of the cGAS-STING pathway: mechanisms, post-translational modifications, and therapeutic potential in immunotherapy. *Drug Design Dev Ther*. (2025) 19:1721–1739. doi: 10.2147/dddt.s501773

44. Zhang Y, Wang Y, Mu P, Zhu X, Dong Y. Bidirectional regulation of the cGAS-STING pathway in the immunosuppressive tumor microenvironment and its association with immunotherapy. *Front Immunol*. (2024) 15:1470468. doi: 10.3389/fimmu.2024.1470468

45. Chen M, Yu S, van der Sluis T, Zwager MC, Schröder CP, van der Vegt B, et al. cGAS-STING pathway expression correlates with genomic instability and immune cell infiltration in breast cancer. *NPJ Breast Cancer*. (2024) 10:1. doi: 10.1038/s41523-023-00609-z

46. Kundu M, Butti R, Panda VK, Malhotra D, Das S, Mitra T, et al. Modulation of the tumor microenvironment and mechanism of immunotherapy-based drug resistance in breast cancer. *Mol Cancer*. (2024) 23:92. doi: 10.1186/s12943-024-01990-4

47. Zhang K-M, Zhao D-C, Li Z-Y, Wang Y, Liu J-N, Du T, et al. Inactivated cGAS-STING signaling facilitates endocrine resistance by forming a positive feedback loop with AKT kinase in ER+HER2– breast cancer. *Advanced Sci.* (2024) 11:e2403592. doi: 10.1002/advs.202403592

48. Duan Y, Hu Z, Han P, Lei B, Wang S, Wang Z, et al. ADSL-generated fumarate binds and inhibits STING to promote tumour immune evasion. *Nat Cell Biol.* (2025) 27:668–82. doi: 10.1038/s41556-025-01627-8

49. Ni H, Zhang H, Li L, Huang H, Guo H, Zhang L, et al. T cell-intrinsic STING signaling promotes regulatory T cell induction and immunosuppression by upregulating FOXP3 transcription in cervical cancer. *J ImmunoTherapy Cancer.* (2022) 10:e005151. doi: 10.1136/jitc-2022-005151

50. Li M, Lu L, Bao Q, Zhou M, Nie B, Liu Y, et al. Radiotherapy-derived engineered stem cell exosomes improve anti-glioma immunotherapy by promoting the formation of tertiary lymphoid structure and improve the release of type I interferon. *J Nanobiotechnology.* (2025) 23:239. doi: 10.1186/s12951-025-03301-5

51. Zhang W, Huang X. Targeting cGAS-STING pathway for reprogramming tumor-associated macrophages to enhance anti-tumor immunotherapy. *Biomarker Res.* (2025) 13:43. doi: 10.1186/s40364-025-00750-w

52. Cossu C, Di Lorenzo A, Fiorilla I, Todesco AM, Audrito V, Conti L. The role of the toll-like receptor 2 and the cGAS-STING pathways in breast cancer: friends or foes? *Int J Mol Sci.* (2023) 25:456. doi: 10.3390/ijms25010456

53. Li Q, Tian S, Liang J, Fan J, Lai J, Chen Q. Therapeutic development by targeting the cGAS-STING pathway in autoimmune disease and cancer. *Front Pharmacol.* (2021) 12:779425. doi: 10.3389/fphar.2021.779425

54. Islam S, Islam MM, Akhand MRN, Park B-Y, Akanda MR. Recent advancements in cGAS-STING activation, tumor immune evasion, and therapeutic implications. *Med Oncol.* (2024) 41:291. doi: 10.1007/s12032-024-02539-7

55. Cai R, Chen Q, Zhao D, Wang Y, Zhou L, Zhang K, et al. A high immune-related index with the suppression of cGAS-STING pathway is a key determinant to herceptin resistance in HER2+ Breast cancer. *Int J Biol Sci.* (2024) 20:3497–514. doi: 10.7150/ijbs.94868

56. Zhao H-Y, Liu Z, Tao J, Mao S, Wang M, He M, et al. An oral tricyclic STING agonist suppresses tumor growth through remodeling of the immune microenvironment. *Cell Chem Biol.* (2025) 32:280–290.e14. doi: 10.1016/j.chembiol.2025.01.004

57. Wu X, Xu L, Li X, Zhou Y, Han X, Zhang W, et al. A HER2-targeting antibody-MMAE conjugate RC48 sensitizes immunotherapy in HER2-positive colon cancer by triggering the cGAS-STING pathway. *Cell Death Dis.* (2023) 14:550. doi: 10.1038/s41419-023-06073-8

58. Aine M, Nacer DF, Arbajian E, Veerla S, Karlsson A, Häkkinen J, et al. The DNA methylation landscape of primary triple-negative breast cancer. *Nat Commun.* (2025) 16:3041. doi: 10.1038/s41467-025-58158-x

59. Aysola K, Desai A, Welch C, Xu J, Qin Y, Reddy V, et al. Triple negative breast cancer - an overview. *Hereditary Genet.* (2013) 2013:001. doi: 10.4172/2161-1041.s2-001

60. Mahendran G, Shangaradas AD, Romero-Moreno R, Wickramarachchige Dona N, Sarasija SHGS, Perera S, et al. Unlocking the epigenetic code: new insights into triple-negative breast cancer. *Front Oncol.* (2024) 14:1499950. doi: 10.3389/fonc.2024.1499950

61. Xu X, Zhou H, Hong R, Gong J, Wan Y, Fu Q, et al. A self-accelerating 'copper bomb' strategy activated innate and adaptive immune response against triple-negative breast cancer. *Bioactive Materials.* (2025) 49:193–206. doi: 10.1016/j.bioactmat.2025.02.019

62. Wang Y, Liu Y, Zhang J, Peng Q, Wang X, Xiao X, et al. Nanomaterial-mediated modulation of the cGAS-STING signaling pathway for enhanced cancer immunotherapy. *Acta Biomaterialia.* (2024) 176:51–76. doi: 10.1016/j.actbio.2024.01.008

63. Pindiprolu SKSS, Singh MT, Magham SV, Kumar CSP, Dasari N, Gummadi R, et al. Nanocarrier-mediated modulation of cGAS-STING signaling pathway to disrupt tumor microenvironment. *Naunyn-Schmiedeberg's Arch Pharmacol.* (2025). doi: 10.1007/s00210-025-03835-3

64. Pan X, Zhang W, Guo H, Wang L, Wu H, Ding L, et al. Strategies involving STING pathway activation for cancer immunotherapy: Mechanism and agonists. *Biochem Pharmacol.* (2023) 213:115596. doi: 10.1016/j.bcp.2023.115596

65. Wang X, Lin M, Zhu L, Ye Z. GAS-STING: a classical DNA recognition pathways to tumor therapy. *Front Immunol.* (2023) 14:1200245. doi: 10.3389/fimmu.2023.1200245

66. Liu L-C, Shen Y-C, Wang Y-L, Wu W-R, Chang L-C, Chen Y-H, et al. Growth-promoting function of the cGAS-STING pathway in triple-negative breast cancer cells. *Front Oncol.* (2022) 12:851795. doi: 10.3389/fonc.2022.851795

67. Xu G, Liang Q, Gao L, Xu S, Luo W, Wu Q, et al. Developing an arene binuclear ruthenium(II) complex to induce ferroptosis and activate the cGAS-STING pathway: targeted inhibiting growth and metastasis of triple negative breast cancer. *J Medicinal Chem.* (2024) 67:19573–85. doi: 10.1021/acs.jmedchem.4c01908

68. Shen Q, Xu P, Mei C. Role of micronucleus-activated cGAS-STING signaling in antitumor immunity. *Zhejiang Da Xue Xue Bao Yi Xue Ban.* (2024) 53(1):25–34. doi: 10.3724/zdxbyxb-2023-0485

69. Wang X, Yang Y, Wang P, Li Q, Gao W, Sun Y, et al. Oxygen self-supplying nanoradiosensitizer activates cGAS-STING pathway to enhance radioimmunotherapy of triple negative breast cancer. *J Controlled Release.* (2024) 376:794–805. doi: 10.1016/j.jconrel.2024.10.049

70. Kim BG, Kim BR, Kim DY, Kim WY, Kang S, Lee SI, et al. Cannabidiol enhances Atezolizumab efficacy by upregulating PD-L1 expression via the cGAS–STING pathway in triple-negative breast cancer cells. *Cancer Immunol Res.* (2024) 12:1796–807. doi: 10.1158/2326-6066.cir-23-0902

71. Zhou B, Chen M, Hao Z, Li L, Zhang Y, Fang B, et al. Zinc-copper bimetallic nanoplatforms trigger photothermal-amplified cuproptosis and cGAS-STING activation for enhancing triple-negative breast cancer immunotherapy. *J Nanobiotechnology.* (2025) 23:137. doi: 10.1186/s12951-025-03186-4

72. Zhong H, Chen G, Li T, Huang J, Lin M, Li B, et al. Nanodrug Augmenting Antitumor Immunity for Enhanced TNBC Therapy via Pyroptosis and cGAS-STING Activation. *Nano Lett.* (2023) 23:5083–5091. doi: 10.1021/acs.nanolett.3c01008

73. Han Q, Zhou Y, Dong Z, Wang W, Wang M, Pang M, et al. SNORA47 affects stemness and chemotherapy sensitivity via EBF3/RPL11/c-Myc axis in luminal A breast cancer. *Mol Med.* (2025) 31:150. doi: 10.1186/s10020-025-01216-3

74. Castagnoli L, Franceschini A, Cancila V, Dugo M, Bigliardi M, Chiodoni C, et al. CD36 enrichment in HER2-positive mesenchymal stem cells drives therapy refractoriness in breast cancer. *J Exp Clin Cancer Res.* (2025) 44:19. doi: 10.1186/s13046-025-03276-z

75. Luo J, Pang S, Hui Z, Zhao H, Xu S, Yu W, et al. Blocking Tim-3 enhances the anti-tumor immunity of STING agonist ADU-S100 by unleashing CD4(+) T cells through regulating type 2 conventional dendritic cells. *Theranostics.* (2023) 13:4836–57. doi: 10.7150/thno.86792

76. Chu Z, Zheng W, Fu W, Liang J, Wang W, Xu L, et al. Implanted microneedles loaded with sparfloxacin and zinc-manganese sulfide nanoparticles activates immunity for postoperative triple-negative breast cancer to prevent recurrence and metastasis. *Adv Sci (Weinh).* (2025) 12:e2416270. doi: 10.1002/advs.202416270

frontiers | Frontiers in Oncology

TYPE Original Research
PUBLISHED 29 July 2025
DOI 10.3389/fonc.2025.1612643

Check for updates

OPEN ACCESS

EDITED BY
Abdul K. Parchur,
Medical College of Wisconsin, United States

REVIEWED BY
Prarthana Pasricha,
Carleton University, Canada
Praveenbalaji Rajendran,
Harvard University, United States

*CORRESPONDENCE
Kuo Men
menkuo126@126.com
Hui Wang
wanghui2@umc.net.cn

†These authors have contributed equally to this work and share first authorship

‡These authors have contributed equally to this work

RECEIVED 16 April 2025
ACCEPTED 30 June 2025
PUBLISHED 29 July 2025

CITATION
Huang X, Guo C, Liu S, Men K and Wang H (2025) Dosimetric analysis of orthogonal collimator configuration in volumetric modulated arc therapy planning: a comparative study. *Front. Oncol.* 15:1612643. doi: 10.3389/fonc.2025.1612643

COPYRIGHT
© 2025 Huang, Guo, Liu, Men and Wang. This is an open-access article distributed under the terms of the Creative Commons Attribution License (CC BY). The use, distribution or reproduction in other forums is permitted, provided the original author(s) and the copyright owner(s) are credited and that the original publication in this journal is cited, in accordance with accepted academic practice. No use, distribution or reproduction is permitted which does not comply with these terms.

Dosimetric analysis of orthogonal collimator configuration in volumetric modulated arc therapy planning: a comparative study

Xin Huang[1,2†], Chenlei Guo[3†], Shuangtong Liu[1,2†], Kuo Men[3*‡] and Hui Wang[1,2*‡]

[1]Department of Oncology, Tianjin Union Medical Center, The First Affiliated Hospital of Nankai University, Tianjin, China, [2]Tianjin Cancer Institute of Integrative Traditional Chinese and Western Medicine, Tianjin Union Medical Center, The First Affiliated Hospital of Nankai University, Tianjin, China, [3]Department of Radiation Oncology, National Cancer Center/National Clinical Research Center/Cancer Hospital, Chinese Academy of Medical Sciences and Peking Union Medical College, Beijing, China

Background: In volumetric modulated arc therapy (VMAT), collimator angle selection impacts dose distribution and plan quality. Conventional VMAT plans use dual arcs with collimators set at 0°. This study explores the dosimetric effects of using orthogonal collimator angles (0° and 90°) in dual-arc VMAT.

Methods: Sixty patients with head and neck, thoracic, and abdominal tumors were analyzed. Two VMAT plans were generated: Plan A (0° collimator angle) and Plan B (0° and 90° collimator angles). Dosimetric endpoints included conformity index (CI), gradient measure (GM), homogeneity index (HI), dose to organs at risk (OARs), mean dose to normal tissues ($D_{mean,\ NT}$), monitor units (MU), and gamma pass rate (GPR).

Results: Plan B improved dosimetric outcomes over Plan A. HI decreased by 0.03 in the rectum, 0.01 in the breast, and 0.01 in the larynx. GM decreased by 0.15 cm in the rectum, 0.05 cm in the breast, and 0.01 cm in the larynx. OAR doses were reduced across sites, with notable decreases in the bladder (–4.62 Gy), left anterior descending artery (–3.99 Gy), and spinal cord (–1.79 Gy). $D_{mean,NT}$ was slightly reduced in the rectum, breast and larynx. MU increased in rectum plans (+41 MU), but decreased in the breast and laryngeal plans by 38 MU and approximately 73 MU, respectively. All plans achieved GPR > 95%.

Conclusion: Incorporating orthogonal collimator angles (0° and 90°) in dual-arc VMAT enhances dose conformity and spares OARs without compromising target coverage or delivery accuracy. This approach is clinically applicable with minimal workflow changes.

KEYWORDS

radiotherapy, radiotherapy treatment planning, volumetric modulated arc therapy, orthogonal collimator angles, dose conformity and homogeneity

1 Background

In the field of radiation therapy, volumetric modulated arc therapy (VMAT) achieves high-precision irradiation of planning target volume through continuous gantry rotation and dynamic adjustment of the multileaf collimator (MLC) while maximizing the protection of the surrounding normal tissues (1–3). The selection of collimator angles has a significant effect on the dose distribution and plan quality of VMAT (4–6). Currently, patients undergoing radiation therapy typically receive double-arc VMAT plans with a collimator angle of 0° (5, 7–10).

Under the conventional double-arc field with a collimator angle of 0°, the beam primarily irradiates the planning target along the anteroposterior direction (i.e., from the front to the back of the patient or vice versa) (11). This arrangement may lead to several limitations. The movement direction of the MLC leaves is parallel to the gantry rotation plane, restricting the flexibility of the leaves in the direction perpendicular to the gantry rotation (3, 12, 13). Additionally, the beam shape of the 0° collimator is relatively fixed and may not adapt well to complex planning target shapes and the protection needs of the surrounding normal tissues (7, 14, 15). In particular, when the planning target has a pronounced concave shape or a large curvature, the 0° collimator may fail to effectively avoid critical organs, leading to increased dose exposure and potential radiation-induced side effects (16). For organs with relatively flexible positioning, such as the small intestine in the pelvic cavity, the 0° collimator arrangement may lead to high doses in certain regions, increasing the risk of small intestine damage such as enteritis or intestinal obstruction (17, 18).

To reduce the dose exposure of normal tissues, this study introduced a 90° collimator angle into a conventional double-arc VMAT plan. This setting leverages the modulating capability of the MLC in the orthogonal direction, which is expected to improve the dose distribution in the planning target and protect critical normal organs. This study aimed to explore a simple and effective optimization method to enhance the quality and therapeutic effects of VMAT plans without significantly increasing the plan complexity. These findings aim to provide a new perspective for the design of radiation therapy plans, particularly in improving treatment efficiency and protecting normal tissues.

2 Methods

2.1 Case selection

This retrospective study randomly selected 60 patients who underwent VMAT at the Tianjin People's Hospital in December 2024. The patient cohort included 20 patients each with laryngeal cancer, 20 with left-sided breast cancer, and 20 with rectal cancer. The prescribed doses for the target volumes were set at 60.06 Gy/33 fractions for laryngeal cancer, 50 Gy/25 fractions for breast cancer, and 48.6 Gy/27 fractions for rectal cancer. The study adhered to the guidelines of the medical ethics committee, and all patient data were anonymized and analyzed. All patients underwent computed tomography (CT) simulation using a 16-slice large-bore CT scanner (General Electric Company. (2015). Discovery RT 590. GE Healthcare).

2.2 Plan design

For each patient, the planning target volume (PTV) and organs at risk (OARs) were contoured using Eclipse Treatment Planning System based on patient imaging data. Two VMAT plans were designed and labeled Plan A and Plan B. Plan A used a conventional double-arc plan with a collimator angle of 0°, whereas Plan B employed a double-arc plan with orthogonal collimator angles of 0° and 90°. All other parameters, such as the beam energy, field size, and optimization objectives, were kept consistent during the planning process, with only the collimator angles being altered. All plans were designed and optimized by the same medical physicist to ensure the reliability and accuracy of the results. In this study, all treatment plans for patients with rectal cancer were standardized to ensure that 100% of the target volume received at least 95% of the prescribed dose.

2.3 Target evaluation

The dose distributions of the target volumes for both plans were meticulously assessed using the conformity index (CI) (19, 20), gradient measure (GM) (21), and homogeneity index (HI) (22).

The CI is a crucial quantitative metric in radiation therapy used to evaluate the conformity of the high-dose region to the PTV. A CI value closer to 1 indicated better conformity between the dose distribution and target, indicating that the shape and size of the high-dose region more closely matched the target. CI was calculated using the following formula:

$$CI = \frac{V_{PTV,ref}}{V_{PTV}} \times \frac{V_{ref}}{V_{PTV}}$$

where, $V_{PTV,ref}$ is the target volume at the prescribed dose, V_{PTV} is the PTV volume, and V_{ref} is the total volume covered by the prescribed dose.

The GM assesses the dose fall-off at the target margins, serving as an important parameter for evaluating the dose transition between the target and surrounding normal tissues. The GM is typically measured in centimeters, representing the distance from the target edge to the 50% prescription isodose line. A higher GM value indicates faster dose fall-off at the target edge, resulting in better protection of the surrounding normal tissues. GM was calculated as follows:

$$GM = \sqrt[3]{\frac{3V_{50\,\%}}{4\pi}} - \sqrt[3]{\frac{3V_{PTV}}{4\pi}}$$

where $V_{50\%}$ is the volume enclosed by the 50% prescription isodose line, and V_{PTV} is the PTV volume.

The HI is a vital metric for evaluating the uniformity of the dose distribution within a target during radiation therapy. An HI value

closer to 0 indicates a more uniform dose distribution within the target. HI was calculated using the following formula:

$$HI = \frac{D_2 - D_{98}}{D_{50}}$$

where D_2 is the dose covering 2% of the target volume, D_{98} is the dose covering 98% of the target volume, and D_{50} is the dose covering 50% of the target volume, respectively.

2.4 OARs evaluation

In radiation therapy, dosimetric evaluation of OARs is crucial for ensuring treatment safety. The OARs of interest are listed in Table 1. The mean dose ($D_{mean,\ OAR}$) to OARs was used to assess the overall dose exposure, whereas the maximum dose (D_{max}) was used to evaluate potential high-dose risks. Additionally, the ratio of total body volume receiving a specific percentage of the prescribed dose (20%, 40%, 60%, and 80%) was assessed and denoted as $V_{20\%}$, $V_{40\%}$, $V_{60\%}$, and $V_{80\%}$, respectively.

The mean radiation dose to normal tissues ($D_{mean,NT}$) refers to the average radiation dose from normal tissues outside PTV in the radiotherapy plan. This is an important indicator for assessing the safety of a radiotherapy plan and reflects the extent of radiation exposure to normal tissues. The equation for calculating $D_{mean,NT}$ is as follows:

$$D_{mean,NT} = \frac{(V_{body} \times D_{mean,body}) - (V_{PTV} \times D_{mean,PTV})}{V_{body} - V_{PTV}}$$

where V_{body} is the total irradiated volume (e.g., body volume), $D_{mean,body}$ is the mean dose to the total irradiated volume, V_{PTV} is the PTV volume, and $D_{mean,PTV}$ is the mean dose to the PTV volume (with volume units in cm^3 and dose units in Gy).

2.5 Plan evaluation

Monitor units (MU) are radiation therapy parameters that describe the total beam-on time required for a treatment plan. They reflect the irradiation intensity of the linear accelerator when executing the treatment plan. Under the same dose distribution, a lower total MU generally indicates a higher plan efficiency. In a treatment plan, the total MU is the sum of the MUs of all the beams.

Plan verification refers to the process of validating the dose distribution of a VMAT treatment plan during radiation therapy to ensure the accuracy and safety of the treatment plan. Since VMAT technology modulates volume by adjusting multiple parameters, such as the shape of the MLC opening, dose rate, and gantry rotation speed, its dose distribution is complex and requires individualized quality assurance (QA). In this study, an electronic portal imaging device (EPID) was used to compare the dose calculated using the planning system with the actual measured dose.

The gamma pass rate (GPR) is the percentage of points that meet specific dose difference and distance-to-agreement (DTA) criteria in gamma analysis. Gamma analysis was used to compare the planned dose distributions with measured dose distributions by calculating the gamma index for each point to assess the consistency between the two. Points with a gamma index < 1 are considered "passed" and the GPR is the percentage of these "passed" points out of the total evaluated points. In clinical practice, a commonly used gamma analysis criterion is a 3% dose difference and 3 mm DTA (3%/3 mm), with a pass rate of 90% being the acceptable standard. A higher GPR indicates better consistency between the planned and measured dose distributions, leading to higher treatment accuracy and safety.

2.6 Statistical analysis

A rigorous statistical treatment and analysis were conducted on the collected data. Comprehensive descriptive statistical analyses, including mean and standard deviation, were performed for all evaluation indicators encompassed by Plan A and Plan B. Given that the sample size for all analyses was only 20, the Kolmogorov–Smirnov (K–S) test (23) was employed to assess the normality of the data. The results of the normality test indicated that the majority of the data did not conform to a Gaussian distribution ($p<0.05$). Consequently, non-parametric methods were utilized for statistical comparisons. Specifically, the Wilcoxon signed-rank test (24) was applied for comparisons between the two groups. All statistical analyses were carried out using OriginPro 2024 software (OriginLab Corporation, Northampton, MA, USA). The significance threshold for this study was set at $p<0.05$.

3 Results

3.1 Target volume

In terms of target conformity, the CI for rectal, breast, and laryngeal cancers showed no significant differences between Plan A and Plan B, indicating consistent conformity between the two plans. The results can be seen in Figure 1a and Table 1. However, the average GM of Plan B was lower than that of Plan A across all three cancers, indicating a faster dose fall-off at the target margins and improved protection of surrounding normal tissues. Notably, the GM reduction in breast cancer was minimal (0.05 cm, $p=0.150$), and some individual cases exhibited higher GM in Plan B. The largest GM reduction was observed in rectal cancer (0.15 cm, $p=0.002$), followed by laryngeal cancer (0.01 cm). Notably, the reduction in breast cancer was minimal, suggesting a limited clinical impact and highlighting anatomical factors that may reduce the modulation advantage of orthogonal collimation in this site. The results are shown in Figure 1b and Table 1. Similarly, the HI of Plan B was lower than that of Plan A, indicating a more uniform dose distribution within the planning target. The HI reductions were 0.03 for rectal cancer ($p<0.001$), 0.01 for breast cancer ($p=0.003$), and 0.01 for laryngeal cancer ($p<0.001$). The results are presented in Figure 1c and Table 1. For clarity, P

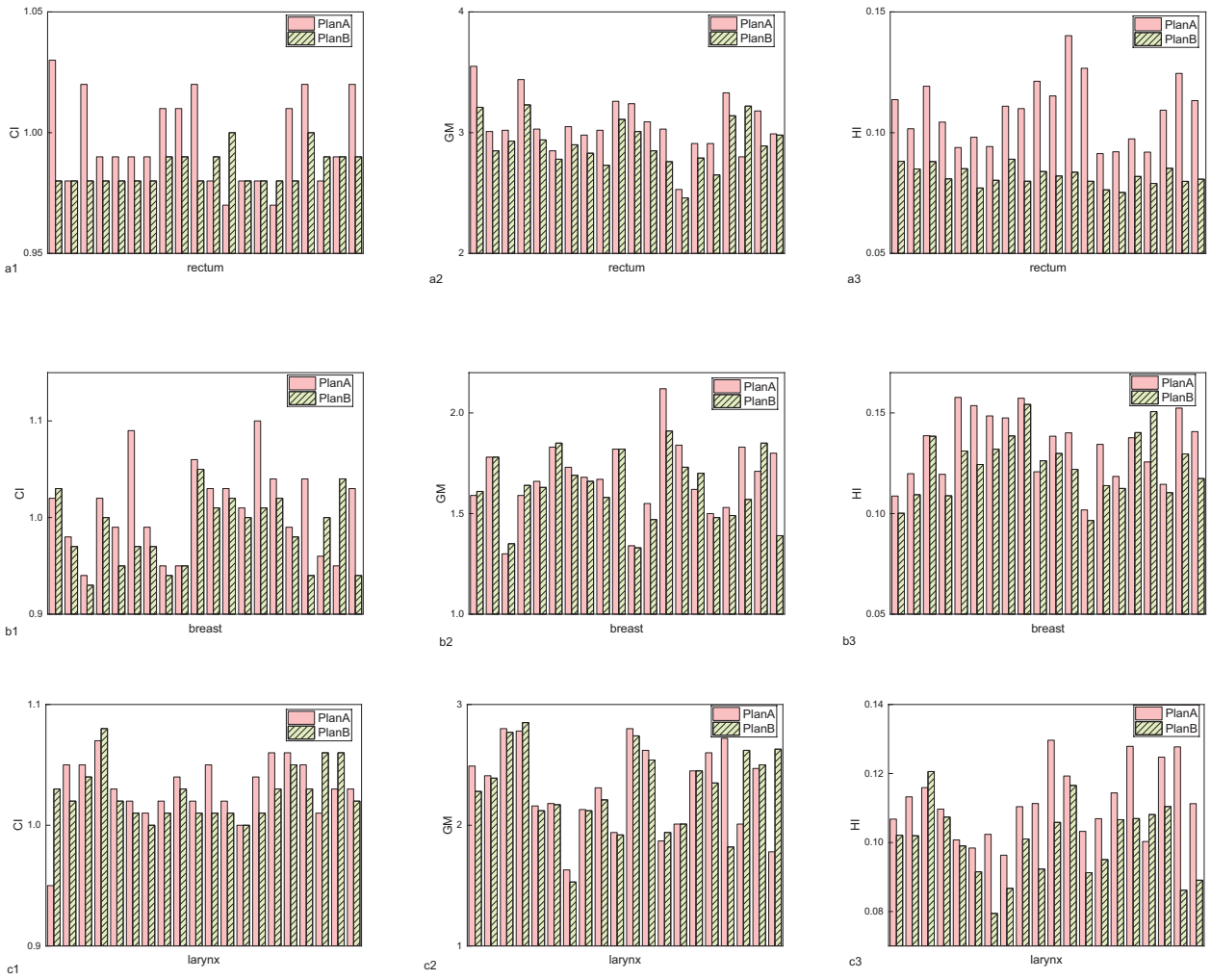

FIGURE 1
The assessment indicators for planning target volumes of rectal cancer, breast cancer, and laryngeal cancer. **(a)** conformity index (CI), **(b)** gradient measure (GM), **(c)** homogeneity index (HI).

values are reported only when the comparison between plans resulted in notable or statistically significant differences.

3.2 OARs

For rectal cancer, Plan B demonstrated a reduction in the D_{mean} to the bladder, pelvis bone, intestine, and both femoral heads by 4.62 ($p<0.001$), 1.11 ($p<0.001$), 1.64 ($p<0.001$), left 2.78 ($p=0.001$) and right 4.29 Gy ($p=0.001$), respectively. The D_{max} to the intestine decreased by 0.68 Gy ($p=0.002$). $D_{mean,NT}$ decreased from 6.65 ± 0.90 Gy in Plan A to 6.53 ± 0.87 Gy in Plan B. The results are presented in Figure 2a and Table 1.

For breast cancer, Plan B resulted in a decrease in the mean dose to the contralateral breast, heart, left anterior descending artery (LAD), ipsilateral lung and contralateral lung by 0.19, 0.24, 3.99 ($p<0.001$), 0.60, and 1.18 Gy, respectively. $D_{mean,NT}$ decreased by 0.19 Gy ($p=0.002$). However, the volume of the affected lung receiving 5 Gy (V_5:+1.92 Gy) increased, whereas the volume receiving 20 Gy (V_{20}: -2.67 Gy) decreased. The results are shown in Figure 2b and Table 1.

For laryngeal cancer, the mean dose to mandible increased by 0.06 Gy, while the maximum dose decreased by 1.7 Gy ($p=0.002$). The mean doses to the oral cavity, left parotid gland, and pharyngeal constrictor decreased by 0.51 ($p=0.029$), 0.46, and 2.54 Gy ($p=0.001$), respectively. The mean dose to the right parotid gland increased by 0.37 Gy. The maximum dose to the spinal cord decreased by 1.79 Gy ($p<0.001$). $D_{mean,NT}$ decreased by 0.27 Gy. The results can be seen in Figure 2c and Table 1.

3.3 Dose lines

In the analysis of isodose line volumes for rectal cancer, the ratios of total body volume receiving 20%, 40%, 60%, and 80% of the prescription dose ($V_{20\%}$, $V_{40\%}$, $V_{60\%}$, and $V_{80\%}$) were numerically lower in Plan B. However, these changes were small (typically <1%) and may reflect variability inherent to small-sample pilot data. The

10.3389/fonc.2025.1612643

TABLE 1 The mean and variance of evaluation indicators for Planning Target Volumes(PTV), Organs at Risk (OARs), Monitor units (MU) and the gamma pass rate in two plans for rectal cancer, breast cancer, and laryngeal cancer.

Disease	Target	Indicator	Plan A	Plan B	P value
Rectum	PTV	CI	1.10 ± 0.02	0.99 ± 0.01	0.023
		GM	3.06 ± 0.23	2.91 ± 0.20	0.002
		HI	0.11 ± 0.01	0.08 ± 0.00	<0.001
	Bladder	Mean dose	25.62 ± 5.63	21.00 ± 2.87	<0.001
	Pelvis	Mean dose	24.03 ± 3.28	22.92 ± 3.02	0.032
	Intestine	Mean dose	22.51 ± 3.70	20.87 ± 3.01	<0.001
		Max dose	49.54 ± 1.15	48.86 ± 0.84	0.002
	Femoral Left	Mean dose	19.33 ± 4.09	16.55 ± 2.69	0.001
	Femoral Right	Mean dose	20.52 ± 5.06	16.23 ± 3.34	0.001
	Body-PTV	$D_{mean,NT}$	6.65 ± 0.90	6.53 ± 0.87	0.225
	Plan	MU	521 ± 100	562 ± 59	0.022
	QA	Gamma	97.14 ± 0.73	97.99 ± 0.38	<0.001
Breast	PTV	CI	1.01 ± 0.05	0.99 ± 0.04	0.015
		GM	1.68 ± 0.19	1.63 ± 0.17	0.150
		HI	0.13 ± 0.02	0.12 ± 0.02	0.003
	Breast	Mean dose	4.27 ± 1.83	4.08 ± 1.31	0.279
	Heart	Mean dose	6.44 ± 1.38	6.20 ± 1.30	0.271
	LAD	Mean dose	24.12 ± 4.87	20.13 ± 3.01	<0.001
	Lung Left	Mean dose	11.43 ± 1.84	10.83 ± 1.75	0.065
		V_5	40.69 ± 10.24	42.61 ± 9.27	0.305
		V_{20}	21.19 ± 6.97	18.52 ± 4.77	0.040
	Lung Right	Mean dose	3.80 ± 0.44	2.62 ± 0.54	0.211
	Body-PTV	$D_{mean,NT}$	3.68 ± 0.45	3.49 ± 0.40	0.002
	Plan	MU	557 ± 70	519 ± 38	<0.001
	QA	Gamma	98.28 ± 0.77	98.58 ± 0.67	0.056
Larynx	PTV	CI	1.03 ± 0.03	1.03 ± 0.02	0.127
		GM	2.31 ± 0.36	2.30 ± 0.35	0.231
		HI	0.11 ± 0.01	0.10 ± 0.01	<0.001
	Mandible	Mean dose	28.71 ± 3.47	28.76 ± 3.66	0.723
		Max dose	61.16 ± 2.81	59.46 ± 1.32	0.002
	OC	Mean dose	30.77 ± 4.74	30.26 ± 4.935	0.029
	Parotid Left	Mean dose	21.52 ± 4.20	21.06 ± 4.12	0.588
	Parotid Right	Mean dose	22.25 ± 3.51	22.62 ± 3.14	0.737
	Pharyngeal	Mean dose	35.59 ± 7.67	33.05 ± 7.84	0.001
	Spinalcord	Max dose	19.77 ± 2.45	17.98 ± 1.90	<0.001
	Body-PTV	$D_{mean,NT}$	8.55 ± 2.45	8.28 ± 2.59	0.162
	Plan	MU	587 ± 35	514 ± 8	<0.001
	QA	Gamma	96.98 ± 0.70	97.07 ± 0.62	0.808

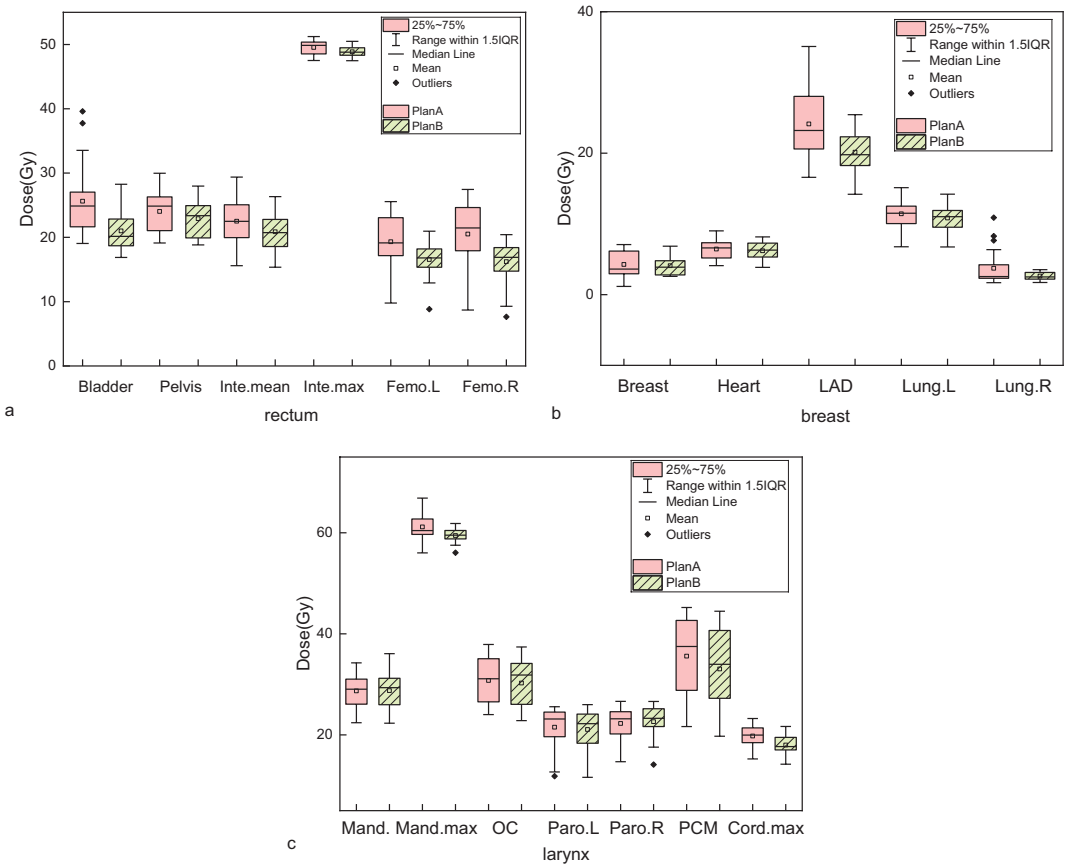

FIGURE 2
Comparison of mean or maximum dose to organs at risk (OARs) between Plan A (dual-arc VMAT with identical collimator angles) and Plan B (dual-arc VMAT with orthogonal collimator angles: 0° and 90°). **(a)** Rectal cancer: bladder, pelvis, small intestine (Inte), left femoral head (Femo.L), and right femoral head (Femo.R); **(b)** Breast cancer: contralateral breast, heart, left anterior descending artery (LAD), ipsilateral lung (lung.L), and contralateral lung (lung.R); **(c)** Laryngeal cancer: mandible (Mand.), oral cavity (OC), left and right parotid glands (Paro.L and Paro.R), pharyngeal constrictor (PCM), and spinal cord. Each group contains 10 patients. Boxplots illustrate the distribution of dose values: boxes represent the interquartile range (IQR), horizontal lines indicate medians, whiskers extend to 1.5×IQR, and open circles denote statistical outliers. Slight dose reductions in Plan B are observed in several OARs, though absolute differences remain small in most cases.

results are shown in Figure 3a and Table 2. For breast cancer, $V_{20\%}$ and increased by 0.43%. While $V_{40\%}$, $V_{60\%}$ and $V_{80\%}$ decreased by 0.37%, 0.36% and 0.15%, respectively. The results are displayed in Figure 3b and Table 2. For laryngeal cancer, $V_{40\%}$ and $V_{80\%}$ slightly increased by 0.03%, and 0.58%, respectively. While $V_{20\%}$ and $V_{60\%}$ decreased by 0.61%, and 0.09%, respectively. The results are displayed in Figure 3c and Table 2.

3.4 Dose-volume histogram

In the analysis of DVH for OARs, Plan B showed significant changes compared to Plan A. For rectal cancer, the DVH for the bladder, pelvis bone, and intestine showed a notable reduction. Specifically, the bladder DVH showed a maximum relative volume reduction of 19.57% within a dose range of 11.1–27.4 Gy. The pelvis bone DVH showed a maximum reduction of 9.23% within the dose range of 22.3–36.6 Gy. The intestine DVH showed a maximum reduction of 4.87% within the dose range of 11.2–40.4 Gy. The left femoral head DVH showed a maximum reduction of 21.51% within the dose range of 14.8–26.1 Gy, while the right femoral head DVH showed a maximum reduction of 31.86% within the dose range of 15.1–26.6 Gy. The results are shown in Figure 4a.

For breast cancer, Plan B showed an increase in the contralateral lung DVH within a dose range of 16.7–27.4 Gy, with a maximum increase of 0.15%. The contralateral breast DVH showed a maximum reduction of 0.15% within a dose range of 16.7–27.4 Gy. The heart DVH showed a maximum reduction of 2.35% within the dose range of 12.6–29.1 Gy. The LAD DVH showed the most significant reduction within the dose range of 15.1–37.0 Gy, with a maximum reduction of 15.76%. The DVH of the affected lung showed a maximum reduction of 0.87% within the dose range of 20.3–49.1 Gy. The results are shown in Figure 4b.

For laryngeal cancer, the mandibular DVH showed a maximum reduction of 2.03% within a dose range of 13.9–34.9 Gy. The oral cavity DVH showed a maximum reduction of 7.44% within a dose range of 29.2–39.9 Gy. The left parotid gland DVH showed a maximum reduction of 1.80% within the dose range of 34.9–56.1 Gy, while the right parotid gland DVH showed a maximum reduction of 1.62% within the dose range of 22.3–50.8 Gy. The

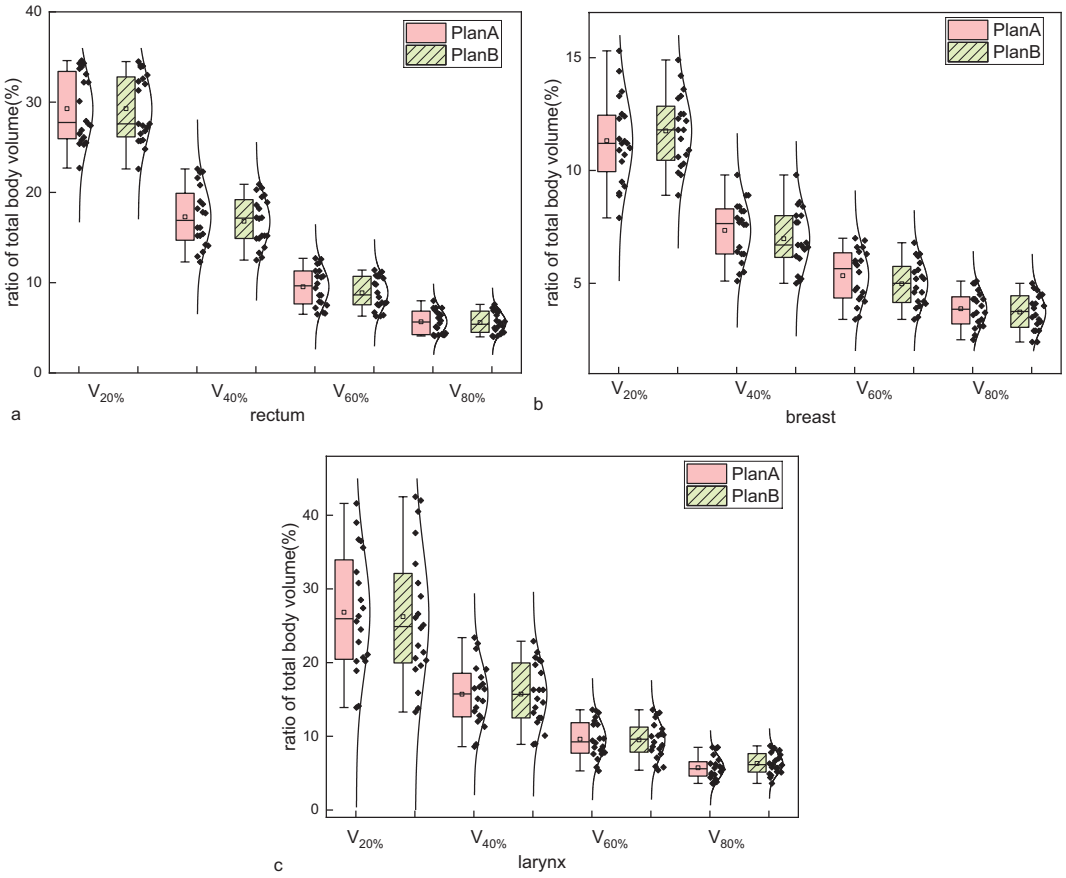

FIGURE 3
Comparison of the ratio of total body volume receiving 20%, 40%, 60%, and 80% of the prescription dose ($V_{20\%}$, $V_{40\%}$, $V_{60\%}$, and $V_{80\%}$) between Plan A and Plan B across three disease sites: **(a)** rectal cancer, **(b)** breast cancer, and **(c)** laryngeal cancer. Each metric reflects the percentage of the entire patient body exposed to respective isodose levels. Each group includes 20 patients. Boxplots represent distribution: the boxes show the interquartile range (IQR), horizontal lines indicate medians, whiskers extend to 1.5×IQR, and open circles represent outliers. Although Plan B showed numerically lower V-values in most cases, the differences were marginal, suggesting limited dosimetric impact on total body exposure.

pharyngeal constrictor DVH showed a maximum reduction of 5.23% within a dose range of 25.7–39.1 Gy. The spinal cord DVH showed a maximum reduction of 18.42% within a dose range of 13.8–22.4 Gy. The results are shown in Figure 4c.

3.5 Plan results

The mean value of MU for rectal (p=0.022), breast (p<0.001), and laryngeal cancers (p<0.001) were 521, 557, and 587 for Plan A,

TABLE 2 Mean and variance of the ratio of total body volume corresponding to the prescribed dose percentages (20%, 40%, 60%, 80%).

Volume (cm^3)		$V_{20\%}$	$V_{40\%}$	$V_{60\%}$	$V_{80\%}$
Rectum	Plan A	29.28 ± 3.87	17.29 ± 3.14	9.55 ± 2.13	5.67 ± 1.30
	Plan B	29.27 ± 3.77	16.80 ± 2.70	8.88 ± 1.82	5.59 ± 1.19
	Pvalue	0.295	0.161	0.001	0.671
Breast	Plan A	11.32 ± 1.91	7.35 ± 1.32	5.34 ± 1.16	3.88 ± 0.79
	Plan B	11.75 ± 1.60	6.98 ± 1.33	4.98 ± 1.00	3.73 ± 0.79
	Pvalue	0.108	0.711	0.004	0.016
Larynx	Plan A	26.84 ± 8.13	15.71 ± 4.21	9.61 ± 2.54	5.73 ± 1.56
	Plan B	26.23 ± 9.06	15.73 ± 4.27	9.52 ± 2.49	6.31 ± 1.47
	Pvalue	0.322	0.831	0.266	0.296

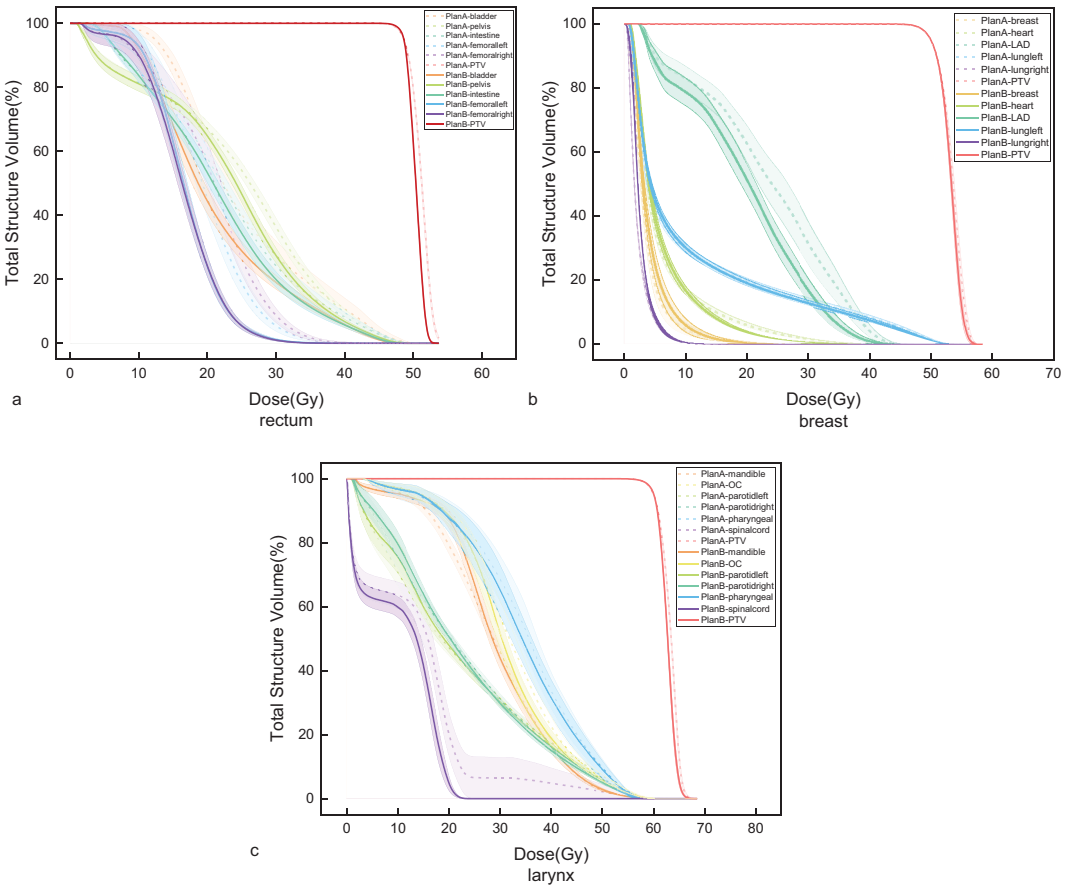

FIGURE 4
Dose-Volume Histogram (DVH) of the Planning Target Volumes(PTV) and Organs at Risk (OARs). **(a)** rectal cancer, **(b)** breast cancer, and **(c)** laryngeal cancer.

and 562, 519, and 514 for Plan B, respectively. The results are shown in Figure 5a. The gamma pass rate (GPR) for all plans exceeded 95%. The results are seen in Figure 5b.

4 Discussion

This study compared VMAT plans using a 90° collimator angle (Plan B) with conventional collimator angle plan (Plan A) to evaluate its potential benefits in optimizing planning target dose distribution and protecting OARs. The results revealed the significant advantages of Plan B in key dosimetric indicators, providing innovative ideas for radiotherapy plan design and holding significant clinical application value.

The results indicated that Plan B was comparable to Plan A regarding target dose coverage, achieving 95% coverage of the prescription dose. This suggests no significant difference in the overall dose coverage capability between the two plans. However, Plan B was significantly superior to Plan A regarding GM and HI. The decrease in the GM of Plan B indicates a faster dose fall-off at the target margins, which could protect the surrounding normal tissues more effectively. Moreover, the reduction in the HI in Plan B suggests a more uniform dose distribution within the target. This may be attributed to the introduction of a 90° collimator angle, which fully uses the modulating capability of the MLC in the orthogonal direction, thereby improving dose distribution.

Regarding OAR protection, Plan B demonstrated a significant dose reduction trend compared with Plan A. In particular, for the intestine, which is located flexibly within the pelvic cavity and close to the target, Plan B significantly reduced the dose exposure to the intestine through the optimized collimator angles. This reduces the risk of complications caused by high-dose irradiation, such as enteritis and intestinal obstruction. Additionally, the decrease in the D_{mean} to the bladder indicates that Plan B can avoid increased dose exposure to the bladder, thereby reducing the incidence of bladder irritation symptoms. For breast cancer, Plan B reduces the dose to important organs such as the contralateral breast, heart, and left anterior descending artery (LAD). Although the V_5 volume of the affected lung increased, the V_{20} decreased, which is favorable for protecting normal tissues overall. This optimization strategy helps reduce the long-term effect of radiotherapy on the heart and coronary arteries while minimizing damage to the affected lung. Notably, V_5 and V_{20} for the left lung (LungL) exhibited considerable inter-patient variability, with standard deviations exceeding 20% of

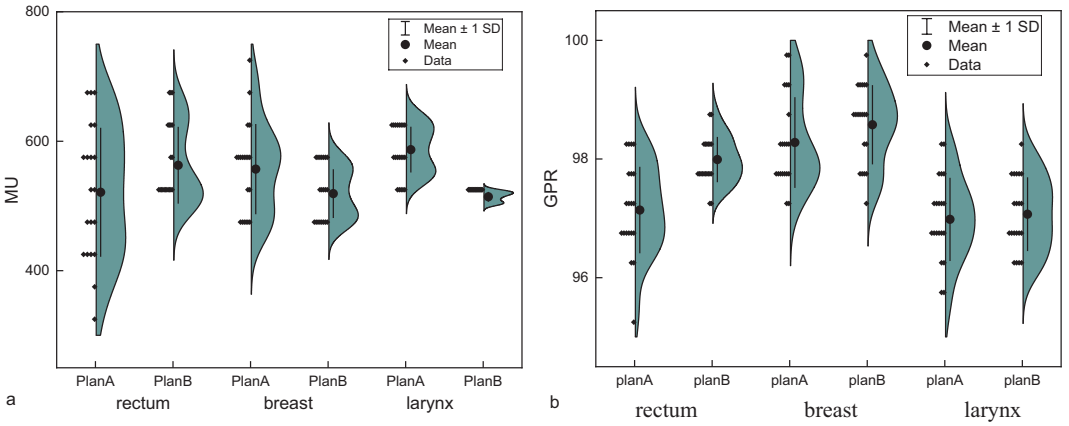

FIGURE 5
(a) Monitor units (MU) of Plan A and Plan B in rectal cancer, breast cancer, and laryngeal cancer. **(b)** The gamma pass rate (GPR) of Plan A and Plan B in rectal cancer, breast cancer, and laryngeal cancer.

the mean in some cases. This variability may arise from differences in chest wall curvature, lung expansion, and beam entry geometry, all of which can affect low-dose bath distribution. As such, these parameters should be interpreted with caution, especially in small pilot cohorts. For laryngeal cancer, Plan B exhibited more precise dose control in areas such as the mandible, oral cavity, parotid glands, and pharyngeal constrictors, with a significant reduction in the maximum dose to the spinal cord. This indicates that Plan B offers greater advantage in protecting important organs and tissues in patients with laryngeal cancer, thereby effectively reducing the risk of radiotherapy-related complications.

In rectal cancers, the ratio of total body volumes receiving 20%, 40%, 60%, and 80% of the prescribed dose ($V_{20\%}$, $V_{40\%}$, $V_{60\%}$, and $V_{80\%}$, respectively) decreased in Plan B. This indicates that Plan B can better protect the surrounding normal tissues during rectal cancer radiotherapy while maintaining adequate tumor irradiation. However, for breast cancer, the changes in Plan B dose lines are more complex. The volumes receiving 20% of the prescribed dose increased, whereas those receiving 40%, 60% and 80% decreased significantly. These changes may be related to the specific shape of the breast cancer target and surrounding tissues. Overall, Plan B effectively controlled the high-dose region volumes in optimizing isodose lines, particularly in radiotherapy plans for rectal and breast cancers. This optimization strategy helps reduce the potential damage to the surrounding normal tissues while ensuring adequate planning target irradiation. For laryngeal cancer, optimizing dose lines in Plan B must consider the balance between the low- and high-dose regions to achieve the best therapeutic effect.

Through a comparative analysis of radiotherapy plans for the three types of cancer, we found significant differences in the mean number of MUs between Plan A and Plan B across different cancer types, with inconsistent trends. These differences may be closely related to factors such as tumor location, radiotherapy techniques, dose distribution optimization strategies, and individual patient anatomy. For example, Plan B may focus on protecting normal tissues within the pelvic cavity in optimizing rectal cancer. By increasing the number of MUs, a more complex dose distribution was achieved to reduce the dose exposure to normal tissues. In the breast cancer optimization process, Plan B may prioritize the uniformity and conformity of the dose distribution. Adjusting the arc angles and MLC movements reduces the demand for the MUs. For laryngeal cancer, Plan B may focus more on precise irradiation of the laryngeal tumor and the cervical lymphatic drainage area. A more precise dose distribution was achieved by reducing the number of MUs.

Adjusting the collimator angle alters the propagation path and dose distribution of the radiation beam within a patient's body. Introduction a 90° collimator angle allows the radiation beam to cover the target area more comprehensively, reducing the dose of cold and hot spots and achieving a more uniform and conformal dose distribution. Moreover, the complementary use of collimator angles at different angles can significantly reduce the dose exposure to OARs, particularly when the target has large curvature changes adjacent to or interwoven with OARs, and the advantages of the 90° collimator angle are more prominent. Target areas with large curvature changes have a concave shape, similar to the two separate targets. Such target structures are prone to problems similar to those of isolated island blockages when designed. Figure 6 illustrates the dose distribution and beam eye view (BEV) for 0° and 90° collimator angles.

The HyperArc orthogonal collimator technique has garnered widespread attention owing to its ability to achieve high-precision dose irradiation among modern radiotherapy techniques. However, applying this technique requires complex equipment and optimization algorithms. By simplifying the technical approach, this study explores whether combining a 90° collimator arc with a 0° arc can achieve effects similar to those of orthogonal collimators while avoiding dose inhomogeneity issues. This study investigates the effects of applying the 90° collimator arc in radiotherapy and the

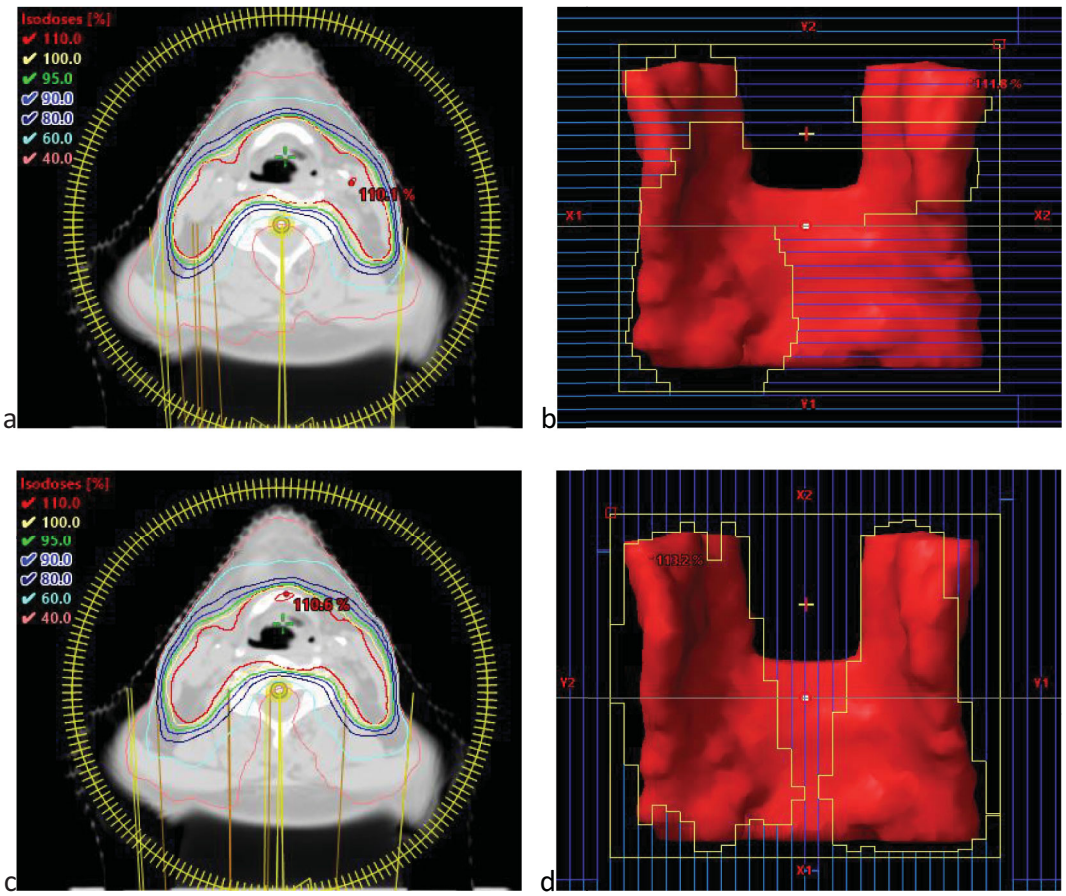

FIGURE 6
(a) The illustration of dose distribution under 0° collimator angles. **(b)** the beam eye view (BEV) under 0° collimator angles. **(c)** The illustration of dose distribution under 90° collimator angles. **(d)** the beam eye view (BEV) under 90° collimator angles.

rationality for its combination with the 0° arc. This approach achieves a high dose conformity similar to the Halcyon orthogonal collimator and effectively improves dose uniformity within the target. This combination optimizes the direction and intensity distribution of dose irradiation through the synergistic action of multiple angles, thereby reducing the dose inhomogeneity caused by a single arc angle.

Although personalized collimator angle settings can potentially achieve improved dosimetric results, they are often associated with increased planning complexity and require substantial time investment, experience, and technical expertise from physicists. In contrast, our study employed a fixed orthogonal configuration with collimator angles of 0° and 90° for the two arcs in Plan B, without additional modulation. This simplified approach not only enhances reproducibility and planning efficiency but is also feasible for implementation on most modern treatment planning systems and linear accelerators, which support assigning different collimator angles for each arc. Therefore, the proposed method offers a practical balance between dosimetric benefit and clinical applicability. They require extensive clinical experience and advanced planning and design skills. In comparison, adding a 90° collimator angle does not require complex adjustments for each case and has strong operability and universality. This can simplify the plan design process and improve work efficiency while ensuring therapeutic effects. In actual radiotherapy, when managing many patients with different types of tumors, there is a need for a method that can ensure therapeutic effects while simplifying the plan design process and improving work efficiency. The VMAT plan optimization method of adding a 90° collimator angle meets this demand and has significant clinical application value.

Despite the advantages of the method design and result analysis, this study has some limitations. First, the sample size was small, with only 60 patients, which may have limited the statistical analysis. This was a proof-of-concept investigation. Future research should validate the statistical effects and clinical applicability by expanding the sample size. Second, future studies should further explore the application effects of the 90° collimator angle at other tumor sites and its comprehensive application value in combination with other optimization techniques, such as adaptive radiotherapy. In addition, this study focused solely on improvement in dosimetric indicators and did not involve long-term follow-up of clinical treatment effects. Future research should combine patient clinical prognostic data to evaluate the efficacy and safety of the optimized plan for actual treatment.

5 Conclusion

In summary, by comparing the dosimetric indicators of conventional 0° collimator angle (Plan A) and 0° and 90° orthogonal collimator angles (Plan B) in VMAT plans, this study explored the effect of the 90° collimator on target dose distribution and OAR protection. The results demonstrated that Plan B significantly outperformed Plan A in key dosimetric metrics, including improved homogeneity index (HI) and gradient measure (GM), as well as reduced dose exposure to OARs, while maintaining complete target coverage and high-precision plan delivery. Moreover, the implementation of Plan B does not require complex individualized adjustments, offering high clinical feasibility and generalizability. This study provides a simple and effective new concept for designing radiotherapy plans with significant clinical value. Future research should expand the sample size to further validate its statistical effects and clinical applicability, and evaluate the actual efficacy and safety of the optimized plan.

Data availability statement

The raw data generated in this study contains clinical information that cannot be disclosed to the journal. Requests to access the datasets should be directed to XH, medicalphysicists@163.com.

Author contributions

XH: Writing – original draft, Formal analysis. CG: Writing – review & editing, Methodology, Formal analysis. SL: Writing – review & editing, Data curation. KM: Writing – review & editing, Project administration. HW: Writing – review & editing, Funding acquisition, Resources.

Funding

The author(s) declare that financial support was received for the research and/or publication of this article. This research was supported by the Fundamental Research Funds for the Tianjin People's Hospital (No.2024YJ021), the Tianjin Key Medical Discipline (Specialty) Construction Project (No.TJYXZDXK-053B), the Tianjin Key Specialty Construction Project for combining traditional Chinese and Western medicine (No.ZDZKKF02), National High Level Hospital Clinical Research Funding (2022-CICAMS-80102022203), and Tianjin Health Research Project (Grant No.TJWJ2025QN051).

Conflict of interest

The authors declare that the research was conducted in the absence of any commercial or financial relationships that could be construed as a potential conflict of interest.

Generative AI statement

The author(s) declare that Generative AI was used in the creation of this manuscript. Generative AI was used in this article for grammatical and linguistic standardization.

Publisher's note

All claims expressed in this article are solely those of the authors and do not necessarily represent those of their affiliated organizations, or those of the publisher, the editors and the reviewers. Any product that may be evaluated in this article, or claim that may be made by its manufacturer, is not guaranteed or endorsed by the publisher.

References

1. Otto K. Volumetric modulated arc therapy: IMRT in a single gantry arc. *Med Phys*. (2008) 35:310–7. doi: 10.1118/1.2818738

2. Macchia G, Deodato F, Cilla S, Cammelli S, Guido A, Ferioli M, et al. Volumetric modulated arc therapy for treatment of solid tumors: current insights. *Onco Targets Ther*. (2017) 10:3755–72. doi: 10.2147/OTT.S113119

3. Peiris GS, Whelan B, Hardcastle N, Sheehy SL. The effect of multi-leaf collimator leaf width on VMAT treatment plan quality. *J Appl Clin Med Phys*. (2025) 26:e70018. doi: 10.1002/acm2.70018

4. Isa M, Rehman J, Afzal M, Chow JC. Dosimetric dependence on the collimator angle in prostate volumetric modulated arc therapy. *Int J Cancer Ther Oncol*. (2014) 2:20419. doi: 10.14319/ijcto.0204.19

5. Kim M, Kim B, Choi E, Shin YS, Park SG, Oh YK, et al. Analyzing collimator rotation angle influence on half-beam VMAT outcomes for prostate cancer: A comparative approach using statistical and machine learning methods. (2024). doi: 10.21203/rs.3.rs-4225871/v1

6. Saeed H, Sadiqullah HM, Ahmad HK, Shafiq S, Ahmed Q, Basit A, et al. The effect of varying collimator angles on VMAT planning of prostate cancer. *Pakistan J Med Health Sci*. (2023) 17:145–8. doi: 10.53350/pjmhs2023174145

7. Sun W, Chen K, Li Y, Xia W, Dong L, Shi Y, et al. Optimization of collimator angles in dual-arc volumetric modulated arc therapy planning for whole-brain radiotherapy with hippocampus and inner ear sparing. *Sci Rep*. (2021) 11:19035. doi: 10.1038/s41598-021-98530-7

8. Li X, Wu J, Palta M, Zhang Y, Sheng Y, Zhang J, et al. A collimator setting optimization algorithm for dual-arc volumetric modulated arc therapy in pancreas stereotactic body radiation therapy. *Technol Cancer Res Treat*. (2019) 18:1533033819870767. doi: 10.1177/1533033819870767

9. Sze HC, Lee MC, Hung WM, Yau TK, Lee AW. RapidArc radiotherapy planning for prostate cancer: single-arc and double-arc techniques vs. intensity-modulated radiotherapy. *Med Dosim*. (2012) 37:87–91. doi: 10.1016/j.meddos.2011.01.005

10. Treutwein M, Hipp M, Koelbl O, Dobler B. Searching standard parameters for volumetric modulated arc therapy (VMAT) of prostate cancer. *Radiat Oncol*. (2012) 7:108. doi: 10.1186/1748-717X-7-108

11. Li MH, Huang SF, Chang CC, Lin JC, Tsai JT. Variations in dosimetric distribution and plan complexity with collimator angles in hypofractionated volumetric arc radiotherapy for treating prostate cancer. *J Appl Clin Med Phys*. (2018) 19:93–102. doi: 10.1002/acm2.12249

12. Ahn BS, Park SY, Park JM, Choi CH, Chun M, Kim JI. Dosimetric effects of sectional adjustments of collimator angles on volumetric modulated arc therapy for irregularly-shaped targets. *PloS One*. (2017) 12:e0174924. doi: 10.1371/journal.pone.0174924

13. Huang SX, Yang SH, Zeng B, Li XH. Personalized selection of unequal sub-arc collimator angles in VMAT for multiple brain metastases. *Appl Radiat Isot*. (2024) 214:111513. doi: 10.1016/j.apradiso.2024.111513

14. Serarslan A, Daştan Y, Aksu T, Yıldız RE, Gürsel B, Meydan D, et al. Ninety-degree angled collimator: a dosimetric study related to dynamic intensity-modulated radiotherapy in patients with endometrial carcinoma. *BMC Cancer*. (2023) 23:515. doi: 10.1186/s12885-023-11033-8

15. Abdulameer MS, Pallathadka H, Menon SV, Rab SO, Hjazi A, Kaur M, et al. Dosimetric effect of collimator rotation on intensity modulated radiotherapy and volumetric modulated arc therapy for rectal cancer radiotherapy. *J Xray Sci Technol*. (2024) 32:1331–48. doi: 10.3233/XST-240172

16. Durmuş IF, Esitmez D, Arslan GI, Okumuş A. Dosimetric comparison of three-dimensional conformal, intensity-modulated radiotherapy, volumetric modulated arc therapy, and dynamic conformal arc therapy techniques in prophylactic cranial irradiation. *Prog Med Phys*. (2023) 34:41–7. doi: 10.14316/pmp.2023.34.4.41

17. Barillot I, Tavernier E, Peignaux K, Williaume D, Nickers P, Leblanc-Onfroy M, et al. Impact of post operative intensity modulated radiotherapy on acute gastro-intestinal toxicity for patients with endometrial cancer: results of the phase II RTCMIENDOMETRE French multicentre trial. *Radiother Oncol*. (2014) 111:138–43. doi: 10.1016/j.radonc.2014.01.018

18. Liao X, Wu F, Wu J, Peng Q, Yao X, Kang S, et al. Impact of positioning errors in the dosimetry of VMAT left-sided post mastectomy irradiation. *Radiat Oncol*. (2020) 15:1–7. doi: 10.1186/s13014-020-01556-w

19. Feuvret L, Noël G, Mazeron J. J., Bey P. Conformity index: A review. *Int J Radiat Oncol Biol Phys*. (2006) 64:333–42. doi: 10.1016/j.ijrobp.2005.09.028

20. Hodapp N. The ICRU Report 83: prescribing, recording and reporting photon-beam intensity-modulated radiation therapy (IMRT). *Strahlenther Onkol*. (2012) 188:97–9. doi: 10.1007/s00066-011-0015-x

21. Duan Y, Lin Y, Wang H, Kang B, Feng A, Ma K, et al. How does the gradient measure of the lung SBRT treatment plan depend on the tumor volume and shape? *Front Oncol*. (2021) 11:781302.

22. Kataria T, Sharma K, Subramani V, Karrthick K. P., Bisht S. S.. Homogeneity Index: An objective tool for assessment of conformal radiation treatments. *J Med Phys*. (2012) 37:207–13. doi: 10.4103/0971-6203.103606

23. Vrbik JSmall-sample corrections to Kolmogorov–Smirnov test statistic. *Pioneer J Theor Appl Stat*. (2018) 15:15–23.

24. McDonald JH. *Wilcoxon signed-rank test - Handbook of Biological Statistics* . Available online at: www.biostathandbook.com (Retrieved September 02, 2021).

frontiers | Frontiers in Oncology

TYPE Original Research
PUBLISHED 13 August 2025
DOI 10.3389/fonc.2025.1623313

Check for updates

OPEN ACCESS

EDITED BY
Poonam Yadav,
Northwestern University, United States

REVIEWED BY
Dikhra Khan,
All India Institute of Medical Sciences, India
Syed Sarmad Bukhari,
Harvard University, United States

*CORRESPONDENCE
Jing Qian
qian.jing@mayo.edu
Debra H. Brinkmann
brinkmann.debra@mayo.edu

RECEIVED 05 May 2025
ACCEPTED 25 July 2025
PUBLISHED 13 August 2025

CITATION
Qian J, Pafundi DH, Breen WG, Brown PD, Hunt CH, Jacobson MS, Johnson DR, Kaufmann TJ, Kemp BJ, Kizilbash SH, Lowe VJ, Ruff MW, Sarkaria JN, Uhm JH, Zakhary MJ, Seaberg MH, Wan Chan Tseung HS, Yan ES, Zhang Y, Laack NN and Brinkmann DH (2025) Analysis of imaging signatures in ^{18}F-DOPA PET of glioblastoma treated with dose-escalated radiotherapy. *Front. Oncol.* 15:1623313. doi: 10.3389/fonc.2025.1623313

COPYRIGHT
© 2025 Qian, Pafundi, Breen, Brown, Hunt, Jacobson, Johnson, Kaufmann, Kemp, Kizilbash, Lowe, Ruff, Sarkaria, Uhm, Zakhary, Seaberg, Wan Chan Tseung, Yan, Zhang, Laack and Brinkmann. This is an open-access article distributed under the terms of the Creative Commons Attribution License (CC BY). The use, distribution or reproduction in other forums is permitted, provided the original author(s) and the copyright owner(s) are credited and that the original publication in this journal is cited, in accordance with accepted academic practice. No use, distribution or reproduction is permitted which does not comply with these terms.

Analysis of imaging signatures in ^{18}F-DOPA PET of glioblastoma treated with dose-escalated radiotherapy

Jing Qian[1*], Deanna H. Pafundi[2], William G. Breen[1], Paul D. Brown[1], Christopher H. Hunt[3], Mark S. Jacobson[3], Derek R. Johnson[3], Timothy J. Kaufmann[3], Bradley J. Kemp[3], Sani H. Kizilbash[4], Val J. Lowe[3], Michael W. Ruff[5], Jann N. Sarkaria[1], Joon H. Uhm[4,5], Mark J. Zakhary[6], Maasa H. Seaberg[7], Hok Seum Wan Chan Tseung[1], Elizabeth S. Yan[1], Yan Zhang[1], Nadia N. Laack[1] and Debra H. Brinkmann[1*]

[1]Department of Radiation Oncology, Mayo Clinic, Rochester, MN, United States, [2]Department of Radiation Oncology, Mayo Clinic, Jacksonville, FL, United States, [3]Department of Radiology, Mayo Clinic, Rochester, MN, United States, [4]Department of Medical Oncology, Mayo Clinic, Rochester, MN, United States, [5]Department of Neurology, Mayo Clinic, Rochester, MN, United States, [6]Department of Radiation Oncology, University of Maryland, Baltimore, MD, United States, [7]Department of Radiation Oncology, University of California San Francisco Medical Center, San Francisco, CA, United States

Background/objectives: ^{18}F-DOPA is an amino acid radiotracer with high uptake in glioblastoma and low uptake in normal brain. Patients underwent pre-radiation and post-radiation ^{18}F-DOPA PET scans on a prospective clinical trial. This analysis investigates quantitative image features correlated with prognosis and treatment response to identify patients who benefit the most from dose-escalated therapy.

Methods: Quantitative image features from ^{18}F-DOPA PET scans of 58 glioblastoma patients were extracted from the high uptake region (TBR>2.0) in both pre-RT and early post-RT follow-up PET images, which were then refined using Pearson pair correlation. To explore the possibility to identify patients who benefit the most from dose-escalated therapy, pre-irradiation features were identified with univariate Cox regression analysis. Classifications with simple threshold or with Decision Tree models were carried out to categorize patients into distinct survival groups. Additionally, the features with notable changes before and after RT were identified and the temporal patterns of these changes between the survival groups were compared. Multivariates cox analysis was performed to assess the prognostic value of delta features in survival analysis.

Results: The pre-irradiation features demonstrated predictive capability in distinguishing survival groups, yielding an accuracy of 0.78 on the reserved test dataset. We also pinpointed eight quantitative features that exhibited a significant difference before and after radiotherapy in patients with MGMT-unmethylated glioblastoma. The change of the features presented different patterns between the survival groups separated by median overall survival and the inclusion of delta features can enhance the accuracy of survival analysis. Conversely, for patients

with methylated MGMT, no feature displayed such significant changes between preRT and early postRT.

Conclusions: Our study showcased the potential of employing quantitative features derived from ^{18}F-DOPA images to refine the stratification of patients with unmethylated MGMT for dose escalated therapy. Moreover, the change of these features can serve as valuable tools for monitoring treatment responses following radiotherapy.

KEYWORDS

glioblastoma, radiotherapy, 18 F-DOPA PET, treatment response, quantitative imaging

Introduction

Glioblastoma (1) is typically treated with maximally safe surgical resection followed by radiotherapy and concomitant and adjuvant chemotherapy, with or without tumor treating fields (2, 3). Despite these incremental advances in multimodality treatment, survival for many patients remains poor with a median survival of 15 months after diagnosis (4). The efficacy of treatment also showed strong correlation with certain biomarkers, for example, patients with methylated O^6-methylguanine methyltransferase (MGMT) promoter often benefit from temozolomide while patients with unmethylated MGMT do not (5), although the heterogeneity of glioblastoma and variability in MGMT expression across tumor regions complicates the correlation between MGMT expression and treatment response (6, 7). The IDH (isocitrate dehydrogenase) status is another important molecular characteristic and prognostic indicator in glioblastoma. Mutant IDH is generally associated with a better prognosis and longer survival than IDH-wildtype glioblastoma (6, 8). Magnetic resonance imaging (MRI) including T1 post-gadolinium and T2 series are the standard for diagnosis, treatment planning and follow-up of glioblastoma, however as the images providing only morphological information, their sensitivity and capability to distinguish tumor from treatment effects are limited (9, 10). Improvements in assessment of treatment response and tumor progression may result from advances in imaging with modalities such as advanced MRI (i.e. perfusion and diffusion MRI (4, 11–14) or PET with amino acid tracers (15–19). As one of the most promising techniques, amino acid PET images provide more specific uptake in tumor tissue than in areas of radiation-induced normal tissue response (20, 21) and have been recommended for assessing glioma progression (22, 23).

Quantitative analysis of amino-acid PET imaging is of significant interest in glioblastoma diagnosis (24, 25) and monitoring (26, 27) due to its ability to quantitatively capture tumor heterogeneity and other prognostic information (28, 29). This analysis could utilize radiomics or other mathematical tools to extract quantitative image features. Traditional radiomics studies (24–27, 30) typically focus on single-time-point data from patients treated with a standard protocol (2). Although it is essential to provide prognostic prediction before the start of therapy, information at a single time point could be restrained in assessing treatment responses to interventions such as radiotherapy (RT) while understanding treatment response is crucial for the post-therapy management. Additionally, although biomarkers like MGMT methylation are strong prognostic indicators of survival (5), they are often excluded in radiomics analysis possibly due to limited data availability. Given the varying survival rates of glioblastoma patients, exploring the potential of quantitative imaging to further stratify patients with the same biomarkers for individualized treatment and post-treatment management is of great interest.

To further improve treatment efficacy, clinical trials suggest that radiation dose escalation targeted to tumor heterogeneity may enhance patient survival (31, 32). However, not all patients benefit from increased radiation doses, and higher doses inevitably raise normal tissue toxicity and complicate post-therapy management. Therefore, identifying patients who may benefit from dose escalation is essential for personalized treatment. To address this challenge, in this study, we extracted quantitative image features from ^{18}F-DOPA PET images of newly diagnosed glioblastoma patients undergoing dose-escalated RT (DERT), at pre-RT and serial post-RT follow-up (FU) timepoints, then performed single-time-point and time-series analyses on the extracted quantitative features. We aimed to identify pre-irradiation radiomic features to further stratify patients with the same MGMT methylation status, in order to determine which patients may benefit most from DERT for more individualized therapy. Additionally, we examined changes in the quantitative features associated with overall survival (OS), highlighting the survival-related response following DECT. Our study is the first to stratify glioblastoma patients for dose escalation, demonstrating the prognostic value of ^{18}F-DOPA and its potential role in monitoring treatment response.

Materials and methods

Patient cohort

This study included patients with newly diagnosed glioblastoma treated with ^{18}F-DOPA guided DERT (31) on an institutional prospective phase II clinical trial (NCT01991977). Patients

enrolled in the trial were treated with chemoradiation with a boost to 76 Gy in 30 fractions guided by ^{18}F-DOPA PET imaging, followed by standard adjuvant temozolomide. Surgical resection took place prior to the acquisition of any images investigated in this study. Extent of resection was categorized as biopsy, subtotal resection or complete resection. MGMT methylation status was defined using a clinical, quantitative methylation-specific PCR assay. The current study is a retrospective analysis of data curated from that clinical trial (31). To simplify the impact from different pathological biomarkers and because most patients in the trial had wild-type IDH, the patients with mutant IDH status were excluded in this study. All the patients in the trial with a pre-RT and at least one FU ^{18}F-DOPA PET/CT scan were included in this current study. The first FU (FU1) images were acquired consistently at 1 month after completing RT with a mean of 32 days from the last session of RT and a standard deviation of 6.5 days, and subsequent FU frequency was determined for each patient based on clinical judgement and availability. The second FU (FU2) has a mean of 82 days from the last session of RT with a standard deviation of 18 days. The distribution of FU1 and FU2 timeframes can be found in Supplementary Figure S1. In this study, only the images at pre-RT, FU1, and FU2 timepoints were considered. Patients were first grouped based on their MGMT methylation status. Within each methylation status grouping, median OS was used as a threshold to classify patients into two subgroups: those with longer survival (LS), defined as OS above the median, and those with shorter survival (SS), defined as OS at or below the median. Informed consent was obtained from all patients, and the study was approved by Institutional Review Board (IRB) and complied with the principles of the Helsinki declaration.

PET imaging and radiomics feature extraction

PET imaging was conducted on either a GE Discovery 690XT or a GE Discovery MI PET/CT system with matched spatial resolution, following a strictly controlled protocol (31, 33). ^{18}F-DOPA was injected intravenously at a dose of 5 mCi ± 10%. PET sinograms were reconstructed using a fully 3-dimensional iterative reconstruction algorithm with corrections for attenuation, scatter, randomness, deadtime, decay, and normalization applied. All PET images were resampled into voxel dimensions of 2x2x2 mm. PyRadiomics (34) was employed to extract 26 shape, 19 first-order and 70 texture quantitative features from each scan, adhering to the definitions outlined by the Image Biomarker Standardization Initiative (35, 36). The list of extracted features is reported in Supplementary Table S1. All shape features are reported in voxel-based units. Additionally, relative delta features were calculated, representing the percentage change of a quantitative feature at a given FU timepoint compared to the pre-RT measurement for each patient.

$$\Delta Feature(t:FU) = 100* \frac{Feature(t:FU) - Feature(t:pre-RT)}{Feature(t:pre-RT)}$$

All features were extracted from the region of high SUV uptake, where the tumor-to-normal-brain-tissue SUV ratio (TBR) exceeded 2.0. The SUVmean of the normal brain tissue was calculated on a wedge of the contralateral brain (33). This high uptake region, referred to as the region of interest (ROI) hereafter, corresponded to the region of dense tumor and exhibited greater predictive value compared to the entire tumor volume, as demonstrated in our prior work (33). The use of an SUV-threshold-based autosegmentation method also eliminated observer bias during tumor delineation. ROIs in each scan were reviewed by an experienced medical physicist and an experienced nuclear medicine physician to exclude physiological uptake, for example striatal uptake.

Feature selection

To explore single timepoint classification into LS and SS survival groups based on pre-RT images, only shape and first-order features were utilized due to their straight-forward interpretation and ease of generalization in future work. For transparency, an exploratory Random Forest model including feature importance analysis is provided in the Supplementary Material. Although texture features may improve model performance, restriction to shape and first order features may improve reliability for datasets with limited size. These features were first filtered with a pairwise correlation coefficient below 0.8, followed by a univariate Cox regression analysis against OS. Only the features with hazard ratio (HR) out of the range [0.99, 1.01] and the p-value less than 0.05 were chosen.

To investigate features correlated to survival-associated treatment response, the feature selection principle involves utilizing features that undergo the most significant changes before and after RT. Therefore, delta quantitative features were employed on an individual variable basis. All extracted features, irrespective of their predictive nature, were incorporated into the analysis. Feature selection was guided by the magnitude of difference observed between the two OS groups, categorized by median OS as the threshold. Specifically, features were chosen if both mean and median values demonstrated a difference of more than 50% between the two survival groups for either FU1 or FU2, and the p-value of the feature was smaller than 0.05 for the LS versus SS comparison. Although all selected features underwent investigation, only those with a pairwise correlation coefficient below 0.8 are presented here to avoid redundancy.

Classification model on pre-RT images

To assess the predictive capability of quantitative features to further stratify patients with the same biomarkers, we conducted simple threshold-based classification with each identified feature and also constructed classification models. Aiming to identify patients who may benefit from DERT, the classification model only utilizes the pre-RT images which were obtained before the DERT started. For each MGMT methylation status, the patient

cohort with were split randomly with 75:25 ratio into train and test dataset. Given the modest size of the patient cohort in this study, considerations for simplicity, interpretability and reproducibility primarily dictated the choices of features and model algorithms. For each identified feature, a simple threshold search was performed on the train dataset to find out the cutoff for best accuracy, and that threshold was applied to the reserved test dataset. For a more complicated model, we opted to use the highly interpretable Decision Tree (DT) Classifier (37), implemented in Scikit-Learn python package (version 1.3.1) (38). The maximum depth of the DT and the maximum number of leaf nodes were both set to 2. The input features were restricted to those identified with univariate Cox analysis, with no attempt made to employ additional features or more complex algorithms to avoid overfitting concerns. Five-fold cross-validation was applied in the model fitting on the train dataset. The prediction on the test data is the average of the predictions from the trained five-fold classification models.

Survival analysis with early FU images

After therapy, it becomes crucial to estimate how long a patient might survive at each FU timepoint. This is expressed as remaining survival (RS), defined as the time between a FU timepoint and the patient's death. Understanding RS enables timely interventions for post-treatment management. RS reflects a combination of factors, including pre-treatment disease characteristics, treatment response, and tumor progression. For each patient, RS was calculated at each FU timepoint and used as the survivals in our analysis. Using early FU imaging, we conducted univariate and multivariate Cox regression analysis to fit RS. To ensure simplicity and reproducibility, we focused exclusively on the identified features in the shape and first-order categories for this analysis. The number of variables was limited to three to minimize the risk of overfitting. By analyzing changes in the Concordance index (C-index) with the inclusion of static and delta radiomic features at corresponding FU timepoints, we evaluated the prognostic value of delta features in predicting RS for patients in this cohort.

Results

Patient

Table 1 displays the categorization of the IDH wild-type patients based on their MGMT status and median OS. Additional clinical details are available in the previous publication of the clinical trial (31). Among patients with unmethylated MGMT, the OS spanned from 5 to 41 months, with a median of 15 months. In contrast, patients with methylated MGMT exhibited an OS ranging from 17 months to over 74 months, with a median of 38 months. The distribution of age and gender is detailed in Table 1, revealing no discernible differences between the various survival groups. The distribution of re-section extent for each subgroup and the p-value of the group comparison is reported in Table 1. The p-values for the age, gender distributions and resection extent between SS and LS group are calculated with Mann-Whitney test.

Feature selection

With univariate Cox regression analysis, only two pre-RT features were identified with strong correlation with OS for the patients with unmethylated MGMT status. Their hazard ratios, confidence interval (CI) and p-values are summarized in Table 2. Maximum is the maximum value of Tumor to Brain Ratio (TBRmax) reported in other literature (39–41). Skewness measures the asymmetry of the distribution of values about the mean TBR value. The same analysis was also applied to the cohort with methylated MGMT status, but no feature satisfying the criteria was identified.

Table 3 presents the delta features that exhibited a significant difference before and after RT as well as between LS and SS groups. Among patients with unmethylated MGMT, eight such features were identified, whereas no delta feature was found to exhibit a significant difference at the same level (more than 50% for both mean and median) for patients with methylated MGMT. For a

TABLE 1 Epidemiology of the selected patients, categorized by MGMT methylation status and median OS.

MGMT methylation	Methylated		Unmethylated	
Median OS [months]	**38**		15	
Survival Group	SS	LS	SS	LS
Patient count	12	11	19	16
Male: Female	50%:50%	64%:36%	58%:42%	56%:44%
p-value: gender	0.543		0.422	
Age [year]: Min: Max	42:68	39:74	42:77	19:70
Age [year]: Median	59	59	59	55
p-value: age	0.828		0.184	
Resection: biopsy:subtotal:total	11%: 58%:32%	25%:31%:44%	8%:42%:50%	10%:45%:45%
p-value: resection	0.97		0.86	

TABLE 2 Summary of univariate Cox regression analysis for pre-RT single timepoint features that have strong correlation with OS for IDH wild-type patients with unmethylated MGMT status.

Feature	HR	95% CI lower	95% CI upper	p-value
Maximum (TBRmax)	1.33	1.07	1.66	0.01
Skewness	3.45	1.80	6.60	<0.01

concise reference, a simplified description of these features is provided in Supplementary Table S2, although a detailed mathematical definition can be found in the PyRadiomics reference (34).

Classification modeling on pre-RT images

Based on the train dataset, the optimized threshold of TBRmax was determined to be between [2.9, 3.2] for the MGMT unmethylated cohort, which gave an accuracy of 0.73 on the train dataset for LS/SS classification and 0.78 on the reserved test dataset. The F1 score for TBRmax was 0.67 on the test dataset. The optimized cutoff value of skewness was determined to be between [0.65, 0.75] which gave an accuracy of 0.73 on the train dataset and 0.67 on the test dataset. The F1 score for skewness was 0.73 on the test dataset. As a contrast, neither TBRmax nor skewness showed prognostic value for the MGMT methylated cohort, with best accuracy achieved of only 0.56.

To evaluate whether prognostic value could be improved with a more complex model, decision tree models were constructed using three different feature sets: Set 1 (TBRmax), Set 2 (Skewness) and Set 3 (TBRmax and Skewness). Training of the model with 5-fold cross validation on the train dataset (Figure 1a) demonstrated that the model with TBRmax still shows slightly better performance than models with other sets, although the difference is not significant. When applying the DT model with TBRmax to the reserved test dataset, an accuracy of 0.78 and a F1 score of 0.67 was obtained, showing no improvement compared to the simple cutoff method. With TBRmax = 3.0 as a cutoff, patients with unmethylated MGMT are grouped into SS and LS survival categories, with their Kaplan-Meier (KM) plots shown in Figure 1b. Additionally, the KM curve for patients with methylated MGMT is provided for reference.

Time series of quantitative features

Figure 2 displays median values of delta radiomics features found to have a significant difference for patients with unmethylated MGMT status, organized by survival groups. This visualization illustrates the changes over early FU time points. Demonstrating the spread of data points, Figure 3 provides a detailed representation of individual data points for two of the features, MeshVolume, SurfaceVolumeRatio, and the ΔSurfaceVolumeRatio at pre-RT, FU1, and FU2 time points. Additional plots showcasing other selected radiomics features can be found in the Supplementary Material (Supplementary Figures S2-S9). The Mann-Whitney Test was used to calculate the p-value for each radiomic feature between the two survival groups.

To visually illustrate tumor changes, co-registered PET images for three example patients are shown in Figure 4 for time points preRT, FU1, and FU2. Patient 1, who had a short OS, exhibited a small change in tumor volume and SurfaceVolumeRatio at FU1, but the tumor volume decreased and the SurfaceVolumeRatio increased at FU2. Patient 2, who also had a short OS, showed a significant increase in tumor volume after RT and nearly identical SurfaceVolumeRatio at FU1, which then increased at FU2. Patient 3, who had a long OS, demonstrated a decrease in SurfaceVolumeRatio at FU2. For reference, the FU1 timepoint with respect to the last session of RT was consistently at 4 weeks for all three example patients, and the FU2 timepoint with respect to the last session of RT was 2, 2 and 3 months for the patients respectively.

TABLE 3 Delta features which showed a significant difference between pre-RT images and FU1 or FU2 images.

Delta feature number	Category	Features	FU1 p-value	FU2 p-value
Unmethylated MGMT				
DF1	Shape	ΔMeshVolume	**0.038**	0.323
DF2		ΔSurfaceVolumeRatio	0.528	**0.012**
DF3	First order	ΔEnergy	**0.045**	0.303
DF4	Texture	gldm_ΔGrayLevelNonUniformity	**0.029**	0.265
DF5		glrlm_ΔShortRunHighGrayLevelEmphasis	0.417	**0.007**
DF6		glcm_ΔContrast	0.928	**0.027**
DF7		glszm_ΔSmallAreaHighGrayLevelEmphasis	**0.016**	0.044
DF8		glszm_ΔZonePercentage	0.601	**0.014**

The first column is assigned feature number, the second column and the third column show the feature category and name. The last two columns show the p-value of the feature between LS and SS comparison, in FU1 and FU2 image respectively.
P-value less than 0.05 are labeled in bold.

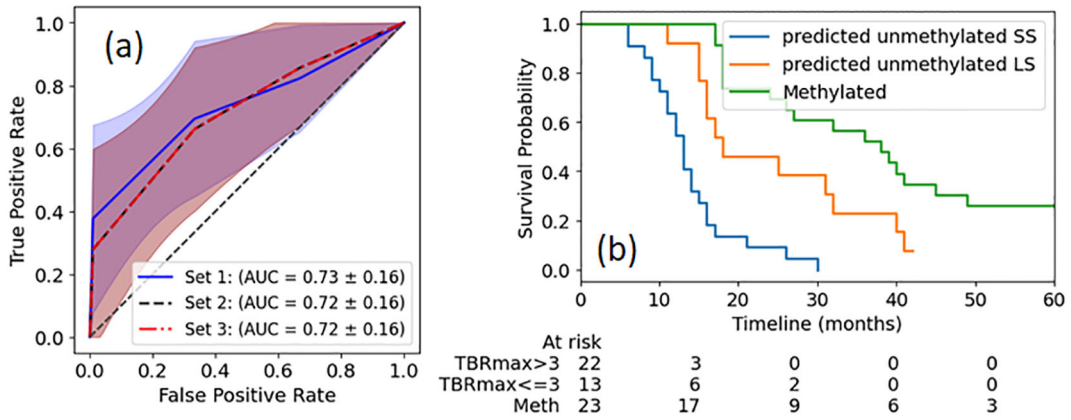

FIGURE 1
ROI (magenta contour) where the TBR ratio exceeded 2.0 for three example patients with different OS at the time points of preRT, FU1 and FU2. The patients with worse outcomes usually have increased SurfaceVolumeRatio.

Survival analysis for RS

Although RS is a dynamic value that updates at each follow-up time point, it exhibits a clear correlation with OS. In the analyses of pre-RT images described in Section 3.2, TBRmax(preRT) was identified as a strong prognostic indicator for OS with a threshold around 3.0. In the RS analysis, TBRmax(preRT) was therefore chosen as the reference baseline. We further assessed the added value of delta features at early FU timepoints. TBRmax(FU) is the TBRmax value measured from FU images. The delta features were evaluated in univariate Cox regression analysis or combined with TBRmax (preRT) in multivariate analysis. While multiple combinations of other delta radiomics features were investigated, none demonstrated a stronger prognostic value than ΔSurfaceVolumeRatio(FU). For clarity and simplicity, Table 4 summarizes the C-index for various feature combinations at different timepoints, highlights the results for ΔSurfaceVolumeRatio(FU), which gives the best achieved results when combined with TBRmax(preRT).

Discussion

Glioblastoma, one of the most aggressive tumors, presents significant treatment challenges. Achieving an optimal balance between maximizing tumor control and minimizing toxicity is critical. While dose escalation targeting tumor heterogeneity has shown promising results, not all patients benefit equally. Identifying those who are most likely to benefit from dose escalation is essential for advancing individualized treatment. Additionally, informed post-treatment management plays a vital role in maximizing patient survival. Static medical images offer a momentary snapshot of the tumor's status. Examining the time series evolution of these images provides a valuable opportunity to investigate how the tumor responds to significant interventions, such as radiation and chemotherapy. Delta features from quantitative imaging serve as a tool specifically designed to discover and quantify these responses over time, capturing imaging characteristics that are often imperceptible to the naked eye. In our study, we extracted quantitative features from ^{18}F-DOPA PET images at multiple time points. We identified interpretable pre-RT prognostic features that could further stratify patients with similar pathological biomarkers for DERT. Additionally, we examined significant changes in the quantitative features between pre-RT and post-RT timepoints, evaluating their prognostic value in predicting remaining survival after follow-up.

As consistently observed in various clinical studies, MGMT methylation serves as a robust biomarker correlated with patient survival (2, 5), a trend reaffirmed in this study. MGMT methylation status is a strong prognosis biomarker for the OS in this study, with significantly different median OS for patients with different MGMT methylation status (Table 1). However, even with the same MGMT unmethylated status, patients show a wide variation in OS and may respond differently to DERT, as illustrated in Figures 1, 2. It is valuable to further stratify patients using imaging biomarkers in addition to MGMT status. Consistent with previous studies on other amino acid PET tracers (e.g., ^{18}FET) (40, 41), TBRmax was identified in this study as a strong pre-irradiation prognostic indicator for OS in patients with unmethylated MGMT. Using a simple threshold of TBRmax = 3.0, these patients can be divided into two distinct survival groups (Figure 1b). A slightly more complex model (DT) does not offer superior performance in accuracy for OS grouping. Among patients with high TBRmax, the SS group had a median survival of 13 months, aligning with the median OS of 13.5 months reported in historical cohorts without dose escalation (31), suggesting limited benefit from dose escalation when TBRmax is high. In contrast, the LS group had a significantly longer median survival of 18 months compared to the historical cohort (13.5 months). TBRmax does not show prognostic value to predict OS of the patients with methylated MGMT in our study. The median OS (38 months) of the methylated MGMT subgroup

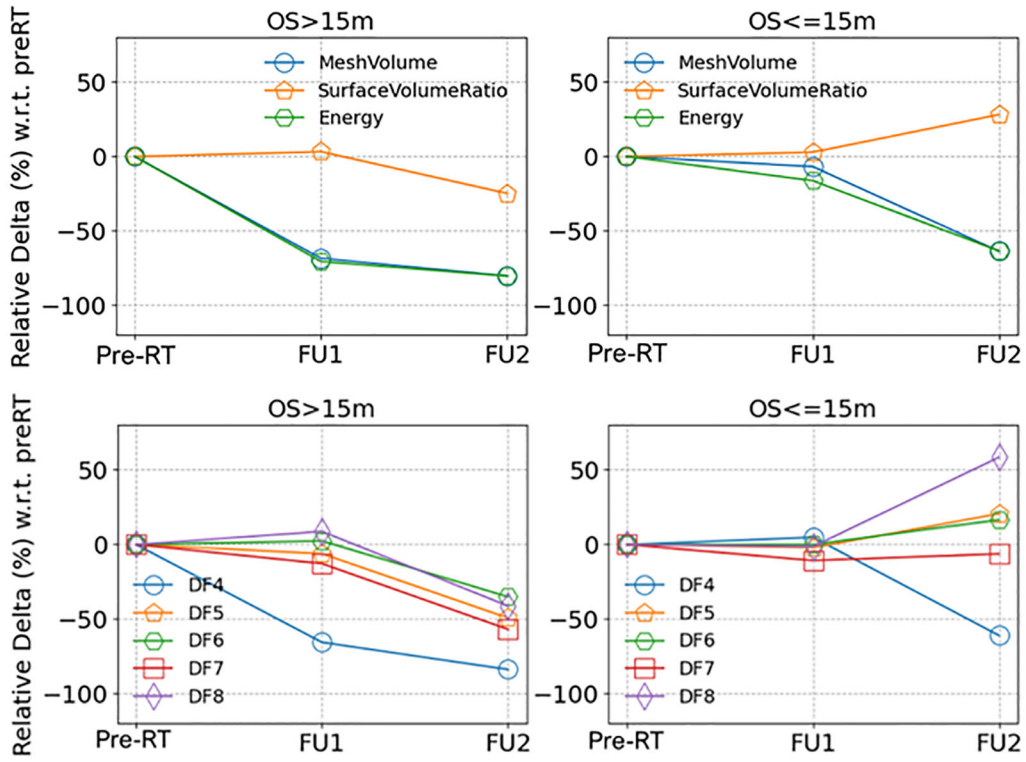

FIGURE 2
(a) ROC curves for survival group classification of MGMT unmethylated patients based on identified radiomics features extracted from single timepoint pre-RT ^{18}F-DOPA PET images. The definitions of feature sets are described in the text. The shadow region depicts the 1 standard deviation. **(b)** KM plots of OS of patients with unmethylated MGMT status, separated by TBRmax cutoff. For reference, KM plot of OS of MGMT methylated patients is also plotted. The p value between any two groups is less than 0.01.

treated with DERT is significantly higher than that of the historical cohort (23.3 months) (31), which may suggest that the patients with methylated MGMT could benefit from dose escalation.

Different survival groups also exhibit different patterns of delta features. We searched for the features showing a significant difference in early FU time points after DERT. Table 2 reports 8 features identified for the cohort with unmethylated MGMT, while no feature was identified for the cohort with methylated MGMT at the early FU timepoints focused on for this work. Notably, while texture features may reflect certain special characteristics of tumors, they are less intuitive to interpret and can be subject to variation in image quality. For the cohort with unmethylated MGMT, Figure 2 illustrates the different patterns of response of image features after DERT. Generally, patients with shorter survival exhibit significant change at FU2 time points, not at FU1. Conversely, patients with longer survival demonstrated early responses in certain features, such as tumor volume and energy, with a significant decrease observed at FU1. This indicates that early tumor response to radiation may be a positive prognostic factor. Notably, for features displaying significant changes at FU2, the direction of change differed between the LS and SS groups. For instance, SurfaceVolumeRatio and ZonePercentage decreased at FU2 in the LS group but increased in the SS group. The variation in the timing of the most substantial percentage change suggests the presence of underlying biological mechanisms related to the radiosensitivity of tumors in different patients, highlighting the need for further investigation. As an example, Figure 3 provides a detailed illustration of the changes in tumor size and SurfaceVolumeRatio, which are among the most interpretable and robust features. SurfaceVolumeRatio has a strong correlation with tumor shape heterogeneity. While the difference of the tumor sizes between LS and SS groups decreased after treatment, the changes of SurfaceVolumeRatio moved in different directions, indicating different responses of the two groups after DERT. The enlarged SurfaceVolumeRatio associated with SS suggested increasing shape heterogeneity, which might be a prognostic indicator of treatment response. Interestingly, this increase in SurfaceVolumeRatio is not observed in patients with methylated MGMT, in either LS or SS groups at FU1 or FU2, although the possibility of such changes at later FU time points was not evaluated in this work. This may indicate differential biologic response to treatment between cohorts. These findings underscore the significance of considering temporal changes in radiomic features and propose potential implications for understanding tumor response and prognosis in the context of treatment interventions. Delta radiomics can also benefit risk analysis for the remaining survival at FU timepoints, as illustrated in Table 4. With treatment effects such as radiation included necrosis, the prognostic value of TBRmax may not hold in the FU images. For example, a significant drop of C-index based on TBRmax(FU) is

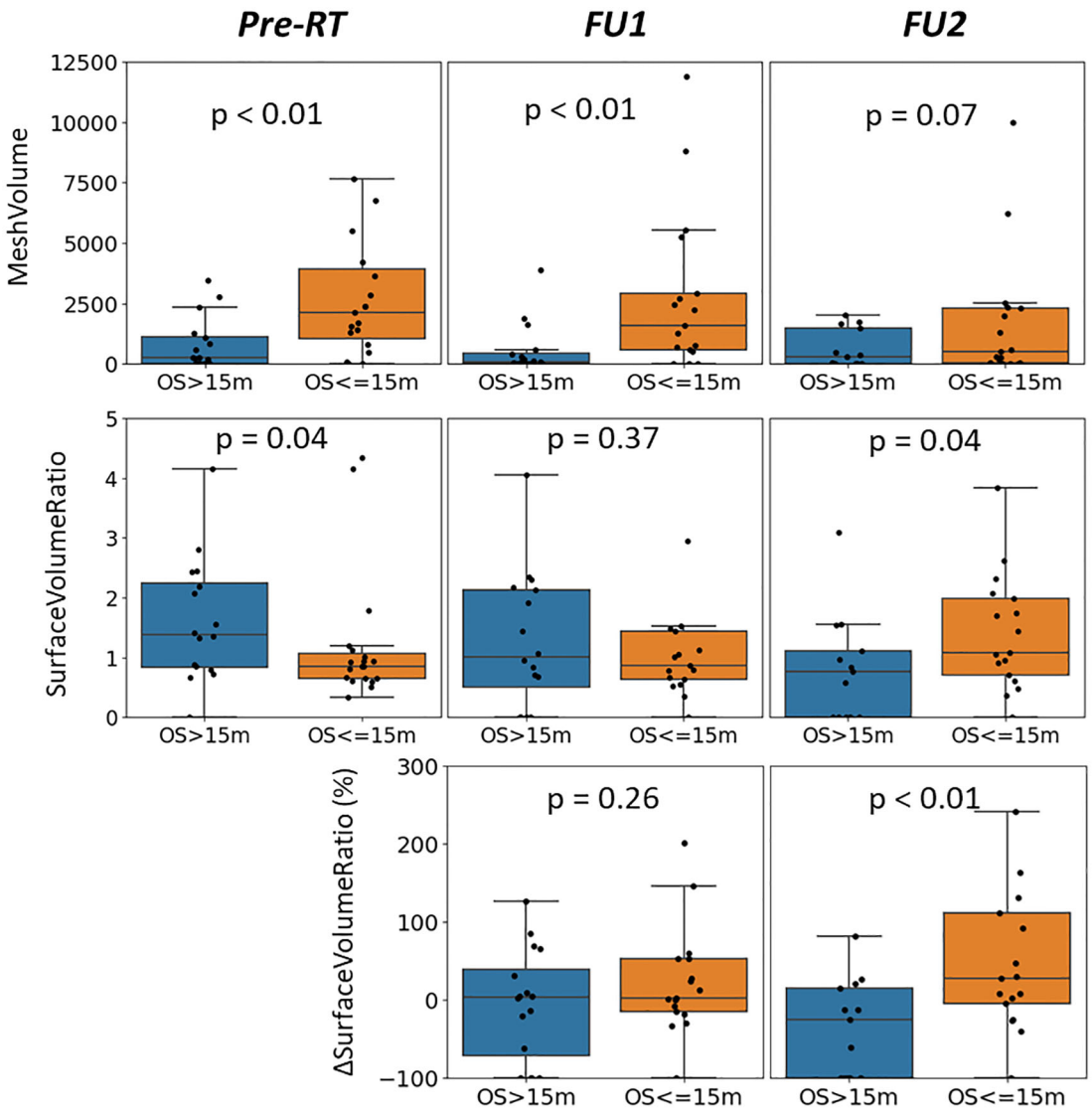

FIGURE 3
Medians of the relative delta of (upper row) shape and first order radiomics features and (lower row) texture radiomics features (full feature names listed in Table 3), separated by longer and shorter survival groups (OS > 15 months or OS <= 15 months), for patients with unmethylated MGMT status.

observed at FU2, while including the delta radiomics can increase C-index and boost the accuracy of risk analysis. Among all the identified delta features, ΔSurfaceVolumeRatio at FU2 shows the most prognostic value. The prognostic delta features provide an opportunity to evaluate treatment response and offer the potential to more effectively differentiate true progression from treatment effects. This is particularly important in cases where traditional criteria, often based on the size of the hyperintense region, may be unreliable due to the effects of high-dose radiation therapy. By leveraging these features, clinicians may enable the timely initiation of salvage treatments while avoiding the premature discontinuation of effective therapies or delays in addressing true progression.

In this study, quantitative image analysis was conducted for both unmethylated and methylated MGMT cohorts, revealing distinct phenotypes between the two groups. The features identified as prognostic for unmethylated MGMT (including TBRmax) generally did not demonstrate prognostic value for methylated MGMT. While further statistical validation is needed, these findings suggest that imaging studies may need to be conducted separately based on MGMT status, as image features in PET images appear to evolve differently in cohorts with different MGMT status.

Several limitations should be acknowledged in this study. Firstly, the small sample size represents a primary constraint. Given that ^{18}F-DOPA PET imaging is an emerging technique not yet approved by the FDA for glioblastoma, its availability, particularly for FU images, is limited in USA. This imposes limitations on the complexity of radiomics feature selection, modeling, and validation. For mitigation, we chose the simple models based on the most reproducible and interpretable features to avoid overfitting. The reported work would

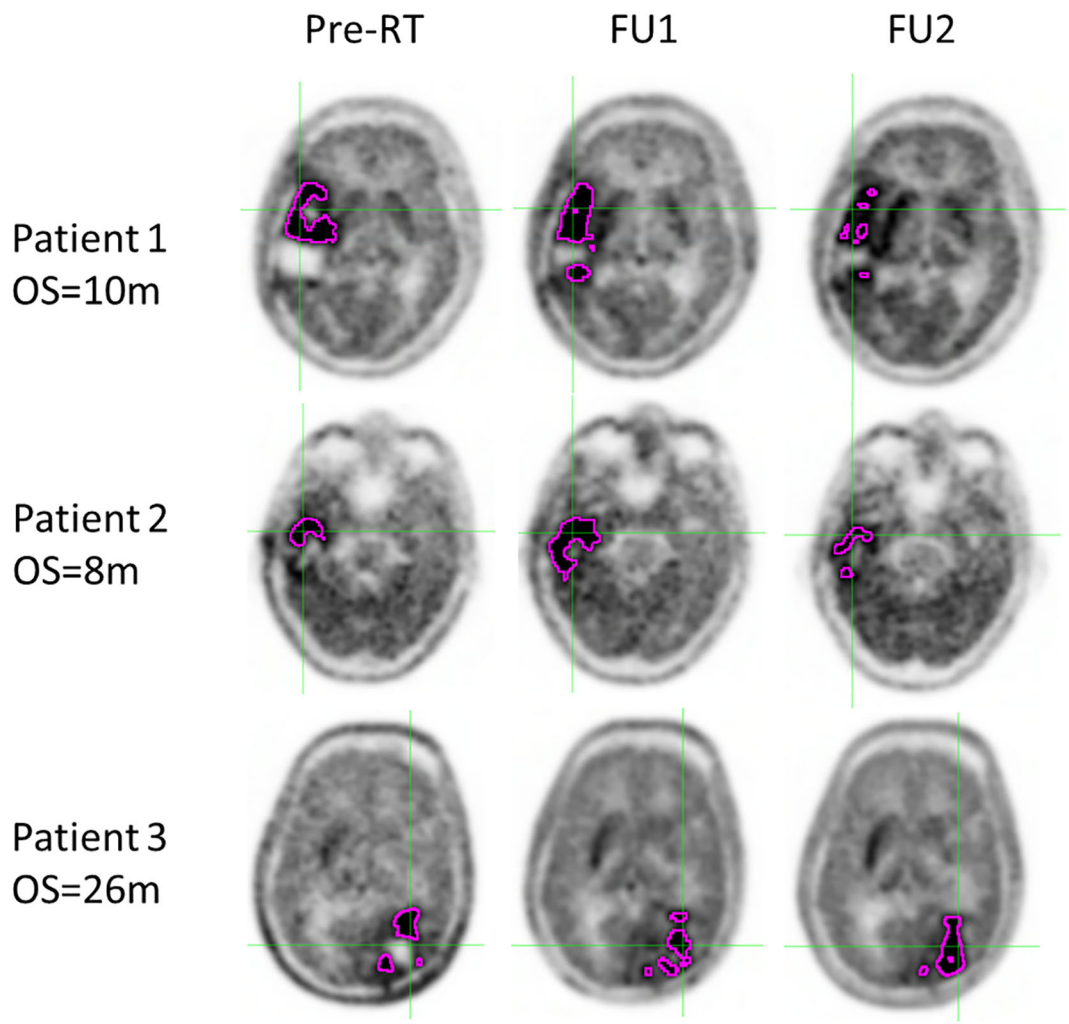

FIGURE 4
Distribution of MeshVolume (top row), SurfaceVolumeRatio (middle row) and ΔSurfaceVolumeRatio (bottom row) of the patients with unmethylated MGMT status, grouped by survival groups and plotted at different time points (left: pre-RT, middle: FU1, right: FU2), with p-value between longer and shorter survival groups reported.

benefit from validation and improvement through additional data, which could be obtained from additional prospective trials utilizing the ^{18}F-DOPA PET tracer. Secondly, this study tries to identify the features with the most significant changes before and after RT, instead of identifying all the features which may exhibit difference with statistical significance. With limited statistics, the threshold used to categorize the difference has not been optimized and is subject to further improvement in the future. Thirdly, the focus of this study is on a single cohort of patients treated with DERT, and the applicability of the identified features to other cohorts requires further investigation. Fourthly, the timing of FU2 had a mean of 2.7 months following the completion of RT with a standard deviation of 0.6 months. Although we consider it as an acceptable variability given the constraints in clinical settings and consistency with National Comprehensive Cancer Network (NCCN) recommendations, reduced variability in the FU2 timepoint could be beneficial for quantitative imaging analysis. Finally, the study primarily concentrates on shape and intensity features. While texture features could offer critical and complementary information (as possibly indicated by the exploratory Random Forest model presented in the Supplementary Material), they are not extensively explored due to concerns about interpretability and susceptibility to image quality. In

TABLE 4 Summary of C-index from Cox regression analysis with feature sets at different time points.

Feature set	Features	C-index		
		preRT	FU1	FU2
1	TBRmax (preRT)	0.66	0.68	0.66
2	TBRmax (FU)	N/A	0.68	0.61
3	ΔSurfaceVolumeRatio (FU)	N/A	0.58	0.7
4	TBRmax (preRT), ΔSurfaceVolumeRatio (FU)	N/A	0.68	0.73
5	TBRmax (preRT), TBRmax (FU), ΔSurfaceVolumeRatio (FU)	N/A	0.69	0.73

the future, with the availability of more data, a revisit and deeper exploration of texture features are warranted.

Conclusions

This study explores the potential to further stratify glioblastoma patients using radiomics features derived from ^{18}F-DOPA PET images and applies delta radiomics features to better understand early treatment responses. Leveraging the high sensitivity of 18F-DOPA PET imaging for glioblastoma, the selected radiomics features, especially TBRmax, from pre-RT images can effectively stratify the patient cohort with un-methylated MGMT and wild-type IDH1, identifying the patients who may benefit most from DERT. The unique characteristics of delta features illuminate distinct treatment response patterns among different survival groups in glioblastoma patients. The observed varied trends in the changes of radiomics feature provide insight into the evolving heterogeneity of tumors following DERT. These findings furnish a valuable tool for evaluating treatment efficacy at an individual patient level and guiding targeted post-treatment interventions when needed. The distinct response pattern also suggests that ^{18}F-DOPA PET images have the potential to be utilized for treatment adaptation during treatment courses.

Looking ahead, we will utilize time series data to separate treatment effects from tumor progression, another important and challenging problem in glioblastoma treatment. We will also expand the research with the addition of MR images. Additionally, we also aim to enlarge the cohort size by incorporating data from diverse protocols and institutions, including the newly launched prospective clinical trial (NCT05781321). This expansion will validate the robustness of our models and prognostic features, paving the way for the development of multi-variable models for more personalized approaches to medicine. With various regimens, we will also investigate whether radiation dose and fractionation influence treatment response. We strongly believe that amino-acid PET tracers, including ^{18}F-DOPA, hold immense potential in enhancing glioblastoma treatment and management, presenting exciting opportunities for both research and clinical applications.

Data availability statement

The original contributions presented in the study are included in the article/Supplementary Material. Further inquiries can be directed to the corresponding authors.

Ethics statement

The studies involving humans were approved by Institutional Review Board, Mayo Clinic, Rochester, MN. The studies were conducted in accordance with the local legislation and institutional requirements. The participants provided their written informed consent to participate in this study.

Author contributions

JQ: Validation, Writing – review & editing, Formal Analysis, Methodology, Writing – original draft, Conceptualization, Software, Visualization, Investigation, Funding acquisition. DP: Funding acquisition, Resources, Writing – review & editing, Data curation, Investigation. WB: Data curation, Investigation, Conceptualization, Writing – review & editing, Funding acquisition. PB: Writing – review & editing, Data curation. CH: Data curation, Writing – review & editing. MJ: Data curation, Writing – review & editing. DJ: Data curation, Writing – review & editing. TK: Data curation, Writing – review & editing. BK: Writing – review & editing, Data curation. SK: Data curation, Writing – review & editing. VL: Data curation, Writing – review & editing. MR: Data curation, Writing – review & editing. JS: Data curation, Writing – review & editing. JU: Data curation, Writing – review & editing. MZ: Writing – review & editing, Data curation. MS: Data curation, Writing – review & editing. HW: Writing – review & editing, Data curation. EY: Data curation, Writing – review & editing. YZ: Writing – review & editing, Data curation. NL: Writing – review & editing, Data curation, Supervision, Funding acquisition. DB: Supervision, Data curation, Investigation, Conceptualization, Resources, Funding acquisition, Writing – review & editing.

Funding

The author(s) declare financial support was received for the research and/or publication of this article. This work was funded by National Cancer Institute of the National Institutes of Health (R01CA178200) and Center for Clinical and Translational Science of Mayo Clinic (2022 Advance the Practice Research Award).

Conflict of interest

VL serves as a consultant for Bayer Schering Pharma, Piramal Life Sciences, Life Molecular Imaging, Eisai Inc., AVID Radiopharmaceuticals, Eli Lilly and Company, and Merck Research and receives research support from GE Healthcare, Siemens Molecular Imaging, AVID Radiopharmaceuticals, and the NIH NIA, NCI. DJ have served on the advisory boards for Telix, Novartis and Cellectar.

The remaining authors declare that the research was conducted in the absence of any commercial or financial relationships that could be construed as a potential conflict of interest.

The author(s) declared that they were an editorial board member of Frontiers, at the time of submission. This had no impact on the peer review process and the final decision.

Generative AI statement

The author(s) declare that no Generative AI was used in the creation of this manuscript.

Any alternative text (alt text) provided alongside figures in this article has been generated by Frontiers with the support of artificial intelligence and reasonable efforts have been made to ensure accuracy, including review by the authors wherever possible. If you identify any issues, please contact us.

Publisher's note

All claims expressed in this article are solely those of the authors and do not necessarily represent those of their affiliated organizations, or those of the publisher, the editors and the reviewers. Any product that may be evaluated in this article, or claim that may be made by its manufacturer, is not guaranteed or endorsed by the publisher.

Supplementary material

The Supplementary Material for this article can be found online at: https://www.frontiersin.org/articles/10.3389/fonc.2025.1623313/full#supplementary-material

References

1. Louis DN, Perry A, Wesseling P, Brat DJ, Cree IA, Figarella-Branger D, et al. The 2021 WHO classification of tumors of the central nervous system: a summary. *Neuro Oncol*. (2021) 23:1231–51. doi: 10.1093/neuonc/noab106

2. Stupp R, Mason WP, van den Bent MJ, Weller M, Fisher B, Taphoorn MJ, et al. Radiotherapy plus concomitant and adjuvant temozolomide for glioblastoma. *N Engl J Med*. (2005) 352:987–96. doi: 10.1056/NEJMoa043330

3. Taphoorn MJB, Dirven L, Kanner AA, Lavy-Shahaf G, Weinberg U, Taillibert S, et al. Influence of treatment with tumor-treating fields on health-related quality of life of patients with newly diagnosed glioblastoma: A secondary analysis of a randomized clinical trial. *JAMA Oncol*. (2018) 4:495–504. doi: 10.1001/jamaoncol.2017.5082

4. Henriksen OM, Del Mar Alvarez-Torres M, Figueiredo P, Hangel G, Keil VC, Nechifor RE, et al. High-grade glioma treatment response monitoring biomarkers: A position statement on the evidence supporting the use of advanced MRI techniques in the clinic, and the latest bench-to-bedside developments. Part 1: perfusion and diffusion techniques. *Front Oncol*. (2022) 12:810263. doi: 10.3389/fonc.2022.810263

5. Hegi ME, Diserens AC, Gorlia T, Hamou MF, de Tribolet N, Weller M, et al. MGMT gene silencing and benefit from temozolomide in glioblastoma. *N Engl J Med*. (2005) 352:997–1003. doi: 10.1056/NEJMoa043331

6. Combs SE, Rieken S, Wick W, Abdollahi A, von Deimling A, Debus J, et al. Prognostic significance of IDH-1 and MGMT in patients with glioblastoma: one step forward, and one step back? *Radiat Oncol*. (2011) 6:115. doi: 10.1186/1748-717X-6-115

7. Ashkan K, Baig Mirza A, Soumpasis C, Syrris C, Kalaitzoglou D, Sharma C, et al. MGMT promoter methylation: prognostication beyond treatment response. *J Pers Med*. (2023) 13(6):999. doi: 10.3390/jpm13060999

8. Yan H, Parsons DW, Jin G, McLendon R, Rasheed BA, Yuan W, et al. IDH1 and IDH2 mutations in gliomas. *N Engl J Med*. (2009) 360:765–73. doi: 10.1056/NEJMoa0808710

9. da Cruz LCH, Rodriguez I, Domingues RC, Gasparetto EL, Sorensen AG. Pseudoprogression and pseudoresponse: imaging challenges in the assessment of posttreatment glioma. *Am J Neuroradiol*. (2011) 32:1978–85. doi: 10.3174/ajnr.A2397

10. Pafundi DH, Laack NN, Youland RS, Parney IF, Lowe VJ, Giannini C, et al. Biopsy validation of 18F-DOPA PET and biodistribution in gliomas for neurosurgical planning and radiotherapy target delineation: results of a prospective pilot study. *Neuro Oncol*. (2013) 15:1058–67. doi: 10.1093/neuonc/not002

11. Patel P, Baradaran H, Delgado D, Askin G, Christos P, Tsiouris AJ, et al. MR perfusion-weighted imaging in the evaluation of high-grade gliomas after treatment: a systematic review and meta-analysis. *Neuro-Oncology*. (2017) 19:118–27. doi: 10.1093/neuonc/now148

12. Leimgruber A, Ostermann S, Yeon EJ, Buff E, Maeder PP, Stupp R, et al. Perfusion and diffusion MRI of glioblastoma progression in a four-year prospective temozolomide clinical trial. *Int J Radiat Oncol Biol Phys*. (2006) 64:869–75. doi: 10.1016/j.ijrobp.2005.08.015

13. Prager AJ, Martinez N, Beal K, Omuro A, Zhang Z, Young RJ. Diffusion and perfusion MRI to differentiate treatment-related changes including pseudoprogression from recurrent tumors in high-grade gliomas with histopathologic evidence. *AJNR Am J Neuroradiol*. (2015) 36:877–85. doi: 10.3174/ajnr.A4218

14. Kim JY, Park JE, Jo Y, Shim WH, Nam SJ, Kim JH, et al. Incorporating diffusion- and perfusion-weighted MRI into a radiomics model improves diagnostic performance for pseudoprogression in glioblastoma patients. *Neuro-Oncology*. (2019) 21:404–14. doi: 10.1093/neuonc/noy133

15. Prather KY, O'Neal CM, Westrup AM, Tullos HJ, Hughes KL, Conner AK, et al. A systematic review of amino acid PET in assessing treatment response to temozolomide in glioma. *Neurooncol Adv*. (2022) 4:vdac008. doi: 10.1093/noajnl/vdac008

16. Cicone F, Galldiks N, Papa A, Langen KJ, Cascini GL, Minniti G. Repeated amino acid PET imaging for longitudinal monitoring of brain tumors. *Clin Transl Imaging*. (2022) 10:457–65. doi: 10.1007/s40336-022-00504-w

17. Nabavizadeh A, Bagley SJ, Doot RK, Ware JB, Young AJ, Ghodasara S, et al. Distinguishing progression from pseudoprogression in glioblastoma using (18)F-fluciclovine PET. *J Nucl Med*. (2023) 64:852–8. doi: 10.2967/jnumed.122.264812

18. Darcourt J, Chardin D, Bourg V, Gal J, Schiappa R, Blonski M, et al. Added value of [(18)F]FDOPA PET to the management of high-grade glioma patients after their initial treatment: a prospective multicentre study. *Eur J Nucl Med Mol Imaging*. (2023) 50:2727–35. doi: 10.1007/s00259-023-06225-0

19. Najjar AM, Johnson JM, Schellingerhout D. The emerging role of amino acid PET in neuro-oncology. *Bioengineering (Basel)*. (2018) 5(4):104. doi: 10.3390/bioengineering5040104

20. Galldiks N, Dunkl V, Stoffels G, Hutterer M, Rapp M, Sabel M, et al. Diagnosis of pseudoprogression in patients with glioblastoma using O-(2-[18F]fluoroethyl)-L-tyrosine PET. *Eur J Nucl Med Mol Imaging*. (2015) 42:685–95. doi: 10.1007/s00259-014-2959-4

21. Galldiks N, Langen KJ. Use of amino acid PET in the diagnostic and treatment management of cerebral gliomas. *Fortschr Neurol Psyc*. (2012) 80(1):17–23. doi: 10.1055/s-0031-1281851

22. Law I, Albert NL, Arbizu J, Boellaard R, Drzezga A, Galldiks N, et al. Joint EANM/EANO/RANO practice guidelines/SNMMI procedure standards for imaging of gliomas using PET with radiolabelled amino acids and [(18)F]FDG: version 1.0. *Eur J Nucl Med Mol Imaging*. (2019) 46:540–57. doi: 10.1007/s00259-018-4207-9

23. Albert NL, Galldiks N, Ellingson BM, van den Bent MJ, Chang SM, Cicone F, et al. PET-based response assessment criteria for diffuse gliomas (PET RANO 1.0): a report of the RANO group. *Lancet Oncol*. (2024) 25:e29–41. doi: 10.1016/S1470-2045(23)00525-9

24. Lohmann P, Lerche C, Bauer EK, Steger J, Stoffels G, Blau T, et al. Predicting IDH genotype in gliomas using FET PET radiomics. *Sci Rep-Uk*. (2018) 8:13328. doi: 10.1038/s41598-018-31806-7

25. Lohmann P, Lerche C, Bauer E, Steger J, Stoffels G, Blau T, et al. Predicting isocitrate dehydrogenase genotype in gliomas using fet pet radiomics. *Neuro-Oncology*. (2017) 19(Suppl 6):vi160. doi: 10.1093/neuonc/nox168.652

26. Lohmann P, Kocher M, Steger J, Galldiks N. Radiomics derived from amino-acid PET and conventional MRI in patients with high-grade gliomas. *Q J Nucl Med Mol Im*. (2018) 62:272–80. doi: 10.23736/S1824-4785.18.03095-9

27. Lohmann P, Lerche C, Bauer E, Steger J, Stoffels G, Blau T, et al. Differentiation of pseudoprogression from tumor progression in glioblastoma patients based on fet pet radiomics. *Neuro-Oncology*. (2017) 19:148–9. doi: 10.1093/neuonc/nox168.607

28. Aerts HJ, Velazquez ER, Leijenaar RT, Parmar C, Grossmann P, Carvalho S, et al. Decoding tumour phenotype by noninvasive imaging using a quantitative radiomics approach. *Nat Commun*. (2014) 5:4006. doi: 10.1038/ncomms5006

29. Hatt M, Krizsan AK, Rahmim A, Bradshaw TJ, Costa PF, Forgacs A, et al. Joint EANM/SNMMI guideline on radiomics in nuclear medicine: Jointly supported by the EANM Physics Committee and the SNMMI Physics, Instrumentation and Data Sciences Council. *Eur J Nucl Med Mol Imaging*. (2023) 50:352–75. doi: 10.1007/s00259-022-06001-6

30. Papp L, Potsch N, Grahovac M, Schmidbauer V, Woehrer A, Preusser M, et al. Glioma survival prediction with combined analysis of *in vivo* (11)C-MET PET features, ex vivo features, and patient features by supervised machine learning. *J Nucl Med*. (2018) 59:892–9. doi: 10.2967/jnumed.117.202267

31. Laack NN, Pafundi D, Anderson SK, Kaufmann T, Lowe V, Hunt C, et al. Initial results of a phase 2 trial of (18)F-DOPA PET-guided dose-escalated radiation therapy for glioblastoma. *Int J Radiat Oncol Biol Phys*. (2021) 110:1383–95. doi: 10.1016/j.ijrobp.2021.03.032

32. Kim MM, Sun Y, Aryal MP, Parmar HA, Piert M, Rosen B, et al. A phase 2 study of dose-intensified chemoradiation using biologically based target volume definition in patients with newly diagnosed glioblastoma. *Int J Radiat Oncol Biol Phys*. (2021) 110:792–803. doi: 10.1016/j.ijrobp.2021.01.033

33. Qian J, Herman MG, Brinkmann DH, Laack NN, Kemp BJ, Hunt CH, et al. Prediction of MGMT status for glioblastoma patients using radiomics feature extraction from (18)F-DOPA-PET imaging. *Int J Radiat Oncol Biol Phys*. (2020) 108:1339–46. doi: 10.1016/j.ijrobp.2020.06.073

34. van Griethuysen JJM, Fedorov A, Parmar C, Hosny A, Aucoin N, Narayan V, et al. Computational radiomics system to decode the radiographic phenotype. *Cancer Res*. (2017) 77:e104–e7. doi: 10.1158/0008-5472.CAN-17-0339

35. Zwanenburg A, Vallieres M, Abdalah MA, Aerts H, Andrearczyk V, Apte A, et al. The image biomarker standardization initiative: standardized quantitative radiomics for high-throughput image-based phenotyping. *Radiology*. (2020) 295:328–38. doi: 10.1148/radiol.2020191145

36. Lei M, Varghese B, Hwang D, Cen S, Lei X, Desai B, et al. Benchmarking various radiomic toolkit features while applying the image biomarker standardization initiative toward clinical translation of radiomic analysis. *J Digit Imaging*. (2021) 34:1156–70. doi: 10.1007/s10278-021-00506-6

37. Myles AJ, Feudale RN, Liu Y, Woody NA, Brown SD. An introduction to decision tree modeling. *J Chemometr*. (2004) 18:275–85. doi: 10.1002/cem.873

38. Pedregosa F, Varoquaux G, Gramfort A, Michel V, Thirion B, Grisel O, et al. Scikit-learn: machine learning in python. *J Mach Learn Res*. (2011) 12:2825–30.

39. Lohmann P, Elahmadawy MA, Gutsche R, Werner JM, Bauer EK, Ceccon G, et al. FET PET radiomics for differentiating pseudoprogression from early tumor progression in glioma patients post-chemoradiation. *Cancers (Basel)*. (2020) 12 (12):3835. doi: 10.3390/cancers12123835

40. Dissaux G, Basse V, Schick U, El Kabbaj O, Auberger B, Magro E, et al. Prognostic value of 18F-FET PET/CT in newly diagnosed WHO 2016 high-grade glioma. *Med (Baltimore)*. (2020) 99:e19017. doi: 10.1097/MD.0000000000019017

41. Muller M, Winz O, Gutsche R, Leijenaar RTH, Kocher M, Lerche C, et al. Static FET PET radiomics for the differentiation of treatment-related changes from glioma progression. *J Neurooncol*. (2022) 159:519–29. doi: 10.1007/s11060-022-04089-2

frontiers | Frontiers in Oncology

TYPE Original Research
PUBLISHED 01 September 2025
DOI 10.3389/fonc.2025.1666489

Check for updates

OPEN ACCESS

EDITED BY
Poonam Yadav,
Northwestern University, United States

REVIEWED BY
Mihaela Ghita-Pettigrew,
Queen's University Belfast, United Kingdom
Beatrice D'Orsi,
National Research Council (CNR), Italy
Inna Gertsenshteyn,
Novartis, United States

*CORRESPONDENCE
Armin D. Tavakkoli
armin.d.tavakkoli.med@dartmouth.edu

†These authors have contributed equally to this work

RECEIVED 15 July 2025
ACCEPTED 13 August 2025
PUBLISHED 01 September 2025

CITATION
Tavakkoli AD, Daley WW, Hunter DI, Allen BA, Carpenter GC, Gladstone DJ, Pogue BW and Hoopes PJ (2025) Anesthesia is a potent determinant of ultra-high dose rate sparing in the murine total abdominal irradiation model. *Front. Oncol.* 15:1666489. doi: 10.3389/fonc.2025.1666489

COPYRIGHT
© 2025 Tavakkoli, Daley, Hunter, Allen, Carpenter, Gladstone, Pogue and Hoopes. This is an open-access article distributed under the terms of the Creative Commons Attribution License (CC BY). The use, distribution or reproduction in other forums is permitted, provided the original author(s) and the copyright owner(s) are credited and that the original publication in this journal is cited, in accordance with accepted academic practice. No use, distribution or reproduction is permitted which does not comply with these terms.

Anesthesia is a potent determinant of ultra-high dose rate sparing in the murine total abdominal irradiation model

Armin D. Tavakkoli[1,2*†], William W. Daley[1†], David I Hunter[1], Beverly A. Allen[1], Gretchen C. Carpenter[1], David J. Gladstone[1], Brian W. Pogue[1] and P. Jack Hoopes[1,2]

[1]Thayer School of Engineering at Dartmouth College, Hanover, NH, United States, [2]Department of Surgery, Geisel School of Medicine at Dartmouth College, Lebanon, NH, United States

Introduction: Radiation therapy is a mainstay of treatment for numerous gastrointestinal (GI) malignancies, where our ability to deliver dose to tumors is limited by acute GI toxicity. Ultra-high dose-rate (UHDR) 'FLASH' irradiation can spare normal tissue, yet its dependence on physiological variables remains incompletely defined.

Methods: We compared FLASH and conventional dose-rate (CDR) 9 MeV electron total abdominal irradiation (TAI) in C57BL/6 mice anesthetized with either intraperitoneal ketamine/xylazine or inhaled isoflurane in room air, deliberately omitting supplemental oxygen. Single doses of 14 or 16 Gy were delivered, and normal-tissue injury was quantified by time-to-25% body-weight loss.

Results: At 14 Gy, UHDR under K/X produced a marked survival advantage: by day 14, 80% of animals had not reached the weight-loss endpoint versus 40% after CDR K/X; no FLASH benefit was discernible with ISO anesthesia. Raising the dose to 16 Gy accentuated these trends; 40% of UHDR K/X mice were still below the endpoint at study termination, whereas all CDR K/X mice met it by day 7. Again, ISO abolished sparing at both dose rates. To probe mechanism, intraperitoneal oxygen tension was measured with an optical reporter in six mice. ISO anesthesia yielded significantly higher pO2 (62 ± 4 mmHg) than K/X (26 ± 10mmHg), a 2.5-fold difference.

Discussion: These findings identify anesthetic-dependent oxygenation as a reproducible confounder in pre-clinical FLASH studies: elevated pO2 under ISO negates abdominal sparing, whereas K/X preserves it across two clinically relevant doses. Rigorous control and reporting of factors that alter tissue oxygenation are therefore essential when designing experiments and, ultimately, translating FLASH radiotherapy.

KEYWORDS

UHDR, flash, anesthesia, oxygen, total abdominal irradiation

Introduction

Radiation therapy (RT) is employed in roughly one-half of all cancer cases and contributes to about 40% of curative treatments worldwide (1). The recent arrival of ultra-high-dose-rate (UHDR), RT has reinvigorated translational efforts to increase the therapeutic ratio by preferentially sparing normal tissue while maintaining tumor control ("FLASH" sparing) (2–4). Elegant proof-of-principle experiments in skin, lung and brain have demonstrated dramatic reductions in toxicity when doses are delivered in micro-second pulses at ≥ 30 Gy/s compared with conventional dose rates (CDR) (5–9). Yet extension of these findings to the abdomen—a site where acute gastrointestinal (GI) syndrome remains a foremost dose-limiting toxicity—has been inconsistent. Whole-abdomen electron FLASH protects crypt stem cells and improves survival in some reports, whereas pencil-beam-scanned proton FLASH and synchrotron proton beams have produced neutral or even worse outcomes relative to CDR irradiation (10, 11). A potential explanation is that the FLASH effect is particularly sensitive to biological context and experimental nuance that is not being controlled for across studies.

A unifying hypothesis for FLASH sparing invokes transient oxygen depletion: extremely intense pulses have been postulated to consume dissolved O_2 faster than it can be replenished, driving tissue into a radioprotective hypoxic state for the brief period in which radical-mediated damage is fixed (12–15). Bulk tissue measurements have refuted this idea through systematic study of skin, and tumor, however still debate exists on whether there could be regional or micro-localized hypoxia induced during the irradiation in FLASH. The data also seems to be dependent upon the total dose as well as the tissue oxygen, and so there seems to be both a minimum and a maximum dose threshold to see the FLASH effect (16, 17). It is therefore likely that oxygen may be a factor in this complex range where FLASH tissue sparing can be seen. If it is true that oxygenation level affects the observation, then any variable that alters baseline or dynamic tissue oxygenation could modulate —or even mask—the FLASH effect. Two variables stand out in small-animal work: the choice of anesthetic and the composition of the carrier or supplemental gas.

Intraperitoneal ketamine/xylazine (K/X) and inhaled isoflurane dominate murine RT studies because they are facile and inexpensive. Unfortunately, they create very different physiological milieus. K/X produces profound bradycardia, respiratory depression, and peripheral vasoconstriction, leading to arterial hypoxemia and tissue pO_2 values as low as 15 mmHg in skin and brain. Isoflurane, in contrast, raises heart rate, increases tidal volume, and vasodilates vessels; when delivered in room air it maintains skin pO_2 near 25–30 mmHg, and when delivered in 100% oxygen it can drive tissue pO_2 above 50 mmHg. Carrier-gas oxygenation matters independently of the volatile agent: supplemental oxygenation during irradiation sharply increases murine skin P_{O2} values and negates the FLASH effect (18–20).

Despite these well-documented effects, anesthetic protocols are rarely reported in pre-clinical FLASH papers, and when they are, oxygen supplementation is common. In a recent systematic review of electron FLASH *in vivo* studies, fewer than one-third specified the fraction of inspired oxygen, and none quantified tissue pO_2. Recent results showed that this omission is not benign: in murine hind-leg skin, breathing 100% oxygen during isoflurane anesthesia abolished FLASH sparing, whereas room-air anesthesia preserved it; moreover, female mice—whose dermis exhibited higher pO_2 than males—ulcerated sooner after UHDR irradiation (18, 21). These data strengthened the link between oxygen tension and FLASH, but they also raised a critical question for abdominal irradiation: does the anesthetic itself, independent of inspired O_2, dictate whether gut tissues experience protection or injury at UHDR?

The small intestine is among the most radiosensitive organs, and weight-loss kinetics as well as crypt-regeneration assays are gold-standard read-outs for acute GI toxicity. Several groups have attempted to exploit FLASH in this setting, yet outcomes have ranged from substantial sparing to overt harm. None of these studies compared different anesthetic regimens head-to-head or measured intraperitoneal oxygenation. Given that intestinal perfusion is highly responsive to vasoactive and respiratory changes, and that K/X and isoflurane exert opposite effects on both, anesthetic selection may be a hidden confounder driving inter-study variability.

Here we directly address this gap by evaluating FLASH sparing in the mouse total abdominal irradiation model, anesthetized with either KX or isoflurane in room air. To mechanistically link any observed differences to oxygen availability, a parallel cohort received intravenous PdG4 Oxyphor and real-time phosphorescence lifetime imaging (OxyLED) was used to record intra-abdominal pO_2 immediately after laparotomy (22).

Methods

Animals and irradiation

All animal experiments were approved by the Dartmouth College Institutional Animal Care and Use Committee (IACUC). Eighty (N=80) male C57BL/6 mice were ordered from Jackson Laboratories and allowed to acclimate to the vivarium for at least 2 weeks. Following the acclimation period, mice were weighed for 3 days to establish baseline weight. On the day of irradiation, mice were anesthetized using either an IP (intra-peritoneal) injection of Ketamine/Xylazine (ketamine 100 mg/kg, xylazine 10 mg/kg; n=10) or inhaled isoflurane anesthesia delivered in room air (SomnoFlo by Kent Scientific, USA) through a non-rebreather mask (3% induction for 3 minutes, then maintained on 1.5%; n=10). A Mobetron linear accelerator (LINAC; IntraOp, Inc, USA) was used to deliver 14 or 16 Gy of 9 MeV electron CDR and UHDR radiation to a 3 cm x 4 cm area centered on the mouse abdomen with a 1 cm air gap. CDR irradiation was delivered at a dose rate of 0.1 Gy/s, while UHDR was delivered at an average dose rate of 420 Gy/s. For the 14 Gy UHDR treatment, the source-to-surface distance (SSD) was set to 37 cm, and each pulse had a width of 3.10 μs delivered at a pulse repetition frequency (PRF) of 90 Hz. A total of four pulses were administered, with each pulse depositing

3.5 Gy, resulting in the prescribed 14 Gy dose. For the 16 Gy UHDR treatment, the SSD was set to 37 cm, and each pulse had a width of 3.54 μs delivered at a PRF of 90 Hz. A total of four pulses were administered, with each pulse depositing 4 Gy, resulting in the prescribed 16 Gy dose. These UHDR beam parameters are consistent with those previously reported in literature for abdominal electron FLASH and meet or exceed the prescribed thresholds for observing FLASH sparing, namely a dose rate > 100 Gy/s (10). CDR treatments were delivered using a PRF of 30 HZ, pulse width of 1.2 us, and the integrated ion chambers were utilized to deliver the prescribed dose.

Dosimetry verification

Prior to the day of live animal irradiation, on "verification day", an in-house beta treatment planning program was used to estimate the necessary treatment parameters for 14 and 16 Gy dose delivery. Briefly, the planning software utilizes cutout specific output data from water-tank measurements and daily output data from LINAC quality assurance procedure to calculate an estimated pulse width, repetition rate, and number of pulses needed for a given dose. These parameters were then used to deliver both CDR and UHDR irradiation to (1) radiochromic film on solid water (EBT-XD, Ashland Inc, USA) (2) pre-calibrated FlashDiamond (uD) detector (PTW Inc., USA) placed at a depth of 1 mm in solid water, and (3) radiochromic film on the abdomen of a mouse phantom. The dose delivered was within 3% of the expected dose. The cutout depth-dose profile is presented in Figure 1.

On the day of live animal irradiation, quality assurance was conducted to verify machine output in CDR and UHDR mode was within 3% of verification day. The calculated output was then inputted into the treatment planning program to determine the final treatment parameters. The final treatment parameters were delivered to the pre-calibrated uD detector at a depth of 1 mm in solid water and dose delivered was once again verified to be within 3% of the expected dose. Finally, individual dose delivery was monitored by placing the uD at the edge of the irradiation field.

Radiation damage assay

Following irradiation, mice were weighed daily and percent weight loss was calculated from the pre-irradiation baseline weight. Time to 25% weight loss was used as the primary endpoint for time to event (survival) analysis.

Oxygen measurements

Six (N=6) additional male C57BL/6 mice were used as (1) a non-irradiated control group and (2) for abdominal oxygen measurements. Following the acclimation period, mice were weighed for 3 days to establish baseline weight. They were then

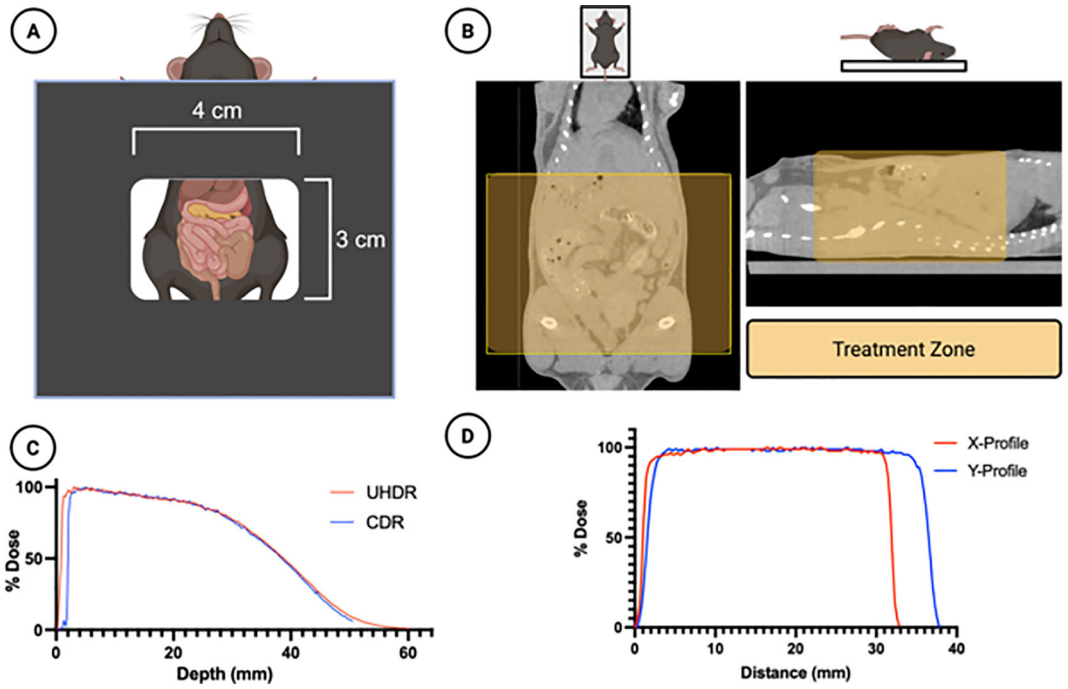

FIGURE 1
Treatment Design. **(A)** A 4x3 cm rectangular cutout was used to irradiate the mouse abdomens. **(B)** A micro-CT scan of the mice demonstrates the treatment zone (shaded yellow) superimposed in two planes. **(C)** The dose-depth characteristics of the cutout for both UHDR and CDR beams are shown in solid water for a 14Gy prescribed dose, obtained using the PTW FLASH diamond detector **(D)** The horizontal and vertical dose profiles of the irradiation field are shown, obtained using EBT-XD radiochromic film. Figure created using Biorender.com.

weighed daily for an additional 14 days, mirroring the irradiated mice. Following this monitoring period, mice received IV injections of PdG4 Oxyphor and were anesthetized using either IP injection of Ketamine/Xylazine (ketamine 100 mg/kg, xylazine 10 mg/kg, n=3) or inhaled isoflurane anesthesia delivered in room air through a non-rebreather mask (3% induction for 3 minutes, then maintained on 1.5%, n=3). Upon verification of the surgical plane of anesthesia, a terminal laparotomy was done to expose the abdominal cavity. Oxygen measurements were taken using the OxyLED (Oxygen Enterprises Inc, USA), with the optical fiber centered at the abdominal cavity.

Statistical analysis

Time to event data were analyzed using log-rank tests. Mice were censored in analyses if death occurred prior to 25% weight loss or if the weight loss was not achieved by 14 days post-irradiation. Oxygen measurements were analyzed using two sample t-tests. All analyses were conducted in Prism (GraphPad Software LLC., USA) with the significance level being $\alpha < 0.05$.

Results

Weight loss

Mice were anesthetized with ketamine/xylazine (K/X) or isoflurane, and irradiated with 14 Gy or 16 Gy of either UHDR or CDR. We used time to 25% weight loss as our primary survival endpoint. Following 14 Gy abdominal irradiation, 14 animals (8 in the UHDR K/X arm, 4 in the CDR K/X arm, and 2 in the CDR ISO arm) never reached the weight-loss threshold before the 14-day study cut-off and were therefore censored. Kaplan–Meier analysis showed that UHDR K/X mice maintained body weight significantly longer than UHDR ISO mice. Median time to endpoint was 6 days for UHDR-ISO and CDR-ISO, whereas it was 7.5 days for CDR-K/X and was not reached for UHDR-K/X, with 80% of those animals still on study at day 14. This is demonstrated in Figure 2.

Following 16 Gy irradiation, 4 animals in the UHDR K/X arm did not reach the weight loss threshold before the study cut off and were censored. Kaplan–Meier analysis showed that UHDR K/X mice maintained body weight significantly longer than CDR K/X mice, whereas the ISO mice did not differ in weight. Median time to endpoint was 6 days for UHDR-ISO, CDR-ISO, and CDR K/X. UHDR K/X mice had a median time to endpoint of 7 days, but 40% remained on study at day 15. This is demonstrated in Figure 3. No mice in the non-irradiated control group show weight loss in the study period.

Oxygen measurements

Bowel oxygen measurements through a laparotomy following systemic administration of PdG4 Oxyphor demonstrated significantly higher oxygen levels in mice anesthetized with isoflurane (mean=62 mmHg, SD=4) compared to mice anesthetized with ketamine/xylazine (mean=27 mmHg, SD=10; Figure 4).

Discussion

Using a 9 MeV electron beam, two previously established doses were delivered, at 14 or 16 Gy, with broad field irradiation to the abdomens of C57BL/6 mice under two commonly interchangeable anesthetics (10): (i) intraperitoneal ketamine/xylazine (K/X, 100/10 mg/kg), and (ii) inhaled isoflurane (ISO, 3% induction, 1.5% maintenance) in room air. Supplemental oxygen was deliberately avoided to isolate anesthetic-specific physiology. Employing time-to-25% weight-loss as an objective endpoint, we asked whether the magnitude of FLASH depended on the anesthetic type.

At the 14 Gy dose, a robust radioprotective effect was seen in UHDR mice anesthetized with K/X compared to ISO. Though a statistically significant sparing effect was not seen between K/X

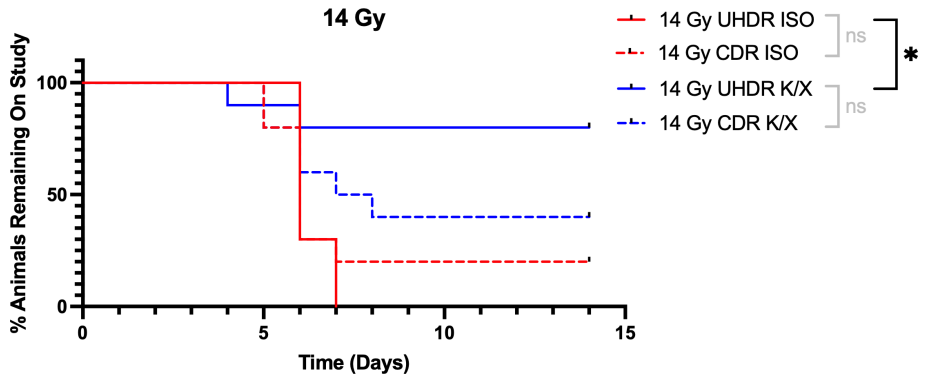

FIGURE 2
Kaplan-Meier curves for mice irradiated with 14 Gy. Mice (N=40) were anesthetized with either isoflurane (ISO) or ketamine/xylazine (K/X) and irradiated with 14 Gy of conventional (CDR) or ultra-high dose rate (UHDR) irradiation (n=10). Mice were removed from study when they reached 25% weight loss from baseline. NS = not significant, *p <0.05.

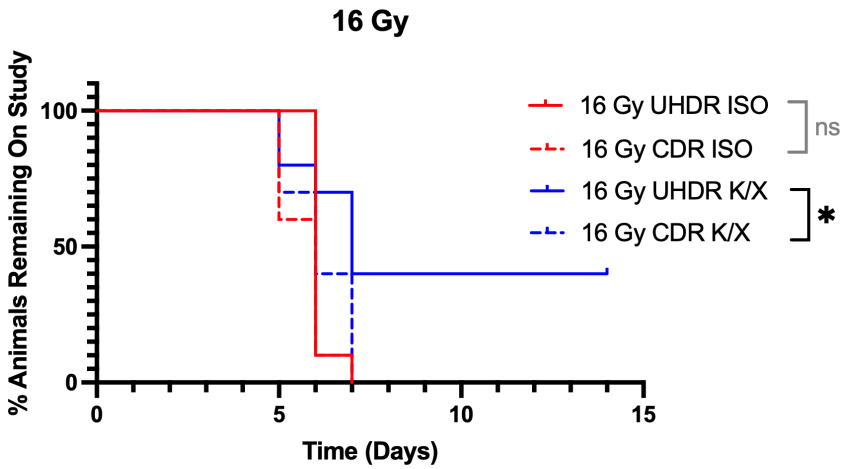

FIGURE 3
Kaplan-Meier curves for mice irradiated with 16 Gy. Mice (N=40) were anesthetized with either isoflurane (ISO) or ketamine/xylazine (KX) and irradiated with 16 Gy of conventional (CDR) or ultra-high dose rate (UHDR) irradiation (n=10). Mice were removed from study when they reached 25% weight loss from baseline. NS = not significant, *p <0.05.

UHDR and CDR mice, it is apparent that this may have been caused by limited statistical power from the few events in the UHDR K/X arm. This is supported by a power analysis showing that a group size (n) of nearly 400 mice is needed to achieve 80% detection power (alpha = 0.05) using the baseline event rate (~0.12) and censoring rate (0.3) observed in the 14 Gy K/X UHDR arm. Regardless, at termination of study (14 days), 80% of UHDR K/X arm had not reached 25% weight loss, compared to 40% in the CDR K/X arm. Importantly though, there is no apparent FLASH effect abdominal sparing in mice anesthetized with ISO, indicating that with ISO anesthesia this would not be seen at this dose level.

At the increased 16 Gy dose, K/X administration showed notable radioprotection to the UHDR irradiated mice, as compared to the CDR mice. A significant sparing effect was seen when comparing UHDR to CDR irradiated mice under the K/X condition as well. At the termination of study, 40% of the UHDR K/X mice had not reached the 25% weight loss endpoint, in comparison to CDR mice who all reached the endpoint by 7 days. These results support the conclusion that ISO anesthesia negates the FLASH sparing effect at this dose level.

To investigate a potential mechanism for loss of sparing under ISO anesthesia, intraperitoneal oxygen measurements were performed using an injected optical oxygen reporter and fiber measurement system in six mice. A significant, nearly 2.5-fold difference in oxygen tension was seen between ISO (average ~62 ± 4 mmHg) and K/X (~26 ± 10 mmHg) conditions. Anesthesia affects tissue oxygenation in a variety of organ systems through multi-modal response including respiratory, cardiac, and vessel

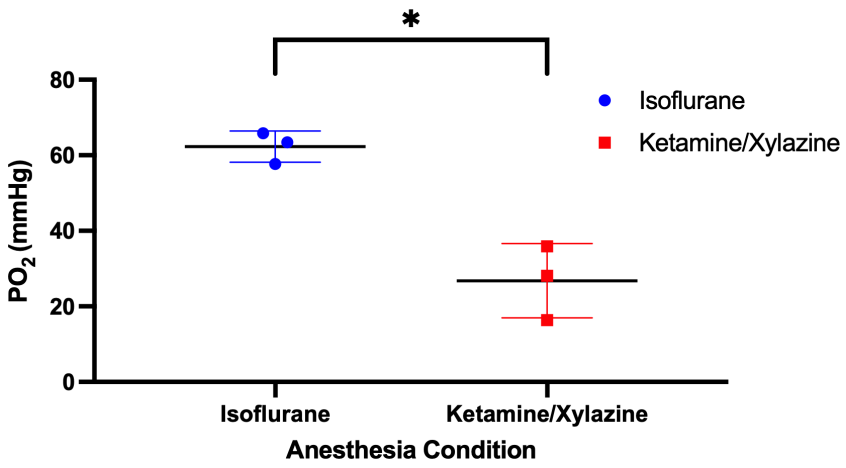

FIGURE 4
Abdomen oxygen measurements. Mice were anesthetized with either isoflurane or ketamine/xylazine, injected with PdG4 Oxyphor, and a laparotomy was done to expose the abdominal cavity. Oxygen measurements were obtained using the OxyLED system. *p <0.05.

tone (perfusion) alteration. Still, the GI system, perfused by mesenteric and splanchnic vasculature, are specially responsive anesthetic effects (23). Considering this in the context of recently published work investigating FLASH sparing under varying oxygen conditions in mouse skin (13, 16, 18, 21), this data supports the interpretation that an oxygen-based mechanism affects the observed differences in radiosensitivity between ISO and K/X anesthesia. We see, again, that FLASH sparing is particularly sensitive to tissue oxygenation, beyond what would be expected from our conventional understanding of oxygen radiosensitization and the oxygen enhancement ratio.

There is now a wide body of literature demonstrating that tissue oxygenation is a key determinant of the magnitude of FLAH sparing across organs (5, 17, 20, 24). This data suggests that an oxygenation threshold or spectrum must exist, above which FLASH sparing is not significant. It is widely known that oxygen enhanced damage through peroxyl formation and DNA damage fixation, and so higher oxygen contributes to higher damage, but this is only seen in the range of local pO_2 <10 mmHg. Thus, it seems plausible that with UHDR irradiation that some local depletion occurs or local change in reactive oxygen species occur, which only significantly affects the normal tissues with lower initial pO_2. Questions remain about what this threshold is, whether it is organ-specific, and if it is modulated by total dose, dose-rate, or fractionation. Once these questions are answered, we can then tackle what we consider to be the key oxygenation question in translational UHDR: Are physiological oxygen values in awake, normally ventilating humans low enough to see a clinically meaningful FLASH sparing effect?

Our study is not without limitations. First, although we see a potent sparing in in mice who were anesthetized with K/X and received 14 Gy of UHDR radiation compared to CDR, we fail to detect a statistically significant difference using Kaplan-Meier (KM) analysis. This is attributed to the limited number of mice meeting the endpoint (2) in the UHDR arm, which affords very little statistical power to the log-rank test. Still, considering the two dose levels 14 Gy and 16 Gy together, FLASH sparing is most apparent under the K/X condition across doses. The second limitation is the inherent uncertainty in the abdominal compartment that is the primary driver of radiation toxicity/weight loss. In Total Abdominal Irradiation (TAI), numerous organs are irradiated with vastly different radiosensitivities. Though weight loss following TAI is typically attributed to small bowel damage, the more nuanced reality is that damage to many of the intrabdominal structures, aside from small bowel, can lead to weight loss and mortality. Although not quantified in this manuscript, significant hydronephrosis, liver damage, gastric enlargement, and enteritis were noted in post-mortem necropsy of mice that very likely contributed to weight loss. This leads to the third limitation, which is the lack of specifity in the abdominal compartment probed in our oxygen measurements. The wide-field oxygen measurements performed centered on the bowel to maximize signal from this organ of interest. This means that these oxygen values are an average of numerous abdominal structures within the irradiation field, rather than any one organ, but were weighted toward the bowel. Still, the results are clear: intrabdominal oxygen levels under ISO anesthesia are significantly higher than under K/X anesthesia. As oxygen measurement technologies advance, more organ-specific measurements would add value to TAI studies.

In summary, by explicitly integrating anesthetic physiology, dosimetry verified to within 3%, and direct oxygen measurements, the present work identified one of the persistent sources of variability relevant to pre-clinical FLASH research, which is anesthesia method. This is particularly important in the light of pre-clinical animal use refinement techniques moving away from injectables toward gaseous anesthesia. There needs to be practical guidance for experimental design as the field advances toward FLASH clinical trials. While direct measurement of tissue oxygen is challenging, future investigations should consider tighter control and reporting of experimental factors that can alter tissue oxygenation.

Data availability statement

The original contributions presented in the study are included in the article/supplementary material. Further inquiries can be directed to the corresponding author.

Ethics statement

The animal study was approved by Dartmouth College Institutional Animal Care and Use Committee (IACUC). The study was conducted in accordance with the local legislation and institutional requirements.

Author contributions

AT: Methodology, Writing – original draft, Writing – review & editing. WD: Data curation, Investigation, Writing – original draft, Writing – review & editing. DH: Writing – review & editing. BA: Writing – review & editing. GC: Writing – review & editing. DG: Conceptualization, Writing – original draft, Writing – review & editing. BP: Funding acquisition, Writing – original draft, Writing – review & editing. PH: Conceptualization, Funding acquisition, Project administration, Resources, Writing – original draft, Writing – review & editing.

Funding

The author(s) declare financial support was received for the research and/or publication of this article. NCI U01CA260446

Conflict of interest

The authors declare that the research was conducted in the absence of any commercial or financial relationships that could be construed as a potential conflict of interest.

Generative AI statement

The author(s) declare that Generative AI was used in the creation of this manuscript in editing of this manuscript.

Any alternative text (alt text) provided alongside figures in this article has been generated by Frontiers with the support of artificial intelligence and reasonable efforts have been made to ensure accuracy, including review by the authors wherever possible. If you identify any issues, please contact us.

Publisher's note

All claims expressed in this article are solely those of the authors and do not necessarily represent those of their affiliated organizations, or those of the publisher, the editors and the reviewers. Any product that may be evaluated in this article, or claim that may be made by its manufacturer, is not guaranteed or endorsed by the publisher.

References

1. Baskar R, Lee KA, Yeo R, Yeoh KW. Cancer and radiation therapy: current advances and future directions. *Int J Med Sci*. (2012) 9:193–9. doi: 10.7150/ijms.3635

2. Daugherty E, Zhang Y, Xiao Z, Mascia A, Sertorio M, Woo J, et al. FLASH radiotherapy for the treatment of symptomatic bone metastases in the thorax (FAST-02): protocol for a prospective study of a novel radiotherapy approach. *Radiat Oncol*. (2024) 19:34. doi: 10.1186/s13014-024-02419-4

3. Matuszak N, Suchorska WM, Milecki P, Kruszyna-Mochalska M, Misiarz A, Pracz J, et al. FLASH radiotherapy: an emerging approach in radiation therapy. *Rep Pract Oncol Radiother*. (2022) 27:344–51. doi: 10.5603/RPOR.a2022.0038

4. No HJ, Wu Y, ML D, Manjappa R, Skinner L, Ashraf MR, et al. Clinical linear accelerator-based electron FLASH: pathway for practical translation to FLASH clinical trials. *Int J Radiat Oncol*. (2023) 117:482–92. doi: 10.1016/j.ijrobp.2023.04.011

5. Montay-Gruel P, Acharya MM, Petersson K, Alikhani L, Yakkala C, Allen BD, et al. Long-term neurocognitive benefits of FLASH radiotherapy driven by reduced reactive oxygen species. *Proc Natl Acad Sci*. (2019) 116:10943–51. doi: 10.1073/pnas.1901777116

6. Vorhees CV, Vatner RE, Williams MT. Review of conventional and high dose rate brain radiation (FLASH): neurobehavioural, neurocognitive and assessment issues in rodent models. *Clin Oncol*. (2021) 33:e482–91. doi: 10.1016/j.clon.2021.09.002

7. Williams MT, Sugimoto C, Regan SL, Pitzer EM, Fritz AL, Sertorio M, et al. Cognitive and behavioral effects of whole brain conventional or high dose rate (FLASH) proton irradiation in a neonatal Sprague Dawley rat model. *Lee J Ed PloS One*. (2022) 17:e0274007. doi: 10.1371/journal.pone.0274007

8. Soto LA, Casey KM, Wang J, Blaney A, Manjappa R, Breitkreutz D, et al. FLASH irradiation results in reduced severe skin toxicity compared to conventional-dose-rate irradiation. *Radiat Res*. (2020) 194(6). doi: 10.1667/RADE-20-00090

9. Fouillade C, Curras-Alonso S, Giuranno L, Quelennec E, Heinrich S, Bonnet-Boissinot S, et al. FLASH irradiation spares lung progenitor cells and limits the incidence of radio-induced senescence. *Clin Cancer Res*. (2020) 26:1497–506. doi: 10.1158/1078-0432.CCR-19-1440

10. Levy K, Natarajan S, Wang J, Chow S, Eggold JT, Loo PE, et al. Abdominal FLASH irradiation reduces radiation-induced gastrointestinal toxicity for the treatment of ovarian cancer in mice. *Sci Rep*. (2020) 10:21600. doi: 10.1038/s41598-020-78017-7

11. Bell BI, Velten C, Pennock M, Kang M, Tanaka KE, Selvaraj B, et al. Whole abdominal pencil beam scanned proton FLASH increases acute lethality. *Int J Radiat Oncol*. (2025) 121:493–505. doi: 10.1016/j.ijrobp.2024.09.006

12. El Khatib M, Van Slyke AL, Velalopoulou A, Kim MM, Shoniyozov K, Allu SR, et al. Ultrafast tracking of oxygen dynamics during proton FLASH. *Int J Radiat Oncol*. (2022) 113:624–34. doi: 10.1016/j.ijrobp.2022.03.016

13. Clark MA, Tavakkoli AD, Petusseau AF, Scorzo AV, Kheirollah A, Davis SC, et al. Dynamic oxygen assessment techniques enable determination of anesthesia's impact on tissue. *Res Sq*. (2024) 3:rs–4751349. doi: 10.21203/rs.3.rs-4751349/v1

14. Jansen J, Knoll J, Beyreuther E, Pawelke J, Skuza R, Hanley R, et al. Does FLASH deplete oxygen? Experimental evaluation for photons, protons, and carbon ions. *Med Phys*. (2021) 48:3982–90. doi: 10.1002/mp.14917

15. Sunnerberg JP, Zhang R, Gladstone DJ, Swartz HM, Gui J, Pogue BW. Mean dose rate in ultra-high dose rate electron irradiation is a significant predictor for O2 consumption and H2O2 yield. *Phys Med Biol*. (2023) 68:165014. doi: 10.1088/1361-6560/ace877

16. Sunnerberg JP, Tavakkoli AD, Petusseau AF, Daniel NJ, Sloop AM, Schreiber W, et al. Oxygen consumption *in vivo* by ultra-high dose rate electron irradiation depends upon baseline tissue oxygenation. *Int J Radiat Oncol Biol Phys*. (2025) 121:1053–62. doi: 10.1016/j.ijrobp.2024.10.018

17. Scarmelotto A, Delprat V, Michiels C, Lucas S, Heuskin AC. The oxygen puzzle in FLASH radiotherapy: A comprehensive review and experimental outlook. *Clin Transl Radiat Oncol*. (2024) 49:100860. doi: 10.1016/j.ctro.2024.100860

18. Tavakkoli AD, Clark MA, Kheirollah A, Sloop AM, Soderholm HE, Daniel NJ, et al. Anesthetic oxygen use and sex are critical factors in the FLASH sparing effect. *Adv Radiat Oncol*. (2024) 9:101492. doi: 10.1016/j.adro.2024.101492

19. Blevins CE, Celeste NA, Marx JO. Effects of oxygen supplementation on injecta ble and inhalant anesthesia in C57BL/6 mice. *J Am Assoc Lab Anim Sci JAALAS*. (2021) 60:289–97. doi: 10.30802/AALAS-JAALAS-20-000143

20. Adrian G, Konradsson E, Lempart M, Bäck S, Ceberg C, Petersson K. The FLASH effect depends on oxygen concentration. *Br J Radiol*. (2020) 93:20190702. doi: 10.1259/bjr.20190702

21. Iturri L, Bertho A, Lamirault C, Brisebard E, Juchaux M, Gilbert C, et al. Oxygen supplementation in anesthesia can block FLASH effect and anti-tumor immunity in conventional proton therapy. *Commun Med*. (2023) 3:1–13. doi: 10.1038/s43856-023-00411-9

22. Esipova TV, Karagodov A, Miller J, Wilson DF, Busch TM, Vinogradov SA. Two new "Protected" Oxyphors for biological oximetry: properties and application in tumor imaging. *Anal Chem*. (2011) 83:8756–65. doi: 10.1021/ac2022234

23. Renard D, Clavier T, Gourcerol G, Desprez C. Impact of anesthesia drugs on digestive motility measurements in humans: A systematic review. *Neurogastroenterol Motil*. (2024) 36:e14855. doi: 10.1111/nmo.14855

24. Pogue BW, Thomas WS, Tavakkoli AD, Jarvis LA, Hoopes PJ. Major contributors to FLASH sparing efficacy emerge from murine skin studies: dose rate, total dose per fraction, anesthesia and oxygenation. *Front Oncol*. (2024) 14:1414584. doi: 10.3389/fonc.2024.1414584

frontiers | Frontiers in Oncology

TYPE Original Research
PUBLISHED 01 September 2025
DOI 10.3389/fonc.2025.1645834

Check for updates

OPEN ACCESS

EDITED BY
Poonam Yadav,
Northwestern University, United States

REVIEWED BY
Peta Lonski,
Peter MacCallum Cancer Centre, Australia
Neda Milosavljevic,
University of Kragujevac, Serbia

*CORRESPONDENCE
Yuexin Guo
guoyx0371@126.com

RECEIVED 12 June 2025
ACCEPTED 04 August 2025
PUBLISHED 01 September 2025

CITATION
Wang H, Pi Y, Liu C, Wang P, Long C, Qi Y, Kong F, Han B, Wang F, Jia F, Liu L, Xu D, Ji T, Wu H and Guo Y (2025) Dosimetric assessment of TomoDirect radiotherapy and TomoHelical radiotherapy in the clinical implementation of total skin irradiation. *Front. Oncol.* 15:1645834. doi: 10.3389/fonc.2025.1645834

COPYRIGHT
© 2025 Wang, Pi, Liu, Wang, Long, Qi, Kong, Han, Wang, Jia, Liu, Xu, Ji, Wu and Guo. This is an open-access article distributed under the terms of the Creative Commons Attribution License (CC BY). The use, distribution or reproduction in other forums is permitted, provided the original author(s) and the copyright owner(s) are credited and that the original publication in this journal is cited, in accordance with accepted academic practice. No use, distribution or reproduction is permitted which does not comply with these terms.

Dosimetric assessment of TomoDirect radiotherapy and TomoHelical radiotherapy in the clinical implementation of total skin irradiation

Haiyang Wang[1], Yifei Pi[1], Chunbo Liu[1], Panfeng Wang[2], Chengzhang Long[2], Yaping Qi[3], Fanyang Kong[1], Bin Han[1], Fangna Wang[1], Fei Jia[1], Lele Liu[1], Dandan Xu[1], Tengfei Ji[1], Huijuan Wu[1] and Yuexin Guo[1]*

[1]Department of Radiation Oncology, The First Affiliated Hospital of Zhengzhou University, Zhengzhou, China, [2]Medical and Ionizing Radiation Metrology Testing Research Center, Henan Provincial Institute of Metrology and Testing Sciences, Zhengzhou, China, [3]Division of Ionizing Radiation Metrology, National Institute of Metrology, Beijing, China

Purpose: This study aims to compare the technical characteristics of TomoDirect (TD) radiotherapy and TomoHelical (HT) radiotherapy in total skin irradiation (TSI) applications. We conducted a comprehensive evaluation of dosimetric parameters and delivery efficiency in TD-based treatment planning to establish clinical guidelines for modality selection in mycosis fungoides.

Materials and methods: This retrospective study analyzed eight mycosis fungoides patients treated with TSI between June 2020 and June 2023, utilizing a 5-mm-thick diving suit bolus to enhance the skin dose distribution with a prescription of 24 Gy delivered in 20 fractions (five fractions/week). Thermoplastic masks (3 mm in thickness) were used for head/neck and thorax/abdomen region immobilization, while the lower limbs were immobilized in a vacuum cushion. Comparative treatment planning employed both TD and HT techniques, with TD plans utilizing 7, 9, and 11 equally spaced coplanar beams (0° starting angle). Ring0, Ring1, Ring2, Ring3, and Ring4, which were 1-cm thick away from the planning target volume (PTV) at distances of 0, 1, 2, 3, and 4 cm, and other normal tissues (NT) were generated. The auxiliary structures were completely blocked during planning. The other plan parameters remained consistent. Plan quality assessment compared the target mean dose (PTVmean), homogeneity index (HI), conformity index (CI), and organ-at-risk (OAR) doses between techniques, with additional evaluation of treatment delivery efficiency through time comparisons.

Results: When using NT, Ring4, and Ring3 auxiliary structures in complete-block mode, TD plans with more than nine beams demonstrate comparable PTVmean, HI, and CI-to-HT plans, whereas TD plans of less than nine beams exhibit inferior target coverage. Neither HT nor TD plans meet the clinical requirements when Ring2, Ring1, or Ring0 structures are fully blocked. Regarding OAR sparing, nine-beam TD and HT plans show equivalent maximum doses to optical structures (lenses, optic nerves, and chiasm) and mean doses to other OARs (oral cavity, salivary glands, lungs, heart, liver, and kidneys) with NT/Ring4/Ring3 blocking. However, both techniques fail to satisfy the OAR constraints when Ring2/Ring1/

Ring0 are blocked. Treatment delivery times remain similar between modalities with NT/Ring4/Ring3 blocking, but the efficiency significantly decreases for both when deeper structures (Ring2/Ring1/Ring0) are included in the blocking protocol.

Conclusion: When employing complete-block mode for NT, Ring4, and Ring3 structures, TD plans utilizing more than nine beams demonstrate comparable dosimetric performance to HT plans in terms of target coverage, OAR sparing, and treatment delivery efficiency. However, both modalities fail to meet the clinical dosimetric requirements when deeper-seated structures (Ring2/Ring1/Ring0) are included in the blocking protocol.

KEYWORDS

TomoDirect, TomoHelical, total skin irradiation, auxiliary ring structures, complete-block mode

1 Introduction

Cutaneous T-cell lymphoma (CTCL), a rare group of mature T-cell malignancies primarily involving the skin, accounts for approximately 71% of primary cutaneous lymphomas, with mycosis fungoides (MF) being the most prevalent subtype (MF) (1). According to the latest data from the National Cancer Institute's "Surveillance Epidemiology and Outcomes", CTCL (mainly MF) is currently growing at a rate of 9.6 cases/million per year, and the incidence rate accounts for approximately 50% of CTCL (2). CTCL is usually highly radiosensitive and has traditionally been treated with total skin electron irradiation (TSEI), which is also clinically considered one of the most effective methods for treating CTCL (3). The conventional Stanford six-field technique presents practical limitations due to extended treatment distances and required patient repositioning (4). With the continuous development of radiotherapy technology, especially with the emergence of HT (5), its unique 360° helical irradiation and pneumatic multileaf collimator can realize ultra-long target treatment (160 cm × 40 cm) and dose sculpture distribution, which is very suitable for the treatment of long and complex targets, such as multiple metastasis irradiation, cranio-spinal irradiation, total body irradiation, total bone marrow irradiation, etc. (6), and it also solves well the drawbacks existing in traditional TSEI. With the gradual development of HT technology, TD treatment technology has been added. Its fixed beam intensity modulation is similar to that of conventional accelerators, but it has the characteristics of up to 12 fixed beams. TD irradiation is intensity-modulated radiation therapy of HT (7), wherein the accelerator head remains fixed at a specific angle while the treatment couch moves along the head–foot direction of the target. This modulation adjusts the intensity of the radiation reaching the target and OARs by controlling the opening and closing MLC to meet clinical and OAR dose requirements. Lin et al. (8) were the first to conduct effectiveness tests on the dose buildup effect of neoprene wetsuits using anthropomorphic phantoms. Hsieh et al. (9) were the first to use a 3-mm diving suit as a bolus to achieve total skin helical tomotherapy (TSHT). Similarly, Haraldsson et al. (10) also used a diving suit as a bolus to perform TSHT, while Wang et al. (11) utilized a 3D-printed total skin bolus for the same purpose. Currently, there is no feasibility study on total skin irradiation using TD irradiation mode. This article will compare the dosimetric differences between TD treatment plans and HT treatment plans with different numbers of beams in TSI treatment by using different auxiliary ring structures to evaluate which plan can achieve better protection of OARs while ensuring target dose distribution, thereby providing more options for the clinical implementation of TSI technology.

2 Materials and methods

2.1 Patients' clinical characteristics

Eight patients with mycosis fungoides underwent total skin irradiation (TSI) at the Radiation Therapy Department of the First Affiliated Hospital of Zhengzhou University between June 2020 and June 2023. The cohort comprised five male and three female patients (Table 1), with an age range of 35–70 years (mean: 59 years), height range of 150–178 cm (mean: 164.8 cm), and weight range of 40–95 kg (mean: 65.1 kg). All methods were carried out in accordance with relevant guidelines and regulations. All experimental protocols were approved by the Zhengzhou University Committee on Ethics Review of Life Sciences (approval number: 2024-KY-0076). Informed consent was obtained from all subjects and/or their legal guardian(s).

2.2 Bolus

Eight patients were dressed in a 5-mm diving suit bolus. The diving suits were tailored according to the patient's external shape to achieve a tight wrap around the body.

TABLE 1 Characteristics of the eight patients.

Patient no.	Age (years)	Sex	Diagnosis	Height (cm)	Body weight (kg)	Treatment technique
1	31	M	MF	170	95	TSHT
2	49	M	MF	178	78	TSHT
3	42	M	MF	165	65	TSHT
4	38	F	MF	150	55	TSHT
5	52	F	MF	160	51	TSHT
6	60	M	MF	168	63	TSHT
7	65	F	MF	155	40	TSHT
8	56	M	MF	172	74	TSHT

2.3 Immobilization

Patients dressed in 5-mm diving suits were immobilized in supine position. Thermoplastic masks (3 mm in thickness) were used for head/neck and thorax/abdomen region immobilization, while the lower limbs were immobilized in a vacuum cushion, ensuring optimal patient positioning and dosimetric accuracy. The upper anatomical reference ("upper mark") was placed at the umbilicus level, and the lower anatomical reference ("lower mark") was positioned at the patella level. The segment line made of lead was located approximately 10 cm above the patella as the boundary between the upper and lower targets.

2.4 Image acquisition at simulation

Computed tomography (CT) scans (Brilliance CT Big Bore, Philips Healthcare, Cleveland, OH, USA) were performed under the following conditions: a scan and reconstruction slice thickness of 5 mm. The patients were scanned in the upper and lower segments—the upper segment was scanned from the skull vertex to 10 cm below the lead wire boundary, and the lower segment was scanned from the toes to 10 cm above the boundary. This 20-cm overlap region (10 cm above and below the wire) ensured proper dose blending between treatment segments while accounting for setup variations and beam penumbra.

2.5 Delineation of target volumes and organs at risk

The CT images were transferred to the eclipse 15.6 workstation (Varian Medical Systems, Inc. Palo Alto, CA, USA). The target volumes and OARs for all patients were delineated by radiation oncologists based on the planning CT according to the ICRU50 (12) and ICRU62 reports (13). The clinical target volume (CTV) was defined as the region between the skin surface and 5 mm beneath it (14). To account for setup errors and the dose buildup effect, the CTV was initially expanded uniformly by 5 mm to create a preliminary PTV. However, since this expansion could extend beyond the body contour (e.g., into air), the outer region of the PTV was retracted by 3 mm to ensure anatomically plausible boundaries while maintaining an adequate target coverage. This approach balanced the geometric uncertainties with physical feasibility, optimizing dose delivery to superficial tissues. OARs were delineated based on the ICRU 83 report (15), including the total bone marrow (head and neck bones, upper limb bones, ribs, spine, pelvis, lower limb bones), eyeballs, lens, parotid, lungs, heart, kidneys, liver, bladder, rectum, spinal cord, brainstem, etc. The junction between the upper and lower sections of the total body irradiation (TBI) had been studied in our previous publication (16). The dose in the overlap region was mostly homogeneous when the distance was equal to the FW.

2.6 Plan designs

The planned CT and contoured structures of each patient were transferred to the treatment planning workstation (version 5.1.6; Accuray, Sunnyvale, CA, USA) for preparation. The dose prescription was 24 Gy in 20 fractions (five fractions/week). The PTV gradually retracted from 1 to 5 cm by 1 cm step to create the ring-shape auxiliary structure as Ring0, Ring1, Ring2, Ring3, Ring4, and other normal tissues (NT). The auxiliary structures were used as an assistant tool for plan optimization to achieve dose objectives. During planning, all the auxiliary structures were set to complete mode one by one. Different number of beam plans for TD and HT were designed. The TD plans with 7, 9, and 11 equally spaced beams were created, starting at an angle of 0°. The planning required at least 95% of the target to receive the prescription dose, with FW of 5 and 2.5 cm, pitches of 0.287 and 0.215, and MF of 4 and 3. The dose grid was 0.195 cm × 0.195 cm (Figure 1). Plans were designed by combining different parameters and auxiliary structures. All other parameters remained consistent, and the final dose calculation was performed after 100 iterations for each plan.

2.7 Assessment of plan parameters

The parameters assessed for the patients included PTVmean, HI, and CI of the target volume. At least 95% of the target volumes reached the prescribed dose. HI was calculated using the formula, HI =

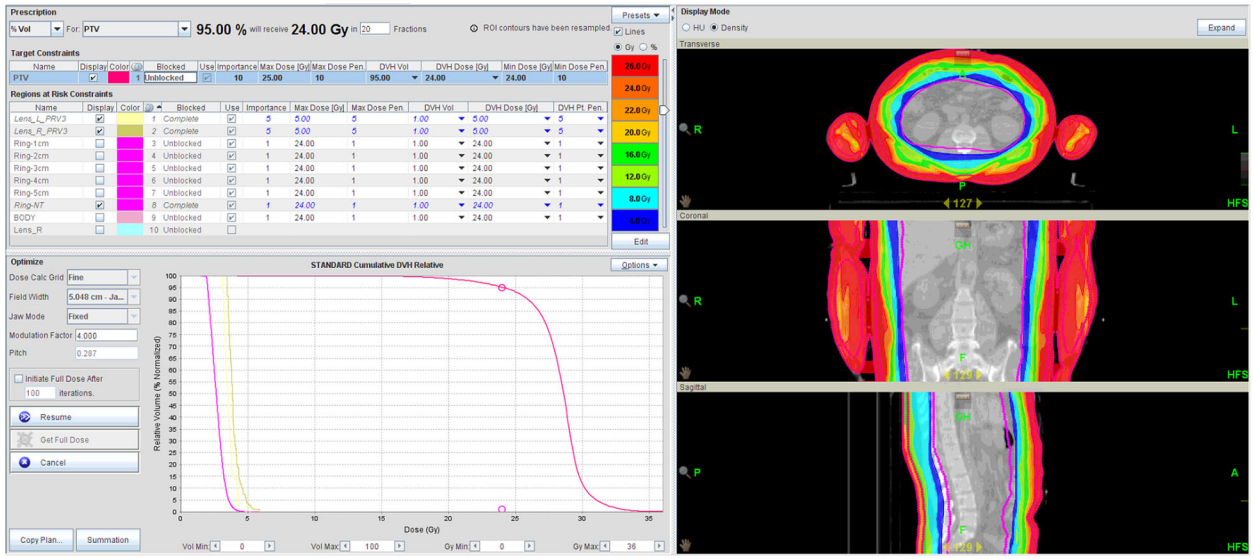

FIGURE 1
TSI-TD treatment plan for the patient.

D5%/D95%, where D5% is the dose received by 5% of the PTV volume, and D95% is the dose received by 95% of the PTV volume. An HI value greater than 1 represents the heterogeneity dose distribution of the target volume. CI was obtained using the following Paddick equation (17), $CI = VT_{,ref}/VT \times VT_{,ref}/V_{ref}$, where $VT_{,ref}$ is the target volume covered by the prescription isodose (cm^3), V_{ref} is the volume encompassed by the prescription isodose (cm^3), and VT is the target volume (cm^3). If the CI value is closer to 1, the better the dose conformity of the target volume is.

2.8 Statistical analysis

All statistical analyses were conducted using SPSS Statistics (version 19.0; IBM Corp., Armonk, NY), with continuous variables presented as mean ± standard deviation (mean ± SD). Graphical representations were generated using OriginPro (version 8.0; OriginLab Corp., Northampton, MA, USA).

3 Results

3.1 Comparisons of dosimetric parameters of target

Figure 2A demonstrates that TD plans utilizing 11 beams and 9 beams achieve prescription dose coverage equivalent to HT plans when NT, Ring4, and Ring3 structures are set to complete-block mode. At the same time, HI (Figure 2B) and CI (Figure 2C) are consistent with the abovementioned results. However, the TD plan with seven beams in the complete mode using the Ring2 auxiliary structure cannot achieve the same prescription dose as the HT plan and is also consistent with the results of HI and CI. This consistency aligns with previous research indicating a consistent relationship between auxiliary structures and target distance, ensuring that when the auxiliary structure distance from the target exceeds or equals 3 cm in the complete mode, the target dose meets the clinical requirements. Our analysis confirmed comparable target coverage between thermoplastic mask-immobilized regions (head/neck/thorax/abdomen) and diving-suit-only areas (lower limbs), with no statistically significant differences (Table 2) in PTVmean (24.1 ± 0.3 Gy vs. 23.9 ± 0.4 Gy, $p = 0.15$) or D95% coverage (96.2% ± 1.1% vs. 95.8% ± 1.3%, $p = 0.22$).

3.2 Comparisons of dosimetric parameters of OARs

Figures 3A–H show the maximum or average doses to the left and right lens, optic nerves, chiasm, oral cavity, bilateral parotid glands, lungs, heart, liver, and bilateral kidneys under the NT, Ring4, Ring3, and Ring2 auxiliary structures in the complete mode, with HT irradiation as well as with the 11-, 9-, and 7-beam TD plans. From the figures, it is apparent that to ensure that organ-at-risk doses remain within clinically acceptable ranges, auxiliary structures must be selected as NT, Ring4, or Ring3. Additionally, the 11- and 9-beam TD plans align with HT plans in terms of OAR doses. However, the Ring2 auxiliary structure and seven-beam TD plan fail to meet the clinical requirements.

3.3 Comparisons of beam on time and gantry period

In Figure 4A, when the auxiliary structures are NT, Ring4, and Ring3, there is little variation in the treatment delivery time between

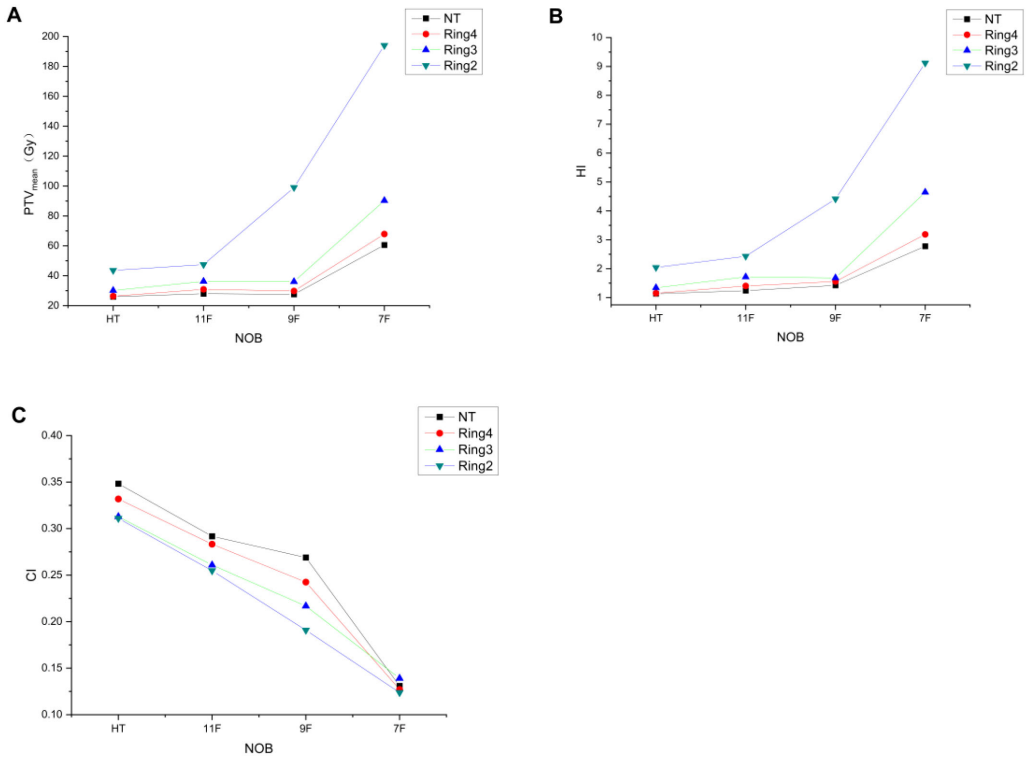

FIGURE 2
Trends of PTVmean **(A)**, HI **(B)**, and CI **(C)** variation with the decreased number of beams (NOB) and irradiation mode under different auxiliary structures.

HT plans and TD plans with 11 and 9 beams, whereas the treatment delivery time significantly increases for the TD plan with seven beams. For the auxiliary structure Ring2, both HT plans and multi-beam TD plans show a significant increase in treatment delivery time, which can no longer meet the clinical treatment demands. In Figure 4B, he MF values of the TD plan are significantly higher than those of the HT plan, with no apparent pattern of variation.

In summary, during TSI treatment, conventional HT mode can be utilized along with TD plans featuring auxiliary structures such as NT, Ring4, and Ring3 with 9 or 11 beams, yielding consistent outcomes. This offers patients requiring TSI treatment a broader range of therapeutic options.

4 Discussion

TD irradiation technology is currently a hot topic in clinical treatment research and application. Primarily, its application in breast cancer irradiation has garnered significant attention. This includes studies on TD irradiation technology in the treatment of unilateral breast cancer (18, 19) as well as its application in the treatment of bilateral breast cancer (20, 21). Additionally, research has also explored its use in cranio-spinal irradiation treatments (22, 23), esophageal cancer therapy (24, 25), and TBI treatment (26, 27). TD irradiation technology is increasingly being applied clinically. However, there are currently no reports of clinical studies on the application of TD in TSI treatment.

Our team previously studied the relationship between different auxiliary structures and outcomes in TSI-HT technology, and we systematically investigated the effects by setting distances from the target at 0, 1, 2, 3, and 4 cm and the remaining volume to generate auxiliary structures Ring0, Ring1, Ring2, Ring3, Ring4, and NT with a uniform thickness of 1 cm each. The auxiliary structures were sequentially set to complete mode in the treatment plan design. The results revealed that when using auxiliary structures with a distance from the target greater than or equal to 3 cm and employing the complete mode, PTVmean, CI, and HI met the clinical requirements. As the distance between the auxiliary structures and the target increased gradually, the treatment delivery time decreased accordingly, but the volume of normal tissues receiving excessive radiation increased. Conversely, when the distance from the target to the auxiliary structures was less than 3 cm and the complete mode was applied, the clinical requirements could not be met (14). In this study, we focused on investigating the effects of 7, 9, and 11

TABLE 2 Comparison of dosimetric parameters between thermoplastic mask regions and diving suit regions.

Dosimetric parameters	Thermoplastic masked regions	Diving suit-only regions	P
PTVmean	24.1 ± 0.3 Gy	23.9 ± 0.4 Gy	0.15
D95% coverage	96.2% ± 1.1%	95.8% ± 1.3%	0.22

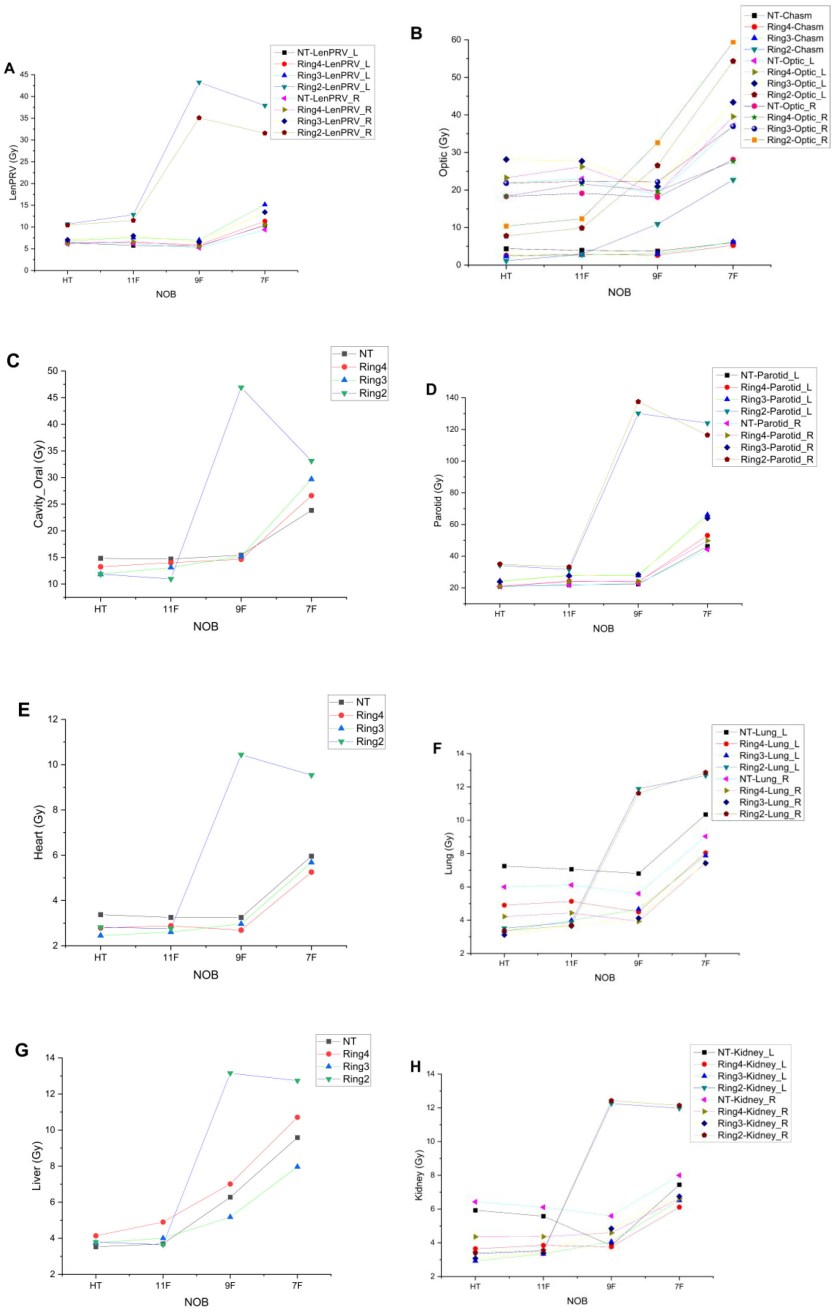

FIGURE 3
Trends of OAR variation with the decreased NOBs and irradiation mode under different auxiliary structures. LenPRV **(A)**, Optic **(B)**, Cavity_Oral **(C)**, Parotids **(D)**, Heart **(E)**, Lungs **(F)**, Liver **(G)** and Kidneys **(H)**.

equalized beams, considering the influence of auxiliary ring structures. We aimed to explore whether TD technology and HT technology have advantages in terms of radiation utilization and treatment delivery time, thereby providing more options for radiotherapy techniques in clinical TSI treatment.

The tomotherapy system has advanced to the fourth generation. The first generation lacks a fixed-beam irradiation mode, while fixed-beam irradiation functionality has been incorporated since the second generation. The functions that can be achieved are the same as those of conventional accelerators: three-dimensional conformal radiotherapy, intensity-modulated radiation therapy, and volumetric-modulated arc therapy. However, their unique attributes differentiate them from conventional accelerators in terms of application and clinical outcomes (7). The institution currently employs a second-generation HT model capable of implementing the aforementioned three treatment modalities. The research discussed in this article is applicable to the second, third, and fourth-generation models. However, since the first-generation HT does not have the described functions, the abovementioned research results are not applicable.

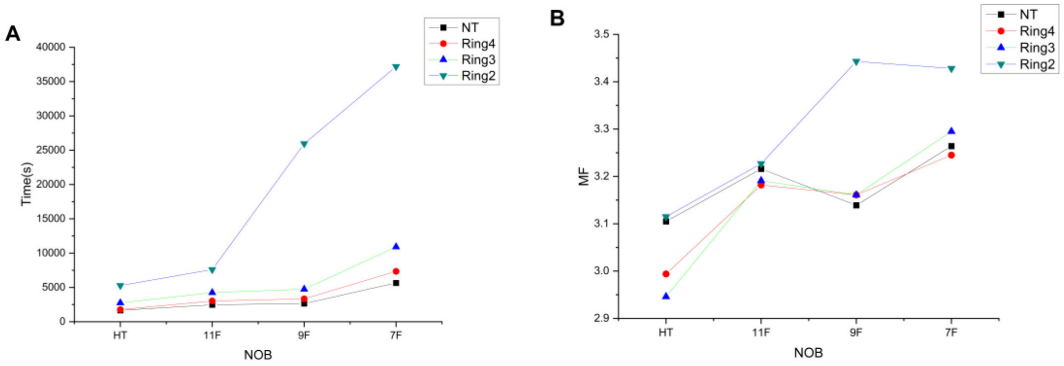

FIGURE 4
Trends of time **(A)** and MF **(B)** variations with the decreased NOBs and irradiation mode under different auxiliary structures.

The TD treatment technique can accommodate up to 12 treatment beams (28), considering that even-numbered beams lead to intersecting beams, which are unfavorable for intensity modulation. Therefore, this study did not investigate them. The focus of this research was on odd-numbered equally spaced beams with fewer than 12 beams. There are reports that the starting angle has no effect on the results in TBI-TD research. Therefore, the starting angles of all fixed beams in this study all start from 0°.

All patients wore a 5-mm diving suit bolus. Unlike previous studies by Hsieh et al. (9), who used a 3-mm diving suit bolus, or Haraldsson et al. (10), who used a 7-mm diving suit bolus, we opted for the most common and widely available 5-mm diving suit bolus. This choice enhances the convenience of procurement and ensures the generalizability of the research findings. While different thicknesses of diving suits may yield minor variations in results, the overall impact is deemed insignificant, thus allowing for broader applicability of the conclusions. However, when considering different materials for a bolus, especially those with significant density variations, further research is needed to confirm conclusions.

The PTV gradually moves inward to form auxiliary structures, creating Ring0, Ring1, Ring2, Ring3, Ring4, and NT auxiliary structures with thicknesses of 1 cm each at distances of 0, 1, 2, 3, and 4 cm and the remaining volume, respectively (14). These auxiliary structures do not represent OARs or the target but are solely used as tools for plan optimization, enabling dose constraints within the body and serving as part of the plan evaluation to study the trend of auxiliary structure dose distribution with varying distances. Generated by moving the PTV inward, Ring0 through Ring4 and the NT auxiliary structure are created with a uniform thickness of 1 cm at specified distances from the target. These structures are generated according to specific requirements on the treatment planning system and remain unchanged due to human efforts, thus ensuring the universality and representativeness of the research findings and their clinical applicability.

This study generated a total of five rings: Ring0, Ring1, Ring2, Ring3, and Ring4 with a thickness of 1 cm and the remaining volume NT. The decision to generate only five rings instead of more auxiliary rings was primarily because the smallest cross-section of the head and neck region is typically approximately 10 cm, making it impractical to generate additional auxiliary rings. It is also noted that the longest distance auxiliary structure used in related research is 5 cm (29). The auxiliary ring structures selected in this study are all 1 cm in thickness, without generating thinner auxiliary rings (such as 8, 5, and 3 mm). The main consideration is that while thinner auxiliary structures might provide more detailed results compared to the 1-cm-thick ones, the changing trend of the research results should be consistent. Thus, this article did not conduct research on thinner auxiliary rings.

This study only collected data from Ring2, Ring3, Ring4, and NT, excluding data from Ring0 and Ring1. This omission is primarily due to the inability to optimize the treatment planning for Ring0 and Ring1 auxiliary structures when used in the complete mode, as their proximity to the target is too close. Therefore, statistical data for Ring0 and Ring1 are not available.

All patients used a 5-mm diving suit bolus. Currently, the most commonly used diving suit on the market is the 5-mm-thick one, which is readily available and offers good material uniformity. Therefore, this conclusion has broader applicability. For the use of other materials as a bolus, especially those with significant differences in density and thickness, this conclusion may not be applicable and requires further investigation.

Previous studies have employed varying bolus thicknesses for TSI treatment. Hsieh et al. (9) used a 3-mm diving suit, achieving an adequate skin dose but with potential underdosing in deeper subcutaneous tissues due to reduced bolus thickness. Haraldsson et al. (10) utilized a 7-mm diving suit, which improved the dose homogeneity but increased the scatter dose to normal tissues. Our study adopted a 5-mm diving suit as a balanced choice, ensuring reliable target coverage while minimizing excessive scatter. This thickness is widely available and clinically practical, with results showing comparable target coverage to HT plans (e.g., PTVmean within ±2% of prescription dose). Minor variations in bolus thickness (3–7 mm) did not significantly alter the clinical outcomes, supporting the generalizability of our protocol.

Our TD-based TSI protocol utilizing 9 or 11 beams with optimized auxiliary structures (Ring3/Ring4/NT) demonstrated clinically acceptable conformity (CI: 0.90 ± 0.03) and homogeneity (HI: 1.05 ± 0.02) indices comparable to HT while reducing the treatment time by 15%–20%. The strategy of

positioning auxiliary structures ≥3 cm from the target effectively controlled high-dose spillage to normal tissues (V20Gy reduction, $p < 0.05$), validating the protocol's efficiency and dosimetric reliability for clinical implementation.

The study systematically evaluated odd-numbered beam configurations (7/9/11) to avoid modulation challenges from beam intersections, establishing 9 and 11 beams as the optimal range for TD-based TSI. By standardizing the 5-mm bolus and auxiliary ring methodology (1-cm increments), we provide a reproducible framework that expands the treatment options, particularly for centers lacking tomotherapy capabilities. This approach not only maintains dosimetric quality but also improves operational efficiency, offering a viable alternative to HT with comparable clinical outcomes.

It is important to acknowledge several limitations in this study. Firstly and most significantly, the study lacks *in vivo* dosimetry verification. We did not use Thermoluminescent Dosimeters (TLDs), Optically Stimulated Luminescence Dosimeters (OSLDs), or films to measure the delivered surface dose, which is a critical component for validating any TSI protocol. While rigorous immobilization and daily Megavoltage Cone Beam Computed Tomography (MVCT) were employed to ensure geometric accuracy, these measures do not substitute for direct dose measurement. Secondly, a formal robustness analysis, which would involve evaluating the plan's sensitivity to setup uncertainties and patient motion, was not performed. The primary scope of this work was to investigate the dosimetric feasibility of TD planning, and these validation steps were beyond that initial scope. Furthermore, our conclusions are drawn from a small patient cohort ($n = 8$), a limitation dictated by the rarity of mycosis fungoides requiring TSI and the preliminary nature of this technical investigation. These limitations together underscore that while our findings establish a promising planning methodology for TD-based TSI, further comprehensive validation—including phantom-based measurements, *in vivo* dosimetry, and robustness analysis—is essential before this technique can be broadly adopted in clinical practice.

While this study primarily focused on establishing the technical feasibility and dosimetric performance of TD-based TSI treatment, we fully agree that investigating patient-specific characteristics (e.g., anatomical variations, disease subtypes, or individual radiosensitivity) could yield valuable insights for personalized treatment optimization.

In conclusion, to achieve results comparable to HT technology in TSI treatment, TD plans with 9 or 11 beams can be utilized, along with auxiliary structures such as NT, Ring4, and Ring3. This study highlights the applicability of TD technology in TSI treatment, thereby offering a wider range of treatment options for TSI therapy.

Data availability statement

The original contributions presented in the study are included in the article/supplementary material. Further inquiries can be directed to the corresponding author.

Author contributions

HYW: Methodology, Writing – original draft. YP: Methodology, Writing – original draft. CBL: Methodology, Writing – original draft. PW: Writing – review & editing. CZL: Writing – review & editing. YQ: Writing – review & editing. FK: Writing – review & editing. BH: Writing – review & editing. FW: Writing – review & editing. FJ: Writing – review & editing. LL: Writing – review & editing. DX: Writing – review & editing. TJ: Writing – review & editing. HJW: Writing – review & editing. YG: Writing – review & editing.

Funding

The author(s) declare financial support was received for the research and/or publication of this article. This study was supported by Henan Province Medical Education Research Project (No. WJLX2024061); Key Scientific Research Projects of Henan Provincial Colleges and Universities (No. 23B320004); and Henan Province Medical Science and Technology Research Program Provincial and Ministry Co-constructed Youth Project (No. SBGJ202103073).

Acknowledgments

The authors thank and acknowledge the support from the First Affiliated Hospital of Zhengzhou University.

Conflict of interest

The authors declare that the research was conducted in the absence of any commercial or financial relationships that could be construed as a potential conflict of interest.

Generative AI statement

The author(s) declare that no Generative AI was used in the creation of this manuscript.

Any alternative text (alt text) provided alongside figures in this article has been generated by Frontiers with the support of artificial intelligence and reasonable efforts have been made to ensure accuracy, including review by the authors wherever possible. If you identify any issues, please contact us.

Publisher's note

All claims expressed in this article are solely those of the authors and do not necessarily represent those of their affiliated organizations, or those of the publisher, the editors and the reviewers. Any product that may be evaluated in this article, or claim that may be made by its manufacturer, is not guaranteed or endorsed by the publisher.

References

1. Willemze R, Jaffe ES, Burg G, Cerroni L, Berti E, Swerdlow SH, et al. WHO-EORTC classification for cutaneous lymphomas. *Blood*. (2005) 105:3768–85. doi: 10.1182/blood-2004-09-3502

2. Yu JB, Blitzblau RC, Decker RH, Housman DM, Wilson LD. Surveillance, epidemiology, and end results (SEER) database analysis of stage IE primary CD30+ Cutaneous T-cell lymphoma (PCCTCL). *Int J Radiat Oncol Biol Phys*. (2007) 69:S536–7. doi: 10.1016/j.ijrobp.2007.07.1777

3. Van Vloten WA, De Vroome H, Noordijk EM. Total skin electron beam irradiation for cutaneous T-cell lymphoma (mycosis fungoides). *Br J Dermatol*. (1985) 112:697–702. doi: 10.1111/j.1365-2133.1985.tb02340.x

4. Piotrowski T, Milecki P, Skórska M, Fundowicz D. Fundowicz total skin electron irradiation techniques: a review. *Postep Derm Alergol*. (2013) 30:50–5. doi: 10.5114/pdia.2013.33379

5. Mackie TR, Balog J, Ruchala K, Shepard D, Aldridge S, Fitchard E, et al. Tomotherap. *Semin Radiat Oncol*. (1999) 9:108–17. doi: 10.1016/s1053-4296(99)80058-7

6. Jeraj R, Mackie TR, Balog J, Olivera G, Pearson D, Kapatoes J, et al. Radiation characteristics of helical tomotherapy. *Med Phys*. (2004) 31:396–404. doi: 10.1118/1.1639148

7. Franco P, Catuzzo P, Cante D, La Porta MR, Sciacero P, Girelli G, et al. TomoDirect: an efficient means to deliver radiation at static angles with tomotherapy. *Tumori*. (2011) 97:498–502. doi: 10.1700/950.10404

8. Lin CT, Shiau AC, Tien HJ, Yeh HP, Shueng PW, Hsieh CH, et al. An attempted substitute study of total skin electron therapy technique by using helical photon tomotherapy with helical irradiation of the total skin treatment: a phantom result. *BioMed Res Int*. (2013) 2013:108794. doi: 10.1155/2013/108794

9. Hsieh CH, Shueng PW, Lin SC, Tien HJ, Shiau AC, Chou YH, et al. Helical irradiation of the total skin with dose painting to replace total skin electron beam therapy for therapy-refractory cutaneous CD4+ T-cell lymphoma. *BioMed Res Int*. (2013) 2013:1–11. doi: 10.1155/2013/717589

10. Haraldsson A, Engleson J, Bäck SÅJ, Engelholm S, Engström PE. A Helical tomotherapy as a robust low-dose treatment alternative for total skin irradiation. *J Appl Clin Med Phys*. (2019) 20:44–54. doi: 10.1002/acm2.12579

11. Wang H, Pi Y, Liu C, Wang X, Guo Y, Lu L, et al. Investigation of total skin helical tomotherapy using a 3D-printed total skin bolus. *BioMed Eng Online*. (2023) 22:57. doi: 10.1186/s12938-023-01118-7

12. ICRU. *Prescribing, Recording, and Reporting Photon Beam Therapy. ICRU Report 50*. Bethesda, MD: International Commission on Radiation Units and Measurements (1993). doi: 10.1118/1.597396

13. Wambersie A, Landberg T. ICRU report 62, prescribing, recording and reporting photon beam therapy (Supplement to ICRU report 50). *ICRU News*. (1999) 17:5–7. doi: 10.1093/jicru/os32.1.Report62

14. Wang H, Pi Y, Guo Y, et al. Influencing factors of total skin irradiation with helical tomotherapy. *Front Oncol*. (2022) 12:852345. doi: 10.3389/fonc.2022.852345

15. International Commission on Radiation Units and Measurements. *Report83. Prescribing, Recording, and Reporting Photon- Beam Intensity-Modulated Radiation Therapy (IMRT)*. Oxford: Pergamon Press (2010). doi: 10.1016/j.canrad.2011.04.003

16. Wang H, Liu J, Pi Y, Liu Q, Mi Y, Yang X, et al. Factors affecting dose distribution in the overlap region of two-segment total body irradiation by helical tomotherapy. *Radiat Oncol*. (2020) 15:1–7. doi: 10.1186/s13014-020-01698-x

17. Singh VP, Kansal S, Vaishya S, Julka PK, Mehta VS. Early complications following gamma knife radiosurgery for intracranial meningiomas. *J Neurosurg*. (2000) 93:57–61. doi: 10.3171/jns.2000.93.supplement_3.0057

18. Chung MJ, Kim SH, Lee JH, Suh YJ. A dosimetric comparative analysis of tomodirect and three-dimensional conformal radiotherapy in early breast cancer. *J Breast Cancer*. (2015) 18:57–62. doi: 10.4048/jbc.2015.18.1.57

19. Haciislamoglu E, Colak F, Canyilmaz E, Dirican B, Gurdalli S, Yilmaz AH, et al. Dosimetric comparison of left-sided whole-breast irradiation with 3DCRT, forward-planned IMRT, inverse-planned IMRT, helical tomotherapy, and volumetric arc therapy. *Phys Med*. (2015) 4:360–7. doi: 10.1016/j.ejmp.2015.02.005

20. Hashimoto H, Omura M, Matsui K, Mukai Y, Hongo H, Yamakabe W, et al. Tangent field technique of tomodirect improves dose distribution for whole-breast irradiation. *J Appl Clin Med Phys*. (2015) 16:5369. doi: 10.1120/jacmp.v16i3.5369

21. Franco P, Migliaccio F, Torielli P, Sciacero P, Girelli G, Cante D, et al. Bilateral breast radiation delivered with static angle tomotherapy (tomodirect): clinical feasibility and dosimetric results of a single patient. *Tumori*. (2015) 101:e4–8. doi: 10.5301/tj.5000264

22. Tsang SW, Collins M, Wong JT, Chiu GA. A dosimetric comparison of craniospinal irradiation using tomodirect radiotherapy, tomohelical radiotherapy and 3D conventional radiotherapy. *J Radiotherapy Pract*. (2017) 16:391–402. doi: 10.1017/S1460396917000309

23. Langner UW, Molloy JA, Gleason JF, Feddock JM. A feasibility study using TomoDirect for craniospinal irradiation. *J Appl Clin Med Phys*. (2013) 14:104–14. doi: 10.1120/jacmp.v14i5.4304

24. Ren R, Zhang Y, Wang H, Huang X, Zhang Q, Sun R, et al. Dosimetric comparison among TomoDirect, Helical Tomotherapy and VMAT in the treatment of upper thoracic esophageal carcinoma. *Chin J Radiological Med Prot*. (2018) 12:32–6. doi: 10.3760/cma.j.issn.0254-5098.2018.01.007

25. Zhang Y, Wang H, Huang X, Zhang Q, Ren R, Sun R, et al. Dosimetric comparison of tomodirect, helical tomotherapy, VMAT, and ff-IMRT for upper thoracic esophageal carcinoma. *Med Dos*. (2018) 5:1–6. doi: 10.1016/j.meddos.2018.05.001

26. Salz H, Bohrisch B, Howitz S, Banz N, Weibert K, Wiezorek T, et al. Intensity-modulated total body irradiation (TBI) with TomoDirect™. *Radiat Oncol*. (2015) 10:1–9. doi: 10.1186/s13014-015-0362-3

27. Wang H, Pi Y, Guo Y. Dosimetric comparison between TomoDirect and Helical Tomotherapy in total body irradiation. *Chin J Radiological Med Prot*. (2019) 12:658–62. doi: 10.3760/cma.j.issn.0254-5098.2019.09.004

28. Shimizu H. Stereotactic body radiation therapy: principles and practices. *Tomotherapy*. (2023), 263–76. doi: 10.1120/jacmp.v14i5.4305

29. Geurts M, Bayliss A, Thapa B, Nelson G. TomoTherapy total skin treatment for mycosis fungoides. doi: 10.1016/j.ejmp.2017.02.005

frontiers | Frontiers in Oncology

TYPE Original Research
PUBLISHED 02 September 2025
DOI 10.3389/fonc.2025.1652684

Check for updates

OPEN ACCESS

EDITED BY
Poonam Yadav,
Northwestern University, United States

REVIEWED BY
Peta Lonski,
Peter MacCallum Cancer Centre, Australia
Renxian Xie,
Shantou University, China

*CORRESPONDENCE
Guanhua Deng
gh.deng@foxmail.com

†These authors have contributed equally to this work

RECEIVED 24 June 2025
ACCEPTED 20 August 2025
PUBLISHED 02 September 2025

CITATION
Tang R, Lan M, Sun X, Luo Y, Gu A, Liu Q, Li Y, Yang G, Pan Z and Deng G (2025) An innovative hippocampal-sparing whole-brain radiotherapy planning approach via the Halcyon system: achieving lower hippocampal doses. *Front. Oncol.* 15:1652684. doi: 10.3389/fonc.2025.1652684

COPYRIGHT
© 2025 Tang, Lan, Sun, Luo, Gu, Liu, Li, Yang, Pan and Deng. This is an open-access article distributed under the terms of the Creative Commons Attribution License (CC BY). The use, distribution or reproduction in other forums is permitted, provided the original author(s) and the copyright owner(s) are credited and that the original publication in this journal is cited, in accordance with accepted academic practice. No use, distribution or reproduction is permitted which does not comply with these terms.

An innovative hippocampal-sparing whole-brain radiotherapy planning approach via the Halcyon system: achieving lower hippocampal doses

Ran Tang[1,2†], Maoying Lan[3†], Xingru Sun[1], Yue Luo[4], Anyan Gu[1], Qing Liu[5], Yingjing Li[6], Guozi Yang[1], Zhenyu Pan[1] and Guanhua Deng[7*]

[1]Department of Radiation Oncology, The Affiliated Huizhou Hospital, Guangzhou Medical University, Huizhou, China, [2]School of Public Health, Nanchang University, Nanchang, Jiangxi, China, [3]Department of Radiation Oncology, The First Affiliated Hospital of Guangzhou Medical University, Guangzhou, China, [4]Department of Radiotherapy, Southern Medical University Hospital of Integrated Traditional Chinese and Western Medicine, Guangzhou, China, [5]People's Hospital of Shaodong, Shaoyang, China, [6]Nanjing Tongrentang Chinese Medicine, Huizhou, China, [7]Department of Radiation Oncology, Guangdong Provincial People's Hospital Guangdong Academy of Medical Sciences), Southern Medical University, Guangzhou, China

Objective: To evaluate the feasibility and dosimetric benefits of Halcyon-based coplanar dual-arc volumetric modulated arc therapy (VMAT) for hippocampal-avoidance whole brain radiotherapy (HA-WBRT).

Methods: Twenty-one HA-WBRT patients were replanned using dual-arc VMAT (collimator 23°/293°) on Halcyon and Truebeam. The planning target volume (PTV) was segmented into three substructures and optimized with different weight parameters. Dosimetric parameters of PTV, monitor units (MUs), does to organs-at-risk(OARs), hippocampal normal tissue complication probability (NTCP) and gamma passing rate were recorded.

Results: All plans met RTOG 0933 criteria. The Halcyon plans demonstrated significantly better homogeneity index (HI) and V_{30Gy} of the PTV (HI: 0.105 *vs.* 0.121, $P<0.001$; V_{30Gy}: 97.1% *vs.* 96.3%, $P<0.001$), alongside reduced hippocampal dose ($D_{100\%}$: 626.8 *vs.* 695.0cGy; D_{mean}: 850.0 *vs.* 898.4cGy; D_{max}: 1348.1 *vs.* 1399.8 cGy; NTCP: 34.16% *vs.* 31.67%, $P \leq 0.001$), OARs sparing improved for Lens D_{max} (495.0 *vs.* 525.8cGy, $P = 0.001$), Optic nerves D_{max}(3047.7 *vs.* 3077.6cGy, $P = 0.006$), and eyes D_{mean}(927.1 *vs.* 937.9cGy, $P = 0.009$). The average gamma passing rates were higher for Halcyon than Truebeam (3%/2mm: 99.96% *vs.* 99.85; 2%/2mm: 99.83% *vs.* 99.49%).

Conclusions: Under the innovative planning approach, redefined hippocampal-sparing radiotherapy using Halcyon system, providing superior prescription dose coverage, improved OAR sparing, and reduced hippocampal NTCP.

KEYWORDS

Halcyon, hippocampus, whole brain radiotherapy, volumetric modulated arc therapy, treatment planning

Introduction

The incidence of brain metastases has been steadily increasing in recent years (1, 2). Despite advances in systemic therapies, the efficacy of chemotherapy in controlling brain metastases remains limited due to the restrictive nature of the blood-brain barrier (3). Whole-brain radiotherapy (WBRT) has demonstrated efficacy in improving local control and extending overall survival in patients with brain metastases (4). However, the neurotoxic effects of WBRT on the central nervous system have become a growing concern (5). Studies have demonstrated that radiation-induced hippocampal damage significantly impairs neurocognitive functions, particularly those related to learning, memory, and spatial processing (6). A multicenter phase II clinical trial (RTOG 0933) revealed that hippocampal-avoidance WBRT (HA-WBRT) effectively preserves patients' neurocognitive functions and improves their quality of life (7).

Over the past decades, HA-WBRT have been developed to use intensity modulated radiation therapy (IMRT), volumetric modulated arc therapy (VMAT), and tomotherapy (TOMO) techniques as listed in Table 1 (8–22). Gondi et al. (8) found that TOMO technology offers more advantages in HA-WBRT. However, the high cost of TOMO equipment makes it unaffordable for many small-scale hospitals. Wang et al. (9) have reported that HA-WBRT based IMRT techniques takes a long time for patients on the couch, which may cause patients discomposure. Dosimetric performance of conventional VMAT for HA-WBRT has been reported in previous studies following RTOG 0933 criteria, suggesting that VMAT irradiations use non-coplanar multi-arc irradiation. However, non-coplanar VMAT techniques increase the risk of tumor movement and extend treatment time.

In recent years, the Halcyon has gained widespread adoption in clinical practice due to its innovative design features. Unlike conventional C-arm accelerators, the Halcyon employs a circular ring gantry structure, eliminating the need for fixed jaws and enabling a ring rotation speed of 24°/s/eedi times that of C-arm LINACs. Additionally, the Halcyon is equipped with a dual-layer multi-leaf collimator (MLC) featuring 29 proximal and 28 distal leaves, which effectively minimizes leakage and transmission. The Halcyon exclusively utilizes a 6 MV flattening filter-free (FFF) photon beam, further enhancing its efficiency and precision in delivering high-quality radiotherapy. To the best of our knowledge, only a few studies have been reports of HA-WBRT using Halcyon. The results from Yokoyama et al. (13) demonstrated that three-arc Halcyon treatment plan was effective in handling hippocampus sparing whole-brain radiotherapy. However, the three-arc design prolonged prolong treatment time and increase costs. Here, we propose a novel coplanar dual-arc VMAT technique on the Halcyon platform that incorporates both target segmentation and collimator angle optimization, and systematically evaluate the dosimetric characteristics of HA-WBRT using coplanar dual-arc VMAT on Halcyon and Truebeam platforms.

Materials and methods

Patient selection

We retrospectively studied twenty-one patients who underwent HA-WBRT from June 2024 to December 2024. The cohort consisted of six males and four females, with a median age of 49 years (range: 33 – 70 years). All patients were diagnosed with non-hematologic malignancies confirmed through histopathological or cytological examination, with magnetic resonance imaging (MRI) showing brain metastases located at least 5 mm away from the hippocampus. Local approval was granted, and written informed consent was obtained.

Simulation

Patients were immobilized in the supine position using a thermoplastic mask. CT images were acquired using a Brilliance Big Bore CT scanner (Philips, Netherlands) with a slice thickness of 2.5 mm, covering the region from the scalp to the upper edge of the second cervical vertebra. Additionally, contrast-enhanced T1-weighted MRI scans with a slice thickness of 1 mm were performed within two weeks before radiotherapy. CT and MRI images were fused in the Eclipse v16.1 treatment planning system to facilitate precise hippocampal delineation by radiation oncologists.

Target and organs at risk delineation

Following the Radiation Therapy Oncology Group (RTOG) atlas, the hippocampus was manually delineated using fused CT and contrast-enhanced T1-weighted MRI images. A 5-mm three-dimensional margin around the hippocampus was designated as the hippocampal avoidance region (HA). The clinical target volume (CTV) was defined as the whole brain excluding the HA region. The planning target volume (PTV) was created by expanding the CTV by 3 mm while excluding the HA region. The prescription dose for the PTV was 30Gy in 10 fractions, with at least 95% of the PTV volume receiving the prescribed dose. Dose constraints for the PTV, hippocampus, and other organs at risk (OARs) are listed in Table 2.

Equipment parameters

The Halcyon designed with a ring gantry from Varian Corporation in the United States was employed, equipped with dual-layer MLCs (29 proximal and 28 distal leaves with a 5-mm resolution) and a 6 MV FFF photon beam with a maximum dose rate of 800 MU/min. For comparison, the Truebeam linac featured a single-layer MLC with 60 leaves (40 central leaves at 5-mm width and 20 peripheral leaves at 10-mm width), a dynamic jaw tracking system,

TABLE 1 Summary of HA-WBRT in the literature.

Ref.	Prescription	Linac and tech.	Plan quality	Hippocampus
Krayenbuehl J, et al. (2017) (10).	30Gy/10F	Trilogy Linac (Varian) 4Arcs_VMAT (2Arcs coplanar and 2Arcs non-coplanar)	$V_{100\%}$=92% HI=0.24	$D_{100\%}$= 8.1Gy D_{mean}=7.3Gy D_{max}=14.1Gy
Wang S, et al. (2017) (11).	30Gy/10F	Truebeam (Varian) 2 Arcs_VMAT coplanar	$V_{100\%}$=91.49% HI=0.28 CI=0.84	$D_{100\%}$=9.275Gy D_{max}=16.0Gy
Gondi V, et al. (2010) (8).	30Gy/10F	Varian linac IMRT Non-coplanar	$V_{100\%}$=93% HI=0.3	D_{max}=15.3Gy
Nevelsky A, et al. (2013) (12).	30Gy/10F	Infinity (Elekta) IMRT Non-coplanar	$V_{100\%}$=92% HI=0.36	$D_{100\%}$=8.37Gy D_{max}=14.35Gy
Yokoyama K, et al. (2022) (13).	30Gy/10F	Halcyon 2–4 Arcs_VMAT Coplanar	$V_{100\%}$=95% HI=0.19	$D_{50\%}$=7.89Gy D_{max}=14.32Gy
		Tomotherapy	$V_{100\%}$=95% HI=0.24	$D_{50\%}$=8.02Gy D_{max}=12.63Gy
Xue J, et al. (2023) (14).	30Gy/10F	Axesse (Elekta) 2 Arcs_VMAT Non-coplanar	$V_{100\%}$=95% HI=0.249 CI=0.821	$D_{100\%}$=8.03Gy D_{mean}=11.71Gy D_{max}=16.81Gy
Zhang HW, et al. (2024) (15).	30Gy/10F	Truebeam 2 Arcs_VMAT Coplanar	$V_{100\%}$=95% HI=1.1 CI=0.84	D_{mean}=11.77Gy D_{max}=17.13Gy
		Tomotherapy	$V_{100\%}$=95% HI=1.05 CI=0.88	D_{mean}=9.23Gy D_{max}=15.42Gy
Yuen AHL, et al. (2020) (16).	30Gy/10F	Truebeam 4 Split-arcs partial_VMAT Coplanar	$V_{100\%}$=94.79% HI=0.23	$D_{100\%}$=7.86Gy D_{mean}=9.16Gy D_{max}=13.23Gy
Yuen AHL, et al. (2022) (17).	30Gy/10F	Truebeam 4 Split-arc partial_VMAT+2 static fields Coplanar	$V_{100\%}$=94.69% HI=0.24	$D_{100\%}$=7.92Gy D_{mean}=9.21Gy D_{max}=13.31Gy
Li MH, et al. (2022) (18).	30Gy/10F	Tomotherapy	$V_{100\%}$=96.56% HI=0.07 CI=0.815	D_{mean}=10.7Gy D_{max}=15.5Gy
		Synergy 4 Arcs_VMAT Coplanar	$V_{100\%}$=92.95% HI=0.219 CI=0.823	D_{mean}=11.2Gy D_{max}=15.2Gy
Takaoka T, et al. (2021) (19).	30Gy/10F	Tomotherapy	$D_{95\%}$=29.9Gy HI=0.259 CI=1.30	$D_{100\%}$=9.3Gy D_{mean}=11.1Gy D_{max}=14.7Gy
Wang BH, et al. (2015) (9)	30Gy/10F	Varian IX 2 Arcs_VMAT Coplanar	$V_{95\%}$=95% HI=0.13 CI=0.88	D_{median}=10.30Gy D_{max}=13.92Gy
Fu Q, et al. (2021) (20).	25Gy/10F	VersaHD (Elekta) 4 Arcs_VMAT	$V_{100\%}$=91.2% HI=0.084 CI=0.839	D_{mean}=6.35Gy D_{max}=7.90Gy
NCT01780675 Trial (21)	25Gy/10F	–	$V_{100\%}$>95% $D_{98\%}$>25Gy $D_{2\%}$<37.5Gy	D_{mean}<8.5Gy
NRG CC001 Trial (22)	30Gy/10F	–	$V_{100\%}$>95% $D_{98\%}$>25Gy $D_{2\%}$<37.5Gy	$D_{100\%}$<9Gy D_{max}<16Gy

and a maximum dose rate of 1400MU/min. All treatment plans were designed using the Eclipse v16.1 treatment planning system.

Plan design

To optimize PTV coverage while sparing the hippocampus, the PTV was segmented into three sub-structures: zPTV_up (from the upper PTV boundary to the superior edge of the HA region), zPTV_mid (the PTV portion overlapping the HA region), and zPTV_down (from the inferior edge of the HA region to the lower PTV boundary). This segmentation strategy enhanced modulation efficiency during treatment planning optimization (Figure 1A).

As illustrated in Figure 1B, to ensure a consistent and unbiased comparative evaluation between the selected machine models under identical clinical conditions, all treatment plans utilized coplanar dual-arc VMAT with collimator angles set at 23° and 293°. Optimization was performed using the photon optimization (PO) algorithm, and dose calculations were conducted with the Acuros XB algorithm at a grid resolution of 2.5 mm. Identical dose constraints and optimization parameters were applied to both Halcyon and Truebeam plans to ensure comparability (Figure 1C).

Plan evaluation

The plan quality was assessed using dose-volume histograms (DVHs). PTV evaluation metrics included V_{30Gy} (%), conformity index (CI), and homogeneity index (HI), calculated using the following Equation 1 (23):

$$\begin{cases} CI = \frac{V_{t,ref}^2}{V_t \times V_{ref}} \\ HI = \frac{D_{2\%} - D_{98\%}}{D_{50\%}} \end{cases} \quad (1)$$

In the formulas, $V_{t,ref}$ represents the volume receiving the prescription dose, is the target volume, and is the volume of the prescription dose within the target volume. $D_{2\%}$, $D_{98\%}$ and $D_{50\%}$ represent the doses received by 2%, 98%, and 50% of the target volume, respectively. The CIcloser to 1 indicates better dose conformity to the target, while the HI closer to 0 reflects more uniform dose distribution within the target.

The evaluation parameters of OARs include $D_{100\%}$, D_{mean}, and D_{max} for the hippocampus; D_{max} for the lens and optic nerves; and D_{mean} for the eyeball. Additionally, the total monitor units (MUs) for all plans were recorded.

Normal tissue complication probability

The normal tissue complication probability (NTCP) is a quantitative measurement of the probability that a dose of radiation will have an undesirable effect on an organ. The following mechanistic of formula is used to calculate the NTCP, as shown in Equations 2, 3 (24):

$$NTCP = \frac{1}{\sqrt{2\pi}} \int_{-\infty}^{t} \exp(-\frac{x^2}{2}) dx \quad (2)$$

$$t = \frac{EQD_2(D_{40}) - TD_{50}}{m \cdot TD_{50}} \quad (3)$$

$EQD_2(D_{40})$ was EQD_2received by 40% of bilateral hippocampal volume, TD_{50} was the $EQD_2(D_{40})$ valuecorresponding to a 50% probability of neurocognitive decline, and m represented the slope of the dose-response curve. Moreover, TD_{50} and m were estimated to be 14.88 Gy and 0.54 by Gondi et al (24).

Biologically equivalent dose in 2-Gy fraction (EQD_2) to 40% of the bilateral hippocampi was evaluated according to the following Equation 4 (25):

$$EQD_2 = D \cdot \frac{d + \alpha/\beta}{2 + \alpha/\beta} \quad (4)$$

Where D represented the total dose and d represented the dose per fraction. An α/β ratio for the hippocampus was assumed to be 2 (25).

Dose verification

3D gamma passing rate analysis on dose images of all treatments was performed using the Portal Dosimetry module in Varian Eclipse. Halcyon plans were verified using its built-in digital megavolt imager, with a pixel resolution of 1280 × 1280 (0.336 mm per pixel) and an active detection area of 43 cm × 43 cm. Truebeam plans were verified using the a-Si1000 electronic portal imaging device, with a pixel resolution of 1024 × 768 (0.39 mm per pixel) and an active detection area of 40 cm × 30 cm. The gamma analysis criteria were set as follows: a dose threshold of 10%, dose tolerance/distance to agreement of 3%/2 mm and 2%/2 mm, respectively. The passing rates for all treatment plans were recorded and analyzed.

Statistical analysis

Statistical analyses were performed using SPSS v25.0 and Origin 2022. The Shapiro-Wilk test was employed to assess data normality. Normally distributed data were expressed as mean ± standard deviation and analyzed using paired t-test, while non-normally distributed data were expressed as median (interquartile range) and analyzed using Wilcoxon test. A two-tailed α-level of 0.05 was considered statistically significant.

Results

Dose distribution and DVH comparison

The Halcyon plan demonstrated superior PTV coverage and hippocampal sparing compared to the Truebeam plan, as illustrated in Figure 2. The DVHs for the same patient, shown in Figure 3, indicate

TABLE 2 Dosimetric compliance criteria for hippocampal avoidance.

Parameter	Dose constraints		
PTV	V_{30Gy}≥95%	$D_{2\%}$≤37.5Gy	$D_{98\%}$≥25Gy
Hippocampus	D_{max} ≤ 16Gy	$D_{100\%}$≤9Gy	
Optic nerves	D_{max} ≤ 33Gy		
Lens	D_{max} ≤ 7Gy		

that both plans met clinical requirements. Notably, the Halcyon plan achieved OAR doses well below tolerance limits and demonstrated a more favorable DVH profile compared to the Truebeam plan.

Dosimetric parameters and monitor unit comparison

All plans achieved ≥ 95% PTV coverage at the prescription dose. The Halcyon plan demonstrated superior coverage at 97.1%, compared to 96.3% for the Truebeam plan (P< 0.001). In terms of dose homogeneity, the Halcyon plan achieved a significantly lower median HI value than the Truebeam plan (0.105 *vs.* 0.121, P< 0.001). Conversely, the CI was marginally better in the Truebeam plan compared to the Halcyon plan (1.105 *vs.* 1.127, P< 0.001). However, the Halcyon plan required significantly more MUs than the Truebeam plan (1083.0 *vs.* 903.0, P< 0.001), as shown in Table 3.

Dosimetric comparison for OARs

The average volume of the hippocampal avoidance region and PTV were 5.4 cm^3 (1.5 - 8.1 cm^3) and 1542.4 cm^3 (1298.3 - 1872.3 cm^3), respectively. The volume of hippocampal avoidance region was accounted for 0.35% of PTV. The Halcyon plan showed superior dosimetric performance for hippocampal protection, achieving significantly lower $D_{100\%}$, D_{mean}, D_{max} and NTCP than the Truebeam plan: 626.8 ± 35.8cGy*vs.* 695.0 ± 31.5cGy (P<0.001), 850.0(837.4, 883.9)cGy*vs.* 898.4 (880.1, 924.7) cGy (P = 0.001), 1348.1 ± 62.2cGy*vs.* 1399.8 ± 74.4cGy (P<0.001), and 34.16 ± 2.02% vs. 31.67 ± 1.57% (p<0.001), as shown in Figure 4.

Additionally, the Halcyon plan achieved a significantly lower D_{max} for the lens and optic nerves and lower D_{mean} for the eyes compared to the Truebeam plan, as shown in Table 4.

Gamma passing rate comparison

All plans successfully passed the quality assurance test under the 3%/2 mm and 2%/2 mm gamma criteria, with passing rates exceeding 97%. As shown in Figure 5, the Halcyon plan demonstrated superior gamma passing rates compared to the Truebeam plan under both criteria: 99.96% ± 0.07% *vs.* 99.85% ± 0.08% for 3%/2 mm (z=16.5, P = 0.008) and 99.83% ± 0.24% *vs.* 99.49% ± 0.17% for 2%/2 mm (z=11, P = 0.003).

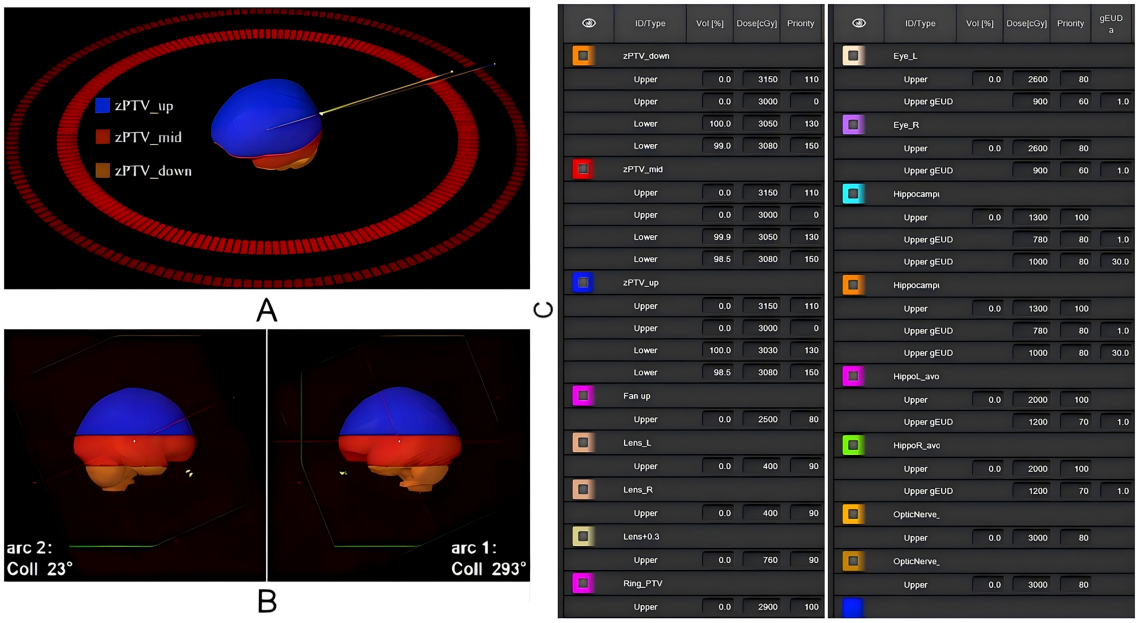

FIGURE 1
Schematic representation of the radiotherapy plan design and key target structure optimization parameters. **(A)** Logical segmentation of the PTV structure; **(B)** Gantry angle settings for dual-arc VMAT; **(C)** Key optimization parameters for target structures in the treatment plan.

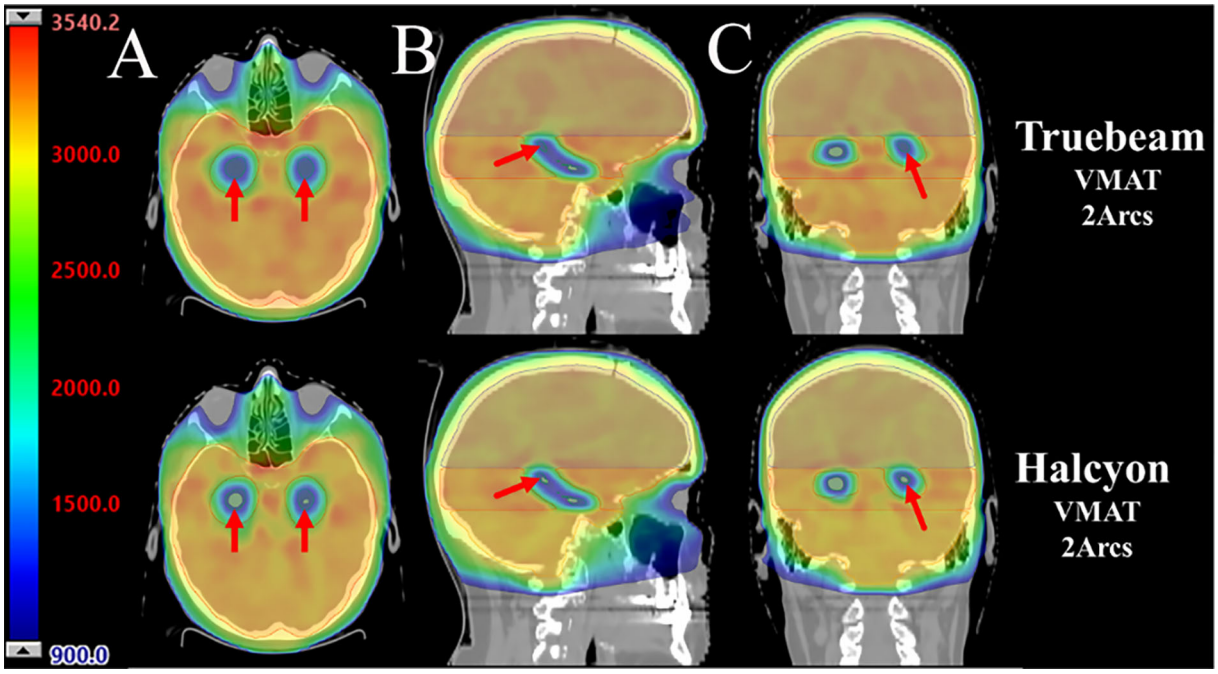

FIGURE 2
The dose distribution of Truebeam and Halcyon applying double arc coplanar VMAT for a representative patient. **(A-C)** Dose distribution at the axial, sagittal and coronal views. The top and bottom figures are the Truebeam and Halcyon plans, respectively.

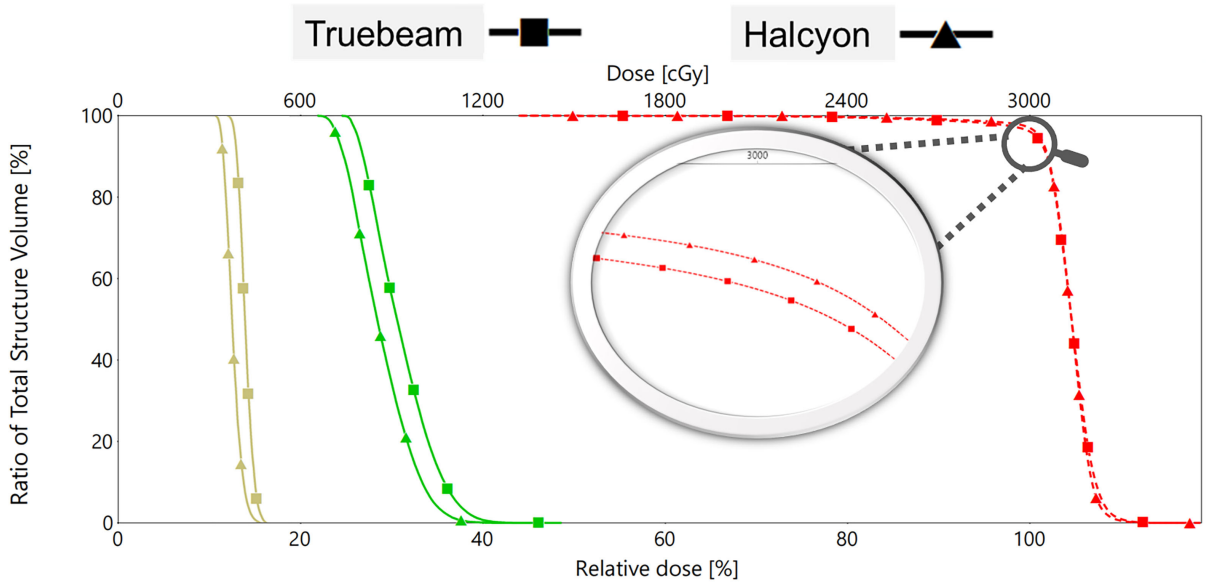

FIGURE 3
DVHs comparison for PTV and OARs between Truebeam and Halcyon applying VMAT. The yellow, green and red line represents the physical dose exposure to the lens, hippocampus and PTV, respectively.

Comparison with other studies in hippocampal-avoidance whole-brain radiotherapy

Compared to previous studies, the Halcyon plan achieved notable milestones in HA-WBRT. The Halcyon plan delivered higher prescription dose coverage ($D_{98\%}$, 29.5 Gy; $D_{2\%}$, 32.8 Gy; $V_{95\%}$, 98.7%; $V_{100\%}$, 97.1%), superior dose homogeneity (HI, 0.105), and excellent hippocampal protection ($D_{100\%}$, 6.27Gy; D_{mean}, 8.50Gy; D_{max}, 13.48Gy). These results are comparable or superior to outcomes reported for Tomotherapy and non-coplanar VMAT techniques.

TABLE 3 Comparison of dosimetric parameters and MUs for PTV [n = 21, $\bar{x} \pm s$/M(Q1, Q3)].

Parameters	Truebeam	Halcyon	t/z value	*P* value
CI	1.105 ± 0.051	1.127 ± 0.059	-7.069	<0.001
HI	0.121 (0.113, 0.125)	0.105 (0.099, 0.108)	-4.015	<0.001
V_{30Gy}/%	96.3 ± 0.3	97.1 ± 0.3	-11.118	<0.001
MU	903.0 (884.5, 918.5)	1083.0 (1053.4, 1140.1)	-4.015	<0.001

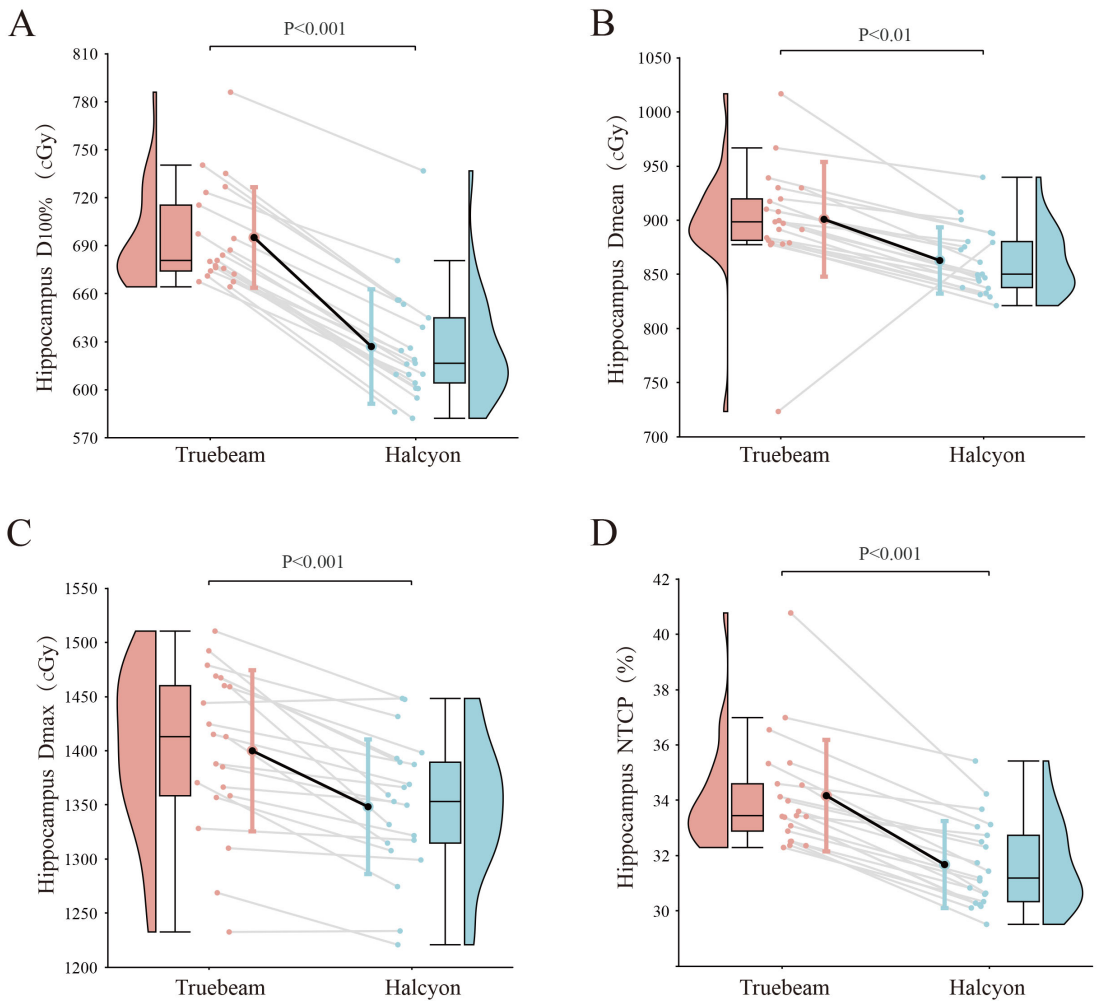

FIGURE 4
Comparison of hippocampus dosimetric parameters. The results are shown for the **(A)** $D_{100\%}$, **(B)** D_{mean}, **(C)** D_{max} and **(D)** NTCP of hippocampus, respectively.

Discussion

HA-WBRT has been shown to be superior to standard WBRT in preserving neurocognitive function and improving patients' quality of life (26), and it has gradually become a widely adopted therapy for brain metastases. In medical centers equipped with both conventional linear accelerators and Halcyon platforms, selecting the optimal radiotherapy device is a critical step in treatment planning. In this study, HA-WBRT plans were generated for both Halcyon and Truebeam accelerators, and differences in dose distributions for target volumes and OARs were analyzed. Both plans met the RTOG 0933 protocol and clinical requirements. The Halcyon plans demonstrated significant advantages in HI and $V_{30Gy}$for the PTV, as well as hippocampal, lens, optic nerves, and eyes. Conversely, Truebeam plans showed a slight advantage in PTV CI, with a marginal 2.0% difference. The Halcyon plans

TABLE 4 Comparison of OARs dosimetric parameters [n = 21, $\bar{x} \pm s$/M(Q1, Q3)].

OARs	Parameters	Truebeam	Halcyon	t/z value	*P* value
Lens	D_{max} (cGy)	525.8 (487.9, 554.4)	495.0 (458.5, 521.3)	-3.285	0.001
Optic nerves	D_{max} (cGy)	3077.6 ± 44.7	3047.7 ± 64.7	3.080	0.006
Eyes	D_{mean} (cGy)	937.9 (916.7, 967.6)	927.1 (906.7, 947.4)	-2.624	0.009

achieved a 15.2% improvement in HI, reflecting superior dose uniformity. Although the Halcyon plans required 16.6% more MUs than Truebeam, the Halcyon's gantry rotation speed is four times faster, significantly reducing treatment delivery time (27). It should be noted that the higher MU requirements of Halcyon systems may exacerbate several potential problems: (i) increased scatter dose, (ii) accelerated machine wear, and (iii) higher treatment costs.

In terms of hippocampal protection, the Halcyon plans demonstrated a significant reduction in $D_{100\%}$ (626.8cGy), achieving a 10.9% decrease compared to the Truebeam plans. The reductions in D_{mean} (850.0cGy *vs.* 898.4cGy) and D_{max} (1348.1cGy *vs.* 1399.8cGy) were more modest, at approximately 4.8%. While statistically significant differences were observed in plan comparisons, the clinical implications of these variations warrant further investigation. To address this issue to some extent, we employed NTCP modeling - a validated quantitative measure for assessing radiation-induced tissue damage severity. Our analysis revealed that Halcyon treatment plans demonstrated the most favorable neurocognitive protection profile, as evidenced by significantly lower NTCP values (p<0.001).These findings suggests that the Halcyon system offers superior protection for normal tissues surrounding by the target volume, particularly in low-dose regions. Several factors may account for this advantage:

1. Jawless Design:

The Halcyon accelerator's jawless configuration positions the MLC leaves closer to the source. Although the leaf tips are rounded, their longer radius and straighter edges minimize the dosimetric leaf gap (DLG) to just 0.1mm (28), significantly reducing the penumbra compared to the 1.8mm DLG observed with Truebeam's MLC design.

2. Dual-Layer MLC:

Halcyon utilizes a dual-layer, staggered MLC configuration with a transmission factor of only 0.47% (29), markedly lower than Truebeam's average transmission of 1.5% for 6 MV beams (30). This design effectively reduces dose leakage and improves the protection of surrounding tissues.

3. Faster Leaf Motion:

The MLC leaves on the Halcyon achieve a maximum speed of 5cm/s, double Truebeam's maximum leaf speed of 2.5cm/s. Previous studies have demonstrated that faster leaf motion enhances the sparing of OARs outside the target region (31), consistent with the findings of this study.

4. Enhanced Modulation Capabilities:

In traditional accelerators, achieving optimal modulation often requires fixing the jaw position due to the limitations of MLC movement when dealing with large target diameters and fields (32). In contrast, the Halcyon's MLC design eliminates this restriction, allowing full extension of the leaves without carriages and enabling seamless modulation across the entire field. Truebeam, by comparison, is limited by a maximum leaf extension of 15 cm beyond the central carriage, which restricts modulation in VMAT plans for larger fields. To address these challenges, techniques such as partial arcs and smaller field sizes have been employed on Truebeam, as reported by Yuen et al. (16), achieving a target HI of 0.23 and a hippocampal D_{mean} of 9.16 Gy. However, the Halcyon platform inherently overcomes these limitations due to its innovative MLC design and superior modulation capabilities.

Rong et al. (33) compared IMRT, VMAT, and TOMO for HA-WBRT, concluding that TOMO provides superior dosimetric distribution, particularly in terms of dose uniformity. In studies conducted by Takaoka et al. (19) and Li et al. (18), TOMO achieved 95% PTV coverage with V_{30Gy}, CI values of 1.3 and 0.815, and hippocampal D_{max} and D_{mean} of 14.7 Gy/11.1 Gy and 15.5 Gy/10.7 Gy, respectively. Hippocampal volume had a large effect on the planning parameters, as shown in Table 4. The treatment planning with the small hippocampal volume resulted in the better dose distribution of target and lower D_{max} values of hippocampus. For instance, the volume of hippocampi was 5.4 cm^3 in our study, whereas the value was 3.95 cm^3 described by Takaoka et al. (19). In our study, Halcyon plans demonstrated better hippocampal sparing (D_{max} of 13.48 Gy, D_{mean} of 8.50 Gy) and achieved exceptional PTV coverage and homogeneity. These findings underscore Halcyon's competitive performance in HA-WBRT and its potential as an effective alternative to TOMO. Yokoyama et al. (13) investigated

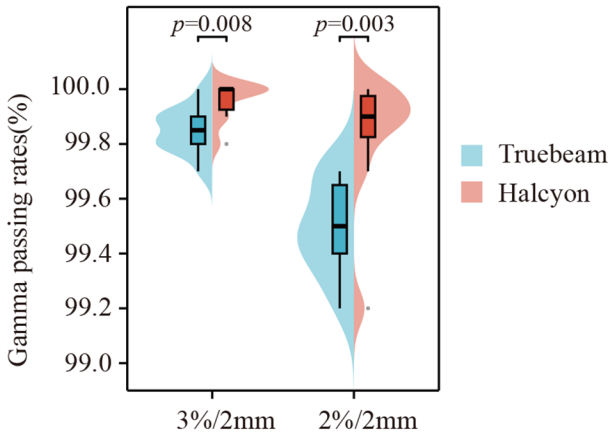

FIGURE 5
Global gamma passing rates of the VMAT plans using Truebeam and Halcyon.

the impact of arc number (2 – 4 arcs) in Halcyon-based VMAT plans, and recommended 3 arcs for HA-WBRT, reporting a hippocampal D_{max} of 14.32 Gy. In our study, the dual-arc VMAT plan achieved a lower hippocampal D_{max} (13.48 Gy *vs.* 14.32 Gy). We attribute this improvement to two innovations in our coplanar dual-arc technique: (i) Target structure segmentation with differential weighting during optimization, enhancing the plan's modulation capability. (ii) The orthogonal collimator angle design facilitates more conformal subfield shapes and better protection of OARs, particularly in complex spatial relationships between the target and OARs.

Non-coplanar IMRT and VMAT techniques have been explored to improve hippocampal sparing. For example, Nevelsky et al. (12) achieved hippocampal D_{max} and D_{mean} of 14.1 Gy and 7.3 Gy, respectively, using nine-field non-coplanar IMRT, though the PTV coverage (92% for V_{30Gy}) was suboptimal. Subsequently, Xue et al. (14) employed a non-coplanar VMAT approach improving the V_{30Gy} coverage to 95%. and achieving a HI and CI values of 0.249 and 0.821, respectively, with hippocampal $D_{100\%}$, D_{max}, and D_{mean} values of 8.03 Gy, 16.81 Gy, and 11.71 Gy. Although Halcyon does not currently support non-coplanar delivery, its HA-WBRT plan quality in our study remains competitive with these reported techniques, demonstrating comparable hippocampal sparing and robust target coverage.

It is worth noting that due to the complexity of HA-WBRT, plan quality is of paramount importance, and selecting appropriate collimator angles is a critical factor for achieving an optimal dose distribution. In this study, the collimator angles for Arc 1 (293°) and Arc 2 (23°) were set with an inter-arc angle of 90°, consistent with previous studies (34). To address the high complexity of the target structure, the zPTV_mid module, which posed greater challenges in meeting planning objectives, was assigned higher optimization weights. This segmentation and weighting strategy improved modulation efficiency during plan optimization, aligning with the modified VMAT techniques reported by Fu et al. (20). Compared to previously published data (as shown in Table 1), the HA-WBRT plans only using coplanar dual-arc technology in our study demonstrated superior prescription dose coverage and dose uniformity. The PTV coverage reached 97.1%, with hotspots ($D_{2\%}$) controlled within 108% of the prescription dose. In terms of hippocampal sparing, the plans achieved groundbreaking results, maintaining an average hippocampal dose below 9 Gy and reducing the lens D_{max} to less than 5 Gy.

Several limitations should be acknowledged in this study. First, this is a retrospective single-center study that lacks validation of long-term clinical outcomes. Second, although our study demonstrated favorable clinical outcomes, the small sample size (n=21) may limit the extrapolation of the results. Third, the potential impact of brain metastasis locations on plan quality was not evaluated. Future longitudinal, multicenter prospective studies will evaluate both cognitive outcomes and survival endpoints in patients with HA-WBRT.

Conclusion

This study demonstrates that the Halcyon accelerator is a viable and efficient platform for HA-WBRT, with excellent PTV dose coverage, superior dose homogeneity, and effective hippocampal sparing while reducing treatment times. These findings provide a robust basis for further exploration and clinical adoption of the Halcyon platform in hippocampal-avoidance radiotherapy.

Data availability statement

The original contributions presented in the study are included in the article/supplementary material. Further inquiries can be directed to the corresponding author.

Ethics statement

The studies involving humans were approved by The Review Committee of Huizhou Third People's Hospital. The studies were conducted in accordance with the local legislation and institutional requirements. The participants provided their written informed consent to participate in this study. Written informed consent was obtained from the individual(s) for the publication of any potentially identifiable images or data included in this article.

Author contributions

RT: Methodology, Conceptualization, Software, Writing – review & editing, Formal analysis, Writing – original draft. ML: Methodology, Writing – original draft, Conceptualization, Funding acquisition. XS: Formal analysis, Writing – review & editing. YL: Writing – review & editing. AG: Writing – review & editing, Data curation, Investigation. QL: Investigation, Writing – original draft. YJL: Writing – original draft, Software, Formal analysis. GY: Validation, Software, Writing – review & editing. ZP: Resources, Writing – review & editing. GD: Supervision, Writing – review & editing, Conceptualization, Project administration, Writing – original draft, Visualization.

Funding

The author(s) declare financial support was received for the research and/or publication of this article. This study was supported by Medical Science and Technology Foundation of Guangdong Province (Grant No. A2023250), Huizhou Science and Technology Innovation Team Project (Grant No. 2023EQ050012), and Huizhou Outstanding Youth Science and Technology Talent Project (Grant No. 2025EQ050018).

Conflict of interest

The authors declare that the research was conducted in the absence of any commercial or financial relationships that could be construed as a potential conflict of interest.

Generative AI statement

The author(s) declare that no Generative AI was used in the creation of this manuscript.

Any alternative text (alt text) provided alongside figures in this article has been generated by Frontiers with the support of artificial intelligence and reasonable efforts have been made to ensure accuracy, including review by the authors wherever possible. If you identify any issues, please contact us.

Publisher's note

All claims expressed in this article are solely those of the authors and do not necessarily represent those of their affiliated organizations, or those of the publisher, the editors and the reviewers. Any product that may be evaluated in this article, or claim that may be made by its manufacturer, is not guaranteed or endorsed by the publisher.

References

1. Arvold ND, Lee EQ, Mehta MP, Margolin K, Alexander BM, Lin NU, et al. Updates in the management of brain metastases. *Neuro Oncol*. (2016) 18:1043–65. doi: 10.1093/neuonc/now127

2. Schimmel WCM, Gehring K, Eekers DBP, Hanssens PEJ, Sitskoorn MM. Cognitive effects of stereotactic radiosurgery in adult patients with brain metastases: A systematic review. *Adv Radiat Oncol*. (2018) 3:568–81. doi: 10.1016/j.adro.2018.06.003

3. Seute T, Leffers P, Wilmink JT, ten Velde GP, Twijnstra A. Response of asymptomatic brain metastases from small-cell lung cancer to systemic first-line chemotherapy. *J Clin Oncol*. (2006) 24:2079–83. doi: 10.1200/jco.2005.03.2946

4. Sperduto PW, Kased N, Roberge D, Xu Z, Shanley R, Luo X, et al. Effect of tumor subtype on survival and the graded prognostic assessment for patients with breast cancer and brain metastases. *Int J Radiat Oncol Biol Phys*. (2012) 82:2111–7. doi: 10.1016/j.ijrobp.2011.02.027

5. Gore EM, Bae K, Wong SJ, Sun A, Bonner JA, Schild SE, et al. Phase iii comparison of prophylactic cranial irradiation versus observation in patients with locally advanced non-small-cell lung cancer: primary analysis of radiation therapy oncology group study Rtog 0214. *J Clin Oncol*. (2011) 29:272–8. doi: 10.1200/jco.2010.29.1609

6. Tallet AV, Azria D, Barlesi F, Spano JP, Carpentier AF, Gonçalves A, et al. Neurocognitive function impairment after whole brain radiotherapy for brain metastases: actual assessment. *Radiat Oncol*. (2012) 7:77. doi: 10.1186/1748-717x-7-77

7. Gondi V, Pugh SL, Tome WA, Caine C, Corn B, Kanner A, et al. Preservation of memory with conformal avoidance of the hippocampal neural stem-cell compartment during whole-brain radiotherapy for brain metastases (Rtog 0933): A phase ii multi-institutional trial. *J Clin Oncol*. (2014) 32:3810–6. doi: 10.1200/jco.2014.57.2909

8. Gondi V, Tolakanahalli R, Mehta MP, Tewatia D, Rowley H, Kuo JS, et al. Hippocampal-sparing whole-brain radiotherapy: A "How-to" Technique using helical tomotherapy and linear accelerator-based intensity-modulated radiotherapy. *Int J Radiat Oncol Biol Phys*. (2010) 78:1244–52. doi: 10.1016/j.ijrobp.2010.01.039

9. Wang BH, Hua W, Gu X, Wang XL, Li J, Liu LQ, et al. Dosimetric study of different radiotherapy planning approaches for hippocampal avoidance whole-brain radiation therapy (Ha-Wbrt) based on fused Ct and mri imaging. *Australas Phys Eng Sci Med*. (2015) 38:767–75. doi: 10.1007/s13246-015-0397-7

10. Krayenbuehl J, Di Martino M, Guckenberger M, Andratschke N. Improved plan quality with automated radiotherapy planning for whole brain with hippocampus sparing: A comparison to the Rtog 0933 trial. *Radiat Oncol*. (2017) 12:161. doi: 10.1186/s13014-017-0896-7

11. Wang S, Zheng D, Zhang C, Ma R, Bennion NR, Lei Y, et al. Automatic planning on hippocampal avoidance whole-brain radiotherapy. *Med Dosim*. (2017) 42:63–8. doi: 10.1016/j.meddos.2016.12.002

12. Nevelsky A, Ieumwananonthachai N, Kaidar-Person O, Bar-Deroma R, Nasrallah H, Ben-Yosef R, et al. Hippocampal-sparing whole-brain radiotherapy using elekta equipment. *J Appl Clin Med Phys*. (2013) 14:4205. doi: 10.1120/jacmp.v14i3.4205

13. Yokoyama K, Kurosaki H, Oyoshi H, Miura K, Utsumi N. Plan quality comparison between hippocampus-sparing whole-brain radiotherapy treated with halcyon and tomotherapy intensity-modulated radiotherapy. *Technol Cancer Res Treat*. (2022) 21:15330338221108529. doi: 10.1177/15330338221108529

14. Xue J, Jin S, Zhang H, Zou K, Sheng J, Tang J, et al. A simplified non-coplanar volumetric modulated arc therapy for the whole brain radiotherapy with hippocampus avoidance. *Front Oncol*. (2023) 13:1143564. doi: 10.3389/fonc.2023.1143564

15. Zhang HW, Hu B, Pang HW. Dosimetric comparison of helical tomotherapy and volumetric modulated arc therapy in hippocampal avoidance whole-brain radiotherapy. *J Appl Clin Med Phys*. (2024) 25:e14218. doi: 10.1002/acm2.14218

16. Yuen AHL, Wu PM, Li AKL, Mak PCY. Volumetric modulated arc therapy (Vmat) for hippocampal-avoidance whole brain radiation therapy: planning comparison with dual-arc and split-arc partial-field techniques. *Radiat Oncol*. (2020) 15:42. doi: 10.1186/s13014-020-01488-5

17. Yuen AHL, Wu PM, Li AKL, Mak PCY. Hybrid split-arc partial-field volumetric modulated arc therapy: an improved beam arrangement for linear accelerator-based hippocampal-avoidance whole brain radiation therapy. *Rep Pract Oncol Radiother*. (2022) 27:352–9. doi: 10.5603/RPOR.a2022.0022

18. Li MH, Chen LJ, Chang CC, Tsai JT, Lin JC. Effect of the simulated half leaf width of a multileaf collimator on volumetric modulated arc therapy plan quality in hippocampal avoidance whole-brain radiotherapy. *J Appl Clin Med Phys*. (2022) 23:e13575. doi: 10.1002/acm2.13575

19. Takaoka T, Tomita N, Mizuno T, Hashimoto S, Tsuchiya T, Tomida M, et al. Dosimetric comparison of helical tomotherapy and intensity-modulated proton therapy in hippocampus- and scalp-sparing whole brain radiotherapy. *Technol Cancer Res Treat*. (2021) 20:15330338211060170. doi: 10.1177/15330338211060170

20. Fu Q, Chen D, Yan H, Chen J, Zhu J, Yan L, et al. Treatment planning of volumetric modulated arc therapy and positioning optimization for hippocampal-avoidance prophylactic cranial irradiation. *J Appl Clin Med Phys*. (2021) 22:15–23. doi: 10.1002/acm2.13217

21. Candiff O, Belderbos J, Wolf AL, Damen E, van Haaren P, Crijns W, et al. Quality assurance and safety of hippocampal avoidance prophylactic cranial irradiation in the multicenter randomized phase iii trial (Nct01780675). *J Natl Cancer Cent*. (2023) 3:135–40. doi: 10.1016/j.jncc.2023.05.004

22. Brown PD, Gondi V, Pugh S, Tome WA, Wefel JS, Armstrong TS, et al. Hippocampal avoidance during whole-brain radiotherapy plus memantine for patients with brain metastases: phase III trial Nrg oncology Cc001. *J Clin Oncol*. (2020) 38:1019–29. doi: 10.1200/jco.19.02767

23. Tang R, Li A, Li Y, Deng G, Wang Y, Xiao Q, et al. Dosimetric comparison of two dose expansion methods in intensity modulated radiotherapy for breast cancer. *Radiat Oncol*. (2023) 18:23. doi: 10.1186/s13014-023-02217-4

24. Gondi V, Hermann BP, Mehta MP, Tomé WA. Hippocampal dosimetry predicts neurocognitive function impairment after fractionated stereotactic radiotherapy for benign or low-grade adult brain tumors. *Int J Radiat Oncol Biol Phys*. (2012) 83:e487–93. doi: 10.1016/j.ijrobp.2011.10.021

25. Prokic V, Wiedenmann N, Fels F, Schmucker M, Nieder C, Grosu AL. Whole brain irradiation with hippocampal sparing and dose escalation on multiple brain metastases: A planning study on treatment concepts. *Int J Radiat Oncol Biol Phys*. (2013) 85:264–70. doi: 10.1016/j.ijrobp.2012.02.036

26. Oskan F, Ganswindt U, Schwarz SB, Manapov F, Belka C, Niyazi M. Hippocampus sparing in whole-brain radiotherapy. A Review. *Strahlenther Onkol*. (2014) 190:337–41. doi: 10.1007/s00066-013-0518-8

27. Sun T, Lin X, Li K, Qiu Q, Duan J, Zhang G, et al. Volumetric modulated arc therapy for hippocampal-sparing prophylactic cranial irradiation: planning comparison of halcyon and C-arm accelerators. *Front Oncol*. (2023) 13:993809. doi: 10.3389/fonc.2023.993809

28. Hernandez V, Saez J, Angerud A, Cayez R, Khamphan C, Nguyen D, et al. Dosimetric leaf gap and leaf trailing effect in a double-stacked multileaf collimator. *Med Phys*. (2021) 48:3413–24. doi: 10.1002/mp.14914

29. Lim TY, Dragojević I, Hoffman D, Flores-Martinez E, Kim GY. Characterization of the halcyon(Tm) multileaf collimator system. *J Appl Clin Med Phys*. (2019) 20:106–14. doi: 10.1002/acm2.12568

30. Li Y, Chen L, Zhu J, Wang B, Liu X. A quantitative method to the analysis of Mlc leaf position and speed based on epid and Ebt3 film for dynamic imrt treatment with different types of Mlc. *J Appl Clin Med Phys*. (2017) 18:106–15. doi: 10.1002/acm2.12102

31. Vorwerk H, Wagner D, Hess CF. Impact of different leaf velocities and dose rates on the number of monitor units and the dose-volume-histograms using intensity modulated radiotherapy with sliding-window technique. *Radiat Oncol*. (2008) 3:31. doi: 10.1186/1748-717x-3-31

32. Rossi M, Boman E, Skyttä T, Kapanen M. A novel arc geometry setting for pelvic radiotherapy with extensive nodal involvement. *J Appl Clin Med Phys*. (2016) 17:73–85. doi: 10.1120/jacmp.v17i4.6028

33. Rong Y, Evans J, Xu-Welliver M, Pickett C, Jia G, Chen Q, et al. Dosimetric evaluation of intensity-modulated radiotherapy, volumetric modulated arc therapy, and helical tomotherapy for hippocampal-avoidance whole brain radiotherapy. *PloS One*. (2015) 10:e0126222. doi: 10.1371/journal.pone.0126222

34. Sun W, Chen K, Li Y, Xia W, Dong L, Shi Y, et al. Optimization of collimator angles in dual-arc volumetric modulated arc therapy planning for whole-brain radiotherapy with hippocampus and inner ear sparing. *Sci Rep*. (2021) 11:19035. doi: 10.1038/s41598-021-98530-7

frontiers | Frontiers in Oncology

TYPE Case Report
PUBLISHED 04 September 2025
DOI 10.3389/fonc.2025.1620637

Check for updates

OPEN ACCESS

EDITED BY
Abdul K. Parchur,
Medical College of Wisconsin, United States

REVIEWED BY
Abdul Karim Ghaith,
Mayo Clinic, United States
Prarthana Pasricha,
Carleton University, Canada
Praveenbalaji Rajendran,
Harvard University, United States

*CORRESPONDENCE
Shosei Shimizu
23s.showsay.shimizu@gmail.com;
23s.shimizu@yz-proton.com

†These authors have contributed equally to this work and share first authorship

RECEIVED 29 April 2025
ACCEPTED 08 August 2025
PUBLISHED 04 September 2025

CITATION
Zhang X, Wang X, Ning W, Liang J, Jin Y, Nie Y, Wang J, Wang Z, Wang W, Zhao J, Kong J, Yang L, Zhou D, Zou Y, Mizumoto M and Shimizu S (2025) Case Report: Multimodal management of a rare pediatric astroblastoma using proton beam therapy and Gamma Knife radiosurgery—a case report and literature review. *Front. Oncol.* 15:1620637. doi: 10.3389/fonc.2025.1620637

COPYRIGHT
© 2025 Zhang, Wang, Ning, Liang, Jin, Nie, Wang, Wang, Wang, Zhao, Kong, Yang, Zhou, Zou, Mizumoto and Shimizu. This is an open-access article distributed under the terms of the Creative Commons Attribution License (CC BY). The use, distribution or reproduction in other forums is permitted, provided the original author(s) and the copyright owner(s) are credited and that the original publication in this journal is cited, in accordance with accepted academic practice. No use, distribution or reproduction is permitted which does not comply with these terms.

Case Report: Multimodal management of a rare pediatric astroblastoma using proton beam therapy and Gamma Knife radiosurgery—a case report and literature review

Xijia Zhang[1†], Xinfa Wang[2†], Weihai Ning[3], Jianfeng Liang[4], Yonglong Jin[5], Yuqian Nie[6], Jie Wang[7], Zishen Wang[7], Wei Wang[8], Jun Zhao[6], Jingjing Kong[6], Lu Yang[6], Dongxue Zhou[6], Yue Zou[6], Masashi Mizumoto[9] and Shosei Shimizu[6,9*]

[1]Department of Neurosurgery, Beijing Tiantan Hospital of Capital Medical University, Beijing, China, [2]Department of Neurosurgery, Children's Hospital of Nanjing Medical University, Nanjing, Jiangsu, China, [3]Department of Neurosurgery, Sanbo Brain Hospital, Capital Medical University, Beijing, China, [4]Department of Neurosurgery, Peking University International Hospital, Beijing, China, [5]Department of Radiotherapy, The Affiliated Hospital of Qingdao University, Qingdao, Shandong, China, [6]Department of Pediatric Radiation Therapy Center, Hebei Yizhou Cancer Hospital, Zhuozhou, Hebei, China, [7]Department of Radiotherapy Physics and Technology, Hebei Yizhou Cancer Hospital, Zhuozhou, Hebei, China, [8]Department of Radiology, Hebei Yizhou Cancer Hospital, Zhuozhou, Hebei, China, [9]Department of Radiation Oncology, University of Tsukuba, Tsukuba, Japan

Introduction: Astroblastoma is an infrequent glial tumor, with the MN1-altered subtype recognized in the 2021 WHO classification. This report details the management of a 4-year-old girl diagnosed with CNS WHO Grade 3 MN1-altered astroblastoma, also found to have a heterozygous BRCA2 mutation. We highlight a sequential multimodal treatment approach involving proton beam therapy (PBT), targeted chemotherapy with a PARP inhibitor, and subsequent salvage Gamma Knife radiosurgery (GKRS).

Main symptoms and findings: The patient presented with right lower extremity weakness and gait disturbance. Initial treatment involved maximal safe resection followed by adjuvant PBT (craniospinal irradiation 36 Gy, local boost to 54 Gy). PBT was selected for its dosimetric advantages, notably minimizing radiation dose to surrounding healthy tissues, thereby reducing potential acute toxicity and long-term risks compared to conventional photon therapy. Despite this, residual tumor persisted. Following the discovery of a BRCA2 mutation, the PARP inhibitor fluzoparib was administered, which was associated with temporary disease stabilization.

Diagnoses, interventions, outcomes: After a second resection confirming residual disease, salvage stereotactic radiosurgery (SRS) using Gamma Knife (30 Gy in 5 fractions) was administered to the remaining lesions. The patient has demonstrated sustained local control with no tumor progression for over 18 months post-SRS, with only mild, asymptomatic perilesional edema and no neurological deficits.

Conclusion - Take-away lesson: This case suggests that leveraging the tissue-sparing benefits of initial PBT may enable effective salvage SRS for managing residual or recurrent high-grade pediatric astroblastoma. Furthermore, it highlights the potential role of molecular profiling to guide targeted therapies in these rare tumors.

KEYWORDS

astroblastoma, proton beam therapy, Gamma Knife radiosurgery, pediatric oncology, case report

Introduction

Astroblastoma represents a rare and infrequent subset of glial tumors within the central nervous system, with an estimated incidence of 0.45% to 2.8% among all neurological tumors (1, 2). While historically considered a predominantly pediatric brain tumor, comprehensive analyses have revealed a bimodal age distribution, exhibiting incidence peaks in both childhood (5–10 years) and young adulthood (21–30 years) (1, 3, 4). Furthermore, a notable female predilection has been consistently observed, with reported male-to-female ratios approximating 1:11 (3, 4). Traditionally, astroblastoma has lacked a specific World Health Organization (WHO) grade due to its intrinsic variability in biological behavior (2, 5). Histopathologically, these tumors have been broadly categorized into "low-grade" or "well-differentiated" variants, generally associated with a more favorable prognosis, and "high-grade" or "anaplastic" counterparts, which typically portend poorer clinical outcomes (6, 7). The clinical spectrum of astroblastoma is diverse, encompassing tumors with relatively indolent progression to those exhibiting aggressive malignant characteristics (2, 3, 8, 9). Notably, the 2021 WHO classification of central nervous system tumors has integrated molecular diagnostics, recognizing "astroblastoma, MN1-altered" as a distinct entity within the category of circumscribed astrocytic gliomas, characterized by the presence of meningioma 1 (MN1) gene alterations (7, 10).

In the management of astroblastomas, the current body of evidence, largely derived from case reports and retrospective analyses, underscores the critical role of maximal safe surgical resection as the primary intervention, aiming to achieve gross total resection (GTR) which correlates with improved tumor control rates and progression-free survival (8, 9, 11–15). Subtotal resection (STR) is generally discouraged as it may not provide equivalent tumor control and often necessitates the consideration of adjuvant therapies (14, 15). The utility of adjuvant radiation therapy (RT), particularly in the context of high-grade and recurrent astroblastomas, suggests a potential survival benefit with postoperative RT (2, 8, 9, 11, 13, 16, 17). However, the optimal dose and target volumes remain under investigation. The role of adjuvant chemotherapy in the management of astroblastoma is even less well-defined, with conflicting reports and a general consensus of unclear benefit in both low- and high-grade tumors, although temozolomide-based regimens have shown some promise in isolated cases (2, 5, 8, 18). This report presents a unique case of high-grade pediatric astroblastoma managed with sequential PBT and GKRS, highlighting the potential feasibility and benefit of this multimodal approach, particularly the role of initial PBT in enabling safe re-irradiation for residual disease and the use of targeted therapy guided by molecular profiling.

Clinical summary

This case involves a 4-year-old girl diagnosed with astroblastoma harboring MN1 alteration, classified as a CNS WHO Grade 3 tumor. At initial presentation, she experienced right lower extremity weakness and gait disturbance. The patient had no significant past medical history, no history of psychiatric illness, and had met age-appropriate developmental milestones prior to presentation. Family history was non-contributory for neurological disorders or malignancy. Further psychosocial details are withheld for privacy. The patient had no relevant past interventions prior to the diagnosis of astroblastoma. Table 1 summarizes the key events during the patient's episode of care. The sequence of imaging findings corresponding to key time points is shown in Figure 1.

In May 2022, the patient developed right lower extremity weakness and unsteady gait without obvious precipitating factors. She was initially diagnosed with synovitis at a local hospital and received conservative treatment, including rest and physical therapy, without improvement. But the weakness gradually worsened. Initial neurological examination confirmed these reported symptoms, although specific details like strength grading were not available. Pre-treatment non-contrast axial CT, performed due to worsening symptoms, revealed a patchy, heterogeneous hyperdense lesion in the left frontal lobe, surrounded by a cystic hypodense area (Figure 1A). Craniotomy and tumor resection were performed, and postoperative MRI revealed a small residual enhancing lesion. Histopathological analysis confirmed the diagnosis of MN1-altered astroblastoma (CNS WHO Grade 3).

TABLE 1 Timeline summarizing key clinical events.

Timeline summarizing key clinical events		
Time Point (Approximate)	Key Event	Corresponding Figure
May 2022 (Month 0)	Onset of symptoms (right leg weakness, unsteady gait); Worsening despite conservative treatment.	
Late May 2022 (Month 0)	Initial CT scan reveals lesion; Craniotomy & maximal safe resection (Surgery 1); Post-op MRI shows residual.	Figure 1A (Pre-op CT)
June 2022 (Month 0-1)	Histopathological Diagnosis: MN1-altered Astroblastoma, CNS WHO Grade 3.	
July-Aug 2022 (Month 1-3)	Adjuvant Proton Beam Therapy (PBT): CSI (36 Gy/20fx) + Local Boost (18 Gy/10fx, Total 54 Gy).	Figure 1B (Pre-PBT MRI). Figure 2 (PBT Plan)
Aug 2022 (Month 3)	Post-PBT MRI: Reduced enhancement, new perilesional edema.	Figure 1C
Sep 2022 (Month 4)	Initiation of oral chemotherapy (Fluzoparib) due to ambiguous MRI findings; Temporary stabilization.	
May 2023 (Month 12)	Follow-up MRI (~9 months post-PBT): Decreased solid component size, persistent mild enhancement.	Figure 1D
June 2023 (Month 13)	Second Craniotomy & Resection; Histopathology confirms residual astroblastoma.	
July 2023 (Month 14)	Salvage Gamma Knife Radiosurgery (GKRS): 30 Gy/5fx.	Figure 3 (GKRS Plan)
Jan 2025 (Month 32)	Last Follow-up (~18 months post-GKRS): MRI shows stable post-treatment changes; No recurrence; No deficits.	Figure 1E

Given the tumor's high grade and potential for dissemination, adjuvant proton beam therapy of Pencil beam scanning was administered, consisting of craniospinal irradiation (CSI) at 36 Gy in 20 fractions (Figure 2A), followed by a local boost of 18 Gy in 10 fractions (Total dose: 54 Gy) (Figure 2B). This dose was selected based on established protocols for pediatric high-grade gliomas, balancing efficacy with the need to minimize long-term toxicity. No significant adverse events were observed during or immediately after treatment. Prior to proton beam therapy, T2-FLAIR imaging demonstrated patchy mild hyperintensity, and contrast-enhanced T1-weighted imaging (T1WI+C) showed heterogeneous mild-to-moderate enhancement of the lesion (Figure 1B). Following completion of proton beam therapy, the extent of contrast enhancement of the solid component was markedly reduced, while new perilesional brain edema was observed (Figure 1C).

Subsequent molecular profiling of the tumor tissue revealed a heterozygous BRCA2 mutation. Based on this finding, oral chemotherapy with the PARP inhibitor fluzoparib (50 mg, twice daily) was initiated as a bridging therapy. This off-label use was discussed extensively with the patient's family, and written informed consent was obtained. The treatment was well-tolerated and was associated with a period of disease stability.

However, approximately 9 months post-proton beam therapy, the solid portion of the lesion had further decreased in size, although mild heterogeneous enhancement persisted (Figure 1D). To confirm the diagnosis and re-evaluate the lesion, a second craniotomy was performed, and histopathology again confirmed residual astroblastoma.

The postoperative MRI showed near-total resection with small, nodular residual enhancing lesions. The interval between PBT and subsequent GKRS was dictated by this period of planned chemotherapy, observation, and the necessary second surgical intervention due to disease persistence. To address the residual disease, stereotactic radiosurgery (Gamma Knife) was performed. Two target volumes were identified within the enhancing lesion, and 30 Gy was delivered in 5 fractions to the 50% isodose line, using the frameless Gamma Knife ICON™ (Elekta) device (Figure 3).

Diagnostic assessment

Diagnostic evaluation included neurological examination, computed tomography (CT), magnetic resonance imaging (MRI) (Figure 1), and histopathological analysis with immunohistochemistry following surgical resection. A key diagnostic challenge was differentiating post-radiation treatment effects (e.g., edema, non-specific enhancement) from true tumor progression on follow-up MRI scans after initial PBT, necessitating careful serial imaging and ultimately a second surgical confirmation. Postoperative pathological examination of the left frontal lobe lesion revealed a high-grade neuroepithelial tumor with both glial and ependymal differentiation, consistent with astroblastoma harboring MN1 alteration, classified as CNS WHO Grade 3. No other differential diagnoses were strongly considered after histopathology.

Immunohistochemistry profile:

- GFAP (partial positive)
- Olig2 (positive)
- S-100 (focally positive)
- Vimentin (positive)
- EMA (partially positive)

10.3389/fonc.2025.1620637

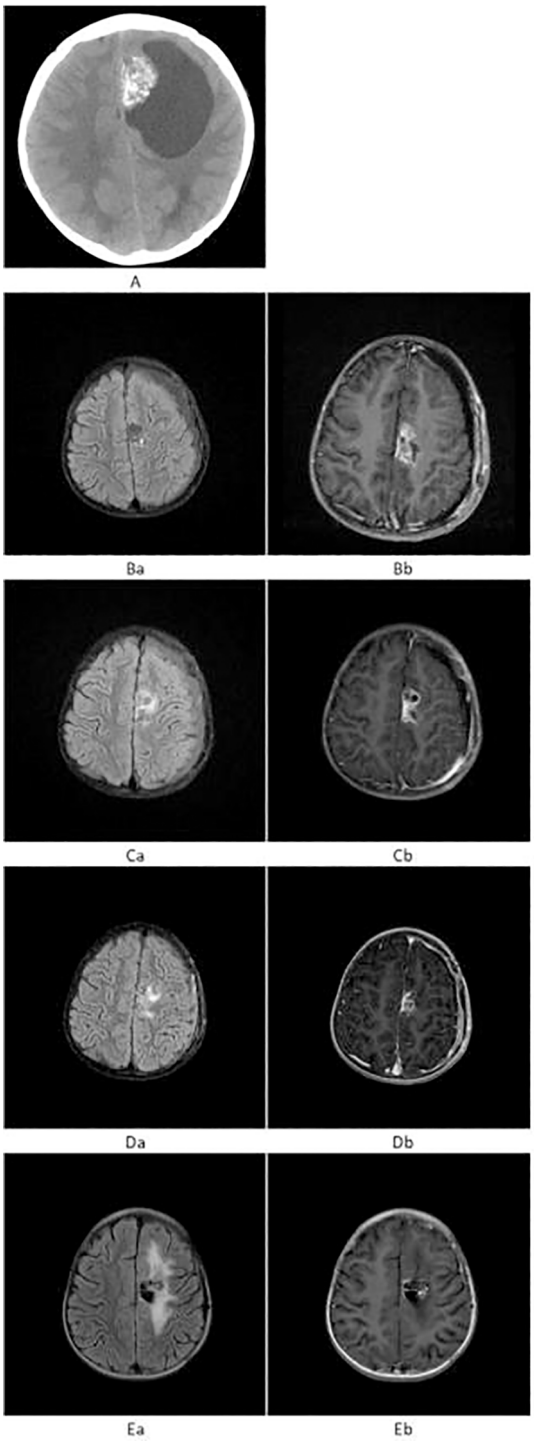

FIGURE 1
(A) Preoperative axial non-contrast CT showing a patchy, heterogeneous hyperdense lesion in the left frontal lobe with surrounding cystic hypodensity. **(B)** Prior to proton beam therapy. **(Ba)** T2-FLAIR shows patchy mild hyperintensity in the left frontal lobe. **(Bb)** T1WI+C reveals heterogeneous mild-to-moderate enhancement of the lesion. **(C)** After proton beam therapy. **(Ca)** T2-FLAIR shows persistent mild hyperintensity. **(Cb)** T1WI+C demonstrates reduced enhancement of the lesion, with new perilesional brain edema. **(D)** At 9 months post-proton beam therapy. **(Da)** T2-FLAIR shows mild patchy hyperintensity. **(Db)** T1WI+C shows reduced size and persistent mild enhancement. **(E)** At 18 months post-Gamma Knife radiosurgery. **(Ea)** T2-FLAIR shows surrounding mild hyperintensity. **(Eb)** T1WI+C reveals no solid enhancement, with only linear enhancement along the cystic margin.

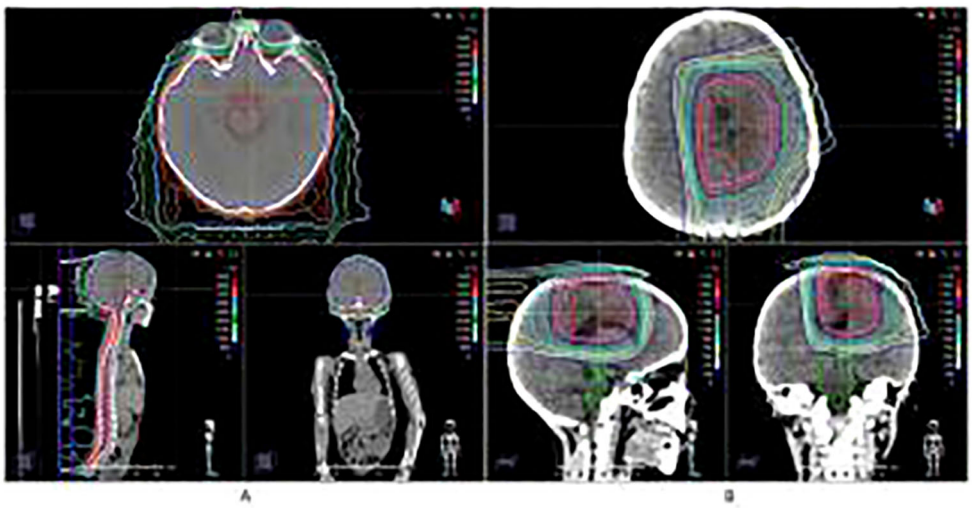

FIGURE 2
Proton Beam Therapy treatment plan and dose distribution. **(A)** Craniospinal irradiation (CSI) at 36 Gy in 20 fractions. **(B)** Local boost of 18 Gy in 10 fractions (Total dose: 54 Gy).

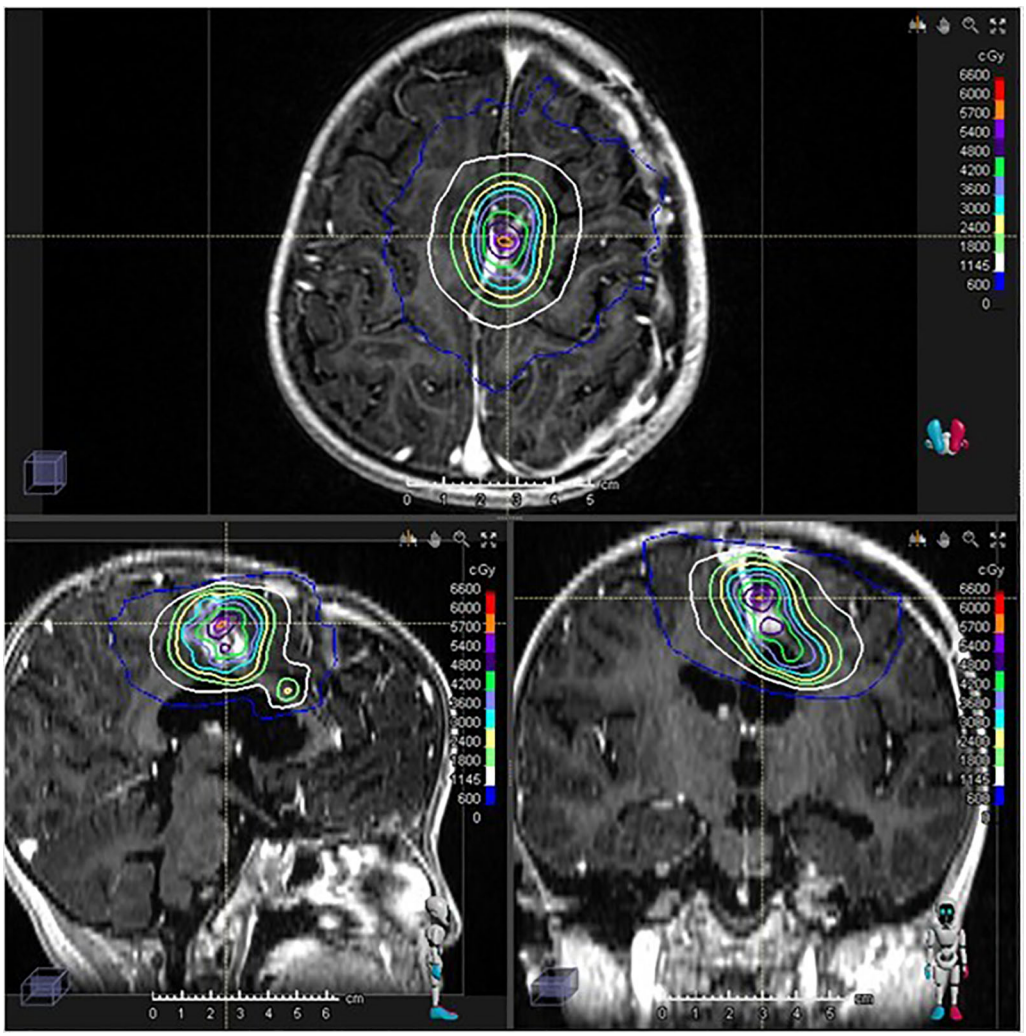

FIGURE 3
Gamma Knife stereotactic radiosurgery treatment plan and dose distribution. 30 Gy/5 fractions was performed.

- D2-40 (positive)
- NeuN, CD34, EZHIP, TTF1-SPT24, CK, YAP-1, BCOR, P53, IDH1-R132H, H3K27M, EGFRvIII, L1CAM, C-myc, SOX10, Calretinin, Neurofilament (NF), and Synaptophysin were negative
- MAP2 (equivocal)
- Ki-67 labeling index: 25–30%
- ATRX (retained expression)
- H3K27me3 (retained expression)
- Cyclin D1 (positive)
- INI-1 and BRG-1 (retained)
- NTRK (1+), with a positive internal control
- Reticulin stain: negative

Molecular Analysis: Further molecular profiling identified a heterozygous BRCA2 mutation.

Prognosis: The tumor was classified as CNS WHO Grade 3, indicating a high-grade malignancy with associated prognostic implications.

Follow-up and outcomes

By 18 months after subsequent Gamma Knife radiosurgery, the lesion no longer demonstrated a definite enhancing solid component; only linear enhancement at the margin of the cystic area was visible, with persistent mild FLAIR hyperintensity surrounding the lesion (Figure 1E). The mild perilesional FLAIR hyperintensity persisted but was asymptomatic and did not require any intervention, such as corticosteroids. No other significant radiation-related toxicities, such as radionecrosis, were observed during follow-up. The patient exhibited no neurological deficits and remained functionally independent in daily life activities. Patient's guardian reported good quality of life with full participation in age-appropriate activities.

Discussion

Although there are therapeutic strategies based on retrospective case series and individual case reports, the rarity of astroblastomas inherently restricts the feasibility of conducting extensive prospective clinical trials (15, 18). Therefore, the optimal treatment modality remains unclear. Maximum safe resection is the treatment of choice as like for other primary brain malignancies (6, 14). Radiation therapy is a crucial adjuvant treatment for high-grade astroblastoma, significantly improving survival rates (3, 4, 6, 8, 16, 18, 19). While its role in low-grade tumors is less clear, radiation can be used after subtotal resection to help control tumor growth (4, 18).

In their series 23 patients, Bonnin and Rubinstein reported that the sole patient who received radiotherapy following biopsy alone survived for 12 years post-diagnosis, indicating a potential benefit of radiotherapy in astroblastoma management (19). Furthermore, they observed that the only patient with high-grade astroblastoma who did not undergo postoperative radiotherapy had the shortest survival duration of 1.5 years, suggesting that the absence of adjuvant radiotherapy may be associated with poorer outcomes in high-grade cases.

Merfeld et al. conducted a retrospective analysis using data from the National Cancer Database to assess the impact of chemotherapy and radiotherapy on astroblastoma outcomes (18). The study found that among patients with high-grade astroblastoma, the 5-year OS of 33.3% for six patients who did not receive radiotherapy was significantly lower, compared to the 5-year OS of 84.6% for the 13 patients who did ($p = 0.075$), highlighting the potential survival benefit of adjuvant radiotherapy in high-grade astroblastoma cases.

Although recurrence in astroblastoma is most often local, dissemination to the spinal cord of astroblastomas have also been observed. Hirano H described a case of a 17-year-old male patient underwent surgery five times (four consecutive intracranial tumor removal surgeries and a final spinal tumor removal surgery) (20). After surgery for the spinal tumor, the patient underwent a course of ICE therapy. Three months after an additional 24 Gy local spinal irradiation was administered, his paraplegia improved slightly for a short period. Thereafter, follow-up head MRIs revealed new tumor recurrence in the basal ganglia. Cyber Knife radiotherapy was then selected to prevent neurological deficits by surgery. Stereotactic radiosurgery controlled the disease for several months, but the patient finally died as a result of the tumor in the middle of 2007.

In central nervous system tumors with a risk of dissemination, craniospinal irradiation (CSI) followed by local treatment, is a key treatment modality for many pediatric cancers, particularly brain tumors where radiotherapy is routinely delivered to the brain or entire craniospinal axis (21, 22). Pilocytic astrocytoma (PA), which is in the same group as astroblastoma, is reported to be disseminating throughout the central nervous system (23–25). In some case series and case report, craniospinal irradiation (CSI) was done for treatment of spinal drop metastasis with good outcome: overall survival time for 9 years, and the patients remained on follow-up (21, 23).

However, the risks of CSI in children include secondary cancers and cognitive impairments. Some studies showed that the different proportions of carcinogenic risks were observed in the lungs, breast, thyroid, stomach, liver, and other organs after different irradiation techniques or carcinogenic models for photon-based CSI radiotherapy (26–28). Bain et al. in 2013, introduced proton beam therapy for craniospinal irradiation (CSI) to minimize the exit dose, thereby concentrating radiation exposure exclusively on the craniospinal axis (23). This approach aimed to reduce radiation exposure to surrounding healthy tissues. Subsequent studies have demonstrated that proton beam CSI (p-CSI) can significantly decrease acute gastrointestinal and hematologic toxicities compared to conventional photon-based CSI, while maintaining comparable disease control outcomes (29).

A study conducted by Howell et al. compared the risks of radiogenic second cancers and cardiac mortality 18 pediatric medulloblastoma patients treated with passively scattered proton or field-in-field photon craniospinal irradiation (CSI), Proton CSI improved normal tissue sparing while also providing more homogeneous target coverage than photon CSI for patients across

a wide age and BMI spectrum (30). Out of 24 evaluated parameters, (V5, V10, V15, and V20 in the esophagus, heart, liver, thyroid, kidneys, and lungs) Wilcoxon signed rank test results indicated 20 were significantly higher for photon CSI compared to proton CSI ($p \leq 0.05$). Specifically, V15 and V20 in all six organs and V5, V10 in the esophagus, heart, liver, and thyroid were significantly higher with photon CSI.

In terms of dose distribution, Yoon et al. evaluated the dosimetric benefits for craniospinal irradiation in cancer in children using three-dimensional conformal radiotherapy (3D-CRT), tomotherapy (TOMO), and proton beam treatment (PBT) in the scattering mode (31). Compared with photon techniques, PBT showed improvements in most dosimetric parameters for CSI patients, with lower organ equivalent doses (OEDs) to organs at risk.

In this case, our management strategy was a sequential, multimodal approach tailored to the evolving clinical and molecular characteristics of the tumor. This included: 1) initial surgery, 2) adjuvant PBT, 3) molecularly-guided systemic therapy with a PARP inhibitor, 4) a second resection for persistent disease, and 5) high-dose salvage GKRS. The cornerstone of this strategy was the initial use of PBT. The physical properties of protons, specifically the Bragg peak, allowed for the delivery of a therapeutic dose to the craniospinal axis and tumor bed while significantly sparing surrounding healthy brain tissue.

After the first surgery, the postoperative MRI revealed a small residual enhancing lesion. Subsequently, considering the tumor's propensity for dissemination, postoperative adjuvant radiotherapy with Proton CSI with a boost to the local tumor was chosen, to reduce the risk of damage to healthy tissue and create conditions for an increased biological dose to the tumor.

This tumor is highly malignant, with a tendency for residual disease, recurrence, and multiple relapses (6, 32). Therefore, in anticipation of secondary recurrence, a combination of repeat surgical resection and stereotactic radiotherapy (SRS) is considered. During the second course of radiotherapy, SRS is often employed for local control (17, 33), and in this context, the superior dose conformity of proton beam therapy—used during the initial treatment instead of conventional photon therapy—becomes a significant advantage, as it preserved a therapeutic window for safe and effective re-irradiation with high-dose GKRS for the residual disease—an option that might have been precluded by the higher integral dose of conventional photon therapy.

Gamma Knife stereotactic radiosurgery (GKRS) has advanced to provide high precision and expanded applicability for re-irradiation cases, including patients with a prior history of radiation therapy. A retrospective study conducted at the Mayo Clinic analyzed 174 patients with recurrent glioblastoma who underwent GKRS between 1991 and 2013. The median overall survival was 10.6 months following GKRS and 19.1 months from initial diagnosis, indicating that GKRS is a safe and modestly effective salvage treatment for recurrent glioblastoma (34).

In this case, Gamma Knife stereotactic radiosurgery (SRS) was administered to the local lesion, shortly after the second surgery of near-total resection. Head MRI 18 months after SRS demonstrated that the lesion remained within the irradiation field, with a decreased area of enhancement compared to pre-radiotherapy imaging, suggesting post-radiation changes. No signs of recurrence or metastasis were observed.

A novel aspect of this case was the use of a PARP inhibitor, fluzoparib, guided by the identification of a heterozygous BRCA2 mutation. While temozolomide is sometimes considered for high-grade gliomas, the presence of a known DNA damage repair pathway defect provided a strong rationale for a targeted approach. Although PARP inhibitor use in astroblastoma is not established, its selection here represents a personalized treatment strategy. This intervention was associated with a period of disease stability, bridging the patient to definitive local therapy.

Furthermore, definitive evidence regarding the optimal radiation dosage for astroblastoma is currently lacking. In the present case, initial treatment involved local irradiation delivering 54 Gy, a boost administered following CSI. Despite this regimen, the contrast-enhancing lesion persisted, and subsequent pathological examination after craniotomy 9 months later the proton beam therapy confirmed residual astroblastoma. This outcome suggests that a total dose of 54 Gy may have been inadequate for achieving local control in this specific instance. Considering that standard treatment protocols for high-grade gliomas typically employ doses around 60 Gy, this established practice could inform the determination of future prescribed doses for astroblastoma. Subsequently, Gamma Knife radiosurgery was administered at a dose of 30 Gy, a level consistent with dosages used for recurrent high-grade glioma irradiation. Notably, the patient has remained free from recurrence for 18 months following this intervention. Despite the limitation of being just one case report, with no large controlled studies yet available, it suggests a potential for controlling secondary recurrence in Astroblastoma.

Strengths and limitations: The strength of this report lies in detailing a multimodal approach combining advanced radiotherapy techniques (PBT and GKRS) for a rare, high-grade pediatric tumor with molecular confirmation (MN1-altered) and providing relatively long-term follow-up (18 months post-SRS). Limitations include its nature as a single case report, making generalizations difficult. The specific contribution of each treatment modality (PBT vs. chemo vs. GKRS) to the final outcome cannot be definitively isolated. Furthermore, optimal radiation doses and volumes for astroblastoma remain uncertain. Nonetheless, this case demonstrates the potential utility of a strategy that combines initial tissue-sparing PBT with molecularly targeted therapy and high-dose salvage SRS to manage this challenging disease.

Primary "take-away" lessons: This case highlights the challenge of managing high-grade pediatric astroblastoma and demonstrates the potential utility of a sequential multimodal strategy involving initial maximal safe resection followed by tissue-sparing adjuvant PBT. The conformal nature of PBT may be advantageous not only for reducing acute and long-term toxicity but also for preserving options for effective salvage therapy, such as high-dose SRS, in the event of residual or recurrent disease.

The patient's perspective:

Our daughter's diagnosis was overwhelming, but we felt supported by the medical team throughout the treatment process.

The initial proton therapy seemed less harsh than we feared. Although needing further treatment with chemotherapy and Gamma Knife was difficult, we are incredibly grateful that she is doing well now, attending school, and living a normal life. We hope sharing her story can help other families facing this rare diagnosis.

Conclusion

We presented a case of high-grade pediatric MN1-altered, BRCA2-mutated astroblastoma managed with maximal safe resection, adjuvant proton beam therapy including craniospinal irradiation, chemotherapy, and subsequent salvage Gamma Knife radiosurgery for residual disease. The clinical presentation, radiologic features, prognostic factors, and management strategies of astroblastomas were reviewed from the current literature. Given the rarity of astroblastoma, the optimal treatment strategy, particularly regarding radiation dose and modality, requires further investigation. We hope this case provides valuable insights into a potential multimodal approach for this challenging disease.

Data availability statement

The datasets presented in this study can be found in online repositories. The names of the repository/repositories and accession number(s) can be found in the article/supplementary material.

Ethics statement

The studies involving humans were approved by Institutional Review Board of Hebei Yizhou Cancer Hospital. The studies were conducted in accordance with the local legislation and institutional requirements. Written informed consent for participation in this study was provided by the participants' legal guardians/next of kin. Written informed consent was obtained from the individual(s), and minor(s)' legal guardian/next of kin, for the publication of any potentially identifiable images or data included in this article.

Author contributions

XZ: Data curation, Writing – original draft, Conceptualization, Investigation, Methodology, Writing – review & editing. XW: Formal analysis, Methodology, Investigation, Writing – review & editing, Writing – original draft, Conceptualization. WN: Investigation, Writing – review & editing, Resources, Data curation, Formal analysis. JL: Formal analysis, Investigation, Validation, Writing – review & editing, Resources. YJ: Investigation, Writing – original draft, Data curation, Formal analysis. YN: Conceptualization, Investigation, Writing – original draft, Data curation. JW: Software, Supervision, Data curation, Writing – original draft, Project administration. ZW: Writing – original draft, Data curation, Conceptualization, Methodology, Software. WW: Resources, Writing – original draft, Methodology, Data curation, Software, Writing – review & editing. JZ: Investigation, Data curation, Conceptualization, Writing – original draft, Project administration. JK: Writing – review & editing, Validation, Resources, Formal analysis, Methodology. LY: Conceptualization, Visualization, Writing – original draft, Investigation, Methodology. DZ: Supervision, Methodology, Conceptualization, Writing – original draft, Formal analysis, Validation. YZ: Visualization, Software, Formal analysis, Project administration, Validation, Writing – review & editing. MM: Project administration, Writing – review & editing, Resources, Supervision, Validation, Conceptualization. SS: Software, Methodology, Writing – review & editing, Supervision, Writing – original draft, Formal analysis, Data curation, Project administration, Validation.

Funding

The author(s) declare financial support was received for the research and/or publication of this article. This work was supported by institutional funds from Hebei Yizhou Cancer Hospital.

Conflict of interest

The authors declare that the research was conducted in the absence of any commercial or financial relationships that could be construed as a potential conflict of interest.

Generative AI statement

The author(s) declare that Generative AI was used in the creation of this manuscript. During the preparation of this work the authors used Gemini in order to improve readability and language. After using this tool/service, the authors reviewed and edited the content as needed and take full responsibility for the content of the publication.

Any alternative text (alt text) provided alongside figures in this article has been generated by Frontiers with the support of artificial intelligence and reasonable efforts have been made to ensure accuracy, including review by the authors wherever possible. If you identify any issues, please contact us.

Publisher's note

All claims expressed in this article are solely those of the authors and do not necessarily represent those of their affiliated organizations, or those of the publisher, the editors and the reviewers. Any product that may be evaluated in this article, or claim that may be made by its manufacturer, is not guaranteed or endorsed by the publisher.

References

1. Caroli E, Salvati M, Esposito V, Orlando ER, Giangaspero F. Cerebral astroblastoma. *Acta Neurochir (Wien)*. (2004) 146:629–33. doi: 10.1007/s00701-004-0230-7

2. Mallick S, Benson R, Venkatesulu B, Melgandi W, Rath GK. Patterns of care and survival outcomes in patients with astroblastoma: An individual patient data analysis of 152 cases. *Childs Nerv Syst*. (2017) 33:1295–302. doi: 10.1007/s00381-017-3410-5

3. Hammas N, Senhaji N, Alaoui Lamrani MY, Bennis S, Chaoui EM, El Fatemi H, et al. Astroblastoma – a rare and challenging tumor: A case report and review of the literature. *J Med Case Rep*. (2018) 12:102. doi: 10.1186/s13256-018-1623-1

4. Jeon C, Kim B, Choi JW. Clinicoradiological and histopathological characteristics and treatment outcomes of cerebral astroblastoma in children: A single-institution experience. *J Neurosurg Pediatr*. (2022) 29:513–9. doi: 10.3171/2022.1.PEDS21389

5. Khan H, Afreen M, Khan A, Ali Malik S, Bhatti MI. Navigating the diagnosis and treatment of astroblastoma: A pediatric case report. *Cureus*. (2024) 16(2):e54901. doi: 10.7759/cureus.54901

6. Sarper B, Bayrak BY, Halis H, Alparslan B, Yeni Bayraktar H. Malignant astroblastoma. *Balk Med J*. (2020) 37(4):224-225. doi: 10.4274/balkanmedj.galenos.2020.2019.11.39

7. Zumaeta J, Martinez R, Santiago Rea N, Anicama-Lima WE, Casavilca-Zambrano S, Valerio J. Hemorrhagic astroblastoma: Atypical presentation of a rare tumor. Illustrative case. *J Neurosurg Case Lessons*. (2025) 9:CASE24486. doi: 10.3171/CASE24486

8. D'Cruze L, Sundaram S, Iyer S, Ganesh K. A rare case of a high-grade astroblastoma with 5-year follow-up. *Asian J Neurosurg*. (2021) 16:183–6. doi: 10.4103/ajns.AJNS_315_20

9. Singh K, Garg S, Rani S, Sandhu P. High-grade intraventricular astroblastoma in a young adult: A rare and controversial tumor to manage. *Asian J Neurosurg*. (2021) 16:567–74. doi: 10.4103/ajns.AJNS_430_20

10. Louis DN, Perry A, Wesseling P, Brat DJ, Cree IA, Figarella-Branger D, et al. The 2021 WHO classification of tumors of the central nervous system: A summary. *Neuro-Oncol*. (2021) 23:1231–51. doi: 10.1093/neuonc/noab106

11. Agarwal V, Mally R, Palande D, Velho V. Cerebral astroblastoma: A case report and review of literature. *Asian J Neurosurg*. (2012) 7:98–100. doi: 10.4103/1793-5482.98657

12. Sprenger F, Da Silva EB, Cavalcanti MS, De Almeida Teixeira BC. Radiology-pathology and surgical correlation in astroblastoma. *Am J Neuroradiol*. (2023) 44:390–5. doi: 10.3174/ajnr.A7824

13. Sadiq M, Ahmad I, Shuja J, Ahmad Z, Ahmed R, Ahmad K. Astroblastoma in a young female patient: A case report and literature review of clinicopathological, radiological and prognostic characteristics and current treatment strategies. *Brain Tumor Res Treat*. (2017) 5:120. doi: 10.14791/btrt.2017.5.2.120

14. Sughrue ME, Choi J, Rutkowski MJ, Aranda D, Kane AJ, Barani IJ, et al. Clinical features and post-surgical outcome of patients with astroblastoma. *J Clin Neurosci*. (2011) 18:750–4. doi: 10.1016/j.jocn.2010.11.007

15. Ahmed KA, Allen PK, Mahajan A, Brown PD, Ghia AJ. Astroblastomas: A surveillance, epidemiology, and end results (SEER)-based patterns of care analysis. *World Neurosurg*. (2014) 82:e291–7. doi: 10.1016/j.wneu.2013.10.035

16. Bhalerao S, Nagarkar R, Adhav A. A case report of high-grade astroblastoma in a young adult. *CNS Oncol*. (2019) 8:CNS29. doi: 10.2217/cns-2018-0012

17. Weintraub D, Monteith SJ, Yen CP, Schlesinger D, Rich T, Sheehan J. Recurrent astroblastoma treated with gamma knife radiosurgery. *J Neurooncol*. (2011) 103:751–4. doi: 10.1007/s11060-010-0430-3

18. Merfeld EC, Dahiya S, Perkins SM. Patterns of care and treatment outcomes of patients with astroblastoma: A national cancer database analysis. *CNS Oncol*. (2018) 7:CNS13. doi: 10.2217/cns-2017-0038

19. Bonnin JM, Rubinstein LJ. Astroblastomas: A pathological study of 23 tumors, with a postoperative follow-up in 13 patients. *Neurosurgery*. (1989) 25:6–13. doi: 10.1097/00006123-198907000-00002

20. Hirano H, Yunoue S, Kaji M, Tsuchiya M, Arita K. Consecutive histological changes in an astroblastoma that disseminated to the spinal cord after repeated intracranial recurrences: A case report. *Brain Tumor Pathol*. (2008) 25:25–31. doi: 10.1007/s10014-007-0224-2

21. Ajithkumar T, Taylor R, Kortmann RD. Radiotherapy in the management of paediatric low-grade gliomas. *Clin Oncol R Coll Radiol G B*. (2019) 31:151–61. doi: 10.1016/j.clon.2018.11.032

22. Stripay JL, Merchant TE, Roussel MF, Tinkle CL. Preclinical models of craniospinal irradiation for medulloblastoma. *Cancers*. (2020) 12:133. doi: 10.3390/cancers12010133

23. Bian SX, McAleer MF, Vats TS, Mahajan A, Grosshans DR. Pilocytic astrocytoma with leptomeningeal dissemination. *Childs Nerv Syst ChNS Off J Int Soc Pediatr Neurosurg*. (2013) 29:441–50. doi: 10.1007/s00381-012-1970-y

24. *Leptomeningeal dissemination of cerebellar pilocytic astrocytoma* (2025). Available online at.

25. Pollack IF, Hurtt M, Pang D, Albright AL. Dissemination of low grade intracranial astrocytomas in children. *Cancer*. (1994) 73:2869–78. doi: 10.1002/1097-0142(19940601)73:11<2869::aid-cncr2820731134>3.0.co;2-i

26. Mori T, Yamaguchi S, Onimaru R, Hashimoto T, Aoyama H. Ronc-19. Two cases of re-irradiation for late recurrent or radiation-induced tumor after radiation therapy for pediatric brain tumors. *Neuro-Oncology*. 22(Supplement_3):iii459. doi: 10.1093/neuonc/noaa222.788

27. Ab BAG. *Clinical outcomes and late endocrine, neurocognitive, and visual profiles of proton radiation for pediatric low-grade gliomas*. *Int J Radiat Oncol Biol Phys*. (2014) 89(5):1060-1068. doi: 10.1016/j.ijrobp.2014.04.053

28. Casey DL, Kushner BH, Cheung NKV, Modak S, Basu EM, Roberts SS, et al. Reduced-dose radiation therapy to the primary site is effective for high-risk neuroblastoma: Results from a prospective trial. *Int J Radiat Oncol Biol Phys*. (2019) 104:409–14. doi: 10.1016/j.ijrobp.2019.02.004

29. Brown AP, Barney CL, Grosshans DR, McAleer MF, de Groot JF, Puduvalli VK, et al. Proton beam craniospinal irradiation reduces acute toxicity for adults with medulloblastoma. *Int J Radiat Oncol Biol Phys*. (2013) 86:277–84. doi: 10.1016/j.ijrobp.2013.01.014

30. Howell RM, Giebeler A, Koontz-Raisig W, Mahajan A, Etzel CJ, D'Amelio AM Jr, et al. Comparison of therapeutic dosimetric data from passively scattered proton and photon craniospinal irradiations for medulloblastoma. *Radiat Oncol*. (2012) 7:116. doi: 10.1186/1748-717X-7-116

31. Yoon M, Shin DH, Kim J, Kim JW, Kim DW, Park SY, et al. Craniospinal irradiation techniques: A dosimetric comparison of proton beams with standard and advanced photon radiotherapy. *Int J Radiat Oncol Biol Phys*. (2011) 81:637–46. doi: 10.1016/j.ijrobp.2010.06.039

32. Fu L, Lao IW, Huang L, Ou L, Yuan L, Li Z, et al. Spinal cord astroblastoma with EWSR1-BEND2 fusion in female patients: A report of four cases from China and a comprehensive literature review. *Am J Surg Pathol*. (2024) 48:1372–80. doi: 10.1097/PAS.0000000000002298

33. Allison CM, Scoones D, Batra A, Sinclair G. Thirteen-year long-term follow-up in a rare case of anaplastic astroblastoma: What makes the difference? *Surg Neurol Int*. (2022) 13:221. doi: 10.25259/SNI_1065_2021

34. Imber BS, Kanungo I, Braunstein S, Barani IJ, Fogh SE, Nakamura JL, et al. Indications and efficacy of gamma knife stereotactic radiosurgery for recurrent glioblastoma: 2 decades of institutional experience. *Neurosurgery*. (2017) 80:129–39. doi: 10.1227/NEU.0000000000001344

frontiers | Frontiers in Medicine

TYPE Original Research
PUBLISHED 16 September 2025
DOI 10.3389/fmed.2025.1661521

Check for updates

OPEN ACCESS

EDITED BY
Poonam Yadav,
Northwestern University, United States

REVIEWED BY
Susovan Jana,
National Institute of Mental Health (NIH), United States
Gayatri Sharma,
Amity University, Noida, India

*CORRESPONDENCE
Narottam Lamichhane
narulamichhane@umm.edu
Hem D. Shukla
hdshukla@som.umaryland.edu

RECEIVED 07 July 2025
ACCEPTED 12 August 2025
PUBLISHED 16 September 2025

CITATION
Keepers Z, Sharma A, Roy S, Ryan H, Bhandary B, Ren L, Lamichhane N and Shukla HD (2025) Mouse pancreatic tumor organoids reveal synergistic efficacy of low-dose anticancer drug and radiation combinations.
Front. Med. 12:1661521.
doi: 10.3389/fmed.2025.1661521

COPYRIGHT
© 2025 Keepers, Sharma, Roy, Ryan, Bhandary, Ren, Lamichhane and Shukla. This is an open-access article distributed under the terms of the Creative Commons Attribution License (CC BY). The use, distribution or reproduction in other forums is permitted, provided the original author(s) and the copyright owner(s) are credited and that the original publication in this journal is cited, in accordance with accepted academic practice. No use, distribution or reproduction is permitted which does not comply with these terms.

Mouse pancreatic tumor organoids reveal synergistic efficacy of low-dose anticancer drug and radiation combinations

Zachery Keepers[1], Aniketh Sharma[2], Sanjit Roy[1], Hurley Ryan[1], Binny Bhandary[1], Lei Ren[1], Narottam Lamichhane[1]* and Hem D. Shukla[1]*

[1]Department of Radiation Oncology, University of Maryland School of Medicine, Baltimore, MD, United States, [2]Department of Biomedical Engineering, University of Illinois at Urbana-Champaign, Urbana, IL, United States

Background: Pancreatic cancer is the fourth-leading cause of cancer death in the United States, with a 5-year survival rate of only 13%. Most patients with locally advanced pancreatic cancer receive chemotherapy with or without radiation therapy (RT). However, current treatment approaches often result in limited clinical response, highlighting the need for novel therapeutic strategies tested in robust model systems. Pancreas tumor-derived organoids offer a promising representative preclinical model for assessing responses to chemotherapy drugs, RT, and combination treatments.
Methods: Pancreatic tumor organoids (PTOs) were derived from Panc02 mouse flank tumors. The PTO microenvironment was characterized and compared with the *in vivo* tumor using immunohistochemical and immunofluorescence staining for alpha-smooth muscle actin (α-SMA) and vimentin. The organoids were treated with fractionated x-ray radiation, gemcitabine, 5-fluorouracil (5-FU), and combinations of drugs with radiation. Treatment response was observed and quantified using brightfield imaging and immunofluorescence to detect reactive oxygen species (ROS) and γH2AX.
Results: Three-dimensional PTOs exhibited expression patterns of α-SMA and vimentin similar to *in vivo* tumors, underscoring their relevance as a translational preclinical model. Dose-dependent growth suppression was observed following treatment with individual chemotherapy agents and radiation. Combination treatments with low-dose chemotherapy and radiation resulted in significantly greater inhibition of organoid growth compared to single-modality treatments. This enhanced effect was validated by reduced vimentin expression, increased γH2AX expression, and elevated reactive oxygen species (ROS) production, indicating amplified DNA damage and cytotoxicity.
Conclusion: Combining low-dose chemotherapy with radiation is significantly more effective at inhibiting pancreatic tumor organoid growth than either treatment alone, likely by targeting distinct signaling pathways. Additionally, the tumor organoid model holds promise for examining drug and radiation treatment responses, with potential for translational impact.

KEYWORDS

pancreatic cancer, radiation therapy, organoid, combination therapy, 5-fluorouracil (5-FU), gemcitabine, ROS, double-stranded breaks (DSBs)

Introduction

Pancreatic cancer is the fourth leading cause of cancer-related deaths. In 2025, the estimated number of pancreatic cancer cases was 67,440, with 51,980 deaths reported (1). The high mortality rate is primarily attributed to late-stage diagnosis, tumor heterogeneity, and resistance to conventional treatments (2). Chemotherapy and radiation therapy remain standard treatment modalities; however, monotherapy often yields variable responses, underscoring the need for individualized treatment strategies (3, 4).

Pancreatic ductal adenocarcinoma (PDAC) has been extensively studied using various models, including two-dimensional cell lines and *in vivo* mouse models. However, these models have limitations and may only offer partial insight into treatment response (4). Two-dimensional cell line models fail to accurately simulate the complexity of the three-dimensional (3D) tumor microenvironment (TME). *In vivo* mouse models, while more representative, are time-consuming and costly. Therefore, in this study, we used a 3D tumor-derived organoid model, which more accurately mimics the diversity and architecture of a tumor, is cost-effective and generally quick to generate, and can be extensively propagated for experimental manipulation (5, 6).

Tumor organoids derived from pancreatic tissue have shown promise as translational models (7, 8). Additionally, 3D organoids mimic functional characteristics of tumors when transplanted into mice (9) and exhibit treatment responses similar to those of the original tumor (3, 10). They also retain the expression of stromal and epithelial markers, enabling study of the response of the TME to different therapies (11).

Standard therapies for PDAC include FOLFIRINOX, which is a combination of 5-fluorouracil (5-FU), oxaliplatin, irinotecan, and leucovorin, or gemcitabine and nab-paclitaxel with or without radiation therapy (RT). However, these approaches are based upon large population studies and could be improved for individualized patient care. Preclinical data show that combining chemotherapeutic agents with low-dose RT could result in tumor suppression due to increased apoptotic signaling, reactive oxygen species (ROS), and DNA damage (12). Currently, there are no studies that analyze the effects of chemotherapy combined with RT on the markers expressed in these changes (13). Evaluating these effects in robust pre-clinical models, such as 3D tumor organoids, may support and unlock insights for individualized care.

This study aims to evaluate the therapeutic potential of combination chemotherapy and radiation therapy using pancreatic tumor organoids (PTOs) derived from murine Panc02 tumors. To evaluate tumor microenvironment fidelity in these PTOs, the expression of two key TME markers, alpha-smooth muscle actin (α-SMA) and vimentin, was assessed using immunohistochemical techniques. PTOs were then treated with single and combination therapies to compare treatment responses. Finally, the effects on ROS and γH2AX were assessed using immunofluorescence.

While some studies have manipulated the expression of specific markers to sensitize pancreatic cancer models to chemotherapy (14), this study evaluated the direct impact of chemotherapy on markers such as ROS and γH2AX. By assessing the efficacy of combining chemotherapy with RT and validating ROS-induced DNA damage as a potential mechanism of PTO inhibition, this study highlights the effects of the combination approach to treatment and the importance of the organoid model as a promising platform for precision medicine in pancreatic cancer (see Figure 1).

Abbreviations: PDAC, Pancreatic ductal adenocarcinoma; RT, Radiation therapy; PTOs, Pancreatic tumor organoids; α-SMA, Alpha-smooth muscle actin; ROS, Reactive oxygen species; γH2AX, Phosphorylated histone H2AX; 5-FU, 5-Fluorouracil; TME, Tumor microenvironment.

Methods

Mouse pancreatic tumor organoid culture

The mouse pancreatic tumor organoids were derived from flank tumors developed in c57bl/6 mice following subcutaneous injection of Panc02 cells. Organoids were grown and cultured in Matrigel® domes on 24-well plates, as described previously (3).

Immunofluorescent and immunohistochemical staining of mouse pancreas tumor organoids and tumor tissue

The mouse pancreatic tumor organoids were generated and propagated in Matrigel® domes in 24-well plates as described above. Immunofluorescence staining was performed as follows: the organoids were fixed in formalin tissue fixation buffer solution with 10% neutral buffer (Sigma Chemical, United States). Before staining, the fixative was removed, and organoids were washed with 1× PBS three times for 5 min each. Organoids were then permeabilized with 0.2% Triton X-100 for 5 min, washed with 1× PBS for 5 min, and blocked with the blocking buffer (Vector Labs, United States) for 1 h. Primary antibodies used were α-SMA (smooth muscle actin): rabbit polyclonal unconjugated 1:100 dilution (ABclonal antibody, #A7248, United States), vimentin: Alexa Fluor 594 conjugated anti-mouse vimentin 1:300 dilution (BioLegend, #699303, United States), and γ-H2AX: phospho gamma S139 H2AX-anti-rabbit (Cell Signaling Technology, #9718S, United States) 1:400 dilution. Incubation with primary antibody was performed overnight in a 1:5 diluted blocking buffer in a 4 °C cold room. Next, the primary antibodies were removed and washed as described above. For the unconjugated α-SMA and γ-H2AX detection, Alexa Fluor 488 rabbit secondary antibody (Thermo Fisher Scientific, #A11008, United States) at 1:300 dilution was used for 1 h. Hoechst 33342 dye (Thermo Fisher Scientific, #H21492, United States) with a concentration of 1 μg/mL was then added for 5–10 min. The antibody and Hoechst dye were then discarded, and the organoids were washed in the same way as described earlier. Finally, the organoids were kept in 1× PBS, and images were captured using an EVOS fluorescence microscope at 20x magnification (Thermo Fisher Scientific, United States). For staining, slides were deparaffinized, unmasked (Vector Labs, United States), and blocked with blocking buffer (Vector Labs, United States). Staining with the α-SMA primary antibody was the same as described above. For the secondary antibody, Vectastain Universal Quick Kit was used according to the manufacturer's instructions. Finally, ImmPACT DAB (Vecta Stain, United States) was used to develop a brown color. After washing with water, the

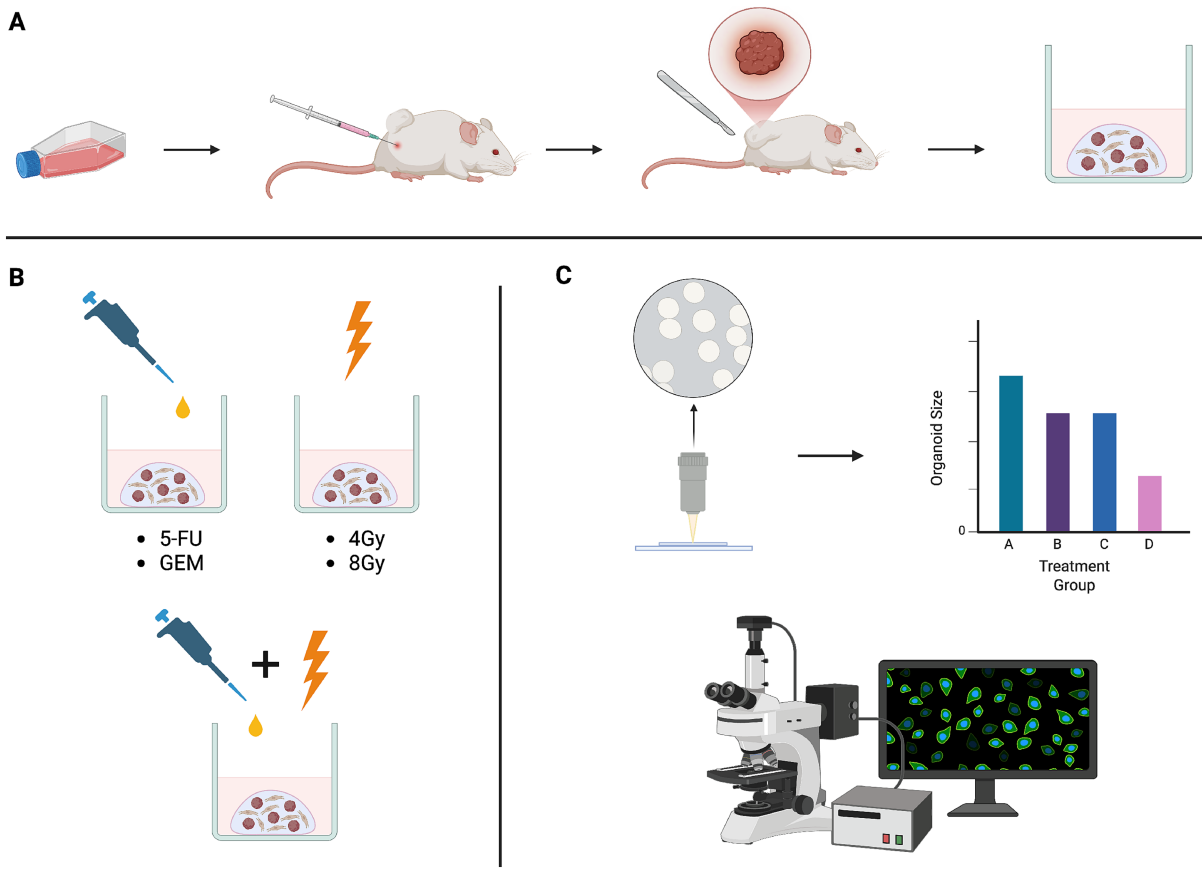

FIGURE 1
(A) Panc02 cells were subcutaneously injected into the flanks of mice and subsequently resected to generate tumor organoids of diverse cell types. **(B)** Tumor organoids were treated with chemotherapy drugs often used in standard-of-care regimens, ionizing radiation, and combinations of chemotherapy and radiation. **(C)** Treatment response was assessed both qualitatively and quantitatively using brightfield imaging and immunofluorescent techniques. Schematic created in BioRender.

slides were air-dried and mounted with cytoseal-60 (Epredia, United States). The images were captured with an EVOS Xl color microscope.

Treatment of organoids with chemotherapy drugs, radiation, and brightfield imaging

The organoids were grown in 25 µL Matrigel® domes on 24-well plates with 500 µL of organoid growth media. Treatment groups included 5-FU (0–100 µM), gemcitabine (5 µM), RT (4 Gy or 8 Gy), and 5-FU or gemcitabine + RT. For the single-modality groups, treatment was administered once, and organoids were allowed to grow for 5 days. For the combination groups, RT was administered 24 h after the initiation of chemotherapy treatment, and organoids were allowed to grow for an additional 4 days. At the end of the treatment, images were captured with an EVOS light microscope and fixed in formalin, as described above. After removal of the fixative, the organoids were washed with 1x PBS, three times each for 5 min, permeabilized with 0.2% Triton X-100 for 5 min, and stained with Hoechst dye (1 µg/mL) for 10 min. The images were captured with an EVOS fluorescence microscope (blue filter).

Measurement of ROS

Organoids were grown and treated as above. At the end of radiation treatment, organoids were incubated with ROS substrate DHE (dihydroethidium, Medchem Express, United States) 20 µg/mL in growth media and incubated for approximately 2 h. Images were captured with the EVOS fluorescence microscope (red filter). Brightfield images were also obtained.

Tumor organoid response and statistical analysis

Tumor organoid response after treatment was assessed by averaging the size of the five largest organoids, as determined by ImageJ. The organoids that did not receive treatment were considered a control group, and all groups' average sizes were normalized to the average size of the control. The responses of the groups were directly compared using a one-sided Student's *t*-test, with a particular focus on comparing groups receiving combination treatments to those receiving the most effective individual component of those combinations. Differences in the average organoid size were considered significant with a p-value of <0.05.

Results

Characterization of mouse pancreas tumor organoids as a model to study chemotherapy drugs and radiation treatment response

It has been shown that mouse PTOs, derived from pancreas tumor tissues or patient-derived xenografts, closely mimic many of the histological, genetic, and phenotypic features of PDAC (9, 10). In this study, we have observed that tumor organoids may maintain the key characteristics of the original TME, expressing α-SMA and vimentin in patterns similar to tumor tissue (Figure 2). Thus, these tumor organoids represent cellular heterogeneity, tumor architecture, and stromal interactions with other important cell types, including but not limited to cancer-associated fibroblasts (CAFs).

Treatment response of mouse pancreas tumor organoids to 5-FU, gemcitabine, and radiation alone and in combination

The sensitivity of mouse PTOs to different doses of 5-fluorouracil (5-FU), gemcitabine, and radiation as monotherapy and combination therapy was evaluated. Tumor organoids were treated with 10–100 μM of 5-FU and monitored for growth inhibition by brightfield imaging. The data showed dose-dependent growth inhibition. Only 100 μM of 5-FU achieved >50% inhibition of tumor organoids, suggesting that single-modality treatment needs high doses to inhibit tumor organoid growth. Notably, co-treatment of 5-FU with radiation (e.g., 25 μM + 8 Gy) yielded synergistic effects and showed significant growth inhibition ($p < 0.05$) compared to single-modality treatments (Figure 3). Furthermore, we observed >70% growth inhibition in tumor organoids treated with 100 μM of 5-FU combined with 8 Gy of radiation. It is also important to note that the combination of 50 μM 5-FU + 8 Gy RT resulted in a response that was not consistent with a dose-dependent trend, which might be expected given the responses to combinations of 5-FU with 4 Gy RT. This is most likely due to the presence of an outlier organoid, which was approximately 2 standard deviations larger than the average of the other organoids in the group and was the largest in any group receiving 8 Gy of RT. Given the totality of the evidence, it is reasonable to conclude that a combination of low doses of 5-FU + radiation reduced organoid viability more effectively than either treatment alone.

The response of PTOs to gemcitabine + radiation treatment was also examined. Tumor organoids treated with a low dose of gemcitabine followed by 4 Gy or 8 Gy of radiation showed greater growth inhibition compared to single-modality treatments. There was approximately 50 and 70% growth inhibition in PTOs treated with 4 Gy + 5 μM gemcitabine and 8 Gy + 5 μM gemcitabine, respectively (Figure 4). While the response of the group treated with 4 Gy + 5 μM gemcitabine was not significant compared to the response of the group treated with gemcitabine alone ($p = 0.10$), it was significant when compared to the group treated with 4 Gy alone ($p < 0.05$). Additionally, immunofluorescent staining revealed a disorganized expression of vimentin following treatment with 4 Gy + 5 μM gemcitabine, which was not observed following treatment with either modality in isolation (Figure 5). These data suggest that the combination treatment was more effective, leading to enhanced PTO growth inhibition and TME disruption.

This study demonstrated that pancreatic tumor organoids exhibit distinct responses to individual and combination treatments. Specifically, the combination treatment of low doses of 5-FU or gemcitabine with radiation shows significant inhibition of

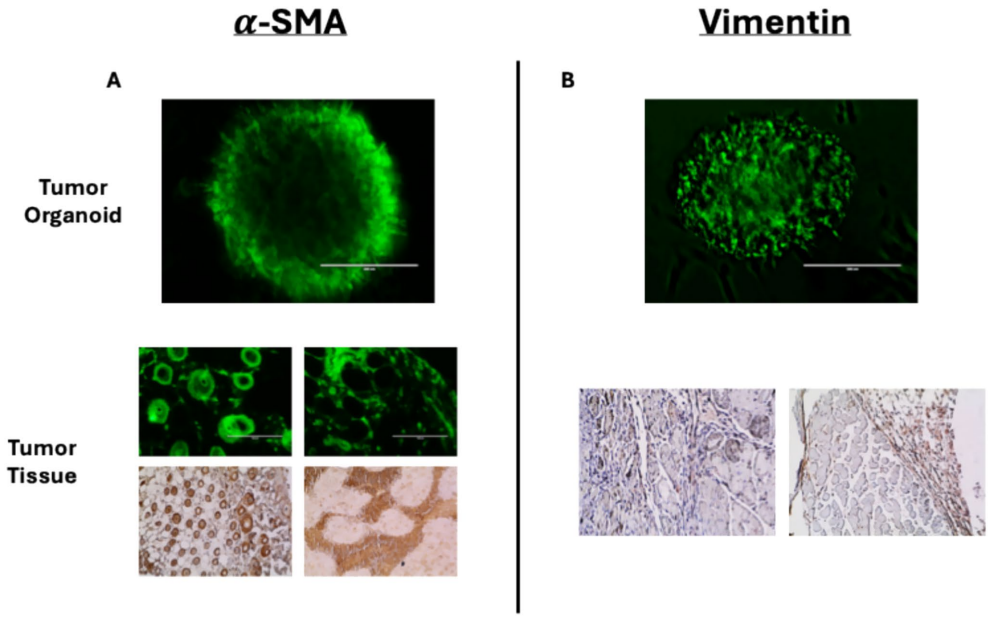

FIGURE 2
Immunofluorescent staining of tumor organoids and immunohistochemical staining of mouse-derived pancreas tumor tissues for **(A)** α-SMA and **(B)** vimentin. Immunofluorescent stains of tumor tissues for α-SMA corroborate the DAB stain.

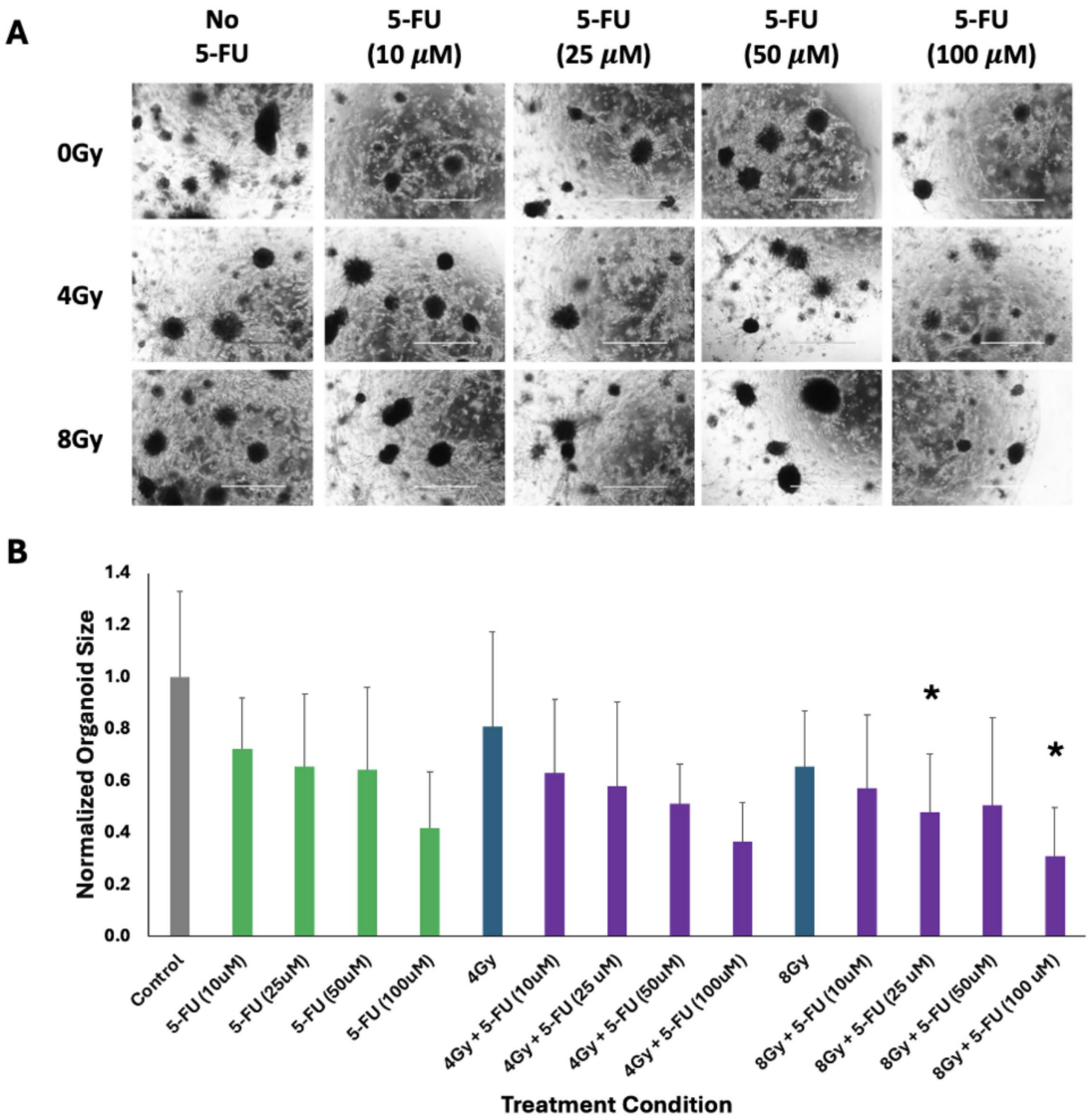

FIGURE 3
Responses of pancreas tumor organoids to treatment with 5-FU (10–100 μM), RT (4 and 8 Gy), and 5-FU + RT at various doses and combinations. The scale bar at the bottom right of each image represents 1,000 μm. **(A)** Brightfield imaging 5 days after the initiation of treatment. **(B)** Average size of the five largest organoids in each of the above images, normalized to the control. Green bars represent those organoids treated with only 5-FU, blue bars represent those treated with only RT, and purple bars represent those treated with a combination of 5-FU and RT. The asterisk indicates a statistically significant ($p < 0.05$) decrease in average organoid size as compared to the most effective single-modality treatment. Error bars represent 1 standard deviation of values.

tumor organoid growth. Therefore, it is reasonable to consider how the combination treatment approach may target different signaling pathways to exert a synergistic effect and overcome therapy resistance.

The combination of chemotherapy and radiation targets different cellular pathways to induce cell death in tumor organoids

Radiation and chemotherapy drugs such as 5-fluorouracil and gemcitabine each use cytotoxic effects through different mechanisms. When used alone or in combination, these therapies target various cellular signaling pathways, leading to cell death via DNA damage, cell cycle arrest, and replication stress (15). When PTOs were treated with either gemcitabine or radiation, cytotoxic ROS were produced; however, the combination of gemcitabine and radiation appeared to generate a greater amount of ROS (Figure 6).

We also assessed the presence of double-strand breaks (DSBs) in tumor organoids treated with gemcitabine and radiation individually and in combination by staining for γH2AX. After treatment, H2AX was quickly phosphorylated at the site of DSBs, which was detected using immunofluorescence microscopy. The data also demonstrated that gemcitabine acts as a radiosensitizer, increasing radiation-induced DNA DSBs (Figure 7). This finding would be consistent with pancreatic cancer cell line work suggesting that gemcitabine synchronizes cells in the S-phase and

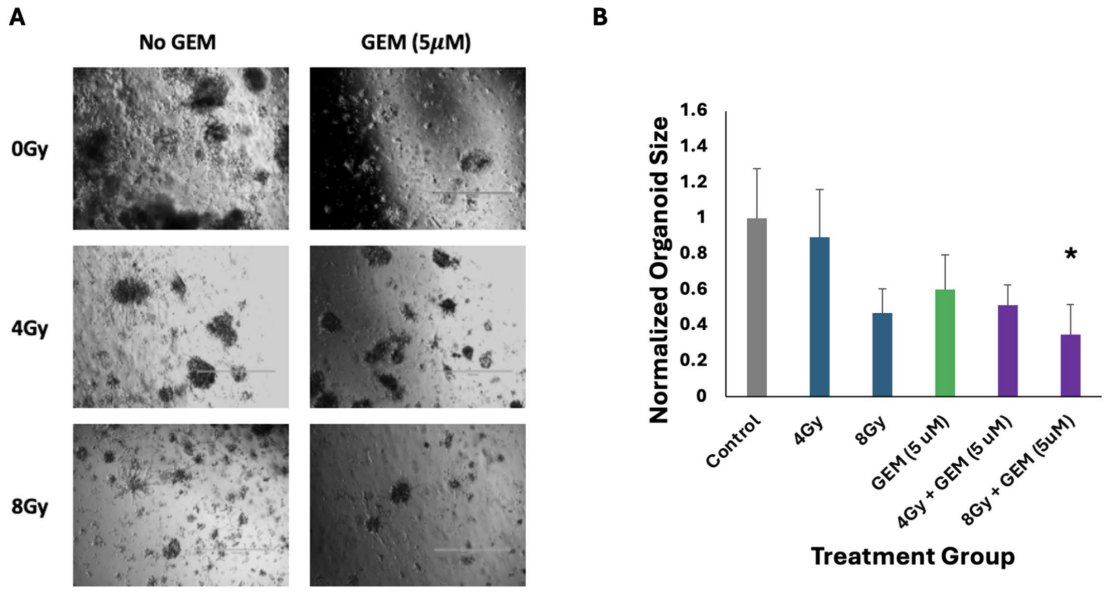

FIGURE 4
Responses of pancreas tumor organoids to treatment with gemcitabine (GEM, 5 μM), RT (4 and 8 Gy), and GEM + RT. **(A)** Brightfield imaging 5 days after the initiation of treatment. The scale bar at the bottom right of each image represents 1,000 μm. **(B)** Average size of the five largest organoids in each of the above images, normalized to the control. The green bar represents those organoids treated with only GEM, the blue bars represent those treated with only RT, and the purple bars represent those treated with a combination of GEM and RT. The asterisk indicates a statistically significant ($p < 0.05$) decrease in average organoid size as compared to the most effective single-modality treatment. Error bars represent 1 standard deviation of values.

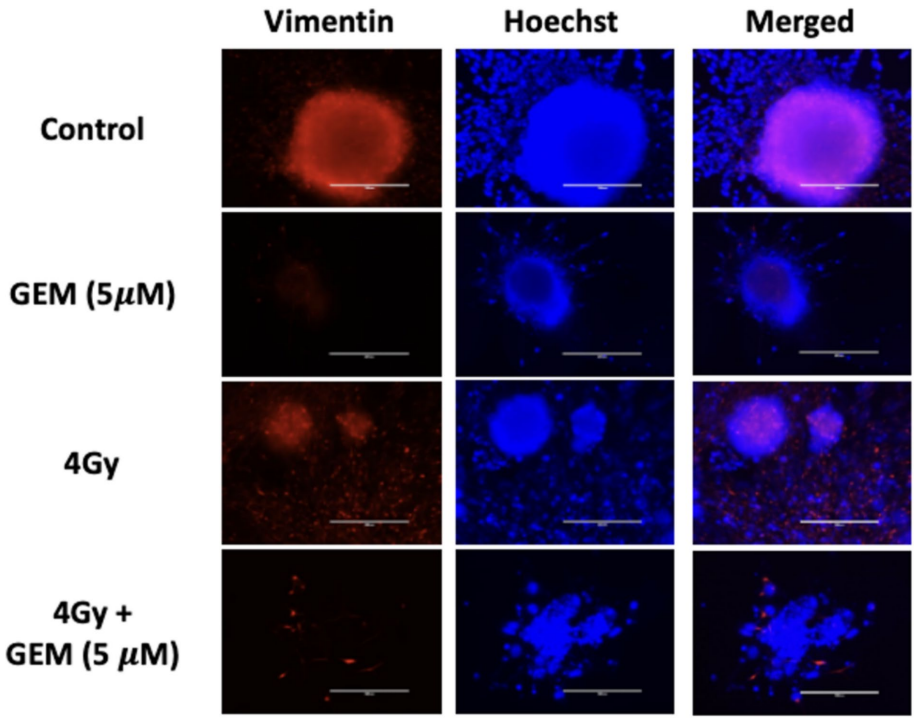

FIGURE 5
Tumor organoid expression of vimentin (red) with nuclear stain (blue) in response to gemcitabine (GEM, 5 μM) alone, RT (4 Gy) alone, and a combination of gemcitabine and RT at the same doses. The scale bar represents 200 μm.

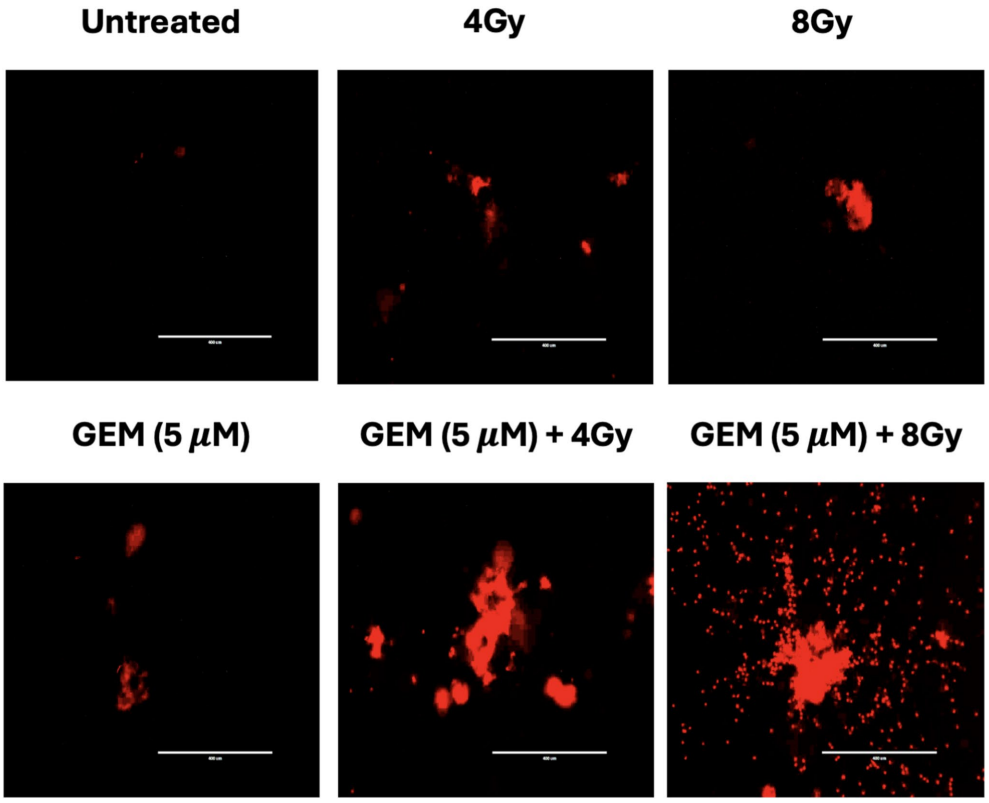

FIGURE 6
Tumor organoid expression of reactive oxygen species (ROS) after treatment with RT (4 and 8 Gy), gemcitabine (GEM, 5 μM), and combinations of gemcitabine and RT. Each label is above the corresponding image. The scale bar represents 400 μm.

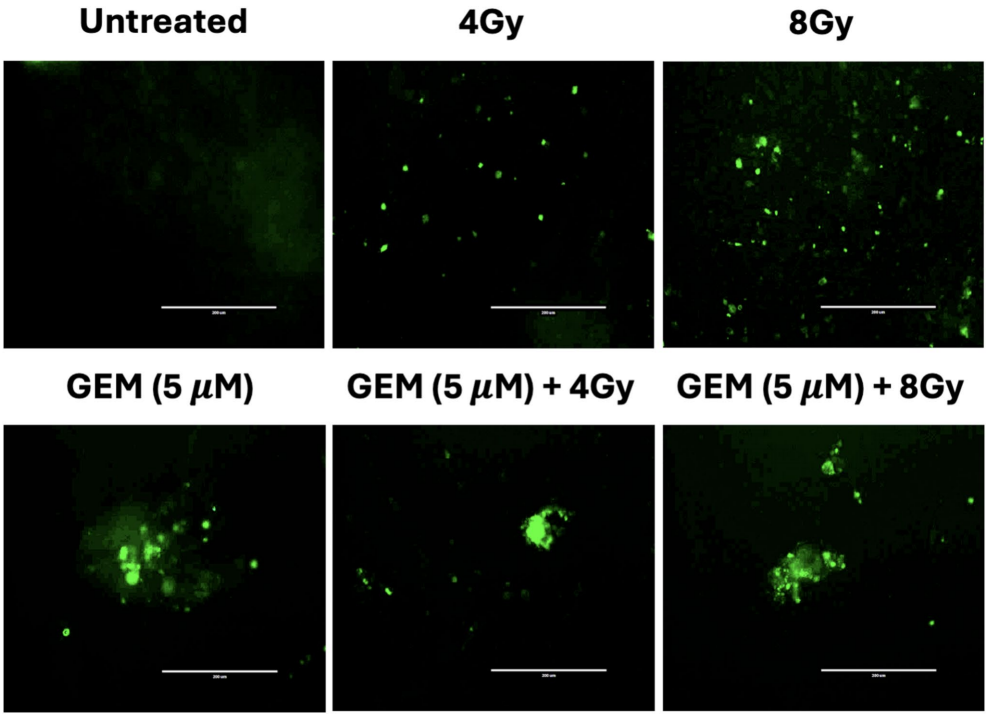

FIGURE 7
Immunofluorescent staining of phosphorylated γH2AX in tumor organoids after treatment with RT (4 and 8 Gy), gemcitabine (GEM, 5 μM), and combinations of RT and GEM shows evidence of DNA double-strand breaks. The scale bar represents 200 μm.

inhibits repair pathways, making them more vulnerable to radiation-induced DSBs (16).

Based on these results, we envisage that 5-FU and gemcitabine both reduce the DNA repair ability of cells and, as a result, cause tumor cells to become more sensitive to radiation-induced DNA strand breaks and cell death.

Discussion

Pancreatic ductal adenocarcinoma continues to be among the most aggressive and lethal malignancies due to its late diagnosis, high metastatic potential, and poor responsiveness to current therapeutic strategies (17). The 2D cancer cell model has long served as a platform to study treatment responses and drug efficacy; however, it has not successfully replicated the complex tumor architecture and tumor microenvironment of patients' tumors (3, 17). While *in vivo* models offer more physiological relevance, they are time-consuming, resource-intensive, and often differ biologically from human tumors (18). The initiation of 3D tumor organoid cultures, derived from tumor tissues or patient-derived xenografts, offers an advanced *ex vivo* system that maintains the histological, molecular, and functional properties of the parent tumor (19, 20). The organoids utilized in this study showed expression of TME markers α-SMA and vimentin in patterns similar to *in vivo* tissues, indicating that key components of tumor-stromal interaction and heterogeneity are also present in tumor organoids. This makes the organoid platform ideal for mimicking the treatment dynamics in PDAC and for exploring therapeutic responses under translational conditions (6, 21). In this study, mouse pancreas tumor organoids were used as a model system to evaluate the dose effectiveness of 5-fluorouracil and gemcitabine combined with ionizing radiation (22).

The results showed that 5-FU monotherapy produced a dose-dependent inhibition of organoid growth, with the highest dose of 100 μM causing approximately a 50% reduction in organoid size. When low doses of 5-FU were combined with radiation (4 Gy and 8 Gy), the treatment efficacy increased (23–25). Furthermore, combinations of 25 or 100 μM 5-FU with 8 Gy radiation produced significantly greater inhibitory effects than either treatment modality administered alone ($p < 0.05$). The latter combination was most effective and inhibited organoids by >70%. Previous studies have also shown that a combination of low-dose chemotherapy and radiation minimizes the cytotoxic effects in normal tissues (26, 27). This suggests that there exists a synergistic effect where the combination of chemotherapy and radiation causes increased DNA damage and reduced DNA repair capabilities, thereby promoting apoptotic cell death more effectively than monotherapy (28, 29).

Similarly, the efficacy of gemcitabine was enhanced when combined with radiation. Compared to the most effective single modality, a low dose of gemcitabine (5 μM) followed by 4 or 8 Gy radiation led to increased inhibition of tumor organoid growth, by approximately 50% ($p = 0.10$) and 70% ($p = 0.05$), respectively. Furthermore, pre-treatment with gemcitabine exhibited radiosensitizing properties, rendering tumor cells more susceptible to radiation-induced DNA damage and apoptotic cell death (12, 28, 30). As previously postulated through research in pancreatic cancer cell line models, the radiosensitizing effect of gemcitabine likely stems from the inhibition of DNA replication and repair pathways, particularly its action on replication forks and the suppression of DNA repair machinery. This effect is especially pronounced when cells are synchronized in the S-phase, thereby amplifying the cytotoxic impact of ionizing radiation (31, 32).

To better understand the mechanistic effects of combining chemotherapy with radiation, we examined the cellular pathways influenced by the combination of treatments. The data suggest that gemcitabine, in combination with radiation, increases intracellular ROS (Figure 6), an important mediator of oxidative DNA damage, mitochondrial dysfunction, and apoptosis (13, 33). Thus, a synergistic enhancement of ROS may be a component of the mechanism underlying the combination effect. Additionally, there is evidence suggesting that combination therapies may activate tumor suppressor pathways such as p53 and checkpoint kinases (Chk1/Chk2), triggering irreversible cell cycle arrest and caspase-mediated apoptosis (34).

The results showed that the combination treatment also increased γH2AX, a marker indicative of DNA double-strand breaks (DSBs). The γH2AX foci formation was of notably high intensity following treatment with gemcitabine or a combination of gemcitabine and radiation, providing evidence of elevated DNA damage in tumor organoids (Figure 7). As a sensitive and quantifiable biomarker, γH2AX serves not only as a marker of therapeutic efficacy but also as a potential tool for optimizing treatment timing and dosage in future clinical applications (35, 36). Pretreatment with gemcitabine may further enhance radiosensitivity by synchronizing cells in a vulnerable phase of the cell cycle and preventing the repair of radiation-induced DSBs.

Collectively, these findings support the use of pancreas tumor organoids as a robust and physiologically relevant model for deriving mechanistic and translatable insights regarding therapeutic approaches. The notably enhanced responses of tumor organoids to combination treatments underscore the potential of multi-modal therapies in overcoming treatment resistance (37, 38). Future studies should aim to identify molecular predictors of treatment response and resistance using patient-derived organoid models, paving the way for the development of more effective, personalized therapeutic strategies.

Data availability statement

The original contributions presented in the study are included in the article/supplementary material, further inquiries can be directed to the corresponding authors.

Ethics statement

The animal study was approved by UMD Institutional Animal Care and Use Committee (IACUC). The study was conducted in accordance with the local legislation and institutional requirements.

Author contributions

ZK: Validation, Data curation, Investigation, Methodology, Writing – review & editing, Formal analysis. AS: Writing – review & editing, Methodology, Data curation. SR: Writing – review & editing. HR: Writing – review & editing, Formal analysis, Methodology, Data curation. BB: Writing – review & editing. LR: Writing – review & editing. NL: Writing – review & editing, Project administration, Conceptualization, Supervision. HS: Funding acquisition, Resources, Writing – original draft, Formal analysis, Project administration, Conceptualization, Supervision, Methodology.

Funding

The author(s) declare that financial support was received for the research and/or publication of this article. This research was supported by an American Cancer Society Institutional Research Grant (ACS-IRG) awarded to HS.

Acknowledgments

The authors thank Dr. William Regine, Chair, Department of Radiation Oncology, University of Maryland, and the American Cancer Society ACS-IRG for financial support to HS.

Conflict of interest

The authors declare that the research was conducted in the absence of any commercial or financial relationships that could be construed as a potential conflict of interest.

Generative AI statement

The authors declare that no Gen AI was used in the creation of this manuscript.

Any alternative text (alt text) provided alongside figures in this article has been generated by Frontiers with the support of artificial intelligence and reasonable efforts have been made to ensure accuracy, including review by the authors wherever possible. If you identify any issues, please contact us.

Publisher's note

All claims expressed in this article are solely those of the authors and do not necessarily represent those of their affiliated organizations, or those of the publisher, the editors and the reviewers. Any product that may be evaluated in this article, or claim that may be made by its manufacturer, is not guaranteed or endorsed by the publisher.

References

1. Siegel RL, Kratzer TB, Giaquinto AN, Sung H, Jemal A. Cancer statistics, 2025. *CA Cancer J Clin*. (2025) 75:10–45. doi: 10.3322/caac.21871

2. Rahib L, Smith BD, Aizenberg R, Rosenzweig AB, Fleshman JM, Matrisian LM. Projecting cancer incidence and deaths to 2030: the unexpected burden of thyroid, liver, and pancreas cancers in the United States. *Cancer Res*. (2014) 74:2913–21. doi: 10.1158/0008-5472.CAN-14-0155

3. Shukla HD, Djukić T, Roy SK, Bhandary B, Gerry AB, Poirier Y, et al. Pancreatic cancer derived 3D organoids as a clinical tool to evaluate the treatment response. *Front Oncol*. (2023) 12:1072774. doi: 10.3389/fonc.2022.1072774

4. Halbrook CJ, Lyssiotis CA, di Magliano MP, Maitra A. Pancreatic cancer: advances and challenges. *Cell*. (2023) 186:1729–54. doi: 10.1016/j.cell.2023.02.014

5. Watanabe S, Yogo A, Otsubo T, Umehara H, Oishi J, Kodo T, et al. Establishment of patient-derived organoids and a characterization-based drug discovery platform for treatment of pancreatic cancer. *BMC Cancer*. (2022) 22:489. doi: 10.1186/s12885-022-09619-9

6. Roy S, Dukic T, Keepers Z, Bhandary B, Lamichhane N, Molitoris J, et al. SOX2 and OCT4 mediate radiation and drug resistance in pancreatic tumor organoids. *Cell Death Discov*. (2024) 10:106. doi: 10.1038/s41420-024-01871-1

7. Porter RJ, Murray GI, McLean MH. Current concepts in tumour-derived organoids. *Br J Cancer*. (2020) 123:1209–18. doi: 10.1038/s41416-020-0993-5

8. Zeng G, Yu Y, Wang M, Liu J, He G, Yu S, et al. Advancing cancer research through organoid technology. *J Transl Med*. (2024) 22:1007. doi: 10.1186/s12967-024-05824-1

9. Boj Sylvia F, Hwang CI, Baker Lindsey A, Chio I, Engle Dannielle D, Corbo V, et al. Organoid models of human and mouse ductal pancreatic cancer. *Cell*. (2015) 160:324–38. doi: 10.1016/j.cell.2014.12.021

10. Le Compte M, De La Hoz EC, Peeters S, Fortes FR, Hermans C, Domen A, et al. Single-organoid analysis reveals clinically relevant treatment-resistant and invasive subclones in pancreatic cancer. *npj Precis Oncol*. (2023) 7:128. doi: 10.1038/s41698-023-00480-y

11. Savary C, Luciana L, Huchedé P, Tourbez A, Coquet C, Broustal M, et al. Fusion-negative rhabdomyosarcoma 3D organoids to predict effective drug combinations: a proof-of-concept on cell death inducers. *Cell Rep Med*. (2023) 4:101339. doi: 10.1016/j.xcrm.2023.101339

12. Huang RX, Zhou PK. DNA damage response signaling pathways and targets for radiotherapy sensitization in cancer. *Signal Transduct Target Ther*. (2020) 5:60–27. doi: 10.1038/s41392-020-0150-x

13. An X, Yu W, Liu J, Tang D, Yang L, Chen X. Oxidative cell death in cancer: mechanisms and therapeutic opportunities. *Cell Death Dis*. (2024) 15:556. doi: 10.1038/s41419-024-06939-5

14. Ahn D, Lee HK, Bae SH, Na H, Choi KC. Downregulation of transforming growth factor-β2 enhances the chemosensitivity to gemcitabine with diminished metastasis in pancreatic cancers. *Biomed Pharmacother*. (2025) 188:118151. doi: 10.1016/j.biopha.2025.118151

15. Zhang Y, Wu L, Wang Z, Wang J, Roychoudhury S, Tomasik B, et al. Replication stress: a review of novel targets to enhance radiosensitivity-from bench to clinic. *Front Oncol*. (2022) 12:838637. doi: 10.3389/fonc.2022.838637

16. Pauwels B, Vermorken JB, Wouters A, Ides J, van Laere S, Lambrechts HAJ, et al. The role of apoptotic cell death in the radiosensitizing effect of gemcitabine. *Br J Cancer*. (2009) 101:628–36. doi: 10.1038/sj.bjc.6605145

17. Roy S, Dukic T, Bhandary B, Tu KJ, Molitoris J, Ko YH, et al. (2022). 3-Bromopyruvate inhibits pancreatic tumor growth by stalling glycolysis, and dismantling mitochondria in a syngeneic mouse model. Am J Cancer Res. 12:4977–4987. Available online at: https://pubmed.ncbi.nlm.nih.gov/36504891/.

18. Jin J, Yoshimura K, Sewastjanow-Silva M, Song S, Ajani JA. Challenges and prospects of patient-derived xenografts for cancer research. *Cancer*. (2023) 15:4352–2. doi: 10.3390/cancers15174352

19. Martinez-Pacheco S, O'Driscoll L. Pre-clinical *in vitro* models used in cancer research: results of a worldwide survey. *Cancer*. (2021) 13:6033. doi: 10.3390/cancers13236033

20. Andrew L, Grundy TE, Fang G, Valdes-Mora F, Gallego-Ortega D. Advancements in 3D cell culture systems for personalizing anti-cancer therapies. *Front Oncol*. (2021) 11:782766. doi: 10.3389/fonc.2021.782766

21. Papargyriou A, Najajreh M, Cook DP, Maurer CH, Bärthel S, Messal HA, et al. Heterogeneity-driven phenotypic plasticity and treatment response in branched-organoid models of pancreatic ductal adenocarcinoma. *Nat Biomed Eng*. (2024) 9:836–64. doi: 10.1038/s41551-024-01273-9

22. Xu M, Zhang T, Xia R, Wei Y, Wei X. Targeting the tumor stroma for cancer therapy. *Mol Cancer*. (2022) 21:208. doi: 10.1186/s12943-022-01670-1

23. Boz G, De Paoli A, Innocente R, Rossi C, Tosolini G, Pederzoli P, et al. Radiotherapy and continuous infusion 5-fluorouracil in patients with nonresectable pancreatic carcinoma. *Int J Radiat Oncol Biol Phys*. (2001) 51:736–40. doi: 10.1016/s0360-3016(01)01708-4

24. Maemura K, Shinchi H, Noma H, Mataki Y, Kurahara H, Maeda S, et al. (2008). Comparison of hyper-fractionated accelerated and standard fractionated radiotherapy with concomitant low-dose gemcitabine for unresectable pancreatic cancer. Anticancer Res. 28:2369–2372. Available online at: https://pubmed.ncbi.nlm.nih.gov/18751420/.

25. Falco M, Masojć B, Sulikowski T. Radiotherapy in pancreatic cancer: to whom, when, and how? *Cancer*. (2023) 15:3382. doi: 10.3390/cancers15133382

26. Mokhtari RB, Homayouni TS, Baluch N, Morgatskaya E, Kumar S, Das B, et al. Combination therapy in combating cancer. *Oncotarget*. (2017) 8:38022–43. doi: 10.18632/oncotarget.16723

27. Liu B, Zhou H, Tan L, Siu KTH, Guan XY. Exploring treatment options in cancer: tumor treatment strategies. *Signal Transduct Target Ther*. (2024) 9:175–44. doi: 10.1038/s41392-024-01856-7

28. Zhao W, Zhou L, Zhao W, Yang H, Lu Z, Zhang L, et al. The combination of temozolomide and perifosine synergistically inhibit glioblastoma by impeding DNA repair and inducing apoptosis. *Cell Death Discov*. (2024) 10:315. doi: 10.1038/s41420-024-02085-1

29. Coquel F, Ho SZ, Tsai KC, Yang CY, Aze A, Devin J, et al. Synergistic effect of inhibiting CHK2 and DNA replication on cancer cell growth. *eLife*. (2025) 13:RP104718. doi: 10.7554/eLife.104718

30. Salah M, Akasaka H, Shimizu Y, Morita K, Nishimura Y, Kubota H, et al. Reactive oxygen species-inducing titanium peroxide nanoparticles as promising radiosensitizers for eliminating pancreatic cancer stem cells. *J Exp Clin Cancer Res*. (2022) 41:146. doi: 10.1186/s13046-022-02358-6

31. Morgan MA, Parsels LA, Maybaum J, Lawrence TS. Improving gemcitabine-mediated radiosensitization using molecularly targeted therapy: a review. *Clin Cancer Res*. (2008) 14:6744–50. doi: 10.1158/1078-0432.CCR-08-1032

32. Kobashigawa S, Morikawa K, Mori H, Kashino G (2015). Gemcitabine induces radiosensitization through inhibition of RAD51-dependent repair for DNA double-strand breaks. Anticancer Res. 35. 2731–2737. Available online at: https://pubmed.ncbi.nlm.nih.gov/25964552/

33. Che PP, Gregori A, Bergonzini C, Ali M, Mantini G, Schmidt T, et al. Differential sensitivity to ionizing radiation in gemcitabine-resistant and paclitaxel-resistant pancreatic Cancer cells. *Int J Radiat Oncol Biol Phys*. (2024) 118:1328–43. doi: 10.1016/j.ijrobp.2023.10.035

34. Wang H, Guo M, Wei H, Chen Y. Targeting p53 pathways: mechanisms, structures, and advances in therapy. *Signal Transduct Target Ther*. (2023) 8:92–35. doi: 10.1038/s41392-023-01347-1

35. Kinders RJ, Hollingshead M, Lawrence S, Ji J, Tabb B, Bonner WM, et al. Development of a validated immunofluorescence assay for H2AX as a pharmacodynamic marker of topoisomerase I inhibitor activity. *Clin Cancer Res*. (2010) 16:5447–57. doi: 10.1158/1078-0432.CCR-09-3076

36. Toapichattrakul P, Autsavapromporn N, Duangya A, Pojchamarnwiputh S, Nachiangmai W, Kittidachanan K, et al. Changing of gamma-H2AX in peripheral blood mononuclear cells during concurrent chemoradiation in locally advanced rectal cancer patients: a potential response predictor. Journal of. *Gastrointest Oncol*. (2024) 15:2117–28. doi: 10.21037/jgo-24-488

37. Gümüşay Ö, Vitiello PP, Wabl CA, Corcoran RB, Bardelli A, Rugo HS. Strategic combinations to prevent and overcome resistance to targeted therapies in oncology. *Am Soc Clin Oncol Educ Book*. (2020) 40:e292–308. doi: 10.1200/EDBK_280845

38. Victoir B, Croix C, Gouilleux F, Prié G. Targeted therapeutic strategies for the treatment of cancer. *Cancer*. (2024) 16:461. doi: 10.3390/cancers16020461

frontiers | Frontiers in Oncology

TYPE Original Research
PUBLISHED 18 September 2025
DOI 10.3389/fonc.2025.1640685

Check for updates

OPEN ACCESS

EDITED BY
Abdul K. Parchur,
University of Maryland Medical Center,
United States

REVIEWED BY
Djamel Eddine Chouaib Eddine Chouaib Belkhiat,
University Ferhat Abbas of Setif, Algeria
Takaaki Matsuura,
Hiroshima University, Japan

*CORRESPONDENCE
Yun Zhang
zhangyun_1983@sohu.com

RECEIVED 04 June 2025
ACCEPTED 03 September 2025
PUBLISHED 18 September 2025

CITATION
Zhou Y, Gong C, Jian J and Zhang Y (2025) Innovative patient-specific delivered-dose prediction for volumetric modulated arc therapy using lightweight Swin-Transformer. *Front. Oncol.* 15:1640685. doi: 10.3389/fonc.2025.1640685

COPYRIGHT
© 2025 Zhou, Gong, Jian and Zhang. This is an open-access article distributed under the terms of the Creative Commons Attribution License (CC BY). The use, distribution or reproduction in other forums is permitted, provided the original author(s) and the copyright owner(s) are credited and that the original publication in this journal is cited, in accordance with accepted academic practice. No use, distribution or reproduction is permitted which does not comply with these terms.

Innovative patient-specific delivered-dose prediction for volumetric modulated arc therapy using lightweight Swin-Transformer

Yongqiang Zhou[1], Changfei Gong[2,3], Junming Jian[2,3] and Yun Zhang[2,3]*

[1]Department of Radiation and Medical Oncology, First Affiliated Hospital of Wenzhou Medical University, WenZhou Radiation Oncology and Translational Research Key Laboratory, Wenzhou, Zhejiang, China, [2]Department of Radiation Oncology, Jiangxi Cancer Hospital & Institute, Jiangxi Clinical Research Center for Cancer, Nanchang, Jiangxi, China, [3]NHC Key Laboratory of Personalized Diagnosis and Treatment of Nasopharyngeal Carcinoma (Jiangxi Cancer Hospital), Nanchang, Jiangxi, China

Background: Volumetric modulated arc therapy (VMAT) necessitates rigorous pre-treatment patient-specific quality assurance (PSQA) to ensure dosimetric accuracy, yet conventional manual verification methods encounter time and labor constraints in clinical workflows. While deep learning (DL) models have advanced PSQA by automating metrics prediction, existing approaches relying on convolutional neural networks struggle to reconcile local feature extraction with global contextual awareness. This study aims to develop a novel lightweight DL framework that synergizes hierarchical spatial feature learning and computational efficiency to enhance VMAT-delivered dose (VTDose) prediction.
Methods: We propose a hybrid architecture featuring a novel hierarchical fusion framework that synergizes shifted-window self-attention with adaptive local-global feature interaction. (termed "STQA"). Specially, strategic replacement of Swin-Transformer blocks with ResNet residual modules in deep layers, coupled with depthwise separable attention mechanisms, enables 40% parameter reduction while preserving spatial resolution. The model was trained on multimodal inputs and evaluated against state-of-the-art methods using structural similarity index (SSIM), mean absolute error (MAE), root mean square error (RMSE), and gamma passing rate (GPR).
Results: Visual evaluation of VTDose and discrepancy maps across axial, coronal, and sagittal planes demonstrated enhanced fidelity of STQA to ground truth (GT). Quantitative analysis revealed superior performance of STQA across all evaluation metrics: SSIM=0.978, MAE=0.163, and RMSE= 0.416. GPR analysis

confirmed clinical applicability, with STQA achieving 95.43%±3.41% agreement with GT (94.63%±2.84%).

Conclusions: STQA establishes a paradigm for efficient and accurate VTDose prediction. Its lightweight design, validated through multi-site clinical data, addresses critical limitations in current DL-based PSQA, offering a clinically viable solution to enhance radiotherapy PSQA workflows.

KEYWORDS

deep learning, Swin-Transformer, volumetric modulated arc therapy, pre-treatment specific quality assurance, multimodal

1 Introduction

Volumetric modulated arc therapy (VMAT) has emerged as a cornerstone of precision radiotherapy, achieving superior dose conformity through synchronized dynamic multi-leaf collimator (MLC) modulation and gantry rotation (1). While this technological complexity enhances treatment plan quality compared to conventional techniques, it simultaneously intensifies the demand for rigorous verification of dose distribution authenticity and deliverability. Pre-treatment patient-specific quality assurance (PSQA) remains an essential clinical safeguard, strongly endorsed by the American Association of Physicists in Medicine (AAPM) to ensure VMAT dose accuracy and patient safety (2). Current clinical workflows employ measurement devices such as diode arrays, ionization chambers, and radiographic films to quantify discrepancies between planned and delivered dose. However, conventional PSQA workflows, which depend on physical measurements, are time-consuming and labor-intensive. They delay treatment initiation and reduce the efficiency of radiotherapy services (3).

Over the past decade, machine learning (ML) has driven advancements in PSQA, particularly in gamma passing rate (GPR) prediction. Early ML approaches, including Poisson regression with Lasso regularization for binary classification (4, 5), regression/classification models for VMAT plans (6), artificial neural networks (ANN) for dosimetry prediction (7), and feature-engineered support vector machines (8, 9), demonstrated moderate success but faced limitations in accuracy and clinical applicability due to manual feature dependency. The emergence of deep learning (DL) revolutionized this field through automated hierarchical feature extraction via convolutional neural networks (CNN). Key innovations include CNN architectures for prostate cancer PSQA (10, 11), transfer learning-enhanced VGG-16 models outperforming domain-expert systems (12), fluence map-based error detection frameworks (13), GANs for EPID-to-dose conversion (14), and log file-informed fluence modeling (15–18). By eliminating manual feature engineering and enabling end-to-end prediction through raw data abstraction, DL methods have significantly improved prediction accuracy and clinical utility compared to traditional ML approaches, establishing a paradigm shift in PSQA optimization.

Extensive studies have validated the potential of ML/DL models in terms of predicting PSQA without performing real measurements (4–18). However, critical analysis of existing methodologies reveals three fundamental limitations requiring attention for clinical implementation of ML/DL-based PSQA models. Firstly, the predominant GPR evaluation paradigm fails to establish quantitative relationships between spatial dose distribution characteristics and validation outcomes, particularly at anatomically complex sites. This limitation obscures detection of subclinical dose deviations and provides insufficient spatial context (e.g., failure point localization, clustered anomalies) for comprehensive clinical assessment (19, 20). Secondly, most models rely on 2D planar dose representations, inherently incapable of capturing the 3D spatial modulation characteristics intrinsic to VMAT's dynamic delivery. This dimensional reduction introduces systematic errors in dose carving pattern recognition. Thirdly, while CNN excel at local feature extraction, their reliance on downsampling operations sacrifices spatial resolution and local detail preservation. The inherent locality of convolutional kernels further restricts global contextual awareness and long-range spatial relationships modeling - critical capabilities for holistic dose distribution analysis.

The remarkable success of Transformers in natural language processing (21) has spurred their adaptation to computer vision, leveraging global self-attention mechanisms to overcome the local inductive bias inherent in CNNs. Pioneering this shift, Kolesnikov et al. developed the Vision Transformer (ViT) (22), achieving state-of-the-art image recognition through patch-based sequence

Abbreviations: VMAT, Volumetric modulated arc therapy; MLC, multi-leaf collimator; PSQA, Patient-specific quality assurance; ML, Machine learning; DL, Deep learning; VTDose, VMAT-delivered dose; CT, Computed tomography; MRI, Magnetic resonance imaging; PET, Positron emission tomography; W-MSA, Window Multihead Self-Attention; SW-MSA, Shifted Window Multihead Self-Attention; LN, LayerNorm; BN, BatchNorm; CV, Computer Vision; CGAN, CycleGAN; TrQA, TransQA; SWNet, Swin-UNet; SSIM, structural similarity index; MAE, mean absolute error; RMSE, Root-mean-square error; GT, Ground truth.

TABLE 1 Clinical characteristics of cancer patients enrolled in this study.

Characteristics	Sample number	Percentage
Gender, no. (%)		
Male	120	60.0%
Female	80	40.0%
Age (years)		
<20y	15	7.5%
20y-60y	100	50.0%
>60y	85	42.5%
Cancer sites		
H&N	38	19.0%
Chest	116	58.0%
Abdomen	46	23.0%

processing. Recent work by Zeng et al. (23) demonstrates a hybrid network integrating Transformers with modified U-Net architectures for predicting measurement-guided volumetric dose in PSQA, enabling quantitative analysis of spatial dose differences between predicted and clinical dose distributions. However, subsequent studies reveal critical limitations of pure Transformer architectures in vision tasks, particularly their inadequate local feature extraction capabilities for dense predictions (24–27). This limitation has motivated hybrid architectures combining CNN and Transformer encoders through serial (e.g., TransUNet (28)) or parallel (e.g., TransFuse (29)) configurations to synergize global context modeling with local feature learning. Concurrently, enhanced variants like Swin Transformer (30) incorporate hierarchical shifted-window mechanisms, demonstrating superior performance in pixel-level prediction tasks and advancing the evolution of vision-specific Transformer architectures.

To address the critical limitations in existing PSQA methodologies, we propose STQA (Swin Transformer-based Quality Assurance) - a novel lightweight network that synergizes hierarchical feature learning with adaptive global-local attention for volumetric dose prediction in VMAT-PSQA. Departing from conventional Transformer adaptations, our architecture introduces three key innovations: 1) A depth-aware hierarchical encoder-decoder framework employing parameter-shared shifted window attention across scales, enabling efficient cross-resolution feature interaction while preserving spatial fidelity; 2) A dual-path feature extraction mechanism combining depth-wise separable local attention with global context modeling through lightweight transformer blocks, effectively capturing both fine-grained dose carving patterns and long-range anatomical dependencies; 3) Bottleneck-adapted skip connections with channel-wise excitation modules that dynamically recalibrate multi-scale features during spatial resolution recovery. Extensive experiments demonstrate STQA's capability to predict 3D dose distributions closely matching actual VTDose, enabling patient-specific VTDose acquisition. Our method not only demonstrates superior overall prediction performance but also consistently outperforms comparative models across multiple cancer sites (head & neck, chest, abdomen). Significantly, STQA achieves a 40% parameter reduction versus Swin Transformer through depth-wise separable attention in shallow layers, hierarchical parameter-shared window processing, and bottleneck adapters within skip connections that strategically compress and reactivate channels, thereby maintaining performance while eliminating architectural redundancy.

2 Methods

2.1 Data collection and preprocessing

The study cohort comprised 200 patients treated with volumetric modulated arc therapy (VMAT) between 2020 and 2024 (Table 1) in Jiangxi Cancer Hospital. The original dataset is split into training (160), validation (20), and test set (20), which contain 7731, 1045 and 1105 images, respectively. All computed tomography (CT) simulations were performed using a Somatom Confidence RT Pro CT scanner (Philips Healthcare, Best, the Netherlands) with 2 mm slice thickness. To ensure precise target delineation, coregistered diagnostic magnetic resonance imaging (MRI) and positron emission tomography (PET) images were integrated into the planning process by board-certified radiation oncologists with >10 years' experience in radiotherapy. VMAT plans were generated using clinically validated treatment planning systems: the Monte Carlo algorithm in Monaco (version 5.11, Elekta AB) with a dose calculation grid of 2 mm. All plans were optimized through multi-criteria iterative optimization to ensure optimal target coverage while adhering to strict organ-at-risk dose constraints. Finalized plans were delivered via 6 MV flattening filter-free beams using an Elekta Infinity linear accelerator equipped with a 160-leaf Agility multileaf collimator (MLC). Prior to treatment, comprehensive quality assurance was performed using the ArcCHECK-3DVH system (Sun Nuclear Corporation, Melbourne, FL, USA), which underwent comprehensive calibration procedures including validation array measurements, beam modeling verification (gamma pass rate >95% at 3%/3 mm), and dose reconstruction accuracy assessments.

To ensure spatial consistency across all data types, both the measured and TPS-planned dose distributions were extracted directly from DICOM RT Dose files and converted into 32-bit floating-point arrays (3). These dose maps were then interpolated to align with the coordinate system of the corresponding CT images and resampled to a uniform grid resolution. Each 3D volume—including CT, planned dose, and measured dose—was initially represented as a matrix of size 512 × 512 × 150 pixels. Zero-padding was applied during interpolation to preserve spatial dimensions. To optimize computational efficiency and memory usage, all images were down-sampled to a resolution of 256 × 256 × 150 prior to model input. Planned dose values were normalized to the maximum dose value within each plan to facilitate stable network training. The model outputs, which are generated in normalized form, are subsequently denormalized back to absolute

dose values in units of Gy by rescaling with the same reference maximum dose. These final predictions are then formatted into DICOM RT-Dose objects compatible with clinical systems, enabling direct use in standard quality assurance procedures such as gamma index analysis and DVH evaluation.

2.2 The overall network structure

The overall architecture of the STQA network proposed in this study, as illustrated in Figure 1, incorporates targeted modifications to the original Swin-UNet framework to better align with our dose prediction objectives. To address the specific requirements of our task and enhance computational efficiency, we implemented two key architectural adjustments: first, replacing consecutive Swin Transformer blocks at the bottleneck layer with final residual network components of ResNet to capitalize on the inherent advantage of residual blocks in maintaining feature extraction capacity while mitigating computational complexity, while preserving original image resolutions and feature dimensions; second, strategically substituting both the loss function and optimization algorithm to facilitate stable training convergence and improve task-specific adaptation. Crucially, STQA retains the essential U-shaped configuration comprising four core components - encoder, bottleneck, decoder, and skip connections - as visually demonstrated in Figure 1, ensuring effective feature propagation and multi-scale information integration throughout the network architecture.

2.3 Swin-Transformer-based feature extraction

The Swin Transformer architecture employs two distinct attention mechanisms as its core feature extraction components: the Window Multihead Self-Attention (W-MSA) module that processes localized image regions through fixed window partitioning, and the Shifted Window Multihead Self-Attention (SW-MSA) module that enables cross-window information exchange through strategic window shifting operations, with their hierarchical arrangement and interaction patterns visually detailed in Figure 2.

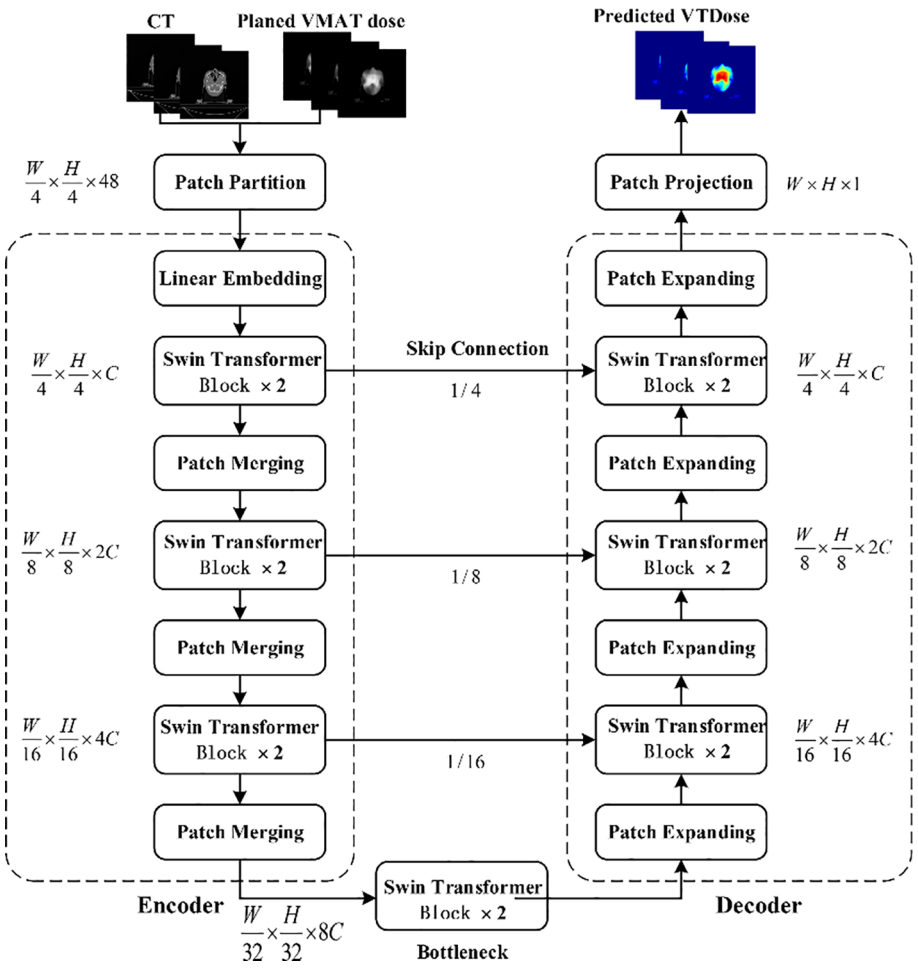

FIGURE 1
Flow chart of the proposed STQA.

SwinUNet utilizes Swin-Transformer layers for feature extraction, Patch Merging and Patch Expanding layers for downsampling and upsampling respectively and incorporates skip connections inspired by U-Net to fuse encoder features in the decoder.

$$\hat{z}^{l} = \mathrm{W-MSA}\left(\mathrm{LN}\left(z^{l-1}\right)\right) + z^{l-1} \tag{1}$$

$$z^{l} = \mathrm{MLP}\left(\mathrm{LN}\left(\hat{z}^{l}\right)\right) + \hat{z}^{l} \tag{2}$$

$$\hat{z}^{l+1} = \mathrm{SW-MSA}\left(\mathrm{LN}\left(z^{l}\right)\right) + z^{l} \tag{3}$$

$$z^{l+1} = \mathrm{MLP}\left(\mathrm{LN}\left(\hat{z}^{l+1}\right)\right) + \hat{z}^{l+1} \tag{4}$$

$$Attention(Q, K, V) = SoftMax\left(\frac{QK^{T}}{\sqrt{d}} + B\right)V \tag{5}$$

In Equations 1–4, $\hat{z}^{l}$ and z^{l} denote the outputs of the $l-th$'s (S) W-MSA model and the MLP model respectively. In Equation 5, $Q, K, V \in R^{M^2 \times d}$ represent the query matrix, key matrix, and value matrix respectively. M^2 represents the number of patches in a window, while d denotes the dimension information of the query or key matrix. Due to the fact that the axis values of relative positions in the model are all within$[-M+1, M+1]$, a smaller deviation matrix needs to be parameterized as $\hat{B} \in R^{(2M-1)\times(2M+1)}$, where B is the value fetched from $\hat{B}$. In Swin Transformer blocks, the input data first pass through a LayerNorm (LN) layer. LN here serves a similar role to BatchNorm (BN) commonly used in Computer Vision (CV). Both are designed to normalize the activations of the previous layer to some extent to avoid the vanishing gradient problem. The difference between LN and BN lies in the dimensions over which normalization is computed. LN computes normalization across the layer dimension, whereas BN computes it across the batch dimension. In the field of NLP, the batch size of networks is typically smaller than in CV, making BN less effective compared to LN. Therefore, LN layers are commonly used in Transformers. The formula for LN is shown in Equation 6.

$$y = \frac{x - \mathrm{E}[x]}{\sqrt{\mathrm{Var}[x] + \varepsilon}} * \gamma + \beta \tag{6}$$

Where $\mathrm{E}[x]$ represents the mean of x and $\mathrm{Var}[x]$ represents the variance of x. ε is a very small number to avoid the possibility of zero denominator, γ and β are learnable parameters.

After passing through the LN layer, it is input into the W-MSA or SW-MSA layer. Compared to multi-head self-attention (MSA), W-MSA saves a significant amount of computation by independently computing each window. For an input image of size (h, w), assuming each window contains patches of size M×M, the computational complexity formulas for MSA and W-MSA are given by Equations 7, 8 respectively.

$$\Omega(\mathrm{MSA}) = 4hwC^2 + 2(hw)^2C \tag{7}$$

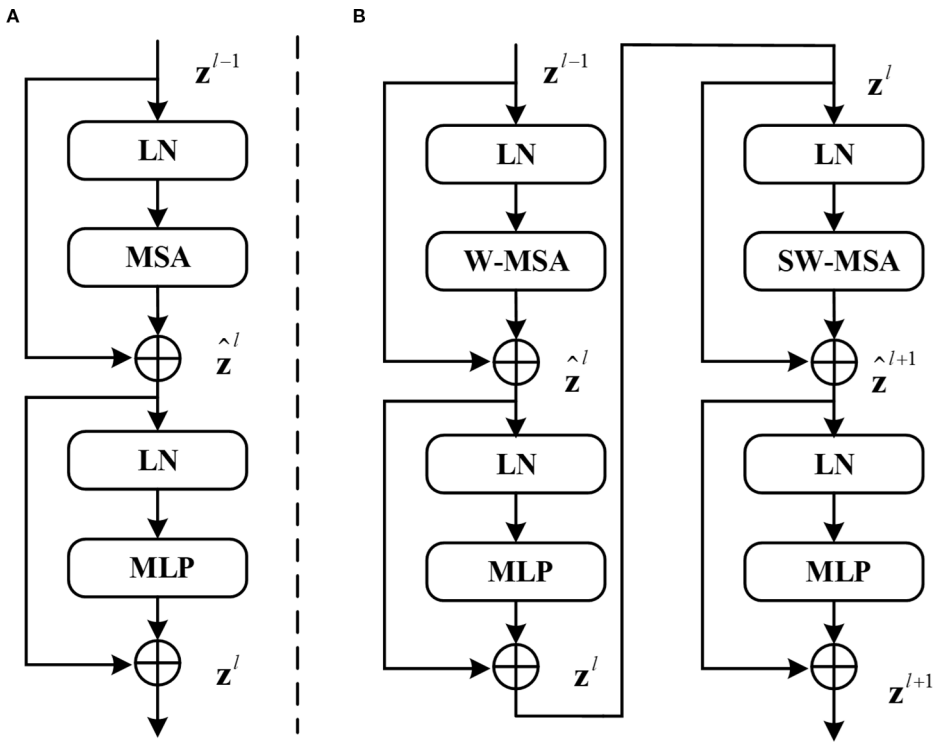

FIGURE 2
(A) Structure of the standard transformer block. **(B)** Two consecutive Swin transformer blocks (renamed W-Trans block and SW-Trans block).

$$\Omega(\mathrm{W}-MSA) = 4hwC^2 + 2M^2hwC \quad (8)$$

W-MSA reduces computation but leads to a lack of information communication between windows. To address this issue, SW-MSA must be computed in subsequent blocks. Information interaction between windows is achieved by shifting the windows down and to the right by half the window size and then computing W-MSA again for the shifted windows. Therefore, W-MSA and SW-MSA need to appear in pairs. It is for this reason that the number of blocks in Swin Transformer is typically even. In Swin-UNet, the number of blocks in Swin Transformer is 2, comprising one W-MSA block and one SW-MSA block. After passing through the W-MSA layer or SW-MSA layer, followed by a BN layer, and finally a multi-layer perceptron (MLP) for feature mapping, the final output is obtained.

2.4 The proposed STQA

Swin-UNet demonstrates powerful capabilities in extracting contextual information and restoring spatial resolution; however, the convergence of transformer modules for image feature computation in deep bottleneck sections remains suboptimal. Considering the challenges of network parameterization as depth increases, this paper proposes enhancements to the deep bottleneck of Swin-UNet. Since the design of residual blocks in ResNet does not reduce feature extraction capacity with increased network depth, replacing two consecutive Swin Transformer blocks in the bottleneck position with ResNet layers is a viable solution. ResNet networks, primarily composed of multiple residual modules—a popular structure in modern neural networks—address the degradation issues caused by deepening layers, thus enabling parameter computation even in thousand-layer networks. After optimization and comparison, we adopt the final layer of the deep ResNet network as the bottleneck of Swin-UNet to improve the model's predictive accuracy in quality assurance of preprocessing patient-specific data, as illustrated in Figure 3; additionally, to reduce parameter computation, 1×1 convolutions are employed for dimensionality reduction on feature vectors.

As data features pass through the last layer of the ResNet deep network, both image resolution and feature dimensions remain unchanged. As shown in Figure 3, this layer comprises three residual blocks, with each residual module consisting of a residual block layer that includes two convolutional blocks, two BN layers, and one ReLU activation. The improved Swin-UNet network maintains the same encoder, bottleneck, and decoder components as the original, but it replaces the Swin-UNet bottleneck with the last layer of the ResNet network—resulting in nearly a 40% reduction in network parameters while achieving better performance.

In the encoder, the image is first divided into patches using a Patch Partition layer, and a linear embedding layer tokenizes the data to produce a C-dimensional representation of size H/4 × W/4. The divided blocks are then concatenated via a Patch Merging layer, which reduces the patch resolution to half of the original; although the merged features are initially four times the original dimension, an additional linear layer is applied to unify the dimension to twice the original. At the bottleneck, leveraging the advantage of ResNet's residual blocks that do not degrade in performance as the network deepens, the fifth layer structure of ResNet is employed to overcome the convergence issues of transformer blocks in deep networks, with the input feature resolution set at W/32 × H/16 and remaining unchanged. Finally, the Patch Expanding layer upsamples the features by doubling the resolution while halving the feature dimension until full-size resolution is restored, and the skip

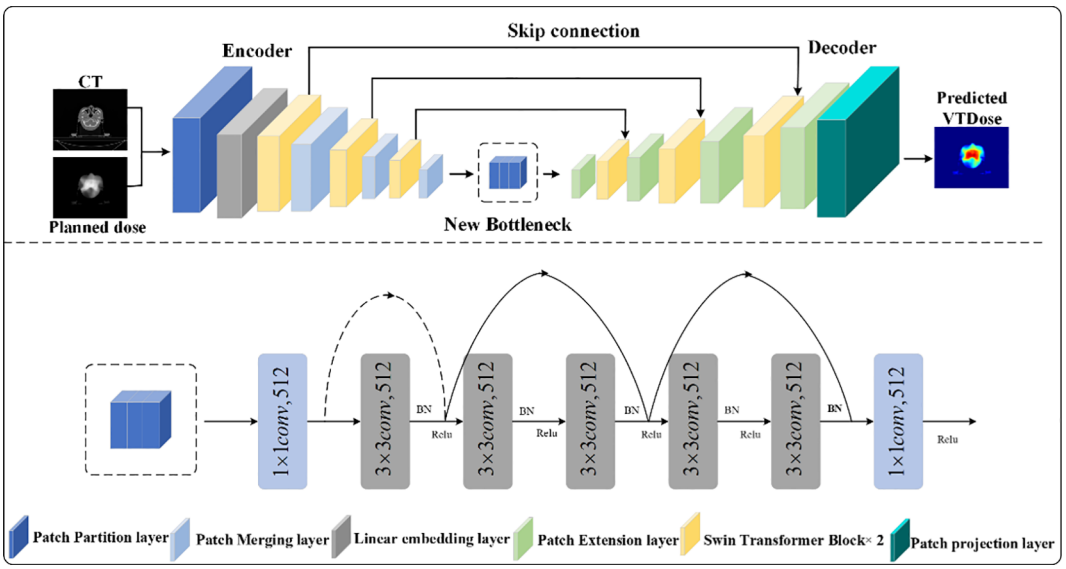

FIGURE 3
The proposed STQA network.

connections fuse multi-scale features from the encoder with the upsampled features to mitigate spatial information loss caused by downsampling. The algorithm flow of STQA is as follows: (see Algorithm 1)

1: Data input
2: while ε has not converged do
3: for t=0, 1, …n do
4: Sample $\{R\ tdose_i\}^m$,$\{CT_i\}^m$, $\{Edose_i\}m \rightarrow P_{data}(H,W,2)$ a batch from the dataset
5: $P_{data}(H,W) \rightarrow P_{data}(H,W,C)$
6: Patch partition(P_{data})
7: Linear embedding(P_{data})
8: Swin transformer(P_{data})
9: Patch merging(P_{data})
10: Conv(P_{data})
11: Patch exanding(P_{data})
12: Linear projection(P_{data})
13: $A_{\varepsilon}^{(L1)} \leftarrow \nabla_w Loss_{L1}(P_{data})$
14: $\varepsilon \leftarrow \varepsilon + \xi A_{\varepsilon}^{(L1)}$
15: end for
16: end while
17: Output predicted VTDose distribution.

Algorithm 1. STQA.

2.5 Experiment setup

To validate the effectiveness of STQA predictions, we compared our method with three established prediction networks using the same test set: U-Net (31), CycleGAN (CGAN) (30), TransQA (TrQA) (23), and Swin-UNet (SWNet) (30). The compared methodologies are summarized as follows: (1) U-Net: A classical encoder-decoder architecture recently adapted for dose prediction tasks (31), demonstrating strong performance in medical image analysis. (2) CGAN: An unsupervised framework proposed by Zhu et al. (32) that employs dual generative adversarial networks with cycle consistency, eliminating the requirement for paired training data. (3) TrQA: A hybrid architecture integrating Transformer's self-attention mechanisms with enhanced U-Net structures, specifically designed for VTDose prediction in PSQA (23). (4) SWNet: A pioneering U-shaped network developed by Lin et al. (30) that incorporates hierarchical Swin Transformer blocks in both encoder and decoder pathways to improve medical image segmentation.

For quantitative evaluation, we adopted three established metrics: structural similarity index (SSIM), mean absolute error (MAE), and root mean square error (RMSE). The experimental dataset comprised paired radiotherapy planning data including CT images, Planned dose distributions, and corresponding VTDose ground truth (GT) maps, collected from multiple cancer patients. To leverage multimodal information, we concatenated CT and Planned dose images along the channel dimension as dual-channel inputs, preserving their distinct information characteristics while providing complementary anatomical and dosimetric features to the network. In addition, GPR analysis serves as the most widely adopted methodology for comparing measured and calculated dose distributions in PSQA for VMAT, where the agreement level is typically quantified through GPR metrics. To further evaluate the prediction accuracy across different methods, we additionally compared the three-dimensional GPR (3%/2mm criterion with a 10% threshold) of various prediction approaches.

The proposed STQA architecture was implemented in PyTorch and trained/tested on an NVIDIA GeForce RTX 3090 GPU with 16GB memory using CUDA-accelerated computation. We employed the Adam optimizer with L1 loss as the primary objective function, setting the initial learning rate to 1e-5 and training for 200 epochs. To ensure fair comparison, all baseline models were re-implemented using identical training protocols and hardware configurations. The total training time for each model was recorded as follows: U-Net: 28 hours, CGAN: 34 hours, TrQA: 41 hours, SWNet: 44 hours, and STQA: 38 hours. After training, each model can generate a full 3D dose distribution within approximately 5–7 seconds, demonstrating compelling inference speed suitable for time-sensitive clinical settings.

Ablation studies were conducted to systematically evaluate key architectural components and parameter settings in our framework. The investigation comprised two main aspects: (1) Performance comparison among three architectural variants: baseline Swin-UNet, our full STQA model, and a hybrid Swin-UNet+ResNet (SURNet) configuration with ResNet blocks directly cascaded at the bottleneck layer. (2) Quantitative analysis of skip connection configurations in STQA, where different numbers of cross-scale connections (0-3) were tested. Specifically, 3 skip connections represent full connections at 1/16, 1/8, and 1/4 resolution levels; 2 connections utilize 1/16 and 1/8 levels; 1 connection employs only the 1/16 level, while 0 connections indicate complete removal of skip connections. This systematic evaluation enables comprehensive understanding of feature propagation mechanisms in our proposed architecture.

3 Results

Table 2 presents the quantitative evaluation results across all test cases. As demonstrated in Table 2, STQA achieves statistically

TABLE 2 Comparison of experiments based on STQA and other prediction network models.

Method	SSIM	MAE(%)	RMSE(%)
U-Net	0.788	0.608	0.931
CGAN	0.891	0.419	0.867
TrQA	0.944	0.251	0.646
SWNet	0.958	0.198	0.597
STQA	0.978	0.163	0.416

significant improvements over U-Net and CGAN across all metrics. When comparing STQA with the state-of-the-art methods TrQA and SWNet, our method exhibits superior performance, particularly in the RMSE metric, where STQA reduces the error to 0.416 compared to 0.646 for TrQA and 0.597 for SWNet. In terms of structural similarity, STQA achieves an SSIM value of 0.978, outperforming TrQA (0.958) and SWNet (0.944) by margins of 0.034 and 0.020, respectively.

For enhanced visual comparison across methodologies, Figure 4 presents representative predicted dose distributions spanning three anatomical regions (head & neck, chest, abdomen) in axial, coronal, and sagittal orientations. Visual inspection of Figure 4 demonstrates that U-Net and CGAN underperform relative to the comparative methodologies, with U-Net exhibiting the most pronounced prediction inaccuracies. The VTDose maps indicate that STQA generates predictions with enhanced dose fidelity, a finding further supported by comprehensive analysis of dose difference maps. Comparative evaluation of discrepancy distributions reveals that Transformer-based models (TrQA, SWNet, and STQA) exhibit significantly reduced deviations compared to conventional approaches. Notably, STQA achieves minimal dose discrepancies across all clinical cases, outperforming other Transformer-based counterparts in maintaining alignment with GT dose distributions. To assess local dose accuracy, we computed mean absolute errors

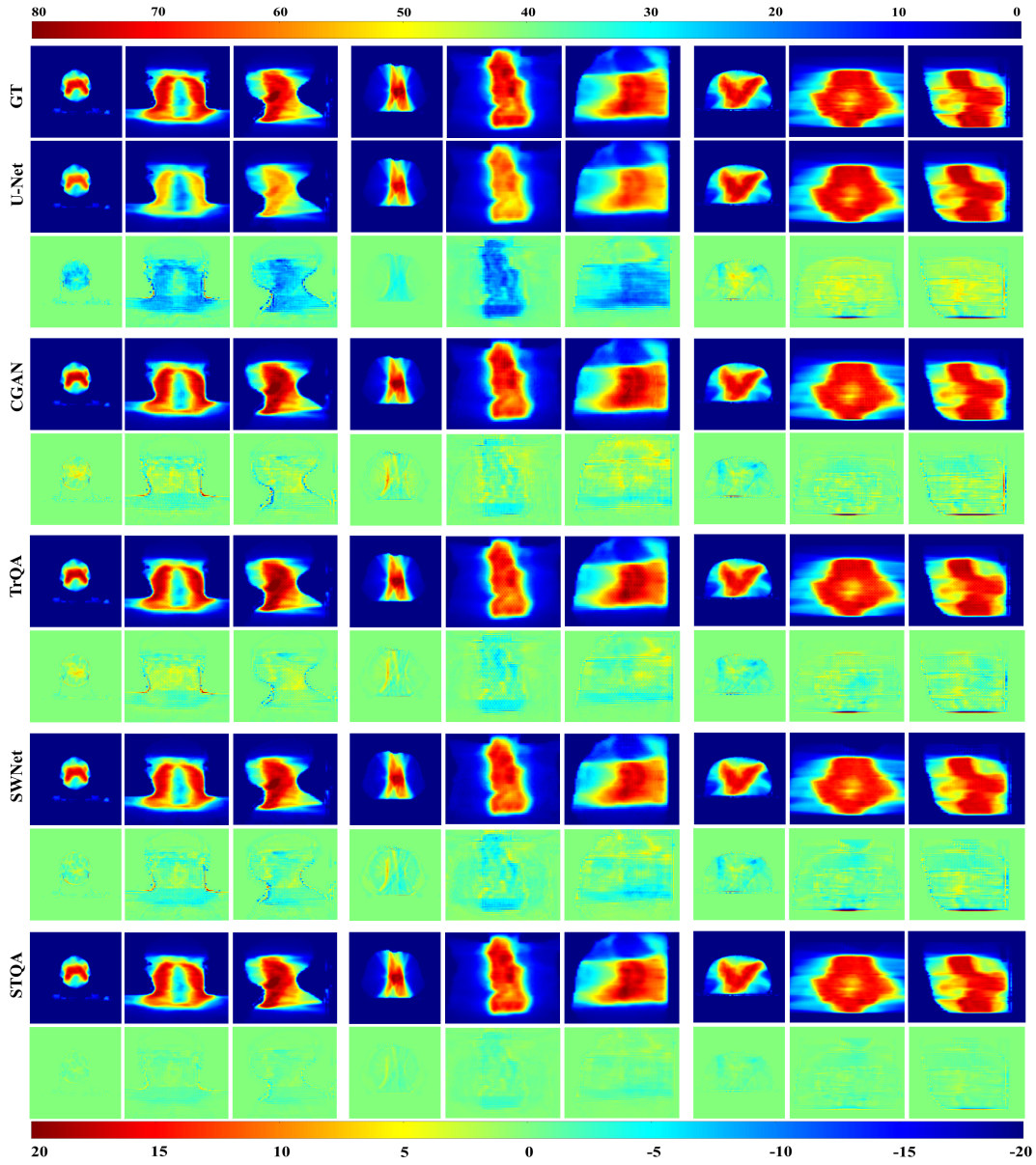

FIGURE 4
Qualitative analysis of predicted VTDose distributions (in Gy) across methodologies. Dose distributions are visualized for head & neck (columns 1-3), chest (columns 4-6), and abdominal (columns 7-9) cases. Rows 3, 5, 7, 9, and 11 demonstrate dose discrepancy maps between GT and predicted results. Anatomical plane assignments follow: columns 1/4/7 display axial dose distributions, columns 2/5/8 depict coronal plane mappings, and columns 3/6/9 correspond to sagittal plane patterns.

for Dmean and Dmax in critical OARs including the spinal cord and parotid glands. STQA achieved errors of 1.08 ± 1.21 Gy and 1.14 ± 0.67 Gy, respectively, outperforming all baselines, followed by SWNet and TrQA, UNet has the worst. This performance advantage suggests STQA's superior capability in preserving dosimetric details while ensuring spatial consistency with GT.

To evaluate the predictive performance of each network for specific cancer sites, tests were conducted separately based on three major cancer sites (head & neck, chest, abdomen), and the results of each method were compared as shown in Table 3. From the comparison across the three metrics, all methods exhibited better dose prediction results for the chest than the other two sites. This may be due to the simpler structure of the thorax compared to the other two sites and the fact that chest patients accounted for the largest number (116, 58%), making it easier for the network to extract features. Additionally, the prediction accuracy of abdominal patients is slightly better than that of head and neck patients, which is likely due to the small number of head and neck patients and the complex anatomical structure. Despite the imbalanced distribution of cancer sites, stratified sampling during data splitting helped mitigate bias, and STQA consistently outperformed baselines across all sites. Overall, STQA achieved the best predictive accuracy across all three cancer sites. This indicates that the STQA network demonstrates the best performance across various shapes and texture differences. Furthermore, the GPR analysis revealed distinct performance differences among models: The U-Net model achieved suboptimal GPR results (98.54 ± 3.42%), showing statistically inferior performance compared to other methods. In contrast, STQA demonstrated the closest agreement with GT measurements, yielding GPR values of 95.43 ± 3.41% versus the GT baseline of 94.63 ± 2.84%. Intermediate performance was observed for CGAN (98.22 ± 2.74%), TrQA (96.91 ± 4.16%), and SWNet (96.20 ± 3.65%), all showing comparable GPR outcomes. The mean errors between the GPR of the VTDose and the predictions were 4.24% for the U-Net, and 3.42%, 2.52%, 1.77%, 1.1% for CGAN, TrQA and STQA, respectively.

Table 4 illustrates the ablation experiment of the performance differences among different model architectures. In the comparison of parameter quantities among the three structural models, we observed that replacing the bottleneck of the original Swin-UNet with ResNet's network layers (STQA) resulted in a reduction of nearly 40% in the memory footprint of the trained model files. Additionally, STQA exhibited a reduction of almost 50% in model file memory compared to SWNet. This indicates that the STQA architecture not only reduces redundant parameters and has a smaller time complexity but also slightly improves performance. While the SURNet model exhibits the best performance, its deeper network structure leads to larger model parameter quantities and higher time complexity. Therefore, considering all factors, we believe that the STQA structure demonstrates the optimal performance. Table 5 demonstrates the impact of the number of skip connections in the network on its performance (ablation experiment 2). We observed that the neural network exhibited the highest predictive accuracy when having 3 skip connections. This is likely because an appropriate number of skip connections can effectively integrate features from different layers, enhancing the network's ability to capture multi-scale information. Too few skip connections may not fully utilize the feature hierarchy, while too many could introduce unnecessary complexity and potential overfitting. Therefore, in this study, we default the number of skip connections to be 3, as it strikes a balance between feature integration and model complexity, leading to optimal performance.

TABLE 3 Comparison of model performance across different cancer sites.

Method	SSIM	MAE(%)	RMSE(%)
	H&n/abdomen/chest	H&n/abdomen/chest	H&n/abdomen/chest
U-Net	0.782/0.816/0.821	0.522/0.513/0.505	0.865/0.841/0.822
CGAN	0.892/0.898/0.901	0.419/0.400/0.381	0.848/0.826/0.805
TrQA	0.948/0.954/0.966	0.250/0.245/0.225	0.637/0.632/0.5724
SWNet	0.964/0.967/0.971	0.195/0.186/0.162	0.583/0.577/0.468
STQA	0.980/0.984/0.985	0.159/0.152/0.145	0.411/0.408/0.365

TABLE 4 Comparison of performance and parameters among different model architectures.

Method	SSIM	MAE(%)	RMSE(%)	Model_size
SWNet	0.951±0.5e-3	0.188±0.05	0.587±0.24	98.1MB
STQA	0.982±0.5e-3	0.160±0.04	0.418±0.31	45.2MB
SURNet	0.988±0.4e-3	0.155±0.02	0.394±0.14	105.4MB

4 Discussion

Artificial intelligence, particularly deep learning (DL) techniques, has found extensive application in multiple facets of radiotherapy treatment planning and delivery, such as tumor target delineation (33), adaptive radiotherapy plans (34), 3D dose prediction (23), and PSQA (35). Accurate and rapid implementation of quality assurance processes for patients' radiotherapy treatments can assist physicists in patient care. In terms of methods, compared to CNN networks, DL networks based on Transformers lack some important inductive biases (e.g., locality and translation equivariance), making their training heavily reliant on large-scale datasets and pre-trained models. However, due to the

TABLE 5 Impact of the number of skip connections on network performance.

Skip connection	SSIM	MAE(%)	RMSE(%)
0	0.815	3.256	8.032
1	0.641	1.577	3.412
2	0.957	0.193	0.543
3	0.977	0.168	0.444

lack of large-scale and well-annotated datasets, the development of DL in the field of medical imaging lags behind that of natural image processing. In particular, there have been few studies applying Transformers to the field of radiotherapy quality assurance. Recently, Hu et al., proposed a U-shaped network called TrDosePred (36), which consists of convolutional patch embedding and several Transformer blocks based on local self-attention. This network aims to generate dose distributions from contour CT images. The dose score on the test dataset was 2.426 Gy, and the DVH score was 1.592 Gy. The results demonstrate that the performance of TrDosePred is comparable to or even better than previous state-of-the-art methods, proving the potential of Transformers in improving treatment planning processes.

In this paper, we aim to obtain global contextual information from radiotherapy volume images to improve the accuracy of VMAT quality assurance. We innovatively improved the Swin-UNet architecture to construct the STQA network, making the network suitable for handling radiotherapy planning data. Specifically, we modified the loss function and optimizer for training the network to L1 loss and Adam, respectively. Moreover, to explore optimal network training, we attempted to train the network using a combination of two loss functions, L1 and L2, with weighted allocation. Most importantly, we replaced two consecutive Swin Transformer modules between the downsampling and upsampling layers of the Swin-UNet network with ResNet layers to overcome the problem of feature extraction degradation due to network depth, thereby improving performance. The inherent properties of Transformers allow them to handle feature representations at a stable and relatively high resolution, accurately meeting the demands for finer-grained and globally consistent predictions in dense prediction tasks. Compared to other state of the art models, we applied Transformer-based DL methods to the VTDose prediction task and achieved better accuracy. This further demonstrates the outstanding achievements of Transformers in medical imaging compared to traditional CNN networks, helping to narrow the development gap between medical imaging DL and natural image processing.

Visual comparisons through representative predicted VTDose distributions reinforce these quantitative findings. STQA's VTDose maps show superior fidelity. The dose difference maps further substantiate this, with STQA exhibiting minimal discrepancies across all cases, especially in high-dose regions and critical anatomical structures. This is particularly important as these areas are often the most challenging to predict accurately due to their complexity and the potential consequences of dosing errors. Tables 2–4 demonstrate that our proposed STQA framework achieves state-of-the-art performance in VTDose prediction across multiple evaluation dimensions. Compared to existing Transformer-based methods (TrQA and SWNet), STQA reduces RMSE by 35.6% and 30.3%, respectively, while improving SSIM by 3.6% and 2.1% over these benchmarks. These advancements almost align with the performance gains reported in recent studies utilizing hybrid architectures for medical image analysis (30). The 16.6-25.3% improvement in SSIM and 18.5–69.5% reduction in MAE for these challenging cases suggests that our multi-scale skip connection strategy and hybrid bottleneck design effectively capture both global contextual relationships and local texture details—a capability not fully realized in pure Transformer architectures (23). The ablation studies further validate STQA's architectural innovations. The 40–50% reduction in model memory footprint compared to SWNet, while maintaining competitive accuracy, resolves a key practical limitation of Transformer-based models. Although SURNet achieved marginally higher SSIM values (0.988 vs. STQA's 0.982), its 2.3× greater parameter count and longer inference time render it clinically impractical. Our results thus suggest that STQA successfully balances computational efficiency with prediction accuracy.

Due to the inherent constraints associated with patient data and DL networks, certain discrepancies between predicted and measured results are unavoidable. Addressing these discrepancies in the future involves augmenting the dataset size or refining DL networks through optimization. The patients in the dataset used in this work come from multiple sites, but they are mixed for both training and testing, rather than having one set for training and another for external testing. Since data from different centers may exhibit significant differences, it can affect the effectiveness of training. In the future, balancing data processing or increasing patient data volume will further improve prediction accuracy. However, it is worth noting that while incorporating multi-institutional data could further improve the model's generalizability by capturing a broader range of anatomical and dosimetric variations, the present study utilized data from a single institution to ensure consistency in imaging and treatment protocols. The inherent rarity and heterogeneity of medical data pose significant challenges to assembling large, diverse multi-center datasets. The predominance of chest cases may introduce a bias toward simpler anatomies, though our model still performed well on more complex sites. Future work will aim to collect a more balanced dataset across cancer sites and institutions. While we did not separately compute voxel-level sensitivity/specificity for gamma-fail classification, operating directly on volumetric VTDose provides the spatial observability required for fail-voxel localization and *post-hoc* gamma-map synthesis; we plan to report a dedicated voxel-wise gamma-fail analysis in future work. Finally, the model still suffers from time complexity, and we will strive to reduce the model's time complexity in future work.

In conclusion, this study proposes a new framework termed STQA for VMAT quality assurance, demonstrating superior performance compared to existing models. To strengthen the model's generalization capacity and convergence properties, we innovatively integrated a ResNet layer into the network's bottleneck to enhance feature extraction capabilities while adopting advanced loss functions and optimization strategies. Comprehensive validation conducted on VMAT-treated cancer patient datasets revealed that STQA achieves state-of-the-art performance in both global dose distribution prediction and edge dose accuracy across various tumor sites. This successful implementation not only addresses critical challenges in VMAT

quality assurance but also paves the way for effective integration of deep learning across medical domains, potentially inspiring novel methodological developments in medical artificial intelligence. From a clinical integration perspective, STQA demonstrates practical feasibility. The average inference time for a full 3D dose prediction is approximately 5–7 seconds on an NVIDIA RTX 3090 GPU, which is compatible with routine QA workflows. The model can be deployed as a standalone application or integrated into existing treatment planning systems via a standardized DICOM RT Dose interface. Future work will focus on user interface development and real-time validation in clinical settings.

Data availability statement

The datasets presented in this article are not readily available because the data used and analyzed during the current study are available from the corresponding author on reasonable request. Requests to access the datasets should be directed to zhangyun_1983@sohu.com.

Ethics statement

Written informed consent was obtained from the individual(s) for the publication of any potentially identifiable images or data included in this article.

Author contributions

YQZ: Project administration, Methodology, Writing – original draft. CG: Writing – review & editing, Conceptualization, Visualization, Formal Analysis, Resources, Funding acquisition. JJ: Writing – review & editing, Conceptualization, Data curation, Investigation. YZ: Conceptualization, Writing – review & editing, Formal Analysis.

Funding

The author(s) declare financial support was received for the research and/or publication of this article. The authors acknowledge the supported by the National Natural Science Foundation of China (No.82360357), WenZhou Radiation oncology and translational research key lab, and “Five-level Progressive” talent cultivation project of Jiangxi Cancer Hospital & Institute (WCDJ2024YQ04).

Conflict of interest

The authors declare that the research was conducted in the absence of any commercial or financial relationships that could be construed as a potential conflict of interest.

Generative AI statement

The author(s) declare that no Generative AI was used in the creation of this manuscript.

Any alternative text (alt text) provided alongside figures in this article has been generated by Frontiers with the support of artificial intelligence and reasonable efforts have been made to ensure accuracy, including review by the authors wherever possible. If you identify any issues, please contact us.

Publisher’s note

All claims expressed in this article are solely those of the authors and do not necessarily represent those of their affiliated organizations, or those of the publisher, the editors and the reviewers. Any product that may be evaluated in this article, or claim that may be made by its manufacturer, is not guaranteed or endorsed by the publisher.

References

1. Ono T, Iramina H, Hirashima H, Adachi T, Nakamura M, Mizowaki T. Applications of artificial intelligence for machine- and patient-specific quality assurance in radiation therapy: current status and future directions. *J Radiat Res.* (2024) 65:421–32. doi: 10.1093/jrr/rrae033

2. Miften M, Olch A, Mihailidis D, Moran J, Pawlicki T, Molineu A, et al. Tolerance limits and methodologies for IMRT measurement-based verification QA: Recommendations of AAPM Task Group No. 218. *Med Phys.* (2018) 45:e53–83. doi: 10.1002/mp.12810

3. Gong C, Zhu K, Lin C, Han C, Lu Z, Chen Y, et al. Efficient dose-volume histogram-based pretreatment patient-specific quality assurance methodology with combined deep learning and machine learning models for volumetric modulated arc radiotherapy. *Med Phys.* (2022) 49:7779–90. doi: 10.1002/mp.16010

4. Valdes G, Scheuermann R, Hung CY, Olszanski A, Bellerive M, Solberg TD. A mathematical framework for virtual IMRT QA using machine learning. *Med Phys.* (2016) 43:4323. doi: 10.1118/1.4953835

5. Valdes G, Chan MF, Lim SB, Scheuermann R, Deasy JO, Solberg TD. IMRT QA using machine learning: A multi-institutional validation. *J Appl Clin Med Phys.* (2017) 18:279–84. doi: 10.1002/acm2.12161

6. Li J, Wang L, Zhang X, Liu L, Li J, Chan MF, et al. Machine learning for patient-specific quality assurance of VMAT: prediction and classification accuracy. *Int J Radiat Oncol Biol Phys.* (2019) 105:893–902. doi: 10.1016/j.ijrobp.2019.07.049

7. Chan MF, Witztum A, Valdes G. Integration of AI and machine learning in radiotherapy QA. *Front Artif Intell.* (2020) 3:577620. doi: 10.3389/frai.2020.577620

8. Hirashima H, Ono T, Nakamura M, Miyabe Y, Mukumoto N, Iramina H, et al. Improvement of prediction and classification performance for gamma passing rate by using plan complexity and dosiomics features. *Radiother Oncol.* (2020) 153:250–7. doi: 10.1016/j.radonc.2020.07.031

9. Granville DA, Sutherland JG, Belec JG, La Russa DJ. Predicting VMAT patient-specific QA results using a support vector classifier trained on treatment plan characteristics and linac QC metrics. *Phys Med Biol.* (2019) 64:095017. doi: 10.1088/1361-6560/ab142e

10. Tomori S, Kadoya N, Takayama Y, Kajikawa T, Shima K, Narazaki K, et al. A deep learning-based prediction model for gamma evaluation in patient-specific quality assurance. *Med Phys.* (2018). doi: 10.1002/mp.13112

11. Tomori S, Kadoya N, Kajikawa T, Kimura Y, Narazaki K, Ochi T, et al. Systematic method for a deep learning-based prediction model for gamma

evaluation in patient-specific quality assurance of volumetric modulated arc therapy. *Med Phys*. (2021) 48:1003–18. doi: 10.1002/mp.14682

12. Interian Y, Rideout V, Kearney VP, Gennatas E, Morin O, Cheung J, et al. Deep nets vs expert designed features in medical physics: An IMRT QA case study. *Med Phys*. (2018) 45:2672–80. doi: 10.1002/mp.12890

13. Kadoya N, Kon Y, Takayama Y, Matsumoto T, Hayashi N, Katsuta Y, et al. Quantifying the performance of two different types of commercial software programs for 3D patient dose reconstruction for prostate cancer patients: Machine log files vs. machine log files with EPID images. *Phys Med*. (2018) 45:170–6. doi: 10.1016/j.ejmp.2017.12.018

14. Jia M, Wu Y, Yang Y, Wang L, Chuang C, Han B, et al. Deep learning-enabled EPID-based 3D dosimetry for dose verification of step-and-shoot radiotherapy. *Med Phys*. (2021) 48:6810–9. doi: 10.1002/mp.15218

15. Kalet AM, Luk SMH, Phillips MH. Radiation therapy quality assurance tasks and tools: the many roles of machine learning. *Med Phys*. (2020) 47:e168–77. doi: 10.1002/mp.13445

16. Pillai M, Adapa K, Das SK, Mazur L, Dooley J, Marks LB, et al. Using artificial intelligence to improve the quality and safety of radiation therapy. *J Am Coll Radiol*. (2019) 16:1267–72. doi: 10.1016/j.jacr.2019.06.001

17. Yang X, Li S, Shao Q, Cao Y, Yang Z, Zhao YQ. Uncertainty-guided man-machine integrated patient-specific quality assurance. *Radiother Oncol*. (2022) 173:1–9. doi: 10.1016/j.radonc.2022.05.016

18. Hu T, Xie L, Zhang L, Li G, Yi Z. Deep multimodal neural network based on data-feature fusion for patient-specific quality assurance. *Int J Neural Syst*. (2022) 32:2150055. doi: 10.1142/S0129065721500556

19. Matsuura T, Kawahara D, Saito A, Yamada K, Ozawa S, Nagata Y. A synthesized gamma distribution-based patient-specific VMAT QA using a generative adversarial network. *Med Phys*. (2023) 50:2488–98. doi: 10.1002/mp.16210

20. Yoganathan SA, Ahmed S, Paloor S, Torfeh T, Aouadi S, Al-Hammadi N, et al. Virtual pretreatment patient-specific quality assurance of volumetric modulated arc therapy using deep learning. *Med Phys*. (2023) 50:7891–903. doi: 10.1002/mp.16567

21. Courant R, Edberg M, Dufour N, Kalogeiton V. Transformers and visual transformers. In: Colliot O, editor. *Machine learning for brain disorders*. Humana, New York, NY (2023).

22. Wolf T, Debut L, Sanh V, Chaumond J, Delangue C, Moi A, et al. (2020). Transformers: State-of-the-art natural language processing, in: *Proceedings of the 2020 conference on empirical methods in natural language processing: system demonstrations*. pp. 38–45. doi: 10.18653/v1/2020.emnlp-demos.6

23. Zeng L, Zhang M, Zhang Y, Zou Z, Guan Y, Huang B, et al. TransQA: deep hybrid transformer network for measurement-guided volumetric dose prediction of pre-treatment patient-specific quality assurance. *Phys Med Biol*. (2023) 68. doi: 10.1088/1361-6560/acfa5e

24. Wu K, Peng H, Chen M, Fu JL, Chao HY. (2021). Rethinking and improving relative position encoding for vision transformer, in: *Proceedings of the IEEE/CVF International Conference on Computer Vision*, . pp. 10033–41. doi: 10.1109/iccv48922.2021.00988

25. Li J, Yan Y, Liao S, Yang XK, Shao L. Local-to-global self-attention in vision transformers. (2021). doi: 10.48550/arXiv.2107.04735

26. Vaswani A, Ramachandran P, Srinivas A, Parmar N, Hechtman B, Shlens J, et al. (2021). Scaling local self-attention for parameter efficient visual backbones, in: *Proceedings of the IEEE/CVF Conference on Computer Vision and Pattern Recognition*, . pp. 12894–904. doi: 10.1109/cvpr46437.2021.01270

27. Liu Z, Lin Y, Cao Y, Hu H, Wei YX, Zhang Z, et al. (2021). Swin transformer: Hierarchical vision transformer using shifted windows, in: *Proceedings of the IEEE/CVF international conference on computer vision*, . pp. 10012–22. doi: 10.1109/iccv48922.2021.00986

28. Chen J, Lu Y, Yu Q, Luo XD, Adeli E, Wang Y, et al. Transunet: Transformers make strong encoders for medical image segmentation. (2021). doi: 10.48550/arXiv.2102.04306

29. Zhang Y, Liu H, Hu Q. (2021). Transfuse: Fusing transformers and cnns for medical image segmentation, in: *Medical Image Computing and Computer Assisted Intervention–MICCAI 2021: 24th International Conference*, Strasbourg, France, September 27–October 1, 2021. pp. 14–24. Springer International Publishing, Proceedings, Part I 24. doi: 10.1007/978-3-030-87193-2_2

30. Lin A, Chen B, Xu J, Zhang Z, Lu GM, Zhang D, et al. Ds-transunet: Dual swin transformer u-net for medical image segmentation. *IEEE Trans Instrumentation Measurement*. (2022) 71:1–15. doi: 10.1109/tim.2022.3178991

31. Ma M, Kovalchuk N, Buyyounouski MK, Xing L, Yang Y. Incorporating dosimetric features into the prediction of 3D VMAT dose distributions using deep convolutional neural network. *Phys Med Biol*. (2019) 64:125017. doi: 10.1088/1361-6560/ab2146

32. Zhu J-Y, Park T, Isola P, Efros AA. (2017). Unpaired image-to-image translation using cycle-consistent adversarial networks, in: *Proceedings of the IEEE international conference on computer vision*, Venice, Italy. pp. 2223–32.

33. Shi J, Ding X, Liu X, Li Y, Liang W, Wu J. Automatic clinical target volume delineation for cervical cancer in CT images using deep learning. *Med Phys*. (2021) 48:3968–81. doi: 10.1002/mp.14898

34. Zou Z, Gong C, Zeng L, Guan Y, Huang B, Yu X, et al. Invertible and variable augmented network for pretreatment patient-specific quality assurance dose prediction. *J Imaging Inf Med*. (2024), 1–12. doi: 10.1007/s10278-023-00930-w

35. Cui X, Yang X, Li D, Dai X, Guo Y, Zhang W, et al. A StarGAN and transformer-based hybrid classification-regression model for multi-institution VMAT patient-specific quality assurance. *Med Phys*. (2025) 52:685–702. doi: 10.1002/mp.17485

36. Hu C, Wang H, Zhang W, Xie Y, Jiao L, Cui S. TrDosePred: A deep learning dose prediction algorithm based on transformers for head and neck cancer radiotherapy. *J Appl Clin Med Phys*. (2023):e13942. doi: 10.1002/acm2.13942

frontiers | Frontiers in Oncology

TYPE Original Research
PUBLISHED 29 September 2025
DOI 10.3389/fonc.2025.1672778

Check for updates

OPEN ACCESS

EDITED BY
Abdul K. Parchur,
University of Maryland Medical Center,
United States

REVIEWED BY
Jaidip Jagtap,
Mayo Clinic, United States
Varekan Keishing,
Mayo Clinic, United States

*CORRESPONDENCE
Yue Yan
yue.yan@dartmouth.edu

RECEIVED 24 July 2025
ACCEPTED 08 September 2025
PUBLISHED 29 September 2025

CITATION
Asher GL, Wang S, Zaki BI, Russo GA, Gill GS, Thomas CR, Prioleau TO, Li Y, Zhang R, Yan Y and Hunt B (2025) Dosimetric evaluations using cycle-consistent generative adversarial network synthetic CT for MR-guided adaptive radiation therapy.
Front. Oncol. 15:1672778.
doi: 10.3389/fonc.2025.1672778

COPYRIGHT
© 2025 Asher, Wang, Zaki, Russo, Gill, Thomas, Prioleau, Li, Zhang, Yan and Hunt. This is an open-access article distributed under the terms of the Creative Commons Attribution License (CC BY). The use, distribution or reproduction in other forums is permitted, provided the original author(s) and the copyright owner(s) are credited and that the original publication in this journal is cited, in accordance with accepted academic practice. No use, distribution or reproduction is permitted which does not comply with these terms.

Dosimetric evaluations using cycle-consistent generative adversarial network synthetic CT for MR-guided adaptive radiation therapy

Gabriel L. Asher[1], Shiru Wang[2], Bassem I. Zaki[3,4], Gregory A. Russo[3,4], Gobind S. Gill[4], Charles R. Thomas[3,4], Temiloluwa O. Prioleau[1], Yuting Li[5], Rongxiao Zhang[2,6], Yue Yan[2,3,4]* and Brady Hunt[2,3]

[1]Department of Computer Science, Dartmouth College, Hanover, NH, United States, [2]Thayer School of Engineering, Dartmouth College, Hanover, NH, United States, [3]Geisel School of Medicine, Dartmouth College, Hanover, NH, United States, [4]Department of Radiation Oncology & Applied Sciences, Dartmouth-Hitchcock Medical Center, Lebanon, NH, United States, [5]Department of Radiation Physics, University of Texas MD Anderson Cancer Center, Houston, TX, United States, [6]Department of Radiation Oncology, University of Missouri, Columbia, MO, United States

Background: Magnetic resonance (MR) guided radiation therapy combines high-resolution image capabilities of MRI with the precise targeting of radiation therapy. However, MRI does not provide the essential electron density information for accurate dose calculation, which limit the application of MRI. In this presented work, we evaluated the potential for Deep Learning (DL) based synthetic CT (sCT) generation using 3D MRI setup scans acquired during real-time adaptive MRI-guided radiation therapy.

Methods: We trained and evaluated a Cycle-consistent Generative Adversarial Network (Cycle-GAN) using paired MRI and deformably registered CT scan slices (dCT) in the context of real-time adaptive MRI-guided radiation therapy. Synthetic CT (sCT) volumes are output from the MR to CT generator of the Cycle-GAN network. A retrospective study was conducted to train and evaluate the DL model using data from patients undergoing treatment for kidney, pancreas, liver, lung, bone, and prostate tumors. Data was partitioned by patients using a stratified k-fold approach to ensure balanced representation of treatment sites in the training and testing sets. Synthetic CT images were evaluated using mean absolute error in Hounsfield Units (HU) relative to dCT, and four image quality metrics (mean absolute error, structural similarity index measure, peak signal-to-noise ratio, and normalized cross correlation) using the deformed CT scans as a reference standard. Synthetic CT volumes were also imported into a clinical treatment planning system and dosimetric calculations re-evaluated for each treatment plan (absolute difference in delivered dose to 3cm radius of PTV).

Results: We trained the model using 8405 frames from 57 patients and evaluated it using a test set of 357 sCT frames from 17 patients. Quantitatively, sCTs were comparable to electron density of dCTs, while improving structural similarity with on-table MRI scans. The MAE between sCT and dCT was 49.2$\pm$13.2 HU, sCT NCC outperformed dCT by 0.06, and SSIM and PSNR were 0.97$\pm$0.01 and 19.9$\pm$1.6

respectively. Furthermore, dosimetric evaluations revealed minimal differences between sCTs and dCTs. Qualitatively, superior reconstruction of air-bubbles in sCT compared to dCT reveal higher alignment between sCT than dCT with the associated MR.

Conclusions: Accuracy of deep learning based synthetic CT generation using setup scans on MR-Linacs was adequate for dose calculation/optimization. This can enable MR-only treatment planning workflows on MR-Linacs, thereby increasing the efficiency of simulation and adaptive planning for MRgRT.

KEYWORDS

deep learning, cycle-consistent generative adversarial network, deformable registration, MRI-guided radiation therapy, synthetic CT

1 Introduction

MR-guided radiation therapy (MRgRT) is a relatively new approach to radiation therapy (RT) which combines the high-resolution imaging capabilities of magnetic resonance imaging (MRI) with the precise targeting of radiation therapy. By using real-time MRI linear accelerator systems (MRI-LINAC) during treatment, MRgRT allows for more accurate targeting of the tumor, which can lead to improved outcomes and reduced side effects for patients (1). Several studies have demonstrated the benefits of MRgRT, including improved target coverage, reduced toxicity, and improved overall survival (2–4). Additionally, MRgRT has been shown to be effective in treating a variety of cancer types, including brain, prostate, and breast cancer (1, 5–7). Overall, MRgRT is an innovative approach to radiation therapy that has the potential to improve the radiation therapy workflow and patient outcomes.

However, a critical weakness of MRgRT is a reliance on electron density maps which are derived from computed tomography (CT) images for dose planning. Thus, to successfully carry out MRgRT, MR images must be co-registered with CT images. Co-registration of CT and MRI images is a critical step in MRgRT, however, it can also be a source of errors which can impact the accuracy of the treatment. The co-registration process aligns the CT and MRI images, allowing for precise targeting of the tumor, but it is prone to errors due to the inherent differences in the imaging modalities. CT images have limited soft tissue contrast and do not provide functional information about the tumor. On the other hand, MRI images have a better soft-tissue contrast, and provide functional information about the tumor, however, they are sensitive to motion artifacts and the presence of metallic objects and contrast agents (1, 8). The co-registration of CT and MRI images is conventionally performed manually, which can also be a source of errors if not done carefully. For example, this co-registration process has a systematic uncertainty of approximately 2–5 mm (9). The errors that can occur during the co-registration process can persist at multiple levels of the treatment workflow and bring systematic errors (10).

Current MR to CT registration techniques involve generating a deformed CT (dCT) from a baseline MR image and an existing CT image of the patient. Many of the conventional CT image registration techniques are time consuming and costly (11). Computational time for atlas-based methods rises linearly with dataset size and bulk segmentation requires longer acquisition time compared to conventional MR sequences (12, 13). Thus, deep learning (DL) based synthetic CT registration has been touted as a promising alternative to previous registration techniques. These deep-learning techniques offer several benefits over other methods. These methods consistently achieve state-of-the-art results in terms of registration performance according to Dice score evaluation. Additionally, these methods offer considerable speedups over traditional registration methods (12, 14, 15). These advantages make deep-learning based CT registration an optimal choice for real-time dose-calculations with novel MR-LINAC systems.

However, despite these advantages, there are several significant hurdles for training generalizable deep-learning synthetic CT generation models. First and foremost, datasets are often small. Training machine-learning (ML) models require ground truth labels, which means that for a MR to CT registration task, paired CT/MR datasets are needed. Thus, datasets used in training synthetic CT models tend to be small by machine learning standards and can be afflicted by batch errors due to limited diversity in acquisition settings such as MR and CT machines. Additionally, many datasets suffer from data leakage, which inflates model performance (16). Finally, large differences between intensity values from different MRI manufacturers means that trained models may struggle to generalize well.

Many studies evaluate the performance of various deep-learning architectures on synthetic CT registration from MR images. Generative adversarial networks (GAN) are among the more popular techniques for mapping MR images to sCTs (17).

However, GANs require strongly paired ground truths to train properly. This poses an issue in the context of dataset generation since MR images and CT images cannot be captured simultaneously. Thus, CycleGANs have shown themselves to be a promising method for synthetic CT generation. Due to a cycle-consistency loss, CycleGANs can train on paired or unpaired data, greatly increasing dataset size. Results from related CycleGAN studies have shown promise, with mean absolute error between ground-truth CT volume and sCT volumes between 30–150 Hounsfield Units (HU) (18–22). However, these studies demand further investigation for the following reasons. Firstly, most prior models were only trained with one or two sites in mind. Lei et al. study the brain and pelvis (21), Farjam et al. the pancreas (23), Wolterink et al. the brain (20), and Yang et al. study the brain and abdomen (with different models for each) (18). Furthermore, due to the limited size of datasets, many prior studies, such as Kang et al, Farjam et al, and Lei et al, do not use a held out validation data set in addition to their final test set (21–23). The lack of this validation set means that these models implicitly overfit on the test data since hyperparameters can be directly tuned on test data. Finally, although some studies evaluated treatment planning dose volumetrics on synthetic CTs (22), many of these studies did not (18–21, 23).

Thus, in this research study, we aim to further evaluate the performance of CycleGAN, a deep-learning algorithm, on synthetic CT generation. We employ a novel, large, paired image dataset with 6 different sites. Furthermore, we employ a rigorous data splitting regime to ensure minimal data leakage and the most generalizable results possible. Finally, we use the model trained from this dataset to investigate two tasks. Firstly, we assess the performance of CycleGAN in generating synthetic CT images that accurately correspond to their ground truths. Secondly, we evaluate our synthetic CT images with treatment planning software to determine whether they have adequate dosimetric outcomes to enable MR-only planning on MR-LINACs.

2 Materials and methods

2.1 Study dataset

This study analyzed patients undergoing stereotactic body radiation therapy using the ViewRay MRIdian MR-LINAC at the Dartmouth-Hitchcock Medical Center (DHMC). Patients underwent radiation therapy between March 2021 and June 2022. All DICOM and treatment delivery records were retrospectively accessed and anonymized before inclusion in the study in accordance with a protocol approved by the DHMC institutional review board. Simulation CT/MR scans were acquired on the same day at the outset of RT treatment planning, typically one hour between scans with CT scanning first. CT scans were acquired using a simulation scanner (Siemens EDGE) using routine clinical settings. MRI scans were obtained using a MR-Linac (ViewRay MRIdian) using built-in clinical protocols. Ground-truth deformed CTs (dCT) were generated using the ViewRay treatment planning system registration pipeline.

2.2 Image pre-processing and data partitioning

After dCT generation, all dCT and MR images were extracted in DICOM format with 144 slices and a 3mm axial resolution. The in-plane dimensions were 310 x 360 pixels with a 1.5mm resolution. DICOM volumes were converted to tiff images using the python open-source pydicom and tifffile packages. After conversion to tiff format, all images were padded to 440x440 pixels. Next, we conducted a stratified k-fold data splitting scheme using treatment site specified in the DICOM data as the category for stratification including: adrenal, pancreas, liver, lung, bone, prostate, and other. This split yielded 58 training patients, 11 validation patients, and 17 testing patients, ensuring that train and test splits contained at least one patient from each treatment site category. Prior to use in model training, all 8405 CT and MR images were normalized. CT images were normalized with the following linear formula:

$$Y = \frac{X - X_0}{\alpha} \tag{1}$$

where X is the input voxel in HU, X_0 =-1024, and α = the 99.99 percentile of HU values in the training set range. To ensure that all normalized values were positive, in Equation 1, X_0 was set to -1024, considering that the minimum HU value in our training set was also -1024. MR images were also normalized with Eq.1, with X_0 set at 0, since MR intensity values are all already nonnegative. Our pre-processing pipeline is described in Figure 1.

2.3 Model and loss formulation

Our study utilized the CycleGAN (Cycle-Consistent Generative Adversarial Network) model architecture (24). Training workflow of the CycleGAN model has been shown in Figure 2. Figure 3 details the architecture of CycleGAN. This architecture is a derivative of the generative adversarial network (GAN) (25), a popular deep-learning architecture which leverages two competing networks: a generator and a discriminator. In GANs, a generator generates a synthetic image from an input image, and the discriminator predicts whether this synthetic image is real of fake. The model stops learning when the generator produces indistinguishable images from the ground truth.

CycleGAN adopts a similar architecture as a GAN with two key differences. Firstly, instead of having one generator and one discriminator, CycleGAN has two generators (G_{MR},G_{CT}) and two discriminators (D_{MR},D_{CT}). The generator G_{CT}takes a CT image and generates an MR image, while the generator G_{MR}takes an MR image

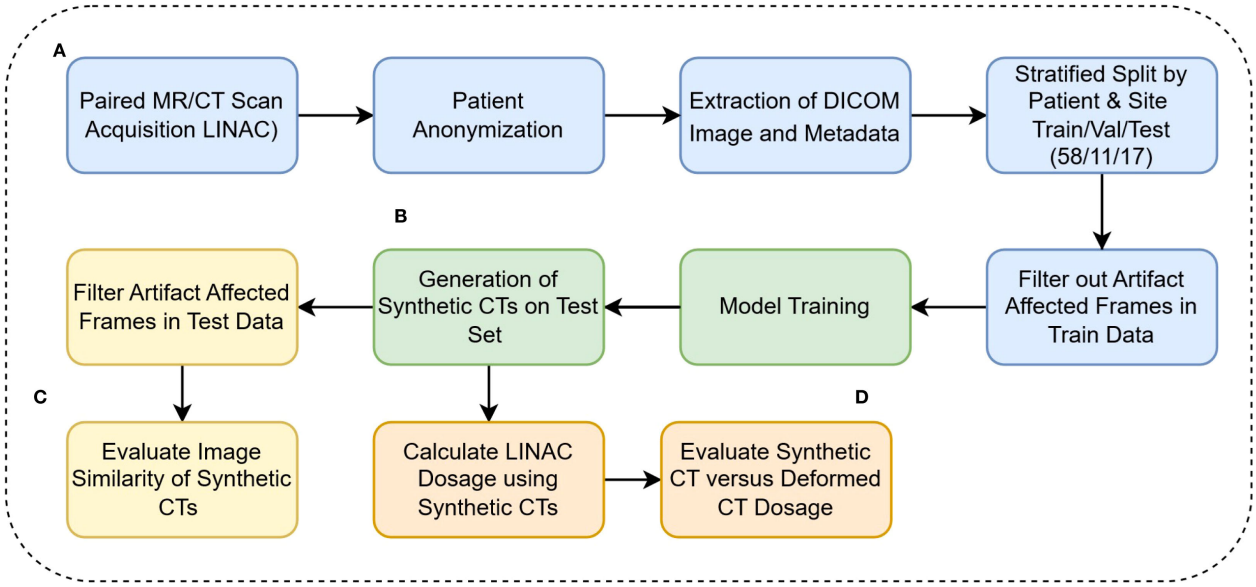

FIGURE 1
(A) DICOM anonymization, preprocessing, and filtration **(B)** Model training and inference calls **(C)** Evaluation of model performance on Hounsfield Unit level **(D)** Clinical evaluation of synthetic CTs.

and generates a CT image. The loss functions used to train the generators and discriminators in a Cycle-GAN typically include three components: the adversarial loss, the cycle-consistency loss, and the identity loss. Adversarial loss is used to ensure that the generated images are realistic and can fool the discriminators. The adversarial loss, L_{adv} is calculated using the mean squared error between the discriminator's output and the ground-truth label. The loss formulation of our discriminators is a summation of the adversarial loss with sCT as input and adversarial loss with dCT as input. Cycle-consistency loss is used to ensure that the generated images preserve the content of the original images and is calculated as the mean absolute error (MAE) between the original image and the translated image that has been translated back to the original domain. The cycle loss, L_{cyc} for the generator G_{CT} is calculated in Equation 2 as:

$$L_{cyc} = \| G_{MR}(G_{CT}(CT_{gt})) - CT_{gt} \| \cdot \lambda \quad (2)$$

, where λ is a weight, and CT_{gt} is a ground truth CT. The identity loss is added to ensure that the images from the same domain should not change after passing through the generator. The identity loss, as shown in Equation 3, L_{idt} for G_{CT} is:

$$L_{idt} = \| G_{CT}(CT_{gt}) - CT_{gt} \| \quad (3)$$

The loss formulations for $G_{MR}$are formulated similarly as G_{CT}. Finally, the total loss as shown in Equation 4, L_{total} is calculated as follows:

$$L_{total} = L_{advMR} + L_{advCT} + L_{cycleMR} + L_{cycleCT} + L_{idtMR} + L_{idtCT} \quad (4)$$

We trained our model on 1 Nvidia RTX 2080 Ti with 12GB of GPU memory. Additionally, we used the following model parameters: random crop to 256x256, batch size of 1, 100 epochs. Our model training code was from: https://github.com/junyanz/pytorch-CycleGAN-and-pix2pix (24, 26).

2.4 Evaluations

After model training, we used the lowest loss model (measured on the validation set) to generate a set of 2464 synthetic CT images from a held-out test set. However, whilst evaluating image similarity, we found a large amount of our test set dCTs were corrupted by artifacts in the beginning and end of each series in the axial plane. Thus, we only conducted our evaluations on the dosimetric relevant images within a 3cm radius of the PTV.

2.4.1 Synthetic image quality assessments

We first evaluated our test set through image quality and similarity metrics. We quantitatively measured the similarity between our sCT and dCT through mean average error (MAE), peak to signal noise ratio (PSNR), and structural similarity (SSIM). The formulas for these metrics are shown in Equations 5–7):

$$MAE = \frac{1}{n}\sum_{i=1}^{n}\left|y_{defCT} - y_{synCT}\right| \quad (5)$$

$$PSNR = 10 \cdot \log_{10}\frac{max(y_{defCT})^2}{\frac{1}{n}(\sum_{i=1}^{n}(y_{defCT} - y_{synCT}^2))} \quad (6)$$

$$SSIM(x,y) = \frac{(2\mu_{ix}\mu_{iy} + C_1)(2\sigma_{ixiy} + C_2)}{(\mu_{ix}^2 + \mu_{iy}^2 + C_1)(\sigma_{ix}^2 + \sigma_{iy}^2 + C_2)} \quad (7)$$

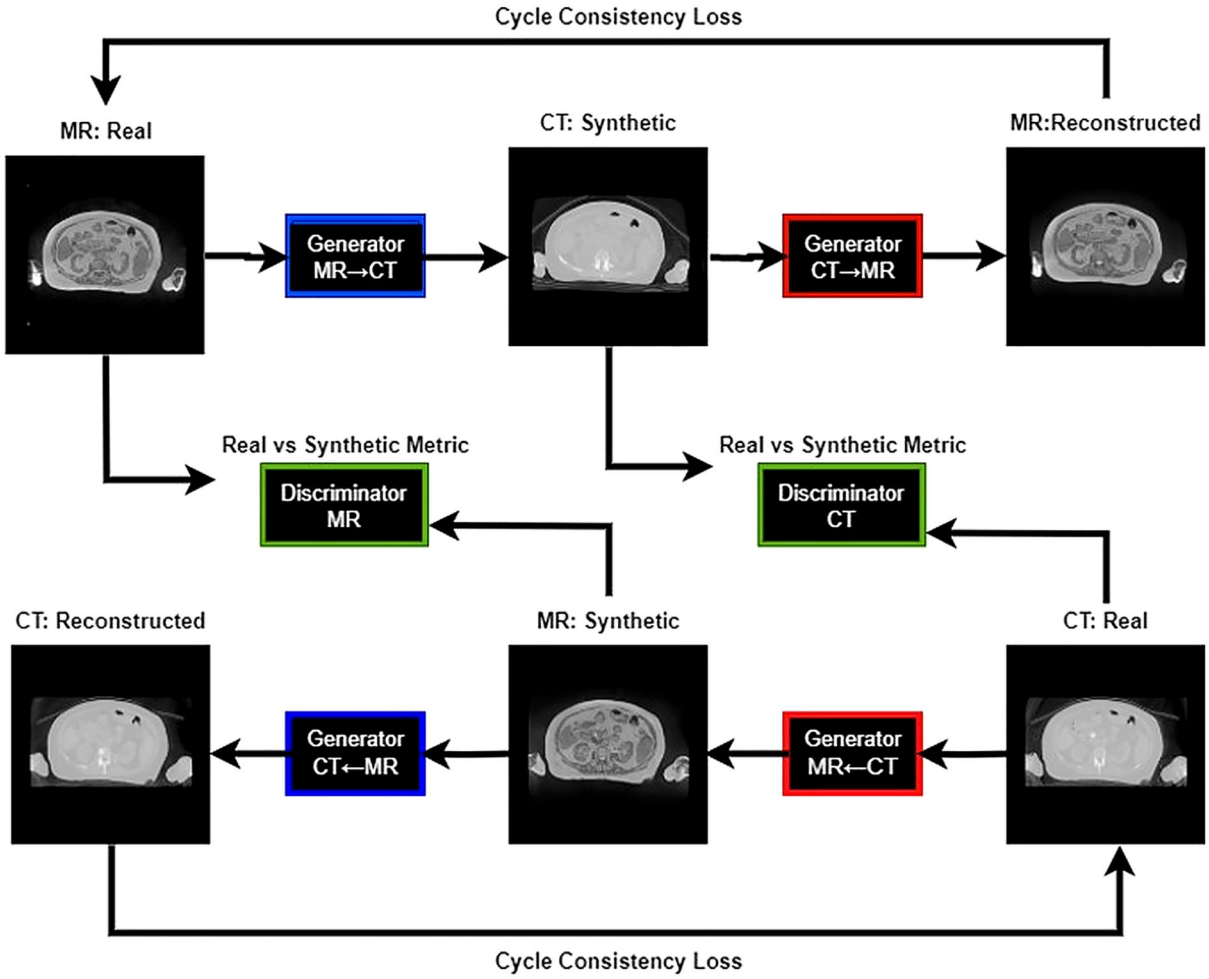

FIGURE 2
Training workflow of the CycleGAN model.

For SSIM, μ_{ix}, u_{iy} are the average HU values for the ith axial slice of our dCT and sCT sieries respectively. $\sigma_{ix}^2, \sigma_{iy}^2$ represent the variance of the aforementioned dCT and sCT slices. Finally, C_1, C_2 are constants applied as suggested by Wang et al (27). Additionally, we evaluated the similarity of sCT and dCT images to their corresponding MR inputs using Normalized Cross-Correlation (NCC). Normalized cross correlation (NCC) is a similarity measure that ranges from -1 to 1, used to determine the degree of similarity between two image regions, with 1 being most similar. NCC was calculated using the xcdskd package on python.

2.4.2 Dosimetric assessments

The second evaluation criteria of our sCTs consists of a comparison between the RT dose calculation in the sCT versus the dCT. In order to calculate these differences, our tiff images were reconverted to DICOM format. This was done by replacing the dCT DICOM "Pixel Data" tag with our generated sCT image. Next, we fed our DICOM sCTs into the ViewRay treatment planning software with the same parameters used on the dCTs to create dose volume histograms (DVHs). These DVHs were used to calculate the absolute difference of dose delivered to the PTV at 95%, 90%, and 85% of the volume. Additionally, we also calculate the difference in dose delivered above 33Gy to all 3cm OAR sites.

3 Results

3.1 Image quantitative comparisons

Table 1 reports the mean absolute error (MAE) of our cycle-GAN model. In total, 357 synthetic CT frames were analyzed from 17 patients. Of the treatment sites analyzed, the most common sites were liver, pancreas, and lung, with 84, 105, and 63 frames respectively. MAE was calculated by comparing synthetic CTs versus deformed CTs. Median MAE values across sites ranged between 44.7.4 HU to 55.6 HU with an overall median MAE of 49.2 HU. Pancreas and lung scans had the highest MAE standard deviations with 20.1 and 9.8 HU respectively. Kidney showed the least difference in MAE between scans with a standard deviation of 1.2 HU.

Table 2 reports SSIM and PSNR metrics, as well as the NCC of our sCTs and dCTs versus our MR image ground truths. Our sCTs

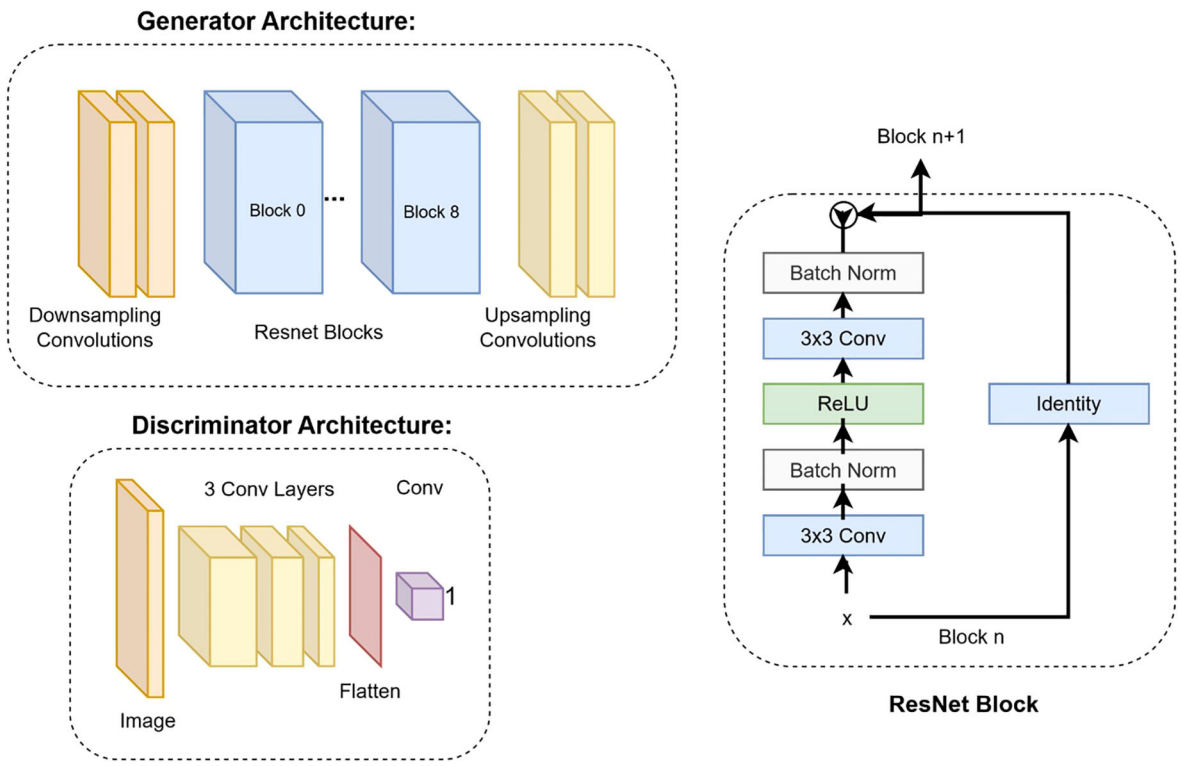

FIGURE 3
Deep learning architectures of the generator and the discriminator. The details of the ResNet block are shown on the right.

TABLE 1 The mean absolute error (MAE) of our cycle-GAN model per site.

Value description	Other	Kidney	Pancreas	Liver	Lung	Bone	Prostate	All
MAE min (HU)	44.4	42.6	37.7	35.6	46.9	52.3	48.3	35.6
MAE median (HU)	49.4	44.7	47.6	44.4	55.6	55.2	51.4	49.2
MAE max (HU)	57.7	47	100.4	67.5	87.8	58.3	53.9	100.4
std (HU)	4.3	1.2	20.1	7.7	9.8	1.6	1.8	13.2
Number of frames	42	21	105	84	63	21	21	357
Number of patients	2	1	5	4	3	1	1	17

TABLE 2 Image quality metrics per site. NCC refers to normalized-cross-correlation, SSIM refers to structural similarity, and PSNR refers to peak signal to noise ratio.

Value description	Other	Kidney	Pancreas	Liver	Lung	Bone	Prostate	All
Deformed NCC	0.769	0.825	0.827	0.839	0.826	0.803	0.707	0.818
Synthetic NCC	0.763	0.826	0.83	0.847	0.83	0.812	0.718	0.824
Median SSIM	0.974	0.978	0.969	0.974	0.967	0.965	0.976	0.971
SSIM std	0.002	0.002	0.016	0.008	0.015	0.003	0.002	0.013
Median PSNR	20.3	20.8	19.6	19.9	19.3	19	20.4	19.9
PSNR std	0.98	0.76	2.05	1.54	1.51	0.17	0.33	1.64
Number of frames	42	21	105	84	63	21	21	357
Number of patients	2	1	5	4	3	1	1	17

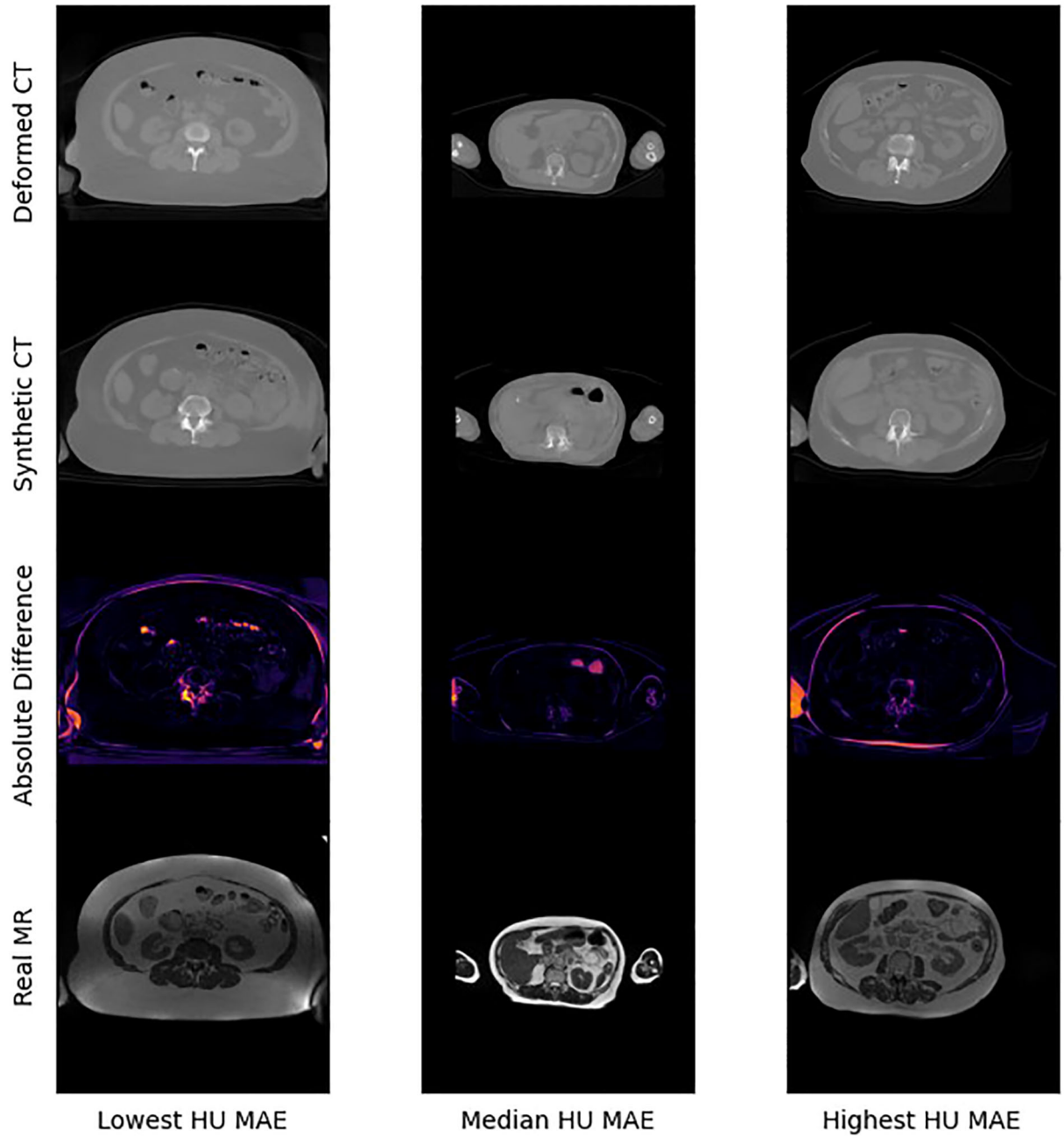

FIGURE 4
The lowest, median, and highest sCT mean average errors (HU) in the test set.

demonstrate a higher (better) NCC value in comparison to deformed CTs in all but one treatment site (Other). Although differences were generally minimal, sCT NCC scores on bone, prostate, and liver showed the largest improvements compared to our deformable registration ground truths. Additionally, we report high SSIM values across all sites, with a median SSIM value of 0.971. Thus, the structural similarity between our sCTs and dCTs is near perfect. Additionally, we report a median PSNR of 19.9 across all sites. This high PSNR value indicates that the sCT is a good representation of the dCT.

Figure 4 presents selected images from the scans with the lowest, median, and highest MAE (HU) from our test set. Figure 5 shows zoomed in panel of spinal region of interest. We compare sCT spinal reconstruction on lowest, median, and highest HU MAE patients. As is evident in all three examples, our model struggled to properly predict skin, bone, and limbs outside of the torso region (arms). Difficulty predicting bone is consistent with prior works (20, 21). Additionally, we view differences between the sCT and dCT with regards to air bubbles. For example, in the median HU images, we observe that our synthetic CT images

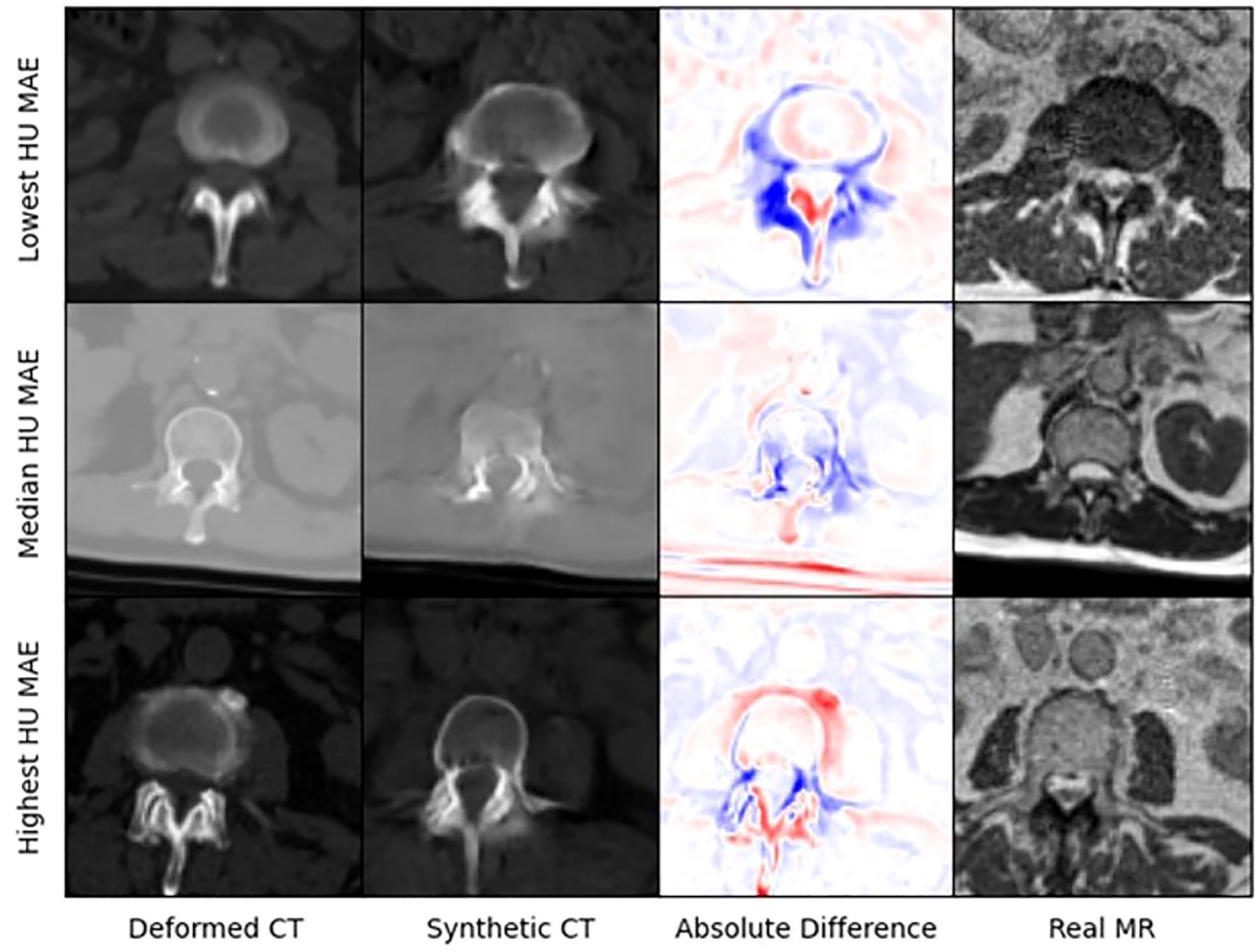

FIGURE 5
Zoomed in panel of spinal region of interest. We compare sCT spinal reconstruction on lowest, median, and highest HU MAE patients.

correctly include air bubbles present in MR, whereas the deformed CTs do not include said bubbles. However, from a qualitative perspective, our sCT reconstructions are minimally different from their deformed CT counterparts.

3.2 Dose comparisons

Table 3 reports the absolute difference of RT dose delivered to PTV at 85%, 90%, and 95% of the volume based on RT dose recalculations using our sCTs. Averaged sCT vs CT dose volumetrics per site is shown in Figure 6. Our results indicate minimal differences in dose delivered using sCTs. Median difference in dose delivered to PTV across all sites is.45Gy,.47Gy, and.46Gy for 85%, 90%, and 95% of volume respectively. Additionally, we found that dose above 33Gy delivered to OARs within 3cm of the PTV also showed minimum differences between sCT and dCT RT dose calculations. The median difference in dose delivered to 3cm OARs minimally increased by 0.01 Gy after switching from sCT to dCT. Additionally, 4 patients had no change in dose delivered to these sites, and 6 patients had less dose above 33Gy delivered to these sites.

4 Discussion

This report presents strong results supporting an MRI-only RT workflow. From a synthetic image quality perspective, our CycleGAN implementation reports comparable or superior MAE compared to prior studies conducted using a CycleGAN architecture (18, 28). Additionally, our results indicate that CycleGAN architecture generalizes well to several treatment sites with minimal additional training data. For example, despite only having 1 kidney, bone, and 3 prostate series each in our training data, we still report a mean MAE of 50.4 HU across these sites. Also, our overall median MAE of 49.2 HU is a strong result in comparison to prior work. This improved synthetic image quality may be a result of a larger dataset. Of the prior CycleGAN studies performed, this study analyzed 86 patient scans, compared with 24, 45, and 38, patients in works from Wolterink et al. (20), Yang et al

TABLE 3 DVH metrics per patient. Reports absolute difference between sCT and CT of dose delivered to 85%, 90%, and 95%.

Patient	Site	Gy diff@85%	Gy diff@90%	Gy diff@95%	Diff OAR dose > 33gy
PT0049	OTHER	0.19	0.21	0.23	0
PT0059	KIDNEY	0.5	0.49	0.47	-0.16
PT0066	PANCREAS	0.23	0.14	0.09	0.07
PT0067	LIVER	0	0.06	0.01	0
PT0069	LIVER	0.48	0.56	0.47	0
PT0070	PANCREAS	1.56	1.16	1.21	-0.26
PT0074	LIVER	0.04	0.04	0.05	0
PT0075	LIVER	0.86	0.82	0.28	-0.18
PT0076	PANCREAS	0.7	0.7	0.45	0.65
PT0077	LUNG	0.16	0.04	0.42	0.98
PT0078	PANCREAS	0.12`	0.07	0.01	-0.19
PT0080	PANCREAS	0.19	0.12	0.21	0.08
PT0081	BONE	0.57	0.57	0.41	NAN
PT0082	PROSTATE	0.16	0.16	0.17	0.25
PT0083	LUNG	1.23	1.64	1.76	0.11
PT0084	LUNG	0.25	0.68	1.13	-1.11
PT0085	OTHER	NAN	NAN	NAN	-0.03
ALL	ALL	0.45	0.47	0.46	0.01

This table also reports the difference in dose delivered above 33Gy in 3cm OAR sites, where a negative value indicates that less dose above 33Gy was delivered with the sCT.

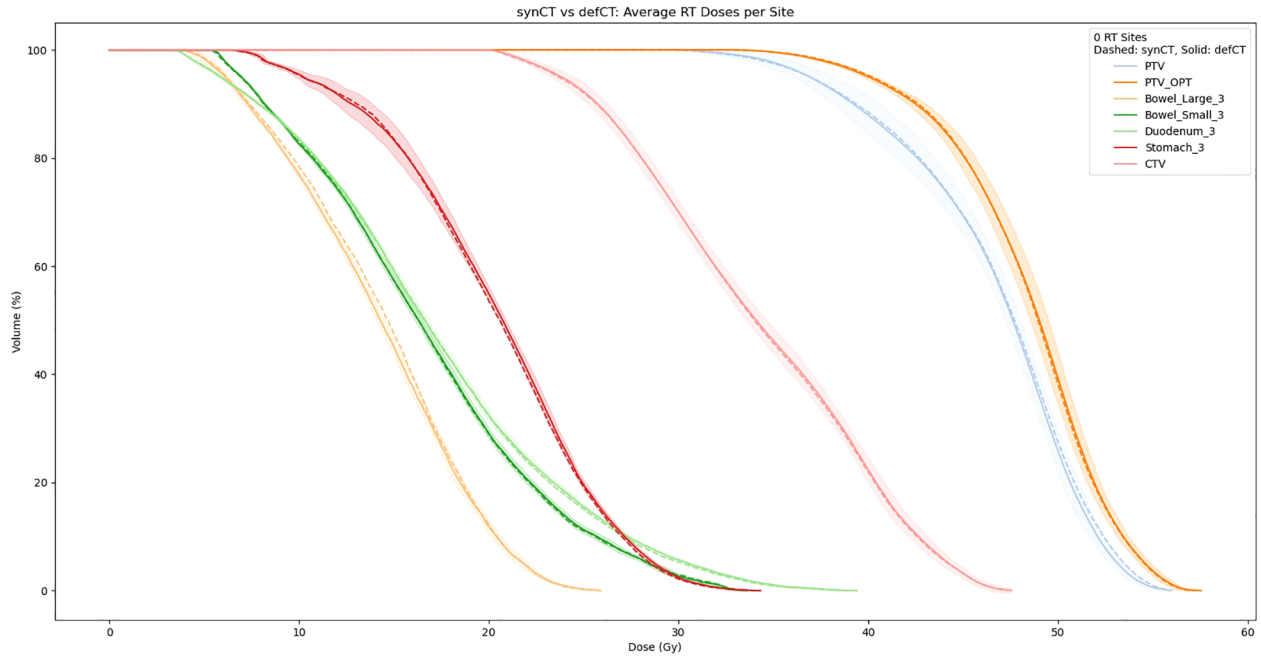

FIGURE 6
Averaged sCT vs CT dose volumetrics per site (dotted = sCT, solid = CT). The shaded region corresponds to the standard deviation between the sCT and CT DVHs.

(18), and Brou et al (28). Thus, given our superior reconstruction results, we demonstrate that dataset size is paramount in creating strong generative synthetic CT models.

Our treatment dose comparison also supports an MRI-only RT workflow. Our 0.45 Gy, 0.47 Gy, and 0.46 Gy average difference in dose delivered to PTV for 85%, 90%, and 95% of the volume indicates that sCTs have minimal effects on dose delivered. Additionally, NCC comparisons in Table 4 indicate that synthetic CTs capture an equivalent to better representation of the MR scans taken during treatment. Thus, we can extrapolate that synthetic CT scans may present a more precise image to calculate RT dose with. Exemplary of this claim are the air bubbles in the median MAE frame of Figure 3. From a visual comparison to the real MR, we can see that the synthetic CT better models air bubbles. Thus, the synthetic CT is likely a better representation to use when performing dose calculations. Another observed benefit of synthetic CTs is the elimination of artifacts compared to deformable CTs. Given that sCT generation is wholly dependent on the MR image fed into the model, if this MR image has no artifacts the resulting sCT will be artifact-free as well.

The key strength of using a deep learning model in synthetic CT generation is speed. Conventional image registration techniques rely on an iterative image update process. However, this process is slow and requires lengthy computation, which is a bottleneck when performing real-time dose calculation. On the other hand, our deep-learning model is fixed after training and requires a single forward pass to generate an output. Therefore, our DL model is much more suited to real-time RT strategies.

Some limitations of our approach include limited frame to frame cohesion on the axial plane. We observed that although primary image structures and features remained fixed, there were some frame-to-frame shifts in axial position along the extremities of each scan. These shifts may have occurred because the CycleGAN architecture trains on a single image at a time as opposed to a whole volume. Therefore, the model has more difficulty learning frame to frame continuance. Another observed limitation to our method is that our model has difficulty predicting HU values for high-intensity regions. For example, in Figure 4, we see that for all 3 image examples our model had difficulty reconstructing and predicting spine intensity values. We believe that this is due to the intrinsic distribution of HU values. Bone HU values are typically above 700, whereas all other tissue HU values fall between -100 and 300 HU. Thus, distribution imbalances may have led to difficulties predicting HU values for high-intensity regions. Finally, we believe that some distribution-matching losses may have caused anomalously shaped structures in certain already hard-to-predict regions such as the spine. For example, the spinal structure of all three sCTs in Figure 4 differs from their dCT ground truths. Given their relative similarity to each other, we believe that these differences may correspond to hallucinated features caused by distribution-matching losses, a phenomenon previously observed in Cycle-GAN based image translation (29).

Future work will involve two key advancements. Firstly, larger and higher quality datasets must be created. Our study shows that despite similar architectures; dataset scale improved our results in comparison to prior studies. Additionally, we believe that on top of scaling dataset, some incorporation of newer DL architectures could improve results. For example, although some work has already been done on MRI to CT conversion using diffusion models (30), given the remarkable performance of diffusion models in other image-processing domains (31), these models are promising for a synthetic CT generation task. As our dataset and compute resources grow, we plan to evaluate volumetric (3D) CycleGAN variants to improve through-plane consistency and integrate them into our framework.

5 Conclusions

In this study, we developed a deep learning algorithm based on CycleGAN (24) to derive sCT from MRI. We have demonstrated that the sCT provides comparable dose accuracy as the clinical CT. Accuracy of deep learning based synthetic CT generation using setup scans on MR-Linacs was adequate for dose calculation/optimization. This can enable MR-only treatment planning workflows on MR-Linacs, thereby increasing the efficiency of simulation and adaptive planning for MRgRT.

TABLE 4 Quantitative evaluation of synthetic versus deformed images across multiple organs.

Value Description	LIVER	PANCREAS	KIDNEY	PROSTATE	LUNG	OTHER	BONE	ALL
Deformed NCC	0.827	0.825	0.817	0.685	0.827	0.759	0.808	0.815
Synthetic NCC	0.838	0.831	0.815	0.705	0.830	0.778	0.824	0.824
SSIM	0.967	0.966	0.974	0.953	0.967	0.969	0.956	0.966
SSIMSTD	0.028	0.052	0.038	0.079	0.010	0.017	0.009	0.040
PSNR	19.406	19.232	20.614	17.978	19.395	19.015	18.496	19.150
PSNR STD	2.050	2.649	1.685	3.367	1.539	1.418	0.923	2.235
Number of Frames	235	340	72	76	228	152	72	1175
Number of Patients	4	5	1	1	3	2	1	17

NCC stands for normalized cross-correlation. SSIM stands for structural similarity. PSNR stands for peak to signal noise ratio.

Data availability statement

The raw data supporting the conclusions of this article will be made available by the authors, without undue reservation.

Ethics statement

The studies involving humans were approved by Dartmouth-Hitchcock Institutional Review Board. The studies were conducted in accordance with the local legislation and institutional requirements. Written informed consent for participation was not required from the participants or the participants' legal guardians/next of kin because The study is a retrospective study based on previous patients' data.

Author contributions

GA: Conceptualization, Formal Analysis, Methodology, Writing – original draft, Writing – review & editing. SW: Methodology, Writing – review & editing. BZ: Data curation, Writing – review & editing. GR: Data curation, Writing – review & editing. GG: Data curation, Writing – review & editing. CT: Data curation, Resources, Writing – review & editing. TP: Methodology, Writing – review & editing. YL: Funding acquisition, Writing – review & editing, Validation. RZ: Supervision, Writing – review & editing. YY: Funding acquisition, Supervision, Writing – review & editing. BH: Methodology, Supervision, Writing – review & editing.

Funding

The author(s) declare financial support was received for the research and/or publication of this article. This work was supported in part by funding from the Dartmouth-Hitchcock Medical Center Department of Medicine through the Scholarship Enrichment in Academic Medicine program.

Conflict of interest

The authors declare that the research was developed in the absence of any commercial or financial relationship that could be construed as a potential conflict of interest.

The author(s) declared that they were an editorial board member of Frontiers, at the time of submission. This had no impact on the peer review process and the final decision.

Generative AI statement

The author(s) declare that no Generative AI was used in the creation of this manuscript.

Any alternative text (alt text) provided alongside figures in this article has been generated by Frontiers with the support of artificial intelligence and reasonable efforts have been made to ensure accuracy, including review by the authors wherever possible. If you identify any issues, please contact us.

Publisher's note

All claims expressed in this article are solely those of the authors and do not necessarily represent those of their affiliated organizations, or those of the publisher, the editors and the reviewers. Any product that may be evaluated in this article, or claim that may be made by its manufacturer, is not guaranteed or endorsed by the publisher.

References

1. Cao Y, Tseng CL, Balter JM, Teng F, Parmar HA, Sahgal A, et al. MR guided radiation therapy: transformative technology and its role in the central nervous system. *Neuro Oncol.* (2017) 19:ii16–29.

2. Chin S, Eccles CL, McWilliam A, Chuter R, Walker E, Whitehurst P, et al. Magnetic resonance-guided radiation therapy: a review. *J Med Imaging Radiat Oncol.* (2020) 64:163–77.

3. Wang W, Dumoulin CL, Viswanathan AN, Tse ZTH, Mehrtash A, Loew W, et al. Real-time active MR-tracking of metallic stylets in MR-guided radiation therapy. *Magn Reson Med.* (2015) 73:1803–11.

4. Wooten HO, Rodriguez VL, Green OL, Kashani R, Santanam L, Tanderup K, et al. Benchmark IMRT evaluation of a Co-60 MRI-guided radiation therapy system. *Radiother Oncol.* (2015) 114:402–5.

5. Tenhunen M, Korhonen J, Kapanen M, Seppälä T, Koivula L, Collan J, et al. MRI-only based radiation therapy of prostate cancer: workflow and early clinical experience. *Acta Oncol.* (2018) 57:902–7.

6. Bohoudi O, Bruynzeel AME, Senan S, Cuijpers JP, Slotman BJ, Lagerwaard FJ, et al. Fast and robust online adaptive planning in stereotactic MR-guided adaptive radiation therapy (SMART) for pancreatic cancer. *Radiother Oncol.* (2017) 125:439–44.

7. Pollard JM, Wen Z, Sadagopan R, Wang J, Ibbott GS. The future of image-guided radiotherapy will be MR guided. *Br J Radiol.* (2017) 90:20160667.

8. Hargreaves BA, Worters PW, Pauly KB, Pauly JM, Koch KM, Gold GE. Metal-induced artifacts in MRI. *AJR Am J Roentgenol.* (2011) 197:547–55.

9. Edmund JM, Nyholm T. A review of substitute CT generation for MRI-only radiation therapy. *Radiat Oncol.* (2017) 12:28.

10. Owrangi AM, Greer PB, GlideHurst CK. MRI-only treatment planning: benefits and challenges. *Phys Med Biol.* (2018) 63:05TR01.

11. Liu Y, Lei Y, Wang T, Fu Y, Tang X, Curran WJ, et al. MRI-based treatment planning for liver stereotactic body radiotherapy: validation of a deep learning-based synthetic CT generation method. *Br J Radiol.* (2019) 92:20190067.

12. Arabi H, Dowling JA, Burgos N, Han X, Greer PB, Koutsouvelis N, et al. Comparative study of algorithms for synthetic CT generation from MRI: consequences for MRI-guided radiation planning in the pelvic region. *Med Phys.* (2018) 45:5218–5233.

13. Rank CM, Tremmel C, Hünemohr N, Nagel AM, Jäkel O, Greilich S. MRI-based treatment plan simulation and adaptation for ion radiotherapy using a classification-based approach. *Radiat Oncol.* (2013) 8:1–13.

14. De Vos BD, Berendsen FF, Viergever MA, Sokooti H, Staring M, Išgum I. A deep learning framework for unsupervised affine and deformable image registration. *Med Image Anal.* (2019) 52:128–43.

15. Sentker T, Madesta F, Werner R. Gdl-fire: Deep learning-based fast 4d ct image registration. In: *International conference on medical image computing and computer-assisted intervention*. Springer International Publishing, Cham (2018). p. 765–73.

16. Yagis E, Atnafu SW, de Herrera AGS, Marzi C, Giannelli M, Tessa C, et al. Deep learning in brain MRI: effect of data leakage due to slice-level split using 2D convolutional neural networks. (2021).

17. Nie D, Trullo R, Lian J, Petitjean C, Ruan S, Wang Q, et al. Medical image synthesis with context-aware generative adversarial networks, in: *Medical Image Computing and Computer Assisted Intervention– MICCAI 2017: 20th International Conference*, Quebec City, QC, Canada, September 11-13, 2017, Proceedings, Part III 20. *Lecture Notes in Computer Science(LNIP)*, Springer, Cham, Switzerland: Springer International Publishing. (2017) 10435, 417–25.

18. Yang H, Zhang Y, Chen Y, Zhang Y, Zhang H, Cai W, et al. Unsupervised MR-to-CT synthesis using structure-constrained CycleGAN. *IEEE Trans Med Imaging*. (2020) 39:4249–61.

19. Olberg S, Choi BS, Park I, Liang X, Kim JS, Deng J, et al. Ensemble learning and personalized training for the improvement of unsupervised deep learning-based synthetic CT reconstruction. *Med Phys*. (2023) 50:1436–49.

20. Wolterink JM, Dinkla AM, Savenije MH, Seevinck PR, van den Berg CA, Išgum I. Deep MR to CT synthesis using unpaired data, in: *Simulation and Synthesis in Medical Imaging: Second International Workshop, SASHIMI 2017*, Conjunction with MICCAI 2017, Québec City, QC, Canada, September 10, 2017 Proceedings 2. *Lecture Notes in Computer Science(LNIP)*, Springer, Cham, Switzerland: Springer International Publishing. (2017) 10557, 14–23).

21. Lei Y, Harms J, Wang T, Liu Y, Shu HK, Jani AB, et al. MRI-only based synthetic CT generation using dense cycle consistent generative adversarial networks. *Med Phys*. (2019) 46:3565–81.

22. Kang SK, An HJ, Jin H, Kim JI, Chie EK, Park JM, et al. Synthetic CT generation from weakly paired MR images using cycle-consistent GAN for MR-guided radiotherapy. *BioMed Eng Lett*. (2021) 11:263–71.

23. Farjam R, Nagar H, Kathy Zhou X, Ouellette D, Chiara Formenti S, DeWyngaert JK. Deep learning-based synthetic CT generation for MR-only radiotherapy of prostate cancer patients with 0.35 T MRI linear accelerator. *J Appl Clin Med Phys*. (2021) 22:93–104.

24. Zhu JY, Park T, Isola P, Efros AA. Unpaired image-to-image translation using cycle-consistent adversarial networks, in: *Proceedings of the IEEE international conference on computer vision (ICCV 2017)*. Los Alamitos, California, USA: IEEE. (2017) pp. 2223–32.

25. Goodfellow I, Pouget-Abadie J, Mirza M, Xu B, Warde-Farley D, Ozair S, et al. Generative adversarial networks. *Commun ACM*. (2020) 63:139–44.

26. Isola P, Zhu JY, Zhou T, Efros AA. Image-to-image translation with conditional adversarial networks, in: *Proceedings of the IEEE International Conference on Computer Vision (ICCV 2017)*. Los Alamitos, California, USA: IEEE. (2017). pp. 1125–34.

27. Wang Z, Simoncelli EP, Bovik AC. Multiscale structural similarity for image quality assessment. In: *The thrity-seventh asilomar conference on signals, systems & Computers, 2003*, vol. 2. Los Alamitos, California, USA: IEEE (2003). p. 1398–402.

28. Brou Boni KN, Klein J, Gulyban A, Reynaert N, Pasquier D. Improving generalization in MR-to-CT synthesis in radiotherapy by using an augmented cycle generative adversarial network with unpaired data. *Med Phys*. (2021) 48:3003–10.

29. Cohen JP, Luck M, Honari S. Distribution matching losses can hallucinate features in medical image translation, in: *Medical Image Computing and Computer Assisted Intervention–MICCAI 2018: 21st International Conference, Granada, Spain*, September 16-20, 2018Proceedings, Part I. *Lecture Notes in Computer Science(LNIP)*, Springer, Cham, Switzerland: Springer International Publishing (2018) 11070, 529–36.

30. Lyu Q, Wang G. Conversion between CT and MRI images using diffusion and score-matching models. *arXiv preprint arXiv:2209.12104*. (2022).

31. Yang L, Zhang Z, Song Y, Hong S, Xu R, Zhao Y, et al. Diffusion models: A comprehensive survey of methods and applications. ACM. *Comput Surv*. (2023) 56:1–39.

frontiers | Frontiers in Oncology

TYPE Original Research
PUBLISHED 29 September 2025
DOI 10.3389/fonc.2025.1653060

Check for updates

OPEN ACCESS

EDITED BY
Abdul K. Parchur,
University of Maryland Medical Center,
United States

REVIEWED BY
Jerry Liu,
Icahn School of Medicine at Mount Sinai,
United States
Yen Cho Huang,
Chang Gung Memorial Hospital, Taiwan
Mouchumee Bhattacharyya,
Bhubaneswar Borooah Cancer Institute, India
Sapna Krishnamurthy,
Jawaharlal Nehru Medical College, India

*CORRESPONDENCE
Heleen Bollen
heleen.bollen@jessazh.be
Sandra Nuyts
sandra.nuyts@uzleuven.be

†PRESENT ADDRESSES
Heleen Bollen,
Department of Radiation Oncology, Limburgs Oncologisch Centrum (LOC), Jessa Hospital 3500 Hasselt, Ziekenhuis Oost-Limburg (ZOL), Genk, Belgium
Elena Onorati,
Universita di Roma, Rome, Italy

RECEIVED 24 June 2025
ACCEPTED 09 September 2025
PUBLISHED 29 September 2025

CITATION
Bollen H, Onorati E, Laenen A, Goedgebeur A and Nuyts S (2025) Strategy to select nasopharyngeal cancer patients for adaptive radiotherapy.
Front. Oncol. 15:1653060.
doi: 10.3389/fonc.2025.1653060

COPYRIGHT
© 2025 Bollen, Onorati, Laenen, Goedgebeur and Nuyts. This is an open-access article distributed under the terms of the Creative Commons Attribution License (CC BY). The use, distribution or reproduction in other forums is permitted, provided the original author(s) and the copyright owner(s) are credited and that the original publication in this journal is cited, in accordance with accepted academic practice. No use, distribution or reproduction is permitted which does not comply with these terms.

Strategy to select nasopharyngeal cancer patients for adaptive radiotherapy

Heleen Bollen[1,2*†], Elena Onorati[3†], Annouschka Laenen[4], Anneleen Goedgebeur[2] and Sandra Nuyts[1,2*]

[1]Laboratory of Experimental Radiotherapy, Department of Oncology, University of Leuven, Leuven, Belgium, [2]Department of Radiation Oncology, Leuven Cancer Institute, University Hospitals Leuven, Leuven, Belgium, [3]Department of Radiation Oncology, Università Campus Bio-Medico di Roma, Rome, Italy, [4]Leuven Biostatistics and Statistical Bioinformatics Center, University of Leuven, Leuven, Belgium

Background: Nasopharyngeal cancer (NPC) patients experience significant anatomical changes during radiation treatment (RT). Adaptive radiotherapy (ART) can be initiated in response to specific events or at scheduled intervals during treatment, prompting questions about patient selection, timing, and reliable triggers for re-CT and replanning. This study aimed to develop a method for selecting NPC patients for ART before treatment and identify the optimal timing for its implementation.

Materials and methods: We retrospectively evaluated NPC patients treated at University Hospitals Leuven between 2016 and 2023, assessing volumetric changes in the parotid glands, air cavities, maxillary sinuses, and body contour at nasopharyngeal and low-neck levels throughout treatment. Structures were contoured on the initial simulation CT, weekly CBCTs, and final treatment day, resulting in eight measurements per parameter. Body contour changes were evaluated at the nasopharyngeal level (odontoid process) and neck level (lower edge of the third cervical vertebra). Measurements included volume, transverse diameters, and radius angles of 50° and 310°. Kaplan-Meier analysis was used for overall survival (OS) and local control (LC), while longitudinal volumetric data were analyzed with linear mixed models. Continuous variables were dichotomized to create a binary variable, for the purpose to define cut-off values for significant predictive variables.

Results: Of the 47 NPC patients analyzed, 2- and 5-year loco-regional control rates were 95%, with overall survival rates of 100% and 93%, respectively. Significant reductions in parotid gland volume and body contour were observed, particularly between weeks 3 and 4. Predictors of parotid gland volume reduction included bulky nodal disease and larger initial parotid volume, with thresholds of 15 mm and 56 cc, respectively. Body contour changes during the fourth week correlated with high N-stage (≥ N3), higher initial BMI (>28 kg/m^2), bulky lymph nodes (15 mm), higher initial mean planned dose to the ipsilateral parotid gland (> 31 Gy) and larger initial primary tumor Clinical Target Volume (> 93 cc). Induction chemotherapy was significantly associated with fewer sinonasal air cavity changes than concomitant chemoradiotherapy.

Conclusion: It is recommended to re-evaluate the RT plan during the period between fractions 15 and 20 of treatment. Patients treated for NCP could be selected for ART based on the following clinical criteria at diagnosis: N3 or higher classification, presence of a bulky lymph node larger than 15 millimeters, initial BMI exceeding 28 kg/m^2, mean planned dose to the ipsilateral parotid glands

greater than 31 Gy, cumulative volume of the parotid glands greater than 56 cc, high-dose CTV of the primary tumor greater than 93 cc, and receiving RT with no prior induction chemotherapy. Validation of these pre-treatment clinical predictors in a large, prospective dataset is essential before clinical usage.

KEYWORDS

adaptive radiotherapy (ART), nasopharyngeal carcinoma, proton therapy, predictors, IMRT (intensity modulated radiation therapy)

Introduction

Nasopharyngeal carcinoma (NPC) is a unique subtype of head and neck cancer (HNC), characterized by distinct etiology and epidemiological patterns (1). Given its anatomical location and intrinsic radiosensitivity, radiotherapy (RT) presents the primary treatment modality for NPC, often in combination with chemotherapy, depending on the disease stage (2). However, treating NPC with radiation presents significant challenges due to its proximity to critical structures. While RT is effective, it carries the risk of both acute and long-term side effects, including feeding tube dependence, hearing impairment, temporal lobe necrosis, and cognitive decline (3–7). Given the generally good prognosis for NPC patients following RT, minimizing these long-term adverse effects is crucial. Proton therapy (PT) has emerged as a promising alternative due to its superior dose distribution and its potential to reduce acute toxicities compared to IMRT (8). Yet, PT also presents unique challenges, such as its sensitivity to changes in tissue density due to the uncertainty of the exact location of the Bragg peak and the sharp distal dose fall-off of protons. Factors like positioning errors, artifacts, tissue deformations, and anatomical changes —often caused by weight loss or tumor response in HNC patients —can shift the Bragg peak (9).

Adaptive radiotherapy (ART) offers a dynamic solution to the variability in patient anatomy during treatment. By incorporating imaging throughout the course of therapy, ART enables adjustments to the treatment plan, enhancing tumor coverage while minimizing dose to OARs (10). However, the optimal timing and criteria for plan adaptation remain unclear, particularly in the context of PT (11). This study aims to address these uncertainties by objectifying anatomical changes occurring during treatment, identifying pre-treatment clinical predictors for these changes, and determining the time points at which the most significant alterations are observed. The ultimate goal is to refine ART strategies, improving the therapeutic ratio in NPC treatment.

Materials and methods

Patient selection and data collection

This retrospective study included patients with histologically confirmed NPC, treated with RT at UH Leuven between 2016 and 2023. Each patient underwent a thorough clinical and radiological evaluation, including MRI of the head and neck and a total body FDG PET-CT scan. Clinical staging was performed according to the American Joint Committee on Cancer (AJCC) 8th edition. After discussion by a multidisciplinary institutional tumor board, patients received treatment at UH Leuven, consisting of RT alone or in combination with chemotherapy, based on disease stage and associated risk factors. Data on patient characteristics, treatment modalities, plan specifications, and anatomical changes during treatment were collected retrospectively. Follow-up adhered to ESMO-EURACAN clinical practice guidelines for NPC (2), with imaging (MRI or FDG PET/CT) three months after RT, then every six months up to the 3rd year, and endoscopic assessment every 3 months in the first year, every 6 months in the second and third years and annually thereafter. Overall survival (OS) was measured from RT initiation to death from any cause. Disease metastasis (DM) was tracked from the start of RT to distant recurrence. Locoregional control (LRC) was assessed from RT initiation to recurrence. Patients still under follow-up or lost to follow-up were censored at their last known date of survival (for OS) or recurrence-free status (for LRC and DM). This study was approved by the Ethics Committee of the University Hospitals of Leuven (S62953).

Radiotherapy

Patients were positioned supine and immobilized using thermoplastic masks covering the head and shoulders. Target volumes and organs at risk were contoured by the radiation oncologist following international guidelines (2). Gross Tumor Volume (GTV) included all detectable disease from CT, MRI, clinical data, and endoscopy. Lymph nodes greater than 1 cm or with necrotic centers were included in the GTV. High-risk Clinical Target Volume (CTV 70) encompassed the primary disease site and grossly involved lymph nodes, with a 1 cm margin added to the GTV. Intermediate-risk CTV (CTV 59.4-P and CTV 59.4-N) was defined by adding a 5 mm margin to the CTV 70-P and CTV 70-N, respectively. CTV 59.4-P also included the entire nasopharynx, clivus, skull base, pterygoid fossae, parapharyngeal space, sphenoid sinus, and portions of the nasal cavity and maxillary sinuses. CTV 59.4-N included the retropharyngeal nodes and elective neck levels

Ib to V bilaterally. Low-Risk CTV (CTV 54) covered the lower neck lymph nodes in cases without gross lymph node involvement. For photon therapy, Planning Target Volumes (PTV 70, PTV 59.4, PTV 54) were generated by adding a 5 mm margin to the respective CTVs. PT plans accounted for setup uncertainties of 3 mm above the mandible and 5 mm below. Treatment plans were developed by medical physicists using Eclipse for photon plans and RayStation for proton plans, adhering to international dose prioritization and acceptance criteria. Dose specifications included: PTV 70: 69.96 Gy in 33 fractions (EQD2 70.66 Gy), PTV 59.4: 59.4 Gy in 33 fractions (EQD2 58.41 Gy) and PTV 54: 54 Gy in 33 fractions (EQD2 52.38 Gy). Photon treatments were delivered using VMAT with Simultaneous Integrated Boost (SIB), while proton treatments used Intensity Modulated Proton Therapy (IMPT) with robust optimization. Daily Cone-Beam CTs (CBCT) were obtained for accurate patient positioning. In-silico proton plans were created for randomly selected patients to compare organ-at-risk dose delivery with equivalent target coverage.

Chemotherapy

Patients received concurrent chemotherapy with high dose cisplatin. Induction chemotherapy included cisplatin alone or in combination with fluorouracil and docetaxel (TPF), gemcitabine, or taxanes.

Delineation of anatomical changes

The study focused on changes in the parotid glands, air cavities, maxillary sinuses, and body contour at the nasopharyngeal and low-neck levels. Each structure was contoured on the initial simulation CT, each weekly CBCT, and on the last day of treatment, yielding eight measurements per parameter. Volume changes in the parotid glands were measured by delineating the parotid glands weekly and calculating the mean volume of both parotid glands (Supplementary Materials 1A). Air cavities at the nasopharyngeal level were measured as a way to evaluate tumor regression indirectly (Supplementary Materials 2A). Maxillary sinus volumes were measured to assess potential non-tumor-related variations impacting proton planning (Supplementary Materials 3A). Body contour changes were assessed at two levels: 1) nasopharyngeal level: volume, measured in cc, at the level of the odontoid process (Supplementary Materials 4A); 2) neck level: volume, measured in cc, at the lower edge of the third cervical vertebra (Supplementary Materials 5A). Additionally, for both the nasopharyngeal and neck regions, radius angles of 50° and 310° were established and measured in centimeters. These measurements were taken from the isocenter of the CT/CBCT to the skin surface at 50° and 310° angles, respectively, corresponding to the levels of the odontoid process and the third cervical vertebra (C3) (Supplementary Materials 6A, 7A). These specific angles were selected because they represent the typical entry trajectory of the anterior proton beam in our planning protocol, where anatomical changes along this path are expected to have the greatest influence on PT dose distribution. Half-fan CBCT images with iterative reconstruction were obtained using Halcyon linacs, in line with University Hospitals Leuven's standard practice for Head and Neck Image-Guided Radiotherapy (IGRT). In instances where the Halcyon machine required maintenance, patients were occasionally treated on a Truebeam linac, following a comparable half-fan CBCT onboard imaging IGRT protocol.

Statistical analysis

Overall survival (OS) was defined as the time from diagnosis to death or the last follow-up, and local control (LC) as the time from diagnosis to local recurrence/progression or last follow-up. OS and LC were estimated using the Kaplan-Meier method. Linear mixed models were used for the estimation of longitudinal volumetric evolutions, and for the analysis of predictive effects of clinical and dosimetric characteristics on volumetric changes. In a second phase, an exploratory analysis was conducted to identify the specific thresholds that most effectively distinguish patients experiencing pronounced anatomical changes during RT from those who did not. To establish binary variables and determine cut-off values for significant predictors, continuous variables were converted into dichotomous categories. The optimal cut-off values were then determined using the likelihood-ratio method, which assessed how well different thresholds fit the model. Statistical analyses were performed using SAS and SPSS software (version 9.4 and 29, respectively).

Results

Forty-seven patients were enrolled in this study. Details on patient demographics, tumor characteristics, and treatments are provided in Table 1. The median follow-up duration was 34.4 months, and the median patient age was 54 years (range: 18–84 years). Males comprised 75% of the cohort, with the majority of patients (47%) diagnosed at stage III. Epstein-Barr virus (EBV)-correlated disease was observed in 77% of cases, and 85% of patients presented with lymph node involvement (N+ disease). RT alone was administered to 6% of patients, while the remaining patients received concomitant chemoradiotherapy. Induction chemotherapy was administered in 55.3% of cases. Only one patient was treated with PT, with the vast majority (98%) receiving IMRT/VMAT. The mean weight loss during treatment was 9% (range: 2.28% to 25.85%). Response to treatment, assessed with PET/CT three months after the end of RT, was known for 44 patients, of which 43 achieved a complete response. Two patients experienced disease recurrence, 6 months and 24 months after treatment. There was one death attributed to NPC. The 2-year and 5-year loco-regional control rates were both 95%, and 2-year and 5-year overall survival rates were 100% and 93%, respectively.

As illustrated in Figure 1A, the cumulative volume of both ipsilateral and contralateral parotid glands decreased from 55.5 cc to 42.2 cc during treatment. The most significant reduction

10.3389/fonc.2025.1653060

TABLE 1 Patient and treatment characteristics.

Variable	Statistic	All
Age	N	47
	Mean	53.38
	Std	14.735
	Median	54.00
	IQR	(44.00; 65.00)
	Range	(18.00; 84.00)
Gender		
Female	n/N (%)	12/47 (25.53%)
Male	n/N (%)	35/47 (74.47%)
Histology		
Others	n/N (%)	12/47 (25.53%)
Keratinizing SCC	n/N (%)	17/47 (36.17%)
Non keratinizing SCC	n/N (%)	18/47 (38.30%)
EBV status		
0	n/N (%)	11/47 (23.40%)
1	n/N (%)	36/47 (76.60%)
T classification		
1	n/N (%)	14/47 (29.79%)
2	n/N (%)	13/47 (27.66%)
3	n/N (%)	11/47 (23.40%)
4	n/N (%)	9/47 (19.15%)
N classification		
0	n/N (%)	7/47 (14.89%)
1	n/N (%)	22/47 (46.81%)
2	n/N (%)	12/47 (25.53%)
3	n/N (%)	6/47 (12.77%)
Stage (AJCC 8th edition)		
1	n/N (%)	1/47 (2.13%)
2	n/N (%)	11/47 (23.40%)
3	n/N (%)	21/47 (44.68%)
4	n/N (%)	14/47 (29.79%)
Bulky N-disease (>15mm)		
Yes	n/N (%)	42/47 (89.36%)
No	n/N (%)	5/47 (10.64%)
Induction chemotherapy		
Yes	n/N (%)	21/47 (44.68%)
No	n/N (%)	26/47 (55.32%)
Concomitant chemotherapy		
Yes	n/N (%)	44/47 (93.62%)
No	n/N (%)	3/47 (6.38%)
Initial weight (pre RT)	N	45
	Mean	80.81
	Std	14.174
	Median	80.60
	IQR	(71.20; 91.10)
	Range	(54.30; 110.00)
Initial weight (kg)		
<90kg	n/N (%)	38/47 (80.85%)
>90kg	n/N (%)	9/47 (19.15%)
Weight loss (kg)	N	47
	Mean	6.73
	Std	3.933
	Median	6.90
	IQR	(3.70; 9.20)
	Range	(-0.30; 16.20)
% Weight loss	N	45
	Mean	8.59
	Std	4.057
	Median	8.56
	IQR	(5.77; 11.24)
	Range	(-0.33; 15.40)
Weight loss		
<10%	n/N (%)	28/47 (59.57%)
>10%	n/N (%)	19/47 (40.43%)
BMI_PRE_RT	N	43
	Mean	26.54
	Std	4.219
	Median	26.80
	IQR	(23.99; 28.77)
	Range	(16.86; 36.42)
Response to RT (CR=1; PR=2; PD=0)		
Persistent disease	n/N (%)	2/47 (4.26%)
Complete response	n/N (%)	42/47 (89.36%)
Partial response	n/N (%)	3/47 (6.38%)
Status (NED=1; AWD=2; DOC=3; DOD=0)		
DOD	n/N (%)	1/47 (2.13%)

(Continued)

TABLE 1 Continued

Variable	Statistic	All
NED	n/N (%)	41/47 (87.23%)
AWD	n/N (%)	4/47 (8.51%)
DOC	n/N (%)	1/47 (2.13%)

SCC, squamous cell carcinoma; BMI, body mass index; RT, radiotherapy; DOD, death of disease; NED, no evidence of disease; AWD, alive with disease; DOC, death of other causes.

occurred between the third and fourth weeks, with a median volume decrease of 3.94 cc (p = 0.0006). While no significant changes were observed in body contour at the nasopharyngeal level, a 10% reduction was noted at the neck level (C3) (Figure 1B). The most significant body contour changes occurred between weeks 3 and 4 of treatment (-1.4 cc; p < 0.001). Additionally, both the 50° and 310° neck diameters showed significant reductions during RT, with the most pronounced decrease occurring between weeks 3 and 4 (Figure 2). The air filling of the nasopharyngeal air cavity increased by 2.34 cm^3 during the first four weeks of treatment (Figure 3) (p = 0.05), while no significant changes were observed in maxillary cavity filling.

Linear mixed modeling identified bulky disease and a greater initial parotid gland volume as significant predictors for parotid gland volume reduction (HR 9.5, p = 0.005; HR 0.31, p < 0.001, respectively). Significant predictors for body contour change included high N-classification, higher initial weight, bulky lymph node disease,

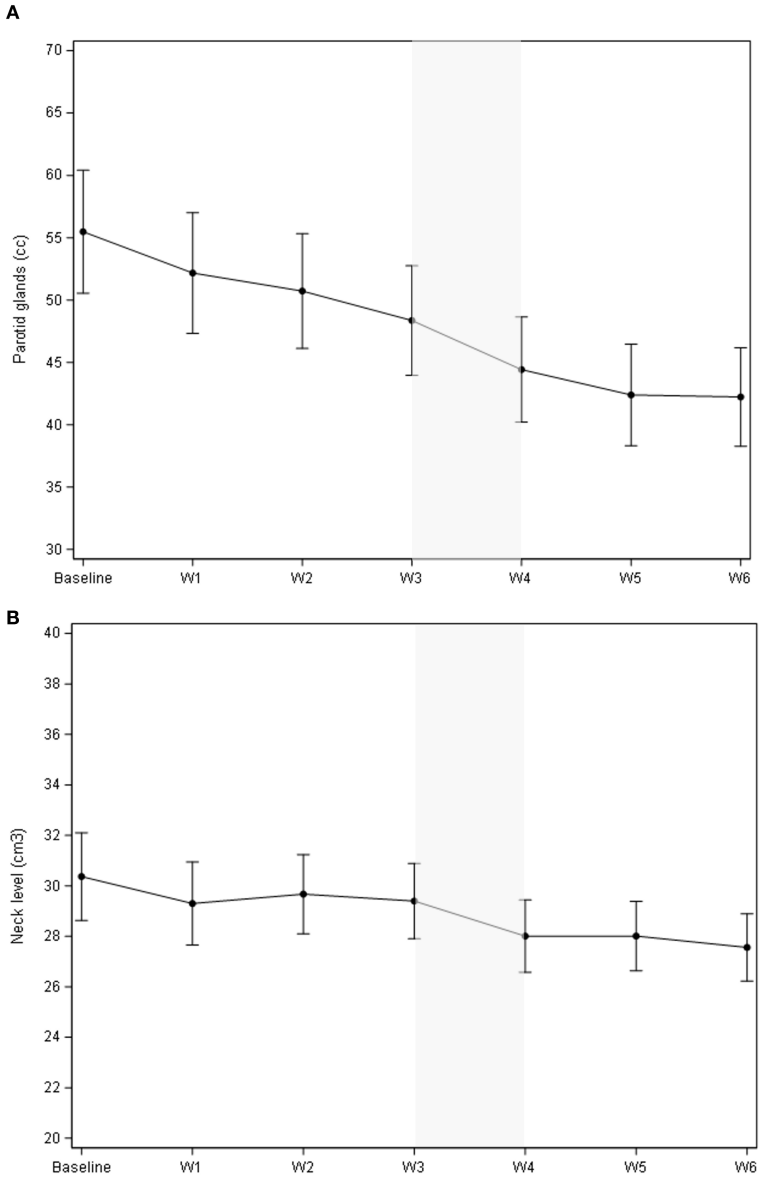

FIGURE 1
Mean volumetric changes (cc) of **(A)** (mean of both) parotid glands during RT, **(B)** the body contour at the level of cervical vertebra C3 (cm^3). **(A)**: Mean change of the parotid glands vs. baseline was -11.1 cc (95% CI -13.7; -8.41), p<.0001; mean change vs. the previous week was -3.94 cc (95% CI -6.16; -1.72), p=0.0006. **(B)**: Mean change of the body contour at C3 vs. baseline was -2.36 cm^3 (95% CI -1.99;-1.78), p<.0001); mean change vs. the previous week was – 1.39 cm^3 (95% CI -1.99;-1.078), p<.0001).

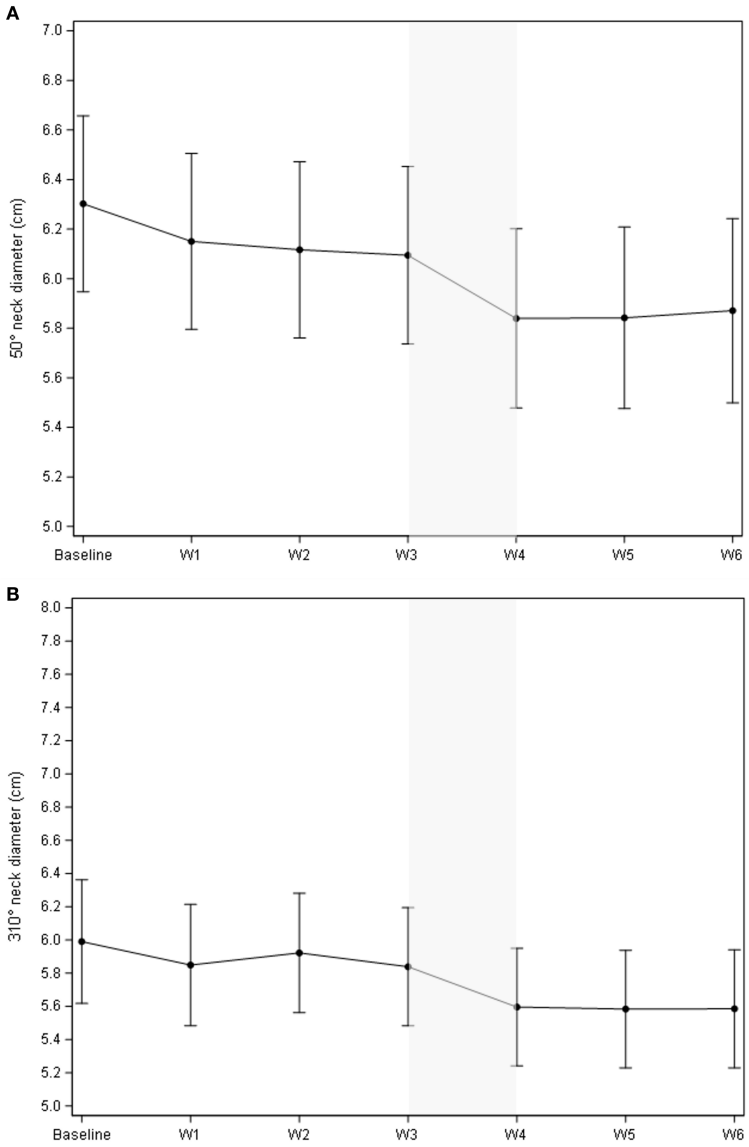

FIGURE 2
Evolution of the body contour at the 50° **(A)** and 310° **(B)** neck diameter (cm). The most significant decrease in radii occurred between weeks 3 and 4, for both the 50° and 310° measurements, exhibiting the steepest slope coefficient during this period. **(A)**: Mean change of the body contour vs. baseline was -0.46 cm (95% CI -0.63; -0.30), p<.0001; mean change of the body contour vs. the previous week was -0.25 cm (95% CI -0.40; -.011), p=0.0005.

higher initial mean planned dose to the ipsilateral parotid gland, and larger initial CTV-P volume. Patients who received induction chemotherapy exhibited less change in nasopharyngeal air cavity filling compared to those who received only concomitant chemoradiotherapy (HR 2.4; $p < 0.01$). Cut-off thresholds for large anatomical changes were established, based on descriptive dichotomization, for bulky lymph nodes (> 15mm), initial parotid gland volume (> 56 c cumulative volume for both glands), N-classification (≥ N3), initial weight (> 88kg, corresponding with a BMI higher than 28 kg/m^2), initial mean planned dose to the ipsilateral parotid gland (> 31 Gy), and the volume of the high-dose CTV-P (> 93 cc). Figure 4 illustrates the identified risk factors associated with the need for adaptive radiotherapy in patients with nasopharyngeal carcinoma.

Discussion

Since ART approach can be initiated both in reaction to a specific event or at predetermined time intervals throughout the course of RT, many questions are rising concerning patient selection, time regimen and dependable methods for triggering re-CT and/or replanning. NPC patients represent an ideal population for studying ART due to their high rate of viral association and favorable response to RT (11). Research by Brown et al. has shown that NPC patients are more likely to require replanning compared to other HNC patients (12). Yang et al. have highlighted that anatomical changes, such as tumor shrinkage, nodal mass reduction, and weight loss, are frequently observed in NPC patients during RT (13). Additionally, Cheng et al.

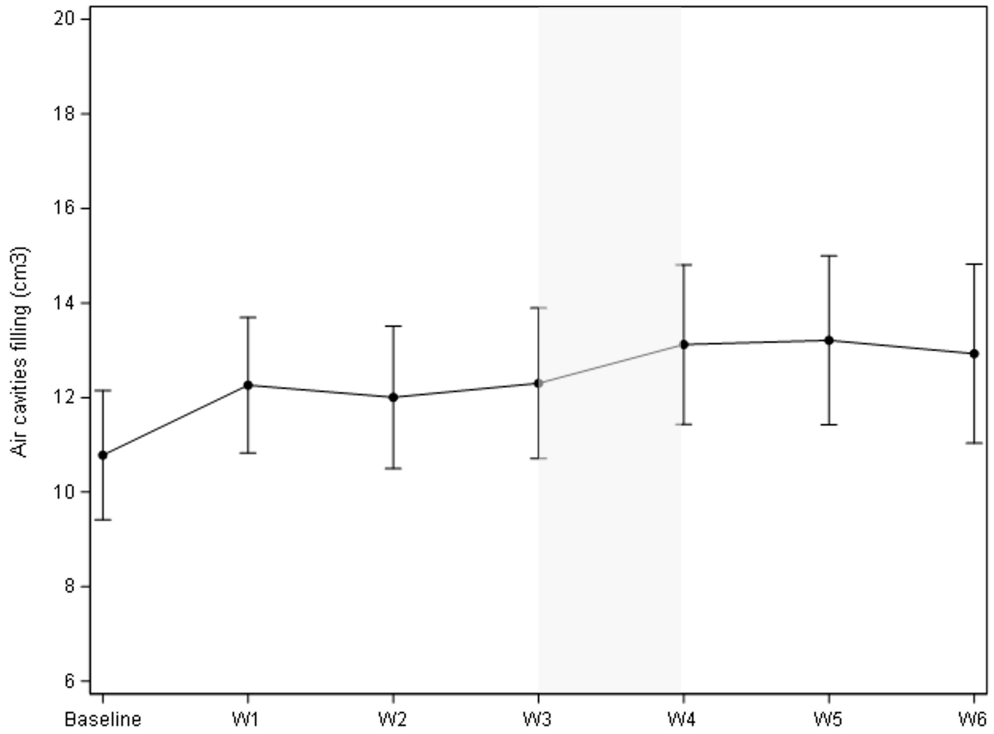

FIGURE 3
Evolution of air cavity diameter (cm^3) during treatment. Mean change of the air cavity diameter vs. baseline was 2.34 cm^3 (95% CI 1.31;3.37), p<.0001; mean change vs. the previous week was 0.81 (95% CI -0.04;1.68), p=0.05.

have noted that NPC patients often receive doses to target volumes (TVs) and critical organs at risk (OAR), such as the brainstem and optic structures, that approach or exceed tolerance levels (14). This underscores the critical role of ART in ensuring dose acceptability and optimizing treatment outcomes for these patients.

This study aimed to identify predictive parameters for the need for ART and re-planning in patients with NPC and to establish the optimal timing for replanning. The analysis incorporated potential pre-treatment selection criteria from recent literature (12, 15–20). Parotid gland volumes were monitored for treatment impact related

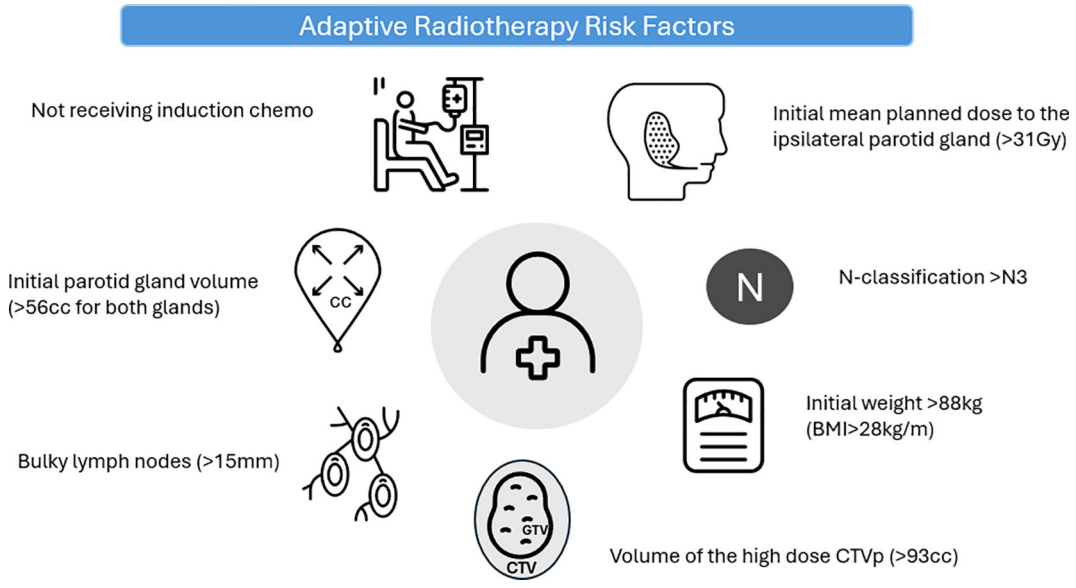

FIGURE 4
Identified risk factors associated with the need for adaptive radiotherapy in patients with nasopharyngeal carcinoma.

to xerostomia, while air cavities and maxillary sinus volumes were assessed to understand tumor regression and variations affecting proton planning, respectively. Our findings suggest that the third week of the treatment is the most suitable time for replanning, based on volumetric changes in the parotid glands, body contour alterations, and air cavity filling. Several pre-treatment predictors for these volumetric changes were identified: higher initial mean dose on the parotid glands, higher initial weight, higher initial BMI, a larger CTV, higher disease stage, initial small volume of the parotid glands, the administration of concomitant chemotherapy and bulkier lymph node disease.

In an additional exploratory analysis, thresholds for these clinical parameters were established. This analysis enables the identification of NPC patients at the time of diagnosis who may be eligible for adaptive radiotherapy (ART) during their radiation treatment. Based on our results, the patient who should be closely monitored during RT to evaluate the need for ART is characterized by N3 or higher classification, presence of a bulky lymph node larger than 15 millimeters, initial BMI exceeding 28 kg/m^2, mean planned dose to the ipsilateral parotid glands greater than 31 Gy, cumulative volume of the parotid glands greater than 56 cc, high-dose CTV of the primary tumor greater than 93cc, and receiving RT with no prior induction chemotherapy.

Patients who received induction chemotherapy experienced fewer anatomical changes during their treatment. During the first four weeks of treatment, the air filling of the nasopharyngeal cavity increased by 2.34 cm^3 (Figure 3, p = 0.05), likely due to tumor regression. This observation helps explain why patients who received induction chemotherapy exhibited less change in air cavity filling compared to those who underwent concomitant chemoradiotherapy. Our findings are consistent with several studies that have identified the mean dose to the parotid gland as a significant predictor of parotid gland volume loss (15, 20–28). However, Brouwer et al. identified a lower cut-off value (22.2 Gy) compared to our analysis (31 Gy).

Other predictors reported in the literature include higher initial mean parotid gland dose, higher initial weight, higher BMI, larger clinical target volume (CTV), advanced T and N stages, smaller initial parotid gland volume, overlap between the parotid gland and target volumes, administration of concomitant chemoradiotherapy, and bulkier disease (12, 16–20). In a study by Brown et al. (12), multivariable analysis demonstrated that NPC patients with N2–3 disease, an initial weight over 100 kg, and larger initial nodal sizes had an 80% or higher likelihood of requiring replanning during treatment. While only two patients in our cohort presented with an initial weight exceeding 100 kg, our analysis similarly identified elevated initial body weight as a predictive factor for significant anatomical changes during treatment, with the relevant threshold set at 88 kg.

The effective integration of ART in the clinical management of HNC necessitates precise timing of the intervention. Currently, there is no consensus on the optimal frequency and timing for replanning in HNC patients (22). Our results align with existing evidence, indicating that the most significant anatomical changes tend to occur between the third and fourth week of the RT course (11). Our findings corroborate the conclusions of Brown et al., who suggested that replanning should be initiated at the start of the third week for patients with NPC and during the fourth week for those with oropharyngeal carcinoma (29).

Strengths of our study include the availability of imaging during RT, the use of multiple methods to assess changes in body contour, the consideration of beam angles for PT, and the exclusive focus on NPC patients. However, our study's retrospective design is a limitation, as is the limited number of patients and the lack of a defined clinically relevant threshold for volumetric change necessitating replanning. In Brown et al.'s study, the need for replanning was determined by radiation oncologists based on the dose to optic structures and the brachial plexus, while Brouwer et al. set their threshold at a 3 Gy mean dose increase to the parotid gland (12, 20, 21,). However, defining such a threshold is challenging. In Brown et al.'s study, only 5 of 110 patients (4.5%) were selected for replanning, an observation that aligns with our clinical experience (12). Furthermore, we need to consider that the high threshold for initiating ART could be partially attributed to the labor-intensive nature of the ART process. We have attempted to address this issue by converting continuous variables into dichotomous categories for establishing cut-off thresholds that most reliably predict the likelihood of a patient experiencing anatomical changes throughout the treatment. However, this approach knows several limitations. First of all, the analysis was performed on only 47 patients, and the clinical parameters were derived from an initial univariate analysis (linear model testing). Secondly, although statistical significance was calculated during the determination of cut-off values, relying solely on significance testing may present an overly optimistic view of the thresholds' accuracy. In any case, our thresholds are hypothesis-generating and validation of these pre-treatment clinical predictors on a large, prospective dataset is essential before clinical usage. Furthermore, in a subsequent study, it will be important to evaluate whether the reported volumetric changes lead to dosimetric implications that may affect acute or late toxicity. A suitable approach would be to incorporate the dosimetric effects into existing Normal Tissue Complication Probability (NTCP) modeling for xerostomia, dysphagia, and tube feeding dependence (30).

In the evaluation of the 310° and 50° NPC radii on both the planning CT and subsequent CBCTs, the anterior point of the dens axis serves as a consistent and clearly identifiable landmark on both imaging modalities. This outermost point of the body can be reliably used to establish the angular radius relative to the imaging midline. However, a key limitation is that small variations in patient orientation —such as pitch, roll, or rotation, often in combination—within the immobilization mask and 3D treatment couch can introduce deviations in the measured radii. These inaccuracies may arise from systematic factors (e.g., treatment couch sagging compared to the CT simulation couch) or random day-to-day variations in patient positioning. Despite these potential sources of error, significant and clinically relevant reductions in radii were still observed.

Conclusion

The time frame between the 15th and 20th fraction is advised as the optimal timing of evaluating the patient's need for ART. This study identified several clinical criteria that may serve as indicators of significant volume changes in patients undergoing RT for NPC: N3 or higher classification, presence of a bulky lymph node larger than 15 millimeters, initial BMI exceeding 28 kg/m^2, mean planned dose to the ipsilateral parotid glands greater than 31 Gy, cumulative volume of the parotid glands greater than 56 cc, high-dose CTV of the primary tumor greater than 93 cc, and receiving RT with no prior induction chemotherapy. To further clarify confounding factors, it will be essential to repeat multivariable analyses and establish cut-off values in larger, well-selected patient cohorts.

Data availability statement

The original contributions presented in the study are included in the article/Supplementary Material. Further inquiries can be directed to the corresponding authors.

Ethics statement

This study was approved by the Ethics Committee Research UZ/KU Leuven (S62953). The studies were conducted in accordance with the local legislation and institutional requirements. This study was conducted retrospectively, and as a result, it was not possible to obtain informed consent from the patients involved. The study was thoroughly reviewed by our institutional ethical committee (UZ Leuven), who determined that obtaining individual patient consent was not necessary under these circumstances. The committee's approval was based on the retrospective design and the anonymization of patient data. Where applicable, all identifiable information has been sufficiently anonymized to ensure that neither the patient nor any third party could identify the individuals involved. In cases where further anonymization was necessary, some details were removed to protect patient privacy.

Author contributions

HB: Resources, Project administration, Data curation, Visualization, Writing – original draft, Conceptualization, Validation, Funding acquisition, Writing – review & editing, Investigation, Supervision, Software, Formal analysis, Methodology. EO: Writing – review & editing, Writing – original draft, Data curation, Methodology. AL: Writing – review & editing, Writing – original draft, Formal analysis, Methodology. AG: Visualization, Data curation, Methodology, Writing – review & editing, Writing – original draft, Conceptualization. SN: Resources, Conceptualization, Data curation, Visualization, Supervision, Validation, Investigation, Project administration, Writing – review & editing, Funding acquisition, Formal analysis, Software, Methodology, Writing – original draft.

Funding

The author(s) declare financial support was received for the research and/or publication of this article. H.B. was supported by a strategic basic research PhD fellowship from the Flemish Foundation of Scientific Research (FWO-Vlaanderen) under grant number 1SE9822N. S.N. is supported by clinical research mandate from the Flemish Foundation of Scientific Research (FWO-Vlaanderen) under grant number 18B4122N.

Conflict of interest

The authors declare that the research was conducted in the absence of any commercial or financial relationships that could be construed as a potential conflict of interest.

Generative AI statement

The author(s) declare that no Generative AI was used in the creation of this manuscript.

Any alternative text (alt text) provided alongside figures in this article has been generated by Frontiers with the support of artificial intelligence and reasonable efforts have been made to ensure accuracy, including review by the authors wherever possible. If you identify any issues, please contact us.

Publisher's note

All claims expressed in this article are solely those of the authors and do not necessarily represent those of their affiliated organizations, or those of the publisher, the editors and the reviewers. Any product that may be evaluated in this article, or claim that may be made by its manufacturer, is not guaranteed or endorsed by the publisher.

Supplementary material

The Supplementary Material for this article can be found online at: https://www.frontiersin.org/articles/10.3389/fonc.2025.1653060/full#supplementary-material

References

1. Chen YP, Chan ATC, Le QT, Blanchard P, Sun Y, Ma J. Nasopharyngeal carcinoma. *Lancet*. (2019) 394:64–80. doi: 10.1016/S0140-6736(19)30956-0/ATTACHMENT/5B569C36-B93B-4C22-8319-D810C2BC476B/MMC1.PDF

2. Bossi P, Chan AT, Licitra L, Trama A, Orlandi E, Hui EP, et al. Nasopharyngeal carcinoma: ESMO-EURACAN clinical practice guidelines for diagnosis, treatment and follow-up. *Ann Oncol*. (2021) 32:452–65. doi: 10.1016/J.ANNONC.2020.12.007/ATTACHMENT/2F4A8739-D07D-45CE-8273-924808A8730C/MMC1.PDF

3. Lee AWM, Ng WT, Hung WM, Choi CW, Tung R, Ling YH, et al. Major late toxicities after conformal radiotherapy for nasopharyngeal carcinoma—Patient- and treatment-related risk factors. *Int J Radiat Oncol Biol Phys*. (2009) 73:1121–8. doi: 10.1016/J.IJROBP.2008.05.023

4. Peng G, Wang T, Yang KY, Zhang S, Zhang T, Li Q, et al. Prospective, randomized study comparing outcomes and toxicities of intensity-modulated radiotherapy vs. Conventional Two-Dimensional Radiotherapy for the Treatment of Nasopharyngeal Carcinoma. *Radiother Oncol*. (2012) 104:286–93. doi: 10.1016/J.RADONC.2012.08.013

5. Pow EHN, Kwong DLW, McMillan AS, Wong MCM, Sham JST, Leung LHT, et al. Xerostomia and Quality of Life after Intensity-Modulated Radiotherapy vs. Conventional Radiotherapy for Early-Stage Nasopharyngeal Carcinoma: Initial Report on a Randomized Controlled Clinical Trial. *Int J Radiat Oncol Biol Phys*. (2006) 66:981–91. doi: 10.1016/J.IJROBP.2006.06.013

6. Dong J, Ng WT, Wong CHL, Li JS, Bollen H, Chow JCH, et al. Dosimetric parameters predict radiation-induced temporal lobe necrosis in nasopharyngeal carcinoma patients: A systematic review and meta-analysis. *Radiother Oncol*. (2024) 195:110258. doi: 10.1016/J.RADONC.2024.110258

7. Wang J, Miao Y, Ou X, Wang X, He X, Shen C, et al. Development and validation of a model for temporal lobe necrosis for nasopharyngeal carcinoma patients with intensity modulated radiation therapy. *Radiat Oncol*. (2019) 14:42. doi: 10.1186/S13014-019-1250-Z

8. Lee A, Kitpanit S, Chilov M, Langendijk JA, Lu J, Lee NYA. Systematic review of proton therapy for the management of nasopharyngeal cancer. *Int J Part Ther*. (2021) 8:119–30. doi: 10.14338/IJPT-20-00082.1

9. Nuyts S, Bollen H, Ng SP, Corry J, Eisbruch A, Mendenhall WM, et al. Proton therapy for squamous cell carcinoma of the head and neck: early clinical experience and current challenges. *Cancers (Basel)*. (2022) 14(11):2587. doi: 10.3390/CANCERS14112587

10. Zhou X, Wang W, Zhou C, Zhu J, Ding W, Chen M, et al. Long-term outcomes of replanning during intensity-modulated radiation therapy in patients with nasopharyngeal carcinoma: an updated and expanded retrospective analysis. *Radiother Oncol*. (2022) 170:136–42. doi: 10.1016/j.radonc.2022.03.007

11. Nuyts S, Bollen H, Eisbruch A, Strojan P, Mendenhall WM, Ng SP, et al. Adaptive radiotherapy for head and neck cancer: pitfalls and possibilities from the radiation oncologist's point of view. *Cancer Med*. (2024) 13(8):e7192. doi: 10.1002/CAM4.7192

12. Brown E, Owen R, Harden F, Mengersen K, Oestreich K, Houghton W, et al. Predicting the need for adaptive radiotherapy in head and neck cancer. *Radiother Oncol*. (2015) 116:57–63. doi: 10.1016/J.RADONC.2015.06.025

13. Yang H, Hu W, Wang W, Chen P, Ding W, Luo W. Replanning during intensity modulated radiation therapy improved quality of life in patients with nasopharyngeal carcinoma. *Int J Radiat Oncol Biol Phys*. (2013) 85:e47–54. doi: 10.1016/J.IJROBP.2012.09.033

14. Cheng HCY, Wu VWC, Ngan RKC, Tang KW, Chan CCL, Wong KH, et al. Prospective study on volumetric and dosimetric changes during intensity-modulated radiotherapy for nasopharyngeal carcinoma patients. *Radiother Oncol*. (2012) 104:317–23. doi: 10.1016/J.RADONC.2012.03.013

15. Yao WR, Xu SP, Liu B, Cao XT, Ren G, Du L, et al. Replanning criteria and timing definition for parotid protection-based adaptive radiation therapy in nasopharyngeal carcinoma. *BioMed Res Int*. (2015) 2015:476383. doi: 10.1155/2015/476383

16. Capelle L, Mackenzie M, Field C, Parliament M, Ghosh S, Scrimger R. Adaptive radiotherapy using helical tomotherapy for head and neck cancer in definitive and postoperative settings: initial results. *Clin Oncol (R Coll Radiol)*. (2012) 24:208–15. doi: 10.1016/J.CLON.2011.11.005

17. Mahmoud O, Reis IM, Samuels MM, Elsayyad N, Bossart E, Both J, et al. Prospective pilot study comparing the need for adaptive radiotherapy in unresected bulky disease and in postoperative patients with head and neck cancer. *Technol Cancer Res Treat*. (2017) 16:1014–21. doi: 10.1177/1533034617717624

18. Hu YC, Tsai KW, Lee CC, Peng NJ, Chien JC, Tseng HH, et al. Which nasopharyngeal cancer patients need adaptive radiotherapy? *BMC Cancer*. (2018) 18 (1):1234. doi: 10.1186/S12885-018-5159-Y

19. Castelli J, Simon A, Rigaud B, Lafond C, Chajon E, Ospina JD, et al. Nomogram to predict parotid gland overdose in head and neck IMRT. *Radiat Oncol*. (2016) 11:1–11. doi: 10.1186/S13014-016-0650-6/FIGURES/6

20. Brouwer CL, Steenbakkers RJHM, Langendijk JA, Sijtsema NM. Identifying Patients Who May Benefit from Adaptive Radiotherapy: Does the Literature on Anatomic and Dosimetric Changes in Head and Neck Organs at Risk during Radiotherapy Provide Information to Help? *Radiother Oncol*. (2015) 115:285–94. doi: 10.1016/J.RADONC.2015.05.018

21. Brouwer CL, Steenbakkers RJHM, van der Schaaf A, Sopacua CTC, van Dijk LV, Kierkels RGJ, et al. Selection of head and neck cancer patients for adaptive radiotherapy to decrease xerostomia. *Radiother Oncol*. (2016) 120:36–40. doi: 10.1016/J.RADONC.2016.05.025

22. Gan Y, Langendijk JA, van der Schaaf A, Van Den Bosch L, Oldehinkel E, Lin Z, et al. An efficient strategy to select head and neck cancer patients for adaptive radiotherapy. *Radiother Oncol*. (2023) 186:109763. doi: 10.1016/j.radonc.2023.109763

23. Sanguineti G, Ricchetti F, Thomas O, McNutt T. Pattern and predictors of volumetric change of parotid glands during intensity modulated radiotherapy. *Br J Radiol*. (2013) 86(1031):20130363. doi: 10.1259/BJR.20130363

24. Vásquez Osorio EM, Hoogeman MS, Al-Mamgani A, Teguh DN, Levendag PC, Heijmen BJM. Local anatomic changes in parotid and submandibular glands during radiotherapy for oropharynx cancer and correlation with dose, studied in detail with nonrigid registration. *Int J Radiat Oncol Biol Phys*. (2008) 70:875–82. doi: 10.1016/J.IJROBP.2007.10.063

25. Broggi S, Fiorino C, Dell'Oca I, Dinapoli N, Paiusco M, Muraglia A, et al. Two-variable linear model of parotid shrinkage during IMRT for head and neck cancer. *Radiother Oncol*. (2010) 94:206–12. doi: 10.1016/J.RADONC.2009.12.014

26. Wang X, Lu J, Xiong X, Zhu G, Ying H, He S, et al. Anatomic and dosimetric changes during the treatment course of intensity-modulated radiotherapy for locally advanced nasopharyngeal carcinoma. *Med Dosim*. (2010) 35:151–7. doi: 10.1016/J.MEDDOS.2009.06.007

27. Sanguineti G, Ricchetti F, Wu B, McNutt T, Fiorino C. Parotid gland shrinkage during IMRT predicts the time to xerostomia resolution. *Radiat Oncol*. (2015) 10:19. doi: 10.1186/S13014-015-0331-X

28. Reali A, Anglesio SM, Mortellaro G, Allis S, Bartoncini S, Ruo Redda MG, et al. Volumetric and Positional Changes of Planning Target Volumes and Organs at Risk Using Computed Tomography Imaging during Intensity-Modulated Radiation Therapy for Head-Neck Cancer: An "Old" Adaptive Radiation Therapy Approach. *Radiol Med*. (2014) 119:714–20. doi: 10.1007/S11547-014-0386-Z

29. Brown E, Owen R, Harden F, Mengersen K, Oestreich K, Houghton W, et al. Head and neck adaptive radiotherapy: predicting the time to replan. *Asia Pac J Clin Oncol*. (2016) 12:460–7. doi: 10.1111/AJCO.12516

30. de Vette SPM, van Rijn-Dekker MI, Van den Bosch L, Keijzer K, Neh H, Chu H, et al. Evaluation of a comprehensive set of normal tissue complication probability models for patients with head and neck cancer in an international cohort. *Oral Oncol*. (2025) 163:107224. doi: 10.1016/j.oraloncology.2025.107224

frontiers | Frontiers in Oncology

TYPE Original Research
PUBLISHED 22 October 2025
DOI 10.3389/fonc.2025.1637443

Check for updates

OPEN ACCESS

EDITED BY
Poonam Yadav,
Northwestern University, United States

REVIEWED BY
Susovan Jana,
National Institute of Mental Health (NIH), United States
Treshita Dey,
Sanjay Gandhi Post Graduate Institute of Medical Sciences (SGPGI), India

*CORRESPONDENCE
Chenbin Liu
chenbin.liu@gmail.com
Zhijian Chen
chenzhijian@cicams-sz.org.cn
Jing Jin
jinjing@csco.org.cn

†These authors have contributed equally to this work

RECEIVED 29 May 2025
ACCEPTED 29 September 2025
PUBLISHED 22 October 2025

CITATION
Xiao N, Yuan C, Zhao T, Xu T, Zhou J, Liao J, Peng M, Liu C, Chen Z and Jin J (2025) Comparative impact of supine vs prone positioning on dose distribution, acute toxicity, and setup error in postoperative radiotherapy for cervical cancer: a multidimensional propensity-matched cohort study. *Front. Oncol.* 15:1637443. doi: 10.3389/fonc.2025.1637443

COPYRIGHT
© 2025 Xiao, Yuan, Zhao, Xu, Zhou, Liao, Peng, Liu, Chen and Jin. This is an open-access article distributed under the terms of the Creative Commons Attribution License (CC BY). The use, distribution or reproduction in other forums is permitted, provided the original author(s) and the copyright owner(s) are credited and that the original publication in this journal is cited, in accordance with accepted academic practice. No use, distribution or reproduction is permitted which does not comply with these terms.

Comparative impact of supine vs prone positioning on dose distribution, acute toxicity, and setup error in postoperative radiotherapy for cervical cancer: a multidimensional propensity-matched cohort study

Nanjie Xiao†, Cuiyun Yuan†, Tianshu Zhao, Tie Xu, Jiaomei Zhou, Junfang Liao, Miao Peng, Chenbin Liu*, Zhijian Chen* and Jing Jin*

Department of Radiation Oncology, National Cancer Center/National Clinical Research Center for Cancer/Cancer Hospital & Shenzhen Hospital, Chinese Academy of Medical Sciences and Peking Union Medical College, Shenzhen, China

Background: Postoperative radiotherapy is standard for high-risk cervical cancer, but acute toxicities—particularly gastrointestinal and hematologic—remain clinically relevant. Patient positioning may influence organ dose exposure and setup accuracy, yet its multidimensional clinical impact is poorly characterized.

Methods: This retrospective cohort study evaluated patients with cervical cancer treated with postoperative volumetric modulated arc therapy between 2019 and 2022. Propensity score matching (2:1) produced a balanced matched cohort of prone and supine treatments for comparative analyses. Primary endpoints included pelvic organ dose-volume parameters, interfractional setup error, and grade ≥2 hematologic and gastrointestinal toxicities, evaluated using multivariable logistic regression and linear mixed-effects models.

Results: In this single-center retrospective cohort (n = 168), propensity score matching (2:1) yielded 112 balanced patients (prone n = 70; supine n = 42). After matching, target coverage was comparable between positions (PTV_D95: 45.52 Gy vs 45.54 Gy, p = 0.24). The prone group showed higher low-dose exposure in bowel bag and rectum at V5–V15 (e.g., V10 difference –9.84%, 95% CI –17.07 to 1.08; adjusted p = 0.040). Setup error was similar across all axes (p > 0.05). The supine group had significantly higher incidence of leukopenia (92.9% vs 71.4%; p = 0.0073), with prone positioning associated with reduced hematologic toxicity (OR = 14.40, 95% CI 1.60–129.74; p = 0.017). Conversely, diarrhea occurred more often in the prone group (44.3% vs 26.2%, p = 0.070), and supine positioning was protective in multivariable analysis (OR = 0.42, 95% CI 0.17–0.97; p = 0.047).

Conclusion: These findings suggest prone positioning may be preferable for patients with limited hematopoietic reserve, while supine positioning may benefit those with gastrointestinal vulnerability. Positioning choice should be individualized based on toxicity risk and functional anatomy to optimize safety in postoperative cervical cancer radiotherapy.

KEYWORDS

cervical cancer, postoperative radiotherapy, patient positioning, hematologic toxicity, gastrointestinal toxicity

Introduction

According to recent data from the International Agency for Research on Cancer (IARC), over 600,000 new cases of cervical cancer and more than 340,000 related deaths were reported globally in 2022, with over 85% of these fatalities occurring in low- and middle-income countries (1). For patients with locally advanced or early-stage disease exhibiting high-risk pathological features, such as positive lymph nodes, positive surgical margins, or deep stromal invasion, adjuvant radiotherapy, including concurrent chemoradiotherapy (CCRT) following radical hysterectomy, is strongly endorsed by major international guidelines, including those from the National Comprehensive Cancer Network (NCCN) and the European Society for Medical Oncology (ESMO), as a standard of care (2, 3). This approach has been shown to significantly reduce pelvic recurrence and improve overall survival. The implementation of advanced radiotherapy techniques, such as intensity-modulated radiotherapy (IMRT) and image-guided radiotherapy (IGRT), has led to substantial progress in optimizing dose conformity and sparing organs at risk (OARs), including the bladder, rectum, bowel, and bone marrow (4, 5). These advancements have enhanced treatment precision and potentially improved patient outcomes. However, treatment-related toxicities, particularly acute gastrointestinal (GI) and hematologic toxicities graded by the Common Terminology Criteria for Adverse Events (CTCAE), remain prevalent and clinically significant (5). Such adverse events can impair treatment adherence, compromise patient-reported quality of life (QoL), and, in severe cases, lead to treatment interruption, which may adversely affect long-term survival outcomes. Consequently, reducing radiation-induced toxicities while maintaining oncological efficacy remains a critical challenge in postoperative radiotherapy for cervical cancer.

Patient positioning, encompassing body posture and immobilization, is central to optimizing postoperative pelvic radiotherapy for cervical cancer, impacting targeting accuracy, organ-at-risk (OAR) sparing, and treatment tolerance. Both prone and supine positions are routinely used (6, 7). Prone positioning with a bellyboard can anteriorly displace small bowel, reducing intermediate-to-high dose exposure and potentially mitigating acute gastrointestinal toxicity (8, 9). Supine positioning, preferred for workflow simplicity, reproducibility, and bladder management, may offer advantages in setup stability and bladder dose control (10, 11). However, most comparative studies are small, single-institution, and methodologically heterogeneous, with few assessing dose–volume metrics, setup accuracy, and multidimensional acute toxicities across key pelvic structures concurrently. We therefore hypothesized that positioning significantly influences pelvic organ dose distribution, setup error, and acute treatment-related toxicities, and that standardized position management may improve safety without compromising target coverage. To test this, we conducted a retrospective analysis using 2:1 propensity score matching to compare prone and supine positioning across multiple endpoints, including OAR dose distribution (bowel bag, rectum, sigmoid colon, and bladder under standardized filling), pelvic bones, setup error, and acute hematologic and gastrointestinal toxicities.

Unlike previous studies that focused on single organs or isolated endpoints, this study employed a comprehensive, multi-organ, and multi-endpoint analytical framework to quantitatively assess the impact of patient positioning during postoperative radiotherapy for cervical cancer. Dosimetric analyses were conducted for key pelvic

Abbreviations: IARC, International Agency for Research on Cancer; NCCN, National Comprehensive Cancer Network; ESMO, European Society for Medical Oncology; CCRT, Concurrent Chemoradiotherapy; IMRT, Intensity-Modulated Radiotherapy; IGRT, Image-Guided Radiotherapy; OAR(s), Organ(s) at Risk; GI, Gastrointestinal; CTCAE, Common Terminology Criteria for Adverse Events; QoL, Quality of Life; VMAT, Volumetric Modulated Arc Therapy; BMI, Body Mass Index; CT, Computed Tomography; CTV, Clinical Target Volume; RTOG, Radiation Therapy Oncology Group; PTV, Planning Target Volume; QUANTEC, Quantitative Analyses of Normal Tissue Effects in the Clinic; DVH, Dose-Volume Histogram; CBCT, Cone-Beam Computed Tomography; WBC, White Blood Cell; Hb, Hemoglobin; PLT, Platelet; NEU, Neutrophil; PSM, Propensity Score Matching; SMD, Standardized Mean Difference; IQR, Interquartile Range; FDR, False Discovery Rate; CI, Confidence Interval; GLMM, Generalized Linear Mixed-Effects Model; PRO(s), Patient-Reported Outcome(s); ABM, Active Bone Marrow; PET, Positron Emission Tomography; MRI, Magnetic Resonance Imaging; PTV_D95, Dose covering 95% of the Planning Target Volume; PTV_mean, Mean dose to the Planning Target Volume; OR, Odds Ratio; AIC, Akaike Information Criterion.

organs, including the bowel bag, rectum, sigmoid colon, bladder, and pelvic bones, evaluating both dose distribution and irradiated volume. Interfractional setup errors were systematically assessed using periodic image-guided radiotherapy (IGRT) data, and the spectrum of acute treatment-related toxicities was thoroughly characterized. By applying propensity score matching, we effectively balanced the baseline characteristics between the prone and supine groups, thereby minimizing selection bias and enhancing the internal validity and generalizability of the findings. The results of this study are expected to expand the current evidence regarding the clinical implications of positioning strategies for postoperative radiotherapy. Quantitative insights from this study may inform evidence-based positioning protocols, improve workflow precision, enhance patient compliance and quality of life, and serve as a methodological foundation for future large-scale, multicenter prospective cohorts and randomized controlled trials. Ultimately, these findings will contribute to the advancement of more precise and individualized radiotherapy strategies for cervical cancer.

Materials and methods

Study design and ethics

This single-center, retrospective cohort study included consecutive patients with cervical cancer who underwent postoperative volumetric modulated arc therapy (VMAT) between November 2019 and October 2022. The inclusion criteria were as follows: (1) histologically confirmed cervical cancer; (2) indication for adjuvant external beam radiotherapy (45.0–50.4 Gy in 25–28 fractions), with or without concurrent chemotherapy, based on National Comprehensive Cancer Network (NCCN) guidelines; and (3) availability of complete radiotherapy planning data and follow-up records. Exclusion criteria were as follows: (1) evidence of distant metastasis; (2) prior pelvic radiotherapy; and (3) active colorectal disease, including but not limited to inflammatory bowel disease and other obstructive or bleeding conditions. The study protocol was approved by the institutional ethics committee (approval no. JS2024-32-1) and the requirement for informed consent was waived. All patient data were anonymized prior to analysis.

CT simulation and positioning

The CT simulation was conducted utilizing a Discovery 590 RT scanner (GE Healthcare, Waukesha, WI, USA) with a slice thickness of 5 mm. Patients positioned prone were immobilized using a belly board system, whereas those positioned supine were immobilized with a thermoplastic mask and a flat tabletop. Bowel preparation involved rectal evacuation and standardized bladder filling. Each patient was instructed to consume 500 mL of water and wait 30 minutes prior to the simulation and each treatment session. Ultrasonography was employed to confirm that the bladder volume ranged between 120 and 150 mL before treatment commencement. The scan range extended from the T10 vertebral body to 5 cm below the ischial tuberosity. The quality of the acquired images was verified to be sufficient for precise delineation of the pelvic structures. Prone patients were immobilized using a belly-board system with pelvic fixation; supine patients were immobilized using a thermoplastic mask and flat tabletop. Bladder filling and bowel preparation were standardized. Daily on-treatment verification (CBCT) was performed during the first five fractions and at least weekly thereafter to ensure reproducibility.

Target volume and organ-at-risk delineation

The target volumes were delineated in accordance with a harmonized protocol integrating elements from the RTOG 0418, 0529, and 0822 guidelines. The clinical target volume (CTV) encompassed the postoperative tumor bed, vaginal cuff, and regional lymphatic drainage areas, including the obturator, internal and external iliac, and presacral regions. In patients exhibiting high-risk pathological features, the upper boundary of the CTV was extended superiorly to the level of the renal vessels, a configuration defined as extended-field irradiation in this study. A uniform 0.5 cm expansion was applied to generate the planning target volume (PTV). Organs at risk (OARs) located within 2 cm of the PTV, including the bladder, rectum, sigmoid colon, and femoral heads, were contoured in accordance with RTOG guidelines. The sigmoid colon was delineated as a distinct structure based on anatomical boundaries. The bowel bag was contoured following the method described by Robyn et al (12).

Radiotherapy planning

All radiotherapy plans were developed using the Eclipse treatment planning system (version 7.3.10; Varian Medical Systems) employing dual-arc volumetric modulated arc therapy (VMAT). The prescribed dose ranged from 45.0 to 48.6 Gy in 25–27 fractions, determined at the discretion of the treating physician based on individual risk factors and clinical judgment. The planning objectives stipulated that at least 95% of the planning target volume (PTV) received 100% of the prescribed dose, with a maximum dose not exceeding 107%. Dose constraints for organs at risk (OARs) were based on the Quantitative Analyses of Normal Tissue Effects in the Clinic (QUANTEC) guidelines. Dose-volume histogram (DVH) parameters were extracted for each OAR at 5 Gy intervals from V5 to V55 and reported as both absolute volume (in cm^3) and relative volume (percentage of total OAR volume).

Image guidance and setup error assessment

Cone-beam computed tomography (CBCT) was performed daily for the first five treatment fractions and weekly thereafter.

Three-dimensional deviations in the lateral (X), longitudinal (Y), and vertical (Z) axes were recorded for each session to evaluate interfractional setup error. Systematic and random error decomposition was not performed. CBCT datasets with missing or unusable data were excluded from the final analysis.

Clinical data collection and toxicity assessment

The body mass index (BMI) was determined by dividing weight in kilograms by height in meters squared (kg/m^2), with weight measurements taken each Wednesday morning under fasting conditions. Complete blood counts were conducted weekly before and during radiotherapy using a standardized laboratory platform. The lowest recorded values during treatment were utilized to evaluate hematologic toxicity, including leukocyte, hemoglobin, platelet, and neutrophil counts. Toxicities were graded according to the Common Terminology Criteria for Adverse Events (CTCAE), version 5.0. Hematological toxicity was defined as grade ≥2 if any of the following thresholds were met: leukopenia (WBC $< 3 \times 10^9$/L), anemia (Hb < 100 g/L), thrombocytopenia (PLT $< 75 \times 10^9$/L), or neutropenia (NEU $< 1.5 \times 10^9$/L). Gastrointestinal toxicity was assessed by the maximum daily bowel movement frequency, with ≥3 stools/day classified as grade ≥2 diarrhea. Other gastrointestinal symptoms were not included in the toxicity analysis.

Propensity score matching

To mitigate baseline confounding between the treatment groups, propensity score matching (PSM) was executed using a multivariable logistic regression model. Covariate selection was informed by prior literature and expert clinical consensus and included age, pathological stage, histological subtype, receipt of neoadjuvant chemotherapy, receipt of concurrent chemoradiotherapy, radiation field size, use of brachytherapy, body mass index (BMI), PTV_D95, PTV_mean, and baseline hematologic indices (white blood cell count, hemoglobin, platelet count, and neutrophil count). A 2:1 nearest-neighbor matching algorithm without replacement was implemented using the MatchIt package in R (version 4.3.1), with a caliper width of 0.45 selected to balance sample retention and matching quality based on a previously published methodology. Matching balance was evaluated using standardized mean differences (SMD), with values <0.1 considered indicative of acceptable balance.

Statistical analysis

Dosimetric comparisons

For each dose-volume threshold from V5 to V55, the median and interquartile range (IQR) of the relative irradiated volume (defined as the percentage of the organ volume receiving at least X Gy) were calculated for both the matched prone and supine groups. Group comparisons were performed using the Wilcoxon rank-sum test. P-values were adjusted for multiple comparisons using the Benjamini–Hochberg false discovery rate (FDR) method. The magnitude of the group differences was quantified using Cliff's delta (Cliff's Δ), with negative values indicating lower values in the prone group. The between-group median differences and their 95% bootstrap confidence intervals were estimated using 2,000 resamples.

Setup error analysis

Interfractional setup errors (X, Y, and Z axes) were analyzed using linear mixed-effects models (lme4 package), with treatment position, fraction number, and their interaction as fixed effects, and patient ID as a random intercept. The model assumptions, including residual normality and variance structures, were verified.

Acute toxicity analysis

To identify potential factors associated with acute toxicity, separate logistic regression models were constructed using grade ≥2 hematologic toxicity and grade ≥2 diarrhea as dependent variables. Univariable logistic regression was first performed for all clinical characteristics and organ-at-risk dose–volume histogram (DVH) parameters. Variables with a p-value of less than 0.20 in the univariable analysis were subsequently incorporated into multivariable logistic regression models. A stepwise backward elimination method was employed for variable selection, and the final models were selected based on the lowest Akaike Information Criterion (AIC) value to optimize model fit and parsimony. Variable selection was entirely based on statistical criteria, with no covariates being forced into the model. Hematologic toxicity and diarrhea were modeled independently. Toxicities were clinician-graded per CTCAE v5.0; validated patient-reported outcomes were not available due to the retrospective nature of the study.

Other statistical tests

Normally distributed continuous variables were analyzed using the Student's t-test, while non-normally distributed variables were assessed using the Wilcoxon rank-sum test. Categorical variables were compared using the chi-squared test or Fisher's exact test, as appropriate. All analyses were performed using R software (version 4.3.1) with the following packages: MatchIt, tableone, rstatix, lme4, and survival. All tests were two-sided, with p-values less than 0.05 considered statistically significant. All statistical analyses were conducted using a complete case dataset, with observations containing missing values excluded from the analysis.

Results

A total of 168 patients were included in the study, comprising 124 patients in the prone position group and 44 patients in the

supine position group. Patients in the prone group exhibited significantly higher PTV_D95 and PTV_mean values compared to those in the supine group (48.60 vs. 45.26 Gy, p = 0.001; 50.60 vs. 47.66 Gy, p = 0.007). Additionally, a greater proportion of patients in the supine position received extended-field irradiation (25.0% vs. 10.5%; p = 0.02) (Table 1). After propensity score matching for clinical and dosimetric variables, including PTV_D95 and PTV_mean, 112 patients were retained, with 70 in the prone group and 42 in the supine group (Figure 1A). The post-matching baseline characteristics were generally well balanced between the two groups. Standardized mean differences (SMDs) were less than 0.1 for most variables, except for hemoglobin (SMD = 0.16), platelet count (SMD = 0.16), and irradiation range (SMD = 0.17); no covariate exceeded an SMD of 0.2 (Table 1, Figure 1B). Following matching, there was no statistically significant difference in PTV_D95 between the prone and supine groups (median [IQR]: 45.52 [44.94–50.90] Gy vs. 45.54 [45.00–50.54] Gy; p = 0.24) (Table 1, Figure 2A, Supplementary Figure S1). No other baseline variables differed significantly between the groups (all p > 0.2).

Dosimetric comparison

Across all dose-volume thresholds (V5–V55), no significant differences were observed between the prone and supine groups in terms of the absolute irradiated volume of the bowel bag (Table 2). However, dose–volume histogram (DVH) analysis revealed significant differences in the relative irradiated volumes at V5, V10, and V55. Specifically, the V5 volume was significantly higher in the prone group than in the supine group (median difference −10.74%, 95% CI −17.05% to −0.96%; Cliff's Δ = 0.32; FDR-adjusted p = 0.040). A similar pattern was observed at V10 (median difference: −9.84%, 95% CI: −17.07% to 1.08%; Cliff's Δ = 0.30; adjusted p = 0.040). While a statistically significant difference was observed at V55 (median difference 0.00%, 95% CI 0.00 to 0.00; Cliff's Δ = −0.15; adjusted p = 0.040), the magnitude of this difference was negligible (Figure 2B). Dose-volume histogram (DVH) analysis of the sigmoid colon revealed no statistically significant differences in the relative irradiated volume between the two groups at any dose level from V5 to V55 (all FDR-adjusted p ≥ 0.05) (Figure 2C). Similarly, no significant differences were detected in the absolute irradiated volume of the sigmoid colon across all dose levels (all p > 0.05) (Table 2). In the rectum, the supine group demonstrated significantly lower irradiated volumes at V10 and V15 compared to the prone group (Figure 2D). At V10, the median relative volume was 97.69% in the supine group versus 100.00% in the prone group (median difference: −2.31%, 95% CI: −7.49% to −2.39%; Cliff's Δ = 0.41; adjusted p = 0.001). At V15, the difference further increased (96.34% vs. 99.97%; median difference, −3.63%; 95% CI, −8.79% to −3.26%; Cliff's Δ = 0.37; adjusted p = 0.003). Although both groups had a median V5 value of 100.00%, the distributions differed significantly (Cliff's Δ = 0.31; unadjusted p = 0.001). No significant differences were found in the absolute irradiated volume of the rectum between the two groups at any dose level (all p > 0.05) (Table 2). Regarding the bladder, the prone group consistently exhibited lower relative irradiated volumes across V5–V55; however, none of these differences reached statistical significance after FDR correction (adjusted p ≥ 0.05) (Table 2, Figure 2E). Prior to adjustment, the supine group showed slightly higher relative pelvic volumes at V5 and V10 (V5: 99.50% [IQR 98.43%–99.85%] vs. 98.95% [94.66%–99.65%], p = 0.01; V10: 96.57% [95.39%–98.37%] vs. 96.28% [89.90%–97.50%], p = 0.01), but these differences were not significant after correction (Figure 2F).

Setup error

Analysis of setup error using a generalized linear mixed-effects model (GLMM) revealed no statistically significant difference in setup error along the x-axis (vertical direction) between the prone and supine groups. The mean displacement was 0.081 cm (95% CI: 0.046–0.117) in the prone group and 0.065 cm (95% CI: 0.019–0.112) in the supine group (p = 0.591). Time, defined as the sequential number of image-guided radiotherapy sessions, was a significant factor affecting displacement along the x-axis (p = 0.006). The interaction between group and time was not significant (p = 0.85) (Figure 3A). Along the y-axis (longitudinal direction), the mean displacement was −0.102 cm (95% CI, −0.154 to −0.049) in the prone group and −0.016 cm (95% CI, −0.084 to 0.053) in the supine group. The difference between groups was not statistically significant (p = 0.051). Time remained a significant factor (p < 0.001), whereas the group–time interaction was not significant (p = 0.55) (Figure 3B). On the z-axis (lateral direction), the mean displacement was 0.071 cm (95% CI, 0.023–0.117) in the prone group and −0.001 cm (95% CI, −0.063–0.060) in the supine group. No significant differences were observed between groups (p = 0.072). Neither time (p = 0.153) nor the interaction term (p = 0.74) was statistically significant (Figure 3C).

Hematologic toxicity

In the matched population of postoperative cervical cancer patients, the incidence of grade ≥2 leukopenia was significantly higher in the supine group compared to the prone group (92.9% vs. 71.4%; absolute difference, 21.4%; 95% CI 6.4–36.5; p = 0.0073). No statistically significant differences were observed between the two groups regarding the incidence of grade ≥2 neutropenia, anemia, or thrombocytopenia (all p > 0.05). When evaluating the composite incidence of any hematologic toxicity (grade ≥2 in any of the four parameters), the supine group again exhibited a significantly higher rate (95.2% vs. 81.4%; absolute difference 13.8%, 95% CI 0.7–26.9; p = 0.046) (Table 3). Multivariable logistic regression analysis indicated that patients receiving radiotherapy in the supine position had a significantly elevated risk of developing grade ≥2 hematologic toxicity compared to those treated in the prone position (odds ratio [OR] = 14.40, 95% confidence interval [CI] 1.598–129.738; p = 0.017) (Figure 4A). For each 1 g/L increase in baseline hemoglobin level, the risk of hematologic toxicity

TABLE 1 Patients' baseline characteristics before and after propensity-score matching.

Characteristics	Original cohort (n =168)		P value	SMD	Matched cohort (n =112)		P value	SMD
	Prone position (n=124)	Supine position (n=44)			Prone position (n=70)	Supine position (n=42)		
Age,year (mean ± SD)	53.01 ± 10.08	51.93 ± 8.77	0.53	0.12	52.66 ± 10.09	51.88 ± 8.91	0.68	0.08
Pathologic stage			0.52	0.20			0.94	0.07
I	46(37.1%)	15(34.1%)			27 (38.6%)	15 (35.7%)		
II	36(29.0%)	10(22.7%)			15 (21.4%)	10 (23.8%)		
III	42(33.9%)	19(43.2%)			28 (40.0%)	17 (40.5%)		
Histological type			0.97	0.04			0.87	0.10
Squamous carcinoma	99(79.8%)	35(79.5%)			57 (81.4%)	34 (81.0%)		
Adenocarcinoma	15(12.1%)	5(11.4%)			8 (11.4%)	4 (9.5%)		
Other	10(8.1%)	4(9.1%)			5 (7.1%)	4 (9.5%)		
BMI,kg/m2 (median,range)	23.31 (17.83-33.20)	21.83 (17.33-31.24)	0.03	0.25	22.9 (17.8–29.6)	22 (17.3–31.2)	0.21	0.09
Leucocyte (median,range)	4.68 (1.48-14.63)	4.68 (1.52-23.85)	0.42	0.01	4.56 (1.48–10.4)	4.67 (1.52–23.9)	0.47	0.02
Hemoglobin (median,range)	108.00 (82-132.00)	106.50 (92-128.00)	0.27	0.16	108 (87–132)	106 (92–128)	0.33	0.16
Platelet (median,range)	241.50 (80-551)	223.50 (72-429)	0.20	0.25	233 (80–403)	232 (72–429)	0.38	0.16
Neutrophil (median,range)	2.67 (0.1-13.55)	2.23 (0.26-17.39)	0.25	0.08	2.63 (0.1–7.95)	2.23 (0.26–17.4)	0.43	0.002
Neoadjuvant chemotherapy			0.21	0.23			1.00	0.02
Yes	74(59.7%)	31(70.5%)			49 (70.0%)	29 (69.0%)		
No	50(40.3%)	13(29.5%)			21 (30.0%)	13 (31.0%)		
Concurrent chemotherapy			0.10	0.28			1.00	0.01
Yes	50(40.3%)	24(54.5%)			37 (52.9%)	22 (52.4%)		
No	74(59.7%)	20(45.5%)			33 (47.1%)	20 (47.6%)		
Irradiation range			0.02	0.38			0.54	0.17
Standard field	111(89.5%)	33(75.0%)			58 (82.9%)	32 (76.2%)		

(Continued)

10.3389/fonc.2025.1637443

10.3389/fonc.2025.1637443

TABLE 1 Continued

Characteristics	Original cohort (n =168)		P value	SMD	Matched cohort (n =112)		P value	SMD
	Prone position (n=124)	Supine position (n=44)			Prone position (n=70)	Supine position (n=42)		
Extension field	13(10.5%)	11(25.0%)			12 (17.1%)	10 (23.8%)		
Brachytherapy			0.66	0.07			1.00	0.01
Yes	19(15.3%)	8(18.2%)			13 (18.6%)	8 (19.0%)		
No	105(84.7%)	36(81.8%)			57 (81.4%)	34 (81.0%)		
Dmean_PTV(Gy) (median,range)	50.60 (46.36-53.43)	47.66 (46.35-52.33)	0.007	0.50	47.40 (46.36–53.23)	47.85 (46.35–52.33)	0.87	0.06
D95_PTV(Gy) (median,range)	48.60 (44.89-51.43)	45.26 (45.00-50.54)	0.001	0.53	45.52 (44.94–50.90)	45.54 (45.00–50.54)	0.24	0.08

SMD, standardized mean difference.

decreased by 13% (OR = 0.87, 95% CI 0.794–0.953; p = 0.0027). Conversely, for each 1 × 10^9/L decrease in platelet count, the risk increased by 1.3% (OR = 0.987, 95% CI 0.976–0.999; p = 0.0347). Compared to patients with pathological stage I disease, those with stage III disease had a significantly higher risk of toxicity (OR = 35.81, 95% CI 2.535–505.663; p = 0.008), whereas no significant difference was observed for patients with stage II disease.

Gastrointestinal toxicity

Among the matched postoperative cervical cancer patients, the incidence of diarrhea with more than three episodes per day was 26.2% in the supine group and 44.3% in the prone group, resulting in an absolute difference of −18.1% (95% CI, −37.7 − 1.5; p = 0.07). Although the prone position was associated with a higher tendency for diarrhea, the difference was not statistically significant (Table 3). In the multivariable logistic regression analysis, patients in the supine position had a significantly lower risk of diarrhea than those in the prone position (OR = 0.42, 95% CI 0.17–0.97; p = 0.047). Neither age nor the receipt of neoadjuvant chemotherapy was significantly associated with the risk of diarrhea (Figure 4B).

Discussion

This study systematically evaluated the differences between the prone and supine positions during postoperative radiotherapy for cervical cancer in terms of target dose distribution, normal tissue exposure, hematologic and gastrointestinal toxicity, and setup errors. Propensity score matching and multivariate statistical adjustments were employed to minimize confounding factors. The results demonstrated that despite overall comparable dose distributions, the choice of treatment position significantly affected low-dose organ exposure and the incidence of specific toxicities. These findings suggest that patient positioning is not a neutral technical variable and should be considered an integral component of individualized radiotherapy planning.

Following propensity score matching, no statistically significant differences were identified between the supine and prone groups concerning key dosimetric parameters, including the dose received by 95% of the planning target volume (PTV_D95) and the mean PTV dose (PTV_mean). This indicates comparable target coverage and overall dose homogeneity between the two positioning strategies. Further analysis of dose–volume histograms (DVHs) revealed that, although the absolute irradiated volumes of the bowel bag and rectum did not differ significantly between groups, the relative volume receiving low-dose exposure (V5–V15) was significantly greater in the prone group. This phenomenon may be attributed to the gravitational shift of mobile abdominal organs, particularly the small bowel, toward the anterior abdominal wall in the prone position (13). This anterior displacement increases the likelihood that these structures fall within the peripheral regions of the radiation field, where beam penumbra and scatter contribute to the so-called “low-dose bath”. Conversely, during

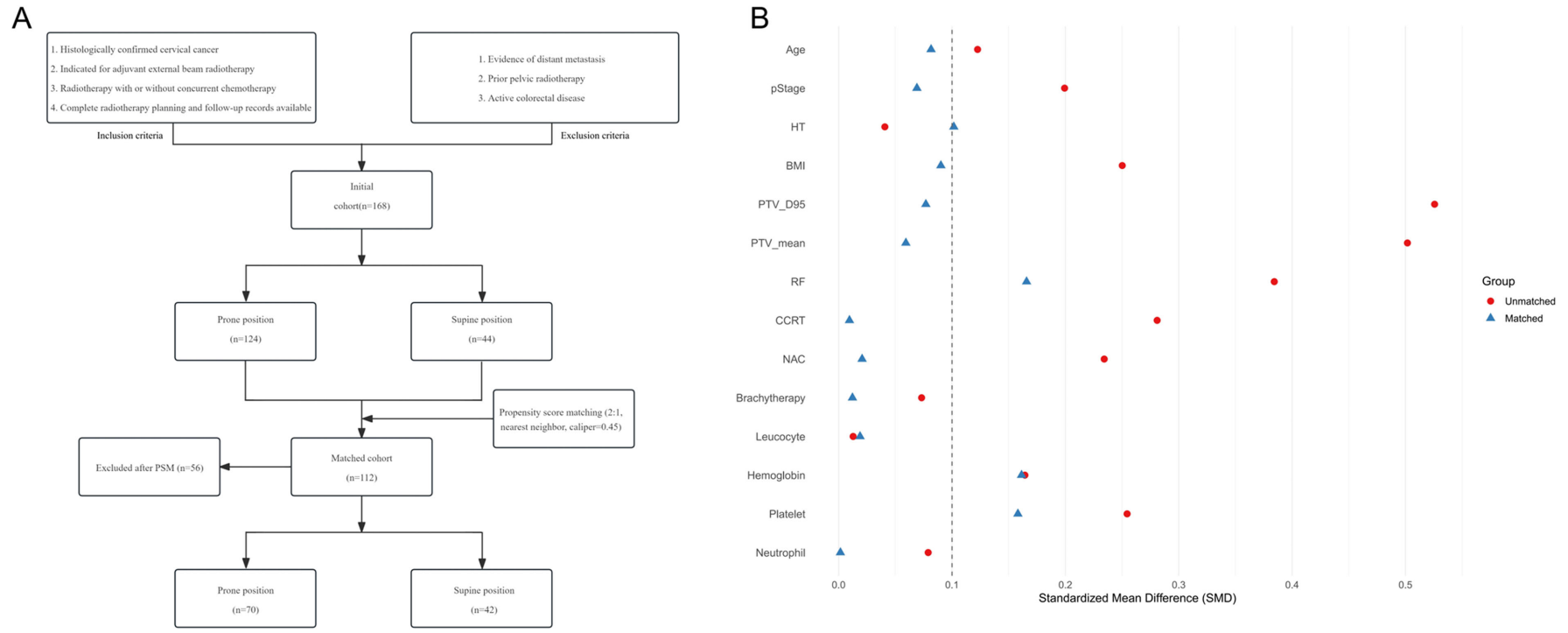

FIGURE 1
Patient selection flow and baseline covariate balance before and after propensity score matching. **(A)** Flow chart of patient inclusion and exclusion. The diagram summarizes the process of patient screening, exclusion criteria, and the final number of cases included in the analysis. **(B)** Love plot showing the standardized mean differences (SMDs) for baseline covariates before and after matching. Each point represents the SMD for an individual covariate; values less than 0.1 after matching are considered indicative of adequate balance between groups. PSM = propensity score matching; SMD = standardized mean difference.

10.3389/fonc.2025.1637443

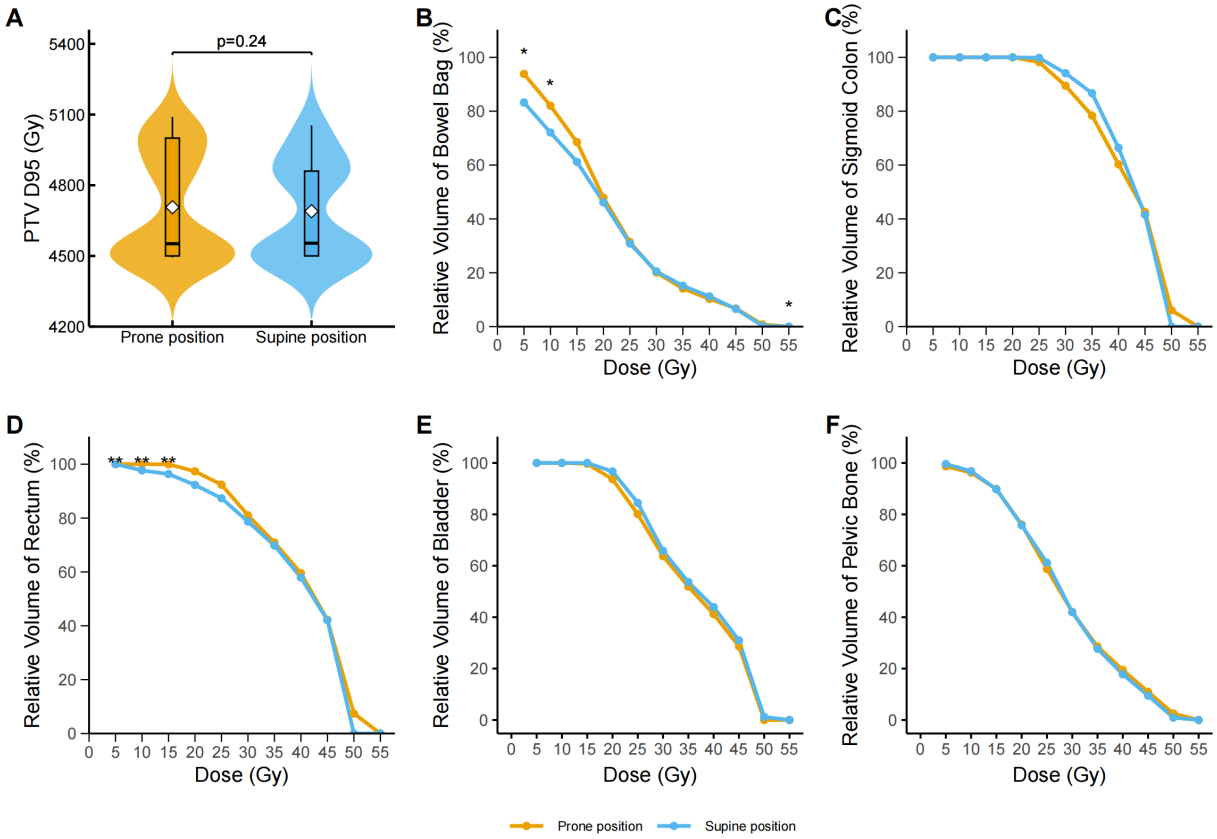

FIGURE 2
Dose–volume analysis of pelvic organs and target volume in prone and supine positions after propensity score matching. **(A)** Distribution of the dose covering 95% of the planning target volume (PTV D95, Gy) in the prone and supine groups. Violin plots display the full distribution with embedded boxplots showing median and interquartile range; white diamonds represent the mean. No significant difference was observed ($p = 0.24$, Wilcoxon signed-rank test). **(B)** Dose–volume histogram (DVH) curves for the bowel bag. The supine group exhibited significantly lower irradiated volumes at V5 ($p = 0.041$), V10 ($p = 0.041$), and V55 ($p = 0.041$) after false discovery rate (FDR) correction. Data represent group medians; asterisks denote statistical significance. **(C)** DVH curves for the sigmoid colon. No statistically significant differences were observed at any dose level (V5–V55) following FDR correction. **(D)** DVH curves for the rectum. The supine group had significantly lower relative volumes at V5 (adjusted $p = 0.0013$), V10 (adjusted $p = 0.0011$), and V15 (adjusted $p = 0.0032$) after FDR correction; asterisks denote statistical significance. **(E)** DVH curves for the bladder. No statistically significant differences were found across any dose levels (V5–V55) following FDR correction. **(F)** DVH curves for the pelvic bone. No statistically significant between-group differences were observed at any dose point after FDR correction. *$p < 0.05$, **$p < 0.01$, ***$p < 0.001$. The asterisk indicates statistical significance in the relative volume at a specific dose level for a given organ-at-risk.

supine positioning, the bowel may shift posteriorly toward the spine or sacrum, potentially reducing exposure to these low-dose regions. Such a pattern of low-dose redistribution has been previously reported in studies of rectal cancer and gynecologic malignancies, with changes predominantly observed in the V5–V15 range (14, 15). Variations in low-dose exposure may not directly cause high-grade toxicity; however, the cumulative low-dose bath and scatter could plausibly contribute to subclinical symptoms through chronic mucosal inflammation and neuroimmune modulation (16). Given that this linkage remains largely associative, prospective studies incorporating quantitative correlative endpoints are needed to establish causality. These findings underscore the potential clinical relevance of monitoring V5–V15 parameters during treatment planning and toxicity risk assessment.

With respect to setup errors, both the prone and supine positions demonstrated comparable accuracy across all three translational directions, with deviations remaining within clinically acceptable thresholds. These findings are consistent with results from large-cohort studies in pelvic radiotherapy that have demonstrated comparable setup accuracy across different treatment positions (17, 18). In the present study, the largest deviations were observed in the longitudinal (superior–inferior) direction, however, these did not reach clinical significance. Treatment duration emerged as an independent factor influencing setup accuracy, potentially reflecting dynamic changes, such as patient fatigue, positional instability, and variations in organ filling. Notably, similar trends of increasing setup errors over the course of treatment have also been observed in postoperative rectal cancer patients (19). While some reports have suggested that the prone position may be associated with larger systematic errors, primarily due to inter-individual anatomical variability and respiratory motion, this study incorporated standardized immobilization protocols and routine image-guided verification, effectively mitigating such concerns. These results support the feasibility and safety of prone positioning in the context of modern radiotherapy techniques (20–22). Daily verification imaging supported the

TABLE 2 Dose–volume parameters in the prone and supine groups after propensity score matching.

Dose-volume parameters (median [IQR])	Bowel bag		P	Sigmoid		P	Rectum		P	Bladder		P	Pelvic bone		P
	Prone station (n=70) (cc)	Supine station (n=42) (cc)		Prone station (n=70) (cc)	Supine station (n=42) (cc)		Prone station (n=70) (cc)	Supine station (n=42) (cc)		Prone station (n=70) (%)	Supine station (n=42) (%)		Prone station (n=70) (%)	Supine station (n=42) (%)	
V5	1968.56 (1559.49–2208.31)	1897.76 (1542.94–2277.11)	0.80	57.17 (41.94–94.71)	65.92 (38.51–99.55)	0.64	37.01 (28.85–52.71)	37.81 (31.07–44.25)	0.61	100 (100–100)	100 (100–100)	0.41	98.95 (94.66–99.65)	99.5 (98.43–99.85)	0.01
V10	1821.44 (1427.64–2008.04)	1708.33 (1412.39–2041.62)	0.92	57.17 (41.94–94.71)	65.92 (38.51–99.55)	0.64	36.66 (28.85–51.5)	36.92 (29.04–44.16)	0.50	100 (100–100)	100 (100–100)	0.14	96.28 (89.9–97.5)	96.57 (95.39–98.37)	0.01
V15	1497.57 (1233.19–1706.08)	1451.88 (1302.16–1761.1)	0.88	57.17 (41.94–94.71)	64.85 (38.51–98.98)	0.68	35.88 (28.03–51.03)	36.25 (28.35–42.94)	0.49	99.61 (95.98–100)	100 (98.85–100)	0.10	89.9 (83.2–93.84)	89.74 (87.58–93.49)	0.31
V20	1076.36 (931.68–1265.71)	1096.18 (960.1–1304.69)	0.69	57.17 (40.64–93.67)	62.27 (38.39–90.19)	0.74	33.17 (27.67–49.67)	35.03 (27.16–42.5)	0.57	93.36 (86.76–98.58)	96.69 (88.43–98.9)	0.21	76.21 (70.83–83.48)	75.77 (71.7–81.38)	0.97
V25	745.92 (645.24–904.71)	769.11 (660.7–898.98)	0.58	56.59 (38.29–85.6)	59.39 (34.61–89.4)	0.89	32.09 (25.61–45.96)	33.06 (26.18–40.28)	0.75	78.1 (70.65–89.8)	84.46 (74.83–91.42)	0.25	59.27 (55.78–65.97)	61.19 (56.52–64.92)	0.56
V30	533.62 (424.29–638.74)	547.54 (467.15–653.46)	0.60	47.51 (32.69–69.64)	51.57 (32.49–83.25)	0.75	30.1 (23.72–40)	31.06 (23.71–36.57)	0.95	63.69 (56.29–70.52)	66.2 (57.68–71.59)	0.33	42.06 (39.2–46.54)	41.97 (38.95–47.38)	0.99
V35	398 (313.51–477.31)	400.11 (339.07–477.79)	0.64	41.23 (27.81–61.65)	45.12 (29.96–75.23)	0.70	26.44 (21.24–36.45)	27.59 (21.92–33.87)	0.85	51.79 (45.58–56.35)	53.88 (46.32–60.29)	0.28	28.57 (25.63–32.42)	27.72 (25.05–30.8)	0.39
V40	305.85 (235.07–363.51)	309.79 (242.73–350.74)	0.93	33.92 (23.58–47.74)	34.81 (21.22–59.26)	0.76	20.96 (17.57–30.79)	23.84 (18.14–30.9)	0.63	41.56 (35.72–46.02)	44.79 (37.27–48.84)	0.20	19.47 (16.47–22.2)	17.78 (16.29–19.95)	0.14
V45	199.55 (154.3–253.4)	188.81 (138.39–254.23)	0.61	21.22 (13.76–32.01)	22.19 (13.89–37.55)	0.65	15.33 (11.87–23.48)	17.01 (13.16–23.16)	0.53	28.78 (23.8–34.43)	30.98 (27.24–37.47)	0.15	10.95 (8.89–14.55)	9.37 (7.88–11.36)	0.06
V50	0 (0–93.5)	7.2 (0–100.61)	0.35	0 (0–5.86)	1.38 (0–3.73)	0.39	0 (0–6.89)	0 (0–7.82)	0.58	0 (0–15.93)	1.48 (0–17.54)	0.22	2.92 (0–7.05)	0.82 (0–3.29)	0.13
V55	0 (0–0)	0 (0–0)	0.86	0 (0–0)	0 (0–0)	0.82	0 (0–0)	0 (0–0)	0.42	0 (0–0)	0 (0–0)	0.17	0 (0–0)	0 (0–0)	0.31

10.3389/fonc.2025.1637443

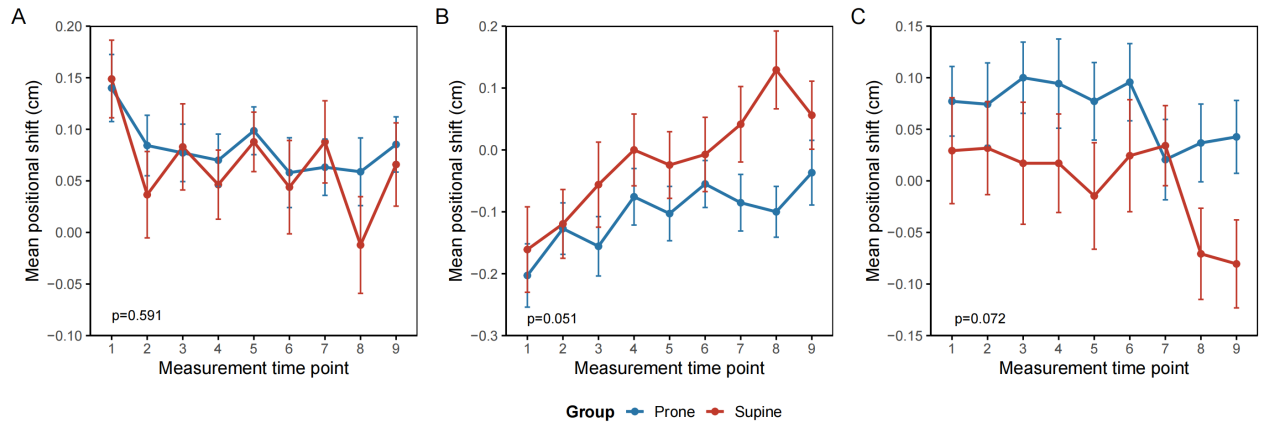

FIGURE 3
Repeated measures of interfractional setup error by treatment position. **(A)** Vertical axis (X) **(B)** Longitudinal axis (Y) **(C)** Lateral axis (Z). Mean interfractional setup deviations (cm) are plotted across treatment fractions (1–9) for patients in the prone (blue) and supine (red) positions. Error bars represent the standard error of the mean. No significant differences were observed between groups across all spatial directions. Trends over time reflect day-to-day variation in patient alignment and organ motion. All measurements were derived from cone-beam computed tomography (CBCT) image guidance.

reproducibility and operational feasibility of prone positioning in routine practice.

Regarding treatment-related toxicity, the prone position demonstrated a significant advantage in terms of hematologic preservation. Patients treated in the supine position exhibited a markedly higher incidence of grade ≥2 leukopenia, with a 14.4-fold increased risk compared to those treated in the prone position, even after multivariable adjustment. This disparity may be attributed to the reduced pelvic bone marrow irradiation volume in the prone position (23). Previous studies have demonstrated that active bone marrow (ABM) located in the iliac and sacral regions exhibits heightened sensitivity to low-dose radiation, with dosimetric parameters such as ABM-V10 and ABM-V20 being closely linked to hematologic toxicity (24–26). Although our study utilized conventional bone structure-based segmentation and identified no significant differences in dose-volume histograms (DVH) between positions, this method may underestimate the actual protective effect of prone positioning on functional marrow. A recent meta-analysis revealed that traditional pelvic DVH metrics, such as V10, can only account for a portion of the variability in hematologic toxicity (25). In contrast, imaging-defined ABM using 18F-FLT PET or IDEAL-IQ MRI, particularly ABM-V20, significantly enhances predictive accuracy (27, 28). Furthermore, we observed that lower baseline hemoglobin levels were associated with an increased risk of toxicity, while a higher pathological stage correlated with greater vulnerability, suggesting that both hematopoietic reserve and tumor burden should be considered in individualized positioning strategies.

In contrast to its hematologic advantage, the prone position was associated with less favorable outcomes concerning gastrointestinal toxicity. Although prone positioning increased low-dose exposure to bowel and rectum, the association with diarrhea approached but did not reach statistical significance in univariable analyses, and multivariable modeling suggested a protective effect for supine. Larger cohorts are required to precisely quantify this relationship. This finding is consistent with our dosimetric results, which indicated significantly higher relative volumes of the bowel bag and rectum exposed to low-dose radiation (V5–V15) in the prone group. Low-dose radiation may not directly induce structural injury, but it can indirectly precipitate symptoms such as diarrhea

TABLE 3 Comparison of grade ≥2 acute toxicities between matched postoperative cervical cancer patients.

Toxicity	Supine station (n=42) (%)	Prone station (n=70)(%)	Absolute difference (Δ, %)	95% CI	P-value
Leucocyte (≥2)	39 (92.9%)	50 (71.4%)	21.4	6.4 - 36.5	0.007
Hemoglobin (≥2)	19 (45.2%)	31 (44.3%)	1	−19.0 - 20.9	1.00
Platelet (≥2)	5 (11.9%)	4 (5.7%)	6.2	−6.9 - 19.3	0.292
Neutrophil (≥2)	28 (66.7%)	39 (55.7%)	11	−9.4 - 31.3	0.320
Hematologic toxicity (≥2)	40 (95.2%)	57 (81.4%)	13.8	0.7 - 26.9	0.046
Diarrhea (≥2)	11 (26.2%)	31 (44.3%)	−18.1	−37.7 - 1.5	0.070

Δ = absolute difference between groups. 95% CI calculated via bootstrapping. p-values are based on Pearson's χ^2 test unless otherwise noted. Fisher's exact test was used when expected cell counts were <5. Hematologic toxicity indicates the presence of grade ≥2 toxicity in any of the following: leucocyte, hemoglobin, platelet, or neutrophil. Toxicities graded per CTCAE v5.0.

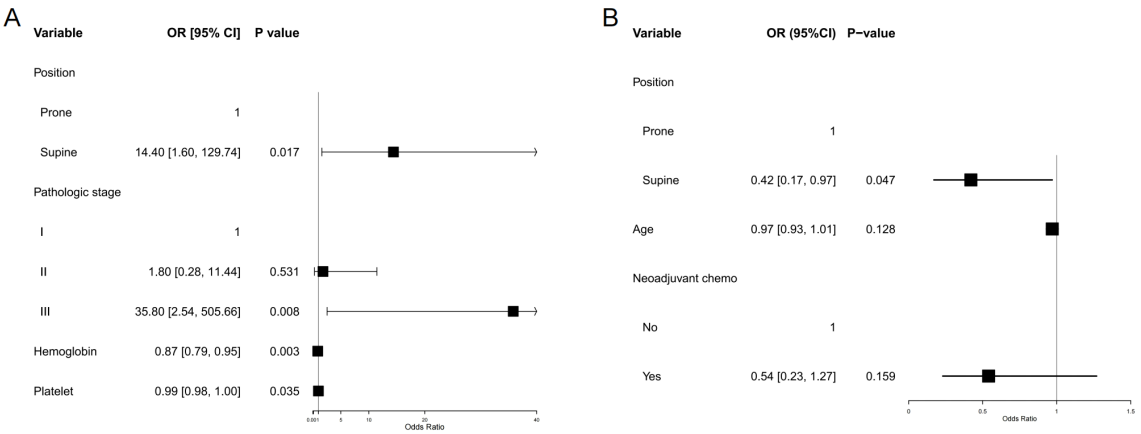

FIGURE 4
Forest plot of multivariable-adjusted associations between treatment position and acute toxicities. **(A)** Hematologic toxicity (grade ≥2). **(B)** Diarrhea (grade ≥2). Forest plots show adjusted odds ratios (ORs) with 95% confidence intervals (CIs) for the association between radiotherapy position (prone vs supine) and the risk of major acute toxicities. Multivariable logistic regression was performed for each endpoint, adjusting for relevant baseline clinical characteristics and dose–volume parameters. Prone positioning was independently associated with a lower risk of hematologic toxicity, while supine positioning was associated with a reduced risk of acute diarrhea. Vertical dashed lines indicate the null value (OR = 1.0); error bars represent 95% Cis.

by compromising intestinal barrier function and eliciting inflammatory responses (29, 30). Moreover, individual factors such as postoperative adhesions and impaired gastrointestinal function may amplify the position-related effects of radiation on the bowel (31). These findings suggest that for patients undergoing concurrent chemoradiotherapy or those with a history of abdominal surgery or underlying gastrointestinal fragility, the supine position may offer a safer therapeutic profile.

This study possesses several methodological strengths. First, the use of propensity score matching and multivariable adjustment minimized baseline confounding factors and enhanced the robustness of the findings. Second, the integration of dosimetric analysis, toxicity profiles, and setup error data provides a comprehensive, multidimensional framework to inform position-related decision-making in postoperative radiotherapy.

Nonetheless, this study has several limitations. First, this retrospective, single-institution design may limit generalizability. Validation in prospective, multi-center cohorts with a broader case mix and diverse practice patterns will be essential to confirm and refine these risk-adaptive positioning recommendations. Second, hematologic risk was estimated from anatomic pelvic bone structures rather than functional marrow imaging (e.g., FLT-PET, MRI), which could more accurately delineate active marrow and strengthen toxicity prediction. Third, exclusive reliance on clinician grading may underestimate symptom burden; future prospective studies should incorporate validated PRO instruments. Fourth, our analyses focused on acute events; subacute and late gastrointestinal and hematologic effects were not captured and warrant standardized longitudinal evaluation. Finally, we did not evaluate adaptive planning across fractions (e.g., variable bladder filling and bowel motion), which may be especially relevant for prone positioning and warrants prospective investigation. Future research should integrate functional imaging, candidate biological or radiomic biomarkers, and adaptive radiotherapy platforms to refine individual susceptibility profiling, guide position-tailored planning and adaptation, and ultimately improve position-selection models toward more precise and safer radiotherapy strategies.

Conclusions

This study demonstrates that the prone position effectively reduces hematologic toxicity and may be more suitable for patients with compromised baseline blood counts or a limited hematopoietic reserve. Conversely, the supine position appears to mitigate the risk of radiation-induced diarrhea and may be preferable for individuals with pre-existing gastrointestinal vulnerability or postoperative adhesions. Optimal positioning for postoperative radiotherapy in cervical cancer should extend beyond a dose-centric paradigm and adopt an individualized framework that incorporates the toxicity spectrum, baseline patient characteristics, and organ functional status.

Data availability statement

The raw data supporting the conclusions of this article will be made available by the authors, without undue reservation.

Ethics statement

The studies involving humans were approved by National Cancer Center/National Clinical Research Center for Cancer/Cancer Hospital & Shenzhen Hospital, Chinese Academy of Medical Sciences and Peking Union Medical College. The studies were conducted in accordance with the local legislation and institutional requirements. Written informed consent for

participation was not required from the participants or the participants' legal guardians/next of kin. Patient consent was waived as this was a retrospective observational study using anonymized data.

Author contributions

NX: Funding acquisition, Writing – original draft, Formal analysis, Visualization, Methodology. CY: Validation, Writing – review & editing, Visualization, Data curation, Project administration. TZ: Visualization, Project administration, Writing – review & editing, Validation, Data curation. TX: Validation, Writing – review & editing, Project administration. JZ: Writing – review & editing, Investigation. JL: Writing – review & editing, Investigation. MP: Investigation, Writing – review & editing. CL: Conceptualization, Writing – review & editing, Resources, Funding acquisition. ZC: Resources, Writing – review & editing, Conceptualization. JJ: Funding acquisition, Resources, Writing – review & editing, Conceptualization.

Funding

The author(s) declare financial support was received for the research and/or publication of this article. This research was supported by Hospital Research Project (No. E010321020, E010124002), Shenzhen High-level Hospital Construction Fund, Shenzhen Key Medical Discipline Construction Fund (No. SZXK013), Sanming Project of Medicine in Shenzhen (No. SZSM202211030), Shenzhen High-level Hospital Construction Fund, National Natural Science Foundation of China (No. 12005301), Guangdong Basic and Applied Basic Research Foundation (No. 2022A1515012456), Shenzhen Science and Technology Program (JCYJ20220530153801004), Natural Science Foundation of Shenzhen City (No: JCYJ20230807150502006), National High Level Hospital Clinical Research Funding and Cooperation Fund of CHCAMS Beijing & Langfang & SZCH (No: CFA202503024), Shenzhen Clinical Research Center for Cancer (No.(2021)287)

Conflict of interest

The authors declare that the research was conducted in the absence of any commercial or financial relationships that could be construed as a potential conflict of interest.

Generative AI statement

The author(s) declare that no Generative AI was used in the creation of this manuscript.

Any alternative text (alt text) provided alongside figures in this article has been generated by Frontiers with the support of artificial intelligence and reasonable efforts have been made to ensure accuracy, including review by the authors wherever possible. If you identify any issues, please contact us.

Publisher's note

All claims expressed in this article are solely those of the authors and do not necessarily represent those of their affiliated organizations, or those of the publisher, the editors and the reviewers. Any product that may be evaluated in this article, or claim that may be made by its manufacturer, is not guaranteed or endorsed by the publisher.

Supplementary material

The Supplementary Material for this article can be found online at: https://www.frontiersin.org/articles/10.3389/fonc.2025.1637443/full#supplementary-material

References

1. Bray F, Laversanne M, Sung H, Ferlay J, Siegel RL, Soerjomataram I, et al. Global cancer statistics 2022: GLOBOCAN estimates of incidence and mortality worldwide for 36 cancers in 185 countries. *CA Cancer J Clin*. (2024) 74:229–63. doi: 10.3322/caac.21834

2. N. National Comprehensive Cancer. *NCCN Clinical Practice Guidelines in Oncology (NCCN Guidelines®): Cervical Cancer*. Plymouth Meeting, PA: National Comprehensive Cancer Network (2025).

3. Cibula D, Raspollini MR, Planchamp F, Centeno C, Chargari C, Felix A, et al. ESGO/ESTRO/ESP Guidelines for the management of patients with cervical cancer - Update 2023. *Int J Gynecol Cancer*. (2023) 33:649–66. doi: 10.1136/ijgc-2023-004429

4. Lee SW, Kim A, Lee SJ, Kim SH, Lee JH. Intensity-modulated radiation therapy for uterine cervical cancer to reduce toxicity and enhance efficacy - an option or a must? *A Narrat Rev Cancer Res Treat*. (2024) 56:1–17. doi: 10.4143/crt.2023.562

5. Anghel B, Serboiu C, Marinescu A, Taciuc IA, Bobirca F, Stanescu AD. Recent advances and adaptive strategies in image guidance for cervical cancer radiotherapy. *Med (Kaunas)*. (2023) 59:1735. doi: 10.3390/medicina5910

6. Gonzalez VJ, Hullett CR, Burt L, Rassiah-Szegedi P, Sarkar V, Tward JD, et al. Impact of prone versus supine positioning on small bowel dose with pelvic intensity modulated radiation therapy. *Adv Radiat Oncol*. (2017) 2:235–43. doi: 10.1016/j.adro.2017.01.005

7. Li C, Xiao YP, Huang L, Jing W, Zhang B, Huang SH, et al. High buttocks supine position to reduce small bowel exposure in gynecological radiotherapy. *Radiat Oncol*. (2024) 19:131. doi: 10.1186/s13014-024-02522-6

8. Wang D, Li B, Chen L, Li Z, Kong F, Yan H, et al. Dosimetric effects of prone immobilization devices on skin in intensity-modulated radiation therapy for gynecologic cancer: a retrospective study. *BMC Cancer*. (2024) 24:1464. doi: 10.1186/s12885-024-13111-x

9. Yan H, Wu M, Wang W, Wang D, Huang X, Dong J, et al. Dosimetry and acute radiation enteritis comparison between prone and supine position in IMRT for gynecological cancers. *J Appl Clin Med Phys*. (2023) 24:e14135. doi: 10.1002/acm2.14135

10. Zheng Z, Liu D, Su Y. Supine/prone position fixation treatment in cervical cancer radiotherapy. *J Cancer Res Ther*. (2025) 21:401–8. doi: 10.4103/jcrt.jcrt_2050_24

11. Ge BB, Liu Y, Jin JH, Wu JT, Liu HT, He CY, et al. Effect of bladder filling status on positioning errors in post-hysterectomy cervical cancer radiotherapy. *Ann Med*. (2023) 55:2249936. doi: 10.1080/07853890.2023.2249936

12. Banerjee R, Chakraborty S, Nygren I, Sinha R. Small bowel dose parameters predicting grade ≥ 3 acute toxicity in rectal cancer patients treated with neoadjuvant chemoradiation: an independent validation study comparing peritoneal space versus small bowel loop contouring techniques. *Int J Radiat Oncol Biol Phys*. (2013) 85:1225–31. doi: 10.1016/j.ijrobp.2012.09.036

13. Stromberger C, Kom Y, Kawgan-Kagan M, Mensing T, Jahn U, Schneider A, et al. Intensity-modulated radiotherapy in patients with cervical cancer. An intra-individual comparison of prone and supine positioning. *Radiat Oncol*. (2010) 5:63. doi: 10.1186/1748-717X-5-63

14. Pinkawa M, Gagel B, Demirel C, Schmachtenberg A, Asadpour B, Eble MJ. Dose-volume histogram evaluation of prone and supine patient position in external beam radiotherapy for cervical and endometrial cancer. *Radiother Oncol*. (2003) 69:99–105. doi: 10.1016/S0167-8140(03)00244-5

15. Drzymala M, Hawkins MA, Henrys AJ, Bedford J, Norman A, Tait DM. The effect of treatment position, prone or supine, on dose-volume histograms for pelvic radiotherapy in patients with rectal cancer. *Br J Radiol*. (2009) 82:321–7. doi: 10.1259/bjr/57848689

16. Wallrapp A, Chiu IM. Neuroimmune interactions in the intestine. *Annu Rev Immunol*. (2024) 42:489–519. doi: 10.1146/annurev-immunol-101921-042929

17. Jadon R, Pembroke CA, Hanna CL, Palaniappan N, Evans M, Cleves AE, et al. A systematic review of organ motion and image-guided strategies in external beam radiotherapy for cervical cancer. *Clin Oncol (R Coll Radiol)*. (2014) 26:185–96. doi: 10.1016/j.clon.2013.11.031

18. Schmidhalter D, Malthaner M, Born EJ, Pica A, Schmuecking M, Aebersold DM, et al. Assessment of patient setup errors in IGRT in combination with a six degrees of freedom couch. *Z fur Med Physik*. (2014) 24:112–22. doi: 10.1016/j.zemedi.2013.11.002

19. Xu H, Zhang Z, Tian B, Li X, Bian Y, Liang X, et al. Evaluation of corrective effect of 6 degree of freedom couch on setup errors in intensity modulated radiotherapy for postoperative rectal cancer patients. *Front Oncol*. (2023) 13:1030599. doi: 10.3389/fonc.2023.1030599

20. Bayley AJ, Catton CN, Haycocks T, Kelly V, Alasti H, Bristow R, et al. A randomized trial of supine vs. prone positioning in patients undergoing escalated dose conformal radiotherapy for prostate cancer. *Radiother Oncol*. (2004) 70:37–44. doi: 10.1016/j.radonc.2003.08.007

21. Mohamed R, Elawadi AA, Alkhanein N, Alharth M, Asiri M. Factors affecting isocenter displacement and planning target volume margin for patients with rectal cancer receiving radiation therapy. *Adv Radiat Oncol*. (2022) 7:101060. doi: 10.1016/j.adro.2022.101060

22. Li J, Kong X, Cheng C, Wang G, Zhuang H, Yang R. Comparison between supine and prone patient setup for lumbosacral spinal stereotactic body radiosurgery with CyberKnife. *Front Oncol*. (2023) 13:959447. doi: 10.3389/fonc.2023.959447

23. Chopra S, Gupta S, Kannan S, Dora T, Engineer R, Mangaj A, et al. Late toxicity after adjuvant conventional radiation versus image-guided intensity-modulated radiotherapy for cervical cancer (PARCER): A randomized controlled trial. *J Clin Oncol*. (2021) 39:3682–92. doi: 10.1200/JCO.20.02530

24. Autorino R, Cusumano D, Rinaldi RM, Giannini R, De Luca V, Campitelli M, et al. Correlation between radiation dose to bone marrow subregions and acute hematologic toxicity inendometrial cancer treated with external beam radiotherapy. *Clin Transl Radiat Oncol*. (2025) 52:100942. doi: 10.1016/j.ctro.2025.100942

25. Corbeau A, Kuipers SC, de Boer SM, Horeweg N, Hoogeman MS, Godart J, et al. Correlations between bone marrow radiation dose and hematologic toxicity in locally advanced cervical cancer patients receiving chemoradiation with cisplatin: a systematic review. *Radiother Oncol*. (2021) 164:128–37. doi: 10.1016/j.radonc.2021.09.009

26. Rahimy E, von Eyben R, Lewis J, Hristov D, Kidd E. Evaluating dosimetric parameters predictive of hematologic toxicity in cervical cancer patients undergoing definitive pelvic chemoradiotherapy. *Strahlenther Onkol*. (2022) 198:773–82. doi: 10.1007/s00066-021-01885-z

27. McGuire SM, Bhatia SK, Sun W, Jacobson GM, Menda Y, Ponto LL, et al. Using [(18)F]Fluorothymidine imaged with positron emission tomography to quantify and reduce hematologic toxicity due to chemoradiation therapy for pelvic cancer patients. *Int J Radiat Oncol Biol Phys*. (2016) 96:228–39. doi: 10.1016/j.ijrobp.2016.04.009

28. Gao T, Wei L, Jiang L, Ma S, Zhang W, Zhang Y, et al. Dose-volume parameters of spared magnetic resonance imaging-defined active bone marrow predict hematologic toxicity in pelvic Malignancies patients undergoing radiotherapy: A cohort study. *Technol Cancer Res Treat*. (2024) 23:15330338241255283. doi: 10.1177/15330338241255283

29. Lu L, Li F, Gao Y, Kang S, Li J, Guo J. Microbiome in radiotherapy: an emerging approach to enhance treatment efficacy and reduce tissue injury. *Mol Med Cambridge Mass*. (2024) 30:105. doi: 10.1186/s10020-024-00873-0

30. Park HY, Yu JH. X-ray radiation-induced intestinal barrier dysfunction in human epithelial Caco-2 cell monolayers. *Ecotoxicol Environ Saf*. (2023) 264:115404. doi: 10.1016/j.ecoenv.2023.115404

31. Shadad AK, Sullivan FJ, Martin JD, Egan LJ. Gastrointestinal radiation injury: symptoms, risk factors and mechanisms. *World J Gastroenterol*. (2013) 19:185–98. doi: 10.3748/wjg.v19.i2.185

frontiers | Frontiers in Medicine

TYPE Review
PUBLISHED 30 October 2025
DOI 10.3389/fmed.2025.1686593

Check for updates

OPEN ACCESS

EDITED BY
Abdul K. Parchur,
University of Maryland Medical Center,
United States

REVIEWED BY
Susovan Jana,
National Institute of Mental Health (NIH),
United States
Silambarasan Anbumani,
The University of Arkansas for Medical
Science, United States

*CORRESPONDENCE
Fada Guan
✉ fguan@mdanderson.org
Yue Yan
✉ yue.yan@dartmouth.edu

RECEIVED 15 August 2025
ACCEPTED 07 October 2025
PUBLISHED 30 October 2025
CORRECTED 25 November 2025

CITATION
Yan Y, Alexander DA, Bednarz BP, Bronk LF, Chen H, Gladstone DJ, Han B, Iannuzzi CM, Li Y, Nguyen N, Mulenga N, Viscariello NN, Wang Y, Weygand J, Zlateva Y and Guan F (2025) Innovative approaches in precision radiation oncology: advanced imaging technologies and challenges which shape the future of radiation therapy.
Front. Med. 12:1686593.
doi: 10.3389/fmed.2025.1686593

COPYRIGHT
© 2025 Yan, Alexander, Bednarz, Bronk, Chen, Gladstone, Han, Iannuzzi, Li, Nguyen, Mulenga, Viscariello, Wang, Weygand, Zlateva and Guan. This is an open-access article distributed under the terms of the Creative Commons Attribution License (CC BY). The use, distribution or reproduction in other forums is permitted, provided the original author(s) and the copyright owner(s) are credited and that the original publication in this journal is cited, in accordance with accepted academic practice. No use, distribution or reproduction is permitted which does not comply with these terms.

Innovative approaches in precision radiation oncology: advanced imaging technologies and challenges which shape the future of radiation therapy

Yue Yan[1,2,3]*, Daniel A. Alexander[1,2], Bryan P. Bednarz[4], Lawrence F. Bronk[5], Huixiao Chen[6], David J. Gladstone[1,2,3], Bin Han[7], Christopher M. Iannuzzi[8], Yuting Li[5], Ngoc Nguyen[6], Natasha Mulenga[3], Natalie N. Viscariello[9], Yuenan Wang[8], Joseph Weygand[1,2], Yana Zlateva[5] and Fada Guan[5]*

[1]Department of Radiation Oncology & Applied Sciences, Dartmouth-Hitchcock Medical Center, Lebanon, NH, United States, [2]Geisel School of Medicine, Dartmouth College, Hanover, NH, United States, [3]Thayer School of Engineering, Dartmouth College, Hanover, NH, United States, [4]Department of Medical Physics, University of Wisconsin Madison, Madison, WI, United States, [5]Department of Radiation Physics, University of Texas MD Anderson Cancer Center, Houston, TX, United States, [6]Department of Therapeutic Radiology, Yale University School of Medicine, New Haven, CT, United States, [7]Department of Radiation Oncology, Stanford University, Stanford, CA, United States, [8]Hartford Health Care Cancer Institute, St. Vincent's Medical Center, Bridgeport, CT, United States, [9]Department of Radiation Oncology, Heersink School of Medicine, University of Alabama at Birmingham, Birmingham, AL, United States

Radiation oncology is undergoing a transformative shift toward precision medicine through unprecedented advances in imaging technologies that enable increasingly personalized and adaptive cancer treatment. This comprehensive review synthesizes the underlying physical principles, current clinical applications, technical challenges, and quality assurance requirements across the complete spectrum of emerging imaging-guided radiation therapy approaches. We examine magnetic resonance-guided radiotherapy systems that enable daily soft-tissue visualization and online plan adaptation, positron emission tomography-guided platforms that allow real-time tracking of metabolically active tumor regions, advanced cone beam computed tomography systems supporting rapid adaptive workflows through artificial intelligence-enhanced image generation, and novel applications including Cherenkov radiation imaging and stereoscopic guidance with surface tracking. For proton therapy, we address innovations spanning dual-energy computed tomography, proton computed tomography, and *in-vivo* range verification that tackle fundamental range uncertainty limitations. In theranostics, we explore sophisticated quantitative imaging for personalized radiopharmaceutical dosimetry. Our analysis reveals that while these technologies converge to enable increasingly adaptive and biology-informed dose delivery, realizing their full clinical potential requires rigorous multicenter validation, standardized quality assurance protocols, integration of multi-omics with functional imaging, trustworthy automation with continuous performance monitoring, interoperable data pipelines, enhanced

workforce training, and attention to equitable access across diverse patient populations. This integrated perspective provides a forward-looking framework to guide clinicians, medical physicists, and researchers in navigating the rapidly evolving landscape of precision radiotherapy while ensuring safe and effective implementation of these transformative technologies.

KEYWORDS

magnetic resonance imaging guided radiotherapy, positron emission tomography, stereoscopic imaging and surface guidance, cone beam computed tomography, generative image synthesis, Cherenkov radiation imaging, imaging innovations in proton therapy, advanced quantitative imaging

1 Introduction

Radiation oncology is experiencing a transformative shift toward precision medicine, driven by unprecedented advances in imaging technologies that enable increasingly personalized and adaptive cancer treatment. Traditional anatomical imaging approaches are rapidly being complemented and, in some cases, superseded by sophisticated modalities that integrate functional, molecular, and real-time biological information into treatment planning and delivery. This evolution represents a paradigm shift from static, one-size-fits-all radiation therapy toward dynamic, patient-specific approaches that can adapt to tumor biology, anatomical changes, and treatment response in real-time.

The emergence of magnetic resonance-guided radiotherapy (MRgRT) systems has enabled daily soft-tissue visualization and online plan adaptation, particularly transforming treatment of mobile targets, such as pancreatic and gastrointestinal malignancies. Simultaneously, the integration of positron emission tomography (PET) with linear accelerators has introduced biology-guided radiotherapy (BgRT), allowing real-time tracking of metabolically active tumor regions. Advanced cone beam computed tomography (CBCT) systems now support online adaptive workflows through rapid, high-quality imaging and artificial intelligence (AI)-enhanced CT generation. Novel applications, such as Cherenkov radiation imaging, stereoscopic guidance with surface tracking, and generative AI-based image synthesis, are further expanding the precision radiotherapy toolkit. In proton therapy, innovations spanning dual-energy CT, proton CT, and *in vivo* range verification address fundamental range uncertainty limitations, while theranostics applications demand sophisticated quantitative imaging for personalized radiopharmaceutical dosimetry.

This comprehensive review aims to provide a critical, integrated assessment of emerging and advanced imaging technologies that are reshaping precision radiotherapy. Unlike previous reviews that examine individual modalities in isolation, we synthesize the underlying physical principles, current clinical applications, technical challenges, and quality assurance requirements across the complete spectrum of imaging-guided radiation therapy (RT) approaches. Our analysis encompasses workflow considerations, automation potential, and standardization needs while highlighting how these technologies converge to enable increasingly adaptive, biology-informed dose delivery.

This article addresses a critical gap in the literature by providing the first comprehensive, cross-platform analysis of how diverse imaging modalities complement each other within modern precision RT workflows. We emphasize practical implementation challenges—including geometric accuracy requirements, quantitative imaging uncertainties, workflow optimization, and workforce training needs—that are essential for successful clinical translation but often underemphasized in technology-focused reviews. Furthermore, we outline a forward-looking framework that integrates multi-omics data with functional and anatomical imaging, supported by trustworthy AI automation and standardized quality assurance protocols. This integrated perspective is designed to guide clinicians, medical physicists, and researchers in navigating the rapidly evolving landscape of precision radiotherapy while ensuring safe, equitable, and effective implementation of these transformative technologies across diverse patient populations.

2 Magnetic resonance imaging-guided radiotherapy

Magnetic resonance imaging (MRI)-guided radiotherapy (MRgRT) allows for direct visualization of soft tissue anatomy during treatment and supports online plan adaptation. Two commercial systems have been deployed clinically. The ViewRay (Oakwood Village OH, USA) MRIdian platform combines a 0.35 T split magnet and was initially designed to utilize three cobalt sources, (1) but it has more recently incorporated a 6 MV linear accelerator (linac) (2). The Elekta (Stockholm, Sweden) Unity platform (3) couples a 1.5 T MRI with a 7 MV linac. Both systems incorporate MRI into the treatment room geometry but differ in field strength, system architecture, and clinical workflow. The MRIdian enables real-time beam gating using multiplanar cine imaging from a balanced steady-state free precession (bSSFP) sequence (4), while Unity employs high-resolution imaging and supports plan adaptation through structured workflows that include "Adapt to Position" and "Adapt to Shape" (5). These capabilities have enabled a shift toward online adaptive planning, where a new radiation treatment plan is created each day, accounting for inter-fractional changes in patient anatomy (6).

2.1 Technological challenges

The technological requirements for MRgRT are non-trivial. Radiation delivery hardware must function reliably in the presence of magnetic fields, and MRI performance must remain stable during beam-on conditions. Integration requires mitigation of mutual interference between linac and MR subsystems, attention to magnetic shielding, and spatial coordination of isocenters. In the case of MRIdian, the split-magnet design permits radiation beam access perpendicular to the B0 field, while modifications to RF shielding and gradient coil structure support simultaneous imaging and irradiation (2). The Unity platform adopts a different approach, positioning the linac outside the magnet bore and delivering radiation along the bore axis (3). These design choices reflect different approaches to managing electromagnetic interference, gradient performance, and beam access geometry (7). Differences in image quality arise largely not only due to differences in field strength (0.35 T for MRIdian vs. 1.5 T for Unity) but also from available sequences and system constraints related to simultaneous imaging and treatment. Sequences such as T2-weighted fast spin echo (FSE) and bSSFP have reduced acquisition times to fit within clinical workflows while preserving the image quality and spatial accuracy required for planning and guidance.

2.2 Clinical applications of MRgRT

In clinical practice, the most commonly used workflow on the MRIdian system involves daily acquisition of a bSSFP image, followed by manual or semi-automated recontouring, re-optimization of the treatment plan, and delivery with respiratory gating. When performed sequentially, the entire process takes approximately 45 min, though newer software versions (A3i) have enabled partial parallelization of workflow steps to reduce overall treatment time (8). Gating is based on direct visualization of the target or a surrogate structure in the cine image, with beam delivery suspended if the structure location exits a predefined boundary. On Unity, adaptation decisions are based on comparison between the reference and daily MR images. In the "Adapt to Position" workflow, the original plan is rigidly shifted, while in "Adapt to Shape," a new plan is generated based on the recontouring of both target and critical structures (5). Unity now supports real-time gating, though this feature was only introduced after several years of clinical use. Its higher field strength enables improved soft tissue contrast and may also facilitate integration of functional imaging (9).

Pancreatic cancer has emerged as a primary disease site in which MRgRT has had a measurable clinical impact, particularly with the MRIdian system, which possesses a much longer gating functionality. Computed tomography (CT)-based planning for pancreatic tumors is limited by poor soft tissue visibility and motion of adjacent gastrointestinal organs, which limits how aggressively they can be treated (10). MR guidance permits direct visualization of the tumor and organs at risk (OARs) at the time of treatment, enabling tighter margins and more aggressive dose prescriptions (11). Initial retrospective series demonstrated the feasibility of delivering 50 Gy in five fractions with acceptable toxicity and local control (12). These results were tested prospectively in the SMART trial, which enrolled 136 patients with locally advanced or borderline resectable pancreatic cancer and treated them using the MRIdian system. The primary endpoint was gastrointestinal toxicity, which was observed in fewer than 5% of patients. Median overall survival exceeded 14 months, and 2-year survival was over 40% (13). These outcomes compare favorably to historical controls and have contributed to the growing interest in MRgRT for tumors in anatomically complex or mobile sites. The pancreas is not the only area of application. There is also emerging evidence in the liver, lung, and prostate, where online adaptation and motion mitigation may offer advantages in selected patients (14, 15). In CNS tumors, although not one of the common applications is present for MRgRT, daily MRI may support tighter margins and improved alignment with evolving anatomical changes during long courses of therapy (16). MRgRT enables treatment in anatomically complex or mobile sites where soft tissue visualization, motion management, or daily adaptation is required.

2.3 Geometric distortion in MRgRT

Geometric accuracy remains a foundational requirement for MRgRT. MRI is inherently prone to spatial distortion from static field inhomogeneities, gradient non-linearities, and magnetic susceptibility differences (17). These distortions can result in discrepancies between the true anatomical position and its appearance on MR images, particularly at the edges of the field of view and in the presence of air–tissue interfaces (18). The magnitude of distortion varies by sequence, field strength, and choice of imaging parameters. The MRIdian system exhibits relatively low distortion due to its low field strength (19, 20). The Unity system, owing to its higher field strength, exhibits greater distortion but benefits from more robust gradient performance and improved signal-to-noise ratio (21). The International Commission on Radiation Units and Measurements (ICRU) recommends a geometric accuracy of 2 mm or better for MRI used in radiotherapy planning and emphasizes the need for routine QA to assess image fidelity (22). These recommendations are particularly relevant for stereotactic treatments (23), with sharp-dose gradients, and for intracranial cases, where millimeter-level accuracy is clinically consequential. Institutions adopting MRgRT should incorporate distortion assessment into their commissioning protocols and account for potential residual uncertainties when defining margins.

2.4 Emerging MRI functional-guided RT

MRI enables the non-invasive interrogation of some biological functions *in vivo* (24–27). Incorporating these capabilities into MR-guided radiotherapy remains an area of active investigation and represents a potential future direction for adaptive treatment. Functional MRI techniques, such as diffusion-weighted imaging (28), dynamic contrast-enhanced MRI (29, 30), and MR spectroscopy (31), offer the possibility of quantifying tumor biology in real time. These approaches are of particular interest in adaptive strategies where the dose may be modulated based on early treatment response. Diffusion imaging has received the most

attention due to its relatively short acquisition times and growing evidence of its correlation with cellular density and therapeutic response (32). Changes in apparent diffusion coefficient (ADC) during treatment have been proposed as an early biomarker of response and may support biologically driven adaptation (33). A recent clinical trial exemplifies this approach using mid-treatment ADC changes along with changes in perfusion to stratify patients with soft tissue sarcoma into dose escalation arms (34). These efforts are preliminary, and further validation is needed to establish the reproducibility and prognostic value of such biomarkers across disease sites and platforms. Nonetheless, the capacity of MRgRT to support quantitative imaging during the course of therapy positions it as a candidate platform for future biologically adaptive radiotherapy (35, 36). Challenges remain in sequence standardization, motion management during functional imaging, and integration with planning software, but these are areas of active investigation (37).

2.5 Summary

MR-guided radiotherapy has created new possibilities for daily adaptation, motion management, and soft tissue visualization. Its clinical use has expanded most rapidly in tumors where conventional image guidance has been limited and intra-fractional motion is substantial, particularly in pancreas and other gastrointestinal malignancies. MR-guided systems enable daily adaptation and motion management while offering a platform for future integration of biologically informed planning. As the field moves toward more precise and personalized therapy, MRgRT offers a platform that supports both current adaptation strategies and future functional imaging applications (38). Its full clinical impact will depend on continued technical refinement, validation of emerging biomarkers, and systematic incorporation into disease-specific treatment paradigms.

3 PET-guided RT: advancing precision in oncology

Positron emission tomography (PET) has revolutionized oncology by providing functional and molecular insights into tumor biology, complementing traditional anatomical imaging. The integration of PET with radiation therapy (RT) has led to the emergence of PET-guided RT, a sophisticated approach aimed at enhancing treatment precision, optimizing dose delivery, and improving patient outcomes (39, 40). This review explores the fundamental principles of PET imaging, its evolution, and diverse applications in radiation oncology, including target delineation, adaptive radiotherapy, and dose painting. It also delves into the development of integrated PET-Linac systems that enable real-time guidance. Furthermore, this addresses the current challenges and limitations in the clinical implementation of PET-guided RT, such as image quantification issues and logistical complexities, while highlighting promising future directions, including the role of artificial intelligence and novel radiotracers.

RT is a cornerstone of cancer treatment, aiming to deliver a precise dose of radiation to malignant cells while sparing surrounding healthy tissues. The evolution of RT has been driven by continuous advancements in imaging technologies, allowing for increasingly accurate tumor localization and treatment delivery. PET, a nuclear imaging technique, has emerged as a critical tool in oncology, offering unique functional insights by visualizing metabolic and molecular processes within the body. Unlike conventional imaging modalities, such as CT and MRI, which primarily provide anatomical information, PET can detect changes at the cellular level, potentially identifying disease in its earliest stages and assessing treatment response (41).

The integration of PET imaging into the RT workflow has paved the way for PET-guided RT, a paradigm shift toward more personalized and biologically informed cancer treatment. This review aims to provide a comprehensive overview of PET-guided RT, covering its underlying principles, clinical applications, technological advancements, current challenges, and prospects.

3.1 Principles of PET imaging and PET-guided radiotherapy

3.1.1 Biophysics of PET

Imaging PET operates on the principle of detecting radiation emitted from radiopharmaceuticals (also known as radiotracers) injected intravenously into a patient. These radiotracers are molecules labeled with a small amount of radioactive material, designed to accumulate in specific tissues or bind to particular proteins, such as those found in tumors or areas of inflammation. The process involves positron emission, annihilation, coincidence detection, and image reconstruction.

3.1.2 PET Radiotracers in oncology

The utility of PET in oncology is significantly enhanced by the availability of various radiotracers that target specific biological processes or cancer types. Fluorine-18 Fluorodeoxyglucose (^{18}F FDG) remains the primary, FDA-cleared radiotracer for SCINTIX BgRT in lung and bone tumors (42). It enables real-time PET-based treatment adaptation using tumor metabolism as a dynamic fiducial marker. Gallium-68/Fluorine-18 Prostate-Specific Membrane Antigen (Ga-68 PSMA/F-18 PSMA) has been shown to enable PET-guided treatment planning for prostate cancer metastases, including bone lesions, within RefleXion® 's BgRT workflow (43–45). It offers superior sensitivity for detecting recurrent disease and precise localization of metastatic lesions, even at low PSA levels. A brief BgRT tracer is summarized in Table 1, in addition to the tracers utilized in the clinic.

3.2 Clinical applications of PET-guided radiotherapy

PET has become increasingly important in oncology, offering molecular-level visualization and quantification of tumor characteristics that extend beyond conventional morphologic imaging (7). These data enable (1) precise delineation of radiotherapy (RT) target volumes; (2) ongoing assessment of treatment response and effectiveness; (3) prediction of failure patterns by identifying sub-regions at high risk of recurrence;

TABLE 1 A summary of the BgRT tracer and its utilization in the clinic.

Tracer (Radiopharmaceutical)	Indication /Tumor types	Role in BgRT
^{18}F-FDG	Lung and bone tumors (primary/metastatic)	Standard tracer for real-time PET-guided BgRT (FDA-cleared for SCINTIX BgRT in lung and bone cancers)
68Ga-PSMA	Prostate cancer with bone metastases	Feasibility demonstrated for SCINTIX BgRT treatment in metastatic prostate cancer
^{18}F-FES (FES = Fluoroestradiol)	ER+ breast cancer lesions	Pilot study comparing FES and FDG PET metrics for BgRT eligibility in breast cancer
64Cu-ATSM	Locally advanced rectal cancer	Studied for hypoxia-guided dose painting in BgRT-like planning (for Phase I feasibility planning only)
FAPI-based tracers (e.g., 68Ga-FAP-CHX, ^{18}F-NOTA-FAPI, 68Ga-FAPI-JH04)	Various epithelial cancers	Promising for tumor microenvironment–guided dose targeting; ongoing dosimetry and biodistribution studies
Nectin-4/αvβ3-targeting tracers (e.g., 68Ga-N188, ^{18}F-FAPI-RGD)	PD-L1/angiogenic tumors	Novel targets being tested via imaging trials; potential for BgRT guidance in immuno-oncology

and (4) individualized dose adaptation, allowing escalation or de-escalation, where clinically warranted.

3.2.1 Target delineation and treatment planning

PET imaging, often combined with CT (PET/CT) (46, 47) or MRI (PET/MRI) (48), provides comprehensive insights into tumor biology, improving diagnostic accuracy and enhancing patient positioning for RT. PET/CT has become a standard tool for cancer detection and staging, helping to identify tumors not visible on anatomical imaging and assessing tumor activity. PET/MRI, due to its high soft tissue contrast, offers unique advantages in T-staging of various cancers and is superior in finding lymph node and distant metastases compared to CT, MRI, and PET/CT.

3.2.2 Adaptive radiotherapy (ART)

Adaptive radiotherapy (ART) is a refined approach that adjusts treatment plans to dynamic anatomical and physiological shifts within a patient's body during therapy. Through frequent imaging, including PET-guided ART (49, 50), it allows specialists to visualize changes like tumor shrinkage or organ movement, enabling precise modification of the radiation dose.

There are three levels of adaptation. (a) Offline ART: Involves adjusting treatment plans between sessions based on periodic imaging assessments. (b) Online ART: Modifies treatment plans immediately before delivery using on-couch imaging, with advanced software and AI facilitating rapid adjustments to daily anatomical variations. (c) Real-Time ART: Continuously adjusts treatment delivery based on real-time changes, creating a "living" picture for immediate detection of changes and ensuring optimal targeting. RefleXion® X1 platform integrates PET imaging before and during treatment sessions, and it is the pioneer that can carry out the above-mentioned offline and real-time ART.

3.3 Integrated PET-linac systems

The integration of PET detectors with linear accelerators represents a technological advancement in RT (51, 52). The RefleXion® X1 system (53, 54), for example, is characterized by its split arc design, employing two 90° PET arcs to guide therapeutic radiation beams in real-time with sub-second latency. This system also incorporates an onboard fan-beam kVCT for anatomical capabilities, offering a hybrid platform for both biologic and anatomic guidance. The workflow for BgRT involves radiotracer injections and X1 PET scans as part of treatment planning, and immediately before and during each fraction for real-time guidance (55). This real-time guidance allows for improved motion management for dose delivery accuracy (56, 57). Figure 1 shows the major components of RefleXion® X1 PET/CT linac.

3.4 Challenges and limitations

3.4.1 Image quality and quantification spatial resolution and noise

Despite the significant advancements, several challenges and limitations persist in the widespread clinical implementation of PET-guided RT.

Image Quality and Quantification Spatial Resolution and Noise: PET images often suffer from low spatial resolution and high noise characteristics, which can make accurate delineation of target regions problematic. The spatial resolution of PET systems is typically limited to around 5 mm.

Image Segmentation: Accurately segmenting tumors from blurred and noisy functional PET images is a difficult issue for PET-based treatment planning. While various segmentation approaches exist (e.g., thresholding, edge detection, and deep learning), their reliable performance on clinically relevant tasks requires objective, task-based evaluation. Inaccuracies can arise from variations in biological processes governing tracer uptake and physical/acquisition phenomena.

Quantitative Accuracy: Fundamental trade-offs between resolution and noise, along with challenges in scatter correction and attenuation correction, affect the quantitative accuracy of PET measurements.

3.4.2 Specificity of radiopharmaceuticals

While radiotracers like 18F-FDG are highly sensitive to many cancer types, they are not always specific to malignant disease,

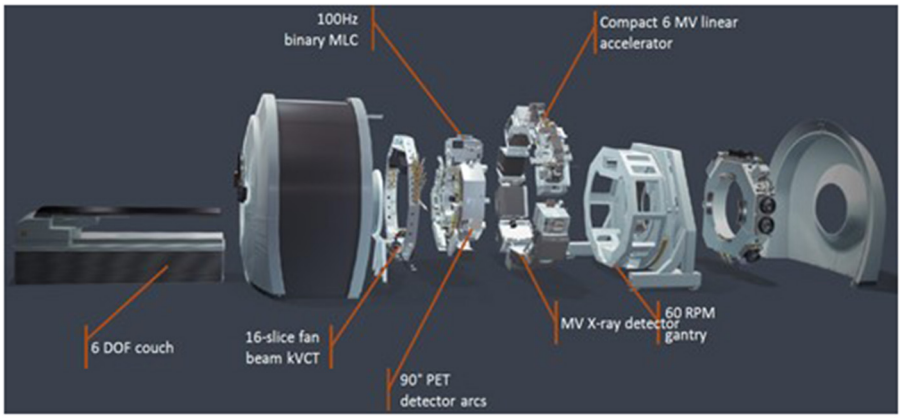

FIGURE 1
Major components: KVCT, PET detector arcs/MLC, MV, and 60 rpm gantry (Courtesy of RefleXion® Medical).

as uptake can occur in other processes with increased glucose turnover, such as infection and inflammation. This can hamper the differentiation between inflammatory changes and neoplastic tissue, or between benign lesions and well-differentiated malignant lesions with low FDG avidity. Although more specific tracers like Ga-68 PSMA have been developed, sources of false positive or negative findings can still exist.

While radiotracers like ^{18}F-FDG are highly sensitive to many cancer types, they are not always specific to malignant disease, as uptake can occur in other processes with increased glucose turnover, such as infection and inflammation. This can hamper the differentiation between inflammatory changes and neoplastic tissue, or between benign lesions and well-differentiated malignant lesions with low FDG avidity. Although more specific tracers like Ga-68 PSMA have been developed, sources of false positive or negative findings can still exist.

The involvement of radiopharmaceuticals in PET-guided radiotherapy and the short half-life of many radiopharmaceuticals, particularly ^{18}F-FDG (110 min), necessitates that cyclotrons be located close to the radiation oncology department. The increased patient treatment time and complexity of the entire BgRT workflow require extra labor forces and seamless coordination among physicians, nurses, nuclear medicine technicians, therapists, and others. Regulation and guidelines, such as task group reports from the American Association of Physicists in Medicine (AAPM), are under development and improvement (58).

3.5 Future directions

The field of PET-guided RT is continuously evolving, with several promising avenues for future development:

- Novel radiotracers: Research is expanding to include available and novel tracers targeting tumor metabolism, hypoxia, vascularity, and proliferation, enabling more precise dose painting and adaptive strategies.
- Artificial Intelligence (AI) and Machine Learning (ML): In PET-guided adaptive radiotherapy, artificial intelligence and machine learning are being applied through several complementary approaches that directly address clinical bottlenecks. Deep learning models, such as 3D U-Net (59), V-Net (60), and residual networks, integrate PET's metabolic data with CT's anatomical details to generate accurate tumor and organ-at-risk contours, reducing the variability and time associated with manual delineation while overcoming challenges of physiologic uptake and heterogeneous tumor activity (61). Radiomics-based methods further enhance treatment personalization by extracting quantitative texture and wavelet features from PET scans to predict response and guide adaptation, including delta-radiomics analyses that track metabolic changes during treatment (62). Together, these AI tools aim to transform PET-based radiotherapy from a labor-intensive, subjective process into a standardized and adaptive workflow that supports real-time clinical decision-making.
- Multiomics Integration: Combining PET imaging with genomic, proteomic, and other omics data to provide more comprehensive biological insights for tailored treatment strategies.
- Polymetastatic Patient Treatment: The ambition to extend BgRT to polymetastatic patients in the future, potentially in conjunction with systemic therapy, represents a significant area of growth.
- Clinical Validation: Standardized segmentation protocols and prospective clinical trials are needed to validate clinical benefits and establish PET-guided RT in routine care.

3.6 Summary

PET-guided RT represents a significant leap forward in precision oncology, moving beyond anatomical targeting to incorporate real-time biological information for optimized treatment delivery. By leveraging the functional insights provided by PET imaging and advanced radiotracers, clinicians can achieve more accurate tumor delineation, implement adaptive treatment strategies, and explore dose painting techniques to personalize

therapy. While challenges related to image quantification, radiotracer specificity, and logistical complexities remain, ongoing technological advancements, particularly in integrated PET-linac systems and the application of AI, are poised to overcome these hurdles. The continued evolution of PET-guided RT holds immense promise for improving disease control, minimizing toxicity to healthy tissues, and ultimately enhancing the quality of life for cancer patients.

4 Stereoscopic imaging and surface guidance techniques for central nervous system tumors

Stereoscopic imaging represents a paradigm shift in precision radiotherapy for central nervous system (CNS) tumors, enabling submillimeter positioning accuracy through dual oblique X-ray imaging systems. Unlike conventional single-plane imaging, stereoscopic techniques provide target localization by triangulating anatomical landmarks from two simultaneously acquired oblique projections. Commercially available systems currently include ExacTrac (Brainlab, Munich, Germany), SyncTraX (Shimadzu, Kyoto, Japan), and CyberKnife (Accuray, Sunnyvale, CA, USA) (63). Among these systems, ExacTrac is the most used as an add-on imaging system to a medical linear accelerator. Stereoscopic imaging has become particularly crucial for intracranial stereotactic radiosurgery (SRS) and spinal stereotactic body RT (SBRT), where high-dose single or hypo-fractionated treatments demand exceptional geometric precision to accurately deliver therapeutic doses to lesions while sparing adjacent critical structures (64–66).

4.1 Technical principles and system architecture

The fundamental architecture of the ExacTrac imaging system consists of two kilovoltage (kV) X-ray sources recessed into the treatment room floor and the corresponding ceiling-mounted amorphous silicon flat panel detectors positioned in an oblique configuration (67). Other stereoscopic imaging systems use some variation of this geometric arrangement. The stereoscopic imaging system is calibrated such that its imaging coordinates are accurately matched to the linac's coordinates. This oblique geometric arrangement enables the acquisition of two instantaneous stereoscopic images without source-detector repositioning, facilitating continuous monitoring throughout treatment delivery, even at non-coplanar patient couch angles where conventional linac-based onboard imaging systems face geometric limitations and the risk of gantry-couch collision.

The dual X-ray generator configuration produces high-resolution stereoscopic images with adjustable kilovoltage, and the tube current parameters are optimized for different anatomical structures and imaging requirements. Typically, 90 kVp and 10 mAs are used for cranial applications, and 120 kVp and 20 mAs are used for spinal applications, though these parameters can be adjusted according to patient size and anatomy. Advancements such as higher heat capacity X-ray tubes support more frequent automated imaging sequences, while enhanced soft tissue contrast and improved readout speeds minimize motion blurring artifacts. Modern systems incorporate larger imaging panels that visualize extended anatomical regions, improving image interpretation and anatomical orientation. Advanced image fusion algorithms match acquired stereoscopic projections with digitally reconstructed radiographs (DRRs) from planning CT datasets, enabling precise six-degrees-of-freedom (6DOF) patient positioning corrections (67).

4.2 Evolution from infrared tracking to thermal surface guidance

Early ExacTrac systems utilized infrared-reflective spheres mounted on patient positioning arrays: a cranial matrix integrated with a face mask or reflective markers attached directly to the mask for intracranial treatments and a reference U-shaped array mounted on the couch sidebar for extracranial applications. Reflective markers can also be directly attached to other immobilization devices or the patient's skin. While effective, this approach required rigid body assumptions and was limited to tracking discrete marker points rather than comprehensive patient surface geometry. The accuracy of the infrared tracking depends on the quality and stability of the reflective markers, which fade with time. The positioning array served merely as a surrogate for patient motion, and its movement could not accurately reflect the patient's actual anatomical displacement. Additionally, the mechanical connection of the U-shaped array to the couch sidebar was inherently unstable, with potential for disconnection or displacement during treatment delivery, which could compromise motion monitoring reliability.

The advancement to the ExacTrac Dynamic system implements markerless surface tracking through 4D thermal camera technology. This system correlates patient heat signatures with reconstructed three-dimensional surface structures, acquiring approximately 300,000 surface points matched to thermal signatures. Thermal surface guidance provides comprehensive patient surface monitoring that eliminates the need for positioning arrays while maintaining submillimeter accuracy.

4.3 Clinical implementation in CNS stereotactic treatments

4.3.1 Initial patient setup and positioning

Patient positioning begins with the placement of the patient on the treatment couch using appropriate immobilization devices. Surface/thermal imaging provides rough initial alignment to the planning CT-generated patient surface contour. After initial stereoscopic X-ray images are acquired, suggested shifts are calculated automatically by matching the X-ray images to the reference DRRs generated from the CT simulation dataset. The calculated shifts will be sent to the 6DOF robotic couch to achieve optimal patient alignment. When positional deviations exceed system correction capabilities, manual patient repositioning is required before re-imaging. This iterative process continues

until all translational and rotational parameters fall within preset tolerance thresholds, which are institution-specific and may vary based on treatment site and clinical experience. For example, tolerances of 0.5 mm/0.5° are commonly used for cranial applications, while spinal treatments may require larger tolerances (e.g., 0.7 mm/0.8°) due to the inherent challenges of reproducing exact spinal curvature and the difficulty of achieving submillimeter precision for vertebral positioning.

4.3.2 Additional verification of positioning accuracy with onboard imagers

Images acquired using the linac onboard imaging system can serve as secondary confirmation of patient positioning accuracy. For cranial cases, a kV/kV image pair acquired at couch angles near zero degrees can be used since it provides optimal anatomical visualization for skull-based registration. Spinal treatments utilize a more comprehensive verification imaging approach, incorporating kV/MV image pairs alongside cone-beam computed tomography (CBCT) to improve vertebral anatomy visualization and account for potential differences in spinal curvature between simulation and treatment setup. This secondary imaging confirmation is particularly crucial for spinal treatments, where vertebral bodies may appear similar on stereoscopic projections, and can reduce the risk of patient setup on incorrect vertebral levels. CBCT imaging allows careful review of the spinal cord canal position relative to the target, providing critical safety verification. In addition, CBCT or kV/MV imaging can also help visualize anatomical changes and patient weight loss/gain. While many centers do not routinely use secondary imaging with ExacTrac, this additional verification step can prevent targeting errors and enhance treatment safety. Deviations detected by onboard imaging are not used to adjust patient positioning. Usually, for CNS cases, only ExacTrac stereoscopic X-ray images are used to calculate and apply couch shifts for patient repositioning. However, this practice is institution-specific and may vary based on treatment site and clinical experience.

4.3.3 Multi-disciplinary image review process

All acquired images undergo systematic review by qualified medical physicists and radiation oncologists to ensure treatment accuracy and patient safety (64, 65). This verification process includes assessment of daily anatomical variation and image registration quality, evaluation of target positioning accuracy, and confirmation of critical structure avoidance. The radiation oncologist provides final approval through the Record and Verify system, while the medical physicist independently verifies all beam parameters and delivery settings before treatment initiation.

4.3.4 Pre-beam and intra-fractional verification protocol

Prior to the delivery of each treatment beam, verification of stereoscopic images is acquired to confirm the maintained patient alignment. When deviations exceed tolerance thresholds but remain within treatment system correction capabilities, calculated shifts are applied, followed by acquisition of confirmatory stereoscopic images. Only after verifying that all positioning parameters are within preset tolerances can treatment beam delivery start. Once positioning verification is achieved, new baseline thermal surface images are created using the 4D thermal camera system, establishing the reference patient surface geometry for subsequent motion monitoring during the selected treatment beam delivery. Figures 2a, b illustrate the verification of stereoscopic images for a cranial and a spinal case, respectively.

4.3.5 Real-time motion monitoring during treatment

Throughout the treatment, continuous thermal surface tracking monitors patient motion in real time. The user defines specific regions of interest for surface tracking based on treatment site and clinical requirements. When patient motion exceeds preset tolerances within these monitored regions, automatic beam-hold functionality is immediately triggered to interrupt the treatment delivery. Surface tracking tolerances of 2.0 mm/2.0° are commonly used for cranial applications. However, for spinal treatments, the threshold may be relaxed since surface tracking is affected by respiratory motion, while the target vertebral structures themselves do not move with respiration. This respiratory artifact may require larger motion tolerances (>1 cm) before beam gating is triggered, limiting the clinical utility of surface monitoring for spinal cases. ExacTrac systems also allow automated X-ray triggering during treatment based on predefined gantry angles or monitor unit intervals, although this feature may not be utilized in all clinical scenarios due to practical considerations, such as limited arc ranges used for certain spine treatments. This continuous monitoring capability ensures maintained positioning accuracy throughout the entire treatment fraction, particularly crucial for lengthy stereotactic procedures where patient comfort and positioning stability may become challenging. Figures 3a, b illustrate the real-time surface motion tracking alongside the pre-beam verification stereoscopic X-ray images for a cranial and a spinal case, respectively.

4.4 Current limitations and future directions

Despite significant advances, stereoscopic imaging maintains inherent limitations as a projection-based technique. Two-dimensional projections may obscure anatomical details compared to volumetric imaging modalities, and the rigid body assumption underlying motion tracking may not capture subtle non-rigid patient movements. Thermal surface tracking may not accurately represent the motion of internal organs and can be affected by environmental factors, such as room temperature variations, air conditioning drafts, patient perspiration, and variations in patient skin temperature, which may alter thermal signatures and compromise tracking accuracy. Patient comfort considerations, particularly with tight-fitting immobilization masks, remain challenging for extended treatment sessions, although different types of masks (basic, open-face, and stereotactic) are available to meet different clinical needs.

Future developments might focus on enhanced thermal surface tracking algorithms that are more robust to environmental and physiological variations, improved soft tissue contrast capabilities,

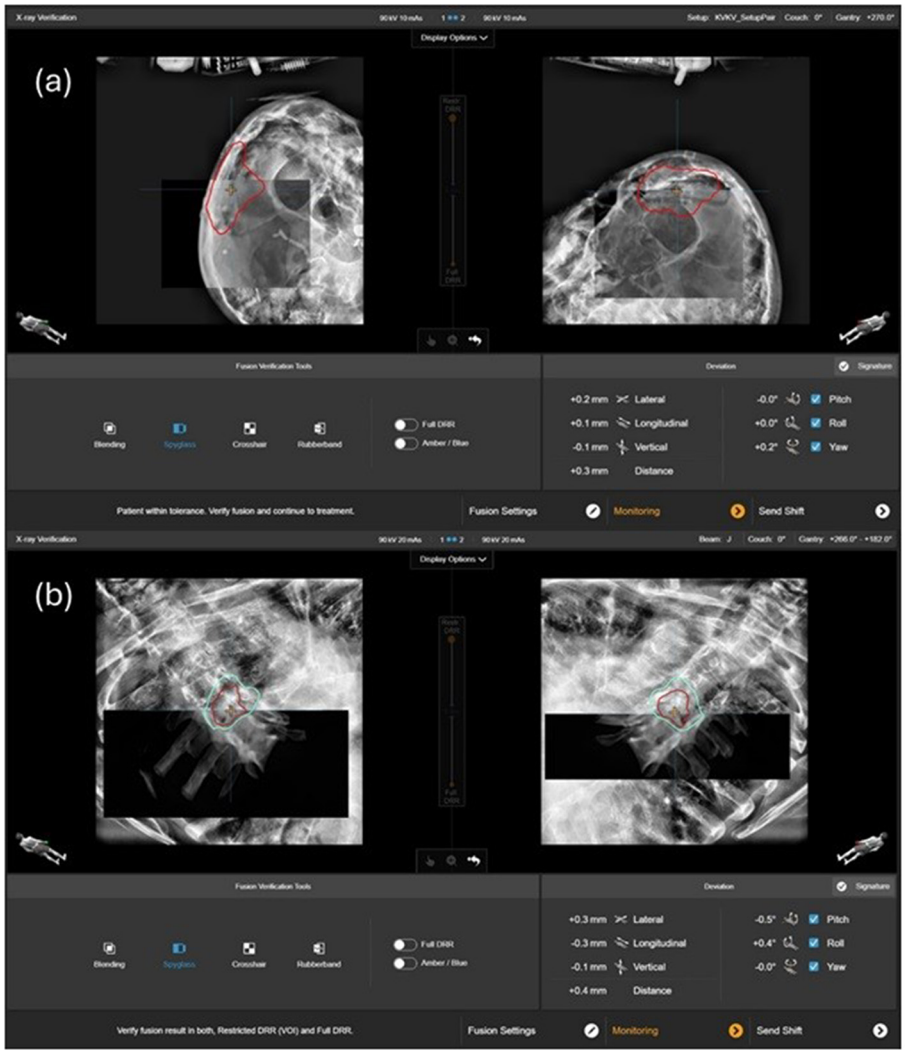

FIGURE 2
X-ray verification of stereoscopic images for a cranial **(a)** and a spinal **(b)** case.

and integration with X-ray and/or magnetic resonance-guided volumetric imaging platforms. Advanced motion prediction algorithms and artificial intelligence-enhanced image fusion represent promising avenues for further improving positioning accuracy and workflow efficiency.

4.5 Summary

In summary, stereoscopic imaging and surface guidance techniques have fundamentally transformed precision radiotherapy for CNS tumors, enabling submillimeter accuracy essential for safe dose escalation in SRS/SBRT applications. The evolution from purely X-ray-based imaging systems to hybrid thermal-surface guidance platforms demonstrates continued technological advancement toward optimal patient positioning and motion management. These innovations directly support the clinical goal of maximizing tumor control while minimizing normal tissue toxicity, particularly crucial for treating lesions adjacent to critical neurological structures.

5 Online adaptive radiotherapy using Ethos

The Ethos linear accelerator (Figure 4) is an online adaptive radiotherapy (OART) system with a ring-shaped gantry and an AI platform. As the FDA-cleared CBCT-guided OART device, Ethos enables high-quality, fast CBCT acquisition and on-couch treatment planning focused on patients' daily anatomical changes.

Ethos utilizes a single energy of 6 MV flattening filter free (FFF) beam and features a dual-layer multi-leaf collimator (MLC) design with staggered leaves, giving an effective 5 mm MLC thickness. The dosimetric leaf gap (DLG) is in the range of tenths of a millimeter, and the leaf transmission coefficient is around 0.01%, which is much smaller than the single-layer MLC design in a conventional C-arm linac. The maximum field size is 28 cm with the full MLC travel range of 28 cm. The bore size is 1 m in diameter, and the couch has three degrees of freedom (DOF). The closed bore and compact design allow for four revolutions per minute (RPM), enabling fast treatment and minimal collision

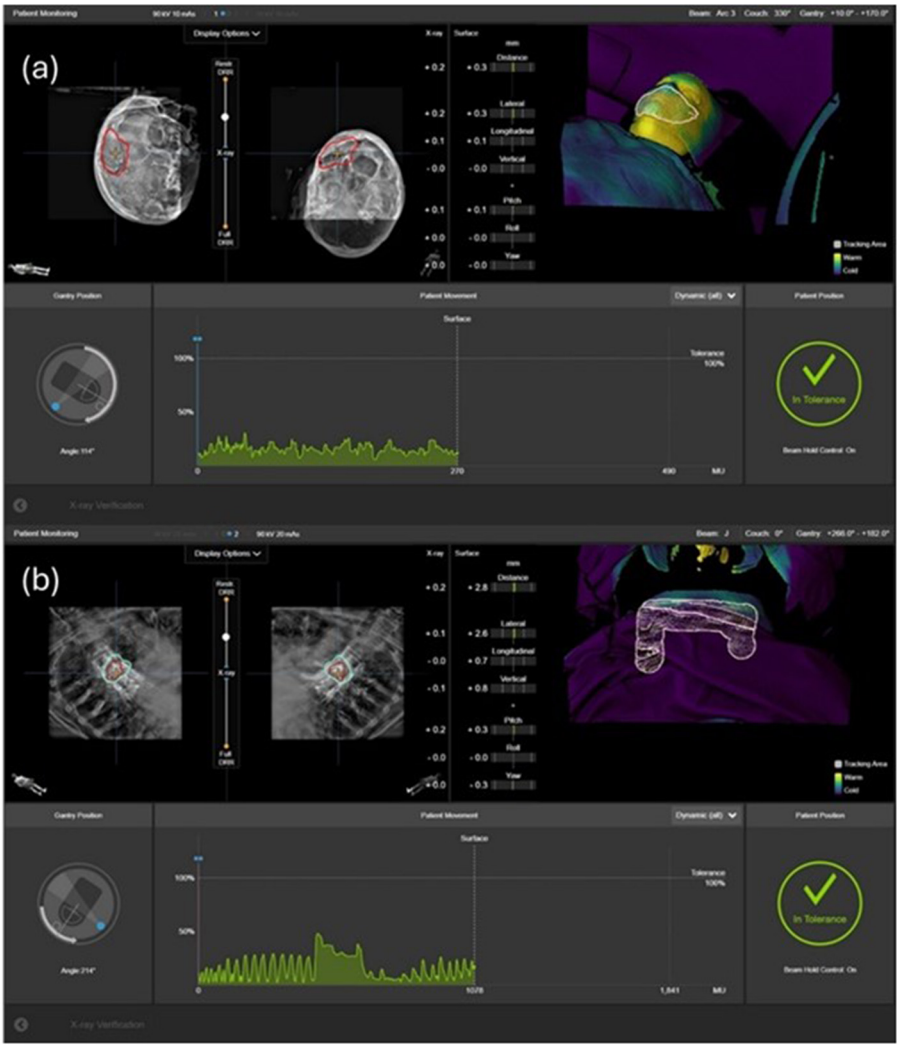

FIGURE 3
Real-time surface motion tracking alongside the pre-beam verification stereoscopic X-ray images for a cranial **(a)** and a spinal **(b)** case.

risk (68). Compared to the conventional C-arm linac, Ethos has no field light, no optical distance indicator (ODI), and no laser marking at the treatment isocenter. Instead, it relies on external lasers for patient alignment and automated shifts in the software. Compared to conventional kV CBCT imaging, Ethos HyperSight provides metal artifact reduction, more accurate HU values, fast acquisition, and superior imaging quality with an extra-large kV imager (~70 cm) and a high-precision iterative CBCT reconstruction algorithm.

Furthermore, Ethos has a dedicated treatment planning system with a pre-configured beam model, an AI-driven automatic contouring, and a plan optimization algorithm called the intelligent optimization engine (IOE) (69). Some Ethos linacs are also equipped with a surface-guided imaging system for motion management and a Mobius quality assurance (QA) system for gamma analysis. All those features in the Ethos platform enable the efficient and accurate on-couch patient adaptive radiotherapy workflows.

5.1 Advanced imaging technology of Ethos OART

In traditional adaptive workflows, such as head and neck re-planning, subsequent CT is acquired after noticeable anatomical changes are observed in the daily CBCT image. Different treatment plans based on patient anatomy changes are created when patients are off-the-couch. Subsequently, daily CBCT images are obtained prior to treatment delivery to verify patient positioning for new plans. This is called image-guided radiotherapy (IGRT) or offline/off-the-couch adaptive radiotherapy. In contrast, Ethos online adaptive process starts with the patient's daily CBCT imaging to visualize anatomy change, followed by recontouring of organs at risk (OAR) and targets, and eventually planning optimization based on that day's patient anatomy while the patient is on the couch. The fundamental difference between the Ethos and traditional RT workflows lies in the timing of CT acquisition for treatment planning. The Ethos system generates adaptive plans based on daily CT scans obtained on each treatment day, whereas

FIGURE 4
The all-in-one Ethos LINAC system, which can be used for CT-simulation, CBCT imaging, AI contours, GPU-based planning, surface guided imaging, QA, and treatment delivery.

traditional adaptive RT relies on CT scans acquired weeks before new adaptive treatment begins. Theoretically, this allows for better OAR sparing and potential target dose escalation than the non-adaptive workflow because a new plan is created every day based on the evolving spatial relationship between tumor and normal tissue. Many body sites can benefit from OART, such as the male and female pelvic region (70–72), the upper abdomen region (73), breast cancer (74, 75), and lung cancer (76) due to variable organ volume or the daily motion. CBCT adaptive therapy is also useful for areas of anticipated weight loss, such as the head and neck (77). A recent study demonstrated that compared to traditional adaptive workflows, the Ethos OART system enables feasible daily adaptive treatments with reduced margins while enhancing target coverage and reducing OAR doses by up to 12 Gy for head and neck patients with oropharynx and larynx cancers (78).

The HyperSight CBCT system has enhanced hardware and software components that contribute to improved scan quality and contour accuracy. The panel utilizes cesium iodide (CsI) scintillator material for higher conversion efficiency and fast readout. Compared to the prior generation of imaging panel, the HyperSight system has twice the active detector area (86 cm × 43 cm) with no lateral offset. This allows for a full-fan trajectory to be used, enabling an image acquisition time of 6 s. This faster scan time has been shown to provide reduced motion artifacts on the planning image (79). Since a plan is created based on daily contours, visualization of targets and OARs is critical to optimizing, calculating, and delivering the plan accurately. Prior to the introduction of HyperSight CBCT, the plan was calculated on a synthetic CT that mapped Hounsfield units (HU) from the simulation CT to the daily CBCT with deformable image registration. With the introduction of HyperSight on Ethos version 2.0, plans may be calculated directly on CBCT images (79). Reconstruction of CBCT images can be performed with the analytical Feldkamp-Davis-Kress algorithm or the iterative CBCT algorithm (iCBCT). An improved metal artifact reduction reconstruction algorithm, iCBCT Acuros MAR, is also included as a reconstruction mode for kV CBCT. Studies have shown that HyperSight CBCT image quality and HU accuracy are comparable to those of CT simulation images, suggesting the utility of the image data for direct dose calculation in adaptive workflows (80). Figure 5 demonstrates a CBCT-based prostate SBRT, where the adapted plan is selected over the scheduled plan for treatment because the target coverage is superior based on the specific bladder and rectal filling prior to treatment on that day.

One promise of direct dose calculation on CBCT is the use of the Ethos linac for simulation-plan-treatment workflows. This CT-simulation free workflow has been suggested for abdominal (81) and spine SBRT (82). By utilizing library plans or diagnostic images or even phantom plans as a "pre-plan," we can acquire the patient's CBCT image and create an adaptive plan on the day of treatment. Therefore, there is a reduction in planning time, with some sessions involving only a single visit (83).

5.2 Planning and workflow considerations for online adaptive radiotherapy

Although most patients theoretically can benefit from adaptive radiotherapy, judicious use of planning and machine time resources is important. Adaptive treatments require extended time on the

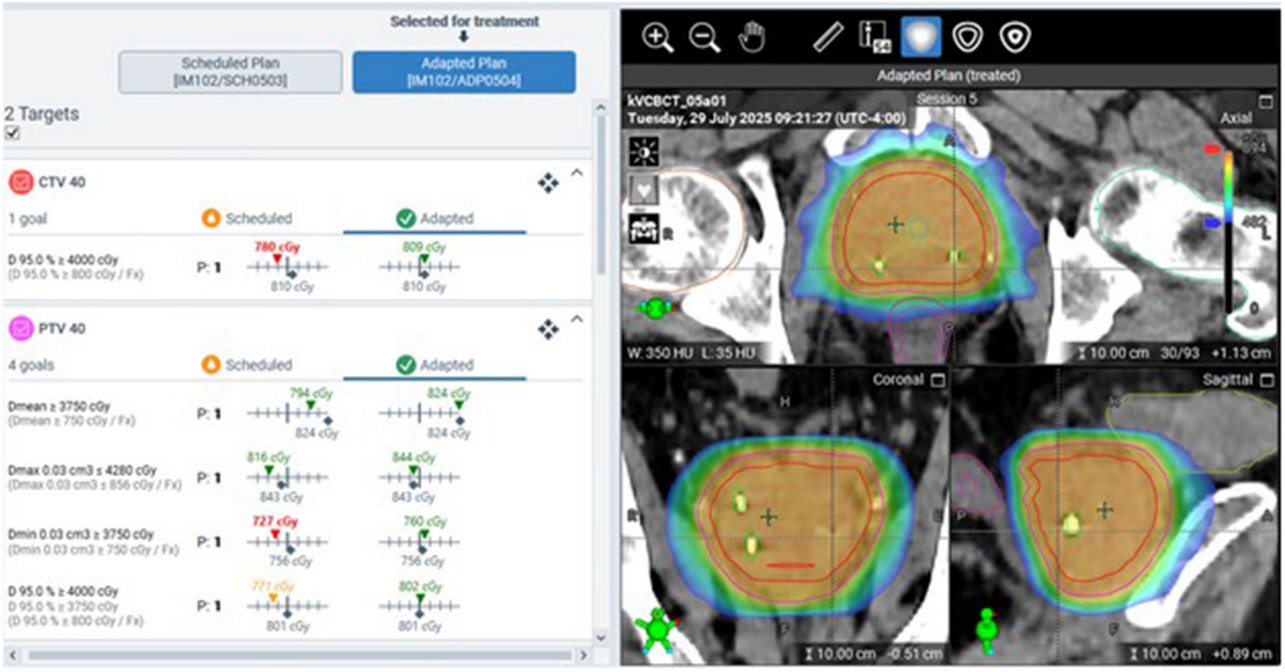

FIGURE 5
The adaptive plan is selected for treatment based on that day's CBCT. Fiducial markers are visible and used as the landmark for positioning verification during the on-couch adaptive process.

machine to allow for contour generation and plan review, leading to potential patient discomfort and movement. In addition, there are additional planning considerations in the Ethos system that require additional dosimetry or physics FTE (84). Workflows vary by clinic, with some having dosimetrists in a traditional role and others utilizing physicists for all Ethos planning (85). During planning, physics and dosimetry must consider visualization of the anatomy at the machine, accuracy of reference targets and structures with their derivations, and the robustness of planning goals to changes in daily patient anatomy. Planning images from simulation should ideally be free of contrast to avoid any issues with synthetic CT (86) or image registration and large enough to cover the anatomy of interest, but small enough for efficient optimization during planning. The Ethos system utilizes daily auto-contouring of patient anatomy to help aid in on-session planning speed, so accurate delineation of these organs at the time of initial planning is important for accurate deformable image registration and target delineation at the time of treatment.

The Ethos intelligent optimization engine (IOE) translates clinical goals input by the planner into planning optimization objectives in a piecewise continuous "quality" function (87). It then iterates the quality function on a priority-quality plane until a goal point is met and does not contribute to lower priority functions. In practice, clinical goals are grouped into priorities, the order of which influences this optimization process greatly. Due to this, the planning goals and their order need to be carefully considered, both on the planning image from simulation CT and with foresight on potential anatomical changes on the CBCT. With robust planning templates, online adaptive radiotherapy has been shown to have dosimetric benefits in several sites, such as breast (75), prostate (88), and lung (80). For example, it has been reported that the adaptive plan was the preference in 95% of fractions for prostate radiotherapy. Online adaptive radiotherapy may allow us to reduce the target margin while maintaining the tumor coverage and sparing critical organs nearby (88).

5.3 Summary

In summary, the high-quality CBCT imaging-guided online adaptive radiotherapy represents a unique opportunity for delivering customized plans based on daily patient anatomy. It uses high-performance kV imaging to visualize a patient's daily changing relationship between tumor and OAR, which is integrated with efficient contouring, intelligent optimization, and precise dose calculation. Therefore, kV CBCT-based online adaptive radiotherapy has great clinical potential for dose escalation in the tumor to enhance the local control, while sparing the critical structures or lowering the toxicity to OAR with reduced target margins.

6 Image synthesis in RT

Generative deep-learning-based image synthesis is an increasingly active area of research in radiation oncology. These techniques can create one imaging modality from another, offering new ways to streamline clinical workflows. CT remains the standard for simulation and treatment planning (89). CT volumes are reconstructed by inverting measurements of the linear attenuation coefficient (μ) collected at multiple projection angles

with the Radon transform (90). As voxel values map directly to electron density, CT is indispensable for accurate dose calculation.

Other modalities, such as MRI, PET, and ultrasound, provide complementary information that can guide accurate dose delivery. However, acquiring these additional scans is often time-consuming, costly, or—under some circumstances—simply impractical for clinicians and patients. Recent advances in deep learning mitigate these barriers by enabling high-quality cross-modal image synthesis, thereby reducing the need for multiple acquisitions and opening new avenues for truly personalized RT.

6.1 Deep learning networks in medical images

Deep learning (DL)—a branch of machine learning built on multi-layered artificial neural networks—now underpins many techniques for generating synthetic images in RT. Recent review articles (91–95) survey the principal DL architectures applied in this field, with convolutional neural networks (CNNs), generative adversarial networks (GANs), and diffusion-based models emerging as the most widely used.

CNNs are a class of deep-learning models inspired by the hierarchical organization of neurons in the human visual cortex (96–98). Purpose-built for grid-like data, they have become ubiquitous in medical imaging applications (99–102). Each convolutional layer deploys a bank of learnable filters that scan the input, capturing local patterns—such as edges and textures—while sharing parameters across the field of view to curb model complexity and ensure translation invariance. Stacking multiple convolutional layers with non-linear activation yields progressively abstract, hierarchical feature representations (103–105). Pooling (106) and other down-sampling operations (107) further condense contextual information, whereas random dropout (108) regularizes the network and mitigates overfitting. By learning features directly from data rather than relying on hand-crafted descriptors, CNNs have become the backbone of image analysis and synthesis tasks in RT. One of the most well-known CNN models is the U-shaped net (U-Net) proposed by Ronneberger et al. (59) (Figure 6). One important modification of the U-Net is direct skip connections between the encoder and the decoder. The U-Net does not have any fully connected layers. Instead, it only uses the valid part of each convolution, which allows the network to propagate context information to the up-sampling layers.

GAN was introduced by Goodfellow et al. (109). Compared to the image generated by the CNNs, it further improves the image quality. GANs learn to synthesize realistic data through a game-theoretic contest between two neural networks: a generator (G) and a discriminator (D). The generator tries to produce realistic images that resemble the real training distribution, while the discriminator simultaneously learns to distinguish generated images from genuine ones. During training, each network improves in response to the other's progress: the generator refines its outputs to fool the discriminator, and the discriminator improves its ability to detect fake images, creating a dynamic "adversarial" loop that gradually drives the generator toward high-fidelity outputs. This framework has enabled breakthroughs in photorealistic image synthesis. Derivative networks, such as Conditional GANs (110, 111) , CycleGAN (112, 113), and StyleGAN (114, 115), extend the idea to guided generation, unpaired domain translation, and finely controllable synthesis, making GANs one of the most versatile and influential tools in modern machine learning.

Another category of generative model is the diffusion model, which was first introduced in 2015 by Sohl-Dickstein et al. (116). Diffusion models generate images by gradually contaminating training data with Gaussian noise and then learning to reverse this process iteratively. Instead of learning the image itself, the model is trained to learn the contaminated noise, which effectively denoises the dataset into realistic samples. Their iterative nature yields high-fidelity detail and inherent diversity, making them more robust to noise contamination in the training dataset. Recent studies show that denoising diffusion probabilistic models can synthesize 3-D MRI and CT volumes with realistic image quality (117, 118). Emerging "foundation" approaches such as MedDiff-FM aim to unify multiple tasks—synthesis, reconstruction, and denoising—within a single large diffusion backbone, pointing toward versatile, privacy-preserving generative pipelines across modalities (119). These advances collectively position diffusion models as a core engine for safe, scalable medical image synthesis.

6.2 Application of image synthesis in RT

Substantial progress has been achieved in image synthesis applications for RT. Notable examples include MRI to synthetic CT (sCT) conversion (120–125) and synthetic MRI (sMRI) (126–134), synthetic PET (sPET) (127, 135, 136), and CBCT to sCT conversion (137, 138).

In recent years, interest in MRI-guided RT has grown substantially within the radiation oncology community. Compared with CT, MRI offers superior soft-tissue contrast and exposes patients to no additional ionizing radiation. This advantage allows more precise delineation of tumors and organs at risk, such as the bowel and optic nerves. MRI signal intensity, however, depends on sequence-specific parameters—e.g., repetition time (TR), echo time (TE), flip angle, and inversion time (TI) (139)—and therefore lacks a direct, one-to-one correlation with electron density. As a result, MRI alone cannot support accurate dose calculation. To address this limitation, generative AI models are now used to synthesize sCT images from MRI data, making MRI-only treatment planning feasible (140, 141). Several studies have quantified the dosimetric differences between sCT and the reference planning CT (125, 142–145). In photon therapy, the mean dose deviation is approximately 1% (142). By contrast, proton therapy is more sensitive: reported proton-beam range shifts reach 5.6 mm in liver cancer (125) and 7.5 mm in prostate cancer (145), which can translate into clinically significant dose errors.

Synthetic MRI leverages advanced machine learning models—most commonly CNNs (96), GANs (109), or diffusion models (116)—to rapidly generate high fidelity MR-like images from either undersampled k-space data or alternative inputs such as CT, quantitative maps, or single contrast scans (127, 146). By learning the complex, non-linear relationship between tissue properties and MR signal formation, these models can synthesize multiple

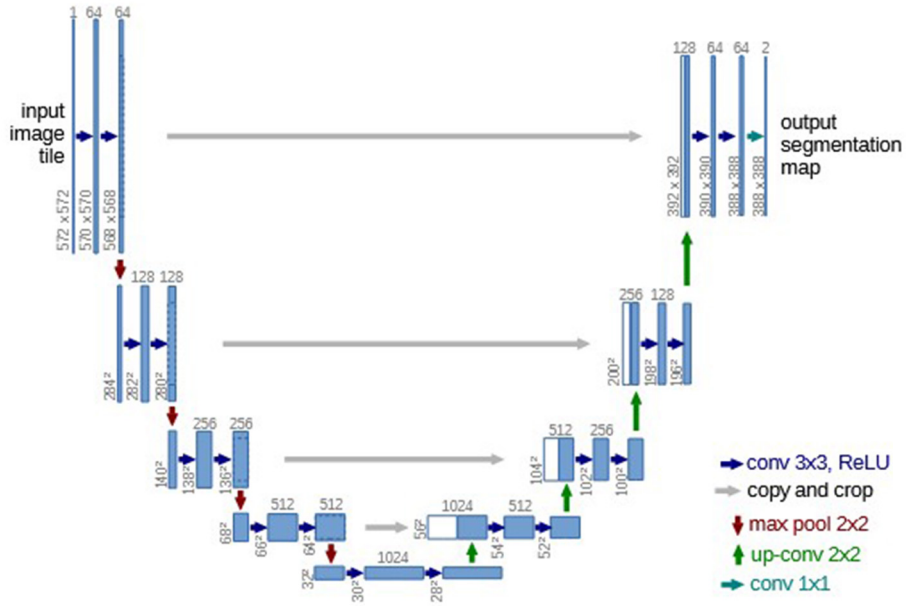

FIGURE 6
Architecture of the U-Net. Reproduced with permission from Ronneberger et al. (59).

contrasts (e.g., T1, T2, or FLAIR weighted images) (147) in a single inference step, standardize intensity across patients, and even predict quantitative relaxation parameters (148). The result is a dramatic reduction in acquisition time and patient motion artifacts, more consistent image quality, and the potential to extend MRI-level soft tissue visualization to scenarios where full MRI is impractical—such as RT workflows that rely primarily on CT (149). As the techniques mature, synthetic MRI is poised to streamline imaging protocols, lower costs, and enable new precision medicine applications ranging from adaptive treatment planning to longitudinal disease monitoring.

PET is already a powerful tool in radiation oncology, which provides functional information about the metabolism of the tissues, but practical and technical barriers keep it from being used whenever it would add value. Synthetic PET imaging is driven by deep learning generators that learn to translate structural or low-count inputs into realistic tracer uptake maps (150). The field began with 3-D U-Nets that capture the global, non-linear correlation between whole-brain MRI volumes and FDG activity (151) and quickly moved to conditional GANs—such as the globally and locally aware GLA GAN (152)—which combine adversarial, pixel-wise, and structural similarity index measure (SSIM) losses so both coarse context and fine lesion details are recovered. Further refinements include frequency-aware U-Nets (153) that process low- and high-frequency bands separately to sharpen edges and textures, and bidirectional or reversible GANs (154, 155) that embed PET semantics in a shared latent space to enforce cycle consistency and boost perceptual fidelity. More recent architectures add Transformer attention to fuse multi-modal MRI/PET cues and model long-range dependencies (156) or adopt diffusion models that iteratively denoise random noise under MRI or textual guidance to yield high-fidelity standardized uptake values (SUVs) (157). These innovations underpin applications such as synthesizing full dose scans from low dose PET or from MRI alone (127, 158, 159), mitigating noise while preserving quantitative accuracy and thereby reducing radiation burden for patients.

CBCT acquired on the treatment machine employs a cone-shaped beam and a flat panel detector; scatter from the whole patient therefore overwhelms the signal, creating streaking, cupping, and other artifacts that corrupt HU (160) accuracy and compromise dose calculation (161). Deep learning pipelines now correct these limitations by translating CBCT into synthetic CT (sCT) volumes with calibrated HUs. Two complementary strategies dominate: projection domain correction (162), in which CNN or GAN models clean hundreds of 2 D x ray projections before reconstruction—leveraging the rich (>300) projection set to converge quickly and bypass many image domain artifacts—and image domain translation (163), where architectures such as U-Net (1), CycleGAN, (112, 113) or attention GAN (137) act directly on the reconstructed CBCT to recover CT-like contrast and bone detail. Projection domain networks can even be trained on non-anthropomorphic phantom projections to learn scatter patterns, enhancing generalizability, while many image domain studies rigidly register CBCT and planning CT to minimize geometric mismatch during training. By restoring HU fidelity, these DL-based CBCT to sCT techniques enable accurate daily dose recalculation, adaptive replanning, and auto contouring, transforming CBCT from a positioning aid into a quantitative backbone for modern image-guided radiotherapy.

6.3 Summary

Generative image synthesis is moving from proof of concept to a practical enabler in RT. More broadly, machine learning is

reshaping the field, but clinical adoption must confront persistent risks of overfitting and domain shift. In radiation oncology, accuracy alone is not enough: even small rates of false negatives or false positives can have serious consequences. Addressing these risks requires rigorous validation, uncertainty reporting, and continuous quality assurance, with medical physicists playing a central role in understanding model limitations, monitoring performance, and integrating these rapidly evolving tools into safe, reliable workflows.

7 Cherenkov radiation imaging: emerging applications in modern RT

Cherenkov radiation emerges when charged particles traverse dielectric media at velocities exceeding the local speed of light. This phenomenon, characterized by its distinctive blue glow, occurs across the electromagnetic spectrum from ultraviolet to near-infrared wavelengths. In RT contexts, Cherenkov emission is generated whenever high-energy radiation interacts with tissue or water-equivalent phantoms, making it an intrinsic component of dose delivery processes (164–166).

The fundamental physics governing Cherenkov production follows well-established principles. The threshold condition requires $\beta \geq 1/n$, where β represents the particle velocity relative to light speed and n denotes the medium's refractive index. For electrons in liquid water, this threshold corresponds to approximately 260 MeV, with characteristic emission angles of ~41°. The Frank–Tamm formula describes Cherenkov intensity as proportional to $1/\lambda$ (2) in the wavelength domain, resulting in the characteristic-blue-weighted spectrum (167).

Under conditions of transient charged particle equilibrium, local Cherenkov intensity demonstrates strong proportionality to absorbed dose for both photon and electron beams (168–171). The presence of Cherenkov emission from radiotherapeutic proton beams has also been investigated (172). However, this relationship becomes complex due to factors including beam quality variations, spectral changes from beam hardening, and anisotropic secondary particle distributions. Furthermore, for *in vivo* applications, the optical transport of Cherenkov photons is dependent on patient-specific spatially heterogeneous tissue optical properties. These complications necessitate correction methodologies for accurate dosimetric applications.

7.1 Physics and detection considerations

The anisotropic nature of Cherenkov emission presents both challenges and opportunities for RT applications. In transparent media like water, Monte Carlo simulations and polarization imaging techniques can provide corrections to account for directional dependencies (169, 173). Alternatively, fluorophore doping can convert anisotropic Cherenkov light to more isotropic fluorescence, simplifying measurements while maintaining dose proportionality (174, 175).

In biological tissues, Cherenkov transport depends critically on optical properties, particularly absorption and scattering coefficients. The effective sampling depth is typically limited to several millimeters beneath tissue surfaces, with sensitivity decreasing exponentially with depth (164, 176–178). Unlike native Cherenkov spectra, tissue-emergent radiation exhibits red-shifted characteristics due to preferential absorption of shorter wavelengths (177).

Detection technologies have advanced significantly, enabling practical Cherenkov measurements in clinical environments. Modern systems employ intensified CMOS cameras to capture the relatively weak Cherenkov signals (on the level of μW cm-2 per Gy s^{-1} for external beam therapy), the sensitivity, and noise characteristics, which have been reported in the literature (179–183). Spectral filtering of ambient lighting and temporal gating synchronized to radiation pulses effectively suppresses ambient light interference, particularly valuable in low-duty cycle applications (184–186).

7.2 Dosimetric applications in phantom studies

Camera-based Cherenkov imaging has demonstrated significant utility for beam characterization and quality assurance in phantom studies. Two-dimensional projection imaging enables rapid profiling of electron and photon beams with excellent spatial resolution (165, 174). Tomographic reconstruction techniques allow three-dimensional dose distribution mapping, validated for intensity-modulated RT (IMRT) and volumetric modulated arc therapy (VMAT) quality assurance (187, 188).

The exceptional spatiotemporal resolution achievable with Cherenkov imaging addresses critical needs in modern RT. Advanced techniques, such as stereotactic radiosurgery, microbeam therapy, and stereotactic body RT, demand precise characterization of small fields with steep dose gradients. Cherenkov imaging provides sub-millimeter spatial resolution in both 2D projection and 3D tomographic modes (175, 189). These favorable properties have been leveraged in the applications of Cherenkov imaging to routing quality assurance, including for MR linacs (190–193).

Ultra-high dose rate (UHDR) RT, known as FLASH-RT, presents unique dosimetric challenges due to dose rates exceeding 40 Gy/s—several orders of magnitude above conventional delivery rates (~2–6 Gy/min). Traditional dosimeters often exhibit dose-rate dependencies that compromise accuracy under UHDR conditions. Cherenkov imaging, combined with fast electronics and feedback systems, has successfully addressed these challenges, enabling dosimetry, monitoring, and control applications in FLASH-RT (194–196).

7.3 Chemical and biological sensing applications

Cherenkov emission spectroscopy has emerged as a powerful tool for non-invasive chemical sensing, particularly for tissue oxygenation monitoring (197) (Figure 7). Conventional oxygen measurement techniques are often invasive and complex, limiting their clinical utility. Cherenkov-based approaches leverage spectral characteristics that correlate with tissue optical properties at varying oxygenation concentrations (198, 199). Multi-channel

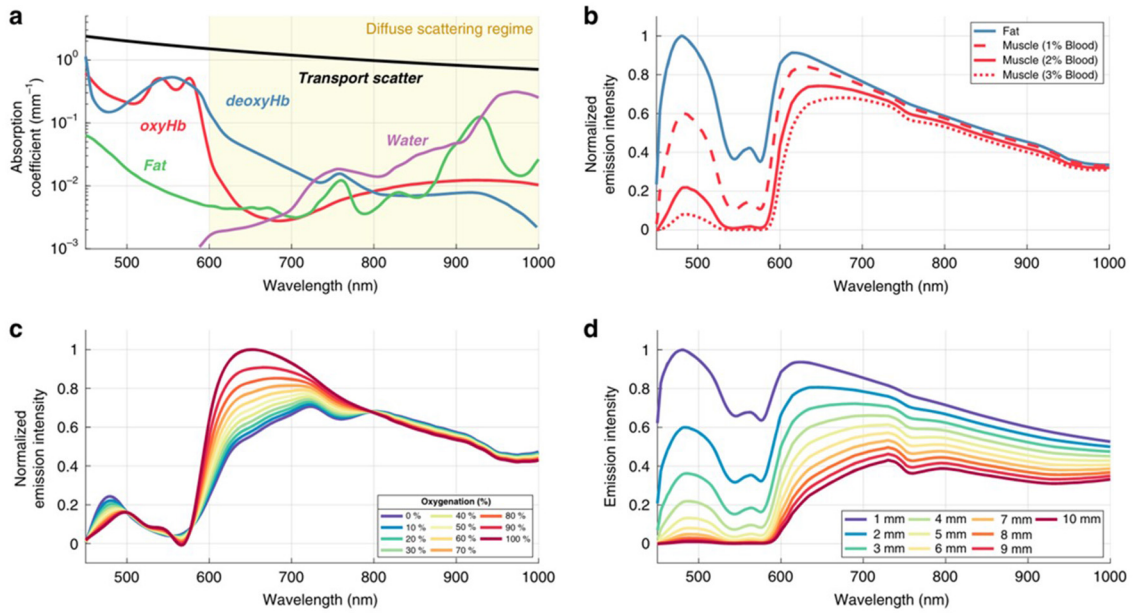

FIGURE 7
Spectral characteristics of tissue-emitted light are primarily determined by the absorption features of oxyhemoglobin, deoxyhemoglobin, water, and lipids, together with the general wavelength dependence of tissue scattering **(A)**. Simulated Cherenkov emission spectra originating from a 5 mm depth are shown for fatty tissue (composition: 90% fat, 9.5% water, 0.5% blood containing equal parts Hb and HbO_2) and for radiodense tissue (mixtures of water and blood in varying ratios, again with equal Hb/HbO_2 contribution) **(B)**. Changes in blood oxygenation within radiodense tissue containing 2% blood modify the Cherenkov spectrum owing to the distinct absorption profiles of oxy- and deoxyhemoglobin **(C)**. Finally, **(D)** illustrates how varying emission depth in radiodense tissue (2% blood) influences the resulting Cherenkov emission observed at the surface. Reprinted from Vasyltsiv et al. (200).

spectral Cherenkov imaging is an emerging technology that can provide additional contrast for subsurface features by leveraging the impact of tissue composition on the emitted Cherenkov spectrum (200). This approach was also used to generate the first color images of Cherenkov emission from patients (197).

The development of Cherenkov-excited luminescence techniques has expanded sensing capabilities beyond direct spectroscopic methods. By introducing oxygen-sensitive optical probes that can be stimulated by Cherenkov light, researchers have demonstrated real-time measurements of partial pressure of oxygen (pO_2), both *in vitro* and *in vivo* (201, 202). Diffuse optical tomography with radiation beam-optimized excitation patterns enables three-dimensional oxygen distribution reconstruction to depths of several centimeters (203, 204).

Cherenkov-excited luminescence scanned imaging (CELSI) represents another jump forward in Cherenkov-based biological sensing. This technique utilizes two-dimensional radiation sheets to generate Cherenkov emission, which subsequently excites luminescence probes distributed throughout biological tissues. By incorporating prior knowledge of beam positioning, three-dimensional optical signal distributions can be reconstructed with high spatial resolution (205–207).

7.4 *In-vivo* clinical applications

Human Cherenkov imaging was first demonstrated in patients with breast cancer receiving external beam RT. Synchronization of frame capture with radiation pulses enabled real-time, background-subtracted imaging at rates exceeding 10 frames per second (166, 208). These proof-of-concept studies revealed field segments projected onto patient surfaces, with intensity correlations to subsequent erythema development.

Clinical applications have expanded to encompass multiple treatment sites and techniques, including total skin electron therapy, head and neck VMAT, and frame-based intracranial stereotactic radiosurgery (209–214). Primary applications focus on motion monitoring, coverage validation, and treatment verification, though quantitative dose correlation remains challenging due to patient-specific factors, such as tissue optical properties, beam geometry, and treatment modality.

Significant progress has been made in addressing quantitative limitations through patient-specific corrections, with a particular focus on breast RT. Spatial frequency domain imaging (SFDI) enables measurement of skin optical properties for Cherenkov intensity correction (215). Additionally, X-ray attenuation values extracted from planning CT scans show a strong correlation with optical absorption, providing an alternative correction approach that utilizes readily available imaging data (216, 217). The patient's skin tone has been incorporated into the correction paradigm by leveraging the intensity of the paired time-delayed images used for online Cherenkov-background subtraction (218). Cherenkov images have been used to monitor and analyze match line quality in half-beam blocked or multi-isocenter treatments (219–221), and there are ongoing attempts to utilize biological features in the images as fiducial markers to track setup accuracy, leveraging classical and deep learning-based image analysis techniques (222–224).

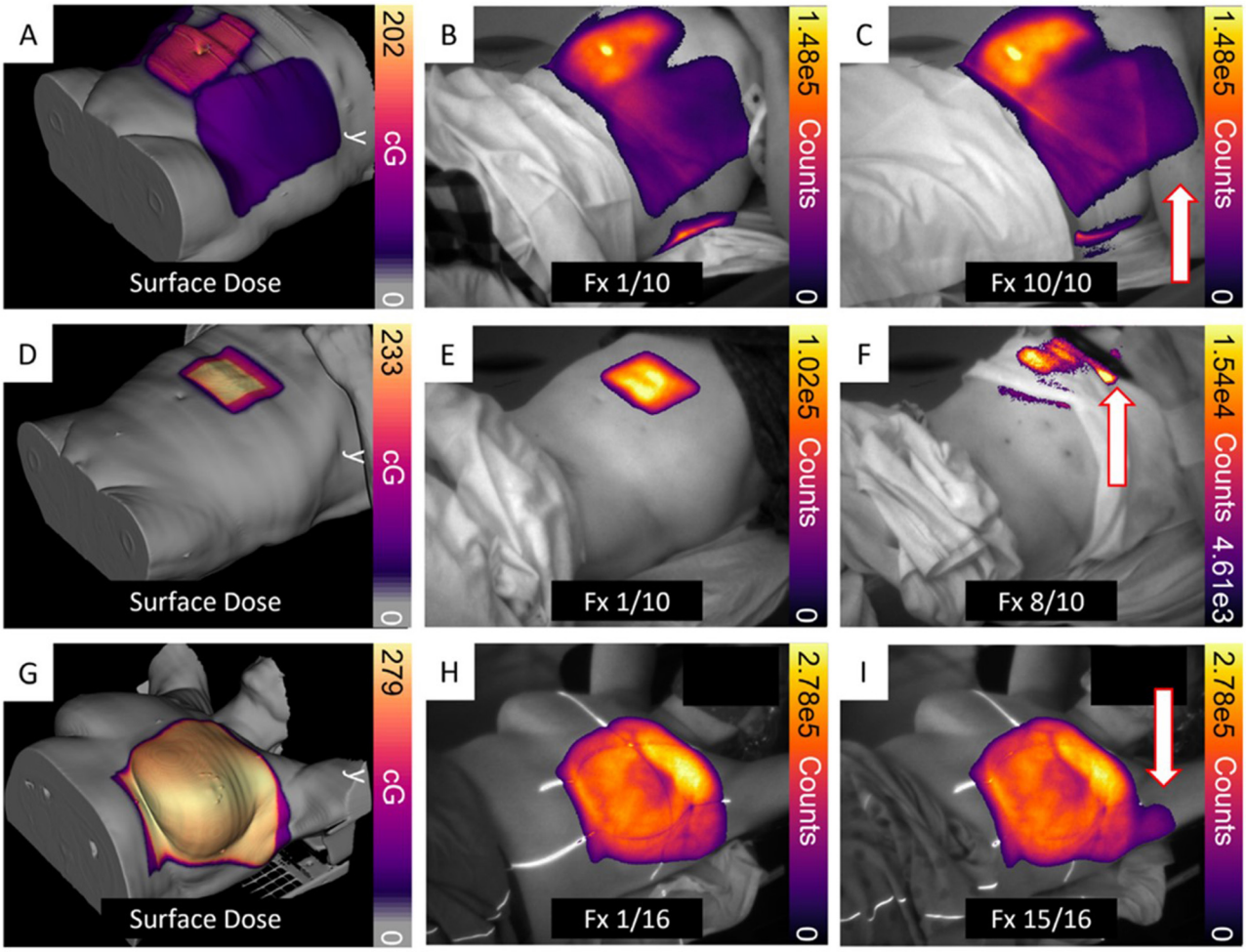

FIGURE 8
Examples of unintended dose delivery are illustrated for Cases 1, 2, and 3. (**A–C**, Case 1) depict incorrect arm positioning during 7 of 10 fractions, resulting in approximately 4.5 Gy exposure from an exit beam. (**D–F**, Case 2) show suboptimal hand placement that produced a small unintended dose in one of the ten fractions. (**G–I**, Case 3) demonstrate additional dose to the left axillary region caused by a slight displacement of the left arm in one of sixteen fractions. For all cases, surface-dose maps derived from the treatment plan were projected onto the corresponding patient CT surface, with red arrows marking the affected regions. Reprinted from Jarvis et al. (228).

Despite quantitative challenges, Cherenkov imaging offers unique advantages as a "free" signal present during any megavoltage RT without additional dose or time requirements. With the introduction of commercially available clinical Cherenkov imaging systems (BeamSite, DoseOptics, Lebanon NH, and DoseRT, Vision RT, London UK), there has been an effort to use the live Cherenkov video feed and the post-treatment cumulative image to monitor beam shape and improve or avoid non-ideal planning, delivery, or setup conditions (225, 226). Published studies on cohorts of 64 to over 600 patients have shown incident rates between 1.5% and 9% that were uniquely identified with Cherenkov imaging (227, 228) (Figure 8). Additionally, there are recent efforts to use Cherenkov images to guide the placement of *in vivo* dosimeters for surface dose measurements on the contralateral breast or verification of implanted electronic device dose limits (229, 230).

Future developments focus on automated anomaly detection through machine learning applications. The large-scale data availability from always-on Cherenkov imaging enables several promising applications, including deep image denoising, motion estimation, automated patient alignment verification, and real-time treatment anomaly detection (210, 211).

7.5 Emerging applications and future directions

FLASH-RT applications represent a rapidly expanding frontier for Cherenkov imaging. The instantaneous nature of Cherenkov emission makes it ideally suited for monitoring UHDR deliveries that typically occur within fractions of a second. Real-time Cherenkov imaging has been successfully demonstrated in large animal FLASH studies, providing quality assurance and delivery control capabilities (196, 231).

Advanced imaging techniques continue to evolve, including multi-spectral Cherenkov imaging for physiological parameter estimation. Time-gated, three-channel cameras have enabled color Cherenkov emission analysis, potentially providing

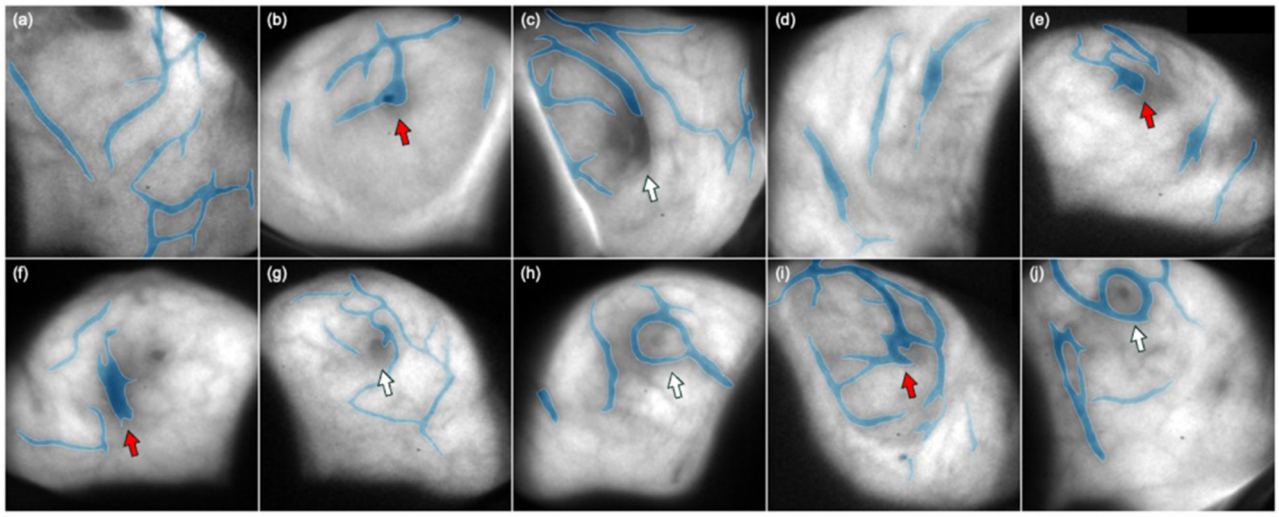

FIGURE 9
Visualization of segmented bio-morphological structures derived from Cherenkov imaging in ten representative breast cancer patients. **(A–J)** display the outputs of a fine-tuned SegResNet model, showing enhanced-edge segmentations of surface features overlaid transparently on the corresponding Cherenkov images. The segmented features primarily represent subcutaneous vasculature on the breast surface, with occasional inclusion of other anatomical details such as scars or nipples. Red arrows in **(B, E, F, I)** highlight segmentation errors involving scars and nipples, whereas white arrows in **(C, G, H, J)** indicate accurate segmentation results where vascular structures are correctly isolated. Reproduced with permission from Wang et al. (224).

information about oxygen saturation, blood volume, and tissue composition (197).

Machine learning integration promises to enhance Cherenkov imaging capabilities significantly. Applications under development include automated treatment verification, real-time anomaly detection, patient-specific dose estimation, and physiological parameter extraction from spectral Cherenkov data (224, 232) (Figure 9).

7.6 Summary

Cherenkov radiation imaging has matured from a laboratory curiosity to a clinically viable technology with diverse applications in RT. While challenges remain in establishing quantitative dose correlations, particularly for *in vivo* applications, the technology offers unique advantages, such as real-time monitoring capabilities, excellent spatiotemporal resolution, and compatibility with emerging UHDR techniques. Continued technological development and clinical validation will likely expand Cherenkov imaging applications in quality assurance, biological monitoring, and treatment verification across conventional and advanced RT modalities.

8 Challenges in precision proton therapy

The popularity of proton therapy is derived from its capacity to spare healthy tissue while providing excellent dose conformity to the tumor due to proton physical properties, particularly the Bragg peak, where protons deposit their maximum energy at the end of their path at a precise depth. Thus, proton therapy is advantageous in pediatric oncology and tumors located near critical organs and structures. However, this unique characteristic comes as a double-edge sword: the precision of proton therapy is vulnerable to any uncertainties contained within the workflow of proton therapy. Even small inaccuracies during this process could lead to significant change in target coverage or unintended irradiation to the normal tissue.

Imaging plays an essential role in every step of proton therapy: from simulation, treatment planning, daily imaging-guided patient setup during treatment, and to potential adaptive planning (Figure 10). This section will first focus on imaging-related challenges in simulation and imaging guidance during daily treatment and then summarize emerging technologies and their future clinical implications.

8.1 Simulation imaging and planning accuracy

8.1.1 Patient positioning and immobilization

Like photon-based treatments, proton therapy treatment begins with simulation, during which high-quality volumetric images, typically a CT scan, are acquired to define tumor target volumes and organs at risk (OARs) and used for dose calculation during treatment planning. Thus, reproducibility of patient setup during simulation is essential to ensure the patient position can be consistently and accurately recreated during treatments. Uncertainties introduced at this stage propagate throughout the entire workflow of the treatment.

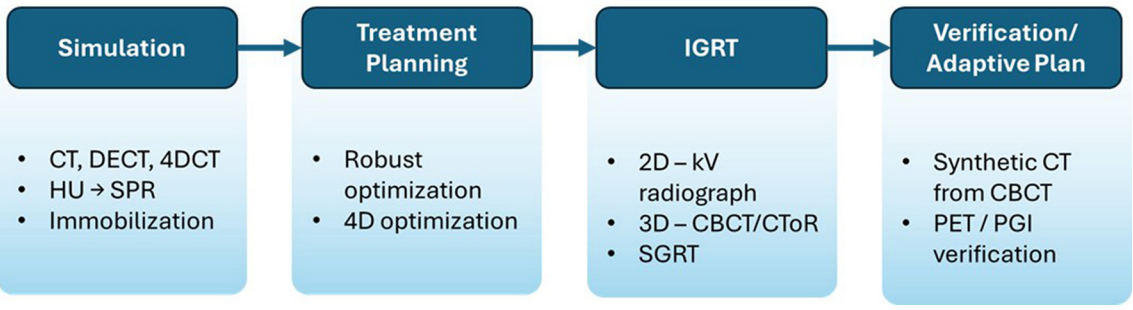

FIGURE 10
Imaging workflow in proton therapy.

Immobilization devices, such as thermoplastic masks for brain and head and neck tumors, VacLok® for other sites, and indexed positioning systems, aid in minimizing variations in patient position. Special attention must be paid to all items that may vary in thickness and location. Changes of these items during the treatment course would significantly impact the dose distribution during daily treatment if placed within a beam path.

8.1.2 CT HU to stopping power ratio (SPR) conversion

The cornerstone of proton therapy planning is the conversion of CT HUs to the stopping power ratio (SPR), which is used to calculate proton dose deposition. Uncertainties in this conversion are the major source of range uncertainty, which is estimated to be 2%—3% and more than 5% in the lung tissue (233, 234).

The standard clinical approach to address range uncertainty is the stoichiometric method, which involves acquiring single-energy CT (SECT) scans of various materials to establish a calibration curve. However, this curve is scanner- and protocol-dependent and assumes consistent image quality and minimal artifacts. Artifacts from metal implants or motion (e.g., respiration) introduce errors in SPR estimation, which ultimately propagate into dose calculation.

8.1.3 Advanced CT imaging techniques

To improve SPR accuracy, the feasibility of using dual-energy CT (DECT) for proton treatment planning is being explored in research and clinical settings (235, 236). DECT acquires two images at different X-ray energies, enabling the calculation of effective atomic number and electron density. This provides a more accurate pathway to SPR estimation than the stoichiometric method. Studies have shown that DECT implementation reduces range uncertainty by more than 1% compared to conventional CT.

Four-dimensional CT (4DCT) is critical in thoracic and abdominal sites where the tumor moves due to respiration and peristalsis. 4DCT allows breathing phase-based sorting of images to capture motion and inform strategies, such as internal target volume (ITV) creation or beam gating. Nowadays, treatment planning system allows users to incorporate different breathing phases during optimization, which greatly reduces the impact of breathing motion on daily dose delivery (237, 238). Proper motion management strategy reduces inter- and intra-fractional motion while improving the robustness of the proton treatment plan.

8.2 Image guidance during treatment in proton therapy

8.2.1 Imaging modalities

Table 2 compares different image modalities in proton therapy. Compared to photon therapy, which is inherently more forgiving for setup inaccuracies, proton therapy is highly sensitive to changes in water equivalent thickness (WET) along the proton beam path due to the finite range. Image-guided RT (IGRT) plays a vital role in verifying patient setup and minimizing uncertainties.

Common IGRT techniques include orthogonal kV radiographs and CBCT. Radiographs are quick and efficient for bony alignment but lack soft tissue visualization. CBCT offers volumetric information but suffers from lower image quality and longer acquisition time. Moreover, CBCT has poor HU accuracy, making it unreliable for proton range calculations (239). Nonetheless, it is superior in anatomy visualization, providing more reliable couch correction to align the anatomy on the treatment day with the simulation CT, reducing the setup uncertainties.

Surface-guided RT (SGRT) is an emerging modality used for patient positioning in superficial tumors or sites with minimal internal motion and for gating or breath-hold cases. It avoids ionizing radiation and provides real-time feedback. However, special attention needs to be paid when relying on SGRT to align the patient since it lacks internal anatomical correlation.

CT-on-Rails (CToR) has been adopted for IGRT modality in proton therapy to address the limitations of CBCT. The image quality of CBCT systems integrated into proton gantries is often compromised due to extended source-to-imager distance (SID) and limited mechanical clearance. In contrast, CToR provides diagnostic-quality volumetric imaging, offering superior soft tissue visualization and improved target delineation, which are requisite for accurate image registration and adaptive dose calculation. When implemented clinically, alignment between the CToR imaging isocenter and the treatment isocenter is critical. This alignment must be established during system installation and commissioning and maintained through

TABLE 2 Comparison of imaging modalities in proton therapy.

Modality	Phase of use	Strengths	Limitations
SECT (CT)	Simulation	Widely available; used for HU-SPR conversion	HU-to-SPR uncertainty; artifact sensitivity
DECT	Simulation	Better SPR accuracy; material decomposition	Limited clinical adoption; more complex workflow
4DCT	Simulation	Captures respiratory motion	Motion artifacts; longer simulation time
CBCT	IGRT/ Verification	Volumetric guidance	Poor HU accuracy; not ideal for replanning; not widely available in all proton centers
CToR	IGRT/ Verification	High-resolution, diagnostic-quality imaging	Set up shift required; space-consuming
pCT	Simulation	Direct SPR measurement	Still under development; resolution and workflow
MRI	Simulation/ Planning	Excellent soft tissue contrast	No intrinsic SPR; image registration needed
PET	Verification	*In vivo* dose verification	Biological washout; logistical and temporal limits
Prompt-Gamma	Verification	Real-time range verification	Limited resolution; detector development ongoing
SGRT	IGRT	Non-ionizing; real-time monitoring	Limited to external surface

routine quality assurance checks. Notably, during imaging, the treatment couch must be rotated or translated away from the treatment position to allow access to the CToR gantry—introducing the potential for setup variability if not properly managed.

8.2.2 Adaptive proton therapy

Given the sensitivity of proton beams to anatomical changes, adaptive therapy is a growing area of interest. Adaptive strategies rely on periodic or daily imaging to assess the impact of changes in patient anatomy on dose delivery and adjust the treatment plan when deemed necessary. Recent research on synthetic CT generation from CBCT using deformable registration or AI techniques holds promise in overcoming its limitation of poor HU reliability (240). CToR images show superior HU accuracy, which would be readily used for adaptive proton treatment planning.

Adaptive therapy can improve target coverage and OAR sparing, particularly in long-course treatments. However, it requires additional clinical resources, including time for recontouring and plan evaluation, making routine implementation challenging.

8.3 Emerging technologies for imaging accuracy

8.3.1 Proton radiography and proton CT

Table 3 summarizes the emerging image techniques for proton therapy. Proton radiography and proton CT (pCT) are imaging modalities that use protons themselves, rather than X-rays, to generate images of patient anatomy. Proton radiography provides 2D images and has been used in research settings for patient alignment and range verification (241). Proton CT, still under clinical development, offers 3D volumetric imaging and direct SPR mapping (242). Studies suggest that pCT can reduce range uncertainty to within 1%, though issues such as limited spatial resolution, longer acquisition times, and system integration remain barriers to clinical implementation.

8.3.2 Prompt gamma and PET imaging for in-vivo verification

Due to its finite range, it is impossible to measure the exit dose from proton delivery during treatment, compared to photon treatment. To verify proton beam delivery during or after treatment, prompt gamma imaging (PGI) and proton-induced PET are under active investigation.

PGI detects gamma photons emitted almost instantaneously as protons interact with nuclei in the patient. The spatial distribution of prompt gammas correlates with the proton range, offering a method for real-time verification. PGI systems are being tested clinically with encouraging results, though detector design and resolution constraints limit full clinical integration (243).

PET imaging leverages the positron-emitting isotopes generated by proton–nucleus interactions. Post-treatment PET can visualize areas where protons deposited energy. However, its clinical utility is limited by biological washout, low signal-to-noise ratios, and logistical challenges, such as the need for on-site PET scanners (243).

8.3.3 Artificial intelligence in imaging accuracy

AI and ML are increasingly being applied to enhance imaging in proton therapy. Applications include:

- Synthetic CT generation from MRI or CBCT, enabling MR-based planning or CBCT-based adaptation with reliable HU/SPR mapping (244).
- Automated segmentation of targets and OARs, reducing variability and speeding up planning.
- Image registration improvements, particularly deformable registration across modalities.
- Artifact correction in CT and CBCT, especially for motion and metal-induced artifacts.

AI tools are being developed to predict anatomical changes and guide adaptive decision-making, potentially reducing the need for daily manual planning and review. As these tools mature, they could enhance the accuracy and efficiency of imaging workflows throughout the proton therapy process.

TABLE 3 Emerging technologies and clinical readiness.

Technology	Purpose	Advantages	Current limitations	Clinical maturity
Dual-energy CT	Improve SPR estimation	Reduced range uncertainty	Needs new calibration and workflow	Moderate
Proton CT (pCT)	Direct SPR measurement	<1% range uncertainty	Resolution, speed, system availability	Low (R&D)
Prompt gamma imaging	*In vivo* range verification	Real-time feedback	Detector complexity, resolution	Low–Moderate
Synthetic CT (from CBCT)	Adaptive planning	Enables CBCT-based replanning	Needs AI or deformable registration	Moderate
AI-based auto-segmentation	Planning/Adaptive	Efficiency, consistency	Validation and generalizability	Moderate
In-room PET	Post-treatment range verification	Biological dose imaging	Washout, timing, scanner access	Low

8.4 Summary

In summary, new technologies are improving the accuracy of proton therapy. Precision is limited by range uncertainty from HU-to-stopping-power conversion, setup/motion, and imaging artifacts. Dual-energy CT tightens SPR estimates, while 4DCT characterizes respiratory motion for robust planning. For image guidance, kV radiographs and CBCT improve daily alignment, SGRT provides non-ionizing motion monitoring, and CT-on-rails offers diagnostic-quality volumetric updates. Adaptive proton therapy leverages periodic or daily imaging to replan when anatomy changes. *In vivo* verification via prompt-gamma and PET supplies range feedback, and pCT can directly inform water-equivalent thickness modeling. AI further enables synthetic CT, automated segmentation, deformable registration, and artifact mitigation. Broad clinical impact will hinge on rigorous validation, standardized QA/reporting, interoperable data pipelines, and staffing/training to sustain adaptive, verification-rich practice.

9 Advanced imaging and dosimetry in theranostics

Radiopharmaceutical therapy (RPT) is a form of internal radiation treatment that combines tumor-targeting molecules with radioactive isotopes to deliver cytotoxic radiation directly to cancer cells. Unlike external beam radiotherapy (EBRT), which delivers radiation from outside the body, RPT administers radiation systemically, typically via the bloodstream, allowing it to target both primary tumors and metastatic sites. This targeted, systemic approach makes RPT particularly well-suited for treating widespread metastatic disease. When used in combination with other therapies, demonstrated promising efficacy and a favorable toxicity profile, often outperforming conventional RPT has systemic treatments in clinical trials (245, 246).

A defining feature of RPT is its compatibility with personalized medicine. As the distribution of radioactive agents can be visualized within the body using imaging—either after administration or through surrogate imaging—the treatment can be precisely tailored to each patient. This imaging capability enables real-time tracking of drug biodistribution and supports individualized dosing based on organ uptake and tumor burden. The term "theranostics" describes this integration of targeted therapy (thera-) with diagnostic imaging (-nostics) (247) and has led to a resurgence in the development and clinical use of RPT over the past two decades.

Theranostics involves the use of molecular imaging, typically with PET/CT or SPECT/CT, to guide patient selection and optimize treatment strategies. A common theranostic approach uses isotope pairs that are chemically identical but differ in their radio-physical properties, such as ^{123}I/ ^{124}I/ ^{131}I and ^{86}Y/ ^{90}Y. In these cases, one isotope is used for imaging to assess biodistribution and receptor targeting, while the other is used for therapeutic radiation delivery. Additionally, theranostic approaches can utilize different elements that can be chelated to the same targeting molecules, such as ^{68}Ga for imaging and ^{177}Lu for therapy, when bound to identical targeting vectors like DOTA-peptides. An alternative strategy involves administering a trace amount of the therapeutic agent and imaging it directly using SPECT/CT to predict the drug's distribution during the treatment. These methods enable clinicians to better evaluate treatment feasibility and personalize RPT to achieve maximum efficacy with minimal toxicity.

9.1 Current RPTs administered in the clinic

Several RPTs have received FDA approval for treating a range of cancers, reflecting the growing role of targeted radionuclide therapy in oncology. Among the most widely used radionuclides in RPT are beta (β^-)-emitters, such as iodine-131 (^{131}I), yttrium-90 (^{90}Y), and lutetium-177 (^{177}Lu). These isotopes are favored for their tissue-penetrating radiation range and ability to induce DNA damage in tumor cells, ultimately leading to cell death.

One of the earliest and most established forms of RPT is radioactive iodine (RAI) therapy, which has been used clinically for nearly a century, particularly for the treatment of differentiated thyroid cancer and benign thyroid disorders such as Graves' disease and toxic multinodular goiter (248). RAI therapy exploits the sodium iodide symporter (NIS)—a transmembrane protein that facilitates active transport of iodide ions into thyroid follicular cells. This transporter is highly expressed in differentiated thyroid cancers, allowing for the selective accumulation of radioactive iodine within malignant tissues.

Beyond therapy, radioactive iodine isotopes are also used for diagnostic imaging. Sodium iodide labeled with ^{123}I ($Na^{123}I$) is commonly used for SPECT/CT imaging due to its favorable gamma photon energy and shorter half-life, which minimizes radiation

dose to the patient. $Na^{124}I$ is a positron-emitting isotope of iodine, which is used for PET/CT imaging, providing higher spatial resolution and quantitative accuracy (249, 250).

Radium-223 dichloride ($^{223}RaCl_2$) was approved by the FDA in 2013 for the treatment of castration-resistant prostate cancer (CRPC) with symptomatic bone metastases. As an alkaline earth metal, $^{223}RaCl_2$ mimics calcium and selectively localizes to areas of increased bone turnover, particularly at sites of metastatic lesions. Patients with metastatic prostate cancer often exhibit elevated bone remodeling activity driven by osteoblasts and osteoclasts, making them ideal candidates for therapies involving calcium mimetics, such as $^{223}RaCl_2$ (251).

^{223}Ra undergoes a six-stage decay process, emitting four alpha particles per decay. These alpha particles account for approximately 95% of the total decay energy, making ^{223}Ra a highly potent source of localized radiation. The emitted alpha particles have high linear energy transfer (LET), which means they deposit a substantial amount of energy along short tracks. This results in efficient induction of DNA double-strand breaks, which are lethal to tumor cells. However, due to their short range (approximately 10–100 μm), the cytotoxic effects of alpha particles are confined to a radius of 2–10 cells, thereby minimizing damage to surrounding healthy tissue.

Meta-iodo-benzyl-guanidine (mIBG) is a norepinephrine analog that targets the adrenergic tissue. When labeled with iodine-131 (^{131}I), mIBG has been used for decades to treat neuroblastoma and other pediatric tumors (252). Despite its long history of clinical use, standard ^{131}I -mIBG does not have formal FDA approval and is therefore prescribed by physicians under investigational or compassionate use protocols (253). One should keep in mind that the prescribed activity for ^{131}I-mIBG is based on patient body weight and is typically much higher than other RPT drugs since pediatric patients can better tolerate bone marrow suppression and can also receive stem cell support following treatment.

More recently, a new formulation known as high-specific-activity (HSA) ^{131}I-MIBG has been developed. This version features a much higher proportion of the mIBG molecules labeled with ^{131}I, significantly increasing its specific activity—the amount of radioactivity per unit mass of drug (254). In standard ^{131}I–mIBG preparations, only about 1% of mIBG molecules are radiolabeled (~123.3 MBq/mg), whereas in HSA ^{131}I–mIBG, nearly 100% of the molecules are labeled (~92,500 MBq/mg) (255). HSA ^{131}I–mIBG received FDA approval in 2018 for the treatment of patients with locally advanced or metastatic pheochromocytoma or paraganglioma who require systemic anticancer therapy. However, the manufacturer of HSA ^{131}I–mIBG discontinued production of the drug in 2023.

^{177}Lu-DOTATATE was approved by the FDA in 2018 for the treatment of gastroenteropancreatic neuroendocrine tumors (GEP-NETs), which are neuroendocrine tumors originating in the pancreas or gastrointestinal tract. GEP-NETs are the most common subtype of well-differentiated neuroendocrine tumors, accounting for more than 70% of cases (256–259). ^{177}Lu-DOTATATE targets somatostatin receptors, which are overexpressed in GEP-NETs. The radiopharmaceutical consists of a somatostatin receptor agonist (SSA), the chelator DOTA, and the therapeutic radionuclide ^{177}Lu (259). To identify appropriate candidates for treatment, the companion diagnostic ^{68}Ga-DOTATATE is used for PET imaging to confirm somatostatin receptor expression in tumors. The standard prescribed activity of ^{177}Lu-DOTATATE is 7.4 GBq, which is administered every 8 weeks for a total of four doses.

The FDA approved ^{177}Lu-PSMA-617 in 2022 for the treatment of castration-resistant prostate cancers (CRPCs) in patients whose tumors overexpress the transmembrane protein prostate-specific membrane antigen (PSMA). PSMA is an ideal therapeutic target due to its high expression on prostate cancer cells and its cell surface localization, which makes it readily accessible to targeted agents. PSMA-617 is a small-molecule PSMA inhibitor that binds specifically to this protein, allowing for targeted delivery of the radioactive isotope ^{177}Lu to cancer cells (260).

The FDA has also approved multiple PSMA-targeted PET radiotracers for identifying patients eligible for ^{177}Lu-PSMA-617 therapy by detecting PSMA expression in tumors. These companion diagnostics are critical in guiding treatment decisions and selecting appropriate candidates for radioligand therapy. Among these, ^{68}Ga-gozetotide (also known as ^{68}Ga-PSMA-11) was the first to receive FDA approval in 2020 for use in PSMA PET/CT imaging. It remains the most extensively studied and widely used radiotracer for PSMA-targeted imaging. In addition, the FDA approved two ^{18}F-labeled tracers: [^{18}F]DCFPyL in 2021 and [^{18}F]rhPSMA-7 in 2023, further expanding the toolbox of PSMA-targeted imaging agents. These radiotracers offer advantages in image resolution and logistical flexibility due to the longer half-life of ^{18}F compared to ^{68}Ga.

Interestingly, the prescribed activity of ^{177}Lu-PSMA-617 is 7.4 GBq per cycle, which matches the dose used for ^{177}Lu-DOTATATE despite targeting entirely different tumors. The treatment is administered every 6 weeks, for up to six cycles, or until disease progression or unacceptable toxicity occurs.

It is increasingly evident that radiopharmaceutical therapy (RPT) is becoming a viable treatment option for a wide range of late-stage cancers. In some cases, RPT may also be used earlier in the course of disease, either as a standalone treatment or in combination with other therapeutic agents. Notably, with the exception of ^{131}I–mIBG and HSA ^{131}I–mIBG, the toxicity profiles observed in clinical trials of approved RPT agents are substantially lower than those associated with many conventional cancer therapies. This suggests that a significant proportion of patients may be clinically underdosed, highlighting an opportunity to optimize treatment delivery. All currently approved RPT agents emit radiation that can be imaged using SPECT/CT, enabling patient-specific dosimetry. This capability allows clinicians to personalize the administered activity for each patient based on their individual biodistribution and organ sensitivity, which is an approach that can be leveraged to maximize therapeutic efficacy while minimizing toxicity.

9.2 Advanced quantitative imaging in radiopharmaceutical therapy

Theranostics relies heavily on advanced imaging modalities to guide and monitor treatment with radiopharmaceuticals. The most commonly used imaging techniques in RPT are positron PET/CT

and SPECT/CT. PET/CT, often using ^{68}Ga- or ^{18}F-labeled tracers, offers high sensitivity and spatial resolution for detecting molecular targets such as PSMA or somatostatin receptors, enabling precise patient selection and treatment planning. SPECT/CT, used with gamma-emitting isotopes, such as ^{131}I or ^{177}Lu, allows for real-time visualization of therapeutic agents and supports quantitative dosimetry to tailor treatment to individual patients. These hybrid imaging techniques not only confirm target expression before therapy but also assess biodistribution, monitor therapeutic response, and detect toxicity—making them essential tools in the practice of personalized medicine within RPT and nuclear oncology.

9.2.1 PET/CT

PET/CT imaging is an advanced medical imaging technique that combines the functional insights of PET with the detailed anatomical information of CT. By integrating these two modalities into a single imaging session, PET/CT provides a comprehensive view of both physiological activity and structural abnormalities within the body. This dual capability has made PET/CT an essential tool in clinical practice, enhancing diagnostic accuracy, guiding treatment planning, and improving overall patient management. The technology continues to advance, with ongoing research aimed at improving image quality, optimizing protocols, and expanding its clinical applications.

PET/CT plays a central role in theranostics by enabling both the selection of appropriate patients for radiopharmaceutical therapy (RPT) and the personalization of treatment. One of its most critical uses is identifying whether a patient's tumor expresses the molecular target required for specific RPTs. For example, ^{68}Ga-PSMA PET/CT is used to detect prostate-specific membrane antigen (PSMA) expression in patients with metastatic prostate cancer, guiding the use of ^{177}Lu-PSMA-617 therapy. Similarly, ^{68}Ga-DOTATATE PET/CT is used to confirm somatostatin receptor expression in patients with neuroendocrine tumors before initiating ^{177}Lu-DOTATATE treatment.

Beyond patient selection, PET/CT is also valuable for treatment planning and dosimetry. By using diagnostic isotopes such as ^{68}Ga or ^{18}F, clinicians can estimate how therapeutic agents like ^{177}Lu or ^{90}Y will distribute throughout the body. This information allows for patient-specific dosimetry calculations, which help determine the optimal therapeutic dose while minimizing toxicity to healthy tissues. PET/CT is also routinely used to monitor treatment response by measuring changes in tracer uptake over time. A decrease in uptake on follow-up PET/CT scans can indicate a reduction in tumor activity or burden, supporting continued therapy or adjustment of the treatment plan.

Additionally, PET/CT enables early detection of disease progression or recurrence, often before structural changes are evident. For instance, ^{68}Ga-PSMA PET/CT is highly sensitive for identifying biochemical recurrence in prostate cancer, even at low PSA levels, allowing for earlier intervention. Finally, PET/CT can help evaluate off-target uptake, such as accumulation in the kidneys, salivary glands, or bone marrow, which may signal potential toxicity risks. This information is essential for refining treatment protocols and protecting critical organs. Overall, PET/CT is a cornerstone of theranostic practice, offering a combination of molecular insight and anatomical precision to guide effective and personalized cancer care.

9.2.2 SPECT/CT

SPECT/CT imaging is a hybrid imaging technique that combines the molecular imaging capabilities of single photon emission computed tomography (SPECT) with the anatomical precision of CT. This integration allows for the simultaneous assessment of functional processes and structural features within the body, enhancing the localization and interpretation of radiopharmaceutical uptake. SPECT/CT has become a valuable tool in clinical practice, particularly in oncology, cardiology, and endocrinology, where it supports accurate diagnosis, guides therapeutic decisions, and aids in treatment response monitoring. Its utility in radiopharmaceutical therapy (RPT) is especially notable, as it enables real-time visualization of therapeutic agent distribution and facilitates quantitative dosimetry. Continuous advancements in detector technology, image reconstruction algorithms, and radiotracer development are further expanding the clinical applications and diagnostic performance of SPECT/CT.

SPECT/CT plays a critical role in theranostics by enabling both the visualization and quantification of radiopharmaceutical distribution, particularly for therapies involving gamma-emitting isotopes. One of its key uses is in patient-specific dosimetry for radiopharmaceutical therapies such as ^{131}I, ^{177}Lu-DOTATATE, and $^{223}RaCl_2$ (298). By providing three-dimensional functional imaging overlaid with anatomical detail, SPECT/CT allows clinicians to assess how the therapeutic agent distributes across tumors and normal organs, enabling precise calculation of absorbed radiation doses. This supports personalized treatment planning aimed at maximizing efficacy while minimizing toxicity. SPECT/CT is also used to monitor treatment response by evaluating changes in radiotracer uptake over time, which can indicate tumor regression or progression. In some cases, a trace amount of the therapeutic agent is administered and imaged with SPECT/CT prior to full-dose therapy to predict biodistribution and assess treatment feasibility. Additionally, SPECT/CT can identify off-target uptake, helping to detect and mitigate potential risks to critical organs such as the kidneys, salivary glands, or bone marrow. Its accessibility, compatibility with a wide range of therapeutic isotopes, and ability to support real-time imaging of therapy delivery make SPECT/CT an important tool in the theranostic workflow.

9.3 Challenges with quantitative imaging

Accurate quantitative PET/CT or SPECT/CT imaging is essential in theranostics because it directly informs critical aspects of personalized treatment planning and clinical decision-making. In theranostics, imaging is not only used for diagnosis and staging but also to measure the *in vivo* distribution of radiopharmaceuticals, enabling patient-specific dosimetry. Precise quantification allows clinicians to calculate the absorbed radiation doses to tumors and normal organs, which is key to balancing efficacy with safety. Inaccurate quantification could lead to underdosing, which reduces therapeutic effectiveness, or overdosing, which increases the risk of toxicity to healthy tissues.

Moreover, quantitative imaging is vital for monitoring treatment response. Changes in standardized uptake values (SUVs) or other quantitative metrics over time provide objective evidence of how well a tumor is responding to therapy. This helps guide decisions about whether to continue, adjust, or stop treatment. It is also crucial for assessing biodistribution in advance of therapy, especially when using a diagnostic surrogate or microdose of the therapeutic agent to predict how the full treatment will behave. Without accurate quantitative imaging, these predictive models become unreliable.

Finally, quantitative PET/CT and SPECT/CT play an important role in clinical research and regulatory approval, where reproducible, measurable outcomes are needed to validate new theranostic agents and protocols. In short, accuracy in quantitative imaging underpins the safety, effectiveness, and precision that define modern theranostic approaches.

Quantifying the distribution of radiopharmaceutical activity within the body is a foundational step in theranostics, as it directly informs absorbed dose calculations and guides patient-specific treatment planning and treatment response assessment. However, achieving accurate quantification is inherently complex and subject to multiple sources of uncertainty. These include limitations in imaging system resolution and sensitivity, patient movement, image noise, and challenges in correcting photon attenuation and scatter. Additionally, variability in segmentation, registration, and calibration processes further complicates the measurement of activity, particularly in small regions of interest, with a heterogeneous uptake (e.g., lesions). Understanding and addressing these sources of uncertainty is critical for improving the accuracy, reproducibility, and clinical utility of quantitative imaging in theranostics. The following sections explore the major technical and procedural factors that contribute to uncertainty in activity quantification.

9.3.1 Quantification of activity

Uncertainty in quantifying activity distribution refers to the challenges and potential sources of error in measuring how a radiopharmaceutical is distributed within the body, especially within specific organs, tissues, or lesions. Accurate quantification is essential in theranostics because it directly impacts dosimetry calculations and, ultimately, the determination of the absorbed radiation dose. Several factors contribute to this uncertainty, including the limited spatial resolution and sensitivity of the imaging system, partial volume effects (which can lead to underestimation of activity in small structures), and inaccuracies in attenuation and scatter correction. Calibration errors in the imaging system can also affect the reliability of activity measurements. Reducing these uncertainties is critical to ensure precise, patient-specific treatment planning in theranostics.

Spatial resolution: Imaging systems such as SPECT and PET have limited spatial resolution, which means they cannot accurately differentiate fine details in small structures. As a result, activity within small organs or lesions may be underestimated due to the partial volume effect (PVE)—a phenomenon where the true activity appears diluted across neighboring voxels, making small structures appear less intense than they actually are. This loss of detail leads to PVE-related inaccuracies in the reconstructed images, which is a well-known limitation of nuclear medicine cameras (261–264).

Sensitivity: The sensitivity of imaging systems varies and refers to the ability of PET or SPECT scanners to detect photons emitted by the radiopharmaceutical. However, no system detects all emitted photons perfectly. Some photons are scattered, absorbed, or missed entirely, which can result in underestimation of total activity and contribute to quantification errors (255, 265, 266).

Noise in Imaging: The signal-to-noise ratio (SNR) plays a critical role in the accuracy of quantitative imaging. Noise can arise from several factors, including limited scan duration, low radiopharmaceutical dose, and patient movement. High noise levels, particularly in areas of low radiotracer uptake (such as surrounding healthy tissue), make it difficult to accurately measure activity. Although increasing scan time and applying noise reduction techniques can improve accuracy, these solutions may reduce patient comfort and limit scanner throughput (255).

Patient motion: Motion during image acquisition, such as respiratory or involuntary movement, can blur the observed activity distribution and introduce quantification errors. This is especially problematic when imaging small structures. For example, one simulation study using ^{90}Y bremsstrahlung SPECT showed that respiratory motion reduced the recovery coefficient of a tumor from 90% to 66% (267, 268).

Calibration: Accurate activity quantification depends on proper calibration of the imaging system, which involves translating detected photon counts into units of radioactivity. This is typically done using radioactive phantoms with known activity distributions. The system is then adjusted to match these known values, establishing a reference for interpreting patient scans. Calibration errors—caused by system performance variability, improper calibration procedures, or aging hardware—can significantly impact quantitative accuracy (255, 269).

9.3.2 Attenuation and scatter correction

During nuclear imaging, photons emitted from radiopharmaceuticals can be absorbed or scattered by tissues as they pass through the body. This process, known as attenuation, is particularly pronounced in denser structures like bone or organs and can lead to underestimation of activity in deeper tissues if not properly corrected. While attenuation correction algorithms are routinely applied, they introduce uncertainty—especially when the patient's anatomy deviates from standard models.

Photon scatter further complicates quantification by reducing image contrast. Scattered photons contribute a diffuse background signal, which can overestimate activity in low-uptake regions and underestimate activity in high-uptake areas like tumors (269). Various scatter correction methods are used to address this, but all introduce potential sources of error depending on imaging conditions, radiopharmaceutical properties, and patient-specific factors (255, 269).

In SPECT imaging, energy window-based methods such as double energy window (DEW) and triple energy window (TEW) are commonly used. These approaches estimate scatter from adjacent energy windows and subtract it from the primary signal. However, their accuracy depends on proper window placement and assumptions about scatter distribution. Misestimation can result in over- or under-correction, affecting final quantification (270–274). For instance, phantom studies have shown that TEW improves contrast-to-noise ratio

over DEW in ^{131}I and ^{177}Lu SPECT, but may produce lower recovery coefficients, suggesting underestimation of true activity (275, 276).

More advanced approaches, such as Monte Carlo (MC)-based scatter correction, simulate individual photon interactions within the patient using detailed physical models (277, 278). These methods account for tissue composition, density, and photon transport, providing more accurate scatter estimation. Comparative studies have shown that MC methods outperform TEW for radionuclides like ^{99m}Tc, ^{111}In, and ^{177}Lu, with TEW overestimating activity by up to 11% in ^{177}Lu imaging due to its inability to capture patient-specific activity distribution (277, 279, 280).

9.3.3 Partial volume effects

The partial volume effect (PVE) occurs when the spatial resolution of an imaging system is insufficient to accurately capture activity within small structures. As a result, activity appears blurred between adjacent regions, leading to underestimation in small, high-uptake areas (e.g., tumors or lymph nodes) and potential overestimation in surrounding low-uptake tissues (261, 262). Structures such as the thyroid, bone marrow, and small tumors are especially vulnerable because their dimensions often fall below the system's resolution, causing activity "spillover" into adjacent areas.

In addition to size, heterogeneous radiopharmaceutical uptake within tumors or organs can be distorted by PVE, obscuring the true distribution of activity. The magnitude of this effect is often characterized using recovery coefficients (RCs), which are derived from phantom studies that measure how much of the true activity is recovered in structures of various sizes and positions. RCs can vary widely—from below 0.1 to above 0.9—depending on factors such as isotope, object size, scanner type, and imaging settings (281). Placement within the field of view also affects RCs; one study using ^{177}Lu demonstrated significantly different RCs for the same sphere size depending on its location in the phantom (281).

To better assess PVE in anatomically relevant settings, anthropomorphic phantoms have been developed for organs such as the kidney (262, 282), liver (283), and the head and neck region (40), allowing more realistic estimation of recovery in complex geometries.

9.3.4 Segmentation

Accurate volume delineation is a critical yet time-consuming step in radiopharmaceutical therapy (RPT) dosimetry and is increasingly complex due to the need to register and interpret multi-timepoint and multimodality imaging (263, 284–286). Inter-observer variability (IOV) in segmentation is widely recognized as the largest source of uncertainty in the dosimetry process (287), potentially impacting both treatment efficacy and toxicity, as well as consistency across clinical centers.

Empirical studies have assessed the impact of segmentation variability by applying controlled changes (e.g., expansions or contractions) to segmented regions of interest (ROIs) and observing the resulting variability in mean absorbed dose (288, 289). These studies show that for organs and large tumors, contour variability is the dominant source of uncertainty, while for small tumors, sensitivity to the recovery coefficient becomes more significant.

Another approach involves directly comparing contours generated by multiple observers. For example, a recent Society of Nuclear Medicine and Molecular Imaging (SNMMI) "Dosimetry Challenge" analyzed dose estimates from 178 participants using common ^{177}Lu-DOTATATE patient data (290–292). The study found segmentation to be a major contributor to dose variability, with normalized activity variability in healthy organs at 7% and lesion variability ranging from 6.7% to 24% (293). These findings support the development of standardized segmentation guidelines to reduce variability and improve the accuracy and reproducibility of RPT dosimetry.

9.3.5 Registration

Accurate image registration is essential for reliable dosimetry in radiopharmaceutical therapy (RPT), yet it remains an underexplored area in the literature. Studies have shown that even small misregistrations—such as translations under 9 mm or rotations under 5°–can cause absorbed dose errors of up to 90% in tumor regions, especially when lesions are located away from the center of the SPECT field of view (294–297). These findings underscore the sensitivity of dose calculations to registration accuracy, particularly in tumor volumes.

While early studies focused on SPECT-only datasets, more recent research has evaluated registration techniques in multi-timepoint SPECT/CT. Comparisons between rigid and non-rigid (deformable) registration methods consistently show that non-rigid approaches provide greater alignment accuracy, especially in complex datasets. CT-based registration—where the CT images guide alignment and the corresponding SPECT data is adjusted—has shown better consistency in activity quantification than SPECT-based methods (296).

Simulated phantom studies further highlight the benefits of non-rigid registration, showing substantial reductions in alignment errors. For instance, spleen and liver misalignments dropped from 15.5% to 2.1% and from 7.3% to 0.2%, respectively, when using deformable registration instead of rigid methods (297). Patient studies echo these findings: in ^{177}Lu-DOTATATE therapy, deformable registration resulted in higher absorbed dose estimates compared to rigid registration, with differences in kidney dose ranging from −19% to 4% and in tumor dose from −67.2% to 100.7% (295).

Proper patient positioning is also critical during multi-timepoint imaging. Movement between scans introduces alignment errors that can persist even after registration, leading to further uncertainties in dosimetry. These findings emphasize the need for careful registration method selection and consistent patient positioning to improve the accuracy of dose estimates in RPT.

9.4 Summary

Radiopharmaceutical therapy (RPT) is an increasingly important modality in oncology, offering targeted, systemic radiation delivery using tumor-seeking molecules labeled with radioactive isotopes. Unlike external beam radiotherapy, RPT can

treat both primary and metastatic disease sites with relatively low toxicity profiles, making it a promising option for patients with late-stage or refractory cancers. A hallmark of RPT is its integration into theranostics—combining diagnostic imaging with therapy to enable personalized treatment planning based on patient-specific biodistribution and molecular target expression.

Multiple RPT agents have gained FDA approval, including ^{131}I for thyroid cancer, $^{223}RaCl_2$ for prostate cancer with bone metastases, ^{177}Lu-DOTATATE for neuroendocrine tumors, and ^{177}Lu-PSMA-617 for prostate cancer. These therapies leverage diagnostic counterparts, such as ^{68}Ga- or ^{18}F-labeled PET tracers, to guide patient selection and assess target expression. Quantitative imaging using PET/CT and SPECT/CT plays a pivotal role in RPT by enabling individualized dosimetry, monitoring therapeutic response, and identifying potential off-target toxicity.

However, accurate quantification of radiopharmaceutical distribution remains technically complex. Sources of uncertainty include limited spatial resolution, sensitivity loss, partial volume effects, attenuation and scatter artifacts, segmentation variability, and image registration inaccuracies. Advances in imaging technologies, standardized protocols, and sophisticated correction algorithms are essential to improve reproducibility and optimize treatment delivery. As RPT continues to evolve, the ability to reduce these uncertainties will be critical to fully realizing the potential of precision medicine in nuclear oncology.

10 Conclusion

In conclusion, emerging technologies are rapidly reshaping the landscape of radiation oncology. Across the RT workflow, advanced imaging is enabling finer target definition, smarter motion management, and increasingly adaptive, biology-informed dose delivery. MR-guided RT brings daily soft-tissue visualization and online adaptation; PET-guided strategies and integrated PET-linac concepts extend guidance to the molecular scale; stereoscopic X-ray with thermal surface guidance supports sub-millimeter CNS positioning; and CBCT-based online adaptation (e.g., HyperSight-enabled workflows) turns daily anatomy into actionable plans. In parallel, generative AI for image synthesis is shortening acquisition chains and improving quantitation, while Cherenkov imaging offers real-time treatment verification and new avenues for QA and FLASH monitoring. In proton therapy, better HU to SPR mapping through DECT, robust motion imaging (4DCT, CToR), and *in vivo* range verification (prompt-gamma, PET) are converging on tighter range uncertainty. Beyond external beam, theranostics couples diagnostic specificity with patient-specific dosimetry to personalize radiopharmaceutical therapy.

Realizing these gains at scale will require rigorous multicenter validation, standardized QA and reporting, integration of multi-omics with functional/quantitative imaging, and trustworthy automation with continuous performance monitoring. Equally important are interoperable data pipelines, workforce training (especially for medical physicists), and attention to access and equity so that precision benefits reach diverse patient populations. Together, these advances point toward safer, more adaptive, and genuinely personalized RT.

Author contributions

YY: Writing – original draft, Writing – review & editing. DA: Writing – original draft. BB: Writing – original draft. LB: Writing – original draft. HC: Writing – original draft. DG: Writing – original draft. BH: Writing – original draft. CI: Writing – original draft. YL: Writing – original draft. NN: Writing – original draft. NM: Writing – original draft. NV: Writing – original draft. YW: Writing – original draft. JW: Writing – original draft. YZ: Writing – original draft. FG: Writing – original draft, Writing – review & editing.

Funding

The author(s) declare that no financial support was received for the research and/or publication of this article.

Acknowledgments

We gratefully acknowledge Dr. Tina Briere of the Department of Radiation Physics at The University of Texas MD Anderson Cancer Center for inspiring discussions and support for this work.

Conflict of interest

The authors declare that the research was conducted in the absence of any commercial or financial relationships that could be construed as a potential conflict of interest.

The author(s) declared that they were an editorial board member of Frontiers, at the time of submission. This had no impact on the peer review process and the final decision.

Correction note

A correction has been made to this article. Details can be found at: 10.3389/fmed.2025.1738811.

Generative AI statement

The author(s) declare that no Gen AI was used in the creation of this manuscript.

Any alternative text (alt text) provided alongside figures in this article has been generated by Frontiers with the support of artificial intelligence and reasonable efforts have been made to ensure accuracy, including review by the authors wherever possible. If you identify any issues, please contact us.

Publisher's note

All claims expressed in this article are solely those of the authors and do not necessarily represent those of their affiliated organizations, or those of the publisher, the editors and the reviewers. Any product that may be evaluated in this article, or claim that may be made by its manufacturer, is not guaranteed or endorsed by the publisher.

References

1. Mutic S, Dempsey JF. The ViewRay system: magnetic resonance–guided and controlled radiotherapy. *Semin Radiat Oncol.* (2014) 24:196–9. doi: 10.1016/j.semradonc.2014.02.008

2. Klüter S. Technical design and concept of a 0.35 T MR-Linac. *Clin Transl Radiat Oncol.* (2019) 18:98–101. doi: 10.1016/j.ctro.2019.04.007

3. Raaymakers BW, Lagendijk JJW, Overweg J, Kok JGM, Raaijmakers AJE, Kerkhof EM, et al. Integrating a 1.5 T MRI scanner with a 6 MV accelerator: proof of concept. *Phys Med Biol.* (2009) 54:N229–N237. doi: 10.1088/0031-9155/54/12/N01

4. Schleffler K, Lehnhardt S. Principles and applications of balanced SSFP techniques. *Eur Radiol.* (2003) 13:2409–18. doi: 10.1007/s00330-003-1957-x

5. Winkel D, Bol GH, Kroon PS, van Asselen B, Hackett SS, Werensteijn-Honingh AM, et al. Adaptive radiotherapy: the Elekta Unity MR-linac concept. *Clin Transl Radiat Oncol.* (2019) 18:54–9. doi: 10.1016/j.ctro.2019.04.001

6. Liveringhouse C, Netzley A, Bryant JM, Linkowski LC, Weygand J, Sandoval ML, et al. Trimodal therapy using an MR–guided radiation therapy partial bladder tumor boost in muscle invasive bladder cancer. *Adv Radiat Oncol.* (2023) 8:101268. doi: 10.1016/j.adro.2023.101268

7. Rammohan N, Randall JW, Yadav P. History of technological advancements towards MR-Linac: the future of image-guided radiotherapy. *J Clin Med.* (2022) 11:4730. doi: 10.3390/jcm11164730

8. La Rosa A, Mittauer KE, Rzepczynski AE, Chuong MD, Kutuk T, Bassiri N, et al. Treatment of glioblastoma using MRIdian® A3i BrainTx: imaging and treatment workflow demonstration. *Med Dosim.* (2023) 48:127–33. doi: 10.1016/j.meddos.2023.02.001

9. Smith BR, St-Aubin J, Hyer DE. Commissioning of a motion management system for a 1.5 T Elekta Unity MR-Linac: a single institution experience. *J Appl Clin Med Phys.* (2025) 26:e70005. doi: 10.1002/acm2.70005

10. Heerkens HD, Van Vulpen M, Erickson B, Reerink O, Intven MP, Van Den Berg CA, et al. MRI guided stereotactic radiotherapy for locally advanced pancreatic cancer. *Br J Radiol.* (2018) 91:20170563. doi: 10.1259/bjr.20170563

11. Chin S, Eccles CL, McWilliam A, Chuter R, Walker E, Whitehurst P, et al. Magnetic resonance-guided radiation therapy: a review. *J Med Imaging Radiat Oncol.* (2020) 64:163–77. doi: 10.1111/1754-9485.12968

12. Rudra S, Jiang N, Rosenberg SA, Olsen JR, Roach MC, Wan L, et al. Using adaptive magnetic resonance image-guided radiation therapy for treatment of inoperable pancreatic cancer. *Cancer Med.* (2019) 8:2123–32. doi: 10.1002/cam4.2100

13. Chuong MD, Lee P, Low DA, Kim J, Mittauer KE, Bassetti MF, et al. Stereotactic MR-guided on-table adaptive radiation therapy (SMART) for borderline resectable and locally advanced pancreatic cancer: a multi-center, open-label phase 2 study. *Radiother Oncol.* (2024) 191:110064. doi: 10.1016/j.radonc.2023.110064

14. Bryant JM, Weygand J, Keit E, Cruz-Chamorro R, Sandoval ML, Oraiqat IM, et al. Stereotactic magnetic resonance-guided adaptive and non-adaptive radiotherapy on combination MR-linear accelerators: current practice and future directions. *Cancers.* (2023) 15:2081. doi: 10.3390/cancers15072081

15. Bryant JM, Cruz-Chamorro RJ, Gan A, Liveringhouse C, Weygand J, Nguyen A, et al. Structure-specific rigid dose accumulation dosimetric analysis of ablative stereotactic MRI-guided adaptive radiation therapy in ultracentral lung lesions. *Commun Med.* (2024) 4:96. doi: 10.1038/s43856-024-00526-7

16. Bryant JM, Doniparthi A, Weygand J, Cruz-Chamorro R, Oraiqat IM, Andreozzi J, et al. Treatment of central nervous system tumors on combination MR-linear accelerators: review of current practice and future directions. *Cancers.* (2023) 15:5200. doi: 10.3390/cancers15215200

17. Mohamed AS, Hansen C, Weygand J, Ding Y, Frank SJ, Rosenthal DI, et al. Prospective analysis of in vivo landmark point-based MRI geometric distortion in head and neck cancer patients scanned in immobilized radiation treatment position: results of a prospective quality assurance protocol. *Clin Transl Radiat Oncol.* (2017) 7:13–9. doi: 10.1016/j.ctro.2017.09.003

18. Weygand J, Fuller CD, Ibbott GS, Mohamed AS, Ding Y, Yang J, et al. Spatial precision in magnetic resonance imaging–guided radiation therapy: the role of geometric distortion. *Int J Radiat Oncol Biol Phys.* (2016) 95:1304–16. doi: 10.1016/j.ijrobp.2016.02.059

19. Ginn JS, Agazaryan N, Cao M, Baharom U, Low DA, Yang Y, et al. Characterization of spatial distortion in a 0.35 T MRI-guided radiotherapy system. *Phys Med Biol.* (2017) 62:4525. doi: 10.1088/1361-6560/aa6e1a

20. Marasini S, Cole M, Curcuru A, Dyke LM, Gach HM, Flores R, et al. Characterization of real-time cine MR imaging distortion on 0.35 T MRgRT with concentric cine imaging QA phantom. *Phys Med Biol.* (2024) 69:065009. doi: 10.1088/1361-6560/ad2d33

21. Otazo R, Lambin P, Pignol JP, Ladd ME, Schlemmer HP, Baumann M, et al. MRI-guided radiation therapy: an emerging paradigm in adaptive radiation oncology. *Radiol.* (2021) 298:248–60. doi: 10.1148/radiol.2020202747

22. Keall PJ, Glide-Hurst CK, Cao M, Lee P, Murray B, Raaymakers BW, et al. ICRU report 97: MRI-guided radiation therapy using MRI-linear accelerators. *J ICRU.* (2022) 22:1–100. doi: 10.1177/14736691221141950

23. Weygand J, Hao Y, Awol M, Joseph AO, Kibudde S, Malloum A, et al. Evaluating the readiness for ultra-hypofractionated prostate and breast radiotherapy in sub-Saharan Africa: a strategic needs-assessment of six leading African institutions. *Ecancermedicalscience.* (2025) 19:1853. doi: 10.3332/ecancer.2025.1853

24. Salzillo T, Hu J, Nguyen L, Whiting N, Lee J, Weygand J, et al. Interrogating metabolism in brain cancer. *Magn Reson Imaging Clin N Am.* (2016) 24:687. doi: 10.1016/j.mric.2016.07.003

25. Wang J, Weygand J, Hwang KP, Mohamed AS, Ding Y, Fuller CD, et al. Magnetic resonance imaging of glucose uptake and metabolism in patients with head and neck cancer. *Sci Rep.* (2016) 6:30618. doi: 10.1038/srep30618

26. Dutta P, Perez MR, Lee J, Kang Y, Pratt M, Salzillo TC, et al. Combining hyperpolarized real-time metabolic imaging and NMR spectroscopy to identify metabolic biomarkers in pancreatic cancer. *J Proteome Res.* (2019) 18:2826–34. doi: 10.1021/acs.jproteome.9b00132

27. Salzillo TC, Mawoneke V, Weygand J, Shetty A, Gumin J, Zacharias NM, et al. Measuring the metabolic evolution of glioblastoma throughout tumor development, regression, and recurrence with hyperpolarized magnetic resonance. *Cells.* (2021) 10:2621. doi: 10.3390/cells10102621

28. Le Bihan D, Breton E, Lallemand D, Grenier P, Cabanis E, Laval-Jeantet M. MR imaging of intravoxel incoherent motions: application to diffusion and perfusion in neurologic disorders. *Radiology.* (1986) 161:401–7. doi: 10.1148/radiology.161.2.3763909

29. Tofts PS, Kermode AG. Measurement of the blood-brain barrier permeability and leakage space using dynamic MR imaging. 1. Fundamental concepts. *Magn Reson Med.* (1991) 17:357–67. doi: 10.1002/mrm.1910170208

30. Tofts PS, Brix G, Buckley DL, Evelhoch JL, Henderson E, Knopp MV, et al. Estimating kinetic parameters from dynamic contrast-enhanced T(1)-weighted MRI of a diffusable tracer: standardized quantities and symbols. *J Magn Reson Imaging.* (1999) 10:223–32. doi: 10.1109/TMI.2009.2019957

31. Weygand J, Carter SE, Salzillo TC, Moussalli M, Dai B. Can an organoid recapitulate the metabolome of its parent tissue: a pilot NMR spectroscopy study. *J Cancer Prev Curr Res.* (2017) 7:00307. doi: 10.15406/jcpcr.2017.08.00307

32. Messina C, Bignone R, Bruno A, Bruno A, Bruno F, Calandri M, et al. Diffusion-weighted imaging in cancer: an update. *Cancer.* (2020) 12:1493. doi: 10.3390/cancers12061493

33. Weygand J, Armstrong T, Bryant JM, Andreozzi JM, Oraiqat IM, Nichols S, et al. Accurate, repeatable, and geometrically precise diffusion-weighted imaging on a 0.35 T magnetic resonance imaging-guided linear accelerator. *Phys Imaging Radiat Oncol.* (2023) 28:100505. doi: 10.1016/j.phro.2023.100505

34. Naghavi AO, Bryant JM, Kim Y, Weygand J, Redler G, Sim AJ, et al. Habitat escalated adaptive therapy (HEAT): a phase 2 trial utilizing radiomic habitat-directed and genomic-adjusted radiation dose (GARD) optimization for high-grade soft tissue sarcoma. *BMC Cancer.* (2024) 24:437. doi: 10.1186/s12885-024-12151-7

35. Jalloul M, Miranda-Schaeubinger M, Noor AM, Stein JM, Amiruddin R, Derbew HM, et al. MRI scarcity in low- and middle-income countries. *NMR Biomed.* (2023) 36:e5022. doi: 10.1002/nbm.5022

36. Munkhtuvshin T, Shagdarsuren B, Bold B, Khurelsukh K, Myagmarsuren D, Bryant JM, et al. Cultivating expertise in MRI physics in Mongolia through international collaboration. *J Med Imaging Radiat Sci.* (2025) 56:101897. doi: 10.1016/j.jmir.2025.101897

37. Pollard JM, Wen Z, Sadagopan R, Wang J, Ibbott GS. The future of image-guided radiotherapy will be MR guided. *Br J Radiol.* (2017) 90:20160667. doi: 10.1259/bjr.20160667

38. Kurz C, Buizza G, Landry G, Kamp F, Rabe M, Paganelli C, et al. Medical physics challenges in clinical MR-guided radiotherapy. *Radiat Oncol.* (2020) 15:93. doi: 10.1186/s13014-020-01524-4

39. Fan Q, Nanduri A, Yang J, Yamamoto T, Loo B, Graves E, et al. Toward a planning scheme for emission guided radiation therapy (EGRT): FDG based tumor tracking in a metastatic breast cancer patient. *Med. Phys.* (2013) 40:081708. doi: 10.1118/1.4812427

40. Shirvani SM, Huntzinger CJ, Melcher T, Olcott PD, Voronenko Y, Bartlett-Roberto J, et al. Biology-guided radiotherapy: redefining the role of radiotherapy in metastatic cancer. *Br J Radiol.* (2021) 94:1117. doi: 10.1259/bjr.20200873

41. Fonti R, Conson M, Vecchio SD. PET/CT in radiation oncology. *Semin Oncol.* (2019) 46:202-9. doi: 10.1053/j.seminoncol.2019.07.001

42. Chau B, Abuali T, Shirvani SM, Leung D, Al Feghali KA, Hui S, et al. Feasibility of biology-guided radiotherapy (BgRT) targeting fluorodeoxyglucose (FDG) avid liver metastases. *Radiat Oncol.* (2024) 19:124. doi: 10.1186/s13014-024-02502-w

43. Wong J, Liu B, Dandapani S, Li Y, Glaser S, Liu J, et al. A prospective pilot study of the RefleXion® X1 PET-CT subsystem imaging performance with [18F]-DCFPyL PSMA in patients with prostate cancer. *J Nucl Med.* (2023) 64:521.

44. Hrinivich WT, Phillips R, Da Silva AJ, Radwan N, Gorin MA, Rowe SP, et al. Online prostate-specific membrane antigen and positron emission tomography guided radiation therapy for oligometastatic prostate cancer. *Adv Radiat Oncol.* (2020) 5:260–8. doi: 10.1016/j.adro.2019.10.006

45. Han C, Bal G, Wong JYC, Williams TM, Liu A. Feasibility of biology-guided radiotherapy with Gallium-68 PSMA-11 radiotracer for bony metastases in prostate cancer patients. *Int J Radiat Oncol Biol Phys.* (2024) 120:79. doi: 10.1016/j.ijrobp.2024.07.137

46. Jarritt PH, Carson KJ, Hounsell AR, Visvikis D. The role of PET/CT scanning in radiotherapy planning. *Br J Radiol.* (2006) 79:S27–35. doi: 10.1259/bjr/35628509

47. Fiorentino A, Laudicella R, Ciurlia E, Annunziata S, Lancellotta V, Mapelli P, et al. Positron emission tomography with computed tomography imaging (PET/CT) for the radiotherapy planning definition of the biological target volume: PART 2. *Crit Rev Oncol Hematol.* (2019) 139:117–24. doi: 10.1016/j.critrevonc.2019.03.008

48. Créhange G, Soussan M, Gensanne D, Decazes P, Thariat J, Thureau S. Interest of positron-emission tomography and magnetic resonance imaging for radiotherapy planning and control. *Cancer Radiothér.* (2020) 24:398–402. doi: 10.1016/j.canrad.2020.02.010

49. Ladbury C, Eustace N, Amini A, Dandapani S, Williams T. Biology-guided radiation therapy: an evolving treatment paradigm. *Surg Oncol Clin.* (2023) 32:553–68. doi: 10.1016/j.soc.2023.02.006

50. Castadot P, Lee JA, Parraga A, Geets X, Macq B, Grégoire V. Adaptive radiotherapy of head and neck cancer. *Semin Radiat Oncol.* (2010) 20:84–93. doi: 10.1016/j.semradonc.2009.11.002

51. Yang J, Yamamoto T, Mazin SR, Graves EE, Keall PJ. The potential of positron emission tomography for intratreatment dynamic lung tumor tracking: a phantom study. *Med Phys.* (2014) 41:021718. doi: 10.1118/1.4861816

52. Oderinde OM, Shirvani SM, Olcott PD, Kuduvalli G, Mazin S, Larkin D. The technical design and concept of a PET/CT linac for biology-guided radiotherapy. *Clin Transl Radiat Oncol.* (2021) 17:106–12. doi: 10.1016/j.ctro.2021.04.003

53. Oderinde OM, Narayanan M, Olcott P, Voronenko Y, Burns J, Xu S, et al. Demonstration of real-time positron emission tomography biology-guided radiotherapy delivery to targets. *Med Phys.* (2024) 51:5672–81. doi: 10.1002/mp.16999

54. Hu Z, Bieniosek M, Ferri V, Iagaru A, Kovalchuk N, Han B, et al. Image-mode performance characterisation of a positron emission tomography subsystem designed for biology-guided radiotherapy (BgRT). *Br J Radiol.* (2023) 96:1141. doi: 10.1259/bjr.20220387

55. Hwang MS, Lalonde R, Huq MS. A detailed process map for clinical workflow of a new biology-guided radiotherapy (BgRT) machine. *J Appl Clin Med Phys.* (2022) 23:e13606. doi: 10.1002/acm2.13606

56. Narayanan M, Zaks D, Olcott PD, Voronenko Y, Burns J, Xu S, et al. Physical validation of biology-guided radiotherapy for delivering a tracked dose distribution to a moving PET-avid target. *Int J Radiat Oncol Biol Phys.* (2021) 111:S22. doi: 10.1016/j.ijrobp.2021.07.078

57. Surucu M, Ashraf MR, Romero IO, Zalavari LT, Pham D, Vitzthum LK, et al. Commissioning of a novel PET-Linac for biology-guided radiotherapy. *Med Phys.* (2024) 51:4389–401. doi: 10.1002/mp.17114

58. U.S. Nuclear Regulatory Commission (NRC). *Standards for protection against radiation: 10 CFR Part 20. Code of Federal Regulations.* Washington, DC: U.S. Government Printing Office (2023).

59. Ronneberger O, Fischer P, Brox T. U net: convolutional networks for biomedical image segmentation. In Navab N, Hornegger J, Wells W, Frangi A, editors. *Medical Image Computing and Computer-Assisted Intervention – MICCAI 2015. MICCAI 2015. Lecture Notes in Computer Science, Vol. 9351.* New York: Springer International Publishing (2015). p. 234–241.

60. Milletari F, Navab N, Ahmadi SA. V-net: fully convolutional neural networks for volumetric medical image segmentation. In *2016 fourth international conference on 3D vision (3DV).* Stanford, CA: IEEE (2016). p. 565–71.

61. Gu S, Dai Z, Wu L, Liu W, Chen L. Dempster-Shafer theory empowered deep learning for enhanced 3D PET-CT medical image segmentation: a first test on automated lesion segmentation in whole-body dataset. In *2024 4th International Conference on Neural Networks, Information and Communication Engineering (NNICE).* Guangzhou: IEEE (2024). p. 350–4.

62. Nakajo M, Jinguji M, Ito S, Tani A, Hirahara M, Yoshiura T. Clinical application of 18F-fluorodeoxyglucose positron emission tomography/computed tomography radiomics-based machine learning analyses in the field of oncology. *Jpn J Radiol.* (2024) 42:28–55. doi: 10.1007/s11604-023-01476-1

63. Perrett B, Ukath J, Horgan E, Noble C, Ramachandran P. A framework for ExacTrac dynamic commissioning for stereotactic radiosurgery and stereotactic ablative radiotherapy. *J Med Phys.* (2022) 47:398–408. doi: 10.4103/jmp.jmp_67_22

64. Benedict SH, Yenice KM, Followill D, Galvin JM, Hinson W, Kavanagh B, et al. Stereotactic body radiation therapy: the report of AAPM Task Group 101. *Med Phys.* (2010) 37:4078–101. doi: 10.1118/1.3438081

65. Cirino E, Benedict SH, Dupre PJ, Halvorsen PH, Kim GGY, Reyhan ML, et al. AAPM-RSS Medical Physics Practice Guideline 9. b: SRS-SBRT. *J Appl Clin Med Phys.* (2025) 26:e14624. doi: 10.1002/acm2.14624

66. Chao ST, Dad LK, Dawson LA, Desai NB, Pacella M, Rengan R, et al. ACR–ASTRO practice parameter for the performance of stereotactic body radiation therapy. *Am J Clin Oncol.* (2020) 43:545–52. doi: 10.1097/COC.0000000000000706

67. Jin J-Y, Yin F-F, Tenn SE, Medin PM, Solberg TD. Use of the BrainLAB ExacTrac X-Ray 6D system in image-guided radiotherapy. *Med Dosim.* 33:124–34. (2008). doi: 10.1016/j.meddos.2008.02.005

68. van de Schoot AJ, Hoffmans D, van Ingen KM, Simons MJ, Wiersma J. Characterization of Ethos therapy systems for adaptive radiation therapy: a multi-machine comparison. *J Appl Clin Med Phys.* (2023) 24:e13905. doi: 10.1002/acm2.13905

69. Visak J, Inam E, Meng B, Wang S, Parsons D, Nyugen D, et al. Evaluating machine learning enhanced intelligent-optimization-engine (IOE) performance for ethos head-and-neck (HN) plan generation. *J Appl Clin Med Phys.* (2023) 24:e13950. doi: 10.1002/acm2.13950

70. Sibolt P, Andersson LM, Calmels L, Sjöström D, Bjelkengren U, Geertsen P, et al. Clinical implementation of artificial intelligence-driven cone-beam computed tomography-guided online adaptive radiotherapy in the pelvic region. *Phys Imaging Radiat Oncol.* (2021) 17:1–7. doi: 10.1016/j.phro.2020.12.004

71. Åström LM, Behrens CP, Storm KS, Sibolt P, Serup-Hansen E. Online adaptive radiotherapy of anal cancer: normal tissue sparing, target propagation methods, and first clinical experience. *Radiother Oncol.* (2022) 176:92–8. doi: 10.1016/j.radonc.2022.09.015

72. Shelley CE, Bolt MA, Hollingdale R, Chadwick SJ, Barnard AP, Rashid M, et al. Implementing cone-beam computed tomography-guided online adaptive radiotherapy in cervical cancer. *Clin Trans Radiat Oncol.* (2023) 40:100596. doi: 10.1016/j.ctro.2023.100596

73. Schiff JP, Price AT, Stowe HB, Laugeman E, Chin RI, Hatscher C, et al. Simulated computed tomography-guided stereotactic adaptive radiotherapy (CT-STAR) for the treatment of locally advanced pancreatic cancer. *Radiother Oncol.* (2022) 175:144–51. doi: 10.1016/j.radonc.2022.08.026

74. Stanley DN, McConnell K, Cardenas CE, Belliveau JG, Meyers K, Hotsinpiller WS, et al. Stereotactic breast radiotherapy delivered via external beam daily online adaptive replanning. *Int J Radiat Oncol Biol Phys.* (2022) 114:e597. doi: 10.1016/j.ijrobp.2022.07.2288

75. Pogue JA, Cardenas CE, Stanley DN, Stanley C, Hotsinpiller W, Veale C, et al. Improved dosimetry and plan quality for accelerated partial breast irradiation using online adaptive radiation therapy: a single institutional study. *Adv Radiat Oncol.* (2024) 9:101414. doi: 10.1016/j.adro.2023.101414

76. Wegener S, Weick S, Schindhelm R, Tamihardja J, Sauer OA, Razinskas G. Feasibility of Ethos adaptive treatments of lung tumors and associated quality assurance. *J Appl Clin Med Phys.* (2024) 25:e14311. doi: 10.1002/acm2.14311

77. Guberina M, Guberina N, Hoffmann C, Gogishvili A, Freisleben F, Herz A, et al. Prospects for online adaptive radiation therapy (ART) for head and neck cancer. *Radiat Oncol.* (2024) 19:4. doi: 10.1186/s13014-023-02390-6

78. Dohopolski M, Visak J, Choi B, Meng B, Parsons D, Zhong X, et al. In silico evaluation and feasibility of near margin-less head and neck daily adaptive radiotherapy. *Radiother Oncol.* (2024) 197:110178. doi: 10.1016/j.radonc.2024.110178

79. Robar JL, Cherpak A, MacDonald RL, Yashayaeva A, McAloney D, McMaster N, et al. Novel technology allowing cone beam computed tomography in 6 seconds: a patient study of comparative image quality. *Pract Radiat Oncol.* (2024) 14:277–86. doi: 10.1016/j.prro.2023.10.014

80. Duan J, Pogue JA, Stanley DN, Shen S, Viscariello NN, Cardenas CE, et al. Assessing HyperSight iterative CBCT for dose calculation in online adaptive radiotherapy for pelvis and breast patients compared to synthetic CT. *J Appl Clin Med Phys.* (2025) 26:e70038 doi: 10.1002/acm2.70038

81. Price AT, Schiff JP, Silberstein A, Beckert R, Zhao T, Hugo GD, et al. Feasibility of simulation free abdominal stereotactic adaptive radiotherapy using an expedited pre-plan workflow. *Phys Imaging Radiat Oncol.* (2024) 31:100611. doi: 10.1016/j.phro.2024.100611

82. Wang D, Kim H, Zhuang T, Visak JD, Cai B, Parsons DD, et al. Simulation-omitting and using library patients for pre-planning online adaptive radiotherapy (SUPPORT): a feasibility study for spine stereotactic ablative radiotherapy (SAbR) patients. *Cancers.* (2025) 17:1216. doi: 10.3390/cancers17071216

83. MacDonald RL, Fallone C, Chytyk-Praznik K, Robar J, Cherpak A. The feasibility of CT simulation-free adaptive radiation therapy. *J Appl Clin Med Phys.* (2024) 25:e14438. doi: 10.1002/acm2.14438

84. Viscariello NN, McConnell K, Harms J, Pogue JA, Ray X, Laugeman E, et al. Quantitative assessment of full-time equivalent effort for kilovoltage-cone beam computed tomography guided online adaptive radiation therapy for medical physicists. *Pract Radiat Oncol.* (2025) 15:e72–81. doi: 10.1016/j.prro.2024.08.007

85. Lin M, Kavanaugh JA, Kim M, Cardenas CE, Rong Y. Physicists should perform reference planning for CBCT guided online adaptive radiotherapy. *J Appl Clin Med Phys.* (2023) 24:e14163. doi: 10.1002/acm2.14163

86. Wang Y, Liu C, Zhang X, Deng W. Synthetic CT generation based on T2 weighted MRI of nasopharyngeal carcinoma (NPC) using a deep convolutional neural network (DCNN). *Front Oncol.* (2019) 9:1333. doi: 10.3389/fonc.2019.01333

87. Archambault Y, Boylan C, Bullock D, Morgas T, Peltola J, Ruokokoski E, et al. Making on-line adaptive radiotherapy possible using artificial intelligence and machine learning for efficient daily re-planning. *Med Phys Int J*. (2020) 8.

88. Byrne M, Teh AY, Archibald-Heeren B, Hu Y, Rijken J, Luo S, et al. Intrafraction motion and margin assessment for ethos online adaptive radiotherapy treatments of the prostate and seminal vesicles. *Adv Radiat Oncol.* (2023) 9:101405. doi: 10.1016/j.adro.2023.101405

89. Hermena S, Young M. *CT Scan Image Production Procedures*. Treasure Island, FL: StatPearls. (2023).

90. Hsieh J. *Computed Tomography: Principles, Design, Artifacts, and Recent Advances.* Bellingham, WA: SPIE Press (2003).

91. Shen C, Nguyen D, Zhou Z, Jiang SB, Dong B, Jia X. An introduction to deep learning in medical physics: advantages, potential, and challenges. *Phys Med Biol.* (2020) 65:05TR01. doi: 10.1088/1361-6560/ab6f51

92. Zhou SK, Greenspan H, Davatzikos C, Duncan JS, Van Ginneken B, Madabhushi A, et al. A review of deep learning in medical imaging: imaging traits, technology trends, case studies with progress highlights, and future promises. *Proc IEEE.* (2021) 109:820–38. doi: 10.1109/JPROC.2021.3054390

93. Wang T, Lei Y, Fu Y, Wynne JF, Curran WJ, Liu T, et al. A review on medical imaging synthesis using deep learning and its clinical applications. *J Appl Clin Med Phys.* (2021) 22:11–36. doi: 10.1002/acm2.13121

94. Meyer P, Noblet V, Mazzara C, Lallement A. Survey on deep learning for radiotherapy. *Comput Biol Med.* (2018) 98:126–46. doi: 10.1016/j.compbiomed.2018.05.018

95. Kazerouni A, Aghdam EK, Heidari M, Azad R, Fayyaz M, Hacihaliloglu I, et al. Diffusion models in medical imaging: a comprehensive survey. *Med Image Anal.* (2023) 88:102846. doi: 10.1016/j.media.2023.102846

96. Eickhoff SB, Rottschy C, Kujovic M, Palomero Gallagher N, Zilles K. Organizational principles of human visual cortex revealed by receptor mapping. *Cereb Cortex.* (2008) 18:2637–45. doi: 10.1093/cercor/bhn024

97. Hilgetag CC, Goulas A. 'Hierarchy' in the organization of brain networks. *Philos Trans R Soc Lond B Biol Sci.* (2020) 375:20190319. doi: 10.1098/rstb.2019.0319

98. Fukushima K. Neocognitron: a self organizing neural network model for a mechanism of pattern recognition unaffected by shift in position. *Biol Cybern.* (1980) 36:193–202. doi: 10.1007/BF00344251

99. Kshatri SS, Singh D. Convolutional neural network in medical image analysis: a review. *Arch Comput Methods Eng.* (2023) 30:2793–810. doi: 10.1007/s11831-023-09898-w

100. Anwar SM, Majid M, Qayyum A, Awais M, Alnowami M, Khan MK. Medical image analysis using convolutional neural networks: a review. *J Med Syst.* (2018) 42:1–13. doi: 10.1007/s10916-018-1088-1

101. Sarvamangala DR, Kulkarni RV. Convolutional neural networks in medical image understanding: a survey. *Evol Intell.* (2022) 15:1–22. doi: 10.1007/s12065-020-00540-3

102. Abdou MA. Literature review: efficient deep neural networks techniques for medical image analysis. *Neural Comput Appl.* (2022) 34:5791–812. doi: 10.1007/s00521-022-06960-9

103. Nair V, Hinton GE. Rectified linear units improve restricted Boltzmann machines. In *Proceedings of the 27th International Conference on Machine Learning (ICML 10)*. Haifa: Omnipress (2010). p. 807–14.

104. Maas AL, Hannun AY, Ng AY. June. Rectifier nonlinearities improve neural network acoustic models. In Proc ICML (Vol. 30, No. 1, p. 3) 2013.

105. Clevert DA, Unterthiner T, Hochreiter S. Fast and accurate deep network learning by exponential linear units (ELUs). *arXiv* [Preprint]. arXiv:1511.07289. (2015). doi: 10.48550/arXiv.1511.07289

106. Akhtar N, Ragavendran U. Interpretation of intelligence in CNN pooling processes: a methodological survey. *Neural Comput Appl.* (2020) 32:879–98. doi: 10.1007/s00521-019-04296-5

107. Zhou DX. Theory of deep convolutional neural networks: downsampling. *Neural Netw.* (2020) 124:319–27. doi: 10.1016/j.neunet.2020.01.018

108. Park S, Kwak N. Analysis on the dropout effect in convolutional neural networks. In Lai SH, Lepetit V, Nishino K, Sato Y, editors. *Computer Vision – ACCV 2016. ACCV 2016. Lecture Notes in Computer Science, vol. 10112.* New York: Springer International Publishing. (2017). p. 189–204.

109. Goodfellow IJ, Pouget Abadie J, Mirza M, Xu B, Warde Farley D, Ozair et al. Generative adversarial nets. *Adv Neural Inf Process Syst.* (2014) 27, 1–9.

110. Wang TC, Liu MY, Zhu JY, Tao A, Kautz J, Catanzaro B. High resolution image synthesis and semantic manipulation with conditional GANs. In *Proceedings of the IEEE Conference on Computer Vision and Pattern Recognition*. Piscataway, NJ: Institute of Electrical and Electronics Engineers (IEEE) (2018). p. 8798–807.

111. Sricharan K, Bala R, Shreve M, Ding H, Saketh K, Sun J. Semi supervised conditional GANs. *arXiv* [Preprint]. arXiv:1708.05789 (2017). doi: 10.48550/arXiv.1708.05789

112. Harms J, Lei Y, Wang T, Zhang R, Zhou J, Tang X, et al. Paired cycle GAN based image correction for quantitative cone beam computed tomography. *Med Phys.* (2019) 46:3998–4009. doi: 10.1002/mp.13656

113. Zhang Y, Liu S, Dong C, Zhang X, Yuan Y. Multiple cycle in cycle generative adversarial networks for unsupervised image super resolution. In *IEEE Trans Image Process, Vol. 29*. Piscataway, NJ: IEEE (2019). p.1101–1112.

114. Karras T, Laine S, Aittala M, Hellsten J, Lehtinen J, Aila T. Analyzing and improving the image quality of StyleGAN. In *Proceedings of the IEEE/CVF Conference on Computer Vision and Pattern Recognition*. Piscataway, NJ: Institute of Electrical and Electronics Engineers (IEEE) (2020). p. 8110–9.

115. Richardson E, Alaluf Y, Patashnik O, Nitzan Y, Azar Y, Shapiro S, Cohen Or D. Encoding in style: a StyleGAN encoder for image to image translation. In *2021 IEEE/CVF Conference on Computer Vision and Pattern Recognition (CVPR)*.Nashville, TN: IEEE (2020). p. 2287–96.

116. Sohl Dickstein J, Weiss E, Maheswaranathan N, Ganguli S. Deep unsupervised learning using nonequilibrium thermodynamics. In Int Conf on Machine Learning (pp. 2256 2265) 2015.

117. Khader F, Müller-Franzes G, Tayebi Arasteh S, Han T, Haarburger C, Schulze Hagenet A, et al. Denoising diffusion probabilistic models for 3D medical image generation. *Sci Rep*. (2023) 13:7303. doi: 10.1038/s41598-023-34341-2

118. Dorjsembe Z, Pao HK, Odonchimed S, Xiao F. Conditional diffusion models for semantic 3D brain MRI synthesis. *IEEE J Biomed Health Inform.* (2024) 28:4084–93. doi: 10.1109/JBHI.2024.3385504

119. Yu Y, Gu Y, Zhang S, Zhang X. Meddiff FM: a diffusion based foundation model for versatile medical image applications. *arXiv* [Preprint]. arXiv:2410.15432 (2024). doi: 10.48550/arXiv.2410.15432

120. Sherwani MK, Gopalakrishnan S. A systematic literature review: deep learning techniques for synthetic medical image generation and their applications in radiotherapy. *Front Radiol.* (2024) 4:1385742. doi: 10.3389/fradi.2024.1385742

121. Yang X, Lei Y, Shu HK, Rossi P, Mao H, Shim H, et al. Pseudo CT estimation from MRI using patch based random forest. In Proc SPIE (Vol. 10133, p. 101332Q) 2017. doi: 10.1117/12.2253936

122. Dinkla AM, Wolterink JM, Maspero M, Savenije MH, Verhoeff JJ, Seravalli E, et al. MR only brain radiation therapy: dosimetric evaluation of synthetic CTs generated by a dilated convolutional neural network. *Int J Radiat Oncol Biol Phys.* (2018) 102:801–12. doi: 10.1016/j.ijrobp.2018.05.058

123. Xu K, Cao J, Xia K, Yang H, Zhu J, Wu C, et al. Multichannel residual conditional GAN leveraged abdominal pseudo CT generation via Dixon MR images. *IEEE Access.* (2019) 7:163823–30. doi: 10.1109/ACCESS.2019.2951924

124. Lei Y, Harms J, Wang T, Liu Y, Shu HK, Jani AB, et al. MRI only based synthetic CT generation using dense cycle consistent generative adversarial networks. *Med Phys.* (2019) 46:3565–81. doi: 10.1002/mp.13617

125. Liu Y, Lei Y, Wang Y, Wang T, Ren L, Lin L, et al. MRI based treatment planning for proton radiotherapy: dosimetric validation of a deep learning based liver synthetic CT generation method. *Phys Med Biol.* (2019) 64:145015. doi: 10.1088/1361-6560/ab25bc

126. Jin CB, Kim H, Liu M, Jung W, Joo S, Park E, et al. Deep CT to MR synthesis using paired and unpaired data. *Sensors.* (2019) 19:2361. doi: 10.3390/s19102361

127. Dayarathna S, Islam KT, Uribe S, Yang G, Hayat M, Chen Z. Deep learning based synthesis of MRI, CT and PET: review and analysis. *Med Image Anal.* (2024) 92:103046. doi: 10.1016/j.media.2023.103046

128. Dai X, Lei Y, Fu Y, Curran WJ, Liu T, Mao H, et al. Multimodal MRI synthesis using unified generative adversarial networks. *Med Phys.* (2020) 47:6343–54. doi: 10.1002/mp.14539

129. Yang H, Sun J, Yang L, Xu Z. A unified hyper GAN model for unpaired multi contrast MR image translation. In de Bruijne M, editors, et al. *Medical Image Computing and Computer Assisted Intervention – MICCAI 2021. MICCAI 2021. Lecture Notes in Computer Science,* vol. 12903. New York: Springer International Publishing (2021). p. 127–37.

130. Kawahara D, Yoshimura H, Matsuura T, Saito A, Nagata Y. MRI image synthesis for fluid attenuated inversion recovery and diffusion weighted images with deep learning. *Phys Eng Sci Med.* (2023) 46:313–23. doi: 10.1007/s13246-023-01220-z

131. Dalmaz O, Yurt M, Çukur T. ResViT: residual vision transformers for multimodal medical image synthesis. *IEEE Trans Med Imaging*. (2022) 41:2598–2614. doi: 10.1109/TMI.2022.3167808

132. Zhang X, He X, Guo J, Ettehadi N, Aw N, Semanek D, et al. PTNet3D: a 3D high resolution longitudinal infant brain MRI synthesizer based on transformers. *IEEE Trans Med Imaging.* (2022) 41:2925–40. doi: 10.1109/TMI.2022.3174827

133. Özbey M, Dalmaz O, Dar SU, Bedel HA, Özturk S, Güngör A, Cukur T. Unsupervised medical image translation with adversarial diffusion models. *IEEE Trans Med Imaging.* (2023) 42:3524–39. doi: 10.1109/TMI.2023.3290149

134. Zhu L, Xue Z, Jin Z, Liu X, He J, Liu Z, et al. Make-a-volume: Leveraging latent diffusion models for cross-modality 3D brain MRI synthesis. In: *International Conference on Medical Image Computing and Computer-Assisted Intervention*. Cham: Springer Nature Switzerland. (2023). p. 592–601. doi: 10.1007/978-3-031-43999-5_56

135. Islam J, Zhang Y. GAN-based synthetic brain PET image generation. *Brain Inform*. (2020) 7:3. doi: 10.1186/s40708-020-00104-2

136. Salehjahromi M, Karpinets TV, Sujit SJ, Qayati M, Chen P, Aminu M, et al. Synthetic PET from CT improves diagnosis and prognosis for lung cancer: proof of concept. *Cell Rep Med*. (2024) 5:101463. doi: 10.1016/j.xcrm.2024.101463

137. Liu Y, Lei Y, Wang T, Fu Y, Tang X, Curran WJ, et al. CBCT based synthetic CT generation using deep attention cycleGAN for pancreatic adaptive radiotherapy. *Med Phys*. (2020) 47:2472–83. doi: 10.1002/mp.14121

138. Landry G, Hansen D, Kamp F, Li M, Hoyle B, Weller et al. Comparing U Net training with three different datasets to correct CBCT images for prostate radiotherapy dose calculations. *Phys Med Biol*. (2019) 64:035011. doi: 10.1088/1361-6560/aaf496

139. Cheng HLM. Investigation and optimization of parameter accuracy in dynamic contrast-enhanced MRI. *J Magn Reson Imaging*. (2008) 28:736–43. doi: 10.1002/jmri.21489

140. Ma X, Chen X, Li J, Wang Y, Men K, Dai, J. MRI-only radiotherapy planning for nasopharyngeal carcinoma using deep learning. *Front Oncol*. (2008) 11:713617. doi: 10.3389/fonc.2021.713617

141. Liu Y, Lei Y, Wang T, Kayode O, Tian S, Liu, et al. MRI-based treatment planning for liver stereotactic body radiotherapy: validation of a deep learning-based synthetic CT generation method. *Br J Radiol*. (2019) 92:20190067. doi: 10.1259/bjr.20190067

142. Shafai-Erfani G, Wang T, Lei Y, Tian S, Patel P, Jani AB, et al. Dose evaluation of MRI-based synthetic CT generated using a machine learning method for prostate cancer radiotherapy. *Med Dosim*. (2019) 44:e64–e70. doi: 10.1016/j.meddos.2019.01.002

143. Thummerer A, Seller Oria C, Zaffino P, Visser S, Meijers A, Guterres Marmitt G, et al. Deep learning–based 4D-synthetic CTs from sparse-view CBCTs for dose calculations in adaptive proton therapy. *Med Phys*. (2022) 49:6824–39. doi: 10.1002/mp.15930

144. Shafai-Erfani G, Lei Y, Liu Y, Wang Y, Wang T, Zhong J, et al. MRI-based proton treatment planning for base of skull tumors. *Int J Part Ther*. (2019) 6:12–25. doi: 10.14338/IJPT-19-00062.1

145. Liu Y, Lei Y, Wang Y, Shafai-Erfani G, Wang T, Tian S, et al. Evaluation of a deep learning-based pelvic synthetic CT generation technique for MRI-based prostate proton treatment planning. *Phys Med Biol*. (2019) 64:205022. doi: 10.1088/1361-6560/ab41af

146. Dayarathna S, Wu Y, Cai J, Wong TT, Law M, Islam K, et al. MU-Diff: a mutual learning diffusion model for synthetic MRI with Application for brain lesions. *npj Artif Intell*. (2025) 1:11. doi: 10.1038/s44387-025-00016-8

147. Haacke EM. *Magnetic Resonance Imaging: Physical Principles and Sequence Design*. New York, NY: Wiley-Liss (1999).

148. Bao S, Liao C, Xu N, Deng A, Luo Y, Ouyang Z, et al. Prediction of brain age using quantitative parameters of synthetic magnetic resonance imaging. *Front Aging Neurosci*. (2022) 14:963668. doi: 10.3389/fnagi.2022.963668

149. Hsu SH, Han Z, Leeman JE, Hu YH, Mak RH, Sudhyadhom A. Synthetic CT generation for MRI-guided adaptive radiotherapy in prostate cancer. *Front Oncol*. (2022) 12:969463. doi: 10.3389/fonc.2022.969463

150. Hussein R, Zhao MY, Shin D, Guo J, Chen KT, Armindo RD, et al. Multi-task deep learning for cerebrovascular disease classification and MRI-to-PET translation. In *2022 26th International Conference on Pattern Recognition (ICPR)*. Montreal, QC: IEEE (2022). p. 4306–12.

151. Sikka A, Peri SV, Bathula DR. MRI to FDG-PET: cross-modal synthesis using 3D U-Net for multi-modal Alzheimer's classification. In International workshop on simulation and synthesis in medical imaging. Springer International Publishing. (2018). p. 80–9. doi: 10.1007/978-3-030-00536-8_9

152. Sikka A, Peri S, Virk JS, Niyaz U, Bathula DR. MRI-to-PET cross-modality translation using globally & locally aware GAN (GLA-GAN) for multi-modal diagnosis of Alzheimer's disease. *J Precis Med Health Dis*. (2025) 2:100004. doi: 10.1016/j.premed.2025.100004

153. Emami H, Liu Q, Dong M. FREA-UNet: frequency-aware U-Net for modality transfer. *arXiv* [Preprint]. *arXiv:2012.15397* (2020). doi: 10.48550/arXiv.2012.15397

154. Fei Y, Zu C, Jiao Z, Wu X, Zhou J, Shen D, et al. Classification-aided high-quality PET image synthesis via bidirectional contrastive GAN with shared information maximization. In *International Conference on Medical Image Computing and Computer-Assisted Intervention*. Cham: Springer Nature Switzerland (2022). p. 527–37.

155. Hu S, Lei B, Wang S, Wang Y, Feng Z, Shen, Y. Bidirectional mapping generative adversarial networks for brain MR to PET synthesis. *IEEE Trans Med Imaging*. (2021) 41:145–57. doi: 10.1109/TMI.2021.3107013

156. Zhang L, Xiao Z, Zhou C, Yuan J, He Q, Yang Y, et al. Spatial adaptive and transformer fusion network (STFNet) for low-count PET blind denoising with MRI. *Med Phys*. (2022) 49:343–56. doi: 10.1002/mp.15368

157. Jang SI, Lois C, Thibault E, Becker JA, Dong Y, Normandin MD, et al. Taupetgen: text-conditional tau pet image synthesis based on latent diffusion models. (2023) *arXiv* [Preprint] arXiv:2306.11984. doi: 10.1109/NSSMICRTSD49126.2023.10338710

158. Pan S, Abouei E, Peng J, Qian J, Wynne JF, Wang T, et al. Full-dose whole-body PET synthesis from low-dose PET using high-efficiency denoising diffusion probabilistic model: PET consistency model. *Med Phys*. (2024) 51:5468–78. doi: 10.1002/mp.17068

159. Zhang J, He X, Qing L, Gao F, Wang B. BPGAN: Brain PET synthesis from MRI using generative adversarial network for multi-modal Alzheimer's disease diagnosis. *Comput Methods Programs Biomed*. (2022) 217:106676. doi: 10.1016/j.cmpb.2022.106676

160. Hurrell MA, Butler APH, Cook NJ, Butler PH, Ronaldson JP, Zainon R. Spectral hounsfield units: a new radiological concept. *Eur Radiol*. (2012) 22:1008–13. doi: 10.1007/s00330-011-2348-3

161. Hou J, Guerrero M, Chen W, D'Souza WD. Deformable planning CT to cone-beam CT image registration in head-and-neck cancer. *Med Phys*. (2011) 38:2088–94. doi: 10.1118/1.3554647

162. Nomura Y, Xu Q, Shirato H, Shimizu S, Xing L. Projection-domain scatter correction for cone beam computed tomography using a residual convolutional neural network. *Med Phys*. (2019) 46:3142–55. doi: 10.1002/mp.13583

163. Shan H, Padole A, Homayounieh F, Kruger U, Khera RD, Nitiwarangkul C, et al. Competitive performance of a modularized deep neural network compared to commercial algorithms for low-dose CT image reconstruction. *Nat Mach Intell*. (2019) 1:269–76. doi: 10.1038/s42256-019-0057-9

164. Zhang R, Fox CJ, Glaser AK, Gladstone DJ, Pogue BW. Superficial dosimetry imaging of Cerenkov emission in electron beam radiotherapy of phantoms. *Phys Med Biol*. (2013) 58:5477. doi: 10.1088/0031-9155/58/16/5477

165. Glaser AK, Davis SC, McClatchy DM, Zhang R, Pogue BW, Gladstone DJ. Projection imaging of photon beams by the Cerenkov effect. *Med Phys*. (2013) 40:012101. doi: 10.1118/1.4770286

166. Jarvis LA, Zhang R, Gladstone DJ, et al. Cherenkov video imaging allows for the first visualization of radiation therapy in real time. *Int J Radiat Oncol Biol Phys*. (2014) 89:615–22. doi: 10.1016/j.ijrobp.2014.01.046

167. Jelley JV. Cerenkov radiation and its applications. *Br J Appl Phys*. (1955) 6:227. doi: 10.1088/0508-3443/6/7/301

168. Glaser AK, Kanick SC, Zhang R, Arce P, Pogue BW. A GAMOS plug-in for GEANT4 based Monte Carlo simulation of radiation-induced light transport in biological media. *Biomed Opt Express*. (2013) 4:741–59. doi: 10.1364/BOE.4.000741

169. Glaser AK, Zhang R, Gladstone DJ, Pogue BW. Optical dosimetry of radiotherapy beams using Cherenkov radiation: the relationship between light emission and dose. *Phys Med Biol*. (2014) 59:3789. doi: 10.1088/0031-9155/59/14/3789

170. Zlateva Y, Muir BR, El Naqa I, Seuntjens JP. Cherenkov emission-based external radiotherapy dosimetry: I. Formalism and feasibility. *Med Phys*. (2019) 46:2370–82. doi: 10.1002/mp.13414

171. Zlateva Y, Muir BR, Seuntjens JP, El Naqa I. Cherenkov emission-based external radiotherapy dosimetry: II. *E*lectron beam quality specification and uncertainties. *Med Phys*. (2019) 46:2383–93. doi: 10.1002/mp.13413

172. Helo Y, Kacperek A, Rosenberg I, Royle G, Gibson AP. The physics of Cerenkov light production during proton therapy. *Phys Med Biol*. (2014) 59:7107–23. doi: 10.1088/0031-9155/59/23/7107

173. Cloutier É, Archambault L, Beaulieu L. Accurate dose measurements using Cherenkov emission polarization imaging. *Med Phys*. (2022) 49:5417–22. doi: 10.1002/mp.15693

174. Glaser AK, Davis SC, Voigt WHA, Zhang R, Pogue BW, Gladstone DJ. Projection imaging of photon beams using Cerenkov-excited fluorescence. *Phys Med Biol*. (2013) 58:601–19. doi: 10.1088/0031-9155/58/3/601

175. Ashraf MR, Bruza P, Pogue BW, et al. Optical imaging provides rapid verification of static small beams, radiosurgery, and VMAT plans with millimeter resolution. *Med Phys*. (2019) 46:5227–37. doi: 10.1002/mp.13797

176. Decker SM, Alexander DA, Hachadorian RL, Zhang R, Gladstone DJ, Bruza P, et al. Estimation of diffuse Cherenkov optical emission from external beam radiation build-up in tissue. *J Biomed Opt*. (2021) 26:098003. doi: 10.1117/1.JBO.26.9.098003

177. Zhang R, Glaser AK, Gladstone DJ, Fox CJ, Pogue BW. Superficial dosimetry imaging based on Cerenkov emission for external beam radiotherapy with megavoltage x-ray beam. *Med Phys*. (2013) 40:101914. doi: 10.1118/1.4821543

178. Zhang R, Glaser AK, Andreozzi J, Jiang S, Jarvis LA, Gladstone DJ, et al. Beam and tissue factors affecting Cherenkov image intensity for quantitative entrance and exit dosimetry on human tissue. *J Biophotonics*. (2017) 10:645–56. doi: 10.1002/jbio.201500344

179. Andreozzi JM, Zhang R, Glaser AK, Jarvis LA, Pogue BW, Gladstone DJ. Camera selection for real-time in vivo radiation treatment verification systems using Cherenkov imaging. *Med Phys.* (2015) 42:994–1004. doi: 10.1118/1.4906249

180. Alexander DA, Bruza P, Farwell JCM, Krishnaswamy V, Zhang R, Gladstone DJ, et al. Detective quantum efficiency of intensified CMOS cameras for Cherenkov imaging in radiotherapy. *Phys Med Biol.* (2020) 65:225013. doi: 10.1088/1361-6560/abb0c5

181. Hallett JE, Bruza P, Jermyn M, Li K, Pogue BW. Noise & mottle suppression methods for cumulative Cherenkov images of radiation therapy delivery. *Phys Med Biol.* (2024) 69:225015. doi: 10.1088/1361-6560/ad8c93

182. Glaser AK, Zhang R, Andreozzi JM, Gladstone DJ, Pogue BW. Cherenkov radiation fluence estimates in tissue for molecular imaging and therapy applications. *Phys Med Biol.* (2015) 60:6701–18. doi: 10.1088/0031-9155/60/17/6701

183. LaRochelle EPM, Shell JR, Gunn JR, Davis SC, Pogue BW. Signal intensity analysis and optimization for in vivo imaging of Cherenkov and excited luminescence. *Phys Med Biol.* (2018) 63:085019. doi: 10.1088/1361-6560/aab83b

184. Ashraf MR, Bruza P, Krishnaswamy V, Gladstone DJ, Pogue BW. Technical note: time-gating to medical linear accelerator pulses: stray radiation detector. *Med Phys.* (2019) 46:1044–8. doi: 10.1002/mp.13311

185. Parks A, Hallett J, Niver A, Zhang R, Bruza P, Pogue BW. Review of Cherenkov imaging technology advances in radiotherapy: single-photon-level imaging in high ambient light and radiation backgrounds. *Biophotonics Discov.* (2024) 1:020901. doi: 10.1117/1.BIOS.1.2.020901

186. Rahman M, Bruza P, Hachadorian R, et al. Optimization of in vivo Cherenkov imaging dosimetry via spectral choices for ambient background lights and filtering. *J Biomed Opt.* (2021) 26:106003. doi: 10.1117/1.JBO.26.10.106003

187. Glaser AK, Voigt WHA, Davis SC, Zhang R, Gladstone DJ, Pogue BW. Three-dimensional Cerenkov tomography of energy deposition from ionizing radiation beams. *Opt Lett.* (2013) 38:634. doi: 10.1364/OL.38.000634

188. Glaser AK, Andreozzi JM, Davis SC, et al. Video-rate optical dosimetry and dynamic visualization of IMRT and VMAT treatment plans in water using Cherenkov radiation. *Med Phys.* (2014) 41:062102. doi: 10.1118/1.4875704

189. Bruza P, Andreozzi JM, Gladstone DJ, Jarvis LA, Rottmann J, Pogue BW. Online combination of EPID Cherenkov imaging for 3-D dosimetry in a liquid phantom. *IEEE Trans Med Imaging.* (2017) 36:2099–103. doi: 10.1109/TMI.2017.2717800

190. Miao T, Bruza P, Pogue BW, Jermyn M, Krishnaswamy et al. Cherenkov imaging for linac beam shape analysis as a remote electronic quality assessment verification tool. *Med Phys.* (2019) 46:811–21. doi: 10.1002/mp.13303

191. Andreozzi JM, Mooney KE, BruŽa P, Curcuru A, Gladstone DJ, Pogue BW, et al. Remote Cherenkov imaging-based quality assurance of a magnetic resonance image-guided radiotherapy system. *Med Phys.* (2018) 45:2647–59. doi: 10.1002/mp.12919

192. Andreozzi JM, Bruža P, Cammin J, Pogue BW, Gladstone DJ, Green O. Optical imaging method to quantify spatial dose variation due to the electron return effect in an MR-linac. *Med Phys.* (2020) 47:1258–67. doi: 10.1002/mp.13954

193. Alexander DA, Bruza P, Rassias AG, Andreozzi JM, Pogue BW, Zhang R, et al. Visual isocenter position enhanced review (VIPER): a Cherenkov imaging-based solution for MR-linac daily QA. *Med Phys.* (2021) 48:2750–9. doi: 10.1002/mp.14892

194. Ashraf MR, Rahman M, Zhang R, Williams BB, Gladstone DJ, Pogue BW, et al. Dosimetry for FLASH radiotherapy: a review of tools and the role of radioluminescence and Cherenkov emission. *Front Phys.* (2020) 8:328. doi: 10.3389/fphy.2020.00328

195. Rahman M, Ashraf MR, Zhang R, Gladstone DJ, Cao X, Williams BB, et al. Spatial and temporal dosimetry of individual electron FLASH beam pulses using radioluminescence imaging. *Phys Med Biol.* (2021) 66:135009. doi: 10.1088/1361-6560/ac0390

196. Rahman M, Ashraf R, Zhang R, Cao X, Gladstone DJ, Jarvis LA, et al. In Vivo Cherenkov imaging-guided FLASH radiotherapy. *Int J Radiat Oncol Biol Phys.* (2022) 114:S139–40. doi: 10.1016/j.ijrobp.2022.07.604

197. Alexander DA, Nomezine A, Jarvis LA, Gladstone DJ, Pogue BW, Bruza P. Color Cherenkov imaging of clinical radiation therapy. *Light Sci Appl.* (2021) 10:226. doi: 10.1038/s41377-021-00660-0

198. Axelsson J, Glaser AK, Gladstone DJ, Pogue BW. Quantitative Cherenkov emission spectroscopy for tissue oxygenation assessment. *Opt Express.* (2012) 20:5133–42. doi: 10.1364/OE.20.005133

199. Rickard AG, Yoshikawa H, Palmer GM, Liu HQ, Dewhirst MW, Nolan MW, et al. Cherenkov emissions for studying tumor changes during radiation therapy: an exploratory study in domesticated dogs with naturally-occurring cancer. *PLoS ONE.* (2020) 15:e0238106. doi: 10.1371/journal.pone.0238106

200. Vasyltsiv R, Jarvis LA, Zhang R, Gladstone DJ, Bruza P. Multispectral analysis of Cherenkov emission for subsurface monitoring of tissue composition and intensity correction. In: *AAPM* (2024). Available online at: https://aapm.confex.com/aapm/2024am/meetingapp.cgi/Paper/13388 (Accessed July 21, 2025).

201. Glaser A, Axelsson J, Zhang R, Gladstone DJ, Pogue BW. Cherenkov emission spectroscopy for tissue oxygen saturation assessment. In *Biomedical Optics and 3-D Imaging, Paper JM3A.15*. Washington, DC: Optica Publishing Group (2012).

202. Zhang R, Glaser A, Esipova TV, Kanick SC, Davis SC, Vinogradov S, et al. Cerenkov radiation emission and excited luminescence (CREL) sensitivity during external beam radiation therapy: Monte Carlo and tissue oxygenation phantom studies. *Biomed Opt Express.* (2012) 3:2381–94. doi: 10.1364/BOE.3.002381

203. Demers JL, Davis SC, Zhang R, Gladstone DJ, Pogue BW. Cerenkov excited fluorescence tomography using external beam radiation. *Opt Lett.* (2013) 38:1364–6. doi: 10.1364/OL.38.001364

204. Holt RW, Zhang R, Esipova TV, Vinogradov SA, Glaser AK, Gladstone DJ, et al. Cherenkov excited phosphorescence-based pO2 estimation during multi-beam radiation therapy: phantom and simulation studies. *Phys Med Biol.* (2014) 59:5317. doi: 10.1088/0031-9155/59/18/5317

205. Zhang R, D'souza AV, Gunn JR, Esipova TV, Vinogradov SA, Glaser AK, et al. Cherenkov-excited luminescence scanned imaging. *Opt Lett.* (2015) 40:827–30. doi: 10.1364/OL.40.000827

206. Pogue BW, Feng J, LaRochelle EP, BruŽa P, Lin H, Zhang R, et al. Maps of in vivo oxygen pressure with submillimetre resolution and nanomolar sensitivity enabled by Cherenkov-excited luminescence scanned imaging. *Nat Biomed Eng.* (2018) 2:254–64. doi: 10.1038/s41551-018-0220-3

207. Jia MJ, Bruza P, Andreozzi JM, Jarvis LA, Gladstone DJ, Pogue BW. Cherenkov-excited luminescence scanned imaging using scanned beam differencing and iterative deconvolution in dynamic plan radiation delivery in a human breast phantom geometry. *Med Phys.* (2019) 46:3067–77. doi: 10.1002/mp.13545

208. Jarvis LA, Gladstone DJ, Pogue BW, Gollub S, Miao T, Bruza P, et al. Cherenkoscopy for treatment verification: correlation of radiation dose to Cherenkov emission intensity in whole breast radiation therapy. *Int J Radiat Oncol.* (2017) 99:E673. doi: 10.1016/j.ijrobp.2017.06.2225

209. Xie Y, Petroccia H, Maity A, et al. Cherenkov imaging for total skin electron therapy (TSET). *Med Phys.* (2020) 47:201–12. doi: 10.1002/mp.13881

210. Zhong W, Ong Y, Miao T, Pogue BW, Zhu TC. Monte Carlo simulation of Cerenkov imaging for total skin electron treatment with CT DICOM realistic patient geometry. *Proc SPIE Int Soc Opt Eng.* (2022) 11940:49–57. doi: 10.1117/12.2609027

211. Petroccia H, Miao T, Maity A, et al. Analysis of cumulative surface dose based on Cherenkov imaging of Total Skin Electron Therapy (TSET). In: *Optical Methods for Tumor Treatment and Detection: Mechanisms and Techniques in Photodynamic Therapy XXVIII. Vol. 10860*. Bellingham, WA: SPIE (2019). p. 40–60.

212. Miao T, Petroccia H, Xie Y, Jermyn M, Perroni-Scharf M, Kapoor N, et al. Computer animation body surface analysis of total skin electron radiation therapy dose homogeneity via Cherenkov imaging. *J Med Imaging.* (2020) 7:034002. doi: 10.1117/1.JMI.7.3.034002

213. Alexander DA, Tendler II, Bruza P, Cao X, Schaner PE, Marshall BS, et al. Assessment of imaging Cherenkov and scintillation signals in head and neck radiotherapy. *Phys Med Biol.* (2019) 64:145021. doi: 10.1088/1361-6560/ab25a3

214. Tendler II, Hartford A, Jermyn M, LaRochelle E, Cao X, Borza V, et al. Experimentally observed Cherenkov light generation in the eye during radiotherapy. *Int J Radiat Oncol.* (2019) 106:422–9. doi: 10.1016/j.ijrobp.2019.10.031

215. Hachadorian R, Bruza P, Jermyn M, Mazhar A, Cuccia D, Jarvis L, et al. Correcting Cherenkov light attenuation in tissue using spatial frequency domain imaging for quantitative surface dosimetry during whole breast radiation therapy. *J Biomed Opt.* (2018) 24:1–10. doi: 10.1117/1.JBO.24.7.071609

216. Hachadorian RL, Bruza P, Jermyn M, Gladstone DJ, Pogue BW, Jarvis LA. Imaging radiation dose in breast radiotherapy by X-ray CT calibration of Cherenkov light. *Nat Commun.* (2020) 11:2298. doi: 10.1038/s41467-020-16031-z

217. Hachadorian RL, Bruza P, Jermyn M, Gladstone DJ, Zhang R, Jarvis LA, et al. Remote dose imaging from Cherenkov light using spatially resolved CT calibration in breast radiotherapy. *Med Phys.* (2022) 49:4018–25. doi: 10.1002/mp.15614

218. Decker SM, Andreozzi JM, Hernandez D, Alexander DA, Wickramasinghe V, Hachadorian RL, et al. Improving Cherenkov-based radiotherapy dose estimates in diverse patient populations via skin luminance imaging. *Phys Med Biol.* (2025). doi: 10.1088/1361-6560/aded68

219. Hachadorian R, Farwell JC, Bruza P, Jermyn M, Gladstone DJ, Pogue BW, et al. Verification of field match lines in whole breast radiation therapy using Cherenkov imaging. *Radiother Oncol.* (2021) 160:90–6. doi: 10.1016/j.radonc.2021.04.013

220. Li Y, Liu H, Huang N, Wang Z, Zhang C. Using Cherenkov imaging to monitor the match line between photon and electron radiation therapy fields on biological tissue phantoms. *J Biomed Opt.* (2020) 25:125001. doi: 10.1117/1.JBO.25.12.125001

221. Geng C, Di X, Li X, Shu D, Zhu L, Tang X. Measurement of field match lines in electron beam radiotherapy using carbon quantum dot sheeting enhanced Cherenkov imaging. *Radiat Meas.* (2023) 169:107030. doi: 10.1016/j.radmeas.2023.107030

222. Zhang R, Andreozzi JM, Gladstone DJ, Beeler WH, Glaser A, Jiang S, et al. Cherenkoscopy based patient positioning validation and movement tracking during post-lumpectomy whole breast radiation therapy. *Phys Med Biol.* (2014) 60:L1–L14. doi: 10.1088/0031-9155/60/1/L1

223. Chen Y, Decker SM, Bruza P, Gladstone DJ, Jarvis LA, Pogue BW, et al. Cherenkov imaged bio-morphological features verify patient positioning with

deformable tissue translocation in breast radiation therapy. *Adv Radiat Oncol*. (2025) 10:101684. doi: 10.1016/j.adro.2024.101684

224. Wang S, Chen Y, Jarvis LA, Tang Y, Gladstone DJ, Samkoe KS, et al. Robust real-time segmentation of bio-morphological features in human Cherenkov imaging during radiotherapy via deep learning. *Med Phys*. (2025) 52:e18002. doi: 10.1002/mp.18002

225. Chen E, Pogue BW, Bruza P, Alexander DA, Andino NL, Decker SM, et al. Clinical implementation of the first Cherenkov imaging system in a community-based hospital. *Tech Innov Patient Support Radiat Oncol*. (2022) 24:1–5. doi: 10.1016/j.tipsro.2022.08.011

226. Robinson A, Tallhamer M, Orman A. Optimizing breast cancer radiation therapy with volumetric modulated arc therapy and skin flash: a case study using deep inspiration breath hold and Cherenkov imaging. *Adv Radiat Oncol*. (2025) 10:101798. doi: 10.1016/j.adro.2025.101798

227. Alexander DA, Decker SM, Jermyn M, Bruza P, Zhang R, Chen E, et al. One year of clinic-wide cherenkov imaging for discovery of quality improvement opportunities in radiation therapy. *Pract Radiat Oncol*. (2023) 13:71–81. doi: 10.1016/j.prro.2022.06.009

228. Jarvis LA, Hachadorian RA, Jermyn M, Bruza P, Alexander DA, Tendler II, et al. Initial clinical experience of Cherenkov imaging in EBRT identifies opportunities to improve treatment delivery. *Int J Radiat Oncol*. (2020) 109:1627–37. doi: 10.1016/j.ijrobp.2020.11.013

229. Decker SM, Matous AL, Zhang R, Gladstone DJ, Grove EK, Williams BB, et al. Cherenkov imaging combined with scintillation dosimetry provides real-time positional and dose monitoring for radiotherapy patients with cardiac implanted electronic devices. *Phys Imaging Radiat Oncol*. (2024) 32:100642. doi: 10.1016/j.phro.2024.100642

230. Decker SM, Bruza P, Zhang R, Pogue BW, Gladstone DJ, Jarvis LA. Visual dose monitoring for whole breast radiation therapy treatments via combined Cherenkov imaging and scintillation dosimetry. *Int J Radiat Oncol Biol Phys*. (2025) 121:365–74. doi: 10.1016/j.ijrobp.2024.08.033

231. El Naqa I, Pogue BW, Zhang R, Oraiqat I, Parodi K. Image guidance for FLASH radiotherapy. *Med Phys*. (2022) 49:4109–22. doi: 10.1002/mp.15662

232. Decker SM, Alexander DA, Bruza P, Zhang R, Chen E, Jarvis LA, et al. Performance comparison of quantitative metrics for analysis of in vivo Cherenkov imaging incident detection during radiotherapy. *Br J Radiol*. (2022) 95:20211346. doi: 10.1259/bjr.20211346

233. Paganetti H. Range uncertainties in proton therapy and the role of Monte Carlo simulations. *Phys Med Biol*. 57:R99–R117. doi: 10.1088/0031-9155/57/11/R99

234. Li B, Lee HC, Duan X, Shen C, Zhou L, Jia X, et al. Comprehensive analysis of proton range uncertainties related to stopping-power-ratio estimation using dual-energy CT imaging. *Phys Med Biol*. (2017) 62:7056–74. doi: 10.1088/1361-6560/aa7dc9

235. Seco J, Spadea MF. Imaging in particle therapy: state of the art and future perspective. *Acta Oncol*. (2015) 54:125–48. doi: 10.3109/0284186X.2015.1075665

236. Yang M, Virshup G, Clayton J, Miller M, Kirby N, Fuss M, et al. Theoretical variance analysis of single- and dual-energy computed tomography methods for calculating proton stopping power ratios of biological tissues. *Phys Med Biol*. (2012) 55:1343–62. doi: 10.1088/0031-9155/55/5/006

237. Taasti VT, Hattu D, Vaassen F, Canters R, Velders M, Mannens J, et al. Treatment planning and 4D robust evaluation strategy for proton therapy of lung tumors with large motion amplitude. *Med Phys*. (2021) 48:4425–37. doi: 10.1002/mp.15067

238. Buti G, Souris K, Montero A, Janssens G, Sterpin E, Vynckier S. Towards fast and robust 4D optimization for moving tumors with scanned proton therapy. *Med Phys*. (2019) 46:5434–43. doi: 10.1002/mp.13850

239. Hua C, Weiguang Y, Takao K, Kazuo T, Saori O, Takenori N, et al. A robotic C-arm cone beam CT system for image-guided proton therapy: design and performance. *Br J Radiol*. (2017) 90.1079:20170266. doi: 10.1259/bjr.20170266

240. Thummerer A, Zaffino P, Meijers A, Marmitt GG, Seco J, Steenbakkers RJHM, et al. Comparison of CBCT based synthetic CT methods suitable for proton dose calculations in adaptive proton therapy. *Phys Med Biol*. (2020) 65:095002. doi: 10.1088/1361-6560/ab7d54

241. Schneider U, Pedroni E. Proton radiography as a tool for quality control in proton therapy. *Med Phys*. (1995) 22:353–63. doi: 10.1118/1.597470

242. Sadrozinski HFW, Bashkirov VA, Johnson RP, Schulte RW. Development of proton computed tomography detectors. *Nucl Instrum Methods Phys Res*. (2013) 699:205–10. doi: 10.1016/j.nima.2012.04.029

243. Knopf AC, Lomax A. In vivo proton range verification: a review. *Phys Med Biol*. (2013) 58:R131–R160. doi: 10.1088/0031-9155/58/15/R131

244. Maspero M, Bentvelzen LG, Savenije MHF, Guerreiro F, Seravalli E, Janssens GO, et al. Deep learning-based synthetic CT generation for paediatric brain MR-only photon and proton radiotherapy. *Radiother Oncol*. (2020) 153:197–204. doi: 10.1016/j.radonc.2020.09.029

245. Bodei L, Herrmann K, Schöder H, Scott AM, Lewis JS. Radiotheranostics in oncology: current challenges and emerging opportunities. *Nat Rev Clin Oncol*. (2022) 19:534–50. doi: 10.1038/s41571-022-00652-y

246. Sgouros G, Bodei L, McDevitt MR, Nedrow JR. Radiopharmaceutical therapy in cancer: clinical advances and challenges. Nat *Rev Drug Discov*. (2020) 19:589–608. doi: 10.1038/s41573-020-0073-9

247. Idée JM, Louguet S, Ballet S, Corot C. Theranostics and contrast-agents for medical imaging: a pharmaceutical company viewpoint. *Quant Imaging Med Surg*. (2013) 3:292–7. doi: 10.3978/j.issn.2223-4292.2013.12.06

248. Hertz S, Roberts A. Radioactive iodine in the study of thyroid physiology; the use of radioactive iodine therapy in hyperthyroidism. *J Am Med Assoc*. (1946) 131:81–6. doi: 10.1001/jama.1946.02870190005002

249. Durski JM, Hruska CB, Bogsrud TV, Ryder M, Johnson GB. 123I scan with whole-body retention measurement at 48 hours for simplified dosimetry before 131I treatment of metastatic thyroid cancer. *Clin Nucl Med*. (2021) 46:e151–3. doi: 10.1097/RLU.0000000000003464

250. Phan HTT, Jager PL, Paans AMJ, Plukker JTM, Sturkenboom MGG, Sluiter WJ, et al. The diagnostic value of 124I-PET in patients with differentiated thyroid cancer. *Eur J Nucl Med Mol Imaging*. (2008) 35:958. doi: 10.1007/s00259-007-0660-6

251. Parker C, Nilsson S, Heinrich D, Helle SI, O'Sullivan JM, Fosså SD, et al. Alpha Emitter Radium-223 and survival in metastatic prostate cancer. *New Eng J Med*. (2013) 369:213–23. doi: 10.1056/NEJMoa1213755

252. Agrawal A, Rangarajan V, Shah S, Puranik A, Purandare N. MIBG (metaiodobenzylguanidine) theranostics in pediatric and adult malignancies. *Br J Radiol*. (2018) 91:20180103. doi: 10.1259/bjr.20180103

253. Wieland DM, Mangner TJ, Inbasekaran MN, Brown LE, Wu JL. Adrenal Medulla imaging agents: a structure-distribution relationship study of radiolabeled aralkylguanidines1. *J Med Chem*. (1984) 27:149–55. doi: 10.1021/jm00368a008

254. Pryma DA, Chin BB, Noto RB, Dillon JS, Perkins S, Solnes L, et al. Efficacy and safety of high-specific-activity 131I-MIBG therapy in patients with advanced pheochromocytoma or paraganglioma. *J Nucl Med*. (2019) 60:623–30. doi: 10.2967/jnumed.118.217463

255. Dickson JC, Armstrong IS, Gabiña PM, Denis-Bacelar AM, Krizsan AK, Gear JM, et al. EANM practice guideline for quantitative SPECT-CT. *Eur J Nucl Med Mol Imaging*. (2022) 50:980. doi: 10.1007/s00259-022-06028-9

256. Modlin IM, Lye KD, Kidd M. A 5-decade analysis of 13,715 carcinoid tumors. *Cancer*. (2003) 97:934–59. doi: 10.1002/cncr.11105

257. Yao JC, Hassan M, Phan A, Dagohoy C, Leary C, Mares JE, et al. One hundred years after "carcinoid": epidemiology of and prognostic factors for neuroendocrine tumors in 35,825 cases in the United States. *J Clin Oncol*. (2008) 26:3063–72. doi: 10.1200/JCO.2007.15.4377

258. Strosberg J, El-Haddad G, Wolin E, Hendifar A, Yao J, Chasen B, et al. Phase 3 trial of 177 Lu-Dotatate for midgut neuroendocrine tumors . *New Eng J Med*. (2017) 376:125–35. doi: 10.1056/NEJMoa1607427

259. Kulke MH, Mayer RJ. Carcinoid tumors. *N Eng J Med*. (1999) 340:858–68. doi: 10.1056/NEJM199903183401107

260. Sartor O, de Bono J, Chi KN, Fizazi K, Herrmann K, Rahbar K, et al. Lutetium-177–PSMA-617 for metastatic castration-resistant prostate cancer. *New Eng J Med*. (2021) 385:1091–103. doi: 10.1056/NEJMoa2107322

261. Marquis H, Willowson KP, Bailey DL. Partial volume effect in SPECT & PET imaging and impact on radionuclide dosimetry estimates. *Asia Ocean J Nucl Med Biol*. (2023) 11:44–54. doi: 10.22038/AOJNMB.2022.63827.1448

262. Tran-Gia J, Lassmann M. Optimizing image quantification for 177Lu SPECT/CT based on a 3D printed 2-compartment kidney phantom. *J Nucl Med*. (2018) 59:616–24. doi: 10.2967/jnumed.117.200170

263. Ljungberg M, Sjögreen-Gleisner K. The accuracy of absorbed dose estimates in tumours determined by Quantitative SPECT: a Monte Carlo study. *Acta Oncol*. (2011) 50:981–9. doi: 10.3109/0284186X.2011.584559

264. Flux G, Bardies M, Monsieurs M, Savolainen S, Strand SE, Lassmann M. The impact of PET and SPECT on dosimetry for targeted radionuclide therapy. *Z Med Phys*. (2006) 16:47–59. doi: 10.1078/0939-3889-00291

265. Fahey FH, Harkness BA, Keyes JW, Madsen MT, Battisti C, Zito V. Sensitivity, resolution and image quality with a Multi-Head SPECT camera. *J Nucl Med*. (1992) 33:1859–63.

266. Bailey DL, Willowson KP. An evidence-based review of quantitative SPECT imaging and potential clinical applications. *J Nucl Med*. (2013) 54:83–9. doi: 10.2967/jnumed.112.111476

267. Kyme AZ, Fulton RR. Motion estimation and correction in SPECT, PET and CT. *Phys Med Biol*. (2021) 66:18TR02. doi: 10.1088/1361-6560/ac093b

268. Bastiaannet R, Viergever MA, De Jong HWAM. Impact of respiratory motion and acquisition settings on SPECT liver dosimetry for radioembolization. *Med Phys*. (2017) 44:5270–9. doi: 10.1002/mp.12483

269. Busemann Sokole E, Płachcínska A, Britten A. Acceptance testing for nuclear medicine instrumentation. *Eur J Nucl Med Mol Imaging.* (2010) 37:672–81. doi: 10.1007/s00259-009-1348-x

270. Hutton BF, Buvat I, Beekman FJ. Review and current status of SPECT scatter correction. *Phys Med Biol.* (2011) 56:R85–112. doi: 10.1088/0031-9155/56/14/R01

271. Can M, Karadeniz I, Çapa Kaya G, Ertay T. A study on energy window-based scatter correction methods in 99mTc and 123I imaging. *J Instrum.* (2023) 18:P10009. doi: 10.1088/1748-0221/18/10/P10009

272. Zaidi H, Koral KF. Scatter modelling and compensation in emission tomography. *Eur J Nucl Med Mol Imaging.* (2004) 31:761–82. doi: 10.1007/s00259-004-1495-z

273. Zaidi H, Koral KF. Scatter correction strategies in emission tomography. *Quant Anal Nucl Med Imaging.* (2006) 205–35. doi: 10.1007/0-387-25444-7_7

274. Hamill JJ, Cabello J, Surti S, Karp JS. Energy-based scatter estimation in clinical PET. *Med Phys.* (2024) 51:54–69. doi: 10.1002/mp.16826

275. Michael K, Frangos S, Iakovou I, Lontos A, Demosthenous G, Parpottas Y. The impact of dual and triple energy window scatter correction on I-123 postsurgical thyroid SPECT/CT imaging using a phantom with small sizes of thyroid remnants. *Life.* (2024) 14:113. doi: 10.3390/life14010113

276. Huizing DMV, Sinaasappel M, Dekker MC, Stokkel MPM, de Wit – van der Veen BJ. 177Lutetium SPECT/CT: evaluation of collimator, photopeak and scatter correction. *J Appl Clin Med Phys.* (2020) 21:272–7. doi: 10.1002/acm2.12991

277. Xiao J, De Wit TC, Zbijewski W, Staelens SG, Beekman FJ. Evaluation of 3D Monte Carlo-based scatter correction for 201Tl cardiac perfusion SPECT. *J Nucl Med.* (2007) 48:637–44. doi: 10.2967/jnumed.106.037259

278. Sakellios NG, Karali E, Lazaro D, Loudos GK, Nikita KS. Monte-Carlo simulation for scatter correction compensation studies in SPECT imaging using GATE software package. *Nucl Instrum Methods Phys Res A.* (2006) 569:404–8. doi: 10.1016/j.nima.2006.08.056

279. Ouyang J, Fakhri G El, Moore SC. Improved activity estimation with MC-JOSEM versus TEW-JOSEM in 111In SPECT. *Med Phys.* (2008) 35:2029. doi: 10.1118/1.2907561

280. Robinson AP, Tipping J, Cullen DM, Hamilton D. The influence of triple energy window scatter correction on activity quantification for (1 7 7)Lu molecular radiotherapy. *Phys Med Biol.* (2016) 61:5107–27. doi: 10.1088/0031-9155/61/14/5107

281. Leube J, Claeys W, Gustafsson J, Salas-Ramirez M, Lassmann M, Koole M, et al. Position dependence of recovery coefficients in 177Lu-SPECT/CT reconstructions - phantom simulations and measurements. *EJNMMI Phys.* (2024) 11:52. doi: 10.1186/s40658-024-00662-y

282. Tran-Gia J, Schlögl S, Lassmann M. Design and fabrication of kidney phantoms for internal radiation dosimetry using 3D printing technology. *J Nucl Med.* (2016) 57:1998–2005. doi: 10.2967/jnumed.116.178046

283. Gear JI, Long C, Rushforth D, Chittenden SJ, Cummings C, Flux GD. Development of patient-specific molecular imaging phantoms using a 3D printer. *Med Phys.* (2014) 41:082502. doi: 10.1118/1.4887854

284. Jackson P, Hardcastle N, Dawe N, Kron T, Hofman MS, Hicks RJ. Deep learning renal segmentation for fully automated radiation dose estimation in unsealed source therapy. *Front Oncol.* (2018) 8:215. doi: 10.3389/fonc.2018.00215

285. Gustafsson J, Sundlöv A, Sjögreen Gleisner K. SPECT image segmentation for estimation of tumour volume and activity concentration in 177Lu-DOTATATE radionuclide therapy. *EJNMMI Res.* (2017) 7:18. doi: 10.1186/s13550-017-0262-7

286. Hagmarker L, Svensson J, Rydén T, Gjertsson P, Bernhardt P. Segmentation of whole-body images into two compartments in model for bone marrow dosimetry increases the correlation with hematological response in 177Lu-DOTATATE treatments. *Cancer Biother Radiopharm.* (2017) 32:335–43. doi: 10.1089/cbr.2017.2317

287. Guzene L, Beddok A, Nioche C, Modzelewski R, Loiseau C, Salleron J, et al. Assessing interobserver variability in the delineation of structures in radiation oncology: a systematic review. *Int J Radiat Oncol.* (2023) 115:1047–60. doi: 10.1016/j.ijrobp.2022.11.021

288. Besemer AE, Titz B, Grudzinski JJ, Weichert JP, Kuo JS, Robins HI, et al. Impact of PET and MRI threshold-based tumor volume segmentation on patient-specific targeted radionuclide therapy dosimetry using CLR1404. *Phys Med Biol.* (2017) 62:6008–25. doi: 10.1088/1361-6560/aa716d

289. Uribe CF, Esquinas PL, Tanguay J, Gonzalez M, Gaudin E, Beauregard JM, et al. Accuracy of 177Lu activity quantification in SPECT imaging: a phantom study. *EJNMMI Phys.* (2017) 4:1–20. doi: 10.1186/s40658-016-0170-3

290. Brosch-Lenz J, Kurkowska S, Frey E, Dewaraja YK, Sunderland J, Uribe C. An international study of factors affecting variability of dosimetry calculations, part 3: contribution from calculating absorbed dose from time-integrated activity. *J Nucl Med.* (2024) 65:1166–72. doi: 10.2967/jnumed.123.267293

291. Brosch-Lenz J, Ke S, Wang H, Frey E, Dewaraja YK, Sunderland J, et al. An international study of factors affecting variability of dosimetry calculations, part 2: overall variabilities in absorbed dose. *J Nucl Med.* 2023 64:1109–16. doi: 10.2967/jnumed.122.265094

292. Uribe C, Peterson A, Van B, Fedrigo R, Carlson J, Sunderland J, et al. An international study of factors affecting variability of dosimetry calculations, part 1: design and early results of the SNMMI dosimetry challenge. *J Nucl Med.* (2021) 62:36S−47S. doi: 10.2967/jnumed.121.262748

293. Kurkowska S, Frey E, Dewaraja Y, Sunderland J, Uribe C. Impact of segmentation methods on healthy organ and tumor activity estimates for 177Lu-DOTATATE therapy â€“ results from SNMMI 177Lu dosimetry challenge. *J Nucl Med.* (2024) 65:242502.

294. Papavasileiou P, Divoli A, Hatziioannou K, Flux GD. The importance of the accuracy of image registration of SPECT images for 3D targeted radionuclide therapy dosimetry. *Phys Med Biol.* (2007) 52:N539–48. doi: 10.1088/0031-9155/52/24/N01

295. Grassi E, Fioroni F, Berenato S, Patterson N, Ferri V, Braglia L, et al. Effect of image registration on 3D absorbed dose calculations in 177Lu-DOTATOC peptide receptor radionuclide therapy. *Phys Med.* (2018) 45:177–85. doi: 10.1016/j.ejmp.2017.11.021

296. Sjögreen-Gleisner K, Rueckert D, Ljungberg M. Registration of serial SPECT/CT images for three-dimensional dosimetry in radionuclide therapy. *Phys Med Biol.* (2009) 54:6181. doi: 10.1088/0031-9155/54/20/010

297. Ao ECI, Wu NY, Wang SJ, Song N, Mok GSP. Improved dosimetry for targeted radionuclide therapy using nonrigid registration on sequential SPECT images. *Med Phys.* (2015) 42:1060–70. doi: 10.1118/1.4906242

298. Adam DP, Grudzinski JJ, Bormett I, Cox BL, Marsh IR, Bradshaw TJ, et al. Validation of Monte Carlo 131I radiopharmaceutical dosimetry workflow using a 3D-printed anthropomorphic head and neck phantom. *Med Phys.* (2022) 49:5491–503. doi: 10.1002/mp.15699

frontiers | Frontiers in Oncology

TYPE Original Research
PUBLISHED 11 December 2025
DOI 10.3389/fonc.2025.1720143

Check for updates

OPEN ACCESS

EDITED BY
Abdul K. Parchur,
University of Maryland Medical Center,
United States

REVIEWED BY
Teresa Pinheiro,
University of Lisbon, Portugal
Lorenzo Manti,
University of Campania Luigi Vanvitelli, Italy

*CORRESPONDENCE
Dalong Pang
pangd@georgetown.edu

RECEIVED 07 October 2025
REVISED 21 November 2025
ACCEPTED 25 November 2025
PUBLISHED 11 December 2025

CITATION
Pang D, Jung M, Velena A, Parke W and Dritschilo A (2025) Proton-boron capture interaction enhances killing of radiation resistant cancer cells.
Front. Oncol. 15:1720143.
doi: 10.3389/fonc.2025.1720143

COPYRIGHT
© 2025 Pang, Jung, Velena, Parke and Dritschilo. This is an open-access article distributed under the terms of the Creative Commons Attribution License (CC BY). The use, distribution or reproduction in other forums is permitted, provided the original author(s) and the copyright owner(s) are credited and that the original publication in this journal is cited, in accordance with accepted academic practice. No use, distribution or reproduction is permitted which does not comply with these terms.

Proton-boron capture interaction enhances killing of radiation resistant cancer cells

Dalong Pang[1]*, Mira Jung[1], Alfredo Velena[1], William Parke[2] and Anatoly Dritschilo[1]

[1]Department of Radiation Medicine, Georgetown University Medical Center, Washington, WA, United States, [2]Department of Physics, George Washington University, Washington, WA, United States

Background/objectives: Studies involving the interaction of protons with boron (^{11}B) have shown potential for enhanced cell killing in cancer cells. However, theoretical analyses conducted using Monte Carlo simulations have not corroborated the experimental findings. Our objective is to independently investigate the effects of proton-boron capture interaction on the killing of cancer cells in SQ20-B and MCF-7 cells.

Methods: Cell survival and DNA damage endpoints were analyzed in radiation resistant SQ-20B cells and in radiation sensitive MCF-7 cancer cells after exposure to ^{11}B (BSH_{11}) and proton irradiation. Clonogenic cell survival curves were assessed to fit the Linear Quadratic (LQ) and Single-Hit Multi-Target (SHMT) models. Additionally, γH2AX foci were quantified to evaluate DNA damage up to 24 hours post irradiation, comparing the effects of proton irradiation alone to proton irradiation in the presence of boron in SQ-20B cells.

Results: Exposure of cells to BSH_{11} resulted in decreased survival of SQ-20B cells following proton irradiation as compared to untreated control cells. Assays measuring γH2AX showed prolonged presence of γH2AX foci in cells after proton exposure in the presence of BSH_{11}. In contrast, cells treated with BSH_{11} and irradiated with Cs-137 γ-rays did not show cell killing enhancement. Additionally, cells treated with BSH_{10}, an analog of BSH_{11} that contains only ^{10}B, displayed no change in survival after proton irradiation compared to untreated cells.

Conclusions: Our data show a small enhancement of cell killing by proton radiation in the presence of BSH_{11} that we attribute to the proton-boron interaction. Analysis of γH2AX demonstrates a prolonged duration of foci formation in cells after proton irradiation in the presence of BSH_{11}. Further research will be needed to better understand the potential clinical applications of proton-boron interaction.

KEYWORDS

boron, proton, irradiation, cell survival, γH2AX, SQ-20B, MCF-7, BSH

Introduction

The primary advantage of proton radiotherapy (RT) compared to photon RT is the unique energy deposition associated with the Bragg peak, which results in no radiation dose delivered beyond this peak (1, 2). In addition to utilizing the inherent physical and biological properties of protons in radiotherapy, further strategies have been explored to enhance their biological effectiveness (3, 4).

One of the strategies is to explore interaction between proton and boron and the products it produces. Upon absorption of a proton, a stable isotope of boron (^{11}B) is converted into a ^{12}C nucleus in an excited state, which subsequently decays to an ^{8}Be nucleus and emits a α particle of energy 3.76 MeV. The ^{8}Be nucleus further decays into two α particles of energy 2.74 MeV each (5). When placed in a cell medium, the three α particles produced in this process possess enough energy to traverse several cancer cells of typical thickness of 10-20 μm. Mindful of the high lethality of α particles (6, 7), one can expect an enhancement of cell killing by proton irradiation when a ^{11}B containing compound is introduced into the cell medium.

The experimental data presented by Cirrone et al. on the effectiveness of proton-boron capture therapy offered the first evidence of the potential efficacy of proton-boron capture therapy (PBCT) (8). However, subsequent theoretical studies have questioned the validity of the mechanisms proposed in this report (5, 9, 10). The concerns are primarily based on Monte Carlo simulation of the proton-boron capture interaction and the amount of energy released in the process, with a consensus among the authors that the energy released is too small to support the magnitude of effects on cell survival reported by Cirrone et al.

This study reports additional experimental data on potential efficacy of proton-boron interaction in cell killing. By employing a ^{11}B containing compound (BSH_{11}) and two cancer cell lines of different radiation sensitivity, we hope to gain insight on the potential cell killing effects of α particles as well as that of protons. To account for the fact that BSH_{11} contains 80% ^{11}B and 20% ^{10}B and the presence of secondary neutrons in the proton irradiation experiments, we irradiated with protons cells treated with BSH_{10} compound that contains over 99.97% ^{10}B to evaluate the possibility of cell killing resulting from ^{10}B and neutron capture interaction. In addition, BSH_{11} treated cells were also irradiated with photons to evaluate potential biological effects of BSH_{11}.

Materials and methods

Two cell lines were used in this study: the radioresistant SQ20-B cell line, which originated from squamous carcinoma of head and neck origin and is known for its radiation resistance and the radiosensitive MCF-7 cell line, which was derived from breast cancer and is more radiosensitive than other cell lines. These two cell lines allow for an analysis of the different radiation effects induced by densely ionizing particles, such as alpha particles which may have the potential to overcome the radiation resistance of cancer cells (6, 7). In addition to colony formation-based survival studies, we assessed DNA double-strand break (DSB) damage by quantifying γH2AX at various time points following irradiation.

Cell growth and cytotoxicity assay

Cells were obtained from the Lombardi Cancer Center Tissue Culture Core Facility at Georgetown University Medical Center. SQ-20B cells were maintained in complete DMEM media: DMEM, 10% Fetal Bovine Serum (FBS), 5% Pen/Strep. MCF-7 cells were cultured in complete RPMI media: RPMI, 10% Fetal Bovine Serum (FBS), 5% Pen/Strep. Both cell lines were kept in logarithmic growth phase at 37^0C and 5% CO_2 environment and tested negative for mycoplasma contamination.

Cytotoxicity assays were performed by exposing cells to graded drug dilutions for 48 hours. Cytotoxicity was measured using the CellTox Green Cytotoxicity Assay (Cat.#G8731, Promega), following manufacturer's instructions. Positive and negative controls were included to ensure proper normalization of the results. Cytotoxicity was assessed by measuring fluorescence at 513 nm excitation/532 nm emission. Cell viability is expressed as a percentage of the control groups. The inhibitory concentration values of 50% (IC_{50}) values and the mean value of IC_{50} were calculated using Prism (GraphPad Software, Inc).

Boron containing BSH compounds

This investigation utilized two BSH compounds: BSH_{11} and BSH_{10}. The compounds, BSH_{11} (sodium mercaptododecaborate or N-BSH, $Na_2[1\text{-}SH^{11}B_{12}H_{11}]$) and BSH_{10} Compound (sodium mercaptododecaborate (10B), BSH, $Na_2[1\text{-}SH^{10}B_{12}H_{11}]$ were purchased from KATCHEM Ltd, a commercial vendor (Czech Republic). The primary compound used in this research was BSH_{11}, which has a boron isotope distribution of 80% ^{11}B and 20% ^{10}B, in contrast, BSH_{10}, which contains 99.97% ^{11}B, served as a control to assess the potential effects of boron neutron capture reaction during interactions with BSH_{11} and protons. The BSH compounds were in powder form and were dissolved in deionized, distilled water to achieve appropriate dilutions, resulting in a concentration of 50 μM, equivalent to 6.6 ppm for B_{11}.

Proton irradiation

Proton irradiations were conducted at the Proton Center of Medstar Georgetown University Hospital using the Mevion S250i pencil beam scanning proton system. The radiation field consisted of a single energy layer of 85 MeV, with a field size of 20x20 cm^2, comprising 1681 spots spaced 5 mm apart. Each spot received a monitor unit (MU) of 1.358. Cells in petri dishes, in a medium 1-mm thick, were positioned on top of a 5-cm solid water plate and CT scanned. Figure 1A shows the transverse CT image of the apparatus, where the light gray colored block shows the solid water plate and 3 containers on top show the petri dishes; the light gray

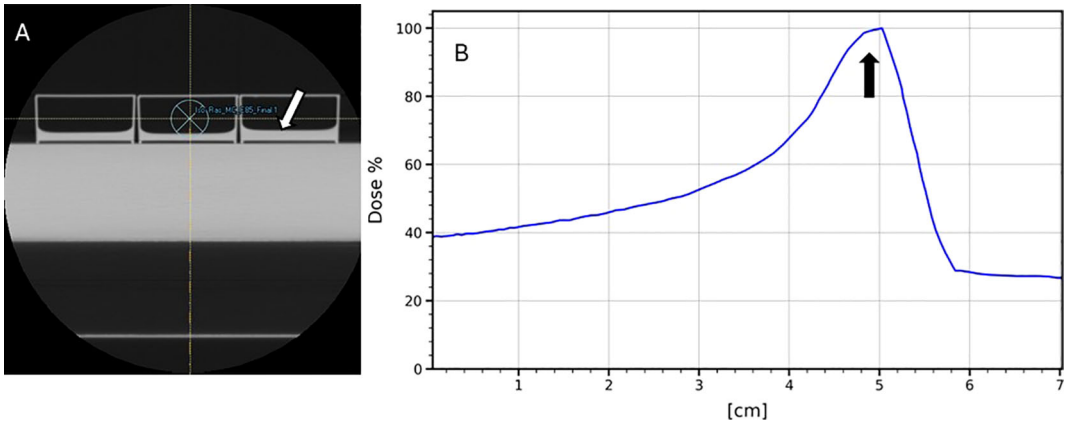

FIGURE 1
CT image of the irradiation apparatus **(A)** and the Bragg peak curve calculated by the Raystation treatment planning system. The arrow in **(A)** shows the location of the cell medium in one of the petri dishes, and the arrow in **(B)** shows the location of cell medium relative to the Bragg peak. The Y-axis shows the calculated RBE dose of proton along the beam path normalized to the maximum dose at the Bragg peak. The X axis shows the distance starting from the bottom of the solid water plate.

colored layers at the bottom of the dishes show the cell containing liquid, as pointed by the white arrow. The CT images were imported into a Raystion treatment planning system (RS11A) by Raysearch Laboratories (Stochholm, Sweden) to generate radiation dose distribution from a single proton beam as defined above and directed posteriorly at the bottom of the solid water plate for irradiation of the cells. Figure 1B shows the Bragg peak curve of the beam and the arrow shows the position of the cells. This setup ensured that the dose delivery to the cell medium was maintained within the proximal 90% to distal 90% region of the Bragg peak. The doses were further measured using a calibrated parallel plate chamber with measurements taken in 1-mm increment along the beam direction to confirm that the dose variation within the irradiated medium is less than 10%. For each radiation delivery, six-well plates containing cells were placed within the treatment field. Doses of 0 (sham), 1, 3, 5, 7 and 9 Gy were administered in triplicate to facilitate statistical error determination.

Photon irradiation

Photon irradiation of the cells was conducted at Georgetown University Lombardi Cancer Center's core facility using a Cs-137 γ–irradiator on BSH_{11} treated SQ-20B cells. The dose rate of this irradiator was 1.56 Gy/min. Sample preparation and the doses delivered were consistent with previously detailed methods, except for the radiation source.

Cell survival assay

Cells were seeded into T25 flasks and treated with the drug for 48 hours prior to proton irradiation. The treatments included a Sham group (no drug) and the BSH_{11} compound at a concentration of 50 μM. As a control to evaluate any potential cell-killing effects of neutron-boron interaction that might occur in the proton-BSH_{11} reaction, the BSH_{10} compound was infused in another batch of SQ-20B cells at the same concentration. Each treatment was conducted in triplicate. Following irradiation, cells were incubated for 10–14 days post radiation until colony formation was observed. The cell survival data were fitted with the Linear-Quadratic (LQ) model for calculation of survival at various dose levels and alpha and beta values, The Single-Hit-Multi-Target (SHMT) model was also used for determination of D_0. Mean and standard deviation were calculated from three repeats of each experiment. Unpaired student t-test was used for evaluation of statistical significance.

H2AX analysis

SQ-20B cells were treated with the BSH_{11} compound at a concentration of 50 μM for 48 hours prior to exposure to 5 Gy of proton radiation. Sham-treated cells served as control. Cells were fixed for 15 min using 4% formaldehyde at various time points (30min, 1hr, 2hrs, 4hrs, 6hrs, 12hrs and 24hrs) following irradiation. After fixation in 4% Formaldehyde, the cells were blocked for 1 hour using a Blocking Buffer (95% PBS, 5% Goat Serum and 0.3% TritonX-100) and incubated with γH2AX antibody (Abcam) overnight at 4^0C, followed by incubation with a secondary anti-rabbit Alexa Fluor 488 for 1hr. Fluorescence images were captured using a Leica SP8 AOBS Laser Scanning Confocal Microscope after mounting the cells with Scale bar = 200 μm for all images. The number of distinct foci in individual nuclei was counted for each condition. Two-sample unpaired t-tests were performed for statistical analysis.

Results

There were no observed cytotoxicities to BSH11 or BSH10 exposures of SQ-20B or MCF7 cells to concentration from 1 to

50 μM. BSH is non-toxic in these cancer cells at the concentrations used in these experiments. Therefore, we selected a concentration of 50 μM for radiation experiments.

Figure 2 shows the cell survival curves for SQ20-B and MCF-7 cells irradiated with protons alone and with protons combined with 50 μM BSH_{11}. Solid curves correspond to SQ-20B, while dashed curves correspond to MCF-7. Across the dose range, the addition of BSH_{11} reduced survival for both cell lines, consistent with a radiation sensitizing effect. Radiation resistant SQ-20B cells consistently exhibited higher survivals than MCF-7 cells.

Dose by dose analysis using the LQ model revealed that BSH_{11} treatment significantly decreased SQ-20B survival at 3 Gy ($p = 0.0069$), 5 Gy ($p = 0.0266$), 7 Gy ($p = 0.0473$), and 9 Gy ($p = 0.0014$) indicating a pronounced effect at intermediate and high doses. For MCF-7, although survival was consistently lower in the BSH_{11} group, the dose points did not reach statistical significance ($p > 0.05$). The LQ model derived D_{10} (dose required to reduce cell survival to 10%) further reflected these differences. In SQ-20B cells, D_{10} decreased from 6.890 ± 0.134 Gy to 5.776 ± 0.080 Gy with BSH_{11} ($p = 0.0002$), corresponding to a dose-modifying factor (DMF - ratio of the dose required to achieve 10% survival without BSH to that with BSH) of 1.19, which indicates an enhanced overall radiation sensitizing effect. In MCF-7 cells, D_{10} decreased from 4.322 ± 0.090 Gy to 3.994 ± 0.512 Gy ($p = 0.3360$), giving a DMF of 1.08, but this change was not statistically significant.

From the SHMT model, the D_0, defined as the dose that reduces cell survival to 37% in the exponential portion of the survival curve, was significantly reduced in SQ-20B cells from 1.874 ± 0.108 Gy (control) to 1.523 ± 0.102 Gy with BSH_{11} treatment ($p = 0.0149$). This decrease indicates an increased intrinsic radiosensitivity of SQ-20B cells in the presence of BSH_{11}. In contrast, MCF-7 cells showed no significant changes in D_0 between control (0.941 ± 0.105 Gy) and BSH_{11}-treated (0.948 ± 0.154 Gy) groups ($p = 0.9529$) which suggests that the intrinsic sensitivity of MCF-7 to proton irradiation was not altered by BSH_{11}.

The BSH_{11} compound contains 80% ^{11}B and 20% ^{10}B; therefore, the ^{10}B component could contribute to the observed cellular effects of BSH_{11} through the boron-neutron interaction. To investigate this possibility, we irradiated SQ-20B cells with protons after treatment with BSH_{10} which contains 99.97% of ^{10}B. Figure 3 shows the resulting survival curves. No statistically significant differences in survival were observed between the BSH_{10}-treated and control groups with D_{10} values of 6.23 ± 0.30 Gy and 5.78 ± 0.23 Gy, respectively ($p = 0.1117$). These findings suggest that ^{10}B, in the absence of ^{11}B, does not significantly alter proton radiosensitivity in SQ-20B cells under the tested conditions.

To further evaluate the role of the proton-^{11}B interaction, we irradiated SQ-20B cells with Cs-137 gamma rays in a Cesium irradiator with and without BSH_{11} treatment. To rule out any purely chemical effects of the BSH compound, the BSH_{11} concentration was increased from 50 to 450 μM. Figure 4 shows the corresponding survival curves. Treatment with BSH_{11} did not produce a statistically significant change in survival when cells were irradiated with gamma photons, with D_{10} values of 7.78 ± 0.23 Gy for control cells and 8.21 ± 0.25 Gy for BSH_{11}-treated cells ($p = 0.0920$). These results indicate that the survival differences observed in proton-irradiated SQ-20B cells are unlikely to be due to chemical effects of BSH_{11} but rather to the specific interaction between protons and ^{11}B.

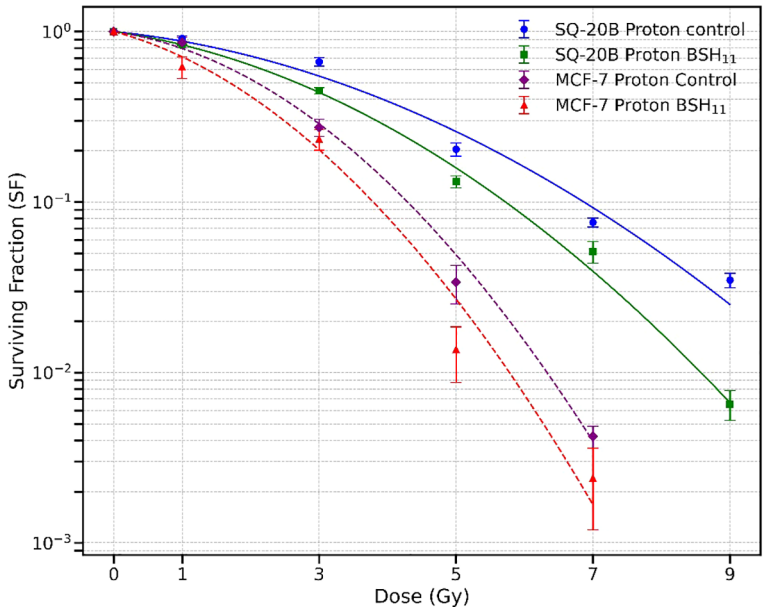

FIGURE 2
Survival curves for SQ-20B (solid lines) and MCF-7 (dashed lines) cell lines following proton irradiation, with and without 50 μM BSH_{11}. For SQ-20B, circles represent control (no BSH_{11}) and squares represent BSH_{11}-treated cells; for MCF-7, diamonds represent control, and triangles represent BSH_{11}-treated cells. Data points represent the mean ± standard error from three independent experiments. Curves were obtained from log-scale least-squares fit the experimental data.

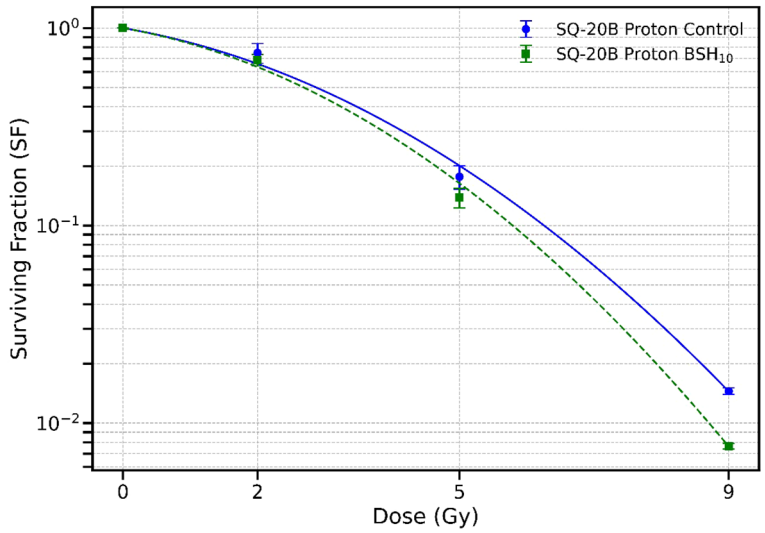

FIGURE 3
Survival curves for SQ-20B cells irradiated with protons alone (circles) or with 50 μM BSH_{10} treatment (squares). Data points represent the mean ± standard error from three independent experiments. Curves were fitted using the Linear–Quadratic (LQ) model. No statistically significant differences in D_{10} were observed between the two groups (p = 0.1117).

H2AX

γH2AX is a highly sensitive molecular marker for detecting the presence of DNA double strand breaks and the subsequent repair of these lesions (11). To investigate whether the observed reduction in cell survival in the presence of BSH_{11} may be the result of a possible change in the DNA DSB pattern, potentially attributable to proton-boron capture interaction, we irradiated the SQ-20B cells with a single fraction, proton dose of 5 Gy, both with and without BSH. We conducted γH2AX analyses on the irradiated cells up to two hours post irradiation.

As shown in Figures 5, the number of foci per cell was significantly higher in BSH_{11} treated SQ-20B cells and persisted longer following exposure to proton irradiation (5Gy) compared to irradiated cells without BSH_{11} treatment (all $P < 0.001$).

We further evaluated the kinetics of the repair processes by assessing foci formation at various time points, ranging from 0

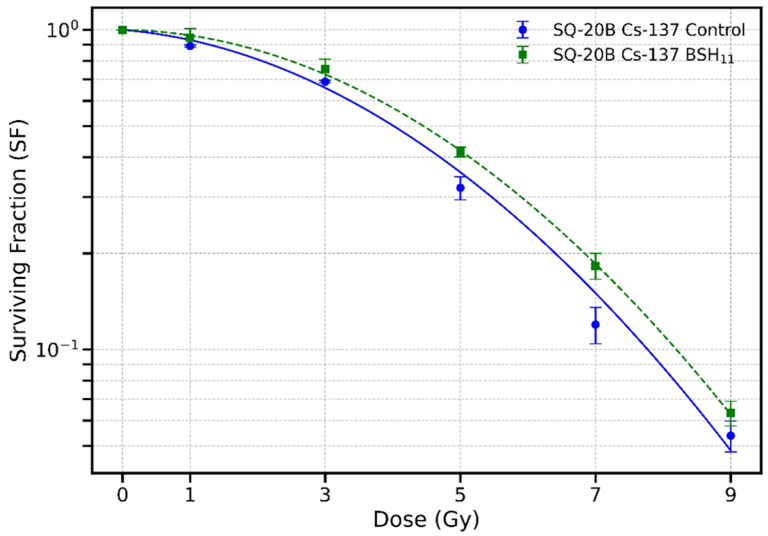

FIGURE 4
Survival curves for SQ-20B cells irradiated with Cs-137 gamma rays in the absence (circle) and presence (square) of 450 μM BSH_{11}. Data points represent the mean ± standard error from three independent experiments. Data fitted with LQ model. No statistically significant difference in survival was observed between the two groups with D_{10} values of 7.78 ± 0.23 Gy (control) and 8.21 ± 0.25 Gy (BSH_{11}) (p = 0.0920).

hours to 24 hours, across three different fields. Each field contained an average of 50 to 100 cells, which were analyzed to determine the number of foci formed. Figure 6 shows the foci numbers peaking at 30 minutes and then decreasing over a 6-hour interval. The proton + BSH_{11} treated cells demonstrate a slower recovery process.

The difference in the number of foci per cell in BSH_{11} treated cells after radiation—compared to cells without BSH_{11} treatment—suggests that nearly all double-strand breaks (DSBs) induced by proton radiation were repaired within 24 hours in SQ-20B cells. In contrast, treatment with BSH_{11} altered this response in two important ways: it increased the number of breaks at the same radiation dose and slowed their repair.

Discussion

Investigations of the effectiveness of proton-boron interaction have produced inconsistent results, ranging from radiation killing enhancement to no apparent effects (8, 12–17). Our experiments comparing two different cancer cell lines, one radioresistant and the other sensitive, reveal a small sensitization of the radiation resistant cells, but not of the radiation sensitive cells. As illustrated in Figure 2, the addition of BSH_{11} to the SQ-20B cells led to statistically significant reduction in survival across all dose levels except at the lowest dose of 1 Gy. For the MCF-7 cells, although the survival appears to be lower in the presence of BSH_{11} at all dose levels, the reductions are not statistically significant.

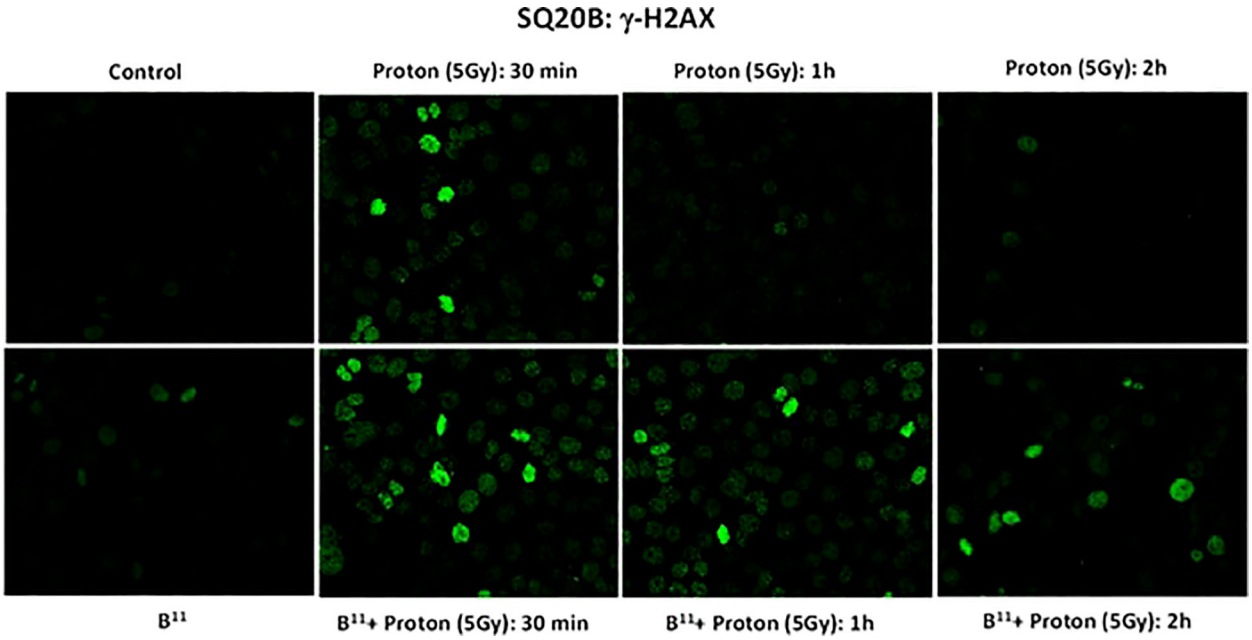

FIGURE 5
γH2AX foci formation for SQ-20B cells post irradiation at 30 mins, 1 hr and 2 hr time intervals.

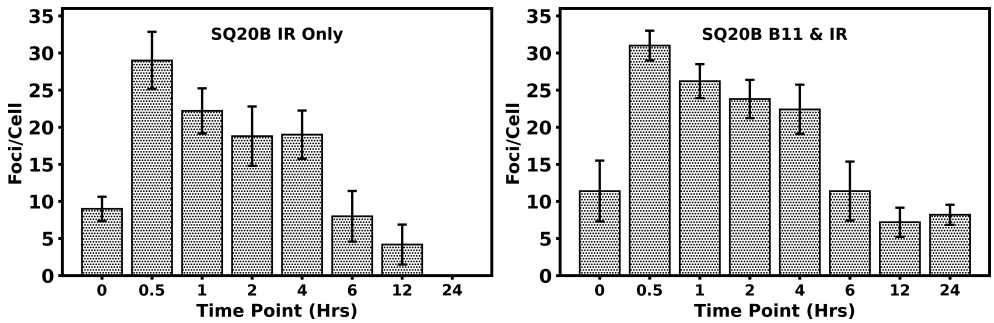

FIGURE 6
Analysis of γH2AX foci in SQ-20B (B) cells. Following treatment at various time points, the number of cells with foci formation was counted in three different fields. Each field contained as average 50–100 cells, which were examined to determine the number of foci formations. The 0-hour samples were treated with BSH_{11} only or subjected to sham irradiation. Error bars represent the standard error, and the percentage of focus-positive cells (cells containing at least 10 foci) is plotted. The histogram was created using the average number of foci in five cells within each field at different time points.

We interpret these observations to support a radiation sensitizing effect of BSH_{11} on radiation resistant cells and suggest that the alpha particles released in the p-^{11}B interaction may contribute to the observed increase in cell killing of the SQ-20B cells. This interpretation is consistent with the observations of high-LET radiation overcoming radiation resistance. For the more radiation sensitive MCF-7 cells, sensitization was observed (Figure 2) but did not reach statistical significance in our experiments. Nonetheless, the sensitization effect on radiation resistant cell lines is the focus of this research.

In a therapeutic proton system, neutrons are also generated due to scattering interactions with various atoms along the beam path. For the Mevion S250i proton system, the neutron contamination in the primary beam is less than 0.1% (18). Despite this low neutron flux, it can still damage certain electronics in the treatment room, potentially including cells in the petri dish used for experiments. Recent Monte Carlo simulations by other investigators have estimated the presence of high energy and thermal neutrons in proton irradiated materials, including cell medium (19, 20) and found a thermal neutron flux on the order of 10^8/cm^2/GyE and potential radiation sensitization due to BNCT effects by irradiating cells of various cell lines treated with BPA (19). A small sensitization was reported at BPA concentration of 80 ppm which was attributed to the BNCT effect (19), suggesting the possibility of thermal neutron contribution in PBCT due to the 20% ^{10}B contained in BSH_{11}. In this research we investigated the potential role of ^{10}B by irradiating cells treated with BSH_{10} which contains over 99.97% ^{10}B with no ^{11}B and found no sensitization and thus ruled out the BNCT effects due to effects of possible thermal neutrons under our experimental conditions.

The results obtained in the p-BSH_{11}, p-BSH_{10} and γ-BSH_{11} experiments support the interpretation that the reduced cell survival in the p-BSH_{11} experiment was likely due to the interaction between proton and ^{11}B which produces three alpha particles. These alpha particles are lethal in cell killing when traversing cells and may induce additional bystander cell killing effects (21, 22).

It is interesting to observe that BSH_{11} induced a statistically significant survival reduction in the radiation resistant SQ-20B cells but not the radiation sensitive MCF-7 cells. Further experiments will be needed to assess the effects of higher concentrations.

Conclusions

The experimental data on cell survival that we present in this report for SQ-20B and MCF-7 cells, following proton and photon irradiation in the presence of BSH, demonstrate a small but statistically significant increase in cell death in the radiation resistant SQ-20B cells but not the radiation sensitive MCF-7 cells. Our findings are less robust but qualitatively support Cirrone's report of enhanced cell kill by protons in the presence of ^{11}B. This enhancement can be attributed to the boron-proton interaction under our experimental conditions. The potential clinical relevance may require further studies.

Data availability statement

The raw data supporting the conclusions of this article will be made available by the authors, without undue reservation.

Ethics statement

Ethical approval was not required for the studies on animals in accordance with the local legislation and institutional requirements because only commercially available established cell lines were used.

Author contributions

DP: Formal Analysis, Writing – review & editing, Project administration, Validation, Writing – original draft, Conceptualization, Supervision, Investigation. MJ: Data curation, Writing – review & editing, Investigation, Formal Analysis, Visualization. AV: Formal Analysis, Writing – review & editing, Data curation. WP: Writing – review & editing, Formal Analysis. AD: Writing – review & editing, Methodology, Investigation, Conceptualization.

Funding

The author(s) declared that financial support was not received for this work and/or its publication.

Acknowledgments

We would like to thank Amrit Kaphle for assistance in statistical analysis.

Conflict of interest

The authors declare that the research was conducted in the absence of any commercial or financial relationships that could be construed as a potential conflict of interest.

Generative AI statement

The author(s) declare that no Generative AI was used in the creation of this manuscript.

Any alternative text (alt text) provided alongside figures in this article has been generated by Frontiers with the support of artificial intelligence and reasonable efforts have been made to ensure accuracy, including review by the authors wherever possible. If you identify any issues, please contact us.

Publisher's note

All claims expressed in this article are solely those of the authors and do not necessarily represent those of their affiliated organizations, or those of the publisher, the editors and the reviewers. Any product that may be evaluated in this article, or claim that may be made by its manufacturer, is not guaranteed or endorsed by the publisher.

References

1. Goitein M, Lomax AJ, Pedroni ES. Treating cancer with protons. *Phys Today*. (2002) 55:45–50. doi: 10.1063/1.1522215

2. Kjellberg R, Sweet W, Preston W, Koehler A. The Bragg peak of a proton beam in intracranial therapy of tumors. *Trans Am Neurological Assoc (US)*. (1962) 87:216–8.

3. Schuemann J, Berbeco R, Chithrani DB, Cho SH, Kumar R, McMahon SJ, et al. Roadmap to clinical use of gold nanoparticles for radiation sensitization. *Int J Radiat Oncol Biol Physics*. (2016) 94:189–205. doi: 10.1016/j.ijrobp.2015.09.032

4. Waissi W, Nicol A, Jung M, Rousseau M, Jarnet D, Noel G, et al. Radiosensitizing pancreatic cancer with PARP inhibitor and gemcitabine: an *in vivo* and a whole-transcriptome analysis after proton or photon irradiation. *Cancers*. (2021) 13:527. doi: 10.3390/cancers13030527

5. Ganjeh ZA, Eslami-Kalantari M. Investigation of proton–boron capture therapy vs. Proton therapy. *Nucl Instruments Methods Phys Res Section A: Accelerators Spectrometers Detectors Associated Equipment*. (2020) 977:164340. doi: 10.1016/j.nima.2020.164340

6. Sgouros G. Alpha-particles for targeted therapy. *Advanced Drug delivery Rev*. (2008) 60:1402–6. doi: 10.1016/j.addr.2008.04.007

7. Brooks A, Newton G, Shyr L-J, Seiler F, Scott B. The combined effects of α-particles and X-rays on cell killing and micronuclei induction in lung epithelial cells. *Int J Radiat Biol*. (1990) 58:799–811. doi: 10.1080/09553009014552181

8. Cirrone G, Manti L, Margarone D, Petringa G, Giuffrida L, Minopoli A, et al. First experimental proof of Proton Boron Capture Therapy (PBCT) to enhance protontherapy effectiveness. *Sci Rep*. (2018) 8:1–15. doi: 10.1038/s41598-018-19258-5

9. Mazzone A, Finocchiaro P, Meo SL, Colonna N. On the (un) effectiveness of proton boron capture in proton therapy. *Eur Phys J Plus*. (2019) 134:361. doi: 10.1140/epjp/i2019-12725-8

10. Shahmohammadi Beni M, Islam MR, Kim KM, Krstic D, Nikezic D, Yu KN, et al. On the effectiveness of proton boron fusion therapy (PBFT) at cellular level. *Sci Rep*. (2022) 12:18098. doi: 10.1038/s41598-022-23077-0

11. Mah L, El-Osta A, Karagiannis T. γH2AX: a sensitive molecular marker of DNA damage and repair. *Leukemia*. (2010) 24:679–86. doi: 10.1038/leu.2010.6

12. Bláha P, Feoli C, Agosteo S, Calvaruso M, Cammarata FP, Catalano R, et al. The proton-boron reaction increases the radiobiological effectiveness of clinical low-and high-energy proton beams: novel experimental evidence and perspectives. *Front Oncol*. (2021) 11. doi: 10.3389/fonc.2021.682647

13. Manandhar M, Bright SJ, Flint DB, Martinus DK, KolaChina RV, Ben Kacem M, et al. Effect of boron compounds on the biological effectiveness of proton therapy. *Med physics*. (2022) 49:6098–109. doi: 10.1002/mp.15824

14. Jelínek Michaelidesová A, Kundrát P, Zahradníček O, Danilová I, Pachnerová Brabcová K, Vachelová J, et al. First independent validation of the proton-boron capture therapy concept. *Sci Rep*. (2024) 14:19264. doi: 10.1038/s41598-024-69370-y

15. Belchior A, Alves BC, Mendes E, Megre F, Alves LC, Santos P, et al. Unravelling physical and radiobiological effects of proton boron fusion reaction with anionic metallacarboranes ([o-COSAN]-) in breast cancer cells. *EJNMMI Res*. (2025) 15:13. doi: 10.1186/s13550-025-01199-6

16. Cammarata FP, Torrisi F, Vicario N, Bravatà V, Stefano A, Salvatorelli L, et al. Proton boron capture therapy (PBCT) induces cell death and mitophagy in a heterotopic glioblastoma model. *Commun Biol*. (2023) 6:388. doi: 10.1038/s42003-023-04770-w

17. Ricciardi V, Bláha P, Buompane R, Crescente G, Cuttone G, Gialanella L, et al. A new low-energy proton irradiation facility to unveil the mechanistic basis of the proton-boron capture therapy approach. *Appl Sci*. (2021) 11:11986. doi: 10.3390/app112411986

18. Prusator MT, Ahmad S, Chen Y. Shielding verification and neutron dose evaluation of the Mevion S250 proton therapy unit. *J Appl Clin Med physics*. (2018) 19:305–10. doi: 10.1002/acm2.12256

19. Shiba S, Shimo T, Yamanaka M, Yagihashi T, Sakai M, Ohno T, et al. Increased cell killing effect in neutron capture enhanced proton beam therapy. *Sci Rep*. (2024) 14:28484. doi: 10.1038/s41598-024-79045-3

20. Safavi-Naeini M, Chacon A, Guatelli S, Franklin DR, Bambery K, Gregoire M-C, et al. Opportunistic dose amplification for proton and carbon ion therapy via capture of internally generated thermal neutrons. *Sci Rep*. (2018) 8:16257. doi: 10.1038/s41598-018-34643-w

21. Deshpande A, Goodwin E, Bailey S, Marrone B, Lehnert B. thE. Alpha-particle-induced sister chromatid exchange in normal human lung fibroblasts: evidence for an extranuclear target. *Radiat Res*. (1996) 145:260–7. doi: 10.2307/3578980

22. Nagasawa H, Little JB. Unexpected sensitivity to the induction of mutations by very low doses of alpha-particle radiation: evidence for a bystander effect. *Radiat Res*. (1999) 152:552–7. doi: 10.2307/3580153

Frontiers in Oncology

Advances knowledge of carcinogenesis and tumor progression for better treatment and management

The third most-cited oncology journal, which highlights research in carcinogenesis and tumor progression, bridging the gap between basic research and applications to imrpove diagnosis, therapeutics and management strategies.

Discover the latest Research Topics

See more →

Frontiers

Avenue du Tribunal-Fédéral 34
1005 Lausanne, Switzerland
frontiersin.org

Contact us

+41 (0)21 510 17 00
frontiersin.org/about/contact